Journal of Turbomachinery

Published Quarterly by ASME

VOLUME 128 • NUMBER 2 • APRIL 2006

TECHNICAL PAPERS

(Contents continued on inside back cover)

This journal is printed on acid-free paper, which exceeds the ANSI Z39.48-1992 specification for permanence of paper and library materials. ∞™
♲ 85% recycled content, including 10% post-consumer fibers.

Editor, **DAVID C. WISLER (2008)**
Assistant to the Editor: **ELIZABETH WISLER**
Associate Editors
Gas Turbine (Review Chair)
R. Abhari (2006)
Aeromechanics
M. MIGNOLET (2006)
M. MONTGOMERY (2008)
A. SINHA (2008)
Boundary Layers and Turbulence
G. WALKER (2008)
Computational Fluid Dynamics
J. ADAMCZYK (2008)
M. CASEY (2008)
Experimental Methods
W.-F. NG (2008)
Heat Transfer
R. BUNKER (2006)
J.-C. HAN (2008)
Radial Turbomachinery
R. VAN DEN BRAEMBUSSCHE (2008)
Turbomachinery Aero
S. GALLIMORE (2008)
D. PRASAD (2008)

PUBLICATIONS DIRECTORATE
Chair, **ARTHUR G. ERDMAN**

OFFICERS OF THE ASME
President, **RICHARD E. FEIGEL**
Executive Director, **VIRGIL R. CARTER**
Treasurer, **T. PESTORIUS**

PUBLISHING STAFF
Managing Director, Publishing
PHILIP DI VIETRO
Manager, Journals
COLIN MCATEER
Production Coordinator
JUDITH SIERANT
Production Assistant
MARISOL ANDINO

Transactions of the ASME, Journal of Turbomachinery (ISSN 0889-504X) is published quarterly (Jan., Apr., July, Oct.) by The American Society of Mechanical Engineers, Three Park Avenue, New York, NY 10016. Periodicals postage paid at New York, NY and additional mailing offices. POSTMASTER: Send address changes to Transactions of the ASME, Journal of Turbomachinery, c/o THE AMERICAN SOCIETY OF MECHANICAL ENGINEERS, 22 Law Drive, Box 2300, Fairfield, NJ 07007-2300. **CHANGES OF ADDRESS** must be received at Society headquarters seven weeks before they are to be effective. Please send old label and new address.

STATEMENT from By-Laws. The Society shall not be responsible for statements or opinions advanced in papers or ... printed in its publications (B7.1, Par. 3). **COPYRIGHT © 2006** by the American Society of Mechanical Engineers. For authorization to photocopy material for internal or personal use under those circumstances not falling within the fair use provisions of the Copyright Act, contact the Copyright Clearance Center (CCC), 222 Rosewood Drive, Danvers, MA 01923, tel: 978-750-8400, www.copyright.com. Request for special permission or bulk copying should be addressed to Reprints/Permission Department.

Canadian Goods & Services Tax Registration #126148048

Downloaded 01 Jun 2010 to 171.66.16.62. Redistribution subject to ASME license or copyright; see http://www.asme.org/terms/Terms_Use.cfm

Journal of Turbomachinery Volume 128, Number 2 APRIL 2006

The ASME Journal of Turbomachinery is abstracted and indexed in the following:

Aluminum Industry Abstracts, Aquatic Science and Fisheries Abstracts, Ceramics Abstracts, Chemical Abstracts, Civil Engineering Abstracts, Compendex (The electronic equivalent of Engineering Index), Corrosion Abstracts, Current Contents, Ei EncompassLit, Electronics & Communications Abstracts, Energy Information Abstracts, Engineered Materials Abstracts, Engineering Index, Environmental Science and Pollution Management, Excerpta Medica, Fluidex, Fuel and Energy Abstracts, INSPEC, Index to Scientific Reviews, Materials Science Citation Index, Mechanical & Transportation Engineering Abstracts, Mechanical Engineering Abstracts, METADEX (The electronic equivalent of Metals Abstracts and Alloys Index), Metals Abstracts, Oceanic Abstracts, Pollution Abstracts, Referativnyi Zhurnal, Shock & Vibration Digest, Steels Alert

Comparison of Turbine Tip Leakage Flow for Flat Tip and Squealer Tip Geometries at High-Speed Conditions

Nicole L. Key

Tony Arts

Von Karman Institute for Fluid Dynamics,
B1640 Rhode Saint Genèse,
Belgium

The tip leakage flow characteristics for flat and squealer turbine tip geometries are studied in the von Karman Institute Isentropic Light Piston Compression Tube facility, CT-2, at different Reynolds and Mach number conditions for a fixed value of the tip gap in a nonrotating, linear cascade arrangement. To the best knowledge of the authors, these are among the very few high-speed tip flow data for the flat tip and squealer tip geometries. Oil flow visualizations and static pressure measurements on the blade tip, blade surface, and corresponding endwall provide insight to the structure of the two different tip flows. Aerodynamic losses are measured for the different tip arrangements, also. The squealer tip provides a significant decrease in velocity through the tip gap with respect to the flat tip blade. For the flat tip, an increase in Reynolds number causes an increase in tip velocity levels, but the squealer tip is relatively insensitive to changes in Reynolds number. [DOI: 10.1115/1.2162183]

Introduction

In modern gas turbine engines, the recent trend of increased combustor outlet temperature to achieve higher thermal efficiency and higher power output poses a challenge to the aerodynamics, heat transfer, and material capabilities of the first stages of the high-pressure turbine. Tip leakage flows are a source of aerodynamic inefficiency and high thermal loading near the tip. It is quite difficult to cool the blade tip through conventional film-cooling techniques. Not only is the leakage flow path three-dimensional in nature, but strong secondary flows also cause very hot mainstream flow to enter the tip clearance region. The blade tip is one of the most frequently inspected and repaired parts of the turbine.

Mayle and Metzger [1] studied heat transfer in a simulated 2-D rectangular tip with and without a rotating shroud. They found that heat transfer at the blade tip was not significantly affected by rotation. Metzger, Bunker, and Chyu [2] confirmed this when studying heat transfer on flat and grooved tip models while introducing a moving shroud surface over the grooved tip model. This was also recently confirmed by Bunker [3]. This justified the experimental investigation of tip flows in stationary cascades.

One of the first large-scale, idealized studies of the tip gap flow on a flat tip blade was done by Sjolander and Cao [4]. They found that the flow separated from the pressure side tip corner and formed a well-organized chordwise vortex above the blade tip. The separation vortex induced a flow back toward the pressure side corner, resulting in the formation of a secondary counter rotating vortex. This attached flow near the pressure side corner could have a reasonably high convective heat transfer coefficient as well as high wall shear stress.

Azad et al. [5] studied the effect of tip gap and inlet turbulence intensity on detailed local heat transfer coefficient distributions on the flat tip surface of the GE-E^3 blade. Pressure distributions on the endwall and in the near-tip region provided complementary information for the transient liquid crystal heat transfer data. They found that different heat transfer regions existed on the tip surface. The leading edge had a low heat transfer region near the suction side. A region of high heat transfer existed along the leakage flow path. The entrance effect caused a higher heat transfer coefficient on the tip surface near the pressure side. Generally, a larger tip gap resulted in a higher overall heat transfer coefficient because a larger amount of tip leakage flow passed through the gap. An increase in turbulence intensity from 6.1% to 9.7% increased the heat transfer coefficient by 15%–20% along the leakage flow path. Yang et al. [6] used these data to validate their computational results. The computed streamlines indicated that the rollup of the tip leakage vortex displaced the suction side flow in the pitchwise direction.

Bunker, Bailey, and Ameri [7] studied the detailed distribution of convective heat transfer coefficients on the first-stage blade tip surface for a large power generation gas turbine. They used a hue-detection-based liquid crystal technique to obtain detailed heat transfer coefficient distributions on the blade tip surface for flat tip surfaces with both sharp and rounded edges. A central “sweet spot” of low heat transfer occurred from the leading edge to mid-chord and extended toward the suction side. A pressure side entry separation vortex aft of the sweet spot created a significant increase in heat transfer rates. They found that a small tip edge radius led to increased leakage flow and higher heat transfer rates. This was similar to the results of Ameri [8] who used numerical analyses to show that a sharp edge performed better than a radiused edge camber line squealer tip in reducing tip leakage flow.

A squealer tip allows for a smaller tip clearance but reduces the risk of catastrophic failure should the blade tip rub into the endwall. It is also thought to act as a labyrinth seal, increasing the resistance to the flow [9]. Tip leakage flow rate is generally a good indicator of tip losses and tip heat transfer in relation to different tip treatments. Usually, lower losses and lower heat transfer rates occur for a smaller tip flow rate.

Not many detailed local heat transfer measurements on a turbine blade squealer tip surface and the near-tip surfaces are available in the open literature. Metzger, Bunker, and Chyu [2] found that there is an optimum value of depth-to-width (cavity width)

Contributed by the International Gas Turbine Institute of ASME for publication in the Journal of Turbomachinery. Manuscript received October 1, 2003; final manuscript received March 1, 2004. IGTI Review Chair: A. J. Strazisar. Paper presented at the International Gas Turbine and Aeroengine Congress and Exhibition, Vienna, Austria, June 13–17, 2004, Paper No. 2004-GT-53979.

ratio beyond which no further flow reduction occurred, and they recommended shallow cavities for an overall reduction in heat transfer to the cavity wall.

Azad et al. [5] investigated six different squealer geometry arrangements in a low-speed linear cascade of the GE-E^3 high-pressure turbine first stage rotor blade. They found that the location of the squealer changed the leakage flow and resulted in very different heat loads on the blade tip. The single squealer on the suction side provided the best seal to the leakage flow and, thus, the lowest heat transfer coefficient. In general, a single squealer reduced the overall heat transfer to the tip better than a double squealer arrangement.

Azad, Han, and Boyle [10] performed the first detailed heat transfer measurements on a squealer tip blade. The transient liquid crystal technique was applied to the GE-E^3 turbine blade. High heat transfer rates were observed in the front-central portion of the cavity floor caused by flow impingement. The pressure side and suction side rims also experienced high heat transfer rates due to flow entrance and exit effects, respectively. A recirculating dead-flow region occurred in the downstream end of the cavity near the trailing edge, resulting in low heat transfer rates. The leakage flow rate through the flat tip gap was higher than the squealer tip for the same tip gap size. The leakage flow direction was shifted toward the leading edge for the squealer tip with respect to the flat tip. The overall heat transfer for the squealer tip decreased with decreased tip gap and was found to be smaller than that observed for the corresponding flat tip geometry.

Yang et al. [11] performed a numerical simulation of the work of [5,10]. They found that the leading edge region for the flat tip had a lower pressure ratio (lower velocity) than the mid-chord and trailing edge regions. This led to low heat transfer rates on the tip near the leading edge [10]. It was also shown that the primary effect of the squealer tip was confined to the vicinity of the tip gap. The leakage vortex associated with the squealer tip was much weaker. In the trailing edge region where no squealer was present, extremely high velocities were observed in the tip gap on both the pressure and suction sides. The flow entering the gap region near the leading edge of the squealer tip blade appeared to be entrained in the streamwise direction into the cavity. This flow would impinge on the inner rim of the pressure side squealer (near mid-chord) and then get deflected toward the suction side which led to a highly three-dimensional flow field in the squealer tip gap. At the larger tip clearance, both the leakage vortex and the separation in the cavity were considerably stronger.

Jin and Goldstein [12] used a naphthalene sublimation technique in accordance with the heat/mass transfer analogy to obtain heat transfer coefficients from measured mass transfer data. The effects of tip clearance, Reynolds number, and turbulence intensity were investigated on a flat tip rotor blade. Papa, Goldstein, and Gori [9] also used the naphthalene sublimation technique to study a squealer tip and a winglet-squealer tip where the winglet was attached to the pressure side of the tip. For all tip gap levels investigated, the highest mass transfer was observed on the cavity floor in a region near to the leading edge, about a distance of one squealer height from the inner part of the squealer. As the tip gap level decreased, this peak moved away from the leading edge and closer to the suction side squealer.

All of the studies described have been performed at low speed. Polanka et al. [13] performed one of the first full rotating, simultaneous pressure and heat transfer measurements to be taken in the turbine tip shroud region in a full-scale rig that operated at matched flow conditions to the true turbine environment. They quantified the effects of Reynolds number, inlet temperature, turbine pressure ratio, and inlet flow temperature profiles. The blade geometry had a sharp- edged flat tip with a nominal tip-to-shroud clearance of about 0.5% blade height. The Reynolds number had a minimal effect on blade loading, but the endwall showed a decrease in the minimum, maximum, and average pressure as the Reynolds number decreased. This could be caused by extra losses in this region at lower Reynolds number. They found that the blade shroud had higher average pressures than the blade tip because of the unsteady range of pressures as the rotor blade passed. This is in contrast to the results of Bunker, Bailey, and Ameri [7] who showed that in a stationary cascade, the tip and endwall pressures were locally similar.

For this study, aerodynamic data of a turbine cascade with a flat tip and squealer tip will be acquired at two different Reynolds numbers based on chord and isentropic exit conditions (450,000 and 900,000) and two different isentropic exit Mach numbers (0.9 and 1.1). The experimental facility allows for independent selection of Reynolds number and Mach number so it will be possible to understand the effect of compressibility and the effect of Reynolds number. These are among the few high-speed cascade data acquired for turbine blade tip flows. This study is part of a larger project including heat transfer measurements, which will be reported later.

Experimental Setup

Measurements are performed in the von Karman Institute Isentropic Light Piston Compression Tube facility CT-2, a stationary blow-down facility. The air in the tube upstream of the test section is isentropically compressed to the specified pressure and temperature of the desired inlet flow. When these conditions are reached, the shutter valve is opened, and flow enters the test section. A sonic throat downstream of the test section allows the exit Mach number of the cascade to be set. The pressure levels in the upstream piston tube and downstream dump tank can be adjusted to achieve a given Reynolds number based on chord and exit isentropic Mach number. Thus, Mach number can be set independently of Reynolds number, and this allows compressibility effects and Reynolds number effects to be understood. The effects of unsteady wakes and blade rotation, which may be important in real operating conditions, are not considered here. The facility maintains a steady flow for approximately 0.4 s. The details of the CT-2 facility, flow quality, and data acquisition characteristics have been well established in the literature for more than 15 years [14].

For these experiments, CT-2 is fitted with a four-bladed linear cascade. Details of the blade profile are provided in [15]. Only four blades are used in the cascade because of the size of the scaled-up blades. Thus, it is necessary to make measurements to ensure that spatial flow periodicity occurs for the instrumented blade. The angle of the tailboard of the cascade is adjusted until the potential field downstream of the instrumented blade appears periodic according to the downstream static pressure tap measurements. The solidity of the cascade is 1.25, the blade aspect ratio (based on chord) is 0.82, and the stagger angle of the cylindrical blades is 125.0 deg with respect to the tangential direction. The inlet flow angle is 32 deg, and the exit flow angle is −62 deg with respect to the axial direction. The tip gap is 1.34% of the blade height. The squealer groove height is 2.68% of the blade height, and the squealer wall width is 1.77% of the blade height.

Figure 1 shows the static pressure tap locations on the instrumented blade. The static pressures are measured with differential pressure transducers. There are 65 static pressure taps on the endwall. Eleven static pressure taps are instrumented on the tip of the blade. For the cascade with the flat tip, there are blade surface static pressure taps at mid-span and 97.3% span (or 98.6% of the blade height). For the cascade with the squealer tip, the blade surface taps at 97.3% span are the same, but instead of mid-span, taps are put on the inner part of the squealer at 97.3% span. This corresponds to tap placement occurring half-way up the squealer. These inner squealer taps occur at the same distance from the leading edge as the mid-span taps.

Measurements have been made to provide appropriate boundary conditions for CFD computations. There are 10 static pressure taps instrumented 24.9% chord upstream of the cascade leading edge plane to provide inlet Mach number information. The inlet

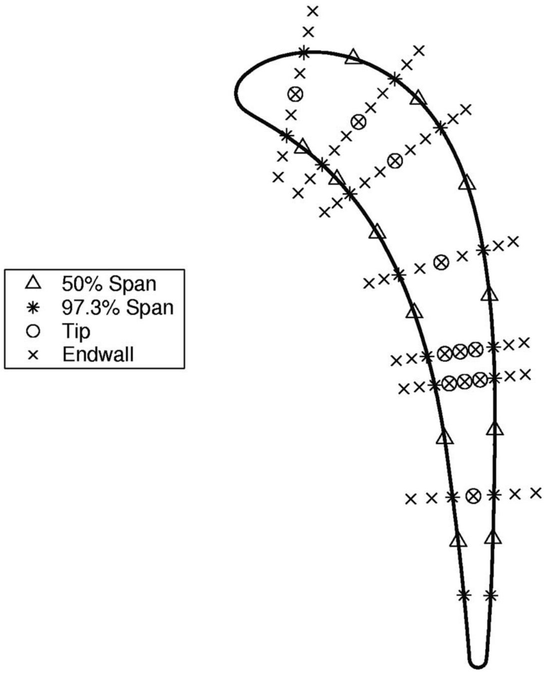

Fig. 1 Instrumented blade

Mach number is about 0.4 for all cases. The upstream boundary layer is traversed using a specially designed total pressure probe. The boundary layer at Re=450,000 is a transitional boundary layer while the boundary layer at Re=900,000 is a turbulent boundary layer.

The downstream total pressure distribution and flow angle are measured over 1.5 blade pitches using a three-hole probe placed on a pneumatic traversing mechanism. These measurements allow the aerodynamic losses of the cascade to be calculated at various spanwise locations of the passage.

The cases with the target Reynolds number of 450,000 are referred to as "low Re," and the cases with the target Reynolds number of 900,000 are designated as "high Re." Similarly, the cases with the target exit Mach number of 0.9 are named "low M," and the cases with the target exit Mach number of 1.1 are called "high M."

Blade Surface Pressure

Static pressure taps are instrumented on the blade at mid-span and near the tip at 97.3% span. The blade surface Mach number distribution is not affected by a change in Reynolds number. The effect of increased exit Mach number is to load up the trailing edge portion of the blade by decreasing the pressure on the suction side while keeping the pressure side unchanged.

Figure 2 compares the local blade loading distribution at mid-span to the surface velocities at 97.3% span for the flat tip blade at high M. The uncertainty in Mach number is ±0.01. Uncertainty bars were not added in this section, as they would be smaller than the symbols used in these figures.

The overall pressures near the tip are lower than the overall pressures at mid-span. The leading edge near the tip is unloaded while the trailing edge is more loaded than at mid-span. There are two phenomena occurring at the tip: the secondary flows and the tip leakage flow. The impact of the tip leakage vortex should increase further downstream along the blade as more flow enters the tip gap and thus, enters the tip leakage vortex. Computations of the condition of low Re, low M with and without tip clearance by means of Fine/TURBO (by Numeca International) were performed for the flat tip geometry only. The main purpose of this computation was to try to separate the effects of secondary flows and tip clearance on the blade pressure distribution. The flow solver solves the Reynolds averaged Navier-Stokes equations using a finite volume, time marching explicit 3D method on a structured mesh with a Baldwin-Lomax turbulence model.

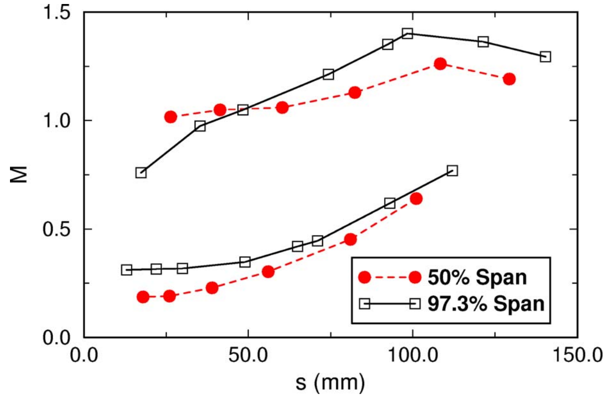

Fig. 2 Surface velocities at high M, high Re

Figure 3 shows the 97.3% span local loading distribution both with and without tip clearance. The experimental data follow the CFD prediction with tip clearance quite well. From this figure, the effect of the tip flow is to decrease the suction side pressure on the rear portion of the blade. This could be caused by the tip leakage vortex interacting with the suction surface. It also causes a slight decrease in the pressure side pressure near the leading edge, which is likely due to flow entering the tip gap. The tip clearance slightly unloads the leading edge and significantly loads up the trailing edge region. Thus, the significant unloading of the leading edge occurring near the tip as seen in Fig. 2 would be mostly caused by the secondary flows, while the tip leakage flow will contribute slightly. The largest pressure difference across the blade occurs at x/c_{axial} of 0.06 to 0.08. This is the portion of the tip where the highest velocities through the tip gap are expected.

Figure 4 shows the comparison between the surface velocity distributions for the flat tip blade and squealer tip blade at the 97.3% span location for the high Re, high M experimental data. Yang et al. [11] showed that the effect of the squealer tip was confined to the vicinity of the tip gap, and, in the present experiment, there is relatively little difference between the profiles at 97.3% span. However, the suction side of the squealer tip blade shows a constant velocity region around $s=40$ mm, indicating a possible separation bubble on the squealer tip blade. There is relatively little change on the pressure side distributions between the flat tip and squealer tip case.

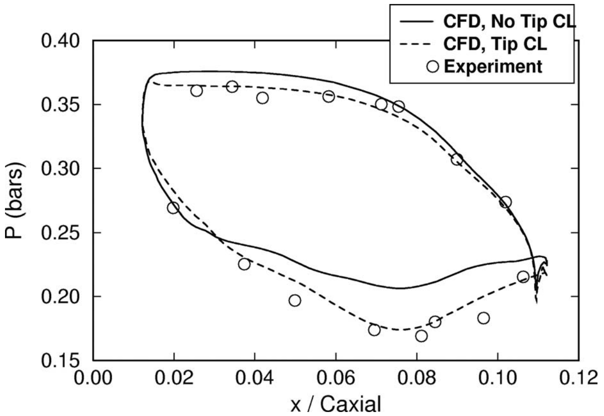

Fig. 3 Comparison of CFD and experimental results for flat tip at 97.3% span

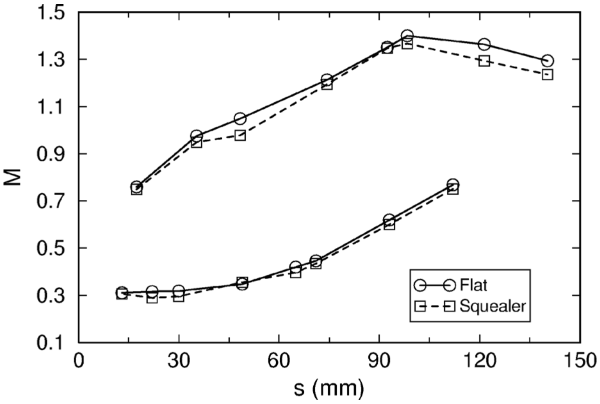

Fig. 4 Flat and squealer tip comparison of 97.3% span surface velocity distributions at high Re, high M

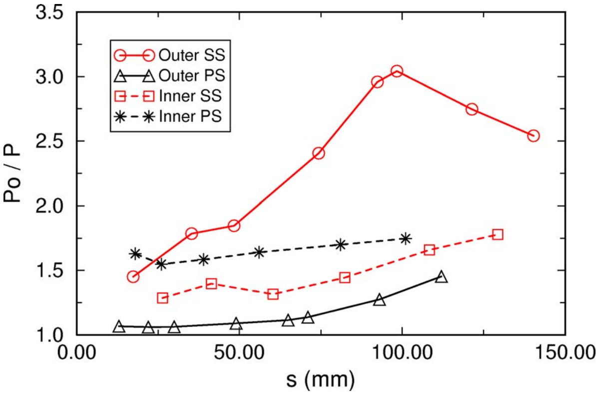

Fig. 6 Pressure ratios on squealer groove at 97.3% span for high Re, high M

Some flow visualizations using an oil and titanium dioxide mixture showed that the flow on the rim of the pressure side squealer is actually moving toward the leading edge (Fig. 5). CFD results could provide crucial information in the leading edge region to help in understanding the flow structures.

Figure 6 shows all of the 97.3% span surface data (inner surface and outer surface) of the squealer blade for the high Re, high M case. All pressure ratios presented in this work are referenced to the freestream inlet total pressure. The pressure ratios on the inner surface of the squealer are mostly within the range of pressure ratios on the outer surface of the squealer. The pressure side squealer shows inner surface pressure ratios that are at a higher level than on the suction side inner surface, which is a reversal of the pressure gradient with respect to the blade surface pressures. This corresponds to the recirculating flow in the squealer cavity. In the rear portion of the blade, the outer pressure distribution sets up a large pressure difference across the tip gap. However, the pressure ratios on the inner surface of the squealers do not seem to be affected by this, indicating a recirculating flow pattern in the squealer cavity. Perhaps, the width of the squealer cavity (blade width) determines the relative difference in pressure ratio between the inner suction side and inner pressure side squealer. For example, near the leading edge, there is a large difference in the inner surface pressure ratios, or velocities, between the two surfaces, but near the trailing edge, there is relatively little difference.

Blade Tip

Figure 7(*a*) shows the flow visualization on the cavity floor of the squealer tip. Near the leading edge suction side, the dots appear smeared, indicating flow impingement. Further along the suction side, the flow seems to travel along the suction side. The flow near the middle of the cavity near the leading edge is traveling from suction side to pressure side, indicating that this is a region of recirculating flow. Thus, the flow near the suction side has to move around this recirculation blockage. The flow in the squealer appears to have a streamwise component of velocity. In the rear part of the blade, the flow near the pressure side is traveling in the streamwise direction while the flow near the suction side is traveling toward the pressure side with a component of streamwise velocity. It appears that the flow continues to travel and accumulate in the trailing edge region of the squealer.

Figure 7(*b*) shows the flow visualization on the tip of the flat tip blade. The dots indicate the location of static pressure taps where tap 1 is near the leading edge and tap 7 is near the trailing edge. The flow that enters the leading edge region appears to maintain an almost purely axial velocity direction. This flow through the gap changes direction between taps 3 and 4. This corresponds to the same region where the largest pressure difference across the blade occurred in Fig. 2. After the flow initially enters from the pressure side, it travels toward the suction side, but it appears that a streamwise component is added to the tip gap flow in this area. Near the suction surface toward the trailing edge, some dots remain intact, and it was verified that they were not dry. Thus, this indicates a local separation region.

A separation vortex on the pressure side due to the flow entering the tip gap is evident by the line of oil that can be seen along the edge of the blade tip near the pressure side. Figure 8(*a*) also indicates the existence of the pressure side separation vortex due to entrance effects. A similar pressure side separation vortex was shown by Ameri and Bunker [16] in their simulation results of flow streamlines over the tip of a sharp-edged blade. Figure 8(*b*) also indicates that there could be a similar separation vortex that

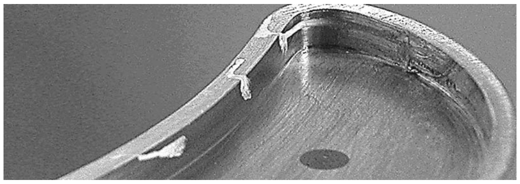

Fig. 5 Flow visualization of inner squealer pressure side rim near leading edge

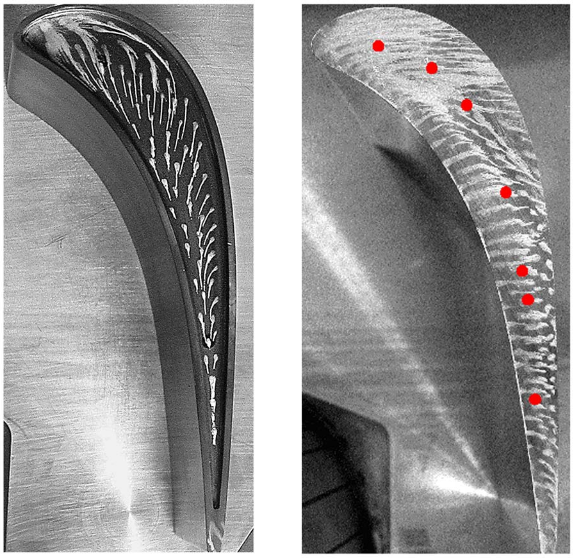

(*a*) (*b*)

Fig. 7 Flow visualization on squealer (*a*) and flat (*b*) tip blades

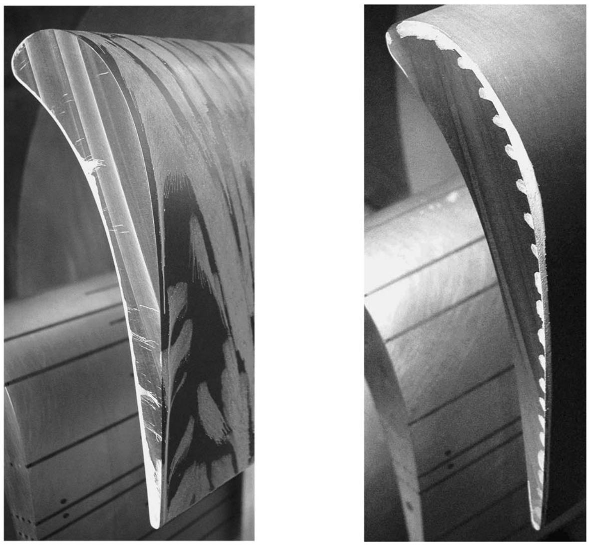
(*a*) (*b*)

Fig. 8 Flow visualization of separation vortices due to entrance (*a*) and Exit (*b*) effects

rolls up along the suction side of the blade surface near the tip due to exit effects. Also, Fig. 8(*b*) shows that some oil has wrapped around the trailing edge and migrated up the pressure side.

Figure 9 shows the tip pressure ratio along the camber line for the high M cases. As already explained in the preceding section, uncertainty bars were not added, as they would be smaller than the symbols.

Tap 1 corresponds to the tap nearest to the leading edge, while tap 7 corresponds to the tap nearest to the trailing edge. For the flat tip geometry, the highest pressure ratios occur for taps 4–7. This indicates along which part of the blade the majority of the tip leakage flow is passing. The high Re case shows a higher pressure ratio (higher velocity indicates higher flow rate). Taps 4–6 correspond to the same region on the blade where the 97.3% span surface loading distribution has the largest pressure difference. This is interesting because there was little difference in the blade loading near the tip for the two different Reynolds number cases. Thus, the large Reynolds number effect in the tip region must be due to viscous effects including the endwall and blade tip boundary layers. The pressure ratio for the squealer tip on Fig. 10 seems to be independent of the Reynolds number. Its pressure ratio remains at almost a constant level, which is much lower than the pressure ratio for the flat tip in Fig. 9. Tap 3 seems to show a slight decreased pressure ratio with respect to the other taps. This corresponds to the same area of the blade that shows the dip in pressure ratio on the suction side in the blade loading results near the tip in Fig. 4.

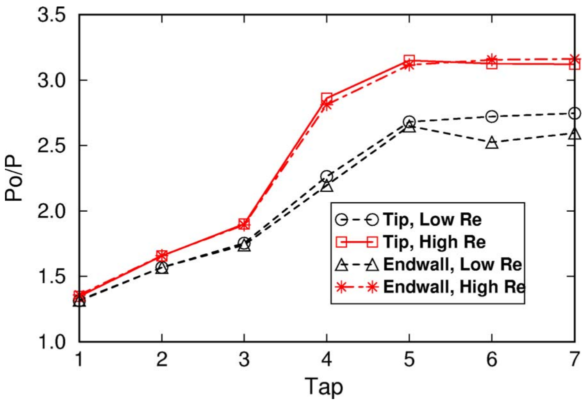

Fig. 9 Comparison of tip and endwall camber line pressure ratios for flat tip blade at high M

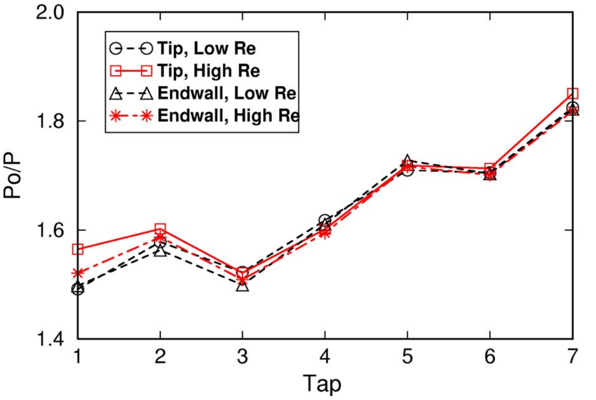

Fig. 10 Comparison of tip and endwall pressure ratio over squealer tip blade at high M

Figures 9 and 10 are comparing the tip pressure ratio along the camber line to the corresponding endwall pressure ratio along the camber line. As for the cases investigated by Bunker, Bailey, and Ameri [7], these figures show that the pressure distribution trends are very similar at both the blade tip and endwall. Note that the scale for pressure ratio in Fig. 9 is broader than that for Fig. 10. For the flat tip, the low Re cases are the most different between the endwall and the tip.

Figure 10 shows just how invariant the squealer tip data along the camber line are not only between the tip and endwall, but also for the two different Reynolds numbers. This is not surprising for purely recirculating flow. The leading edge region shows some slight variations between the endwall and blade tip pressures at high Re only. In fact, when investigating these types of data at all test conditions, the only major difference in the squealer tip data occurs in the trailing edge where a higher pressure ratio occurs for the higher exit Mach number case because of the more loaded trailing edge region for the high M cases.

At the high M condition, Fig. 11(*a*) shows the flat tip at low Re, and Fig. 11(*b*) shows the squealer tip at low Re. The squealer tip has reduced the pressure ratio (velocity) directly above the surface of the blade, but it seems that on the endwall suction side of the blade near the trailing edge, the pressure ratio is actually increased for the squealer tip. Figure 11(*c*) shows the flat tip at high Re, high M while Fig. 11(*d*) shows the squealer tip at high Re, high M. At the higher Reynolds number, the flat tip blade experiences higher pressure ratios. When comparing the two Reynolds number cases of the flat tip results, it can be seen that the same region of the blade has the higher pressure ratio, while the high Re has a higher level of pressure ratio. The high Re case has a high pressure ratio region that extends to the suction side toward the trailing edge. There is relatively little difference for the squealer tip between the two different Reynolds numbers. The region of elevated pressure ratio on the squealer tip near the pressure side leading edge exists for all test conditions.

It was shown in Figs. 9 and 10 that the endwall pressure ratio is a fair reflection of the tip pressure ratio. Thus, it can be said that the flat tip blade will have the lowest pressure ratio near the leading edge of the blade. This corresponds to low velocities and, thus, low heat transfer coefficients. This was seen by Yang et al. [6] in the leading edge region of their flat tip blade, and they called it the “sweet spot.”

For the flat tip blade studied by Azad et al. [5], the leading edge region was the area of lowest heat transfer coefficients, but there were high heat transfer coefficients along the leakage flow path. The lowest velocities over the flat tip were shown in Fig. 11(*a*)

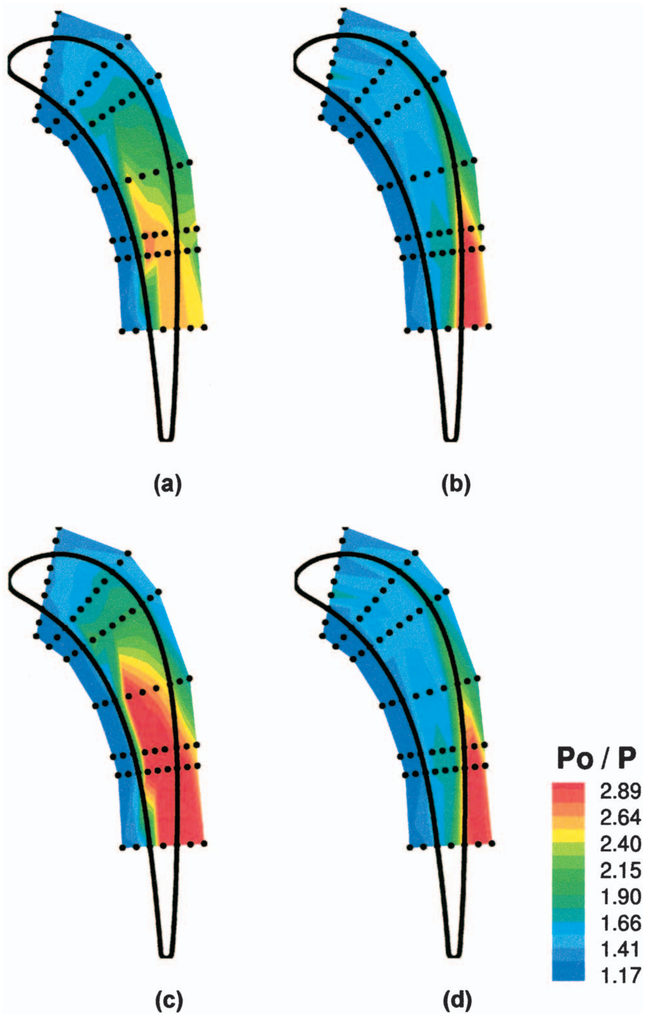

Fig. 11 Endwall pressure ratios for flat (*a*) and squealer (*b*) at high Re, high M

near the leading edge. The high-velocity regions are shown to correspond to the last half of the blade. This is also the region of the blade that had the largest pressure differential across the tip set up by the loading distribution.

For the squealer tip studied by Papa, Goldstein, and Gori [9], the highest mass transfer (thus heat transfer by analogy) region occurred on the cavity floor in the region near the leading edge. The numerical work by Yang et al. [11] also showed that the flow into the gap at the leading edge was entrained in the streamwise direction. Instead of a recirculating region of dead flow at the leading edge, the flow actually has a significant velocity. This is seen to be the case in the results for Fig. 11(*b*). Unfortunately there are no endwall taps further toward the leading edge. Azad, Han, and Boyle [10] also report high heat transfer coefficients near the leading edge (due to impingement) and on the suction side and pressure side squealer rims (due to entrance/exit effects). The flow visualization on the cavity floor of the squealer tip (Fig. 7(*a*)) also showed evidence of flow impingement near the leading edge since the oil dots became large and smeared.

Aerodynamic Loss

The downstream total pressure distribution is measured by traversing a three-hole pneumatic pressure probe across 1.5 pitches during a test. The measurement of blade losses requires the downstream probe to traverse at speeds of about 500 mm/s because of the short duration of the test. Therefore, it is necessary to determine the dynamic response of the pneumatic probe for a given pressure transducer and tube length. The digital compensation technique used is the direct least squares method developed by Paniagua and Denos [17].

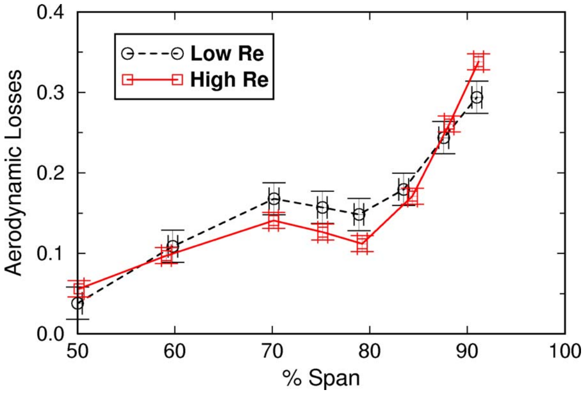

Fig. 12 Loss distribution on flat tip blade at low M

At low Reynolds number, the experimental uncertainty in ζ is ± 0.02, and at high Reynolds number, $\Delta\zeta = \pm 0.01$. The uncertainty in the radial position of the downstream probe is ±0.5 mm.

The spanwise location of the downstream probe is changed between runs to obtain the radial distribution of the losses over half of the span near the tip. Equation (1) is used to compute the aerodynamic losses [14]. The central cavity of the three-hole probe provides the P_{02} measurement, which is averaged over one pitch. The upstream total pressure measured in the compression tube provides P_{01}. This signal is averaged over the time it took the downstream probe to traverse the pitch. The downstream static pressure taps used for the periodicity investigation provide the measurement of the local P_2, which is also averaged over the same pitch for which the probe traverse measurements are taken.

$$\zeta = 1 - \frac{1-\left(\dfrac{P_2}{P_{o2}}\right)^{(\gamma-1)/\gamma}}{1-\left(\dfrac{P_2}{P_{01}}\right)^{(\gamma-1)/\gamma}} \tag{1}$$

Figure 12 shows the loss distribution at low M for the flat tip blade. The losses are increasing toward the tip. This is because of the endwall boundary layer and the tip leakage flow. The local maximum occurring near 70% span is caused by secondary flows. The pressure side horseshoe vortex moves across the blade passage, from pressure side to suction side. It carries the low momentum fluid of the inlet boundary layer. The low Re case has higher losses in the 70% span region because the inlet endwall boundary layer for the low Re cases is thicker than for the high Re cases. The tip results show higher velocities in the tip gap region for the higher Reynolds number cases. These higher velocities would cause higher losses near the tip, as shown in Fig. 12. The results for the high M cases are qualitatively similar except there is a more evident blockage effect caused by the probe.

The loss profile for the flat tip is compared to the squealer tip at low Re, low M in Fig. 13. The squealer tip blade appears to have a similar loss level at mid-span where the effect of the tip flows should not be felt. The squealer tip has a lower overall level of loss for the rest of the span. It appears that the peak associated with the secondary flows is shifted to a higher radial location for the squealer tip blade. Figure 14 shows the tip comparison for the high Re, low M case. Similarly, the overall levels of loss for the squealer tip are slightly below those for the flat tip case. Again, there is a radial shift in the secondary flow peak. If the tip leakage vortex associated with the flat tip is stronger than that associated with the squealer tip, then it could displace the secondary flows further down the blade. The computations by Yang et al. [6] found

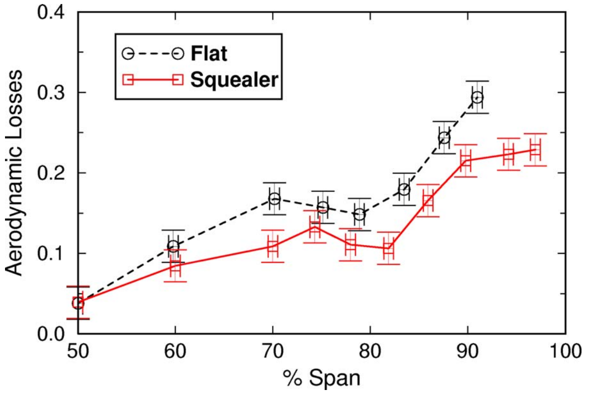

Fig. 13 Loss distribution comparison between flat and squealer tip at low Re, low M

that the roll up of the tip leakage vortex displaced the suction side flow in the pitchwise direction. Yang et al. [11] also saw that the leakage vortex associated with the squealer tip was much weaker than that for the flat tip. The different character in the losses near the tip between the squealer tip and the flat tip confirms that the tip leakage vortex is quite different for the two cases.

Flow visualizations were performed on the suction surface of the blades near the tip to try to learn more about the structure of the tip leakage vortex. Figure 15 shows the flow visualization results for the flat tip blade. At a distance of about $\frac{1}{8}$ of the span from the tip, there is an apparent line separating flow that goes toward mid-span (characteristic of the secondary flows) and flow that goes toward the tip. This line is the impingement line of the tip leakage vortex. The oil that goes toward the tip seems to meet up with a line of oil that has been traced along the blade's surface on the rear suction side near the tip. It is apparently some sort of liftoff line. The flow from the suction side does not penetrate the small 2 mm zone near the tip of the blade.

Further downstream along the blade, the size of the tip leakage vortex increases, and it affects a larger spanwise extent of the blade. Figure 16 shows the oil paint visualization for the suction side of the squealer tip blade. As with the flat tip, there is evidence of the suction side separation vortex in the top 2 mm of the blade. For the corresponding flat tip case in Fig. 15, this suction side separation vortex/counter tip vortex appears to affect a larger part of the suction side for the squealer tip blade, especially in the rear part of the blade. A reattachment line is visible indicating where the tip leakage vortex impinges on the blade. The tip leakage vortex appears to be slightly larger for the squealer tip blade than for the flat tip blade according to the location of the reattachment line. This could indicate that the tip leakage vortex is weaker (and thus larger) for the squealer tip blade than for the flat tip blade. If the velocity through the squealer tip gap has been reduced with respect to the flat tip case, the tip leakage vortex would be weaker. Yang et al. [11] found that the leakage vortex associated with the squealer tip was much weaker than for the flat tip.

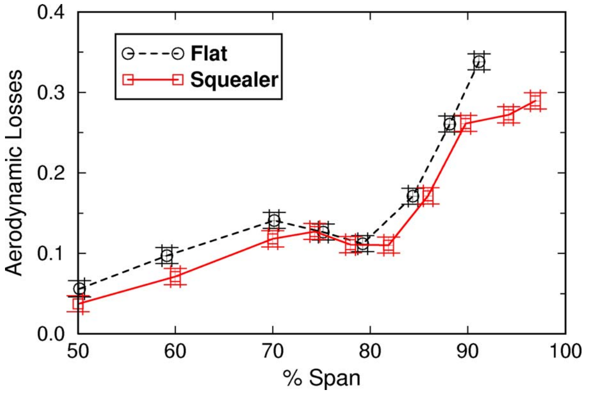

Fig. 14 Loss distribution comparison between flat and squealer tip at high Re, low M

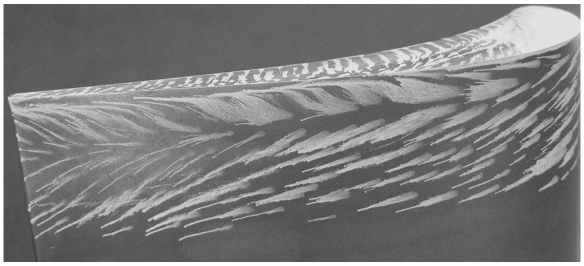

Fig. 15 Flow visualization of suction side (flat tip)

Conclusions

Surface pressure measurements along with a CFD computation indicate that the effect of the secondary flows near the tip are mainly to unload the front portion of the blade while the effect of the tip leakage flows are to load up the rear portion of the blade. Comparison in 97.3% span surface pressures show that a small region of constant pressure occurs for all cases with a squealer tip between the second and third taps from the leading edge on the suction side of the blade. This is the only difference in the surface pressures at 97.3% span between the flat tip and squealer tip cases. The loading data also show that the highest pressure differential across the tip of the blade occurs at an x/c_{axial} of 0.06–0.08, and this is confirmed as a region of high leakage flow rate from the tip camber line data.

For the flat tip blade, a pressure side separation vortex is apparent on the tip of the blade. There is also a region just downstream of the leading edge region where the flow along the tip changes direction and actually travels in the streamwise direction for a distance. For the squealer tip blade, flow visualization results are in line with a recirculating flow within the squealer tip cavity. Evidence of flow impingement exists near the leading edge. The flow on the cavity floor travels from the suction surface to the pressure surface with a significant component of streamwise velocity. Interesting results of oil dots on the inner surface of the pressure side squealer near the leading edge show that the flow exits the cavity and travels along the squealer rim toward the leading edge.

The tip data are compared to endwall data where there are corresponding pressure taps, and it is shown that there is relatively little difference in the pressure ratios reported at the surface of the tip to the pressure ratios reported on the endwall. The camber line data for the squealer tip show that its behavior is independent of Reynolds number. The only difference occurs in the trailing edge of the blade between the two Mach number conditions because the surface pressure distributions at the higher Mach number are more aft loaded.

For the endwall data, the squealer tip shows a significant decrease in pressure ratios over the blade surface with respect to the

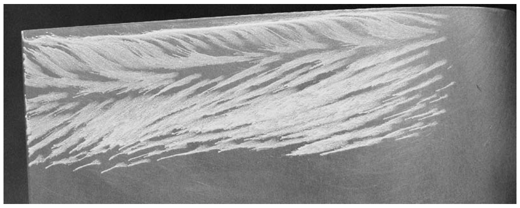

Fig. 16 Flow visualization of suction side (squealer tip)

flat tip blade. The flat tip blades show a region of high pressure ratio extending downstream of the leading edge region. The squealer tip starts to show an increased pressure ratio along the suction side in the rear portion of the blade but not directly over the blade itself. For the flat tip, an increase in Reynolds number causes an increase in pressure ratio levels, but the squealer tip is relatively insensitive to changes in Reynolds number. This is interesting because the blade loading near the tip of the flat tip blade shows relatively no Reynolds number effect. However, the tip flows for the flat tip blade are largely affected by the Reynolds number. The only region of the endwall where the squealer tip does not result in a lower overall pressure ratio compared to the flat tip is in the endwall row of taps nearest to the leading edge. Flow visualization indicates that flow impingement occurs in the leading edge portion of the squealer cavity.

The aerodynamic loss data show that the squealer tip cases result in a shift of the peak associated with the secondary flows toward the tip. This could be caused by a weaker tip leakage vortex associated with the squealer tip geometry. The squealer tip cases provide lower aerodynamic losses for all cases, which could be due to a decrease in mixing losses since the squealer tip leakage flow has lower velocities in the tip gap with respect to the flat tip blade.

This study is part of a larger project that seeks to acquire heat transfer data on these and other tip geometries. These data are important for CFD validation since the flow physics in the tip region are difficult to correctly model with current tools. Eventually, CFD could provide insight to some of the detailed flow structures that have been indicated in the flow visualizations.

Acknowledgment

The reported work was performed within the European research project "Aerothermal Investigation of Turbine Endwalls and Blade" (AITEB, 5FP, G4RD-CT-1999-00055). The permission for publication is gratefully acknowledged by the authors. The CFD calculation was performed at VKI by J. Prinsier.

Nomenclature

c = chord length
M = isentropic Mach number
P = static pressure
Re = Reynolds number
s = distance along blade surface
x = axial direction in cascade coordinates

Greek Symbols

Δ = experimental uncertainty
γ = specific heat ratio
ζ = aerodynamic losses

Subscripts

0 = Total condition
1 = cascade inlet
2 = cascade exit

References

[1] Mayle, R. E., and Metzger, D. E., 1982, "Heat Transfer at the Tip of an Unshrouded Turbine Blade," Proceedings, 7th International Heat Transfer Conference, Hemisphere Publishing Corp., pp. 87–92.

[2] Metzger, D. E., Bunker, R. S., and Chyu, M. K., 1989, "Cavity Heat Transfer on a Transverse Grooved Wall in a Narrow Flow Channel," ASME J. Heat Transfer, **111**, pp. 73–79.

[3] Bunker, R. S., 2004, "Turbine Blade Tip Design and Tip Clearance Treatment," VKI LS 2004–02 on *Blade Tip Heat Transfer and Coolong Techniques*.

[4] Sjolander, S. A., and Cao, D., 1995, "Measurements of the Flow in an Idealized Turbine Tip Gap," ASME J. Turbomach., **117**, pp. 578–584.

[5] Azad, G. S., Han, J., Teng, S., and Boyle, R. J., 2000, "Heat Transfer and Pressure Distributions on a Gas Turbine Blade Tip," ASME J. Turbomach., **122**, pp. 717–724.

[6] Yang, H., Acharya, S., Ekkad, S. V., Prakash, C., and Bunker, R., 2002, "Flow and Heat Transfer Predictions for a Flat-Tip Turbine Blade," ASME Paper No. GT-2002–30190.

[7] Bunker, R. S., Bailey, J. C., and Ameri, A. A., 2000, "Heat Transfer and Flow on the First-Stage Blade Tip of a Power Generation Gas Turbine: Part 1—Experimental Results," ASME J. Turbomach., **122**, pp. 263–271.

[8] Ameri, A. A., 2001, "Heat Transfer and Flow on the Blade Tip of a Gas Turbine Equipped with a Mean-Camberline Strip," ASME J. Turbomach., **123**, pp. 704–708.

[9] Papa, M., Goldstein, R. J., and Gori, F., 2002, "Effects of Tip Geometry and Tip Clearance on the Mass/Heat Transfer from a Large-Scale Gas Turbine Blade," ASME Paper No. GT-2002-30192.

[10] Azad, G. S., Han, J., and Boyle, R. J., 2000, "Heat Transfer and Flow on the Squealer Tip of a Gas Turbine Blade," ASME J. Turbomach., **122**, pp. 725–732.

[11] Yang, H., Acharya, S., Ekkad, S. V., Prakash, C., and Bunker, R., 2002, "Numerical Simulation of Flow and Heat Transfer Past a Turbine Blade with a Squealer-Tip," ASME Paper No. GT-2002-30193.

[12] Jin, P., and Goldstein, R. J., 2002, "Local Mass/Heat Transfer on Turbine Blade Near-Tip Surfaces," ASME Paper No. GT-2002-30556.

[13] Polanka, M. D., Hoying, D. A., Meininger, M., and MacArthur, C. D., 2002, "Turbine Tip and Shroud Heat Transfer and Loading Part A: Parameter Effects including Reynolds Number, Pressure Ratio, and Gas to Metal Temperature Ratio," ASME Paper No. GT-2002-30186.

[14] Arts, T., and Lambert de Rouvroit, M., 1992, "Aerothermal Performance of a Two-Dimensional Highly Loaded Transonic Turbine Nozzle Guide Vane: A Test Case for Inviscid and Viscous Flow Computation," ASME J. Turbomach., **114**, pp. 147–154.

[15] Denos, R., Arts, T., Paniagua, G., Michelassi, V., and Martelli, F., 2001, "Investigation of the Unsteady Rotor Aerodynamics in a Transonic Turbine Stage," ASME J. Turbomach., **123**, pp. 81–89.

[16] Ameri, A. A., and Bunker, R. S., 2000, "Heat Transfer and Flow on the First-Stage Blade Tip of a Power Generation Gas Turbine: Part 2—Simulation Results," ASME J. Turbomach., **122**, pp. 272–277.

[17] Paniagua, G., and Denos, R., 2002, "Digital Compensation of Pressure Sensors in the Time Domain," Exp. Fluids, **32**, pp. 417–424.

Large-Eddy Simulation of Unsteady Surface Pressure Over a Low-Pressure Turbine Blade due to Interactions of Passing Wakes and Inflexional Boundary Layer

S. Sarkar[1]
Department of Mechanical Engineering,
Indian Institute of Technology,
Kanpur 208016, India
e-mail: subra@iitk.ac.in

Peter R. Voke
School of Engineering,
University of Surrey,
Guildford GU2 7XH, UK
e-mail: p.voke@surrey.ac.uk

The unsteady pressure over the suction surface of a modern low-pressure (LP) turbine blade subjected to periodically passing wakes from a moving bar wake generator is described. The results presented are a part of detailed large-eddy simulation (LES) following earlier experiments over the T106 profile for a Reynolds number of 1.6×10^5 *(based on the chord and exit velocity) and the cascade pitch to chord ratio of 0.8. The present LES uses coupled simulations of cylinder for wake, providing four-dimensional inflow conditions for successor simulations of wake interactions with the blade. The three-dimensional, time-dependent, incompressible Navier-Stokes equations in fully covariant form are solved with* 2.4×10^6 *grid points for the cascade and* 3.05×10^6 *grid points for the cylinder using a symmetry-preserving finite difference scheme of second-order spatial and temporal accuracy. A separation bubble on the suction surface of the blade was found to form under the steady state condition. Pressure fluctuations of large amplitude appear on the suction surface as the wake passes over the separation region. Enhanced receptivity of perturbations associated with the inflexional velocity profile is the cause of instability and coherent vortices appear over the rear half of the suction surface by the rollup of shear layer via Kelvin-Helmholtz (KH) mechanism. Once these vortices are formed, the steady-flow separation changes remarkably. These coherent structures embedded in the boundary layer amplify before breakdown while traveling downstream with a convective speed of about 37% of the local free-stream speed. The vortices play an important role in the generation of turbulence and thus to decide the transitional length, which becomes time dependent. The source of the pressure fluctuations on the rear part of the suction surface is also identified as the formation of these coherent structures. When compared with experiments, it reveals that LES is worth pursuing as an understanding of the eddy motions and interactions is of vital importance for the problem.* [DOI: 10.1115/1.2137741]

Introduction

Efforts towards the decrease of weight and cost of modern LP turbines by reducing the number of blades come up against the problem of boundary layer separation on the suction surface of blades owing to enhanced loading. Wakes shed from upstream blade rows interact with the separated boundary layer of downstream blades, and make the flow and bubble highly unsteady. Although the benefit of incoming wakes is recognized in periodic suppression of bubble over the suction surface of a highly loaded LP turbine blade, the unsteady and the turbulence effects owing to the wake-bubble interactions must be taken into account for the design of a modern LP turbine blade. Although several studies have been made on wake-induced transition based on attached boundary layers [1–6], the behavior of a separated boundary layer under the influence of unsteady wakes has not been adequately addressed.

LP Turbines operate at relatively low Reynolds numbers in the range $0.9-2\times10^5$; this coupled with high levels of diffusion lead the laminar boundary layer to separate on the suction surface under steady flow. Rapid transition then occurs within the separated layer. This may be attributed to the increased receptivity of free-stream disturbances near the point of separation. The resulting turbulent-like layers will re-energize the flow and reattach to form a separation bubble [7,8]. Separation bubbles were classified as *short* or *long* based on their effect on the main flow inviscid pressure distribution [9]. However, the definition of bubbles based either on their physical length or on the effect of local pressure distribution is ambiguous. A realistic classification of bubbles proposed by Hatman and Wang [10,11] was based on the state of boundary layer at separation and subsequent structure of separated flow including vortex dynamics. It was observed that boundary layers that separate in laminar state behave differently from those that are already transitional or highly unstable (pretransitional) at separation. Downstream of separation, the KH instability sets in; the rollup vortex periodically forms, grows, pairs and finally interacts with the wall. There are studies [1,12] that provide basic information about how transition originates and develops in separated boundary layers. Correlations for the development of intermittency within the separated region are provided by the turbulent

---

[1] To whom correspondence should be addressed.

Contributed by the International Gas Turbine Institute (IGTI) of ASME for publication in the JOURNAL OF TURBOMACHINERY. Manuscript received October 1, 2004; final manuscript received February 1, 2005. IGTI Review Chair: K. C. Hall. Paper presented at the ASME Turbo Expo 2005: Land, Sea and Air, Reno, NV, June 6–9, 2005, Paper No. GT2005-68867.

spot theory with a high spot production rate. It is commonly accepted that the detached laminar layer is inherently unstable and promote the growth of disturbances leading to an early transition. The separated flow transition may or may not involve Tollmien-Schlichting (TS) instability.

For a high-lift turbine, wakes shed from upstream blade rows interact with the separated boundary layer over the suction surface of downstream blade, and make the flow and bubble highly unsteady. The high turbulence intensity of the wake induces transition in the attached boundary layer at a location upstream of separation. The fuller turbulent or calmed velocity profiles withstand greater adverse pressure gradient and thus the boundary layer remains attached resulting in suppression of bubble [5]. As the influence of the wake decays, the velocity profiles return to their undisturbed state re-establishing the separation bubble. The boundary layer behavior depends on the wake-passing frequency and the wake strength. The mechanism controlling the re-establishment of bubble and transition process in an unsteady environment are not fully understood. Few relevant studies on the instability mechanism of a separation bubble under the influence of periodic artificial disturbances have been reported [13–15]. D'Ovidio et al. [13,14] have attempted to extend the correlations for predicting transition length in turbomachinery applications; the physics of transition owing to the interactions of convective wake and the separation bubble is not very complete. Walmuff [15] illustrated that the instability mechanism governing the amplification of the wave packet in a separated bubble is predominantly inviscid. In the vicinity of the reattachment, the nonlinear interaction and the rollup of shear layer evolve large-scale vortex loops (*coherent structures*) that retain their presence far downstream of separation. There are experimental evidences that these coherent structures, formed inside the boundary layer, may cause large pressure fluctuations. The recent work Stieger et al. [16] using PIV measurements over a small area on the suction surface of the T106 LP turbine cascade has revealed the presence of rollup vortices due to the perturbation of separated layer by the convective wake passing.

The present study employs LES as a high-resolution time-dependent calculation to investigate the unsteady pressure over the suction surface of a high-lift LP turbine blade owing to wake passing. LES is often the preferred method of making certain advances in fundamental understanding of dynamical processes in complex turbulent flows, where an understanding of the eddy motions and interactions is the key to comprehension of the flow. The highly unsteady flow in turbomachinery, where the wakes from upstream blade rows interfering periodically with the downstream blades, involves complex interactions between spatial and temporal scales of turbulent eddies impinging on unstable boundary layers. The complexity of such flow cannot be captured by Reynolds-averaged Navier-Stokes calculations. The aim is to assess the ability of LES in resolving the appearance of coherent structures within the inflexional layer over the rear half of the suction surface, the source of large pressure fluctuations, as reported experimentally [16]. An attempt is made to describe the mechanism of formation of these coherent structures, their interactions and downstream convection over the suction surface.

Numerical Methods

LES is the method of predicting turbulent flows by simulating directly large-scale eddies while modeling statistically the effects of those smaller than a defined cut-off scale, usually related to the mesh size. The computational techniques employed have previously been applied to flat-plate bypass transition [17] and also to transition with reattachment following a geometry-induced separation [18]. The Navier-Stokes equations in the fully covariant form are solved on a staggered grid using the finite volume method. The explicit second-order accurate Adams-Bashforth scheme is used for the momentum advancement. The pressure equation is discrete Fourier transformed in one dimension (in which periodicity of the flow and so uniformity of the geometry is imposed) and solved iteratively using multigrid acceleration in the other two dimensions. The spatial discretization is second-order accurate using a symmetry-preserving central difference scheme, which is widely used in LES owing to its non-dissipative and conservative property.

Any small-scale motions (smaller than the mesh or control volume) are averaged out and are accounted by the subgrid-scale model. For modeling the nonresolvable subgrid scales, it was decided to use the classical Smagorinsky model [19] considering the computation economy and the nature of the problem. A reduced value of 0.125 is chosen as model constant. The Smagorinsky model is absolutely dissipative; it is incapable of predicting the reverse cascade regions and overestimates the subgrid-scale dissipation. Part of the problem is due to the fact that the model is only based on local large-scale quantities and predicts nonzero residual stresses even in the laminar region. This limitation can be overcome in many ways. In the present study, the low-Reynolds number model of Voke [20], which is derived following the dissipation spectrum and is expected to simulate the transition flow, has been used. The work of Huai et al. [21], who compared the performance of a localized dynamic model with those of the low-Reynolds number Smagorinsky model and Smagorinsky model with the intermittency modification to simulate the transitional flow over a flat plate, indicated that simple corrections to the Smagorinsky model are worth pursuing. In computations of turbulent flows, the length scale is often multiplied by a damping function to account for the fact that the growth of turbulent structures is inhibited by the presence of the wall. The damping function as suggested by Piomelli et al. [22] is used here to damp the near-wall length scale. In the laminar flow regime, the maximum subgrid-scale dissipation is around 3.0% of the viscous dissipation when the low-Reynolds number correction along with the damping function are used to evaluate the subgrid viscosity.

Details of Numerical Computation. The large-scale simulations of wake passage over a highly cambered blade (T106 profile) for a Reynolds number of 1.6×10^5 based on the chord and exit velocity (V_{2is}) are performed using wake data extracted from precursor simulations of flow past a thin cylinder. For the present study, a H-grid of good quality within the blade passage is developed by applying power-law to the control functions appearing in the elliptic grid generation scheme of Hsu and Lee [23]. The grid lines generated are nearly orthogonal to boundaries and the grid transformation Jacobian and matrices do not show any considerable discontinuity in their distributions within the highly distorted blade passage. Figure 1 shows T106 blade profile and the grid illustrating the smoothly varying grid size and near-wall orthogonality even in the critical regions of leading and trailing edges. The inlet plane of the computational domain is placed at half of axial chord (C_X) upstream of the leading edge, whereas, the outlet plane is at one full axial chord downstream of the trailing edge to resolve the vortex shedding behind the blade. The domain in the spanwise direction is considered 10% of chord that was found to be sufficient to allow three-dimensional (3D) instability and turbulent structure to develop. Wu and Durbin [24] considered the spanwise dimension as 12% of chord with the same blade profile. Further details of T106 cascade and flow configurations are provided in Table 1.

The simulations are performed on a grid with 384 points in the streamwise, 192 in the blade-to-blade plane and 32 in the spanwise directions. Among 384 streamwise grid points, 80 points are distributed upstream of the leading edge, 180 points are used within the blade passage and the remaining 124 points are distributed downstream of the blade. The mesh size varies over the domain but the mean figures for the central region within the blade passage are $\Delta x^+\approx\Delta y^+\approx 40$ and $\Delta z^+\approx 16$ (based on the averaged wall shear stress). The y-mesh is stretched to concentrate points near the wall from $\Delta y^+\approx 40$ in central region of the blade-passage

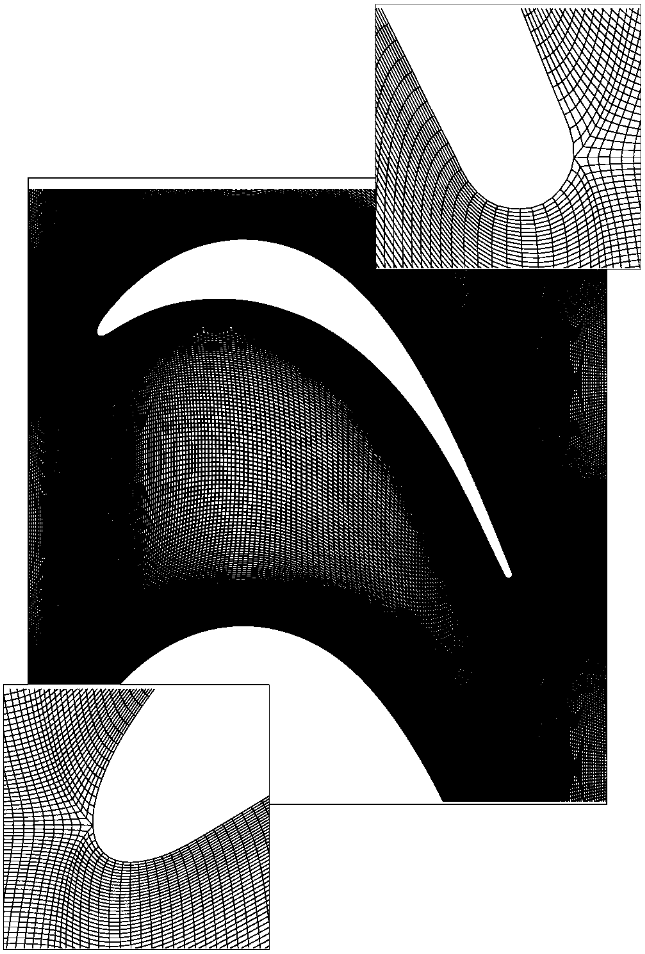

Fig. 1 Computational grid for the T106 blade profile and zoomed view of leading and trailing edges

to a minimum of $\Delta y^+ \approx 1.3$ at the wall, while the x-mesh on the blade surface varies from $\Delta x^+ \approx 10-45$. In the rear half of the blade suction surface, where the boundary layer is transitional, there are approximately 35–43 points inside the boundary layer with η^+ around 0.5 at the first grid point. The time step was about $\Delta t = 1.224 \times 10^{-4}\ C/V_{2is}$ in nondimensional unit. This time step kept the Courant number below 0.2 for the entire simulation and the viscous stability number was much lower. Each wake passing cycle corresponds to 12,000 time steps. The flow field was allowed to evolve for five wake passing cycles and then the data were collected for the phase averaging over eight cycles. This compromise was made considering computational resources and time. The earlier work by Wu and Durbin [24] considered ten wake passing cycles for statistics. The phase averaging was performed by dividing each passing period into 30 equal subdivisions. The computation required 13.5 micros/iteration/grid based on 32 processors of an Origin 3000. In practice the simulation took about two months to perform.

Table 1 Cascade T106 details and flow configurations

Chord	[mm]	198
Cascade pitch	[mm]	158
Blade stagger	[deg]	59.3
Inlet flow angle	[deg]	37.7
Design exit flow angle	[deg]	63.2
Bar diameter	[mm]	3.96
Bar pitch	[mm]	158
Axial distance: Bar to the leading edge	[mm]	85
Reduced frequency of wake passing, $f_r = fC/V_{2is}$		0.68
Flow coefficient, $\phi = V_{X1}/U_b$		0.83

The data generated are analyzed by both the time- and phase-averaging. The time-averaging is represented by an overbar, whereas, averaging at a particular phase $t^m_{n_T} = mT + n_T T$ (m is an integer and n_T is a fraction of the wake passing period T), is denoted by $\langle\bullet\rangle$. Thus, the phase-averaged mean velocity component can be evaluated as

$$\langle u_i\rangle(t_{n_T}) = \frac{1}{N}\sum_{m=1}^{N} u_i(t^m_{n_T}),$$

where, N is the total number of periods within which the phase-averaging is performed. Additional space-averaging over the homogeneous spanwise direction is implied in both the time- and phase-averaging. Time- and phase-averaged velocities are related via $\bar{u}_i = \overline{\langle u_i\rangle}$. Thus, the instantaneous velocity component can be decomposed as

$$u_i = \langle u_i\rangle(t_{n_T}) + u_i'(t_{n_T}) = \bar{u}_i + \tilde{u}_i(t_{n_T}) + u_i'(t_{n_T})$$

where, $\tilde{u}_i(t_{n_T}) = \langle u_i\rangle(t_{n_T}) - \bar{u}_i$ is the periodic velocity fluctuation with respect to the time-averaged mean and $u_i'(t_{n_T})$ is the true stochastic turbulence fluctuation.

Inflow and Other Boundary Conditions. The unsteady wake-induced flow over a turbine blade has been traditionally studied through experiments by sweeping a row of wake-generating cylinders upstream of a cascade. The moving row of wake-generating cylinders is replaced by a precursor large-scale simulation of the flow past a thin cylinder (2% of the blade chord) for a Reynolds number of 1842 based on the inlet velocity (derived from the integrated mass flow through the cascade) and the diameter of the cylinder. A grid of 248 points in the streamwise plane, 384 along the bar-pitch (grid number along the pitch is doubled as compared to the cascade) and 32 in the spanwise direction are used. The wake-data are collected from a plane 5.25 D downstream of cylinder and are interpolated at the inlet plane of cascade considering the kinematics of flow by matching the velocity triangles. Thus, the present LES uses coupled simulations of cylinder for wake, providing four-dimensional inflow conditions for successor simulations of wake interactions with the blade.

The periodic boundary conditions, for instantaneous and statistical variables, are enforced at upstream and downstream of blades to simulate an infinite row of blades in cascade. On the blade surface, no-slip boundary conditions are imposed. At exit of the computational domain, convective boundary conditions are used, that allow passing of trailing vortices through the outflow boundary without any significant mass redistribution. The use of a H-grid poses a problem while solving the discretized Poisson equation as a part of the boundary is periodic and a part is no-slip. In the present study, a homogeneous Neumann condition for pressure is applied on the inflow and outflow, as well as the turbine blade wall and a cyclic matching is applied to the pressure and the associated velocity at upstream and downstream of blades.

Results and Discussion

In this section, unsteady flow developed over the suction surface of a modern LP turbine blade subjected to a periodic wake passing is discussed. A separation bubble on the suction surface of the blade was found to form under the steady state condition. Large amplitude of pressure fluctuations over the rare part of the suction surface are observed as the wake passes over the separation region. LES results are analyzed to understand the physics of these pressure fluctuations in conjunction with the earlier experimental studies [4,5,16].

The unsteady wakes produce an incident flow that has two distinctive characteristics: A free-stream velocity defect described by

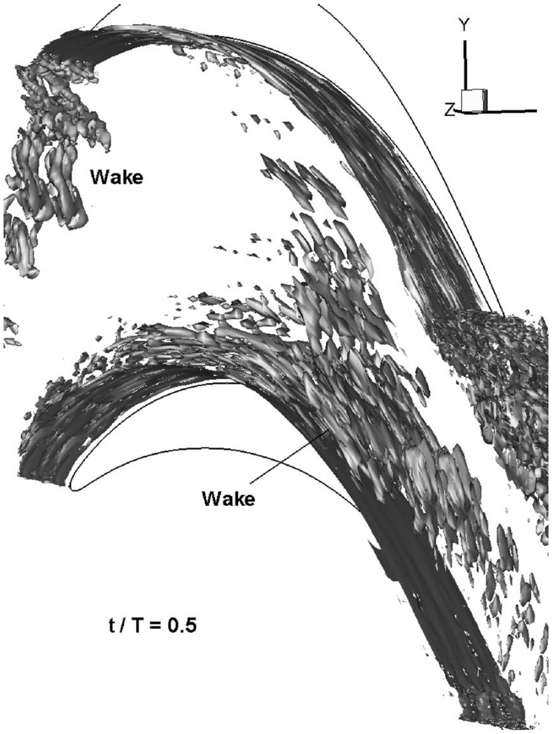

Fig. 2 Iso-surface of vorticity $|\omega|$ at an instant of time through the wake passing cycle

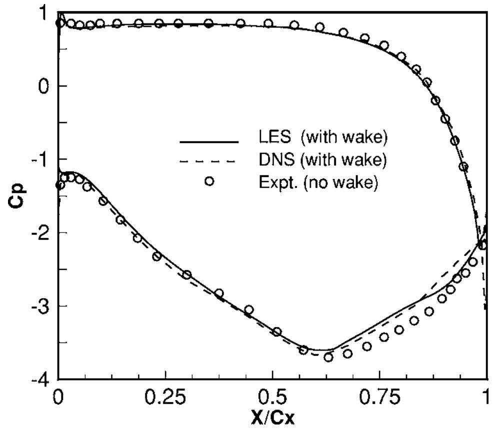

Fig. 3 Time-averaged wall static-pressure coefficient Cp: Present LES; DNS by Wu and Durbin [24] and experiment by Stadtmüller and Fottner [28]

kinematics and associated high turbulence during the wake passing. Although the kinematics of the wake is partly responsible for the boundary layer character developing over the downstream blade rows, the effect of wake turbulence and its convection through the blade passage are also very important. As the present calculation methodology uses wake data from a precursor simulation, the realistic representation of wake data is vital for the successor simulation of wake convection through a turbine cascade passage. The turbulence statistics, and pressure coefficients (not shown) of the computed wake data are in close agreement with the previous experiments and simulations [25,26]. The wake illustrates small-scale eddy structures with organized vortex shedding in the streamwise direction. Spectral analysis of streamwise component of velocity has indicated the value of *Strouhal number* of 0.2 with a wide spectrum in the spanwise direction. The wake data that are kinematically transferred to the cascade inlet have a level of turbulence intensity of about 5.5%.

The kinematics of wakes as it migrates through the high-lift LP turbine blade passage are described in details by Sarkar and Voke [27]. The instantaneous iso-surface of vorticity magnitude $|\omega|$ at an instant of time through the wake passing cycle illustrates three-dimensional visualization of the wake distortion inside the blades passage, Fig. 2. After being segmented at the leading edge, the suction- and the pressure-side wakes behave differently. Straining of incoming wakes near the stagnation point of suction surface has started with hairpin vortices, but these are quickly broken down to random small-scale structures. A bow forms between the pressure- and suction-side wakes owing to different convection speeds. In the apex region of the distorted wake, enhancement of turbulence occurs with growing random small-scale structures and loss of preferred orientation. The pressure side wake suffers from severe stretching and thinning with the decay of turbulence. Sharp turning of the turbine passage causes the pressure-side wake to descend towards the wall over the downstream half of the pressure surface, whereas the suction-side wake after warping around the leading edge travels relatively above the surface. This highly strained wake fluid and generated small-scale structure interact periodically with the inflexional boundary layer over the suction surface; an example of complex interactions between spatial and temporal scales of turbulent eddies impinging on unsteady boundary layer. A well-resolved LES, although difficult to implement for the concerned flow configuration, is expected to illustrate the interactions.

Unsteady Surface Pressure. The time-averaged wall-static pressure coefficients $[C_p=(\bar{P}-\bar{P}_1)/(\bar{V}_1^2/2)]$ with wake passing over the T106 blade from the present LES are compared with the corresponding results from the DNS of Wu and Durbin [24], Fig. 3. The surface pressure distributions from experiments by Professor L Fottner's group at the University der Bundeswehr München, Germany [28] are also superimposed. The agreement between the present LES and DNS of Wu and Durbin is seen to be excellent. Small discrepancies between the simulations and the experiment over the inflexional region of the suction surface may be attributed to different inflow conditions, endwall effects and compressibility. In the experiments the inflow was seeded with grid turbulence but with no passing wakes.

The phase-averaged distributions of unsteady surface pressure coefficients $[\langle C_p\rangle=(\langle P_{01}\rangle-\langle P\rangle)/(\langle P_{01}\rangle-\langle P_2\rangle)]$ at a series of eight time instants through the wake passing cycle are shown in Fig. 4. The time-averaged values of C_p both from the simulation and experiment [16] are also superimposed. When compared with the

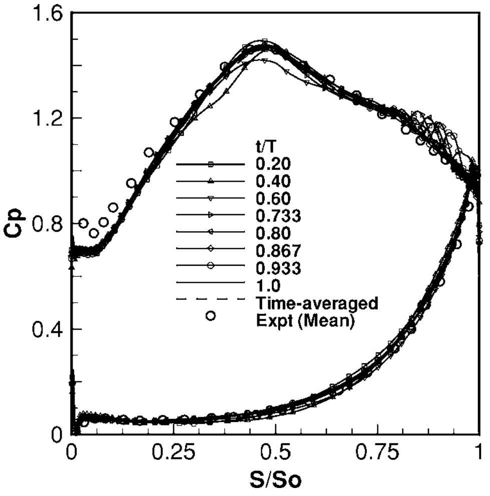

Fig. 4 Phase-averaged Cp distributions on the T106 blade: Present LES and experiment [16]

Table 2 Approximate position of the wake center near to the suction surface during the wake passing cycle

Time (t/T)	Position of the wake center (S/So)
0.30	0.260
0.40	0.395
0.50	0.525
0.60	0.655
0.70	0.785
0.80	0.920
0.90	1.050

time-mean values of surface pressure, the disagreement is observed in the front part of the suction surface. This may be attributed to the change in flow incident angle owing to wake passing from that of the experiment. However, the agreement is good on the pressure surface and downstream of $S/So=0.25$ on the suction surface, particularly downstream of the peak suction, which is the region of primary interest. Experimental data reveal the existence of a laminar separation bubble over the rear part of the suction surface for flow without passing wakes. The bubble starts at $S/So=0.6$ and extends to $S/So=0.8$, where the separated layer undergoes transition and reattaches by $S/So=0.9$. Though the time-mean results of the present LES supports the experiment [5] illustrating the suppression of separation bubble owing to wakes passing, a trace of separation is felt over the region $0.80<S/So<0.90$.

As the wake is convected along the suction surface, phase-averaged surface pressure $\langle C_p\rangle$ is seen to reduce as compared to its steady values over the front part of the blade (Fig. 4), which can be explained by the negative jet model of Meyer [29]. The negative jet when incident on the suction surface causes the local increase of pressure and thereby reduction of $\langle C_p\rangle$ is reflected. At $t/T=0.4$, the wake arrives near the mid-chord ($S/So=0.4$), and the peak suction is reduced by $\Delta\langle C_p\rangle=0.1$. The corresponding experimental value is 0.15 [16]. A remarkable change in the distributions of $\langle C_p\rangle$ on the suction surface occurs as the wake convects over the steady flow separation region. A series of large-amplitude pressure oscillations are observed on the suction surface for $t/T>0.65$ and for the wake position downstream of $S/So=0.70$ (the position of the wake centerline over the suction surface during the wake passing cycle is mentioned in Table 2). The peak-to-valley amplitude of these pressure fluctuations is $\Delta\langle C_p\rangle=0.15$. The corresponding experimental value is 0.3. During the time $0.3<t/T<0.65$ when the boundary layer relaxes to its pre-transitional state owing to the removal of stimulus of early transition after the wake passing over the unstable separated region, no pressure fluctuations are observed. This is partly attributed to the calmed region of flow characterised by higher shear stress and full velocity profiles. It is worthwhile to mention that these pressure fluctuations on the suction surface are dependent on the turbulence intensity and length scale of passing wakes.

The process of phase averaging eliminates random fluctuations and illustrates large amplitude fluctuations. So the pressure oscillations reflected in the phase-averaged results indicate that they are formed by deterministic coherent structures in the flow. Recent work of Stieger et al. [16] has shown that the formation of rollup vortices as the wake passes over the separating boundary layer is the cause of these pressure oscillations. Following sections will be dedicated to discuss that how successfully the instant LES has resolve these coherent structures responsible for pressure fluctuations and flow transition under wake passing.

Space Time Diagram. Important insight to the dynamical effects of wake passing, as well as comparison with similar analysis of available experimental results, can be obtained by studying the variation of key diagnostic parameters as a functions of a single spatial variable and time. Contours of phase-averaged surface pressure $\langle C_p\rangle$ as a function of distance along the suction surface and time from the instant LES are presented in Fig. 5(*a*), Space Time (ST) diagram. To aid visualization of periodic unsteady process, the data are reproduced to form a cycle of three passing periods. The corresponding experimental results [16] are shown in Fig. 5(*b*).

As explained, the effect of a migrating wake can be modelled by a negative jet, which impinges on the suction surface and splits into two streams. One pointing downstream accelerates the flow downstream of the approaching wake and other pointing upstream retards the flow after the wake has passed. The two trajectory lines A and B drawn on the Fig. 5(*a*) represent the maximum and minimum velocity resulting from the kinematics of wake passing. The center of the wake can be thought to lie half way between the lines A and B. Upstream of the steady flow separation region ($S/So<0.7$), the convection of the wake is evident by the reduction in $\langle C_p\rangle$ between lines A and B. The negative jet causes the pressure to increase locally due to migration of wake fluid resulting in reduction of observed values of $\langle C_p\rangle$ on the suction surface. The nature of pressure traces in the region where the wake passes

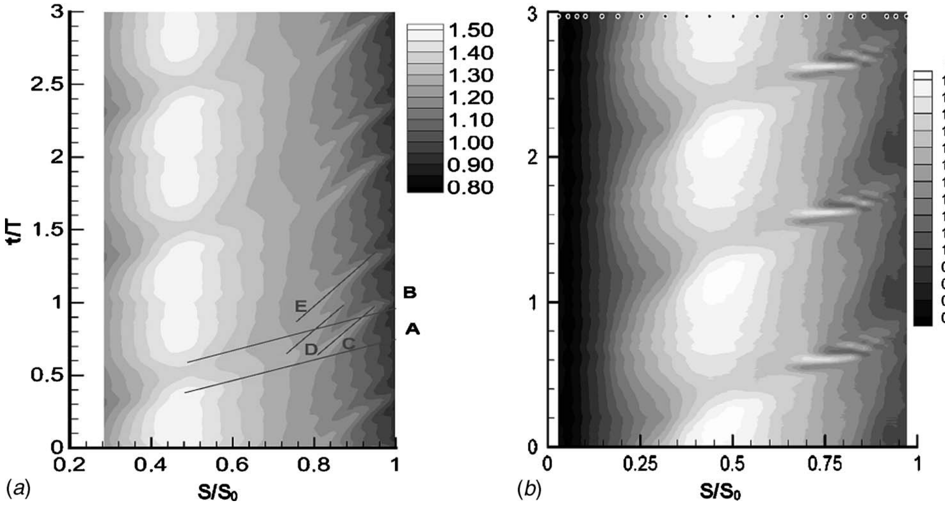

Fig. 5 S-T diagram of phase-averaged Cp over the suction surface of the T106 blade; (*a*) LES, (*b*) experimental [16]

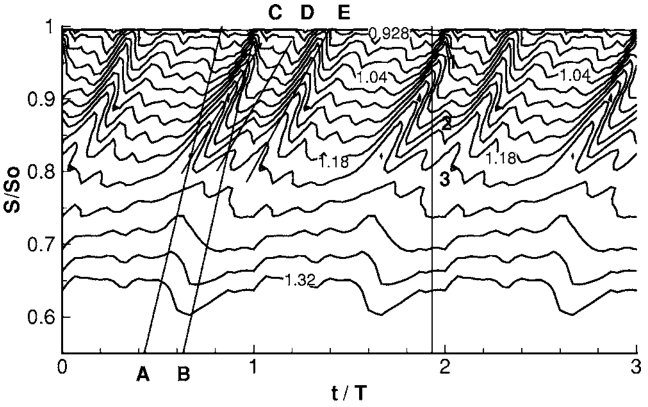

Fig. 6 Traces of phase-averaged Cp over the rear of the suction surface: Trajectories A and B represent local peaks of free-stream velocity, U and C represents 0.37U

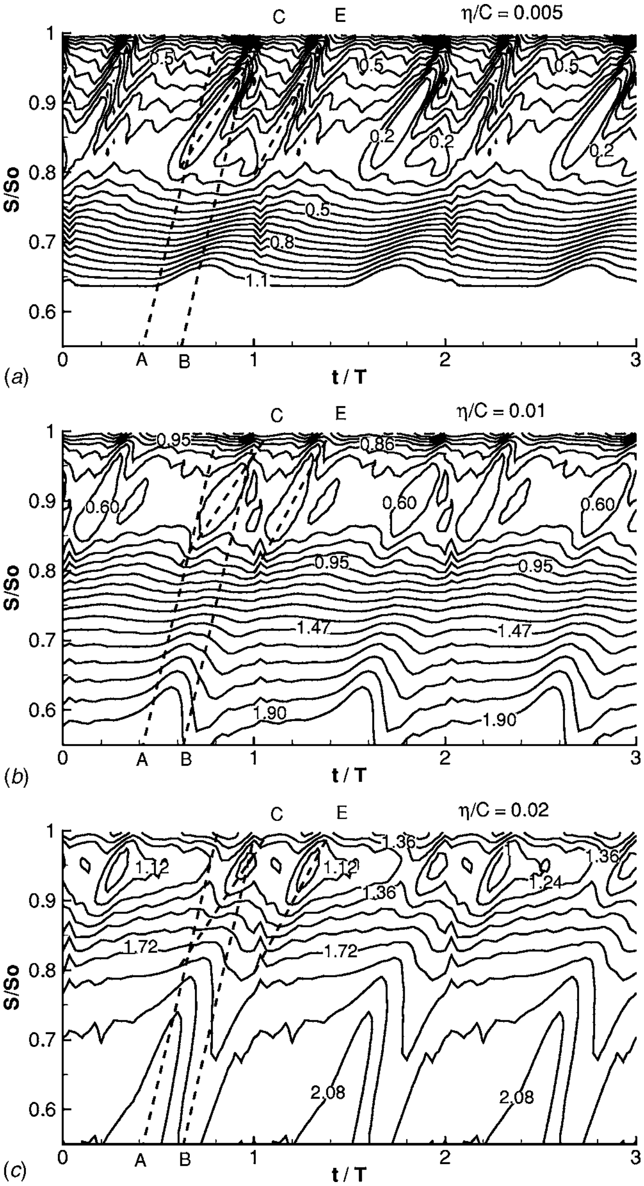

Fig. 7 Phase-averaged contours nondimensional streamwise component of velocities at different sections of boundary layer on the suction surface: Trajectories A and B represent local peaks of free-stream velocity, U and C drawn from 0.37U

the steady flow separation bubble is dramatically different from upstream where the boundary layer is laminar and attached. As the wake arrives at $S/So=0.70$, the onset of pressure fluctuations occurs and a stream of distinct disturbance followed by a relatively weaker one, marked as C and D, travel downstream at a speed much lower than the local free-stream speed. Figure 5(*a*) further illustrates that even after the wake has passed over the region, a stream of disturbance makes its appearance, marked as E, and travels downstream before relaxation of boundary layer. The experimental observations of Stieger et al. [16] presented in Fig. 5(*b*) are similar to those resolved by the present LES, however the experiment does not show such a lagging but prominent stream of fluctuation with respect to wake center.

To illustrate the region of pressure fluctuations further, phase-averaged surface pressure $\langle C_p \rangle$ traces on the suction surface for the rear part of the blade are depicted in Fig. 6. The line A is again the trajectory of peak velocity induced by the migrating wake and thus represents the free-stream velocity. The onset of pressure fluctuations, as indicated in Fig. 6, falls along different trajectories parallel to line A. These phenomena are observed in experiment [16] illustrating that the onset is controlled by wake convection. Thus the LES supports the argument that was put forward that the onset of pressure oscillations is not controlled by the turbulent spots or instability waves within the boundary layer as they convect slower than the free-stream. The onset is also not controlled by an acoustic mechanism as these would travel at much higher speed than the convective wake in an incompressible medium.

In Fig. 6, the pressure fluctuations are observed to originate at $S/So=0.7$, the amplitude of fluctuations increases up to $S/So=0.8$ and thereafter remains approximately constant. The amplitude of fluctuations reduces slightly downstream of $S/So=0.92$, the region of recovery from the steady separation bubble and the region of turbulent mixing. It should also be noted that the number of maxima and minima in the phase-averaged pressure traces is not the same over the rear part of the suction surface. At $S/So=0.7$, one maximum and minimum is observed, whereas at $S/So=0.8$, three sets of maxima and minima have appeared. Two very prominent streams of disturbance marked as C and E travel downstream at approximately 37% of the local free-stream velocity, whereas the experimental value of the convection speed of these structures is about half of the free-stream velocity. It should also be emphasized that the onset of pressure fluctuations E, that was not prominent in experiment, appears to originate from the trajectory line B, which is the trace of the minimum velocity due to the negative jet effect of wake. Thus the onset of pressure fluctuations is not restricted along the wake centerline, but spread over the region bounded by two trajectories A and B, that can be thought of as the zone of influence of the passing wake. These onsets following different trajectories result in coherent structures travelling downstream and form a band of disturbances. The appearance of more than one coherent structure is due to the fact that, once formed, the structures convect slower than the wake, thus allowing the wake to generate new structures at points further downstream as it passes over inflectional velocity profiles. Furthermore convection of coherent structures and nonlinear interactions generate new eddies that result in a series of trajectories of pressure fluctuations causing a delay in boundary layer relaxation as appeared in Fig. 6.

To investigate further the origin of these coherent structures, contours of the phase-averaged streamwise component of velocities nondimensionalized with respect to the inlet velocity are presented on S-T diagrams for different sections of boundary layer profiles, Figs. 7(*a*)–7(*c*). The average boundary layer thickness over the rear part of the blade ($S/So>0.8$) is approximately 5.5% of chord. Figure 7(*a*) corresponds to the inner part of the boundary layer revealing the two distinct migrating disturbances, corre-

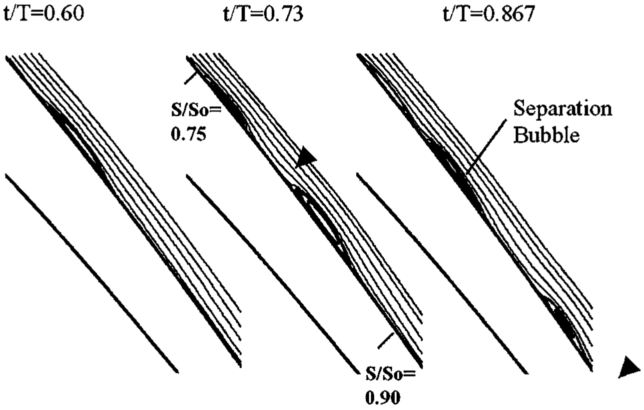

Fig. 8 Phase-averaged streamlines on rear half of the suction surface at selective phases during the wake passing cycle: The location of wake centerline is marked by a triangle

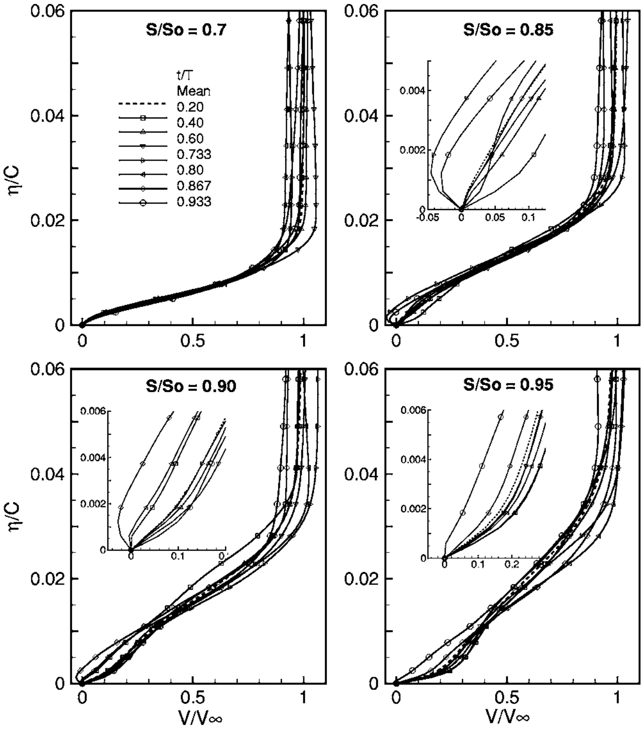

Fig. 9 Phase- and time-averaged nondimensional velocity profiles on the suction surface during the wake passing cycle

sponding to C and E in Fig. 6. Figures 7(*b*) and 7(*c*) also depict these structures, although they are progressively diluted and by $\eta/C=0.02$, which is near the mid-section of boundary layer, the coherent structures tend to disappear. Near the edge of the boundary layer, no appearance of structures are observed, only the effects of the negative jet reflecting acceleration and retardation of local free-stream velocity on either side of the wake centerline are prominent. Thus the observation confirms that the coherent structures appear from the inner-layer of the velocity profile owing to the enhanced receptivity of disturbances of the inflexional boundary layer, and while traveling downstream they remain within the boundary layer.

Unsteady Velocity Profiles. Streamlines from the phase-averaged streamwise velocity over the rare half of the suction side are depicted in Fig. 8. It reveals the changing numbers and positions of thin bubbles, from one to a maximum of three embedded in the boundary layer, appear in the rear part of the suction surface during wake passing. A close look at Fig. 8 confirms that the number of prominent coherent structures in space and time (Fig. 6) can be linked with bubbles forming on the suction surface. Thus, these apparent bubbles embedded in the boundary layer are nothing but the remains of the vortices formed by the inviscid instability as the wake passes over the inflexional boundary layer. The coherent structures, that form owing to the rollup of the separated shear layer [27], induce a backflow resulting in thin separating bubbles.

The phase-averaged velocity profiles with magnified views for the near wall regions at few representative locations over the rear half of the blade are presented in Fig. 9. This also illustrates that the occurrence of flow reversals owing to wake passing depends on the phase. For example, at $S/So=0.85$, flow reversal occurs at two phases. Hence, it can be imagined from the shape and time dependent nature of velocity profiles that bubbles appear to oscillate over the rear part $(0.7<S/So<0.95)$ of the suction surface. Although phase-averaged velocity profiles depict the existence of thin separation bubbles over the rear half of the blade, time-averaged velocity profiles illustrate the suppression of the separation bubble as a result of wake passing confirming the mean flow configuration of Schulte and Hodson [5].

Figure 10 presents the streamwise periodic velocity fluctuations $\langle u\rangle-\bar{u}$ over the rear part of the suction surface for different sections of the boundary layer. Profiles of $\langle u\rangle-\bar{u}$ at the inner part of boundary layer ($\eta/C=0.003$) display a systematic undulation with appearance of dips for phases $t/T>0.60$. These dips in the profile of $\langle u\rangle-\bar{u}$ can be related to the coherent vortices and hence to the bubbles appearing over the blade in Fig. 8. A thin separation bubble is expected beneath a rollup vortex. For example, at $t/T=0.6$, a dip in the $\langle u\rangle-\bar{u}$ profile has appeared near $S/So=0.8$, which corresponds to the formation of a bubble on the surface around the same location. At $t/T=0.733$ and 0.867, respectively, two and three dips in the $\langle u\rangle-\bar{u}$ profiles have formed and those exactly correspond to two and three bubbles appearing on the surface as depicted in Fig. 8. Moreover, magnitude and location of pressure oscillations ($P\approx V^2$) as seen in Fig. 6 can be correlated with the dip in $\langle u\rangle-\bar{u}$ profiles, marked as 1, 2, 3 on the Figs. 6 and 10 for the same phase. The discussion linking the following Figs. 6, 8, and 10 confirms that the pressure fluctuations on the rear part of the suction surface are attributed to the rollup vortices formed by instability of the shear layer through the inviscid mechanism.

Figure 10 also indicates that for $t/T<0.6$, as the wake approaches the steady flow separation region, profiles of $\langle u\rangle-\bar{u}$ present no remarkable dip. This illustrates that rollup vortices form owing to interactions of the passing wake and the flow separation. The presence of the vortical structures is not distinguishable at a normal distance of 2% of chord from the wall. This is in agreement with Fig. 7, confirming that the vortical structures remain within the boundary layer as they are convected downstream. The core of these vortical structures lies approximately at a third of the local time-averaged boundary layer thickness from the wall, which compares good with the core locations of similar vortical structures an evidenced experimentally by Stieger et al. [16]. The variation of $\langle u\rangle-\bar{u}$ obtained at $\eta/C=0.045$ simply reflects the effect of the negative jet.

Visualization of Flow Structure on the Suction Surface. A zoomed view of instantaneous velocity vectors, streamlines, and iso-contours of spanwise vorticity (ω_z) along the mid-span section for the rear part of the blade at instants of time during the wake passing cycle can be very revealing. Velocity vectors are shown on alternate mesh points. For instance, velocity vectors plot at $t/T=0.8$ [Fig. 11(*a*)] indicate that velocity profile becomes inflexional at about $S/So=0.8$ and a small separation bubble has formed. This is followed by two large regions of flow reversal. The streamlines patterns illustrate that these separated regions are

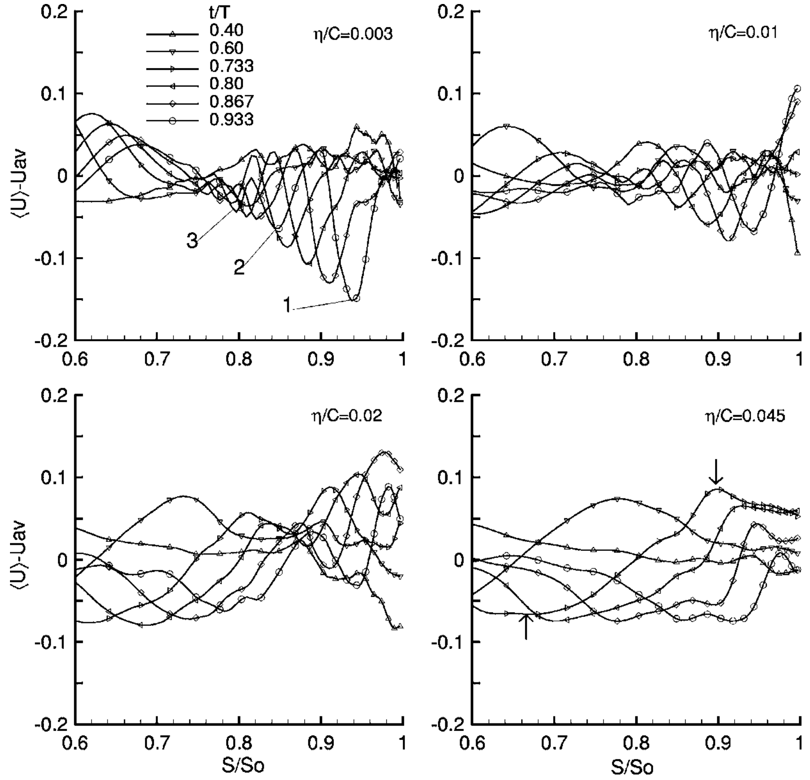

Fig. 10 Streamwise component of phase-averaged velocity perturbations $\langle U\rangle - \bar{U}$ at different sections of boundary layer over the suction surface. Arrows indicate the maximum and minimum velocity by the negative jet

nothing but the manifestation of vortices formed as the wake has passed over the region of inflexional velocity profiles. Isocontours of spanwise vorticity depict the development of cat's eye patterns in the computed flow field, typical of the KH instability; thus these vortices embedded in the boundary layer are formed by rollup of the separated shear layers through an inviscid instability as the shear layers are perturbed by the wake fluid. Once the vortices are formed, the region of steady flow separation changes remarkably by convection of these coherent structures. Positive values of vorticity, indicated by black patches on the surface, represent regions of thin flow reversal induced by these convective vortices. Figures 11(*b*) and 11(*c*) demonstrate the same flow features as explained illustrating growth of vortices while they convect downstream. The coherent vortices retain their presence even near to the training edge. Walmuff [15] observed appearance of a cat's eye pattern in contours of measured spanwise vorticity while studying amplification of the wave packet in a separation bubble and he concluded that the instability mechanism is predominantly inviscid. In the present study, the instability mechanism, the nonlinear interaction and the roll-ups of shear layer evolve large-scale vortex loops (*coherent structures*), that retain their presence far downstream of separation before breakdown, are similar to those observed by Watmuff [15]. There are evidences both experimental [30,31] and numerical [32] that these coherent structures forming inside the boundary layer may cause large pressure fluctuations.

Iso-surface of spanwise component of instantaneous vorticity (ω_z) are also plotted in Fig. 12 to illustrate the three-dimensional flow structures. Apart from the formation of 3D vortex loop in the boundary layer, its downstream convection and growth owing to nonlinear interactions before breaking down to small structures, the figure reveals the appearance of longitudinal streaky structures, characteristics of transition boundary layer [6,33,34]. It appears that the steaks are nothing but elongated legs of Λ-vortices created by vortex stretching process. Thus the transition is characterized by the breakdown of these Λ-vortices over the separating shear layer. The breakdown of the streaks into small and irregular structures that enhance turbulence is observed downstream of $S/So=0.9$. The very similar mechanism is proposed by Alam and Sandham [35] through DNS while studying the transition mechanism of a laminar separation bubble. The appearance of periodic 3D coherent structures that retain their identity far downstream before breaking down influences on generation of turbulence and the transition process becomes time-dependent. It is worthwhile to mention that the unsteady Reynolds-averaged Navier-Stokes (URANS) calculations with transition and turbulence models may fairly reproduce the surface characteristics and losses, but they fail to capture the details of dynamics of separation bubble and the onset of instabilities when interacted by the passing wakes [36]. DNS and LES are successful in this regard at the cost of computational time.

Flow topology generating coherent structures owing to the interactions of migrating wakes and the separated shear layer over T106 blade profile can be schematically illustrated in Fig. 13. Figure 13(*a*) depicts the flow as the wake is approaching the separated shear layer. The shape of the bubble is approximated by the separating stream surface. The wake can be modeled as a negative jet, which impinges on the blade and splits into two streams; one pointing downstream that accelerates the flow downstream of the approaching wake and other pointing upstream that retards the flow after the wake has passed. As the wake convects over the separation bubble, the normal component of negative jet deforms the separation bubble as shown in Fig. 13(*b*). The separated layer is naturally unstable and the enhanced perturbation created by the convective wake develops rollup of shear layer via KH instability. The process results in two coherent vortices and can be correlated to those denoted by C and E while discussing on phase-averaged surface pressure in Fig. 6. These rollup vortices convect at 37% of the local free-stream velocity and thus the wake, which convects

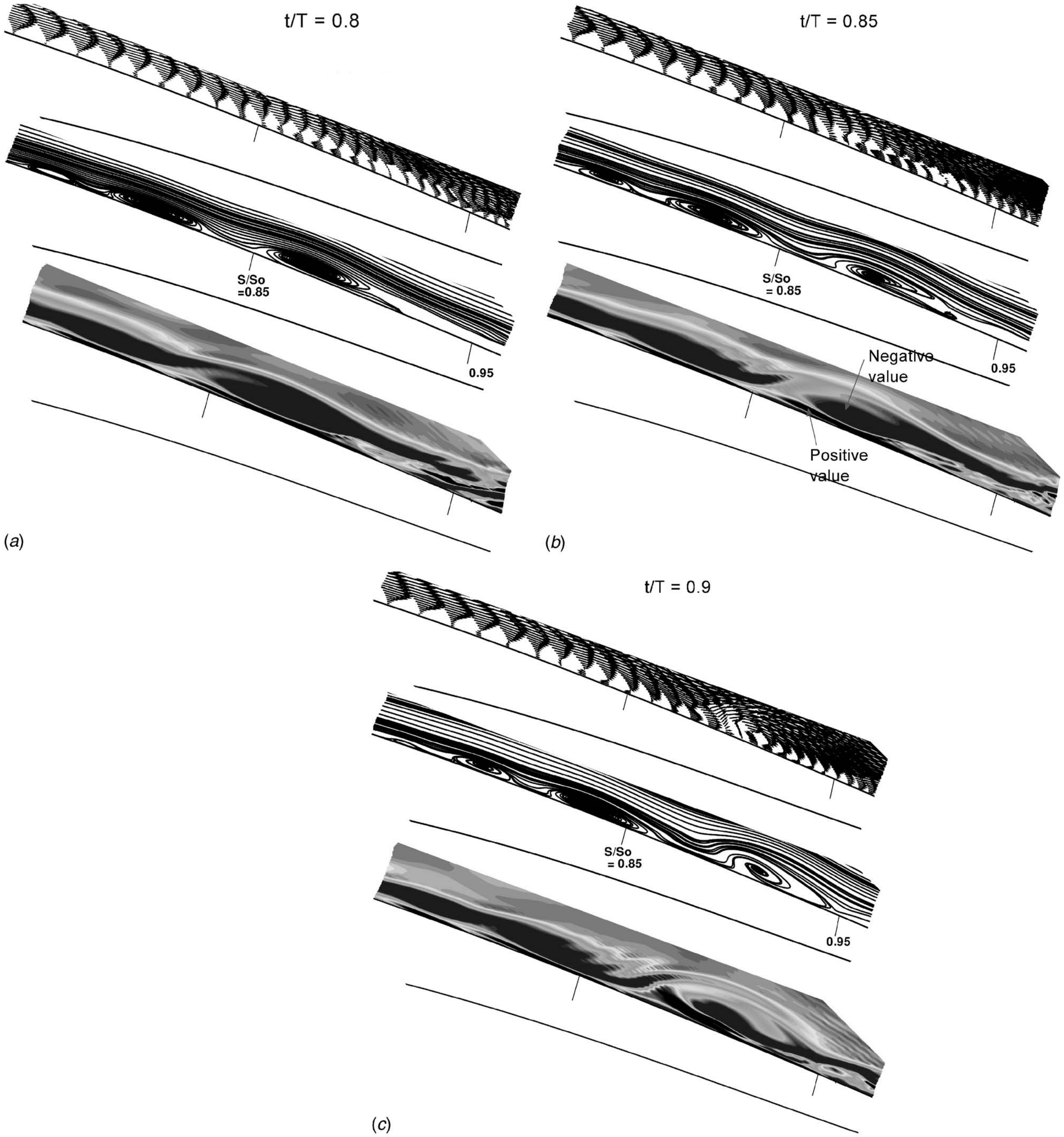

Fig. 11 Instantaneous velocity vectors, streamline, iso-contour of spanwise vorticity over the rear of the suction surface

with the free-stream, moves ahead of these structures and perturbs the separated layer further downstream. This results in generation of further rollup vortex marked as D in Fig. 13(*c*). As the wake has crossed the separated region, a train of apparently three prominent coherent vortices appear for the case studied and retain their presence far downstream before breakdown to small structures, Fig. 13(*d*). Once the influence of passing wake has subsided, the shear layer again begins to separate.

Conclusions

The present LES in conjunction with the earlier experiments reveal that the enhanced receptivity of perturbations associated with the inflexional velocity profile is the cause of instability of the boundary layer over the suction surface of a LP turbine. Coherent vortices form over the rear half of the suction surface by the rollup of shear layer via Kelvin-Helmholtz mechanism as the wake passes over the separation region. These coherent structures embedded in the boundary layer amplify before breakdown while traveling downstream with a convective speed of about 37% of the local free-stream speed. Once the vortices are formed, the steady-flow region of separation changes remarkably. Thin regions of flow reversals are induced beneath these vortices. The transition process on the suction surface can be thought of as the combined effects of breakdown of the longitudinal streaks and the convection of periodic coherent structures appeared owing to the wake passing over the inflexional layer. Pressure fluctuations of large amplitude occur on the suction surface as the wake passes over the rear half of the blade. The numerical flow visualizations

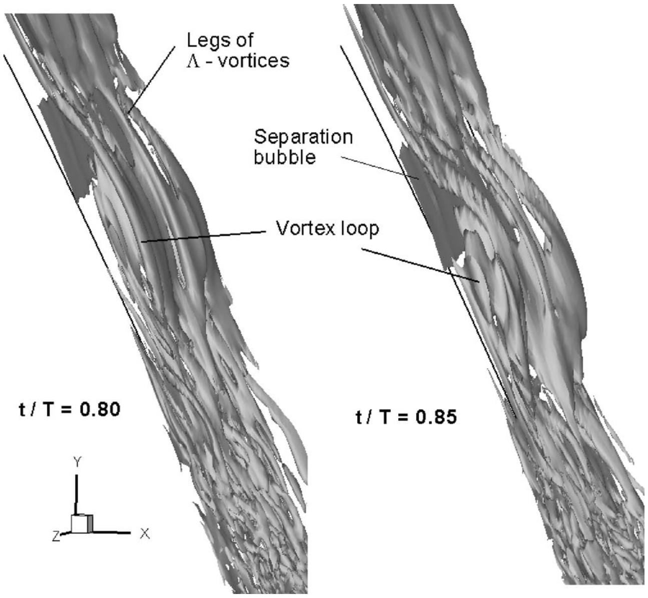

Fig. 12 Instantaneous iso-surface of spanwise component of vorticity on the rear half of the suction surface

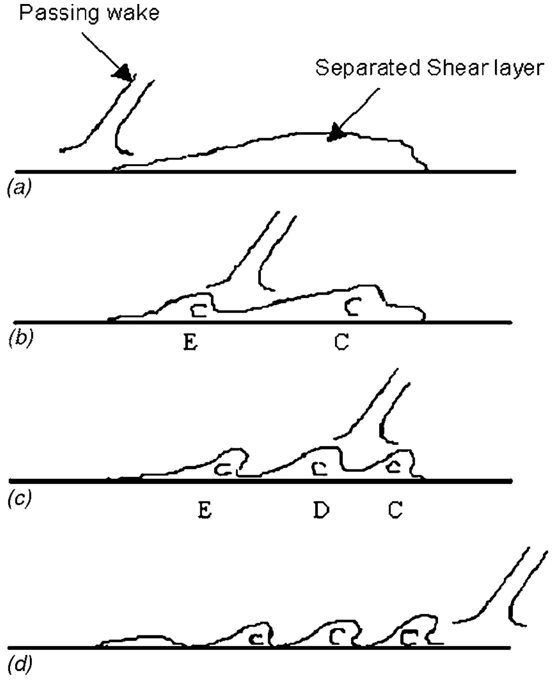

Fig. 13 Schematic of coherent vortices formation mechanism

identify that the coherent structures appeared in the boundary layer are the source of large pressure fluctuations over the rear half of the suction surface.

Acknowledgment

The support for a part of this work from the UK Engineering and Physical Sciences Research Council and Rolls Royce plc is gratefully acknowledged.

Nomenclature

C = chord
C_X = axial chord
D = bar diameter
f = bar passing frequency
P = local surface pressure
Re = Reynolds number$=V_{2is}C/\nu$
S = distance along blade surface
So = suction surface length
t = time
T = bar passing period
U_b = bar speed or blade speed
V = velocity
x,y,z = Cartesian coordinates
$\Delta x^+,\Delta y^+,\Delta z^+$ = mesh size in wall units
V_X = axial velocity
η = wall-normal axis
η^+ = wall-normal distance in wall units
ν = kinematic viscosity

Subscripts

0 = total
1 = inlet
2 = exit
is = isentropic

References

[1] Mayle, R. E., 1991, "The Role of Laminar Turbulent Transition in Gas Turbine Engines," ASME J. Turbomach., **113**, pp. 509–537.

[2] Liu, X., and Rodi, W., 1992, "Measurement of Unsteady Flow and Heat Transfer in a Linear Turbine Cascade," ASME Paper No. 92-GT-323.

[3] Walker, G. J., 1993, "The Role of Laminar Turbulent Transition in Gas Turbine Engines: A Discussion," ASME J. Turbomach., **115**, pp. 207–217.

[4] Halstead, D. E., Wisler, D. C., Okiishi, T. H., Walker, G. J., Hodson, H. P., and Shin, H. W., 1997, "Boundary Layer Development—Part 1: Composite Picture; Part 2: Compressors; Part 3: LP Turbines; Part 4: Computational Analysis," ASME J. Turbomach., **119**, pp. 114–138.

[5] Schulte, V., and Hodson, H. P., 1998, "Unsteady Wake-Induced Boundary Layer Transition in High Lift LP Turbine," ASME J. Turbomach., **120**, pp. 28–35.

[6] Wu, X., Jacobs, R. G., Hunt, J. R. C., and Durbin, P. A., 1999, "Simulation of Boundary Layer Transition Induced by Periodically Passing Wakes," J. Fluid Mech., **398**, pp. 109–153.

[7] Horton, H. P., 1969, "A Semi-Empirical Theory for the Growth and Bursting of Laminar Separation Bubbles," ARC CP 1073.

[8] Roberts, W. B., 1980, "Calculation of Laminar Separation Bubbles and Their Effect of Airfoil Performance," AIAA J., **18**, pp. 25–31.

[9] Tani, I., 1964, "Low Speed Flows Involving Separation Bubbles," *Progress in Aeronautical Science*, Pergamon, New York.

[10] Hatman, A., and Wang, T., 1998, "Separated-Flow Transition, Part 1—Experimental Methodology, Part 2—Experimental Results, Part 3—Primary Modes and Vortex Dynamics," ASME Paper Nos., 98-GT-461, 98-GT-462 and 98-GT-463.

[11] Hatman, A., and Wang, T., 1999, "A Prediction Model for Separated-Flow Transition," ASME J. Turbomach., **121**, pp. 594–602.

[12] Malkiel, E., and Mayle, R. E., 1996, "Transition in a Separation Bubble," ASME J. Turbomach., **118**, pp. 752–759.

[13] D'Ovidio, A., Harkins, J. A., and Gostelow, J. P., 2001, "Turbulent Spot in Strong Adverse Pressure Gradient: Part 1—Spot Behavior," ASME Paper No. 2001-GT-0194.

[14] D'Ovidio, A., Harkins, J. A., and Gostelow, J. P., 2001, "Turbulent Spot in Strong Adverse Pressure Gradient: Part 2—Spot Propagation and Spreading Rates," ASME Paper No. 2001-GT-0407.

[15] Watmuff, J. H., 1999, "Evolution of a Wave Packet Into Vortex Loops in a Laminar Separation Bubble," J. Fluid Mech., **397**, pp. 119–169.

[16] Stieger, R., Hollis, D., and Hodson, H., 2003, "Unsteady Surface Pressures Due to Wake Induced Transition in Laminar Separation Bubble on a LP Turbine Cascade," ASME Papar No. GT2003-38303.

[17] Voke, P. R., and Yang, Z. Y., 1995, "Numerical Study of Bypass Transition," Phys. Fluids, **7**, pp. 2256–2264.

[18] Yang, Z. Y., and Voke, P. R., 2001, "Large-Eddy Simulation of Boundary Layer Separation and Transition at a Change of Surface Curvature," J. Fluid Mech., **439**, pp. 305–333.

[19] Smagorinsky, J., 1963, "General Circulation Experiments With the Primitive Equations. I: The Basic Experiment," Mon. Weather Rev., **91**, pp. 99–164.

[20] Voke, P. R., 1996, "Subgrid-Scale Modeling at Low Mesh Reynolds Number," Theor. Comput. Fluid Dyn., **8**, pp. 131–143.

[21] Huai, X., Joslin, R. D., and Piomelli, U., 1997, "Large-Eddy Simulation of Transition to Turbulence in Boundary Layers," Theor. Comput. Fluid Dyn., **9**(2), pp. 149–163.

[22] Piomelli, U., Ferziger, J. H., and Moin, P., 1987, "Models for Large Eddy Simulation of Turbulent Channel Flows Including Transpiration," Thermoscience Division, Department of Mechanical Engineering, Stanford University, Report TF-32.

[23] Hue, K., and Lee, S. L., 1991, "A Numerical Technique for Two-Dimensional Grid Generation With Grid Control at All of the Boundaries," J. Comput. Phys., **96**, pp. 451–469.

[24] Wu, X., and Durbin, P. A., 2001, "Evidence of Longitudinal Vortices Evolved from Distorted Wakes in Turbine Passage," J. Fluid Mech., **446**, pp. 199–228.

[25] Williamson, C. H. K., and Roshko, A., 1990, "Measurements of Base Pressure in the Wake of a Cylinder at Low Reynolds Number," Z. Flugwiss. Weltraumforsch., **14**, p. 38.

[26] Ghosal, S., and Rogers, M. M., 1997, "Anumerical Study of Self-Similarity in a Turbulent Plane Wake Using Large-Eddy Simulation," Phys. Fluids, **9**, pp. 1729–39.

[27] Sarkar, S., and Voke, P. R., 2003, "LES of Passing Wakes Influencing Transition on Turbine Blades" Direct and Large-Eddy Simulation V, *Proceedings of ERCOFTAC workshop*, R. Friedrich, B. J. Geurts, and O. Métais, ed., Kluwer Academic Publishers, Dordreecht.

[28] Stadtmüller, P., and Fottner, L., 2002, "A Test Case and Experimental Measurements on T106," private communication with Lothar Hilgenfeld.

[29] Meyer, R. X., 1958, "The Effects of Wakes on the Transient Pressure and Velocity Distributions in Turbomachines," ASME J. Basic Eng., **80**, pp. 1544–1552.

[30] Lee, S., and Bershader, D., 1994, "Head-On Parallel Blade-Vortex Interaction," AIAA J., **32**, pp. 16–22.

[31] Saathoff, P. J., and Melbourne, W. H., 1997, "Effects Do Free-Stream Turbulence on Surface Pressure Flactuations in a Separation Bubble," J. Fluid Mech., **337**, pp. 1–24.

[32] Luton, A., Ragab, S., and Telionis, D., 1995, "Interaction of Spanwise Vortices With a Boundary Layer," Phys. Fluids, **7**, pp. 2757–2765.

[33] Alfredsson, P. H., and Matsubara, M., 1996, "Streak Structure in Transition," *Transitional Boundary Layer in Aeronautics*, (R. A. W. M. Henkes and L. J. Ingen, eds., pp. 374–386, Elsevier, New York.

[34] Westin, K. J. A., Boiko, A. V., Klingmann, B. G. B., Kozlov, V. V., and Alfredsson, P. H., 1994, "Experiments in a Boundary Layer Subjected to Free Stream Turbulence. Part 1. Boundary Layer Structure and Receptivity," J. Fluid Mech., **281**, pp. 193–218.

[35] Alam, M., and Sandham, N. D., 2000, "Direct Numerical Simulation of Short Laminar Separation Bubbles With Turbulent Reattachment," J. Fluid Mech., **410**, pp. 1–28.

[36] Michelassi, V., Wissink, J. G., and Rodi, W., 2003, "Direct Numerical Simulation, Large Eddy Simulation and Unsteady Reynolds-Averaged Nanier-Stokes Simulations of Periodic Unsteady Flow in a Low-Pressure Turbine Cascade: A Comparison," Bussei Kenkyu, **217**, pp. 403–411.

Brian M. Holley
Department of Mechanical Engineering,
University of Connecticut,
191 Auditorium Road,
U-3139,
Storrs, CT 06269

Sandor Becz
Pratt & Whitney,
400 Main Street,
MS 169-29,
East Hartford, CT 06108

Lee S. Langston
Department of Mechanical Engineering,
University of Connecticut,
191 Auditorium Road,
U-3139,
Storrs, CT 06269

Measurement and Calculation of Turbine Cascade Endwall Pressure and Shear Stress

The complex three-dimensional fluid flow on the endwall in an axial flow turbine blade or vane passage has been extensively investigated and reported on in turbomachinery literature. The aerodynamic loss producing mechanisms associated with the endwall flow are still not fully understood or quantitatively predictable. To better quantify wall friction contributions to endwall aerodynamic loss, low Mach number wind tunnel measurement of skin friction coefficients have been made on one endwall of a large scale cascade of high pressure turbine airfoils, at engine operating Reynolds numbers. Concurrently, predictive calculations of the endwall flow shear stress have been made using a computational fluid dynamics (CFD) code. Use of the oil film interferometry skin friction technique is described and applied to the endwall, to measure local skin friction coefficients and shear stress directions on the endwall. These are correlated with previously reported measured local endwall pressure gradients. The experimental results are discussed and compared to the CFD calculations, to answer questions concerning endwall aerodynamic loss predictive ability. [DOI: 10.1115/1.2137744]

Introduction

The first jet engine-powered flight took place in Germany and the first operation of a gas turbine to generate electrical power occurred in Switzerland, both in 1939. Since then, initial thermal efficiencies of about 18% have risen steadily over the years to contemporary values well into the 40–45% range. Over the last half century, countless contributions from engineering research, and continuous improvements in design and performance analysis, have brought about this steady thermodynamic efficiency advancement, to make the gas turbine the flexible, versatile and economic energy converter it is today, for both aviation flight and electrical power generation.

Fundamental to this steady improvement in gas turbine efficiency have been advances made in experimental and analytical understanding of gas path aerodynamics, i.e., in an axial flow machine, the flow through blades and vane airfoil passages. Early on, designers were able to use two-dimensional descriptions of gas path flows. Now, with modern machines characterized by higher blade loadings and fewer stages, designers depend on full three-dimensional fluid flow descriptions—both experimental and computational fluid dynamic (CFD) models—on which to base gas path design.

The subject of this paper deals with three-dimensional flow in one type of gas turbine component, an axial flow turbine, as depicted in Fig. 1 (see Ref. [1]). The hardware sketched in Fig. 1 represents a plane (or linear) cascade, depicting the airfoils and endwalls in an axial flow turbine with a very large (infinite) radius. For many years now, experimenters studying complex three-dimensional flows in axial turbines, have made use of planar cascades to sort out and measure fluid flow and heat transfer features. Numerical calculators modeling these flows have also relied on simple plane cascade geometries to attempt to "postdict" existing cascade data, or to separate out the effect of various analytical techniques (such as turbulence models).

The part of the gas path flow influenced by the inner and outer casings of an axial flow turbine is defined by the designer as secondary or endwall flow, depicted in Fig. 1 by the ribbon arrows on the endwall of the plane cascade of turbine airfoils. This flow phenomenon constitutes one of the most commonplace and widespread three-dimensional flows, arising in axial flow turbomachinery generation of electrical and motive (air) power. The basic flow picture depicted in Fig. 1 has been validated by many investigators, too numerous to mention here. Sieverding [2] gives a detailed summary of earlier secondary flow work and Langston [3] provides a survey and evaluation of open literature investigations carried out since the Sieverding review was published.

Endwall flows are responsible for a loss of lift (loss of turbine work) and an increase in aerodynamic loss (increase in gas path entropy). In typical modern day turbine designs, endwall flows can account for over 30% of the total pressure loss through a turbine stage, which can lead to a reduction in turbine efficiencies on the order of three points of turbine efficiency.

There are no closed form analytical solutions to completely describe the secondary endwall flow depicted in Fig. 1. Since the 1980's (e.g., see Hah [4]) numerical calculators using CFD codes have been able to predict many features of the secondary flow. However, their ability to routinely predict aerodynamic losses accurately has been unsuccessful (e.g., see Langston [3]). When endwall flows can cause 30% (or more) of such losses, this inability is a serious handicap for a company's engine design system.

For some years, the lack of an accurate turbulence model has been the accepted reason for the inability of CFD models to predict endwall losses. But there is strong evidence that turbulence is not a first order effect. Early work by Senoo [5] and later by Langston, Nice, and Hooper [6] had indicated that the highly skewed and very thin portions of the endwall boundary layer are laminar. Subsequent experimental studies by Harrison [7,8] have clearly shown that these endwall boundary layer regions are indeed laminar.

Harrison [7] was able to measure endwall shear stresses using an oil-drop viscosity balance method, which enabled him to present a map of constant wall shear stress lines and shear stress coefficients for his cascade endwall. He concluded that the wall shear stress values were high, but that the endwall boundary layer did not have an overriding significance in the generation of cascade aerodynamic loss.

However, Harrison's reasoning on the contribution of the high

---

Contributed by the International Gas Turbine Institute (IGTI) of ASME for publication in the JOURNAL OF TURBOMACHINERY. Manuscript received October 1, 2004; final manuscript received February 1, 2005. IGTI Review Chair: K. C. Hall. Paper presented at the ASME Turbo Expo 2005: Land, Sea and Air, Reno, NV, June 6–9, 2005, Paper No. GT2005-68256.

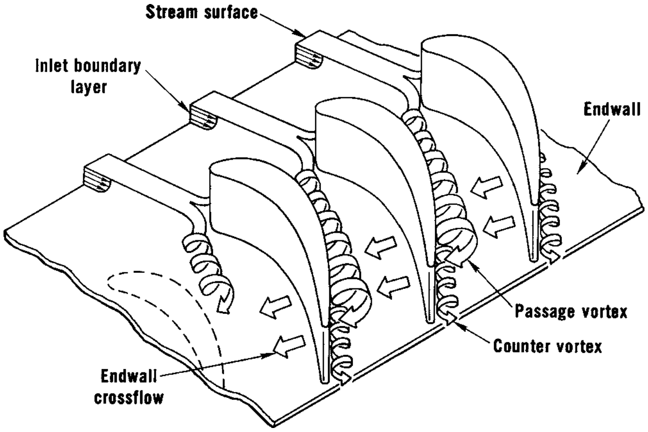

Fig. 1 The three-dimensional separation of a boundary layer entering a planar turbine cascade (from Langston [1])

shear stresses measured on the cascade endwall to loss was based on two-dimensional boundary layer arguments. Also, he did not report on the endwall pressure distribution he measured. Knowledge of the pressure gradients on the endwall are necessary if one is to model or understand the endwall shear stress values produced by the highly skewed endwall boundary layer.

What will be done in this paper is to carry on the earlier work of Harrison [7], to see what extent endwall shear stresses contribute to the loss. Data will be presented on measured endwall skin friction coefficient using an oil film interferometry (OFI) technique. This will be complimented by endwall pressure distribution data taken from Langston, Nice, and Hooper [6] to yield local endwall pressure gradients. Both the endwall pressure gradient data and the endwall shear stress data will then be compared with CFD calculations to try to answer the questions concerning endwall aerodynamic loss predictive ability. Both sets of data, the endwall shear stress and pressure gradient values and locations, are necessary for fully understanding and modeling the endwall boundary layer itself.

Description of Experiment

The current endwall shear stress data and the previously acquired end wall pressure data were collected from the same large scale, low speed cascade wind tunnel. The cascade consists of four JT9D-34 turbine airfoils scaled to ten times engine size. The geometry of the cascade is given in Fig. 2 and as follows:

Axial chord	$b_x = 0.281$ m
Chord/axial chord	1.2242
Pitch/axial chord	0.9555
Span/axial chord	0.9888
Mean camber line angles	43.99 deg, 25.98 deg

Periodicity of the cascade is established through adjustment of the tailboards and bleeds so that the flow around airfoil two and the pressure side of airfoil three matches the potential flow solution as indicated by midspan static pressure taps on the airfoils. The agreement between the static pressure measurements and potential flow solution is shown in Fig. 3. Very good agreement is seen, giving confidence that the data taken from the measurement passage will be representative of an infinite cascade. The inlet angle of the cascade is set at 44.7 deg, and the nominal Reynolds number based on axial chord and cascade inlet velocity (usually about 34 m/s) is 5.9×10^5. The boundary layer is described at the upstream location (Fig. 2) with the following:

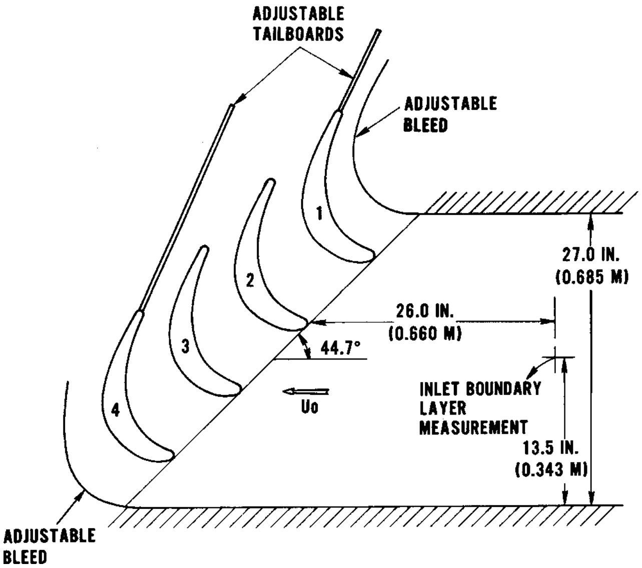

Fig. 2 Schematic of the large-scale airfoil cascade used for measurements of total pressure loss, endwall static pressure, and endwall skin friction coefficient. The inlet boundary layer measurement location also serves as a reference location for total pressure and velocity head.

Boundary layer thickness	3.30 cm
Displacement thickness	0.376 cm
Momentum thickness	0.279 cm
Shape factor	1.35
Momentum thickness Reynolds number	5338

The boundary layer thickness was measured to be within 3% of that measured by Langston, Nice, and Hooper [6]. The skin friction coefficient at this upstream location was measured using OFI, and found to be $C_f = 0.0034$. Text book correlations using the measured momentum thickness for turbulent flow over a flat plate yielded $C_f = 0.0031$, showing good agreement.

Measurements of total and static pressures along with velocity direction were acquired with a five-hole probe. The probe tip diameter is 2.41 mm, and the measurements were taken with the probe nulled in yaw. Further detail of the five-hole probe measurements is provided by Langston, Nice, and Hooper [6].

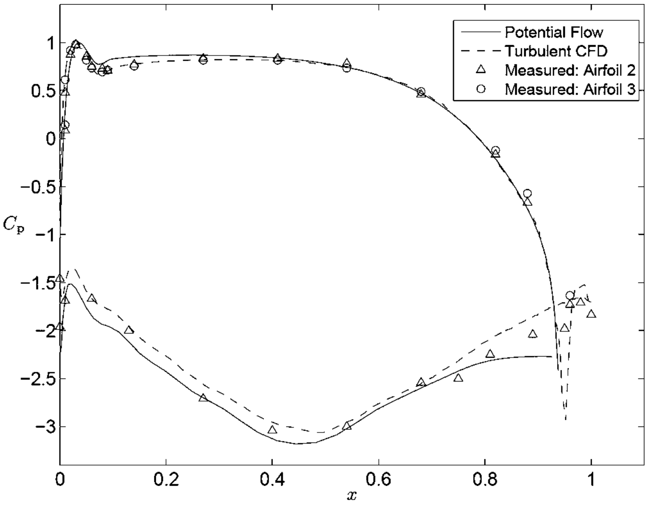

Fig. 3 Agreement among midspan airfoil static pressures from potential flow, turbulent CFD, and measurement

The endwall pressure data treated here are also taken from the work of Langston, Nice, and Hooper [6]. The pressure data were collected using the same cascade wind tunnel and airfoils, and under identical test conditions, as reported on here for the endwall shear stress measurements.

In the earlier work, one endwall of the tunnel was constructed with 13 sliding bars embedded in it. Each slider can be traversed gapwise and had provisions for accepting a fixture for measuring wall static pressure. This arrangement permitted data acquisition at various axial positions upstream of, within, and downstream of the cascade. The endwall and sliders were sealed with Teflon gaskets and lapped to form a smooth composite surface.

The OFI technique was used to measure endwall skin friction coefficients. An oil film on a surface in a wind tunnel will spread and thin due to the shear acting upon it. Under appropriate conditions, the film thickness will be reduced enough for it to be measured interferometrically. Knowledge of the film thickness profile in the direction of flow over it provides shear stress information. Good explanations of the technique are provided by Naughton and Sheplak [9], Driver [10], and Davy et al. [11]. The following equation is used to evaluate C_f

$$C_f = \frac{2\ell\sqrt{n_o^2 - n_a^2 \sin^2 \alpha}}{\lambda \int \frac{1}{2}\frac{\rho U_o^2}{\mu_o}dt} \tag{1}$$

The equation represents three main quantities: (1) the slope of the oil film height versus length, (2) the reference velocity head, and (3) the oil viscosity, the latter two being integrated over the wind tunnel run time. The indices of refraction are tabulated properties of air and oil. The oil used is Dow Corning 200 Silicone fluid with nominal viscosities of 100 and 1000 cSt. Temperature corrections used for oil viscosity were taken from Naughton and Sheplak [9]. The viscosity of the oils were measured at six temperatures ranging from 15–40°C, and the measurements agreed with the correlation within 0.5%. The angle of reflection is dependent on the optical arrangement, and is measured. The light wavelength is a property of the source used, which was for this study a low pressure sodium lamp ($\lambda = 589.0, 589.6$ nm). Velocity head was measured with a Pitot-static probe at the reference location (midspan), which also served as the location for the reference inlet boundary layer measurement (Fig. 2). Ambient temperature along with the temperature in the cascade entrance section were measured using thermocouples. LabVIEW data acquisition software was used to record the velocity head and temperature quantities throughout a wind tunnel run.

The collection and analysis of fringes is described as follows. Prior to each run a rectangular piece of 0.05 mm thick nickel (14% wt. Tungsten) foil was adhered to the endwall. A series of oil patches was applied to the nickel, and the wind tunnel was brought up to the nominal Reynolds number, where it was maintained within ±2%. When fringes were apparent on the nickel under ambient light, the wind tunnel was shut down, and the nickel was removed for photographs under the monochromatic light source. See Fig. 4 for examples of fringe patterns. The fringe spacing from one pattern to the next varies due to varying shear along the surface. Regions of higher shear yield longer fringe spacing. The leading edge of the foil had no observable effect on the skin friction coefficient measurement, unless an oil patch began very close to the foil edge ($\lesssim 1$ mm). Provided the oil patches were applied more than that distance away from the foil leading edge, skin friction coefficient measurements were insensitive to location on the foil. The fringe images were analyzed using XFIG, a drawing package. The fringe spacing is taken as an average over typically five fringes, the midpoint along that length being the location assigned to the skin friction coefficient value. The spatial, pressure, and temperature data were analyzed using MATLAB, a numerical computation software. The analyzed data yielded skin friction coefficients and shear directions. An uncertainty analysis pertaining to Eq. (1) and its particular application in this paper was performed, and the skin friction coefficient measurements are expected to have an experimental uncertainty of ±3% (others have quoted ±4% [9]). The main contributions to error are in ℓ and temperature, which affects μ_o.

Fig. 4 Fringe patterns due to light interference from an oil patch thinned due to shear

CFD Modeling

A computational solution using CFD software from Fluent, Inc. was developed for the same cascade geometry and test conditions as the shear stress measurement data. A Reynolds averaged Navier-Stokes (RANS) solution was obtained using an unstructured grid with a viscous mesh and the shear-stress transport (SST) version [12] of the k-ω turbulence closure model. The leading edge grid region and internal passage grid are shown in Fig. 5. The first node of the endwall grid was set to be within a distance of $y^+ \leqslant 1$, with additional grid clustering near the wall. In addition, using the built-in adaptation within Fluent, regions of large velocity gradient were identified and their mesh densities continually increased until no further change in mass-averaged total pressure loss was evident. Grid independence was achieved using this technique. The final grid consisted of 318,972 nodes. The inlet boundary conditions were set to exactly duplicate the cascade conditions at which endwall shear stress was measured. This involved imposing an inlet boundary layer velocity profile which matched measurements taken at the reference location of Fig. 2. As an additional check on the suitability of the prescribed boundary layer, shear stress measurements were also taken at the reference location to compare with the computationally determined results. The measured value of C_f was 0.0034, while the value from the CFD simulation was 0.0035, in very close agreement with the data.

The inlet turbulence quantities were set by prescribing turbulence intensity and length scale values representative of previous measurements made in the existing cascade. Turbulence intensity was set to 1.0%, while the length scale was set to 6.4 mm. The turbulence intensity values are lower than what is typically encountered in a gas turbine engine. However, the intention here is to model the exact conditions of the experimental cascade rather than represent typical engine conditions. It can be noted, however, that previous research has shown turbulence intensity to have a weak effect on aerodynamic loss [13–15].

One passage of the experimental cascade was modeled, with a periodic boundary condition set in the pitchwise direction to reproduce an infinite cascade. One half of the span was included in the model, with a symmetry plane condition set at the passage midspan. A second order discretization was used for all solved quantities, including turbulence parameters. Additional information regarding specifics of the numerical solver, including validation and verification of the CFD code, can be found in the Fluent user's manual [16]. When attempting to predict secondary flow features, it is important to ensure correct airfoil loading in the

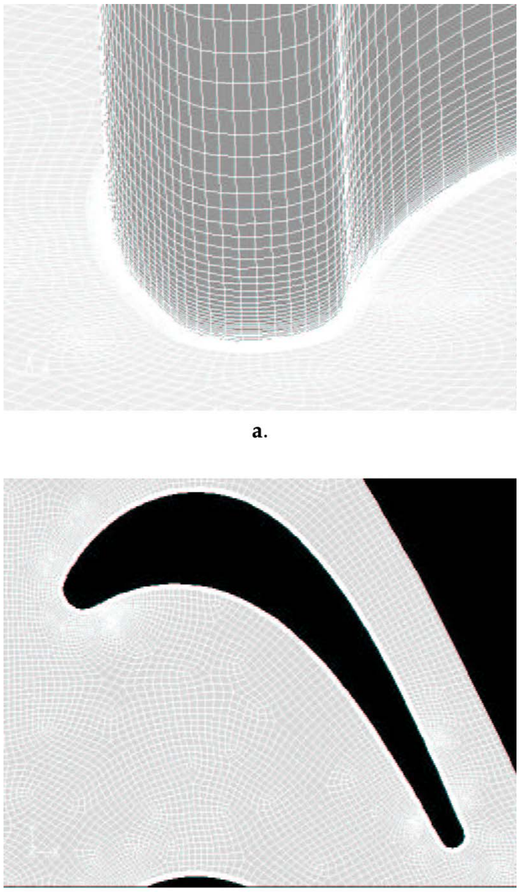

Fig. 5 Computational grid at (*a*) airfoil leading edge and on the endwall (*b*)

simulation, since this will have a direct impact on secondary flow loss. To check the CFD results in this regard, the midspan pressure distributions from the simulation were compared with the experimentally measured values used to establish periodicity in the cascade. The comparison is shown in Fig. 3. The simulation is clearly in excellent agreement with the data.

Results and Discussion

The primary concerns of this study are to better understand endwall aerodynamic loss producing mechanisms and, through this understanding, to improve loss predictive ability. This is addressed first by demonstrating an example of current loss predictive ability, using a proven readily available CFD code. Following that are comparisons between predicted and measured features of the flow: endwall static pressures and skin friction coefficients.

Total Pressure Distribution. One of the stated motivations for these experiments is the inability of CFD to accurately predict the overall total pressure loss in a turbine passage. For the turbine cascade in this study, the CFD model overpredicts aerodynamic losses significantly. Given this behavior, it is instructive to determine where the deviations between prediction and measurement occur. Figure 6 presents a plot of the evolution of mass-averaged total pressure loss coefficient from just upstream of the airfoil leading edge to approximately 40% of axial chord downstream of the trailing edge. As the flow moves through the passage, the measured values of loss stay relatively flat until the area of uncovered turning (defined as the area of the passage beyond the throat in the streamwise direction), starting at approximately 80% of axial chord. In contrast, the CFD solution predicts a sharper increase in loss as soon as the flow has entered the passage, rising well above the experimental values. The computational values do show the same trend in sharp loss increase in the area of uncovered turning, maintaining approximately the same percentage of overprediction in total pressure loss through the remainder of the region considered. By the time the flow has moved to the final point at 40% of axial chord downstream of the trailing edge, the CFD has overpredicted the mass-averaged total pressure loss by about 30%. This CFD simulation errs most on a percentage basis in the region between the cascade entrance and the area of uncovered turning.

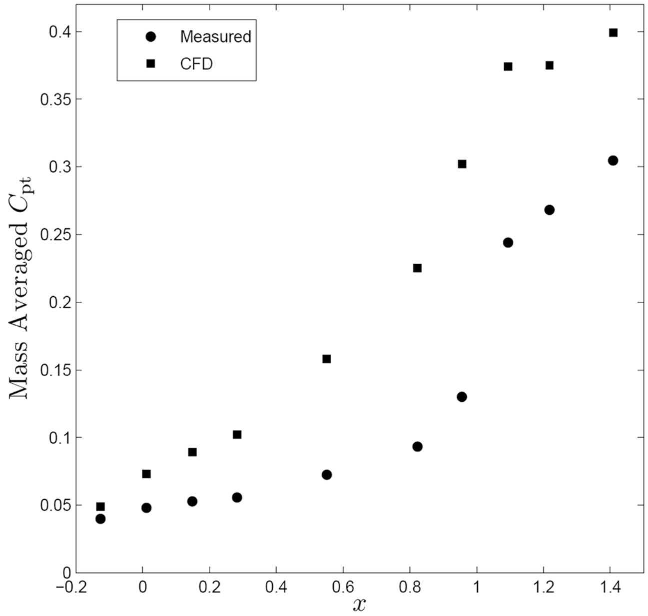

Fig. 6 Development of measured and turbulent CFD predicted mass averaged total pressure coefficient through cascade

Figure 7 is a plot of the percentage difference between the predicted and measured mass-averaged total pressure loss coefficient, with the measured values used as the reference. Upon entrance to the cascade the agreement between measured and predicted values is within 25% for a small value of C_{pt}. The largest difference between measured and predicted values occurs at x

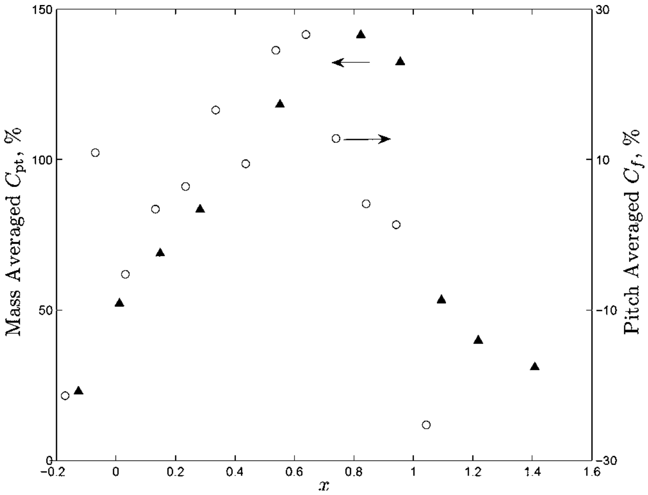

Fig. 7 Comparison between measured and turbulent CFD prediction along the axial coordinate: percent difference between mass averaged total pressure coefficient and pitch averaged skin friction coefficient

Table 1 Summary of mass-averaged total pressure loss coefficient from experiment and calculation ($x=1.1$)

Source	C_{pt}
Measured	0.246
Turbulent CFD solution	0.374
Laminar CFD solution	0.285

$=0.8$ (nearly 150%), but at the cascade exit the loss is again within 30%, a C_{pt} value eight times higher than at the entrance. Since the level of overprediction stays relatively constant after the area of uncovered turning and into the region of mixing downstream of the trailing edge, it is logical to conclude that the computational solution is primarily misrepresenting the loss within the passage itself. A better understanding of why this overprediction occurs may come with a more detailed description of the flow features, and the following sections will take a closer look at endwall pressure and shear stress distributions to determine how these areas contribute to the incorrect loss predictions.

It is interesting to note that Moore and Gregory-Smith [17] found better agreement in exit plane mass-averaged total pressure loss when the flow was modeled with a Navier-Stokes solution which included an intermittency variable to allow laminar and transitional treatment of the endwall boundary layer. To see if this same behavior would hold in the cascade geometry under consideration here, the CFD model described previously was solved using a strictly laminar flow topology. Surprisingly, the laminar simulation provides a much better prediction of total pressure loss than the RANS calculation. Table 1 presents a summary of the loss predicted with the turbulent and laminar solutions, as well as the measured value. The extreme rise in loss in the turbine passage predicted by the turbulent CFD solution, and the much better agreement in exit plane loss between the experimental and laminar flow solution, clearly points out the need for not simply a better turbulence representation with which to model the flow, but a better understanding of the endwall flow boundary layer.

Endwall Pressure Distribution. The ability to predict endwall losses in a CFD simulation is dependent upon the ability to predict endwall static pressures. The sensitivity of this dependence is not clear, but it is a matter of satisfying a boundary condition. Given the differences between measured and predicted loss, it might be expected that there are differences in the measured and predicted endwall static pressures. Figures 8(*a*) and 8(*b*) present distributions of endwall static pressure coefficient, C_p, from experimental and predicted results, respectively. While the CFD simulation does well at predicing the range of endwall static pressures, the distribution indicates differences in the predicted passage vortex and the gradients along the endwall that affect shear stress.

Immediately noticeable with the isobars of Fig. 8(*b*) is the narrow "gully" of low pressure contours underneath the center line of the calculated pressure vortex, running from near the saddle point ($x=0$, $y=1.4$) across the passage to the suction surface of airfoil two. The steep walled pressure contour gully shows the effect of a concentrated steady-state passage vortex, as predicted by CFD. In contrast, the pressure contours of Fig. 8(*a*) show evidence of a less concentrated passage vortex in the experiment, with a static pressure gully that is broad, having gentler wall slopes. This broad gully could also be caused by a fluctuating vortex, but this is not possible to validate from the time-averaged measurements that were taken. However, measurements made by Harrison [7] using high response hot film instrumentation on a similar endwall experiment, do not show evidence of a fluctuating vortex. In any case, the differences in measured and predicted loss coincide with differences in endwall static pressures.

Skin Friction Coefficients on Endwall. The skin friction coefficient data reveal prominent features of the flow along the endwall. Figure 9 shows vectors in the direction of shear (or limiting streamlines) with magnitude C_f. Each vector in Fig. 9(*a*) represents a "nearest neighbor" average of several skin friction coefficient measurements; over 250 OFI measurements were used to produce the map of 130 vectors in Fig. 9(*a*). The CFD data are interpolated to the same grid in Fig. 9(*b*), and in Fig. 9(*c*) both measured and predicted vectors are overlaid. In these vector plots, the saddle point appears below and to the left of the leading edge

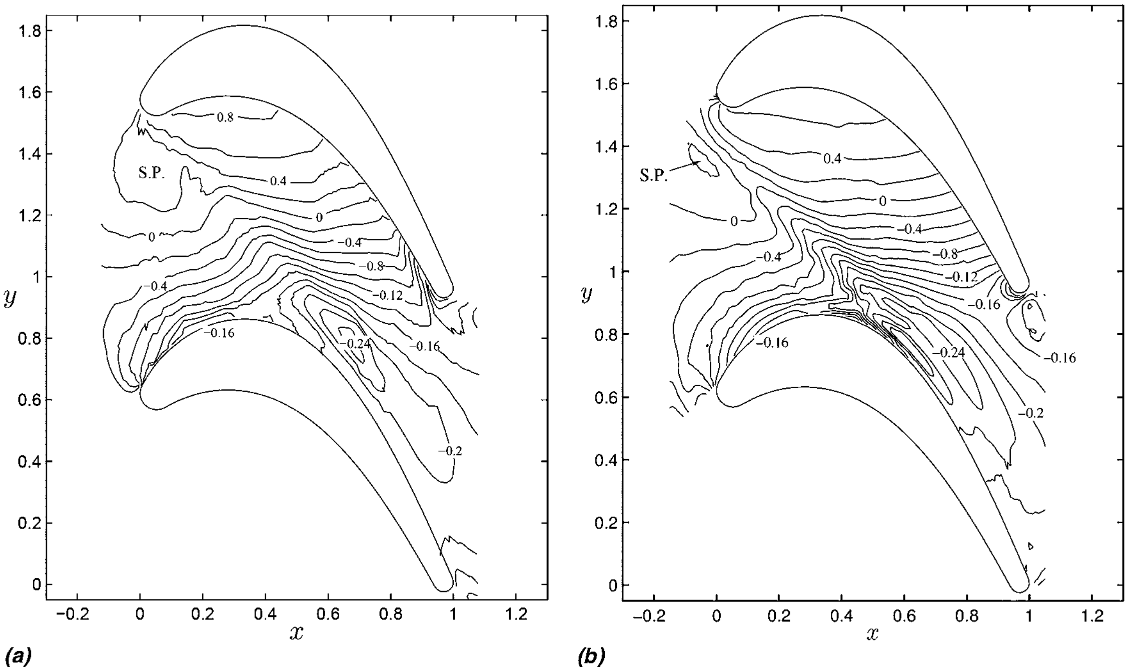

Fig. 8 Measured (*a*) and turbulent CFD (*b*) endwall static pressure coefficients with saddle point (S.P.) locations indicated

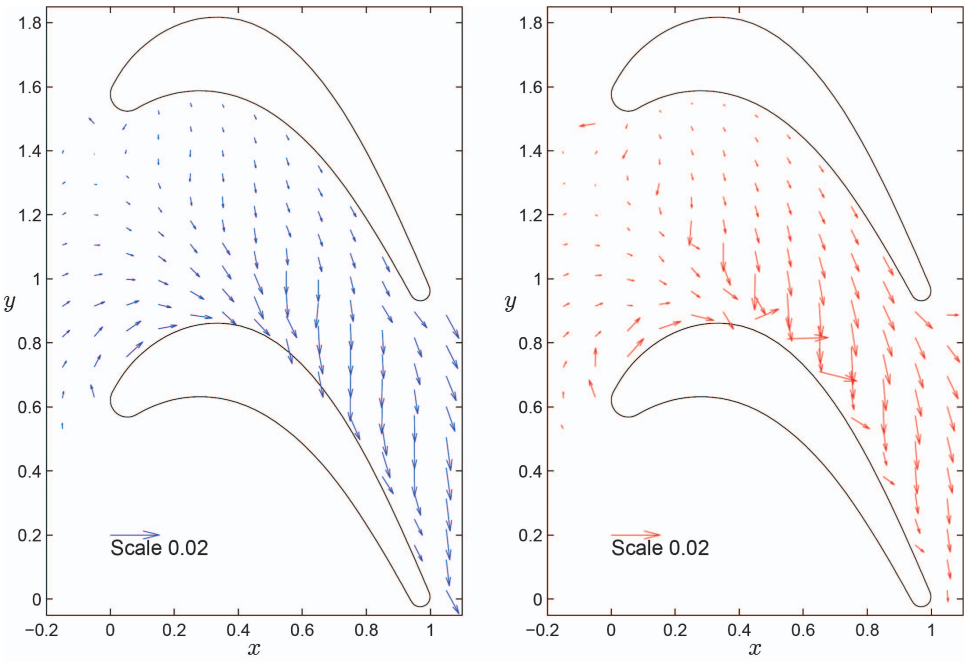

a. Measured

b. Turbulent CFD

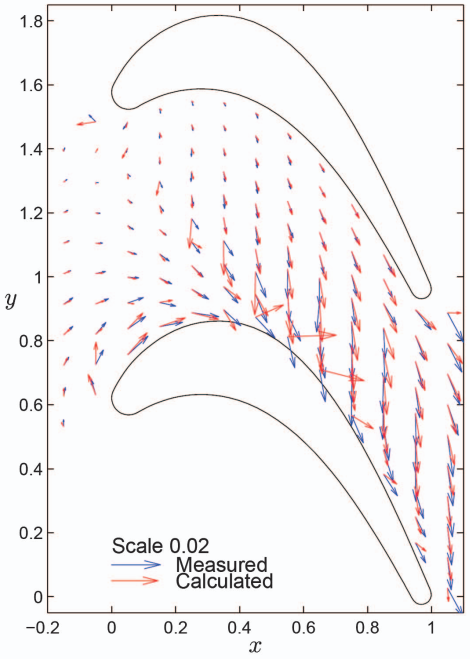

c. Overlay of measured and predicted values

Fig. 9 Measured and predicted "skin friction vectors" $\equiv C_f \tau_w / |\tau_w|$

of the upper airfoil. The vectors near the saddle point indicate the limiting streamlines leading toward and away from the saddle point. Another feature is the passage vortex separation line, which extends from the saddle point toward the throat region of the lower airfoil.

The CFD model underpredicts the crossflow in the three-dimensional boundary layer but overpredicts the shear. The predicted values of shear stress are higher overall than measured values, and the angle of the shear stress vectors generally errs towards the streamwise direction. The standard deviation between the measured and turbulent CFD skin friction coefficient data sets is 38%. The maximum predicted value of skin friction coefficient is 23% higher than the maximum measured value. In the region of highest shear, between the separation line and trailing edge plane, the skin friction coefficient values are overpredicted by 5% on average, compared to 3% over the whole data set. From this perspective the CFD appears to be doing quite well. In the region between the separation line and trailing edge plane, the shear vectors consistently err toward the streamwise direction, with mean angle between measured and predicted shear vectors being 7 deg. The measured data exhibit lower values of shear, but with more

Table 2 Maximum skin friction coefficient: comparison among measurements and turbulent CFD predictions in this study, along with measurements from Harrison's [7] experiment

Source	$\max(C_f)$
Measured	0.018
Turbulent CFD	0.021
Measured [7]	0.020

crossflow. Along the separation line, higher predicted shear is consistent with the higher gradients (denser packing of contour lines) of static pressure seen in Fig. 8 in that same location.

Skin friction data can be compared with measurement data of Harrison [7]. Shear stress values are reported, but the skin friction coefficient data are based on local flow velocities. However, the cascade inlet Reynolds number can be computed from the reported Reynolds number based on true blade chord and exit flow, in addition to the axial chord and inlet and exit flow angles. One needs to assume only a flow temperature (20°C is used here) to obtain the cascade inlet velocity head used to scale the shear stress values. The result is a maximum skin friction coefficient value of 0.02, equal to that of the CFD model. Table 2 lists the maximum predicted and measured values of skin friction coefficient. The location of maximum shear in Harrison's work is in the throat on the suction side of the airfoil, whereas in this study the maximum shear occurs in the region of uncovered turning. The maximum predicted skin friction coefficient value lies about one third across the throat from the suction side.

As is consistent with the observations of the measured and predicted endwall static pressures, prominent differences exist between the measured and predicted shear stress distributions. Most evident is the relative smoothness of the measured vectors, which is consistent with the shallower gradients in endwall static pressure along the passage vortex and in the throat region on the suction side. Further distinctions can be made between measured and predicted shear that show how the distribution of endwall shear and loss coincide.

The contribution of endwall shear to the mass-averaged total pressure loss is not clear, but both measured and predicted quantities of mass-averaged total pressure loss and pitch-averaged skin friction coefficient take on similar profiles along the passage. Figure 10 is a plot of pitch-averaged skin friction coefficient values, measured and calculated, as a function of axial distance through the cascade passage. Figure 6 shows the sharp increase in mass-averaged total pressure loss along the passage. Coincidentally, Fig. 10 shows a sharp increase in the pitch-averaged skin friction coefficient along the passage. Furthermore, the axial location where mass-averaged total pressure loss is most overpredicted coincides with the location where pitch-averaged skin friction coefficient is most overpredicted. As indicated in Fig. 7, the difference between the predicted and measured pitch-averaged skin friction coefficient is not smooth, but the the values are for the most part overpredicted. Aerodynamic loss generation has not been shown here to be due primarily to endwall shear, but it has been shown that the region of sharpest increase in loss coincides with the region of worst loss prediction and worst endwall shear prediction. Also, the loss data shown in Fig. 6 and the endwall shear data shown in Fig. 10 exhibit strikingly similar behavior as functions of axial distance.

Summary and Conclusion

Experimental measurements and CFD predictions were made of the low Mach number air flow through a turbine cascade passage in a large scale planar cascade of high turning, low convergence ratio, low aspect ratio turbine airfoils. The predictions were made using Fluent, a modern, commercially available CFD program. Direct experimental measurements of endwall skin friction coefficient were made using OFI. These were complimented by earlier measurements of endwall static pressures and of mass-averaged total pressure loss coefficient development through the cascade passage and downstream of the cascade exit. The following was concluded.

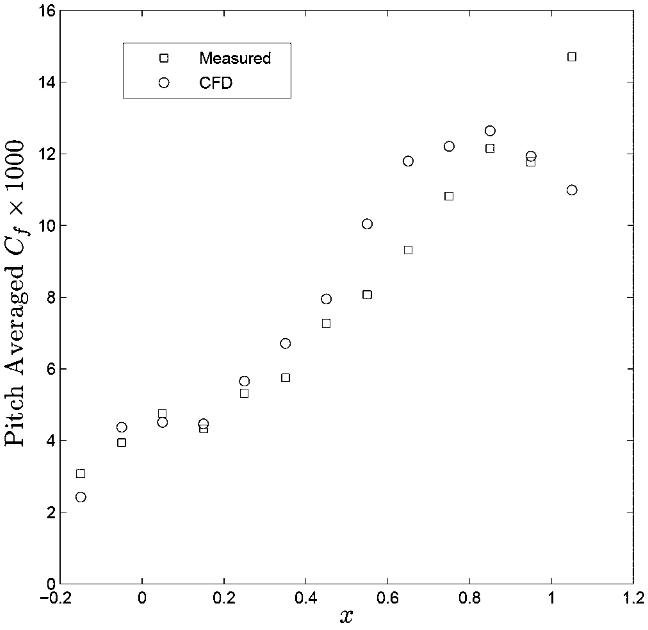

Fig. 10 Development of measured and turbulent CFD predicted pitch-averaged skin friction coefficient through cascade

The CFD predicted values of aerodynamic loss in and downstream of the cascade passage were higher than measured values. At an exit plane just downstream of the cascade the predicted values were 40–60% higher than those measured. This overestimation of loss is commonly seen in CFD calculations of this type, as evidenced in the early work of Hah [4]; and more recent CFD studies reviewed by Langston [3].

Based on a more detailed comparison of experimental measurements and CFD predictions on the cascade endwall itself, it was concluded that:

1. General agreement was found between measurements and predictions of endwall static pressures. However, the measured pressure distributions showed evidence of a less concentrated passage vortex, when compared with CFD results. Steeper gradients were observed in the predicted endwall pressures as compared with measurements, and this was consistent with endwall shear stress distribution.
2. The CFD simulation yielded both underpredicted and overpredicted endwall skin friction coefficient magnitudes. Although skin friction predictions were only 3% high on average in comparison with data obtained from the OFI measurements, the standard deviation between predicted and measured values was about 38%. Despite this varying agreement, the region of highest overprediciton in shear coincided with the region of sharpest loss increase and highest loss overprediciton. In addition, crossflow was somewhat underpredicted.

Based on these results, it is a recommendation that future efforts be directed to getting a more complete set of endwall and airfoil skin friction and surface pressure measurements to compliment existing loss measurements. Such detailed surface and loss measurements would provide a higher level of validation to a CFD simulation than loss measurements alone. Furthermore, the current measurements indicate where more attention should be paid in the CFD simulation for improvement in accuracy.

Acknowledgment

The work reported here was supported by the National Science Foundation under Grant No. 0412929. We thank NSF and NSF Program Director, Dr. Michael Plesniak, for their sponsorship. The nickel-tungsten foil was provided by AMETEK Specialty Metal Products, Wallingford, CT.

Nomenclature

b_x = axial chord, m
C_f = skin friction coefficient, $\tau_w / \frac{1}{2}\rho_o U_o^2$
C_p = static pressure coefficient, $(P-P_o)/\frac{1}{2}\rho_o U_o^2$
C_{pt} = total pressure coefficient, $(P_{to}-P_t)/\frac{1}{2}\rho_o U_o^2$
ℓ = interferometry fringe separation, m
n_o = index of refraction of oil
n_a = index of refraction of air
P = pressure, Pa
P_t = total pressure, Pa
t = elapsed wind tunnel run time, s
U_o = cascade inlet velocity, m/s
x = axial coordinate, scaled by b_x
y = pitch-wise coordinate, scaled by b_x
y^+ = non-dimensional wall coordinate, $=y\sqrt{\tau_w \rho}/\mu$
z = coordinate normal to endwall, scaled by b_x

Greek Symbols

α = angle of light incidence, rad
λ = wavelength of light, m
ρ = Density, kg/m^3
μ = viscosity, Pa·s
μ_o = oil viscosity, Pa·s
τ_w = wall shear stress, Pa

Subscripts

o = upstream
t = total
w = wall

References

[1] Langston, L. S., 1980, "Crossflows in a Turbine Cascade Passage," ASME J. Eng. Power, **102**, pp. 866–874.
[2] Sieverding, C. H., 1985, "Recent Progress in the Understanding of Basic Aspects of Secondary Flows in Turbine Blade Passages," ASME J. Turbomach., **107**, pp. 248–257.
[3] Langston, L. S., 2001, "Secondary Flows in Axial Turbines—A Review," *Heat Transfer in Gas Turbine Systems*, Annals of New York Academy of Sciences, Vol. 934, New York Academy of Sciences, pp. 11–26.
[4] Hah, C., 1984, "A Navier-Stokes Analysis of Three-Dimensional Turbulent Flows Inside Turbine Blade Rows at Design and Off-Design Conditions," ASME J. Eng. Gas Turbines Power, **106**, pp. 421–429.
[5] Senoo, Y., 1958, "The Boundary Layer on the Endwall of a Turbine Nozzle Cascade," Trans. ASME, **80**, pp. 1711–1720.
[6] Langston, L. S., Nice, M. L., and Hooper, R. M., 1977, "Three-Dimensional Flow Within a Turbine Cascade Passage," ASME J. Eng. Power, **99**, pp. 21–28.
[7] Harrison, S., 1990, "Secondary Loss Generation in a Linear Cascade of High-Turning Turbine Blades," ASME J. Turbomach., **112**, pp. 618–624.
[8] Harrison, S., 1992, "The Influences of Blade Lean on Turbine Losses," ASME J. Turbomach., **114**, pp. 184–190.
[9] Naughton, J. W., and Sheplak, M., 2002, "Modern Developments in Shear-Stress Measurement," Prog. Aerosp. Sci., **38**, pp. 515–570.
[10] Driver, D. M., 2003, "Application of Oil-Film Interferometry Skin-Friction Measurement to Large Wind Tunnels," Exp. Fluids, **34**, pp. 717–725.
[11] Davy, C., Alvi, F. S., and Naughton, J. W., 2002, "Surface Flow Measurements of Micro-Supersonic Impinging Jets," *22nd AIAA Aerodynamic Measurement Technology and Ground Testing Conference*, Paper No. AIAA 2002–3196.
[12] Menter, F. R., 1994, "Two-Equation Eddy-Viscosity Turbulence Models for Engineering Applications," AIAA J., **32**(8), pp. 1598–1605.
[13] Zhang, Q., Lee, S. W., and Ligrani, P. M., 2004, "Effects of Surface Roughness and Turbulence Intensity on the Aerodynamic Losses Produced by the Suction Surface of a Simulated Turbine Airfoil," ASME J. Fluids Eng., **126**(2), pp. 257–265.
[14] Hohn, W., 2003, "Numerical and Experimental Investigation of Unsteady Flow Interaction in a Low-Pressure Multistage Turbine," Bussei Kenkyu, **217**(A2), pp. 211–217.
[15] Whitehouse, D. R., Moustapha, S. H., and Sjolander, S. A., 1993, "The Effects of Axial Velocity Ratio, Turbulence Intensity, Incidence and Leading Edge Geometry on the Mid-Span Performance of a Turbine Cascade," Can. Aeronautics Space J., **39**(3), pp. 150–156.
[16] Fluent 6.0 User's Guide, Fluent, Inc., Lebanon, NH.
[17] Moore, H., and Gregory-Smith, D. G., 1996, "Transition Effects on Secondary Flows in a Turbine Cascade," ASME Paper No. 96-GT-100.

Thermal-Mechanical Life Prediction System for Anisotropic Turbine Components

F. J. Cunha
e-mail: frank.cunha@pw.utc.com

M. T. Dahmer

Pratt & Whitney,
United Technologies Corporation,
East Hartford, CT 06108

M. K. Chyu
Department of Mechanical Engineering,
University of Pittsburgh,
Pittsburgh, PA
e-mail: mkchyu@engr.pitt.edu

Modern gas turbine engines provide large amounts of thrust and withstand severe thermal-mechanical conditions during the load and mission operations characterized by cyclic transients and long dwell times. All these operational factors can be detrimental to the service life of turbine components and need careful consideration. Engine components subject to the harshest environments are turbine high-pressure vanes and rotating blades. Therefore, it is necessary to develop a turbine component three-dimensional life prediction system, which accounts for mission transients, anisotropic material properties, and multi-axial, thermal-mechanical, strain, and stress fields. This paper presents a complete life prediction approach for either commercial missions or more complex military missions, which includes evaluation of component transient metal temperatures, resolved maximum shear stresses and strains, and subsequent component life capability for fatigue and creep damage. The procedure is based on considering all of the time steps in the mission profile by developing a series of extreme points that envelop every point in the mission. Creep damage is factored into the component capability by debiting thermal-mechanical accumulated cycles using the traditional Miner's rule for accumulated fatigue and creep damage. Application of this methodology is illustrated to the design of the NASA Energy Efficient Engine (E^3) *high pressure turbine blade with operational load shakedown leading to stress relaxation on the external hot surfaces and potential state of overstress in the inner cold rib regions of the airfoil.* [DOI: 10.1115/1.2137740]

Introduction

Modern turbine hot gas-path blades are subjected to extremely high gas temperatures operating in oxidizing and corrosive environments under high mechanical loads. Turbine blades must maintain adequate strength throughout long service intervals for commercial engines as well as throughout many complex mission types for military engines. In order to achieve required component life, cast nickel single crystal superalloys are used. The first generation single crystal alloys entered commercial service in the early 1980s and military service shortly thereafter. Up to the present time, fourth generation single crystals have been developed. The composition of these superalloys has evolved parallel with advancements in investment casting processes. Single crystal alloys are precipitation-strengthened, cast, mono-grain superalloys based on the Ni-Cr-Al system [1]. The macrostructure is characterized by parallel continuous primary dendrites spanning the casting without interruption in the direction of solidification. Secondary dendrites perpendicular to the solidification axis define the interdendritic spacing. Solidification of these dendrite arms continues in the $\langle 001 \rangle$ direction. If seed crystals are used in the casting process to generate the single crystal component, the primary and secondary crystal orientations can both be selected. However, the secondary direction normal to the solidification growth direction is considered random, as the starting grain selectors in the current casting process can only be used to determine the secondary orientation without controlling it. The $\langle 001 \rangle$ direction is coincident with the primary loading axis. This is done to achieve the lowest elastic modulus in the direction of blade pull for rotating turbine blades. Single crystal components have been aimed at high-temperature creep strength and low ductility. Moreover, current blade durability is further enhanced with the use of thermal barrier and metallic coatings for oxidation and high temperature corrosion resistance.

All of the modern single crystal alloys are two-phase alloys with a large volume fraction of γ' precipitates, based on the intermetallic compound, Ni_3Al, interspersed in a coherent face-centered cubic γ matrix comprised of nickel, Ni, with smaller weight percentages of various other elements in solid solution. These elements include: cobalt, Co; aluminum, Al; chromium, Cr; tungsten, W; molybdenum, Mo; tantalum, Ta; hafnium, Hf; rhenium, Re; and ruthenium, Ru. The elements Re and Ru are introduced in the latest generation of single crystal alloys. All these elements have different attributes which can be summarized as follows: Cr, Al, and Hf are used as surface protection elements; Mo, W, and Ta are used in solid solution strengthening; and Re and Ru are used for high creep strength. In general, the large atomic radii elements such as Mo, W, Re, and Ru act as barriers to dislocation motion at high temperatures providing the alloy with excellent high temperature creep properties.

The strength of these single crystal alloys is mainly a function of the size and the percentage of γ' precipitates. Experimentally, it has been determined that the peak creep strength is achieved with a volume fraction of γ' of 60%–65% [2]. Much of the behavior of these alloys can be explained on the basis that high volume fraction γ' alloys deform by shearing of the γ' precipitates. The high volume fraction of precipitates precludes dislocation bypass at low and intermediate temperatures, forcing precipitate shearing. However, the energies resisting dislocation shearing of the precipitates are those required to form a local reversal of Al–Ni order or antiphase boundary in the stacking fault of the Ni_3Al superlattice. The energies associated with the antiphase boundary in the superlattice stacking faults determine the strength, fatigue, and fracture characteristics of these alloys. This is also evident by the increase in yield strength at moderate to high temperatures before a monotonic decrease in yield strength at higher temperatures.

The excellent, high-temperature creep and fatigue resistance of

---

Contributed by the International Gas Turbine Institute (IGTI) of ASME for publication in the JOURNAL OF TURBOMACHINERY. Manuscript received October 1, 2004; final manuscript received February 1, 2005. IGTI Review Chair: K. C. Hall. Paper presented at the ASME Turbo Expo 2005: Land, Sea and Air, Reno, NV, June 6–9, 2005, Paper No. GT2005-68107.

these superalloys is a result of a combination of solid-solution strengthening, absence of deleterious grain boundaries, and a high volume fraction of precipitates that act as barriers to dislocation motion [3]. It should be pointed out, however, that fatigue crack initiation also depends on the microscopic defects, which can be categorized as intrinsic defects and deviant material defects. Intrinsic defects include carbides, undissolved eutectic pools, and associated microporosity concentrated in interdendritic regions of the casting. Even though the intrinsic defects are normal features of the alloy microstructure, deviant defects such as crystallographic defects related to low and high angle grain boundaries, freckles and sliver grains, and porosity are considered rejectable defects in the material quality if they exceed specified limits. They are not intentionally included in life capabilities for the superalloy [1].

Modern single crystal superalloys are face-centered, single crystal superalloys with cubic symmetry. There are three independent mechanical properties: The modulus of elasticity, E; the shear modulus, G; and the Poisson ratio, ν. The superalloy mechanical and thermal-physical properties are also a function of temperature and change with crystal orientation leading to anisotropic behavior of the material. During the casting process, the single crystal orientation is such that the primary crystal orientation is in the $\langle 001\rangle$ direction coincident with the blade stacking axis within a specified tolerance. Generally, no seed crystals are used in the casting process and the secondary orientation has nearly a random orientation. After the casting process, a series of standard heat treatments (i.e., solution annealing, coating heat treatment, and precipitation heat treatment) are used to optimize microstructures of the material [4].

Since the introduction of single crystal components in the 1980s, a generation of crystal plasticity or slip system modeling has emerged. Single crystals deform by shearing along the $\{111\}$ planes, sometimes referred to as octahedral planes in a crystal coordinate system. Material fatigue is then evaluated from a lifing point-of-view by examining the shear strain amplitudes on the slip system. Material creep behavior can be also evaluated by considering the most relevant deformation mechanisms. Some single crystal nickel superalloys exhibit an incubation period in addition to the usual primary, secondary, and tertiary creep behavior [4]. The incubation period and primary creep behavior is attributed to the $\{111\}\langle 112\rangle$ slip system. In secondary creep behavior at high temperatures, slip occurs in the $\{111\}\langle 101\rangle$-slip system [2]. The latter has been referred to as Type I slip, while the former as Type II slip. Precipitates are resistant to Type I slip, except at very high stresses. Type I dislocations reside chiefly within the interconnected γ channels, and although slip may be hindered by the γ' precipitates, climb and cross slip processes provide ways for continued progress through the structure on a cube slip system, particularly for thermally activated processes. Type II slip is also activated at high stresses having shear stress components [5].

Owing to the wide range of temperatures experienced by turbine blades and vanes as they operate through every point in the mission profile, both Type I and II octahedral deformations and cube slip deformations will be active in the turbine components. In total, there are 30 slip system directions. That is, 24 octahedral slip system directions and six cube slip system directions [6]. The maximum shear strain amplitude on these slip systems can then be used as the governing parameter to assess life capability for a turbine component subjected to fatigue and creep damage. Arakere [6] used a similar approach based on maximum shear stress amplitude on the 30 slip system directions. Naik et al. [7] also used a similar octahedral approach to determine the critical plane fatigue modeling and characterization of single crystal nickel superalloys. Thus, the evaluation of the slip system characteristics in conjunction with the material capability from test data should establish the foundation for a turbine component life prediction system. This is the topic developed in this paper. However, a review of past studies was undertaken to consider previous relevant contributions.

Previous Studies. In the past, nonlinear finite element codes have been developed to perform three-dimensional (3D) thermal, elasto-plastic stress, and creep analysis. These nonlinear programs have been used either as exploratory studies or for contributions to early design stages. This limited application was mainly due to the extensive work and required significant time to obtain a solution. That is, once the cyclic stress-strain and creep behavior of the component material has been determined, the finite element thermal-structural analysis is performed. The result is a local 3D temperature-stress-strain versus time response of the material at critical locations of the component, including areas with stress concentrations, such as airfoil film cooling holes. Then, from the knowledge of fatigue, creep, and fracture resistance of the alloy, a prediction of the lifetime of the component could be made.

The number of examples of past work in the area of life prediction for turbine components is limited, and, in most cases, comprehensive contributions were only conducted at the technical lifing groups of major original equipment manufacturers (OEMs). In this category, McKnight et al. [8] reported on research to verify the utility of advanced structural analysis techniques for life assessment of gas turbine hot section components. Soechting [9] reported the results of a 36-month study on a turbine low cycle fatigue design program for gas turbine airfoils. Arvanitis et al. [10] provided a method based on a ductility exhaustion approach for a multiaxial life prediction system for turbine components. These three contributions were based on a global stress system with empirical test correlations for material capability. Heine et al. [11] also reported on a comprehensive experimental thermal-mechanical fatigue program for coated blades. Moreno et al. [12] summarized the activities performed during an extensive program aimed at improving the high temperature crack initiation life prediction technology for gas turbine hot section components. These two contributions started to examine the influence of microscopic effects on the material capability. Nissley et al. [13] reported on life prediction constitutive models for engine hot section anisotropic materials. More recently, MacLachlan and Knowles [14] used a slip system model and structural elasto-viscoplastic calculation procedures for analysis of turbine components. These more recent contributions provided a platform to examine life prediction in terms of a slip system and characterize the anisotropic behavior of superalloys.

This paper will focus primarily on the progress of the development of a multi-axial life prediction system using a slip system for determining the maximum shear strain amplitude to yield total accumulated cycles in fatigue. The material fatigue capability is debited to account for high temperature creep damage in segments of the component mission profile. A typical cooled uncoated blade, the NASA E^3 high-pressure turbine (HPT) blade, designed by Pratt and Whitney in 1982 [15] is considered to illustrate the application of the life prediction methodology.

Analysis

Multi-Axial Fatigue-Creep Models. The analysis used to determine the maximum shear strain amplitude begins with the modeling of a 3D section of the blade as a solid model and then proceeds by using a finite element code, such as ANSYS [16], for analysis. The blade used in this analysis was created under a NASA contract summarized in the E^3 HPT detailed design report [15]. The blade solid model is shown in Fig. 1(*a*), whereas the finite element ANSYS model is shown in Fig. 1(*b*). As can be appreciated from the transparent solid model of Fig. 1(*a*), the blade is cooled by convection with cavity wall trip strips, not shown, and with a set of pedestals in the trailing edge. While external surfaces are locally film cooled from the leading edge with three rows of showerhead holes, there are no film cooling

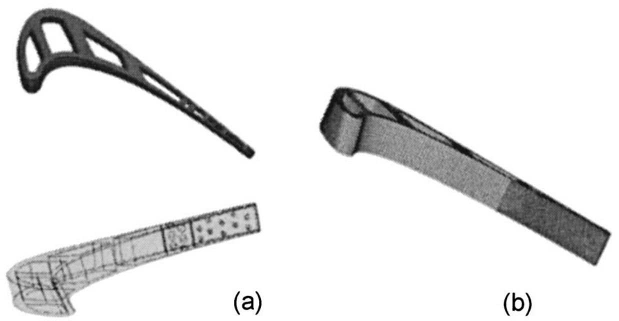

Fig. 1 HPT blade solid model and finite element mesh

holes on either the pressure or suction surfaces of the airfoil. The trailing edge has a centerline cooling flow ejection. The ANSYS model is depicted in Fig. 1(*b*). Details of the finite model are described in the Cooled Airfoil Study presented in the Results and Discussion section of this paper. After the creation of the solid and finite element mesh models, the material properties are specified as a function of temperature.

The boundary conditions become the next building block in the analysis to simulate the thermal and mechanical loads that the part experiences throughout the mission. Different coating systems can be modeled as modified equivalent heat transfer coefficients. For uncoated blades, as is the case here, this latter step is not executed. The external and internal thermal boundary conditions are implemented leading to mixed type boundary conditions of film temperatures and convective heat transfer coefficients for the external and internal walls of the airfoil. Further details are covered in the Cooled Airfoil Study presented in the Results and Discussion section. A thermal conduction analysis is performed with ANSYS to obtain the temperature fields in the blade before proceeding to a structural analysis. The next step is to apply the boundary conditions for a structural analysis. Further details of this simulation are again described in the Results and Discussion section. As the mechanical boundary conditions are prescribed to the model, the stress and strains fields are determined from a subsequent ANSYS run. The thermal-mechanical results are then used as input to the following life analysis.

The constitutive equation relative the crystal coordinate system is written in a matrix notation as

$$\{\varepsilon\}=[S]\{\sigma\}, \tag{1}$$

where: $\{\varepsilon\}=\{\varepsilon_1,\varepsilon_2,\varepsilon_3,\gamma_{12},\gamma_{13},\gamma_{23}\}$ and $\{\sigma\}=\{\sigma_1,\sigma_2,\sigma_3,\tau_{12},\tau_{13},\tau_{23}\}$.

These vectors are the engineering strain and the stress vectors obtained from the contracted strain and stress tensors. The relationship between the engineering and tensor strains is as follows: $\{\varepsilon_1,\varepsilon_2,\varepsilon_3,\gamma_{12}/2,\gamma_{13}/2,\gamma_{23}/2\}=\{\varepsilon_1,\varepsilon_2,\varepsilon_3,\varepsilon_{12},\varepsilon_{13},\varepsilon_{23}\}$. These stress and strain results can be obtained from an ANSYS coupled thermal-structural run under a set of specified boundary conditions and material property data. The matrix $[S]$ is the elastic compliance matrix whose elements have been grouped together by Bekhterev and described by Lekhnitskii [17].

Since no seed crystals are used in the casting process, the secondary orientation has nearly a random orientation [4]. Therefore, the principal crystal coordinate system needs to be transformed into a new system in order to capture the effects of the secondary crystal orientation. To transform Eq. (1) from a principal coordinate system into another coordinate system, denoted here with a prime superscript, the following transformation is followed [17]:

$$S'_{ij}=\sum_{m=1}^{6}\sum_{n=1}^{6}S_{ij}q_{mi}q_{nj}, \tag{2}$$

where: $i,j=1,2,\ldots,6$, and the coefficients q_{mn} denote elements belonging to the mth row and the nth column in Table 1. In this table, the coefficient a_{mn} represents the direction cosines such that $a_{mn}=\cos(m,n)$, with m and n representing the old and new coordinate axes, respectively.

The stress vector transformed to the new coordinate system is given the relationship [17]:

$$\{\sigma'\}=[Q]\{\sigma\}, \tag{3}$$

where the elements of matrix $[Q]$ can also be found in Table 1. The following is an illustrative example of how the elements of a stress vector in the new coordinate system (primed variables) relate to the old coordinate system (unprimed variables),

$$\sigma'_1=\sigma_1a_{11}^2+\sigma_2\sigma_{12}+\sigma_3\sigma_{13}+2\tau_{12}a_{12}a_{11}+2\tau_{13}a_{13}a_{11}+2\tau_{23}a_{12}a_{13}$$

$$\cdots$$

$$\tau'_{23}=\sigma_1a_{21}a_{31}+\sigma_2a_{22}a_{32}+\sigma_3a_{22}a_{33}+\tau_{12}(a_{22}a_{31}+a_{21}a_{32})$$
$$+\tau_{13}(a_{21}a_{33}+a_{23}a_{31})+\tau_{23}(a_{22}a_{33}+a_{23}a_{32}).$$

For the new coordinate system, the equations for the generalized Hooke's law are:

$$\{\varepsilon'\}=[S']\{\sigma'\}. \tag{4}$$

Having obtained the compliance matrix and stress vector with Eqs. (2) and (3), respectively, one proceeds to compute the shear stresses on the local octahedral and cube slip planes.

Dame [2] provided the transformation equation that takes the applied stress acting on a plane α, with normal n^{α}, to the local shear stress component in the β direction on the α plane as follows:

$$\tau^{\alpha\beta}=\sum_{i=1}^{3}\sum_{j=1}^{3}\sigma'_{ij}n_i^{\alpha}l_j^{\alpha\beta}. \tag{5}$$

Knowledge of the normal and directional vectors n_i^{α} and l_j^{ab} with the information about σ'_{ij} allows calculation of the required shear stress amplitudes. This operation leads to 30 shear stresses; 24 shear stresses on the octahedral slip system, and six shear stresses on cube slip systems. These will be denoted by $\tau^1,\tau^2,\ldots,\tau^{30}$. The resolved shear strains can also be determined from applied shear

Table 1 Transformation matrix q_{mn}

	m					
n	1	2	3	4	5	6
1	a_{11}^2	a_{12}^2	a_{13}^2	$2a_{11}a_{12}$	$2a_{11}a_{13}$	$2a_{12}a_{13}$
2	a_{21}^2	a_{22}^2	a_{23}^2	$2a_{21}a_{22}$	$2a_{21}a_{23}$	$2a_{22}a_{23}$
3	a_{31}^2	a_{32}^2	a_{33}^2	$2a_{31}a_{32}$	$2a_{31}a_{33}$	$2a_{32}a_{33}$
4	$a_{11}a_{21}$	$a_{12}a_{22}$	$a_{13}a_{23}$	$a_{12}a_{21}+a_{11}a_{22}$	$a_{11}a_{23}+a_{13}a_{21}$	$a_{22}a_{13}+a_{12}a_{23}$
5	$a_{31}a_{11}$	$a_{32}a_{12}$	$a_{33}a_{13}$	$a_{32}a_{11}+a_{31}a_{12}$	$a_{31}a_{13}+a_{11}a_{33}$	$a_{13}a_{22}+a_{33}a_{12}$
6	$a_{21}a_{31}$	$a_{22}a_{32}$	$a_{23}a_{33}$	$a_{22}a_{31}+a_{21}a_{32}$	$a_{21}a_{33}+a_{23}a_{31}$	$a_{22}a_{33}+a_{23}a_{32}$

strains in a similar manner. The shear strains on the 24 octahedral slip system are given by [18]:

$$\begin{Bmatrix} \gamma^1 \\ \gamma^2 \\ \gamma^3 \\ \gamma^4 \\ \gamma^5 \\ \gamma^6 \\ \gamma^7 \\ \gamma^8 \\ \gamma^9 \\ \gamma^{10} \\ \gamma^{11} \\ \gamma^{12} \end{Bmatrix} = \frac{1}{\sqrt{6}} \begin{bmatrix} 2 & 0 & -2 & 1 & 0 & -1 \\ 0 & -2 & 2 & -1 & 1 & 0 \\ 2 & -2 & 0 & 0 & 1 & -1 \\ -2 & 0 & 2 & 1 & 0 & -1 \\ -2 & 2 & 0 & 0 & -1 & -1 \\ 0 & 2 & -2 & -1 & -1 & 0 \\ 2 & -2 & 0 & 0 & -1 & -1 \\ 0 & 2 & -2 & -1 & 1 & 0 \\ 2 & 0 & -2 & -1 & 0 & -1 \\ 0 & -2 & 2 & -1 & -1 & 0 \\ -2 & 0 & 2 & -1 & 0 & -1 \\ -2 & 2 & 0 & 0 & 1 & -1 \end{bmatrix} \begin{Bmatrix} \varepsilon_1' \\ \varepsilon_2' \\ \varepsilon_3' \\ \gamma_{12}' \\ \gamma_{13}' \\ \gamma_{23}' \end{Bmatrix} \tag{6}$$

$$\begin{Bmatrix} \gamma^{13} \\ \gamma^{14} \\ \gamma^{15} \\ \gamma^{16} \\ \gamma^{17} \\ \gamma^{18} \\ \gamma^{19} \\ \gamma^{20} \\ \gamma^{21} \\ \gamma^{22} \\ \gamma^{23} \\ \gamma^{24} \end{Bmatrix} = \frac{1}{3\sqrt{2}} \begin{bmatrix} -2 & 4 & -2 & 1 & -2 & 1 \\ 4 & -2 & -2 & 1 & 1 & -2 \\ -2 & -2 & 4 & -2 & 1 & 1 \\ -2 & 4 & -2 & -1 & -2 & -1 \\ -2 & -2 & 4 & 2 & 1 & -1 \\ 4 & -2 & -2 & -1 & 1 & 2 \\ -2 & -2 & 4 & 2 & -1 & 1 \\ 4 & -2 & -2 & -1 & -1 & -2 \\ -2 & 4 & -2 & -1 & 2 & 1 \\ 4 & -2 & -2 & 1 & -1 & 2 \\ -2 & 4 & -2 & 1 & 2 & -1 \\ -2 & -2 & 4 & -2 & -1 & -1 \end{bmatrix} \begin{Bmatrix} \varepsilon_1' \\ \varepsilon_2' \\ \varepsilon_3' \\ \gamma_{12}' \\ \gamma_{13}' \\ \gamma_{23}' \end{Bmatrix} \tag{7}$$

The shear strains on the six cube slip systems are [17]:

$$\begin{Bmatrix} \gamma^{25} \\ \gamma^{26} \\ \gamma^{27} \\ \gamma^{28} \\ \gamma^{29} \\ \gamma^{30} \end{Bmatrix} = \frac{1}{\sqrt{2}} \begin{bmatrix} 0 & 0 & 0 & 1 & 1 & 0 \\ 0 & 0 & 0 & 1 & -1 & 0 \\ 0 & 0 & 0 & 1 & 0 & 1 \\ 0 & 0 & 0 & 1 & 0 & -1 \\ 0 & 0 & 0 & 0 & 1 & 1 \\ 0 & 0 & 0 & 0 & -1 & 1 \end{bmatrix} \begin{Bmatrix} \varepsilon_1' \\ \varepsilon_2' \\ \varepsilon_3' \\ \gamma_{12}' \\ \gamma_{13}' \\ \gamma_{23}' \end{Bmatrix} \tag{8}$$

The analysis is performed first at the so-called durability design point under steady state conditions. However, the effect of transients during loading and unloading of the turbine blade in a mission cycle needs to be considered as part of overall blade thermal response. This can be done directly through an ANSYS transient run as well. However, this direct approach can take several hours with long run times, depending on the model complexity. It requires a large amount of data, computing resources, and slow turn-around time, particularly for complex missions. Fortunately, there are ways to perform transient thermal analysis with reduced amount of effort and computing resources, as presented in the next section.

Transient Modeling. Analytical simplification is carried through a section cut at the blade mid-span to obtain the airfoil model as shown in Fig. 1. The airfoil can then be analyzed separately for its entirety and for local lumped regions of interest. Regions of interest may include fast thermal responding regions, such as regions limited to the blade leading or trailing edges in an airfoil span for instance. The general governing equation for thermal transient responses is given by the following general heat balance expression, where T_m denotes metal temperature as the independent variable:

$$\underbrace{\rho c V \frac{dT_m}{dt}}_{\substack{\text{Energy} \\ \text{Storage}}} + \underbrace{m c_p (T_{co} - T_{ci})}_{\substack{\text{Cooling} \\ \Delta\ \text{Enthalpy}}} = \underbrace{h_g A_g (T_g - T_m)}_{\substack{\text{Thermal} \\ \text{Load}}}. \tag{9}$$

The various subscripts of the temperature variable, T, define the corresponding location in the blade, cooling path, or external gas path locations. That is, subscript, m, is for metal; g, is for gas; co, is for coolant out; and ci, is for coolant in. All other variables are defined in the nomenclature.

The governing Eq. (9) can be simplified by introducing the concept of cooling effectiveness, φ, defined as

$$\varphi = \frac{T_g - T_m}{T_g - T_c}. \tag{10}$$

If this definition is introduced in Eq. (9), the governing transient equation can be written as an ordinary differential equation:

$$\frac{1}{\lambda} \frac{dT_m}{dt} + T_m = (1 - \varphi) T_g + \varphi T_c, \tag{11}$$

where: λ=reciprocal of time constant: $\tau = \rho c V / h_g A_g$. The airfoil thermal response can be obtained from the solution of Eq. (11) to a series of step changes in gas temperature, ΔT_g, during a mission cycle. For the purposes of illustration, a closed form solution is obtained for one unit step change in gas temperature. In this case, the thermal response would assume the form:

$$T_m = \underbrace{\{(1 - \varphi) \Delta T_g (1 - e^{-\lambda t})\}}_{\text{Transient response to } \Delta T_g} + \underbrace{\{(1 - \varphi) T_g + \varphi T_c\}}_{\text{Steady-state}}. \tag{12}$$

In general, typical missions can be characterized with several unit steps in gas temperature at different time points in the mission cycle leading to the Duhamel's theorem of superposition principle with fundamental solutions of unit step functions [19]. However, a numerical Runge-Kutta method is a more practical method for solving (11) under complex boundary conditions [20]. This method is adopted in this paper. Figure 2 shows typical boundary condition profiles to be used either for commercial or military engines. These profiles could represent relative gas temperature profiles of the free-stream approaching the blade at different times in the mission. Profiles for the blade coolant supply temperatures would have similar shapes, however the magnitude would be directly related to the compressor discharge pressure. In general, the relative gas temperatures are defined at specified aero stations in the turbine gas path. The coolant temperatures are functions of compressor discharge pressure, which are modified to account for heat addition due to windage and pumping. The flow at different cycle points is obtained as a percentage of design point flow at the compressor inlet station. Typical profiles will be presented in the results section when the blade of Fig. 1 is analyzed. Knowledge of these cycle parameters is then used to determine the blade metal temperature as a function of time in the mission, $T_g(t)$.

The solution of governing equation (11) is performed numerically due to the complexity of a typical mission cycle profile using the Runge-Kutta numerical integration formulation [20]. This operation requires that a set of variables be defined first, as follows:

$$\underbrace{\frac{dT_m}{dt} = \lambda [(1 - \varphi) T_g + \varphi T_c - T_m]}_{\text{Physical Domain}} \Rightarrow \underbrace{\frac{dX_i}{dt} = f_1(t, X_1, \ldots, X_m)}_{\text{Mathematical Domain}}, \tag{13}$$

Subject to initial (t^0, X_i^0);

$$\text{where } X_i = \{X_1, X_2, X_3, X_4\} = \{T_m, T_g, T_c, \lambda\};$$

$$\text{with } \lambda^{(n)} = \lambda_{ss} \left(\frac{\% m}{100} \right)^{0.8}; T_g^{(n)} = T_g^{(n-1)} + \frac{dT_g}{dt} \Delta t;$$

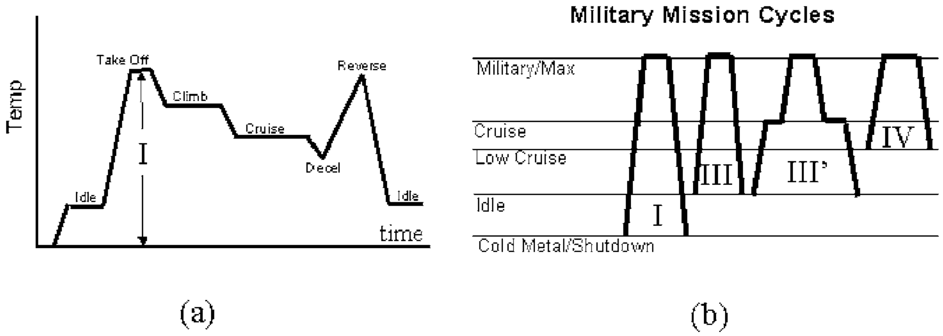

Fig. 2 Different mission cycles for commercial and military engines

$$T_c^{(n)} = T_c^{(n-1)} + \frac{dT_c}{dt}\Delta t.$$

This numerical methodology relies on the fourth-order Runge-Kutta numerical integration to solve a system of three first-order ordinary differential equations for T_m, T_g, and T_c. The temperature rates, dT_g/dt and dT_c/dt are also obtained numerically. In the solution process, solutions for T_g and T_c are used to evaluate the solution of interest, T_m.

Monitoring T_m can be done for any particular airfoil span. These may include a root section with the highest centrifugal stresses, a pitch section with the highest thermal load, or a tip section with the potential for thermal-mechanical fatigue assisted with oxidation. The modeling decision is left to the analyst. In this paper, a pitch section is presented as an example for applying the methodology. Points of interest in these sections could be fast thermal response regions of the airfoil; but then again the selection of the region of interest is left to the analyst.

To determine thermal responses of the regions of interest, time constants need to be calculated. The suitable control volume for these calculations is left to the analyst, and should be consistent with the region of interest. The overall time constant for the entire airfoil section is also calculated. The local metal temperatures, for the region of interest, and for the bulk temperature, for the airfoil span, are obtained for every single point in the mission profile using this numerical procedure. The transient state of thermal strains in the airfoil is subsequently calculated from the local and bulk metal temperatures as described next.

As in the terminology of Ref. [21], the displacement stress and the displacement strain represent the stress and strain produced by actual loads and equivalent tractions, $E\alpha T$, acting on a body element, where E is the modulus of elasticity and α is the coefficient of thermal expansion. The displacement strains, ε_d, that these loads produce are observable strains that can be measured. The associated displacement stress is $E\varepsilon_d$, and the true stress is $(E\varepsilon_d - E\alpha T)$. When there is residual stresses, σ_r, prior to load application or if there are stresses σ_k, due to stress concentrations, of film holes for instance, the net stress is:

$$\sigma = E\varepsilon_d + (\sigma_r + \sigma_k) - E\alpha T. \tag{14}$$

If one assumes a blade composed by a multi-element assembly as a first approximation [21], it will be assumed that each element is subject to a different surface traction, $E_j\alpha_j T_j A_j$, where j denotes a particular element in the assembly. If it is assumed that there is no extra stresses, σ_r, and σ_k, then superposition of a centrifugal load P on the assembly yields the stress in each element as follows [21]:

$$\sigma_i = E_i\left[\frac{\sum_{j=1}^{n} E_j\alpha_j T_j A_j + P}{\sum_{j=1}^{n} E_j A_j} - \alpha_i T_i\right]. \tag{15}$$

The first term inside the brackets, ignoring the mechanical load P for the time being, can be interpreted as the bulk temperature if E and α are factored out. This gives $T_b = \Sigma(\mathrm{TA})_j / \Sigma A_j$. It implies that the local stress is calculated from the difference between bulk stress, $E\alpha_b T_b$, and local stress, $E\alpha_i T_i$. In terms of strain, Eq. (14) can be used to yield the result:

$$\varepsilon_{\text{local}} = \alpha_b(T_b - T_{\text{ref}})w_b - \alpha_{\text{local}}(T_{\text{local}} - T_{\text{ref}})w_{\text{local}} + \varepsilon_0. \tag{16}$$

The reference temperature, T_{ref}, is the reference temperature for the thermal expansion coefficient. The factors w_b and w_{local} are taken as bulk and local weighting factors, which are found by least squares fit to known thermal strain results. In this case, $\varepsilon_{\text{local}}$ is taken as the maximum shear strain amplitude from a set of 30 shear strains $(\gamma^1, \gamma^2, \ldots, \gamma^{30})$, determined from Eqs. (6)–(8). The constant, ε_0, is determined from knowledge of the centrifugal load P at a particular cross sectional area of the blade.

As the bulk and local temperatures are obtained for all the points in mission, it is observed that bulk temperature response may be lagging a response associated with points at higher local metal temperature during the loading portion of the cycle in the mission. The opposite occurs during the unloading part of the cycle in the mission. Using this procedure, local temperatures are computed along with local maximum shear strains, which when plotted together yield the so-called temperature versus strain "peanut curve." This will be presented in the results section. There will be points in the peanut curve that will have temperature response in-phase with strain response while other points will be out-of-phase with strain responses. This phase relationship will yield different fatigue capability to be considered in life prediction calculations.

Fatigue Capability. Blade fatigue capability is defined as the number of cycles to crack-initiation in the part due to cyclic operating conditions. This capability is directly related to the type of cycles in a mission. Figure 2 depicts representations of typical mission types. Unlike commercial missions, military missions are characterized by multiple throttle excursions associated with maneuvers such as climb, intercept, and air-to-air combat. A diagram of a commercial mission is shown in Fig. 2(*a*), while a diagram for military mission is shown in Fig. 2(*b*). In these figures, Roman numerals I, III, and IV refer to different cycle types. Type I is characterized by the operation profile segments from cold metal to maximum power and back to engine shutdown. Type III is characterized by the profile segments from idle to maximum power and back to idle, whereas Type IV is characterized by segments from low cruise to maximum power and back to low cruise. Note that Type II is not used here for clarity, as it usually describes a type of thermal mechanical fatigue during lab testing [11]. Also note that the mission types described here are not to be confused with the types described in the introduction for microscopic octahedral damage.

The total accumulation of cycles in a mission profile is defined

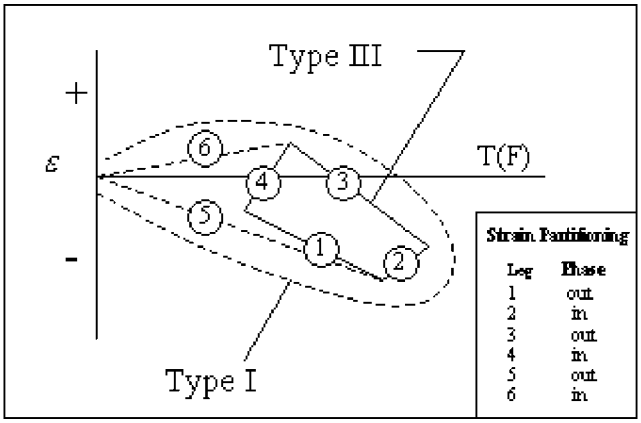

Fig. 3 Overall peanut curve for strain versus temperature for a point in the blade

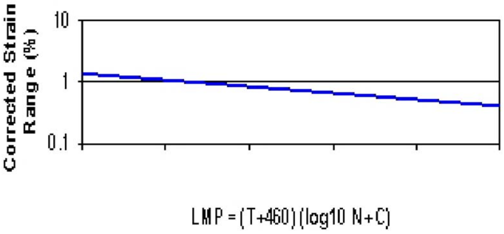

Fig. 4 Typical fatigue data curve

as TACs=Type I+1/4 Type III+1/40 Type IV. As described before, typical commercial type cycles are simpler than military cycle types, as depicted in Fig. 2, and they can be defined by Type I cycles.

As the peanut curve is obtained from the transient analysis, a set of segments is placed around the peanut curve response to characterize the overall thermal-mechanical response of a local region in the blade. Figure 3 depicts one such envelope in the strain versus temperature plot. In this figure, the inner cycle, described by 1-2-3-4 segments, corresponds to a type III cycle, whereas the outer cycle, described by 5-2-3-6 segments, corresponds to a Type I cycle. A Type IV cycle would be characterized like Type III but with smaller inner cycles.

The different legs of the cycle can be either in-phase or out-of-phase in the temperature-to-strain relationship. Therefore, each segment leg will produce different fatigue damage. The material capability, N, is taken as the maximum number of cycles-to-crack-initiation for a particular segment in the peanut curve with maximum strain range and a maximum metal temperature point in that segment. The material fatigue capability is based on minus 3σ capability data [11]. In general, material fatigue capability curves can be provided in terms of temperature, stress ratios, frequencies, and environment. In this case, strain range was related to the number of cycles to crack initiation through a fatigue Larson-Miller parameter, defined as $\mathrm{LMP}=(T+460)[\log(N)+C]$ in the Appendix. A typical representation for the material fatigue capability curve is presented in Fig. 4. It has been observed that most of the fatigue data coalesces onto a single curve when plotted for corrected strain range versus fatigue Larson-Miller parameter as shown in Fig. 4.

For a simple cycle with four segments or legs, as shown in Fig. 3, the overall fatigue capability, N, would be obtained for cycle Types I, III, and IV, as follows:

$$N_{\mathrm{I,III,IV}} = \left\{ \frac{1}{1/2N_{\text{1st Leg}} + 1/2N_{\text{2nd Leg}} + 1/2N_{\text{3rd Leg}} + 1/2N_{\text{4th Leg}}} \right\}_{\mathrm{I,III,VI}}. \tag{17}$$

The factor 2, used in Eq. (17) accounts for one load direction of the cycle segment. This provides a capability higher than that of a cycle testing data, N, where the load path is reversed continuously. To calculate the overall fatigue life, N_f, the lives for each mission profile are calculated using the results of Eq. (17), as follows:

$$\frac{\mathrm{TACs}}{N_f} = \frac{\text{Type I}}{N_{\mathrm{I}}} + \frac{\text{Type III}}{N_{\mathrm{III}}} + \frac{\text{Type IV}}{N_{\mathrm{IV}}},$$

$$\text{where: TACs} = \text{Type I} + \frac{1}{4}\text{Type III} + \frac{1}{40}\text{Type IV}. \tag{18}$$

Having determined the fatigue capability of the material, the creep capability assessment is presented next. In the end, the component life will be determined when creep damage is factored in the component capability by debiting thermal-mechanical accumulated cycles using Miner's rule for damage.

Fatigue-Creep Capability. In general, creep involves thermally activated processes that show dependence on temperature through the factor, $\exp(-\Delta H_i/RT)$, where ΔH_i is the activation energy for the controlling process, R is the Universal gas constant, and T is the absolute temperature [22]. When viewed at the microscopic scale, creep involves thermally activated processes that can be expressed as:

$$\dot{\varepsilon} = \sum_i Z_i \sigma_i(T,S) \exp\left(\frac{-\Delta H_i(T,S)}{Rt} \right), \tag{19}$$

where, the function Z_i includes the frequency of vibration of the flow unit; entropy change; temperature, T; a structure term, S; σ_i is the stress function which may include temperature and the structure term; and ΔH_i is the true activation energy for the ith mechanism controlling creep [22]. The number, distribution, and length of dislocations, type (e.g., edge, screw, pileup, etc.), and dispersion of precipitates, and other geometrical details are included in the structure term, S. Since creep depends on thermally activated rate processes, it is likely that for these processes, the applied stress will tend to lower the potential barrier resisting creep deformation. In such cases, the apparent activation energy, ΔH_c, should be stress-dependent and is given by [22]:

$$\Delta H_c = \Delta H_i - Vf(\sigma), \tag{20}$$

where, V is the activation volume and σ is the applied stress. If the stress function involves internal shear stresses, which are related to the shear modulus, then the function $f(\sigma)$ will also be temperature dependent. This stress effect is expected to decrease with increasing temperature. On the other hand, V may increase in temperature. Since V and σ_i may vary in opposite sense with temperature, the effect on the apparent activation energy, ΔH_c, can be used in the creep rate equation (19) directly for determining

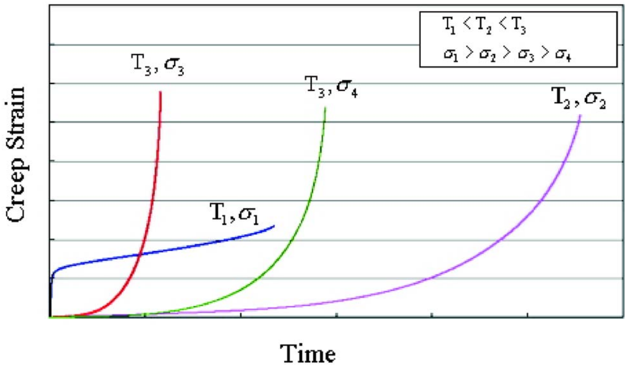

Fig. 5 Typical creep curves

material creep deformation [22].

Isothermal, constant load, creep tests are usually conducted on uncoated specimens in air at different conditions. Specimens were tested for each condition in order to insure a modicum of statistical validity for the creep properties measured. Displacement versus time data logged during the creep tests are then converted into typical creep strain versus time plots as shown in Fig. 5.

The creep curve obtained at T_1, σ_1 exhibits a strong primary creep component. In contrast, primary creep is negligible at a higher temperatures and lower stress values, T_3, σ_3. The former condition results in steady state creep observed over much of the creep test and a relatively short tertiary creep regime. On the other hand, the creep curve obtained at T_3, σ_3 shows no steady state creep. Instead, the tertiary stage involving a continuous increase in the creep rate represents the major portion of the creep curve. No single equation has been found suitable to model the creep rate in all three regimes and for the entire range of temperatures and stresses. However, as a first approximation the following constitutive equation can be used:

$$\dot{\varepsilon} = [A\sigma^n \exp(-\Delta H_c/RT)]t^m, \tag{21}$$

where, $\dot{\varepsilon}$ is the creep strain rate, σ is the applied stress, t is time, and T is absolute temperature. In this case, the creep equation (21) assumes that the strain rate depends upon time from the beginning of the creep process as $\dot{\varepsilon} \propto t^m$, and is therefore classified as a time-hardening-creep-rate behavior.

The high temperature regime is modeled by Eq. (21) where the coefficient, A, is taken as an empirical constant. For the lower temperatures, the time component, t^m, is not necessary in the creep strain equation, and the coefficient, A, can be replaced by the time function $A = A_0 t + A_1[1\text{-exp}(\text{-}rt)]$, where A_0, A_1, and r are empirical constants [23].

Creep data is then used to analyze this component in terms of the creep strain versus time and time required for attaining a limiting strain. Knowledge of design limiting creep strain and times required to attain those limit values yield the creep damage fraction as follows:

$$\text{Creep Damage} = \frac{\text{time}|_{\sigma,T}}{\text{time limit}} = \frac{t}{t_L}. \tag{22}$$

To determine the number of service cycles, n, the following Miner's fraction rule is used:

$$\overset{\substack{\text{Overall}\\\text{Mission}\\\text{Cycle}}}{\sum_{k=1}} \left\{ \underbrace{\overset{\substack{\text{Creep}\\\text{Load}\\\text{Cycles}}}{\sum_{i=1}} \left[\frac{t_i}{t_{L,i}}\right]}_{\text{Creep Damage}} + \underbrace{\overset{\substack{\text{Fatigue}\\\text{Cycles}}}{\sum_{i=1}} \left[\frac{n_i}{N_{f,i}}\right]}_{\text{Fatigue Damage}} \right\} = 1, \tag{23}$$

where, t stands for time at a temperature to induce creep damage in the part, t_L, stands for time to attain limiting strain, either a pre-determined value or the ultimate stress-rupture point, and N_f is the fatigue capability provided by Eq. (18). Application of this methodology is now illustrated to the design of the NASA E^3 HPT blade.

Results and Discussion

Cooled Airfoil Study. The NASA E^3 HPT blade is used as a vehicle to demonstrate the thermal-mechanical life prediction system for uncoated anisotropic turbine components. This analysis follows the material described in the previous sections. The 3D model was already described in Fig. 1, using ANSYS, and is composed of 21,567 elements, 13,494 of which are 3D-10 node tetrahedral structural solid elements in the trailing edge, while 8073 are 3D-20 node structural solid elements in the rest of the airfoil. This hybrid finite element model was used to improve the meshing of the pedestals in the trailing edge region of the airfoil.

In the analysis for this blade model, the durability design point is obtained first for the performance parameters of interest in terms of pressure and temperature. The setup of thermal boundary conditions for the model is a very laborious process. On the external side, computational fluid dynamic codes are used to set-up external pressure and Mach number distributions for free-stream conditions with specified turbulence intensity levels. Boundary layer programs are used to establish the external heat transfer coefficients based on expected wall roughness. Gas recovery temperatures and film cooling effectiveness, usually obtained from previous testing, are used to determine the adiabatic wall (film) temperatures. In the end, external heat transfer coefficients and film temperatures are specified as external boundary conditions for the model. Inside the airfoil, flow network models are used to determine internal pressure drops and Mach number distributions. Heat transfer correlations, based on previous testing, can be used to determine the internal heat transfer characteristics of the blade cooling system under the effects of rotation. Thus, the network flow analysis provides the means to determine internal heat transfer coefficients and coolant temperatures as internal boundary conditions for the model. The thermal results are shown in Fig. 6. These results were compared with the results presented in report [15] and compare well.

The mechanical boundary conditions for the model are such that the bottom plane must remain fixed in the direction of the blade stacking axis, the ⟨001⟩ axis, or the z direction. One node near the middle of an aft internal rib remains fixed in space for all three directions, ⟨100⟩, ⟨010⟩, and ⟨001⟩, and one other node near the leading edge is fixed in the ⟨010⟩ axis or y direction. The top plane nodes are constrained to remain coupled and planar. The primary crystal coordinate system has the ⟨001⟩ axis coincident with pull direction of the centrifugal force experienced by the blade at rated design speed. In order to simulate this, a uniformly distributed load is applied normally to the top face of the blade section. The planar boundary condition applied this way is a first approximation to boundary conditions that may be experienced by the blade section. The assumption is that there is sufficient constraint, because of the surrounding blade material, to counteract bending moments seen as a result of temperature gradients and nonuniform deformation rates [5]. The blade deformation will largely be controlled by the conditions at the ends of the blade. At the root, the blade will experience a relatively lower and more uniform temperature. Thus, if the root of the blade experiences a more uniform temperature, any other cross section will be forced to deform at a uniform rate [5]. Therefore, to a first approximation, the constraint of planar sections has been applied in the blade model. The results of this structural analysis are shown in Fig. 7 in terms of von Mises total strains. It should be noted that the analysis provided here could be applied to a more complex blade model as well.

Since no seed crystal is used in the casting process, the secondary orientation has nearly a random orientation. Therefore, the principal crystal coordinate system is rotating through a sequence

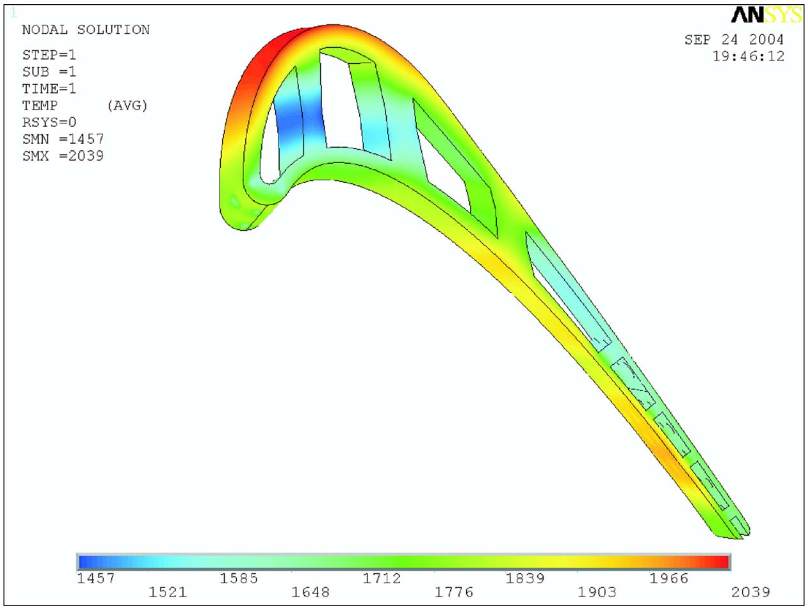

Fig. 6 NASA E^3 HPT blade thermal results

of in-plane angles (in a plane perpendicular to the ⟨001⟩ direction) to determine the worst effect in terms of compliance matrix, given by Eq. (2). The transformed stress vector is given by Eq. (3). In this case, the coordinate system was rotated by an in-plane angle of 45 deg. The slip system shear stress amplitudes are then calculated using Eqs. (6)–(8) to give 30 shear stresses: 24 shear stresses on the octahedral planes and six shear stresses on cube slip systems, denoted as $(\tau^1, \tau^2, \ldots, \tau^{30})$. These can be obtained for every point in the airfoil. The corresponding strain results are then used to obtain the weighting factors of Eq. (15) for a subsequent transient analysis.

The transient analysis is illustrated here for a point on the convex or suction side point on the high-curvature region of the airfoil. The time constants required for the solution are calculated as well. The temperature profile for T_g and T_c are obtained from profiles similar to that of Fig. 8. The mass flow is also needed to calculate the time constants. Figure 9 illustrates a profile for the mass flow rate. It should be noted that these profiles are for a typical commercial aircraft engine. For military engines, other suitable profiles would have been obtained, however the transient solution procedure remains the same.

As a result, the transient strain versus temperature peanut curve can be obtained for any point in the airfoil. Figure 10 illustrates the strain versus temperature peanut curve for a point on the suction side high-curvature region of the airfoil.

In this plot, the take-off segment culminates on a point with the maximum temperature followed by climb and cruise segments. At the end of the cruise segment, the plane starts the descent part of the cycle and during landing, the thrust reversal leads again to relatively higher strains and temperatures of the inner peanut

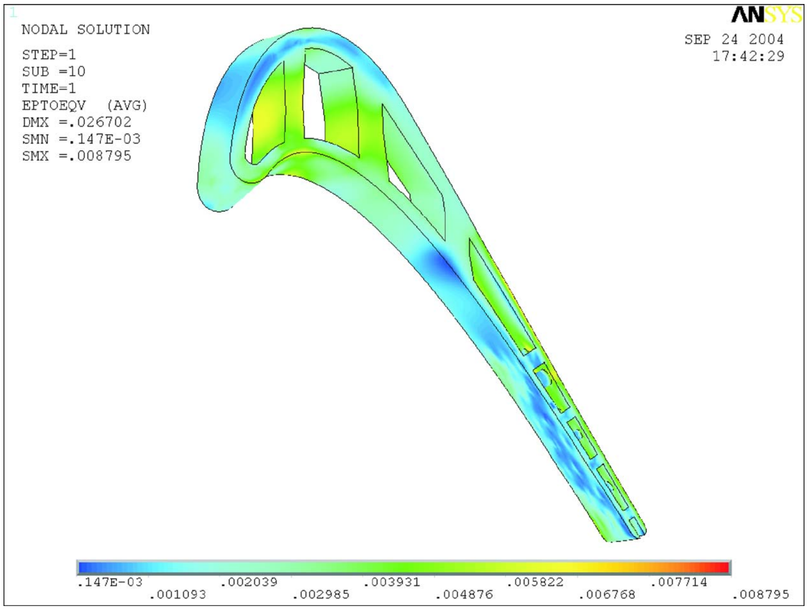

Fig. 7 NASA E^3 HPT blade thermal-mechanical results in terms of equivalent strains

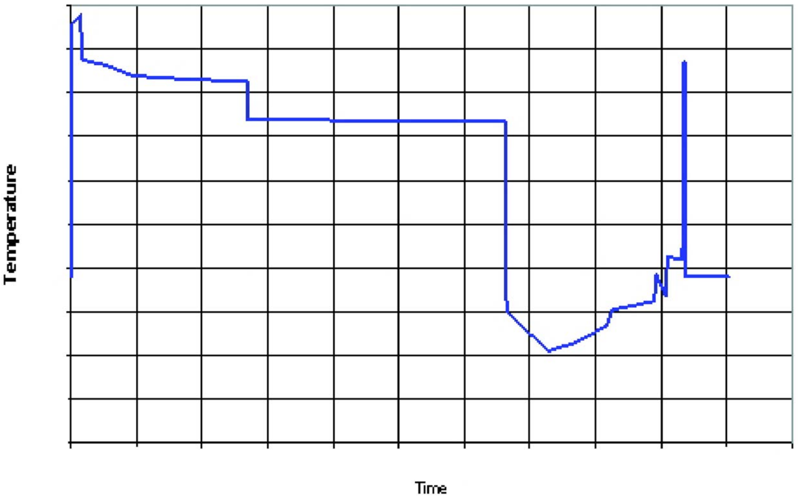

Fig. 8 Performance parameters for a typical commercial aircraft engine mission

curve loop before taxiing to the gate.

The fatigue cyclic counting method, expressed by Eqs. (17) and (18), is then used to calculate the fatigue capability for this point in the airfoil. This same procedure could be applied for all points in the airfoil, and it is up to the analyst to select the desired number of points. Finally, a creep analysis is performed to debit the fatigue life using Miner's rule for damage as per Eq. (23).

In this case, the creep rate equations were modeled in ANSYS along with a bilinear kinematic plasticity model to determine the total number of hours required to achieve a limiting strain level for the design. During the creep run, most of the external points in the airfoil experience stress relaxation, while inner rib points inside the airfoil experience a state of overstress. This is illustrated in Figs. 11 and 12.

Figure 11 depicts the behavior of two points: (1) A suction side high curvature point with the highest metal temperature, which experiences stress relaxation, and (2) another rib point with the coldest temperature which experiences a state of overstress.

Figure 12 illustrates the overall state of stress of the airfoil section at the initial time and after 50 h of hot time at the durability design point. This figure clearly depicts the state of stress relaxation associated with the external points of the airfoil, and the state of potential overstress associated with the cold ribs inside the airfoil section.

In the present case, 10,187 cycles were calculated using the fatigue counting method of Eqs. (17) and (18). Then, using the results of this analysis, Eq. (23) is used to calculate the fatigue-creep capability of the selected point(s). It was found the fatigue results would have to be updated to account for creep damage yielding 2910 cycles for the point of interest located on the suction side high curvature region of the airfoil. In the original report [15], 2200 flight missions were targeted as a requirement for this airfoil during a service life of 10,000 h.

Fig. 9 Core flow for a typical commercial aircraft engine mission

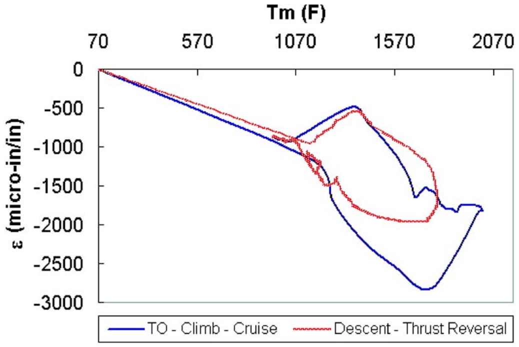

Fig. 10 NASA E^3 HPT blade strain vs temperature "peanut" curve

This illustrative example concludes the technical presentation of the procedure for thermal-mechanical life prediction. It should be mentioned that this procedure could be extended to any point in the turbine component, including stationary vanes, shrouds, and rotating blades.

Conclusions

The durability design of ever-improving components subject to high rotational speeds and gas temperatures is reaching a point where understanding of the fatigue and creep damage mechanisms has become critical to the design and life assessment of gas turbine engine components. This paper examines the problem and has identified the need for very detailed three-dimensional thermal, stress, strain, and life analysis to allow more reliable gas turbine engine designs.

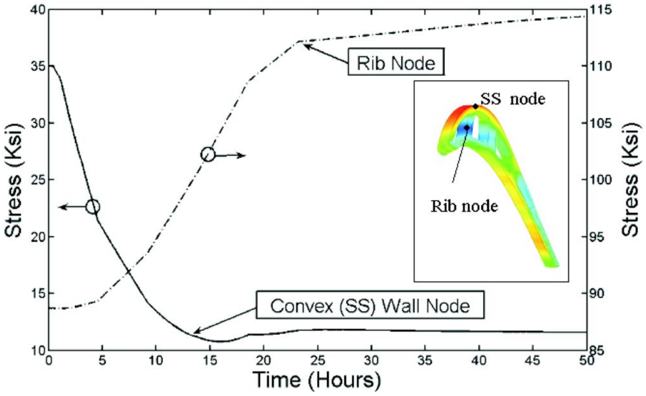

Fig. 11 Structural transient response showing von Mises stress profile for two airfoil points: (1) External suction side point experiencing high temperatures and (2) rib point experiencing relative cold temperatures

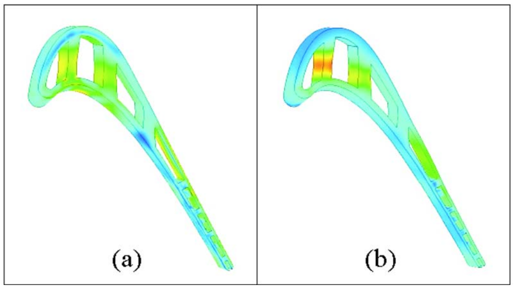

Fig. 12 Structural transient response at (a) initial time, and (b) at 50 h of hot time illustrating stress relaxation on the external points of the airfoil, and overstress on the cold rib regions of the airfoil

A method of determining the mission maximum amplitude of octahedral shear strain has been conceived and developed. The necessary information for use of this method is the knowledge of the 3D state of stress of the component at the durability design point. The transient analysis is developed to determine the response of different parts in the airfoil. A set of strain-versus-temperature peanut curves could then be used as a platform for fatigue cycle counting. This procedure could be applied to one or many points of interest in the airfoil, where the required time constants are determined for each point.

Creep behavior of a component in a mission needs to be determined, as each point in the airfoil will behave differently. This involves a 3D finite element creep analysis with the required modeling equations. Once creep behavior is established, cumulative creep damage can be used in lifing calculations.

The life due to fatigue and creep interaction is performed with the traditional Miner's rule method to assess creep and fatigue damage. The method has been applied to the NASA E^3HPT cooled blade. The results correlate well with the original design calculations and are in agreement with the design life requirements for this blade.

Nomenclature

A = surface area
a_{mn} = direction cosines
c = specific heat
c_p = fluid specific heat at constant pressure
E = modulus of elasticity
h = heat transfer coefficient
H_i = activation energy of ith process
H_c = apparent activation energy
l = directional vector
m = flow rate
n = normal vector or mission point
N = cycle capability
Q = transformation matrix for stress
q_{ij} = element of transformation matrix
R = universal constant
S = structural term for creep equation
T = temperature
TACs = total accumulated cycles
t = time
V = volume
X = variable in Runge-Kutta formulation
W = weighting factor
Z = state variable for creep equation

Greek Symbols

α = thermal expansion coefficient or slip plane
β = slip direction
Δ = denotes difference
ε = strain
φ = $(T_g - T_m)/(T_g - T_c)$, cooling effectiveness
γ = shear strain
ρ = metal density
λ = reciprocal of time const
σ = stress
τ = shear stress or time constant

Subscripts

b = airfoil bulk
c = coolant
co = coolant out
ci = coolant in
d = displacement

g = gas
f = fatigue
i = ith process
L = limit
m = metal or variable counter
r = residual
ref = reference quantity
ss = steady state

Appendix

A brief description of the thermal-mechanical fatigue (TMF) test setup is provided first followed by the derivation of the fatigue parameter similar to that proposed by Larson and Miller [24] for creep testing. In the test setup, the temperature controller controls the induction heater that provides the temperature-time profile to test specimen. The extensometer measures the specimen strain during the testing, and the servo-controller provides feedback loop to the test specimen [8]. After stabilization and calibration runs, the resulting cyclic test data leads to a relationship between strain-range to number of cycles-to-crack-initiation, N, for different metal temperatures. The condition for the specimen to reach the cycle-to-crack-initiation stage is usually based on a pre-determined value of test load compliance. Naturally, several curves are fitted to strain-range versus cycles-to-crack-initiation, N, data for a specified metal temperature. These curves can be further reduced into a master curve of strain-range, corrected by the ratio of local modulus of elasticity to that of the primary crystal direction, versus a cycle-temperature parameter. That is, as the strain rate is related to the fatigue damage; the damage function takes the form, following Larson and Miller [24], as

$$N^{-1} = Z' e^{(-\Delta H/T)}. \tag{A1}$$

where the various terms are defined similar to those for Eq. (19). Equation (A1) is easily reduced to the general form:

$$(T + 460)[\log N + Z] = \text{constant}, \tag{A2}$$

where the resulting constant is set equal to the Larson-Miller parameter for fatigue, denoted by LMP. The empirical constant, Z, is determined by testing at the onset of crack propagation and is given the numerical value of 2, for fatigue processes, which is considerably different than that used for creep processes attaining numerical values between 18 and 20 [24].

Even tough, this paper deals with fatigue capability of uncoated gas turbine components, the addition of metallic or bond coatings (BC) will debit the strain capability of the coated components for a pre-determined Larson-Miller parameter value. This debit in fatigue capability can be offset by the application of thermal barrier coating (TBC) onto the metallic coating and metal substrate. In general, TBC systems reduce thermal loads to the part, BC systems reduce oxidation and corrosion rates. The overall coating system will have a lower fatigue capability than that of uncoated components. But, since the gas turbine thermal loads are extremely high, application of TBC and BC systems trade favorably for the durability of the gas turbine components. These topics will be analyzed in detail in a follow-up paper on this subject.

References

[1] DeLuca, D. P., and Annis, C. G., Jr., 1995, "Fatigue in Single Crystal Nickel Superalloys," Office of Naval Research (ONR) Paper No. FR-23800.
[2] Dame, T. L., 1985, "Anisotropic Constitute Model for Nickel Base Single Crystal Alloys: Development and Finite Element Implementation," Ph.D. thesis, University of Cincinnati.
[3] MacLachlan, D. W., and Knowles, D. M., 2000, "Creep-Behavior Modeling of Single-Crystal Superalloy CMSX-4," Metall. Mater. Trans. A, **31**, pp. 1401–1411.
[4] Seetharaman, V., 2002, "Thickness Debit Properties of PW1484," Pratt and Whitney Materials and Processes Engineering, Interim Report, Nov.
[5] MacLachlan, D. W., and Knowles, D. M., 2001, "The Effect of Material Behavior on the Analysis of Single Crystal Turbine Blades: Part I—Material Model," Fatigue Fract. Eng. Mater. Struct., **25**, pp. 385–398.
[6] Arakere, N. J., 2001, "High-Temperature Properties of Single Crystal Superalloys in Air and Hydrogen," ASME Paper No. 2001-GT-0585.
[7] Naik, R. A., DeLuca, D. P., and Shah, D. M., 2004, "Critical Plane Fatigue Modeling and Characterization of Single Crystal Nickel Superalloys," ASME J. Eng. Gas Turbines Power, **126**, pp. 391–400.
[8] McKnight, R. L., Laflen, J. H., and Spamer, 1981, "Turbine Blade Tip Durability Analysis," Paper No. NASA CR-165268.
[9] Soechting, F. O., 1985, "Turbine Low Cycle Fatigue Design Program," Wright-Patterson Final Report No. AFWAL-TR-86-2124.
[10] Arvanitis, S. T., Symko, Y. B., and Tadros, R. N., 1986, "Multiaxial Life Prediction System for Turbine Components," ASME Paper No. 86-GT-242.
[11] Heine, J. E., Warren, J. R., and Cowles, B. A., 1988, "Thermal Mechanical Fatigue of Coated Blade Materials," Wright-Patterson Final Report No. ERDC-TR-89-4027.
[12] Moreno, V., Nissley, D. M., Lin, and L. S., 1985, "Creep Fatigue Life Prediction for Engine Hot Section Materials (Isotropic) Second Annual Report," Paper No. NASA CR-174844.
[13] Nissley, D. M., and Meyer, T. G., 1992, "Life Prediction and Constitutive Models fro Engine Hot Section Anisotropic Materials Program," Paper No. NASA CR-189223.
[14] MacLachlan, D. W., and Knowles, D. M., 2001, "The Effect of Material Behavior on the Analysis of Single Crystal Turbine Blades: Part II—Component Analysis," Fatigue Fract. Eng. Mater. Struct., **25**, pp. 399–409.
[15] Thulin, R. D., and Howe, D. C., 1982, "Energy Efficient Engine High-Pressure Turbine Design Report," Paper No. NASA CR-165608, PWA-5594-171.
[16] ANSYS User's Manual, Swanson Analysis Systems, Inc., Volumes I,II,III,IV, Revision 5.0.
[17] Lekhnitskii, S. G., 1963, *Theory of Elasticity of an Anisotropic Elastic Body*, 1st Ed. Holden-Day, San Francisco.
[18] Stouffer, D. C., and Dame, L. T., 1980, *Inelastic Deformation of Metals Models, Mechanical Properties and Metallurgy*, 1st Ed. Wiley, New York.
[19] Ozisik, M. N., 1980, *Heat Conduction*, 1st Ed. Wiley, New York.
[20] Scheid, F., 1988, *Theory and Problems in Numerical Analysis*, 2nd Ed. McGraw-Hill, New York.
[21] Burgreen, D., 1968, "Structural Growth Induced by Thermal Cycling," ASME Paper No. 68-WA/Met-14.
[22] Garafalo, F., 1965, *Fundamentals of Creep and Creep-Rupture in Metals*, Macmillan, New York.
[23] Shames, I. H., and Cozzarelli, F. A., 1997, *Elastic and Inelastic Stress Analysis*, 1st ed. Taylor and Francis, London.
[24] Larson, F. R., and J. Miller, 1952, "A Time-Temperature Relationship for Rupture and Creep Stress," Trans. ASME, **1**, pp. 765–775.

Experiments With Three-Dimensional Passive Flow Control Devices on Low-Pressure Turbine Airfoils

Douglas G. Bohl

Ralph J. Volino
e-mail: volino@usna.edu

Department of Mechanical Engineering,
United States Naval Academy,
Annapolis, MD 21402

The effectiveness of three-dimensional passive devices for flow control on low pressure turbine airfoils was investigated experimentally. A row of small cylinders was placed at the pressure minimum on the suction side of a typical airfoil. Cases with Reynolds numbers ranging from 25,000 to 300,000 (based on suction surface length and exit velocity) were considered under low freestream turbulence conditions. Streamwise pressure profiles and velocity profiles near the trailing edge were documented. Without flow control a separation bubble was present, and at the lower Reynolds numbers the bubble did not close. Cylinders with two different heights and a wide range of spanwise spacings were considered. Reattachment moved upstream as the cylinder height was increased or the spacing was decreased. If the spanwise spacing was sufficiently small, the flow at the trailing edge was essentially uniform across the span. The cylinder size and spacing could be optimized to minimize losses at a given Reynolds number, but cylinders optimized for low Reynolds number conditions caused increased losses at high Reynolds numbers. The effectiveness of two-dimensional bars had been studied previously under the same flow conditions. The cylinders were not as effective for maintaining low losses over a range of Reynolds numbers as the bars. [DOI: 10.1115/1.2137743]

Introduction

Boundary layer separation is a known problem on some modern low-pressure turbine (LPT) airfoils, due to the strong adverse pressure gradients created when designers impose higher loading in an effort to improve efficiency and lower cost by reducing airfoil count in engines. Separation bubbles, particularly those which fail to close, can result in a significant loss of lift and a subsequent degradation of engine efficiency (e.g., Hourmouziadis [1], Mayle [2], and Sharma et al. [3]). The problem is particularly relevant in aircraft engines. Airfoils optimized to produce maximum power under takeoff conditions may still experience boundary layer separation at cruise conditions, due to the lower density and therefore lower Reynolds numbers at altitude. A component efficiency drop of 2% may occur between takeoff and cruise conditions in large commercial transport engines, and the difference could be as large as 7% in smaller engines operating at higher altitudes [4,5]. Prediction and control of suction side separation, without sacrifice of the benefits of higher loading, is therefore, crucial for improved engine design.

Separation on airfoils is complicated by boundary layer transition. Separated flow transition in the LPT has been the focus of several recent studies. Volino [6] provides a review and describes as follows the transition process on the suction side of a typical LPT airfoil. The strong acceleration on the leading section of the airfoil keeps the boundary layer thin and laminar, even in the presence of elevated freestream turbulence. In most cases Volino [6] observed that the boundary layer separated just downstream of the suction peak. If transition then occurred in the shear layer over the separation bubble, it caused the boundary layer to reattach.

A few recent studies have focused on control of transition and reattachment in the LPT. Some have used active devices. Huang et al. [7] and Hultgren and Ashpis [8] employed high voltage electrodes to produce glow discharge plasma in a boundary layer to control separation. Bons et al. [4] used steady and pulsed vortex generator jets. Volino [9] used oscillating vortex generator jets with no net mass flow. Sieverding et al. [10] used adjustable devices built into the suction surface.

While active flow control provides a means for adjusting to changing flow conditions and in some cases the benefits of calmed regions [4,9], passive flow control holds the advantage of simplicity. Van Treuren et al. [11], Lake et al. [12], Murawski and Vafai [13], Byerley et al. [14], Volino [15], Sieverding [10], Vera et al. [16], and Zhang and Hodson [17] used various passive devices under LPT conditions to control separation and in many cases reduce losses. Most employed a relatively simple modification, such as a small trip wire or bar (essentially roughness), on the suction surface of an airfoil.

Successful flow control results in a thin, attached boundary layer at the trailing edge of an airfoil, thereby reducing losses. The consensus of the studies listed above is that a device on the suction surface should be placed at or slightly downstream of the pressure minimum. This is a logical result, since the effects of a device farther upstream would be damped by the favorable pressure gradient, and a device too far downstream would lie under the separation bubble and be ineffective. Volino [15] used rectangular bars and found that the optimal bars were not large enough to immediately trip the boundary layer to turbulent, but instead allowed a small separation bubble to form. The bars introduced small disturbances that grew and caused transition and reattachment to move upstream of their location in the uncontrolled case, as explained in Volino and Bohl [18]. The optimal bar height depended on the flow conditions. As Re or freestream turbulence is lowered, the separation bubble becomes larger, so a larger bar is needed to produce enough of a disturbance to move transition sufficiently far upstream. A flow control device producing too small a disturbance will allow a larger separation bubble than desired, resulting in a thicker boundary layer downstream of reattachment and higher losses. Similarly, too large a disturbance will

---

Contributed by the International Gas Turbine Institute (IGTI) of ASME for publication in the Journal of Turbomachinery. Manuscript received October 1, 2004; final manuscript received December 1, 2004. IGTI Review Chair: K. C. Hall. Paper presented at the ASME Turbo Expo 2005: Land, Sea and Air, Reno, NV, June 6–9, 2005, Paper No. GT2005-68969.

move transition farther upstream than necessary, resulting in a longer turbulent region and higher losses. Volino [15], Sieverding et al. [10], and Zhang and Hodson [17] all found that under steady flow conditions, devices optimized for low Re tend to increase losses at high Re. Devices optimized for high Re can be too small to be effective at low Re. Unsteady wakes from upstream airfoils promote transition and reattachment, and Zhang and Hodson [17] found that in unsteady flow optimal control was achieved using smaller devices than in comparable steady flow cases. This made it possible in unsteady flow to reduce losses with a single device over a wider range of Re.

Passive flow control devices of various geometries have been tested, but it is still uncertain if any particular device is superior. In preliminary testing, Volino [15] considered trip wires, rectangular bars, and delta wing vortex generators. All produced similar results. Sieverding et al. [10] found that straight trip wires were somewhat better than rows of spherical roughness elements, but only a limited number of cases were tested. Lake et al. [12] found dimples superior to other devices, presumably because the dimples produced less blockage than devices that protruded into the flow. Again, however, the number of cases considered was limited, and more recent evidence [15,17] suggests that optimal devices should be quite small and produce minimal blockage even if they do extend into the flow. Zhang and Hodson [17] noted differences in transition location with straight and "wavy" trip wires and rectangular bars. The sharp backward facing step on a bar, for example, produced an earlier transition than a round trip wire of the same height. Still, this does not preclude that a bar and a slightly larger wire could produce comparable results.

It is still possible that some devices might prove better for reducing losses than others. Reynolds number can vary by an order of magnitude during engine operation given the change in ambient pressure between takeoff and cruise. Since passive devices by definition cannot be adjusted as conditions change, it is highly desirable to use devices that reduce losses over as large a Reynolds number range as possible. Given the potential payoff of a more efficient engine, it is worthwhile to further consider passive flow control devices of different geometries.

A row of small vertical cylinders is considered in the present study. The cylinders are located at the pressure minimum on the suction surface and the spacing between cylinders is varied. The geometry was chosen in the hope that in comparison to two-dimensional bars or trips wires of the same height, isolated elements might produce a stronger disturbance due to the three-dimensional nature of the flow around them, while presenting less blockage due to the gaps between elements. The net result would presumably be successful separation control with lower losses. Experimental conditions match the low freestream turbulence cases of Volino [15]. Details of the experimental conditions and the results are presented below.

Experiments

Experiments were conducted in a low speed wind tunnel, described by Volino et al. [19]. Briefly, air enters through blowers and passes through a honeycomb, a series of screens, two settling chambers, and a three-dimensional contraction before entering the test section. At the exit of the contraction, the mean velocity is uniform to within 1%. The freestream turbulence intensity is 0.5% ±0.05%. Nearly all of this freestream "turbulence" is actually streamwise unsteadiness at frequencies below 20 Hz and is not associated with turbulent eddies. The root-mean-square intensities of the three components of the unsteadiness are 0.7%, 0.2%, and 0.2% in the streamwise, pitchwise, and spanwise directions, respectively.

The test section, shown in Fig. 1, follows the contraction and consists of the passage between two airfoils. Details are listed in Table 1 and more information is available in Volino [6]. A large span to chord ratio of 4.3 was chosen to insure two-dimensional flow at the spanwise centerline of the airfoils, where all measurements were made. Upstream of each airfoil are flaps, which control the amount of bleed air allowed to escape from the passage. The flaps, along with a tailboard on the pressure side of the passage, are adjusted to produce the correct leading edge flow and pressure gradient along the airfoils. The flow in the passage matches that in a multiblade cascade. The geometry of the passage corresponds to that of the Pak-B airfoil, which is an industry supplied research airfoil that is representative of a modern LPT design. It has been used in several studies, as noted in Volino [6].

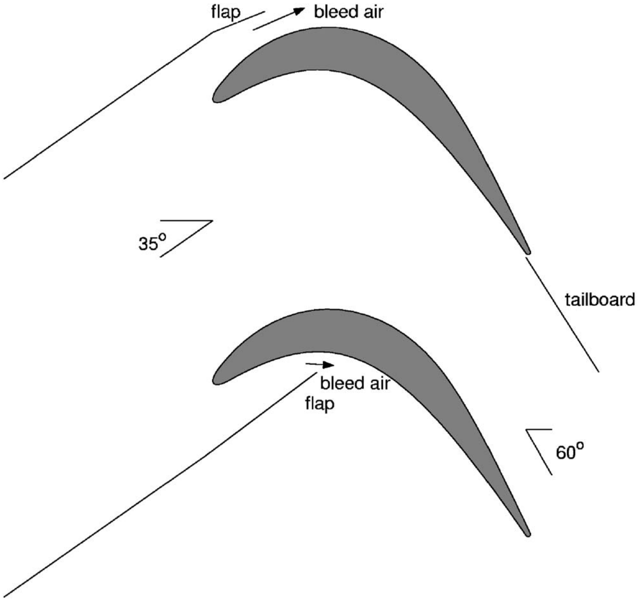

Fig. 1 Schematic of the test section

Experimental conditions match the smooth airfoil baseline cases of Volino [6], who considered five Reynolds numbers (Re $=25{,}000$, 50,000, 100,000, 200,000, and 300,000). Reynolds numbers are based on the exit velocity from the passage and the suction surface length, L_s. Comparison data from cases with passive-bar flow control are from Volino [15]. The bars were of uniform rectangular cross section and extended along the airfoil, as shown in Fig. 2. The trailing edge of the bar was located at $s/L_s=0.51$, near the suction surface velocity peak. All bars were 6 mm wide in the streamwise direction. Bar heights of 0.4, 0.8, and 1.6 mm were used. The bar heights were all less than 1% of L_s. They compare to local boundary layer thickness at the bar location of about 3.8, 2.7, 2.0, 1.4, and 1.2 mm in the base line $\mathrm{Re}=25{,}000-300{,}000$ cases, respectively.

A row of small vertical cylinders is used in the present experimental cases. The cylinders are $D=6$ mm in diameter with one end affixed to the suction surface and the other extending into the flow. The cylinders are located in a line at the suction peak, in the same location as the bars described above, as shown in Fig. 2. Cylinder heights of 0.4 and 1.6 mm were considered, matching the smaller and larger bar heights of Volino [15]. Center to center cylinder spacings ranging from a pitch, P, of $1D$ (i.e., the cylinders were touching) to $30D$ were considered.

Measurements. Pressure surveys were made for each case using a pressure transducer (0–870 Pa range Validyne transducer) and a Scanivalve. Stagnation pressure was measured with a pitot tube upstream of the passage inlet, and 11 pressure taps were located on each airfoil along their spanwise centerlines. The uncertainty in Cp is 7% at $\mathrm{Re}=25{,}000$, and 4% in other cases. Most of this uncertainty is due to bias error. Stochastic error was minimized by averaging pressure transducer readings over a 10 s period. The flow control cylinders were moved in the spanwise di-

Table 1 Test section parameters

Axial chord (mm)	True chord (mm)	Pitch (mm)	Span (mm)	Suction side, L_s (mm)	Inlet flow angle	Exit flow angle	$\frac{U_e}{U_{\text{inlet}}}$
153.6	170.4	136.0	660.4	228.6	35 deg	60 deg	1.64

rection allowing documentation with the pressure taps directly downstream of the center of one cylinder and with the taps midway between the centers of two adjacent cylinders.

Profiles of the streamwise velocity component in the suction side boundary layer were measured for the $\text{Re}=50{,}000$ and 300,000 cases near the trailing edge at $s/L_s=0.944$. Profiles were measured at several spanwise locations relative to the position of the upstream cylinders. Data were acquired with a hot-wire anemometer (AA Lab Systems model AN-1003) and a single sensor boundary layer probe (TSI model 1218-T1.5). The sensor diameter is 3.8 μm, and the active length is 1.27 mm. At each measurement location, data were acquired for 26 s at a 20 kHz sampling rate (2^{19} samples). Data were acquired at 60 wall normal locations in each profile, extending from the wall to the freestream, with most points concentrated in the near wall region. The closest point was within 0.1 mm of the wall, which corresponds to $y/L_s=0.0004$ and between 0.02 and 0.04 boundary layer thicknesses. Uncertainties in the mean velocity are 3–5% except in the very near wall region where near-wall corrections (Wills [20]) were applied to the mean velocity. Uncertainties in the momentum and displacement thicknesses computed from the mean profiles are 10%. Uncertainty in the shape factor, H, is 8%. The uncertainty in the fluctuating streamwise velocity is below 10%, except in the very near wall region ($y<1$ mm, $y/L_s<0.004$) of the $\text{Re}=300{,}000$ cases, where spatial averaging effects, due to the finite length of the hot-wire sensor, may become important. This is discussed in Volino [6].

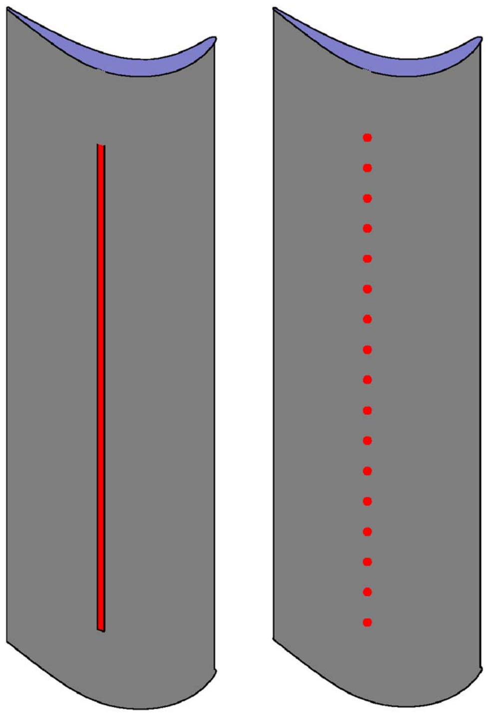
(*a*) (*b*)

Fig. 2 Scale drawing of suction side airfoil showing location of (*a*) bar, or (*b*) cylinders

Results

Pressure Profiles. Suction side pressure profiles for the cases with larger (1.6 mm high) cylinders are shown in Figs. 3–5. Also shown in each figure are the corresponding baseline results from Volino [6], the 1.6-mm-thick bar case results from Volino [15], and an inviscid solution for flow through the passage. Figure 3 shows results at $\text{Re}=25{,}000$ with various cylinder spacings and the pressure taps directly downstream of one cylinder. The data agree with the inviscid solution in the favorable pressure gradient region. The near wall flow slows as it approaches a cylinder or bar, causing a drop in the measured Cp below the inviscid solution at the fifth pressure tap. If the boundary layer separates and does not reattach, there is a drop in the suction peak, as indicated by low Cp values. In addition to this effect, if the blockage caused by a bar or cylinder is sufficiently high, the streamlines immediately downstream will be displaced as they flow over the sixth pressure tap, which may cause the measured local Cp to either rise or fall relative to the inviscid solution, depending on the geometry of a particular case. For controlling separation, cylinders with spacing of $P=2D$ or more are ineffective at $\text{Re}=25{,}000$. There is a plateau in Cp in the adverse pressure gradient region extending to the trailing edge, indicating a separation bubble that does not reattach. The $P=1D$ (touching) cylinders and the solid bar result in a large separation bubble which appears to be starting to reattach by the trailing edge, as indicated by the drop in Cp back toward the inviscid value at the last pressure tap. Figure 4 show the results at $\text{Re}=50{,}000$ with the pressure taps directly downstream of one cylinder ($z/P=0$, Fig. 4(*a*)) and with the taps downstream of the midpoint between adjacent cylinders ($z/P=0.5$, Fig. 4(*b*)). In the base line case, the boundary layer does not reattach.

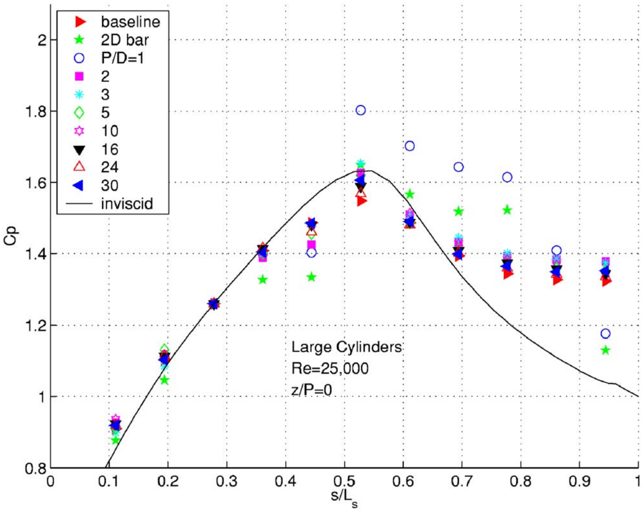

Fig. 3 Pressure profiles, large cylinders, $\text{Re}=25{,}000$, $z/P=0$

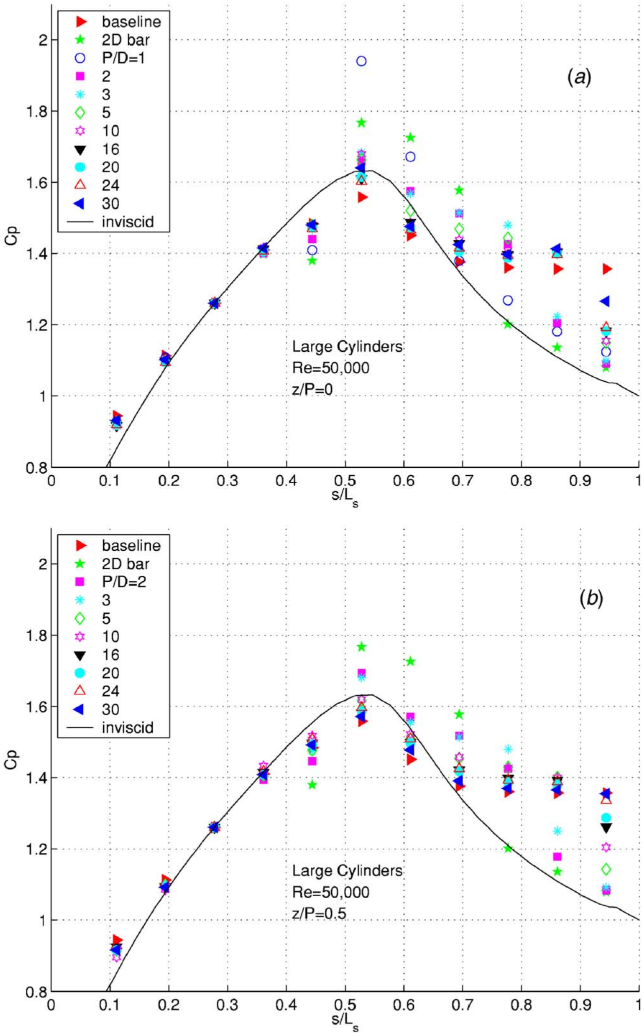

Fig. 4 Pressure profiles, large cylinders, Re=50,000, (*a*) *z/P* =0, (*b*) *z/P*=0.5

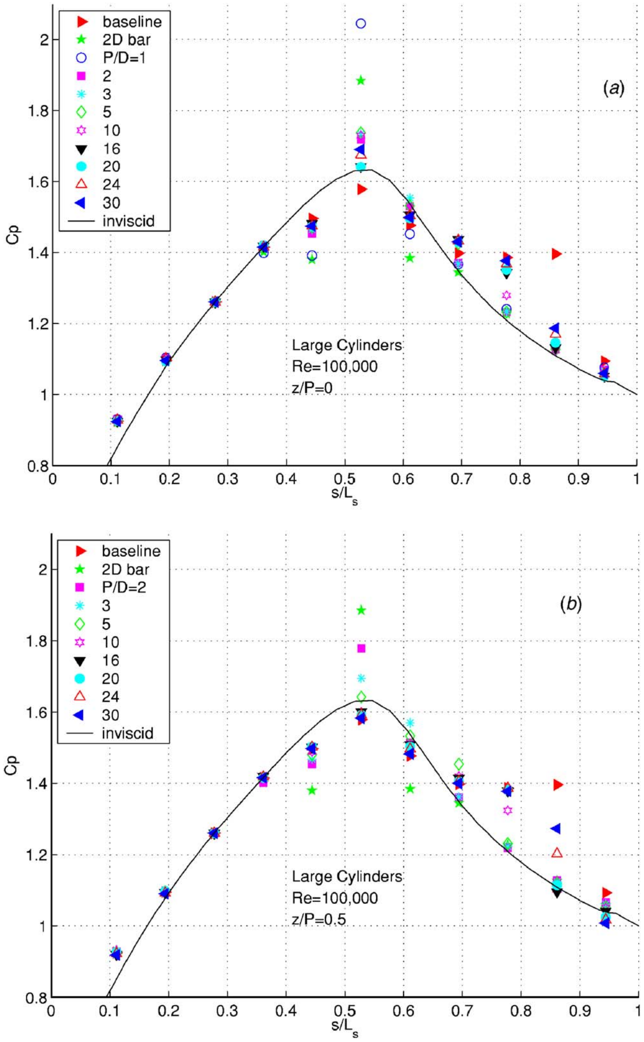

Fig. 5 Pressure profiles, large cylinders, Re=100,000, (*a*) *z/P*=0, (*b*) *z/P*=0.5

With $P=1D$ or the solid bar, reattachment moves upstream to $s/L_s=0.78$. With $P=2D$ reattachment occurs at $s/L_s=0.86$. With $P>2D$ the effect of the cylinders is not observed until the last pressure tap, but even with $P=30D$ there is some effect on Cp at $s/L_s=0.94$ and $z/P=0$. As the spacing increases, the Cp values increase from the inviscid solution toward the baseline case value. At $z/P=0.5$ and $s/L_s=0.94$, Cp is affected for spacings up to $20D$, although not as strongly as it is at $z/P=0$. For $P=24D$ and $30D$, the cylinders are too far apart to affect Cp at $z/P=0.5$. The results at $\mathrm{Re}=100{,}000$ are shown in Fig. 5. In the base line case, there is a clear separation bubble, and it reattaches near the trailing edge. With $P\leqslant 3D$, the separation is essentially eliminated. With $P=5D$ there is a separation, but reattachment by $s/L_s=0.78$. For $P\leqslant 5D$, the Cp values are nearly uniform across the span. For $10D\leqslant P\leqslant 30D$, the boundary layer appears to be at least starting to reattach by $s/L_s=0.86$, with the effect on Cp greater at $z/P=0$. Results for the $\mathrm{Re}=200{,}000$ cases (not shown) are similar to those described above. The boundary layer separates in the base line case and reattaches by $s/L_s=0.86$. Cylinders with $P\leqslant 16D$ effectively suppress the separation across the span. For $P>16D$, the boundary layer is attached at $s/L_s=0.78$ and $z/P=0$, but is still separated at $z/P=0.5$. At $\mathrm{Re}=300{,}000$ there is only a small separation bubble in the base line case, and it reattaches by $s/L_s=0.78$. Cylinders with spacing up to $30D$ appear to suppress this small bubble across the span.

Comparing the results at $z/P=0$ and $z/P=0.5$, the spanwise influence of each cylinder can be estimated. If the region affected by the cylinder is assumed to spread linearly in the spanwise direction as the flow convects downstream, the half angle for the spreading is between roughly 30 and 40 deg. Changes in Cp at $z/P=0.5$ could be due to local turbulence arising from the cylinder induced disturbances. It is also possible, however, that these changes in Cp are due to changes in the mean flow resulting from the cylinder induced changes at $z/P=0$.

The smaller (0.4 mm high) cylinders and bar are ineffective at $\mathrm{Re}=25{,}000$ and 50,000. The boundary layer separates and does not reattach. At $\mathrm{Re}=100{,}000$, as shown in Fig. 6, the cylinders cause the first indication of reattachment to move upstream from near the trailing edge to $s/L_s=0.78$ or 0.86. Cylinder spacings up to $10D$ were considered, and the Cp values decrease from the base line case values toward the inviscid solution as P is decreased. No significant spanwise variation in Cp was observed. The results at $z/P=0.5$ are essentially the same as those shown in Fig. 6 for $z/P=0$. Results for the $\mathrm{Re}=200{,}000$ cases are shown in Fig. 7. The results are very similar to those of the $\mathrm{Re}=100{,}000$ cases, but with reattachment shifted about $0.08L_s$ upstream. When $\mathrm{Re}=300{,}000$ the base line separation bubble is small, and cylinders effectively eliminate it for all value of P.

The presumably more complex three-dimensional flow around isolated $(P>1D)$ cylinders did not produce disturbances better

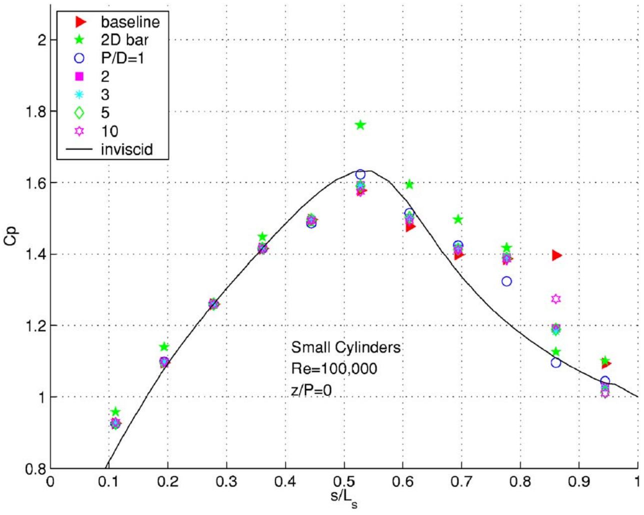

Fig. 6 Pressure profiles, small cylinders, Re=100,000, $z/P=0$

able to control separation than the touching $(P=1D)$ cylinders or two-dimensional bars. In fact, the opposite was observed. The pressure profiles show that as the spacing between cylinders increases, their ability to promote reattachment decreases. This is not simply due to the finite spanwise influence of each cylinder, as very little spanwise variation was observed for cases with $P<10D$. Whether increasing the spacing results in reduced flow blockage and losses will be considered next as the velocity profile results are considered.

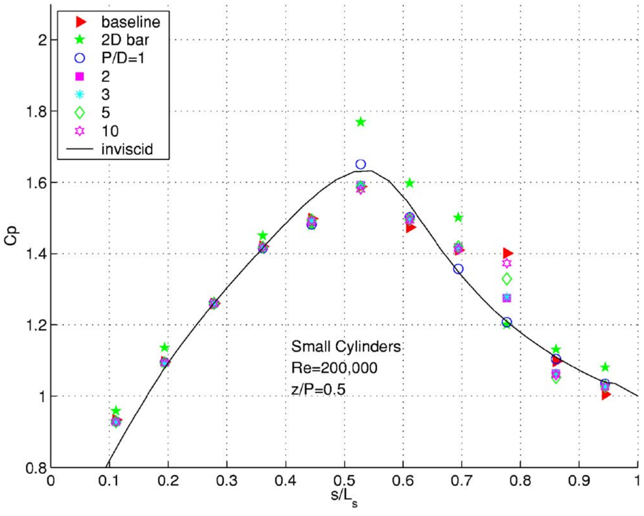

Fig. 7 Pressure profiles, small cylinders, Re=200,000, $z/P=0$

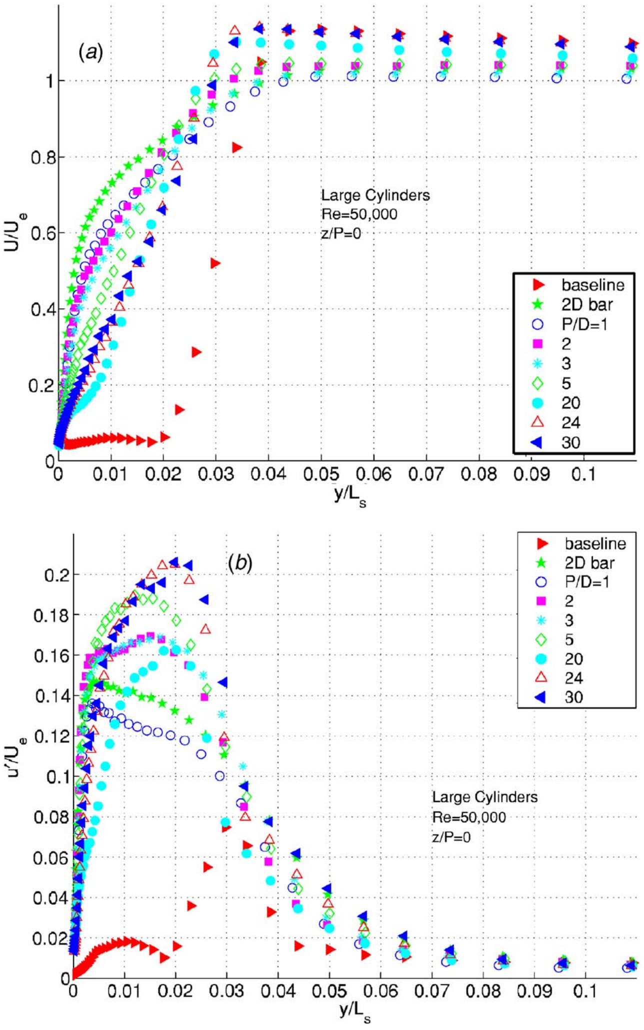

Fig. 8 Trailing edge velocity profiles, large cylinders, Re =50,000, $z/P=0$, (*a*) U/U_e, (*b*) u'/U_e

Velocity Profiles. Mean and fluctuating streamwise velocity profiles for the large cylinder Re=50,000 cases at $z/P=0$ are shown in Fig. 8. Data were acquired near the trailing edge $(s/L_s=0.94)$. The base line case shows a thick separation bubble in the mean profile and a small peak in u' in the shear layer over the bubble. The two-dimensional bar case exhibits a fully attached turbulent mean profile shape and a typical turbulent u' profile with a near wall peak. For the cases with cylinder spacing up to $P=5D$, the mean profiles appear attached and turbulent, but the trend is toward a less full profile as P increases. This trend continues for the cases with $P\geqslant 20D$, with the mean profiles in these cases appearing only partially reattached. The peaks in the u' profiles increase in magnitude and move farther from the wall as the cylinder spacing is increased. High peaks away from the wall are typical of transitioning and reattaching boundary layers. Transition begins in the shear layer over the separation bubble, so u' should be high at this location.The high u'peaks result from the switching between intermittently attached-turbulent-like and separated-laminar-like states. Figure 9 shows the profiles at $z/P=0.5$. For $P\leqslant 5D$, the profiles appear essentially the same as those at $z/P=0$. For $P\geqslant 20D$ the mean profiles show a separation bubble, somewhat thinner than that of the base line case, and u' profiles with only a small peak in the shear layer over the separation bubble. Figure 10 shows the velocity profiles at several spanwise positions for the $P=30D$ case. The progression from attached flow at $z/P=0$ to separated flow at $z/P=0.5$ is clear. The profiles at $z/P=0.13$ and 0.20 are on the edge of the attached flow region with u' peaks between the high peaks at low z/P and the small shear layer peaks at higher z/P. The influence of the cylinders to a spanwise position between $z/P=0.13$ and 0.20 suggests a half angle for the spread of the cylinder influence of about 20 deg. The velocity profile data of Figs. 8–10 are consistent with the conclusions drawn from the corresponding pressure coefficient data of Fig. 4.

The information concerning separation in the mean profiles can be presented in terms of the shape factor, H. The shape factor rises to about 4 when a laminar boundary layer separates, and reaches higher values as a separation bubble thickens. This is due to an increase in the displacement thickness while the momentum thickness remains nearly constant. If the boundary layer reattaches, the

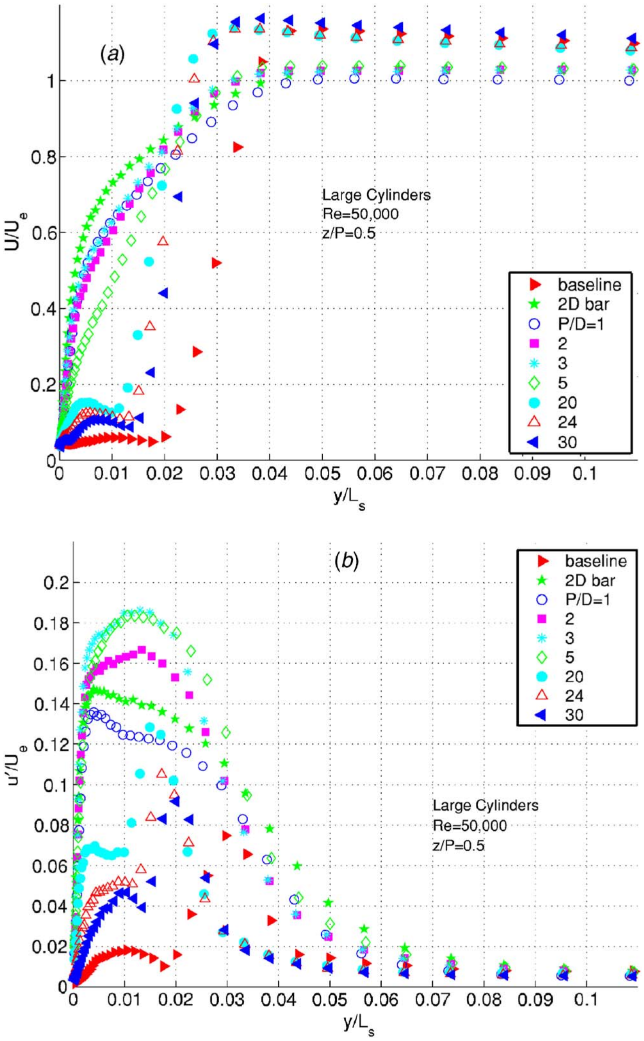

Fig. 9 Trailing edge velocity profiles, large cylinders, Re =50,000, $z/P=0.5$, (*a*) U/U_e, (*b*) u'/U_e

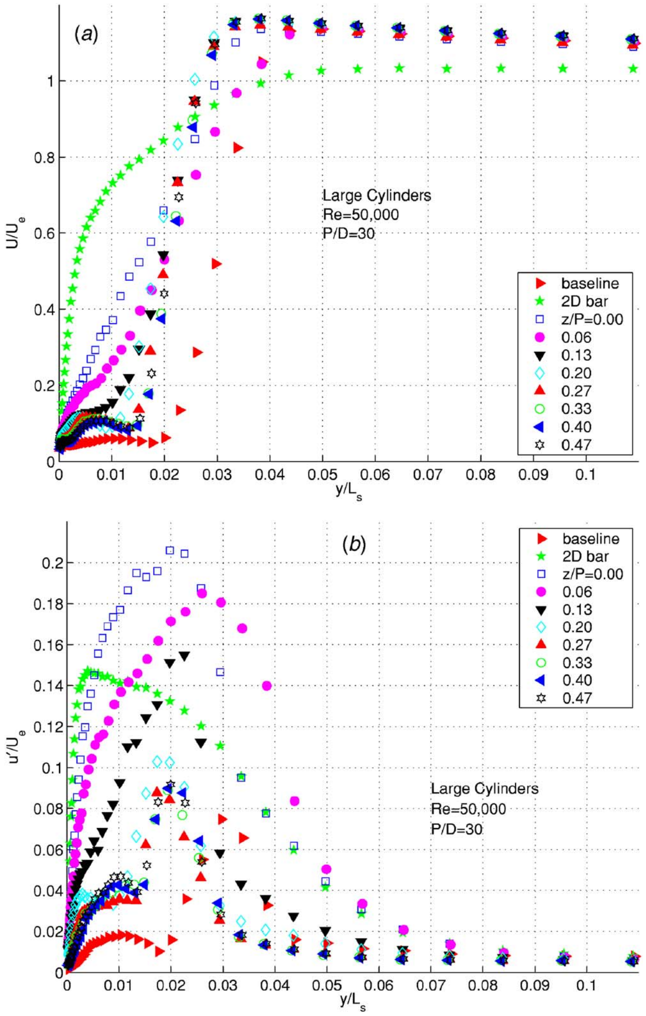

Fig. 10 Trailing edge velocity profiles, large cylinders, Re =50,000, $P/D=30$, (*a*) U/U_e, (*b*) u'/U_e

displacement thickness drops and the momentum thickness begins to rise. The shape factor reaches a turbulent value of about 1.4 after recovering from the separation. Figure 11 shows H as a function of z/P for the Re=50,000 cases with the larger cylinders. In the base line case, $H=6.5$, indicating a thick separation bubble. With the two-dimensional bar, $H=1.6$, indicating that the boundary layer has reattached and is nearing fully developed turbulent conditions. With cylinder spacing up to $P=5D$, H is spanwise uniform. With $P=5D$, H is about 2.3, indicating that the boundary layer has reattached but is not fully recovered from the separation. For $P\geqslant 20D$, $H\approx 3$ at $z/P=0$, indicating the boundary layer has just begun to reattach at this location. For $P\geqslant 20D$ and higher z/P, H is between 4 and 5.5 indicating the boundary layer is still separated. These values are still below the base line value of 6.5, however, indicating that even the widely spaced cylinders are effective in keeping theseparation bubble thinner.

Velocity profiles for the Re=300,000 cases with the larger bar and cylinders are shown in Figs. 12–14. Figure 12 shows the profiles at $z/P=0$. The mean profiles show that the boundary layer is attached in all cases. The u' peaks are near the wall, as expected for attached turbulent boundary layers. The base line case has the highest u' peak, indicating that it is the case with the least developed turbulence. The bar and cylinders move transition upstream, resulting in a more developed turbulent boundary layer by the trailing edge. Both the mean and u' profiles collapse for the cases with $P\geqslant 20D$. This suggests that the cylinders are far enough apart in these cases so that they act as if isolated from each other. Both the mean and u' profiles show that the boundary layer becomes thicker as the cylinder spacing is decreased. The $P=1D$ case has a second u' peak away from the wall that is not present

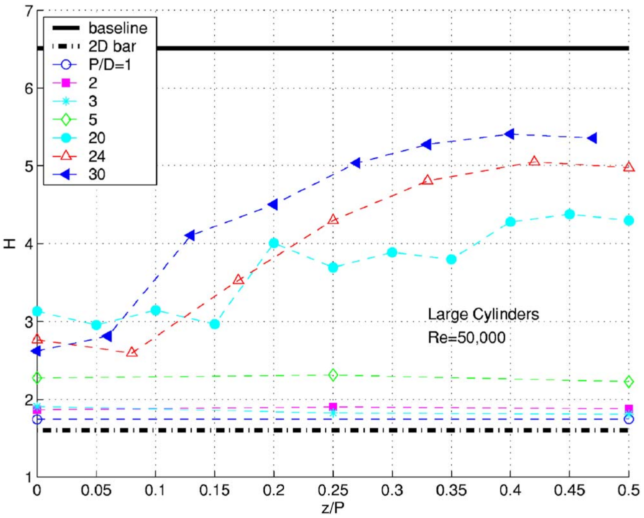

Fig. 11 Shape factor, *H*, at trailing edge, large cylinders, Re =50,000

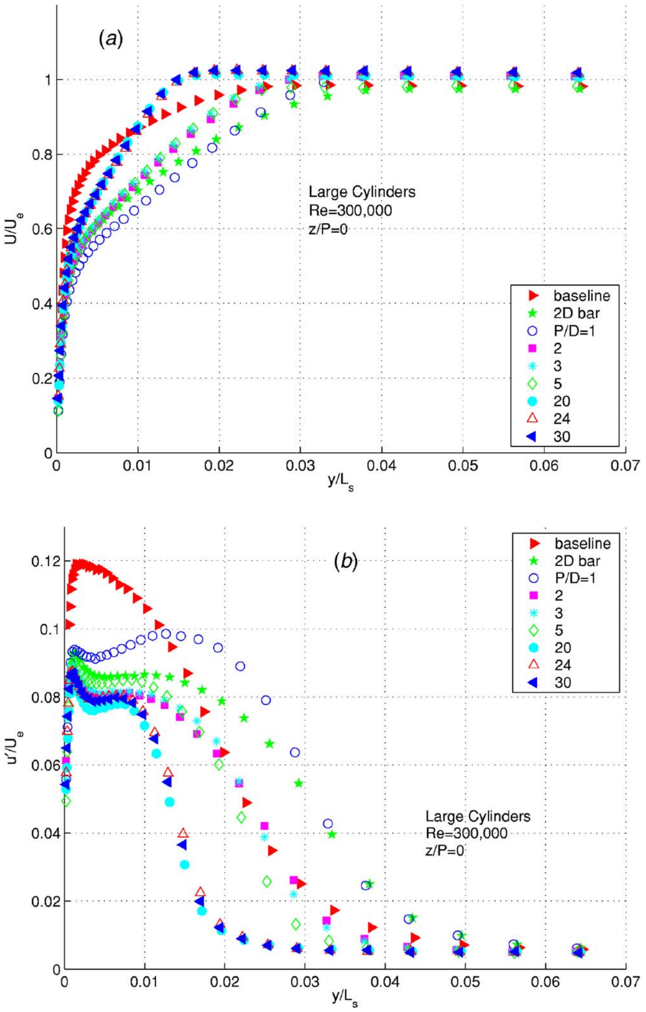

Fig. 12 Trailing edge velocity profiles, large cylinders, Re =300,000, $z/P=0$, (a) U/U_e, (b) u'/U_e

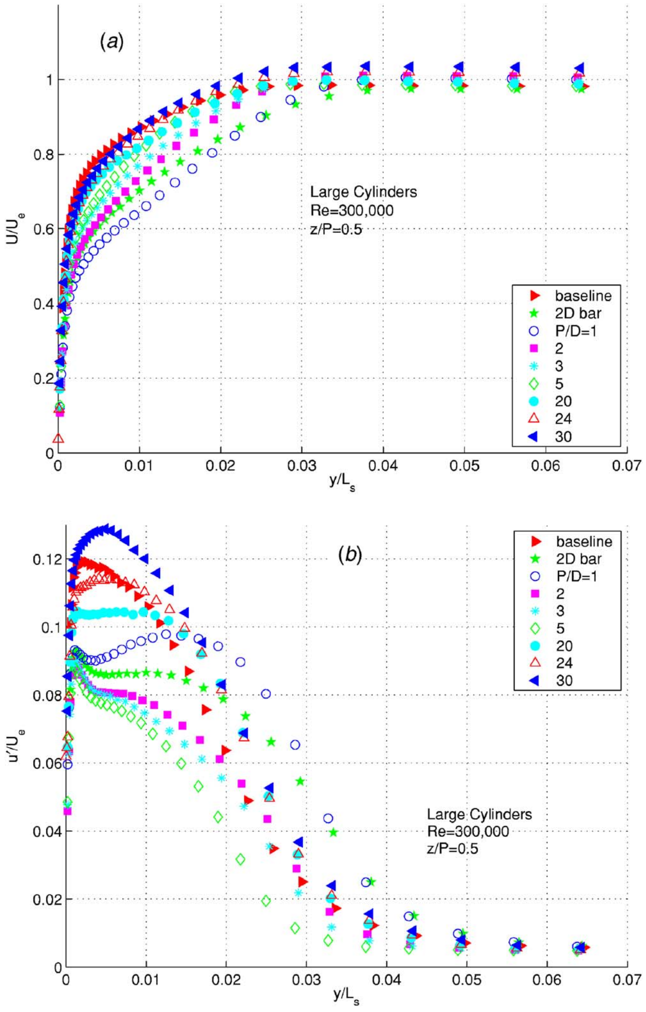

Fig. 13 Trailing edge velocity profiles, large cylinders, Re =300,000, $z/P=0.5$, (a) U/U_e, (b) u'/U_e

in the two-dimensional bar case. The touching cylinders appear to generate more turbulence than the bar. Figure 13 shows the profiles at $z/P=0.5$. The profiles for the $P=24D$ and $30D$ cases are very similar to the baseline results, again suggesting that with large enough spacing the cylinders are effectively isolated from each other and cannot directly influence the flow across the entire span. As P is reduced, the boundary layer becomes thicker, and u' assumes a more turbulent like shape. Figure 14 shows the profiles at several spanwise positions for the $P=30D$ case. The cylinders appear to influence the boundary layer u' nearly uniformly from $z/P=0$ to $z/P=20$. For $z/P>27$, the cylinders have little influence and the profiles are very similar to the base line case profiles. The spanwise extent of the cylinder influence spreads at a half angle of about 20 deg for a strong effect on the boundary layer and about 30 deg for some effect.

Figure 15 shows the shape factor at $s/L_s=0.94$ for the profiles of the Re=300,000 cases with the larger cylinders. The boundary layer is attached, so the shape factor is between 1.4 and 1.7 in all cases. Figure 16 shows the momentum thickness for these cases. The momentum thickness is related to losses in the boundary layer, and in cases with equal shape factor and exit flow angle, the momentum thickness is directly proportional to profile losses (Howell et al. [21]). In the Re=50,000 cases, the large variation in H (Fig. 11) precludes a comparison of losses based on θ, but with the smaller range of H at Re=300,000 (Fig. 15) the comparison is appropriate. Figure 16 shows that the cylinders cause a rise in momentum thickness above the base line case value and that the effect increases as cylinder spacing is decreased. Since the separation bubble is small even in the base line case, the cylinders and bars add an unnecessary disturbance and increase losses. The more widely spaced cylinders cause less blockage and create less of a disturbance, therefore the losses are lower.

Velocity profiles for the Re=50,000 cases with the smaller bar and cylinders are shown in Fig. 17. Cylinder spacings up to $P=5D$ were considered. No variation was observed between the results from different spanwise locations, so only the results from $z/P=0$ are shown. The boundary layer did not reattach for cases with $P\geqslant 2D$, although the separation bubble was slightly thinner and there was a slight increase in the u' peak compared to the base line case. With $P=1D$ the boundary layer appears to be on the verge of reattachment, and with the two-dimensional bar the boundary layer has just begun to reattach. The smaller cylinders are inadequate for control of the boundary layer at this Reynolds number, as previously indicated by the pressure profiles.

The effect of the smaller cylinders on the velocity profiles at Re=300,000 are shown in Fig. 18. No spanwise variation was observed, so only results from $z/P=0$ are shown. The mean profile for the $P/D=1$ case is noticeably different than those for the other cases, including the two-dimensional (2D) bar case. As was noted above, the touching cylinders apparently generate more turbulence that the 2D bar, resulting in a thicker boundary layer. As was the case with the larger cylinders (Fig. 12), the smaller cylinders cause a drop in the u' peak from the base line case value, indicating that the cases with cylinders are closer to fully devel-

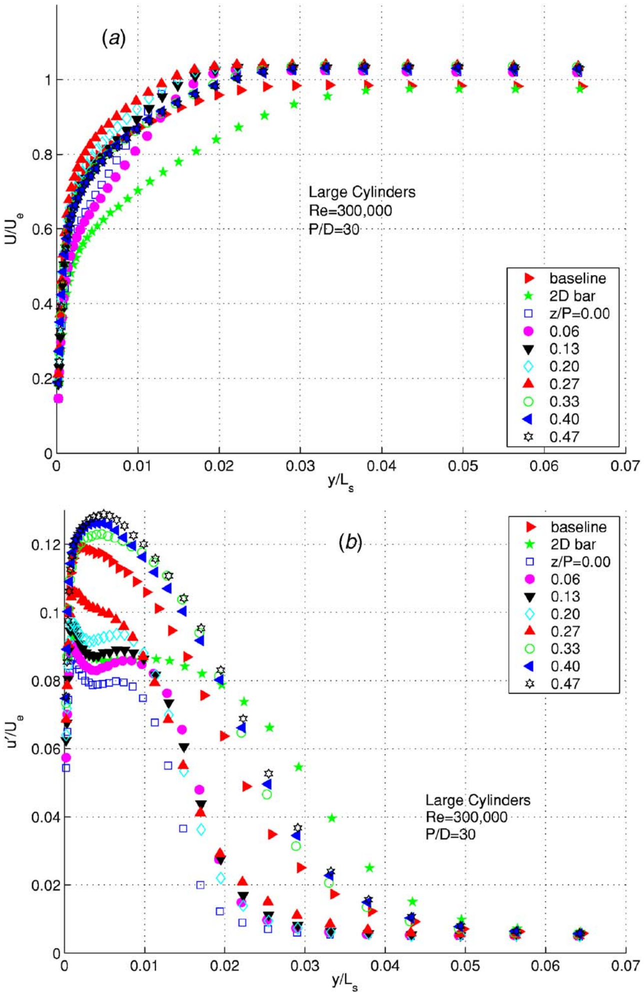

Fig. 14 Trailing edge velocity profiles, large cylinders, Re =300,000, $P/D=30$, (a) U/U_e, (b) u'/U_e

oped turbulent behavior. Shape factors are shown in Fig. 19 as a function of spanwise position. There is little variation between cases, as expected since the separation bubble is small and the boundary layer has fully reattached in all cases. The momentum thickness is shown in Fig. 20. All of the cases with cylinders have higher momentum thickness than the base line case. The case with $P=1D$ has the highest values, again indicating that the touching cylinders generate higher losses than the two-dimensional bars or more widely spaced cylinders.

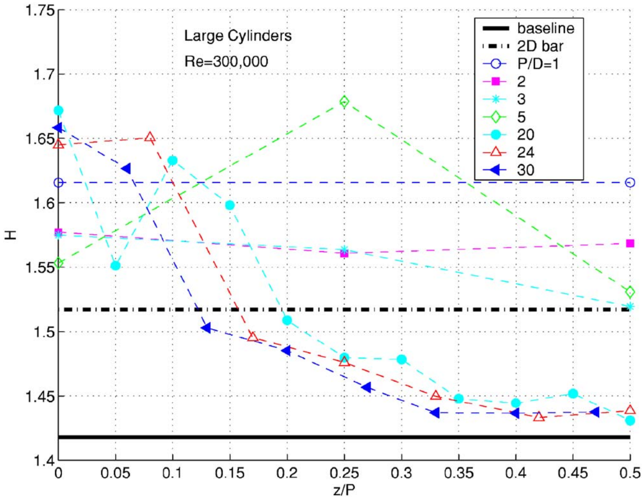

Fig. 15 Shape factor, H, at trailing edge, large cylinders, Re =300,000

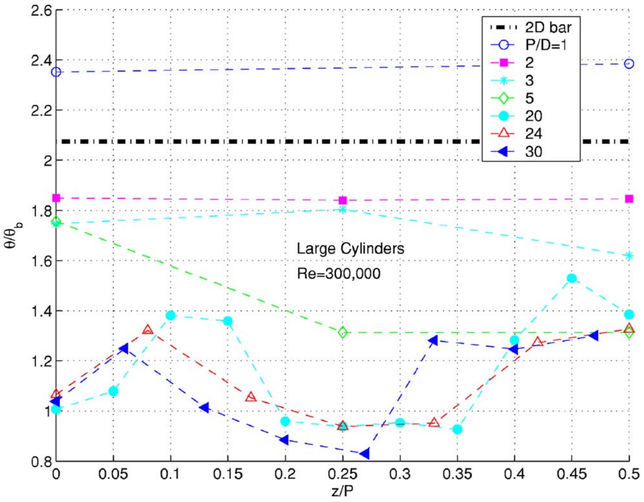

Fig. 16 Momentum thickness at trailing edge, large cylinders, Re=300,000

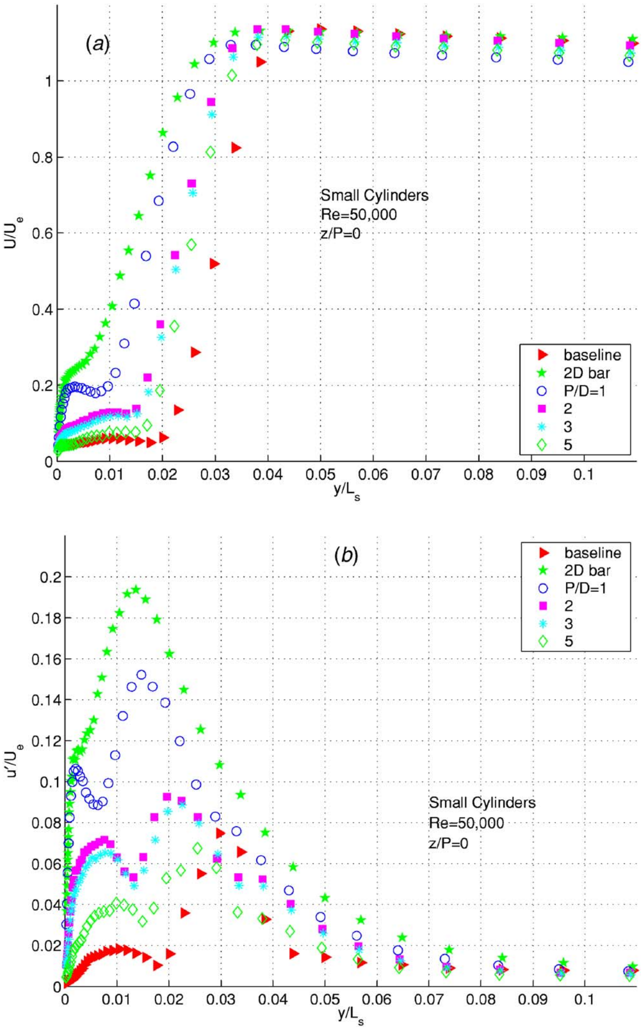

Fig. 17 Trailing edge velocity profiles, small cylinders, Re =50,000, $z/P=0$, (a) U/U_e, (b) u'/U_e

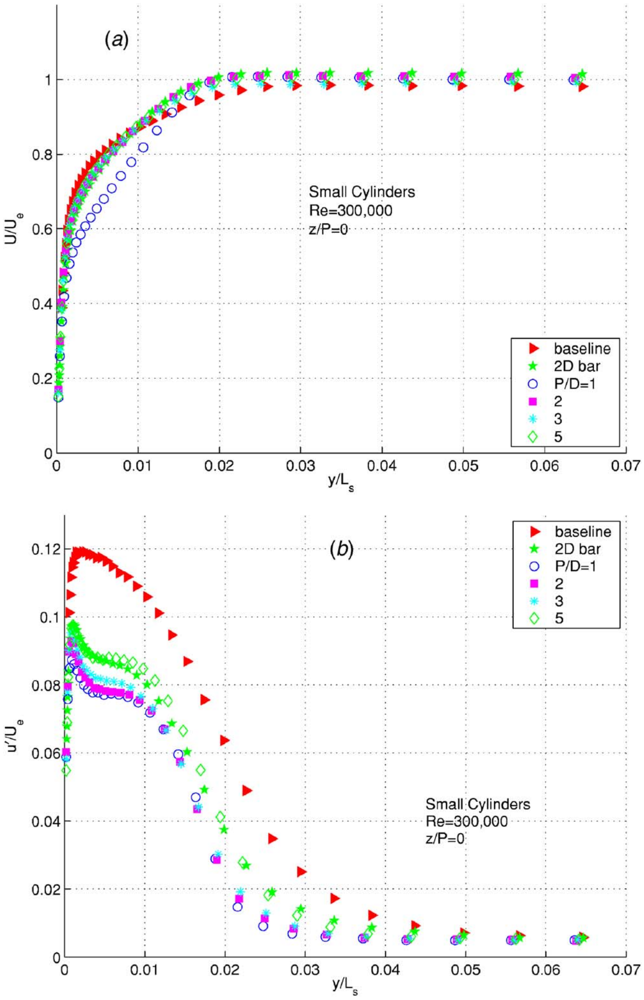

Fig. 18 Trailing edge velocity profiles, small cylinders, Re =300,000, $z/P=0$, (*a*) U/U_e, (*b*) u'/U_e

Discussion

The results presented above suggest that the half angle for the spreading of the disturbances from the cylinders is about 30 deg. This is a rough estimate due to the finite spacing between pressure tap locations and the finite number of cylinder spacings investigated, but the half angle roughly agrees with the spreading angle for turbulent spots in an adverse pressure gradient, as given by D'Ovidio et al. [22]. This angle suggests that a cylinder spacing of between $P/D=5$ and $P/D=10$ is necessary to insure flow control across the span. The velocity profiles showed good spanwise uniformity for $P/D<10$.

The optimal spacing for spanwise disturbances was investigated in an analytical study by Tumin and Ashpis [23]. They considered disturbances in both favorable and adverse pressure gradient flows, including the favorable pressure gradient found in the upstream region of the present test section. Although these results do not apply directly to the adverse pressure gradient region of the present study, they can be extrapolated to the present conditions. They suggest an optimal spacing for maximum disturbance growth in the Re=50,000 cases of $P/L_s \approx 0.03$. For the Re =300,000 cases, the optimal spacing would be $P/L_s \approx 0.012$. With the present cylinder diameter of 6 mm, these spacings correspond to $P/D=1$ and $P/D=0.4$, respectively, and could not be achieved unless the cylinders were touching. Consistent with this, the present results show that the disturbance created by the cylinders decreases as the spacing increases. To better test the Tumin and Ashpis [23] results, however, smaller diameter, separated cylinders with the recommended spacing should be considered.

The results at Re=50,000 show that the larger cylinders with the closest spacing are needed to effectively control separation. At Re=300,000, the separation bubble is small in the base line case, and cylinders or bars cause transition to move upstream, increasing losses. Hence, the thinnest, most widely spaced (which in the limit means nonexistent) devices are optimal. The cylinders which are best at Re=50,000 cause significantly higher losses at Re =300,000. This is the same result found by Volino [15] using two-dimensional bars, and agrees with other findings in the literature, as noted above. So long as the cylinders are close enough to provide spanwise uniformity, it appears that varying the cylinder (or bar) thickness and varying the cylinder spacing are both effective for controlling the transition location and moving it to an optimal location for minimizing losses.

The present results can address the question of whether separated cylinders provide an advantage over a two-dimensional bar. A case with a two-dimensional bar that is capable of controlling separation while keeping losses to a minimum at a low Reynolds number should be compared to a case with cylinders that are thicker than this optimal bar but produce the same reattachment and low losses. Cases with these same geometries should then be compared at a high Reynolds number to see which results in lower high-Re losses. The thin bar in the present study results in mar-

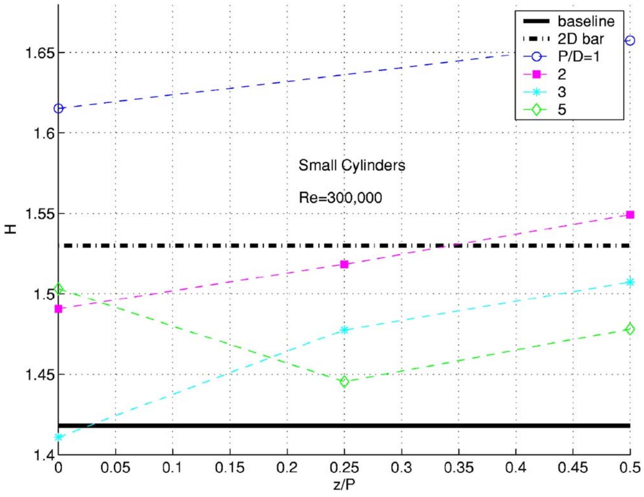

Fig. 19 Shape factor, *H*, at trailing edge, small cylinders, Re =300,000

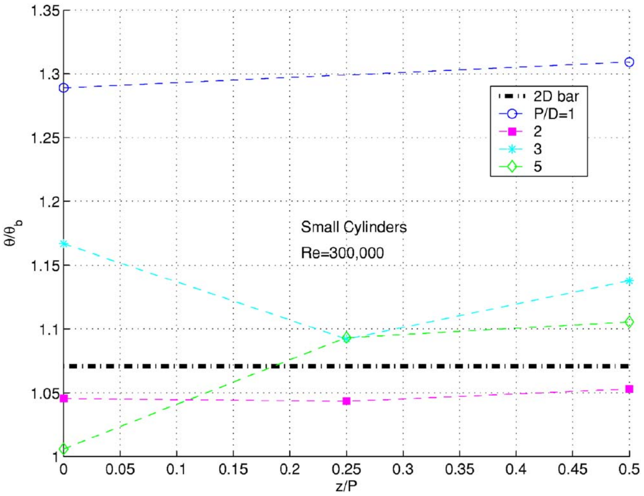

Fig. 20 Momentum thickness at trailing edge, small cylinders, Re=300,000

ginally reattached flow at Re=50,000. The larger cylinders result in spanwise uniform reattachment at Re=50,000 when $P/D=5$. The momentum thicknesses at $s/L_s=0.94$ for these two cases are within 8% of each other. At Re=300,000 the thin bar results in a momentum thickness 7% above the base line case value, while the thick, $P/D=5$ cylinders result in a spanwise averaged momentum thickness that is 46% above the baseline value. Clearly the thin two-dimensional bar is superior to the thicker cylinders. This comparison is not completely adequate, however, since the thin bar only causes marginal reattachment at Re=50,000, while the thick cylinders result in a somewhat more complete reattachment. Volino [15] also considered an intermediate bar with thickness twice that of the thin bar considered above. At Re=50,000 the intermediate bar induced complete reattachment with $H=1.8$ and $\theta/\theta_b=1.23$. These results are very close to those obtained with the large cylinders spaced at $P/D=3$. At Re=300,000 the intermediate bar resulted in $H=1.59$ and $\theta/\theta_b=1.29$. The thick, $P/D=3$ spaced cylinders resulted in an approximately equal shape factor, but $\theta/\theta_b=1.72$. With this better comparison, it is still clear that a thin bar is superior to larger cylinders.

The present results support the conclusions of Sieverding [10] and Zhang and Hodson [17] who found that two-dimensional bars or trips are as good or better than three-dimensional devices for controlling separation. The present results cannot be considered absolutely conclusive, however, since only a single geometry was considered under a limited number of conditions. The number of possible geometries and spacings for three dimensional devices is infinite, so it will never be possible to prove conclusively through experiments that two-dimensional devices are always better. Further study of devices such as the dimples considered by Lake et al. [12] would be useful. The effects of high freestream turbulence and unsteady wakes should also be considered. Perhaps thinner, smaller diameter cylinders with spacings closer to those extrapolated from Tumin and Ashpis [23] could provide better separation control with lower losses. This is merely speculation. What can be said is that the present results add to the evidence that simple two-dimensional bars are preferable.

Conclusions

A row of small cylinders located at the suction peak on a LPT airfoil were effective for separation control. The reattachment of the boundary layer moves upstream as the cylinder height is increased or the cylinder spacing is decreased. The half angle of the spreading of the disturbance created by the cylinders was of the order 30 deg. This is roughly the same as the expected spreading angle for a turbulent spot under the same adverse pressure gradient conditions. Based on this angle, the maximum allowable spacing for spanwise uniform separation control can be determined. By varying the cylinder height and spacing, an optimal reattachment location can be achieved for minimum losses at a given Reynolds number. Cylinders optimized for low Reynolds numbers resulted in higher losses at high Reynolds numbers. The present results add to the evidence that three-dimensional passive flow control devices are not as effective as two-dimensional bars for minimizing losses over a range of Reynolds numbers.

Acknowledgment

This work was sponsored by the NASA Glenn Research Center. The grant monitor was Dr. David Ashpis. The first author received matching support from the Office of Naval Research.

Nomenclature

$Cp = 2(p_T - p)/\rho U_e^2$, pressure coefficient
D = cylinder diameter
H = shape factor, δ^*/θ
L_s = suction surface length
P = center to center spacing of cylinders
p = pressure
p_T = upstream stagnation pressure
Re = $U_e L_s/\nu$, exit Reynolds number
s = streamwise coordinate, distance from leading edge
U_e = nominal exit freestream velocity, based on inviscid solution
u = mean streamwise velocity
u' = rms streamwise fluctuating velocity
y = cross-stream coordinate, distance from wall
z = spanwise coordinate
δ^* = displacement thickness
ν = kinematic viscosity
ρ = density
θ = momentum thickness
θ_b = momentum thickness in base line case

References

[1] Hourmouziadis, J., 1989, "Aerodynamic Design of Low Pressure Turbines," AGARD Lecture Series 167.
[2] Mayle, R. E., 1991, "The Role of Laminar-Turbulent Transition in Gas Turbine Engines," ASME J. Turbomach., **113**, pp. 509–537.
[3] Sharma, O. P., Ni, R. H., and Tanrikut, S., 1994, "Unsteady Flow in Turbines," AGARD Lecture Series 195, Paper No. 5.
[4] Bons, J. P., Sondergaard, R., and Rivir, R. B., 2001, "Turbine Separation Control Using Pulsed Vortex Generator Jets," ASME J. Turbomach., **123**, pp. 198–206.
[5] Volino, R. J., and Hultgren, L. S., 2001, "Measurements in Separated and Transitional Boundary Layers Under Low-Pressure Turbine Airfoil Conditions," ASME J. Turbomach., **123**, pp. 189–197.
[6] Volino, R. J., 2002, "Separated Flow Transition Under Simulated Low-Pressure Turbine Airfoil Conditions: Part 1—Mean Flow and Turbulence Statistics," ASME J. Turbomach., **124**, pp. 645–655.
[7] Huang, J., Corke, T., and Thomas, F., 2003, "Plasma Actuators for Separation Control on Low Pressure Turbine Blades," AIAA Paper No. 2003-1027.
[8] Hultgren, L. S., and Ashpis, D. E., 2003, "Demonstration of Separation Delay With Glow Discharge Plasma Actuators," AIAA Paper No. 2003-1025.
[9] Volino, R. J., 2003, "Separation Control on Low-Pressure Turbine Airfoils Using Synthetic Vortex Generator Jets," ASME J. Turbomach., **125**, pp. 765–777.
[10] Sieverding, C. H., Bagnera, C., Boege, A. C., Antòn, J. A. C., and Luère, V., 2004, "Investigation of the Effectiveness of Various Types of Boundary Layer Transition Elements of Low Reynolds Number Turbine Bladings," ASME Paper No. GT2004-54103.
[11] Van Treuren, K. W., Simon, T., von Koller, M., Byerley, A. R., Baughn, J. W., and Rivir, R., 2002, "Measurements in a Turbine Cascade Flow Under Ultra Low Reynolds Number Conditions," ASME J. Turbomach., **124**, pp. 100–106.
[12] Lake, J. P., King, P. I., and Rivir, R. B., 2000, "Low Reynolds Number Loss Reduction on Turbine Blades With Dimples and V-Grooves," AIAA Paper No. 00-738.
[13] Murawski, C. G., and Vafai, K., 1999, "Effect of Variable Axial Chord on a Low-Pressure Turbine Blade," J. Propul. Power, **15**, pp. 667–674.
[14] Byerley, A. R., Störmer, O, Baughn, J. W., Simon, T. W., VanTreuren, K. W., and List, J., 2002, "Using Gurney Flaps to Control Laminar Separation on Linear Cascade Blades," ASME J. Turbomach., **125**, pp. 114–120.
[15] Volino, R. J., 2003, "Passive Flow Control on Low-Pressure Turbine Airfoils," ASME J. Turbomach., **125**, pp. 754–764.
[16] Vera, M., Hodson, H. P., and Vazquez, R., 2004, "The Effects of a Trip Wire and Unsteadiness on a High Speed Highly Loaded Low-Pressure Turbine Blade," ASME Paper No. GT2004-53822.
[17] Zhang, X. F., and Hodson, H., 2004, "Combined Effects of Surface Trips and Unsteady Wakes on the Boundary Layer Development of an Ultra-High-Lift LP Turbine Blade," ASME J. Turbomach., **127**, pp. 479–488.
[18] Volino, R. J., and Bohl, D. G., 2003, "Separated Flow Transition Mechanisms and Prediction With High and Low Freestream Turbulence Under Low Pressure Turbine Conditions," ASME Paper No. GT2004-63360.
[19] Volino, R. J., Schultz, M. P., and Pratt, C. M., 2001, "Conditional Sampling in a Transitional Boundary Layer Under High Free-Stream Turbulence Conditions," ASME J. Fluids Eng., **125**, pp. 28–37.
[20] Wills, J. A. B., 1962, "The Correction of Hot-Wire Readings for Proximity to a Solid Boundary," J. Fluid Mech., **12**, pp. 65–92.
[21] Howell, R. J., Ramesh, O. N., Hodson, H. P., Harvey, N. W., and Schulte, V., 2001, "High Lift and Aft-Loaded Profiles for Low-Pressure Turbines," ASME J. Turbomach., **123**, pp. 181–188.
[22] D'Ovidio, A., Harkins, J. A., and Gostelow, J. P., 2001, "Turbulent Spots in Strong Adverse Pressure Gradients: Part 2—Spot Propagation and Spreading Rates," ASME Paper No. 2001-GT-0406.
[23] Tumin, A., and Ashpis, D. E., 2003, "Optimal Disturbances in Boundary Layers Subject to Streamwise Pressure Gradients," AIAA J., **41**, pp. 2297–2300.

Experimental and Numerical Investigation of the Unsteady Surface Pressure in a Three-Stage Model of an Axial High Pressure Turbine

Carmen E. Kachel[1]
e-mail: carmen.kachel@siemens.com

John D. Denton

Whittle Laboratory,
Engineering Department,
Cambridge University,
Cambridge, UK

This paper presents the results of a numerical and experimental investigation of the unsteady pressure field in a three-stage model of a high pressure steam turbine. Unsteady surface pressure measurements were taken on a first and second stage stator blade, respectively. The measurements in the blade passage were supplemented by time resolved measurements between the blade rows. The explanation of the origin of the unsteady pressure fluctuations was supported by unsteady three-dimensional computational fluid dynamic calculations of which the most extensive calculation was performed over two stages. The mechanisms affecting the unsteady pressure field were: the potential field frozen to the upstream blade row, the pressure waves originating from changes in the potential pressure field, the convected unsteady velocity field, and the passage vortex of the upstream blade row. One-dimensional pressure waves and the unsteady variation of the pitchwise pressure gradient due to the changing velocity field were the dominant mechanisms influencing the magnitude of the surface pressure fluctuations. The magnitude of these effects had not been previously anticipated to be more important than other recognized effects. [DOI: 10.1115/1.1860378]

1 Introduction

In all turbomachines, the velocity and pressure field is affected by both unresolved (random) and time-resolved (deterministic) unsteadiness. The first group includes all forms of aperiodic unsteadiness for example turbulence, transition or mixing. This unsteadiness is characterized by a high but not specific frequency with short length scales. The work presented in this paper focuses on the second group which includes blade row interaction effects that are caused by the relative movement of the stationary and rotating blade rows. These are predominantly periodic at a relatively low frequency, generally the blade passing frequency and its higher harmonics. An example of deterministic unsteadiness at higher frequencies is trailing edge vortex shedding. This is generally of low amplitude and is therefore less significant than unsteadiness due to blade passing. Spatial effects are usually referred to as clocking effects. These interactions take place between disturbances, for example, wakes or vortices, generated by an upstream object or blade row with no relative movement to the affected blade row and are typically of a convective nature.

Time-resolved deterministic unsteadiness originates either within the blade row itself, e.g., tip leakage effects or from neighboring blade rows, for example, convection of wakes and secondary flow features, potential effects and shroud leakage. Potential effects act both up-and downstream of their origin. All the other effects are convective and thus act only downstream. An overview of the types of unsteadiness, their origin and nature is presented in Table 1.

The unsteady interaction mechanisms in Table 1 also affect the blade static surface pressures periodically. Typically they occur simultaneously and at different strength, some dominating others, some reinforcing each other. Shock waves, for example from the trailing edge shock in transonic turbines, are generally the strongest source of unsteady interactions affecting the downstream blade surface pressures. Because of this most published experimental research on unsteady surface pressures has been carried out on instrumented rotors in transonic test facilities, due to the severity of the shock interaction relative to other unsteady interaction effects [1–7]. Generally there are however few publications on unsteady surface pressure measurements available.

For subsonic blade rows the two main sources of unsteadiness are the periodic inviscid potential-flow variation of the stator and rotor blade rows as they move relative to each other and the viscous wakes shed from the trailing edge of the upstream blade row. Few publications on unsteady surface pressure measurements in subsonic flow are available [8–10].

2 Experimental Setup

The experiments described in this paper were carried out on the model multistage turbine of the Whittle Laboratory in Cambridge, UK, see Fig. 1. This test facility is representative of the high pressure stages of steam turbines. The working fluid is air, which passes through an inlet with filter and honeycomb flow straightener before it enters the turbine. Atmospheric air is sucked through the facility by a fan downstream of the turbine. In addition to the experiments described in this paper detailed steady and unsteady traverses were also performed after each blade row of this facility. All blade rows are shrouded and sealed using axial abradable balsa seals.

The operating point is set by the fan power and the dynamometer brake and is controlled by the flow coefficient $\phi = V_x/U$ measured at the turbine inlet. The shaft speed U is measured on an

---

[1] Currently at Siemens PG, Mülheim, Germany

Contributed by the International Gas Turbine Institute (IGTI) of ASME for publication in the JOURNAL OF TURBOMACHINERY. Manuscript received October 1, 2003; final manuscript received March 1, 2004. IGTI Review Chair: A. J. Strazisar. Paper presented at the International Gas Turbine and Aeroengine Congress and Exhibition, Vienna, Austria, June 13–17, 2004, Paper No. 2004-GT-53626.

Table 1 Sources and types of unsteadiness in turbomachinery applications

Deterministic unsteadiness	Unresolved unsteadiness
-periodic	-aperiodic
-low frequency	-high frequency
-long time scale	-short time scale
-frequency multiple of rotor frequency	-no specific frequency
Timewise	**Mixing**
upstream bladerow:	two flows:
-tip leakage	*-tip leakage*
-secondary flow	*-shroud leakage*
-vortex shedding from t.e.	*-coolant injection*
-wake	shear layers:
-secondary and shed vortices	*-wake*
-shroud leakage	*-secondary and shed vortices*
up/downstream bladerow	**Turbulence**
-potential field	freestream:
-shock waves	boundary layer
Spatial	*-endwall*
upper stage:	*-blade surface*
-clocking	

Table 2 Experimental facility

Design operating point data and geometric parameters		
Flow coefficient ϕ	0.384	
Stage loading $\Psi=\Delta h_0/U^2$	1.5	
Inlet Mach number	0.035	
Design speed (rpm)	680	
Number of stages	3	
Blade row spacing $\Delta z/l_{xsb}$	0.33	
Blade parameters	Stator	Rotor
True chord l (mm)	101.8	97.0
Aspect ratio h/l	0.74	0.77
Blade number N	32	40
Reynolds number[a]	$3.2\cdot 10^5$	$2.8\cdot 10^5$

[a] Based on true chord and exit velocity

optoelectronic speed pickup. The axial velocity at turbine inlet is measured implicitly via a mass flow measurement in the exhaust section and a density measurement at inlet.

The experiments described here were performed on 30% reaction blading at the design operation conditions shown in Table 2. Additional measurements were performed at various flow coefficients ranging from 0.30 to 0.42, which are not presented here.

The characteristic parameters of the model multistage turbine and its blading are also listed in Table 2. Whilst all other parameters are scaled to represent typical high pressure steam turbine conditions, the Reynolds number, based on exit velocity and true chord, is much lower than that in a real turbine. The blade parameters presented in Table 2 are taken at midspan. In anticipation of the unsteady calculations, the number of rotor and stator blades was chosen to have as high a common factor as possible while allowing for reasonable aerodynamic design considerations. This was to reduce the number of blade passages per blade row that needed to be calculated.

2.1 Experimental Set-Up for Time-Resolved Static Surface Pressure Measurements. Time-resolved static pressure measurements were carried out at midspan of stator 1 and stator 2 and additionally at 10% and 90% of the span on stator 2. The unsteady pressures were measured using miniature fast response pressure sensors from Kulite (LQ-062-Series) with a measuring range of 5 psi(~35 kPa). The transducers (Fig. 2(*a*)) were 1.4 mm high and 9.6 mm long. Six slots of 2.7 mm depth and 3 mm width were machined into the pressure surface and suction surface of two blades, respectively (Fig. 2(*b*)). The transducers could be set flush with the rest of the blade surface at any spanwise position within these slots. The connections to the transducers ran within the slots and were held by plasticine, which was also used to fill the open part of the slot flush with the rest of the surface. The slots were positioned approximately equidistant along the surface and located at positions where they would coincide with pressure tappings used for time-resolved static pressure measurements on a different set of instrumented blades (Fig. 3). The sensor positions are indicated by dots on the space axis of the $s-t$ diagrams [e.g., 8, 12, 15, 16]. The advantage of this system was that with the same transducers a large range of surface positions on other sets of blading could be measured and recovered thereafter. Additionally, it was found advantageous that the transducers could be interchanged and that the system was also applicable to three-dimensional blading. However, their installation proved laborious and required a high degree of manual skill.

The unsteady surface pressure fluctuations were expected to be very small in comparison to the measuring range of the transducer. To enable maximum amplification of the output signal the back pressures of the transducers were connected to the equivalent pressure tapping on the instrumented blade used for time-mean static surface pressure measurements (Fig. 3). Unsteady variations on the static side were dampened out by connecting several metres of tubing between the two ends. The time-resolved data was collected using an ensemble averaging technique. The data was taken at a sampling rate of 62.5 kHz over 8 rotor blade passing cycles. This is equivalent to a resolution of 142.5 measuring points per rotor pitch. The start of each of the 100 time traces was phase locked with the rotor and triggered by a signal from the speed pickup.

2.2 Numerical Methods. The experimental unsteady flow investigations were accompanied and aided by unsteady flow calculations. These were essential for understanding the flow behavior in areas where it was not possible to take measurements. The calculations were performed with Denton's unsteady multistage

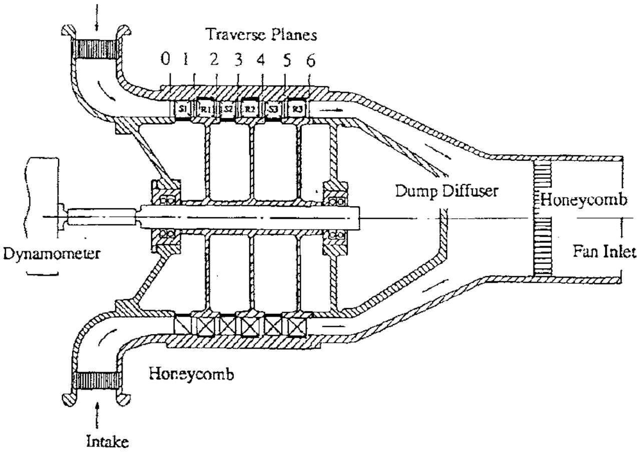

Fig. 1 Schematic of multistage turbine rig

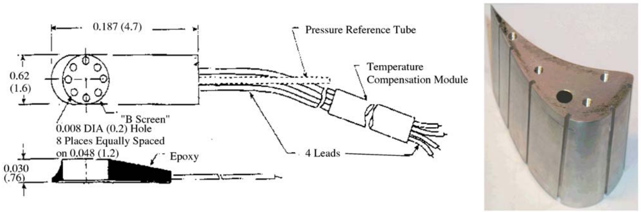

Fig. 2 Instrumentation for time resolved static pressure measurements; (*a*) pressure transducer for time resolved surface pressure measurements, (*b*) slots for pressure sensors

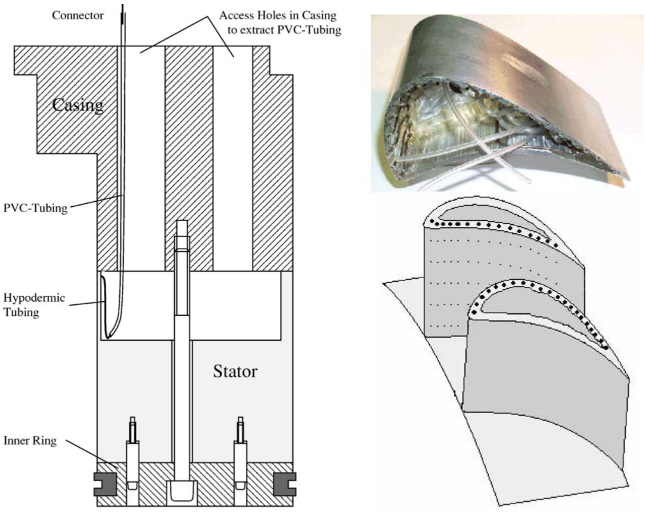

Fig. 3 Instrumentation for time-mean static pressure measurements

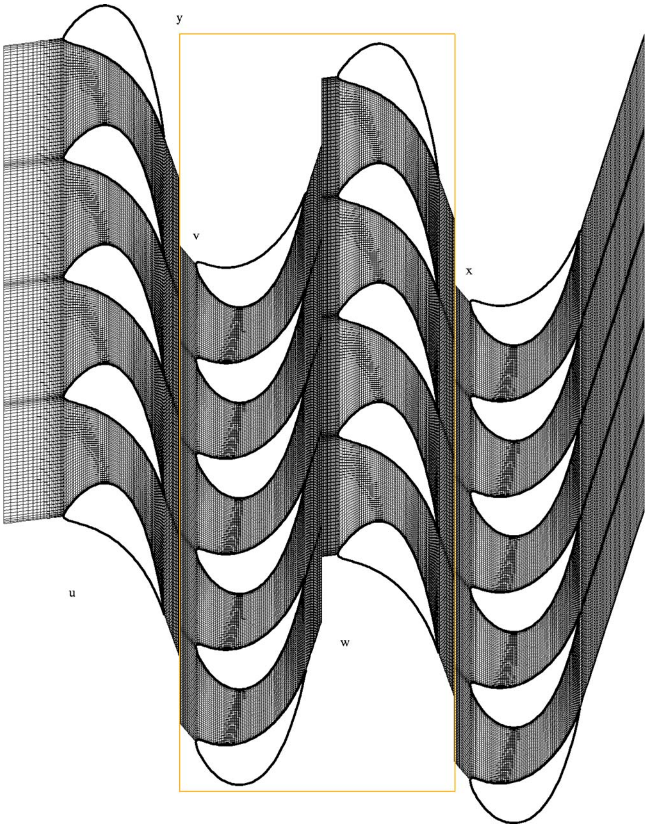

Fig. 4 UNSTREST mesh for 2-stages and for rotor-stator calculation, quasi-stream surface, midspan; rotor-stator calculation, stator 1, rotor 1, stator 2, rotor 2

turbomachine flow solver UNSTREST. This is basically a modified version of the steady MULTIP code and a full account of the programs capabilities is given for example in [11]. The code is a three-dimensional compressible explicit finite-volume Euler solver, described in [12]. The effects of viscosity are modelled by a body force term in the momentum equation. The shear stress is distributed over the flow field via a mixing length model of eddy viscosity.

An H mesh was used to grid the flow domain. To account for the true ratio of blade counts calculations were performed with 4 blades per stator row and 5 blades per rotor row. This resulted in a mesh size to $41\times(4\times41)\times100$ (stator) and $41\times(5\times41)\times100$ (rotor), an example of the grid is shown in Fig. 4. The most extensive of these unsteady calculations was performed over two stages. Additional calculations were performed on 1.5 stages and with two half stages (rotor row followed by stator row). Because of the low Mach number, convergence was improved by performing the calculations at double the operational speed with the flow coefficient chosen to closely match that of the measurement at inlet to stator 2. The increased speed was mainly chosen to conform with steady calculations that were also performed for the two geometries. Later independent investigations by [13] showed that UNSTREST was capable of being run at the low speed of the real model multistage turbine. The unsteady calculations were carried out over the first two stages. Additionally one unsteady calculation was carried out for the first rotor preceded by the second stator. The boundary conditions for this calculation were taken from the respective 2-stage calculation. This was done to isolate the unsteady effects of rotor 1 onto stator 2 and study them in this simplified environment. For all three calculations surface data was written out every 145 time-steps over a cycle of 5 rotor passages. This is 1/5th of the time-resolution of the measurements. The calculated unsteady static pressure data was taken from the blade surface grid points $I=1$ on the suction side and $I=\text{IMR}$ on the pressure side of the same blade passage. Additionally, the calculated unsteady entropy variation was taken two grid points away from the blade surface at $I=3$ and $I=\text{IMR-2}$.

3 Theoretical Analysis

The following one-dimensional models are aimed at aiding the interpretation of the measured static pressure fluctuations. For unsteady inviscid flow along a streamline:

$$\frac{\partial u}{\partial t}+\frac{d}{ds}\left(\frac{u^2}{2}\right)=-\frac{1}{\rho}\frac{dp}{ds} \tag{1}$$

with s being the distance along the streamline. With $u_{(s,t)}=\bar{u}_{(s)}+\tilde{u}_{(s,t)}$ and $p=\bar{p}_{(s)}+\tilde{p}_{(s,t)}$ and by subtracting the steady flow equation $\bar{u}(d\bar{u}/ds)=-(1/\rho)(d\bar{p}/ds)$ as well as neglecting small terms of the order $\hat{u}^2$ Eq. (1) can be rewritten as:

$$\frac{\partial\tilde{u}}{\partial t}+\bar{u}\frac{d\tilde{u}}{ds}+\tilde{u}\frac{d\bar{u}}{ds}=-\frac{1}{\rho}\frac{d\tilde{p}}{ds} \tag{2}$$

Assuming a sinusoidal disturbance propagating with speed Q and variable amplitude $\hat{u}_{(s)}$ along the streamline, the form of the disturbance velocity is

$$\tilde{u}_{(s,t)}=\hat{u}_{(s)}\sin\omega\left(t-\frac{s}{Q}\right) \tag{3}$$

The wavelength of this disturbance is $L=2\pi Q/\omega$. Substituting $\omega(t-(s/Q))=\Phi$ gives

$$\omega\hat{u}_{(s)}\cos\Phi-\bar{u}\hat{u}_{(s)}\frac{\omega}{Q}\cos\Phi+\bar{u}\sin\Phi\frac{d\hat{u}}{ds}+\hat{u}_{(s)}\sin\Phi\frac{d\bar{u}}{ds}=-\frac{1}{\rho}\frac{d\tilde{p}}{ds} \tag{4}$$

Thus, the amplitude $\hat{p}$ of a pressure disturbance can be estimated as the change in pressure over a distance $L/2$ as

$$(Q-\bar{u})\pi\hat{u}_{(s)}\cos\Phi+\left(\bar{u}\frac{d\hat{u}}{ds}+\hat{u}_{(s)}\frac{d\bar{u}}{ds}\right)\frac{\pi Q}{\omega}\sin\Phi=-\frac{\hat{p}}{\rho} \tag{5}$$

By replacing u with w in the relative frame, Eq. (5) can be applied along a streamline in both the relative and the absolute frame of reference. Several cases can now be studied:

3.1 Wake Disturbance. The propagation speed Q of a wake travelling along a streamline is equal to the freestream velocity so that $Q=\bar{u}$. Thus, the first two terms in Eq. (5) cancel out, leaving:

$$\left(\bar{u}\frac{d\hat{u}}{ds}+\hat{u}\frac{d\bar{u}}{ds}\right)\frac{\pi Q}{\omega}\sin\Phi=-\frac{\hat{p}}{\rho} \tag{6}$$

The remaining terms represent two causes of pressure disturbances due to a wake. The first term represents the pressure disturbance due to wake deformation. Typically wake elements are stretched or compressed as they are convected through a bladerow or duct. Wake stretching leads to a decrease of the velocity deficit in the wake, while wake compression increases the velocity deficit in the wake [14]. The magnitude of the change in the pressure perturbation amplitude is proportional to $\rho\bar{u}\Delta\hat{u}_L$ where $\Delta\hat{u}_L$ is the change in the velocity deficit of the wake segment over one-half of a wavelength. From the second term it can be seen that an unperturbed wake convecting through a nonuniform flow field will also generate a pressure disturbance. This is proportional to $\rho\hat{u}\Delta\bar{u}_L$ where $\Delta\bar{u}_L$ is the change in mean streamwise velocity over a half wavelength of the disturbance. Thus, the total magnitude of the pressure perturbation caused by a convected wake is

$$\hat{p}\propto\rho\bar{u}\Delta\hat{u}_L+\rho\hat{u}\Delta\bar{u}_L \tag{7}$$

In a turbine the length of a wake element is initially reduced within a blade row so that the velocity deficit is increased and $\Delta\hat{u}_L$ is positive. Simultaneously the flow is accelerated so that $\Delta\bar{u}_L$ is also positive. Thus, a wake convected through a turbine blade row will generate an increasing pressure perturbation near the leading edge. Towards trailing edge both mechanisms are reversed, i.e., the wake is stretched and the flow is decelerated. In the inter blade row gap neither the wake segments nor the flow field undergo significant changes along a stream line. Thus, the velocity deficit within a wake has negligible influence onto the static pressure field between the blade rows.

3.2 Pressure Variation due to Vortex-Shedding and Secondary Flow Vortices. In a stationary flowfield the streamlines of a vortex are circular. These must be supported by a radial pressure gradient $(u^2/R)=-(1/\rho)(dp/dn)$. This leads to a reduction of the pressure in the vortex core in comparison to the freestream pressure.

In the presence of a vortex street the time-averaged static pressure will be slightly reduced by the periodic reduction of static pressure in the passing vortex cores [15]. This concept is not restricted to a vortex street, but applies also to any vortical disturbance which fits these characteristics. For example a secondary flow vortex might be represented in this form. In a turbine the length of a streamwise vortex element is initially reduced within the blade row and later stretched again towards trailing edge. The stretching of the vortex with circulation $\Gamma=2\pi ru$ will reduce its radius and thus increase the velocity and the necessary pressure drop in the vortex core. Vice versa, the reduction of the length of a vortex line will increase its radius and thus decrease the velocity so that the pressure in the vortex core is increased. Note that this is exactly contrary to the effect of a wake element.

3.3 Potential Disturbance. In a steady flow field the potential field of a blade row is frozen to that blade row. An observer in relative motion sees the potential field as a periodic and, well away from the blade row, almost sinusoidal disturbance, the amplitude of which is only dependent on the axial distance away from the blade row. The decay rate of the first harmonic is proportional to $\exp(-2\pi x/S)$ [16], where x is the axial distance away from trailing or leading edge and S is the blade pitch. However, a real flow field is not steady as the blade row in relative motion causes a disturbance to the stationary blade row, and vice versa. This can cause the potential field to change with relative position of the two blade rows. Thus, the magnitude of the potential field becomes a function of the relative position of the two blade rows.

The amplitude of the potential pressure field determines the amplitude of the velocity perturbation via Eq. (5). On the assumption that the effect of the neighboring blade row on the potential field is small, the potential field of the moving blade row can be considered to be frozen to that blade row. Under this assumption the propagation velocity of the disturbance in the axial direction is zero, so that the disturbance travels with the wheel speed $Q=U$ (rotor) or $Q=-U$ (stator) along the circumferential component of the streamline and the disturbance length scale $L=2\pi U/\omega=S$. S is the pitch of the blade row from which the pressure wave originates. As the potential field decays quickly $\hat{u}_{(s)}(d\bar{u}/ds)$ can be neglected in Eq. (5) and we can write:

$$(U-\bar{u})\pi\hat{u}_{(s)}\cos\Phi+\bar{u}\frac{d\hat{u}}{ds}\frac{S}{2}\sin\Phi=-\frac{\hat{p}}{\rho} \tag{8}$$

The potential field of the rotor causes unsteady fluctuations in the absolute frame of reference, where $U-\bar{u}=\bar{w}$ and $S=S_{rb}$. Similarly the potential field of the stator causes unsteady fluctuations in the relative frame, where u must be replaced with w, $-U-\bar{w}=\bar{u}$ and $S=S_{sb}$.

3.4 One-Dimensional Wave. For a one-dimensional disturbance travelling at the speed of sound $Q=c$ and the decay rate $\hat{u}=0$. In a low speed facility such as the model multistage turbine $c\gg\bar{u}$. Thus, the second and third term on the left-hand side of Eq. (5) can be neglected and so the pressure disturbance will be proportional to

$$-\frac{\hat{p}}{\rho}\propto\hat{u}c \tag{9}$$

In a flow field in which a pressure disturbance due to a wake and a one-dimensional pressure wave of the same magnitude are present the inherent velocity fluctuations relate to each other at a ratio of $\hat{u}_{\text{wave}}/\hat{u}_{\text{wake}}=\bar{u}/c$. This means that in a low speed facility the velocity fluctuations $\hat{u}_{\text{wave}}\ll\hat{u}_{\text{wake}}$ for similarly sized pressure waves. Thus, a one-dimensional pressure wave is unlikely to be seen in the unsteady velocity field.

3.5 Cyclic Back Pressure Variation. If the back pressure of a blade passage changes periodically it can cause mass flow fluctuations through this blade passage. If the frequency of the variation is slow, so that the chord length l is much smaller than the wave length L $(l\ll L)$, applying the continuity equation:

$$\frac{\partial\rho}{\partial t}+\frac{\partial\rho u}{\partial s}=0 \tag{10}$$

where A is the area of the blade passage. If we replace $\rho u=\dot{m}/A$ and $\partial\rho=\partial p/c^2$ and assume that c is constant with s and t and that $\dot{m}=f(t)$ only, then for $\partial s\ll L$ we obtain:

$$\frac{\partial p}{\partial t}=-\frac{\dot{m}(t)c^2}{A^2}\frac{\partial A}{\partial s} \tag{11}$$

Integration over 1/2 period, for which $\partial s=c\partial t$ gives the pressure amplitude as:

$$\hat{p}_{(s)}=-\frac{\hat{\dot{m}}c}{A(s)} \tag{12}$$

where $\hat{\dot{m}}$ is the amplitude of the mass flow fluctuation. This can also be obtained from the familiar form $\hat{p}=-\widehat{\rho\bar{u}}c$ with $\widehat{\rho\bar{u}}A=\hat{\dot{m}}$ =const. Thus, for a cyclic mass flow variation within a blade passage a pressure wave will propagate upstream with increasing amplitude if the passage is contracting or with decreasing amplitude if the passage is diverging.

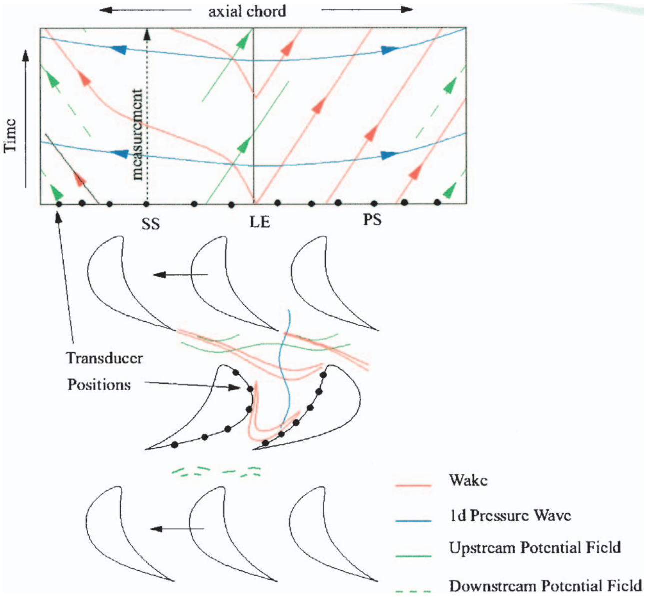

Fig. 5 Systematic of the *s*–*t* diagrams used for unsteady surface data; axial chord; time; measurement, SS, LS, PS; transducer position, wake; 1*d* pressure wave; upstream potential field; downstream potential field

4 Experimental and Numerical Results

The data is presented in form of $s-t$ diagrams, where s is the projection of the blade surface onto the axial chord plotted from the suction side trailing edge to the leading edge to the pressure side trailing edge and t is the measurement time. A schematic of an $s-t$ diagram is shown in Fig. 5. The dots on the s-axis and blade surface mark the position of the transducers. The arrows in the schematic indicate the propagation direction and speed of the various effects. The origin of a disturbance is indicated by the line type. Effects originating from upstream are indicated as solid lines; effects originating from downstream are indicated as dashed lines. The wake is convected downstream along the red lines at the local flow speed. The acceleration of the flow towards the peak suction point is indicated by the slope of the lines. The propagation of 1D pressure waves at the speed of sound relative to the flow is indicated by the straight blue lines. The potential pressure fields of the rotors can be considered to be largely frozen to the rotors with their propagation speed being circumferential, neglecting small fluctuations dependent on the rotor relative position to the stator. Their interaction with the stator surfaces is indicated in green. Their axial extent is limited as indicated by the restricted range in which they are drawn.

As indicated in Fig. 5 the various disturbances affecting the unsteady pressure field are moving at different and sometimes varying speeds through the blade passage. In the present case the frequencies of the periodic disturbances are identical, as the upstream and downstream blade row have the same blade number. Thus, although the wavelength, wave shape and the phase between the disturbances will vary throughout the passage, at each discrete point of the passage the phase difference between the disturbances will be constant during one cycle. The amplitude and phase of the resultant will depend on the magnitude of each disturbance and the phase difference between them. Therefore only if one disturbance is dominant over the others is the phase of the pressure wave in the $s-t$ diagram a direct measure of the propagation speed of that effect. Vice versa, if the propagation speed of the resultant pressure fluctuation is identical to that of a certain disturbance, this disturbance must be the dominant one in that particular area.

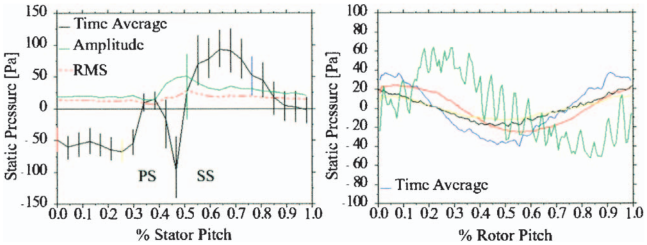

Fig. 6 Pitchwise static pressure variation, measurement in traverse plane 1 (midspan); (*a*) absolute frame of reference, with bars of maximum and minimum pressure; (*b*) rotating frame of reference, time averaged and time resolved pressure PS SS, % stator pitch, % rotor pitch, static pressure [Pa] ×2; time average; amplitude; rms

4.1 Upstream Potential Effects

4.1.1 Stator-Rotor-Interaction on Stator 1. Measurements on the stator 1 were used to study the upstream potential interaction of a rotor with a stator. Since there is no moving bladerow upstream of the stator, periodic fluctuations can be unambiguously related to the rotor potential field. Measurements were taken at mid-span only, where the flow is expected to be most two-dimensional. To assess the expected pressure fluctuations on the blade surface the unsteady static pressure field in the traverse plane was evaluated. The unsteady static pressure field was obtained by superpositioning hot-wire and fast response pressure probe results. Figure 6(*a*) shows the pitchwise variation of the time-averaged static pressure at midspan and bars of the local maximum and minimum of the time-resolved static pressure. The red dashed line shows the rms of the time-resolved pressure and the green line shows the amplitude of the pressure fluctuations. The position of the stator wake is at about midpitch of the measuring range where a deficit in static pressure occurs. This can be explained by the existence of a vortex street shed from the trailing edge as is shown in Sec. 3. Both, fluctuation amplitude and rms increase almost linearly towards the suction side and drop rapidly across the wake. At the suction side both pressure amplitude and rms are about 6 times higher than on the pressure side. Thus, the potential field of the rotor varies with the relative position of the rotor to the stator. This implies that the pressure fluctuations are not explicable solely in terms of the time-averaged static pressure field of the rotor.

Figure 6(*b*) shows the time-averaged static pressure in the relative frame of the rotor, black line, and the time-resolved static pressure at 4 stator pitch positions, coloured lines, position marked by the color of the bars in Fig. 6(*a*). The four time traces are shifted such that their phase should be identical. It can be seen that the potential field of the rotor is not only changed in amplitude but also slightly in shape and phase. This can be explained by the circumferentially varying stator exit angle, i.e., incidence onto the rotor. The variation in incidence alters the position of the stagnation point and changes the leading edge loading of the rotor. This modifies the shape and amplitude of the potential field which is reflected in the time traces.

Outside the wake the pressure field over one rotor pitch is almost sinusoidal. However the time-resolved signal within the stator wake (in Fig. 6(*b*) green) has a higher frequency content. At this position higher frequency oscillations with an amplitude of about 20% of the original sinusoidal wave can be seen. FFT-analysis of the raw signal (Fig. 7(*a*)) shows a well defined peak at 29× the blade passing frequency. In comparison the FFT at midpitch Fig. 7(*b*) shows only a very weak frequency peak at 29× blade passing frequency. The Strouhal number

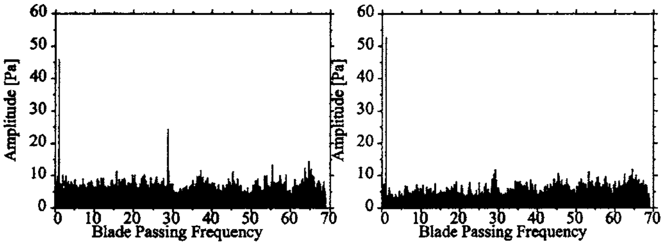

(a) Within Wake (Green Pos.in Fig.6(a)) (b) At Mid Pitch (Red Pos. in Fig.6(a))

Fig. 7 FFT of raw signal from fast response pressure probe (traverse plane 1, midspan)

$$\mathrm{St} = \frac{fD}{V} \tag{13}$$

based on this frequency f, the trailing edge diameter D and the average velocity V at midspan is $\mathrm{St}=0.26$. This is within the expected range for vortex shedding. ($\mathrm{St}=0.1-0.4$ according to [17]; $\mathrm{St}=0.24-0.28$ according to [15].) Thus, the pressure fluctuation within the wake can be associated with a vortex street. The locking of the vortex street into the blade passing frequency is probably due to a fluctuating change of boundary layer thickness caused by the interaction with the downstream potential flow field. The locking of the frequency was also observed in numerical observations by [18,19]. The vortex street, phase shift, and amplitude variation is also clearly visible in the $s-t$ diagram of static pressure in Fig. 9. The vortex street shed from a blade row can cause high frequency pressure oscillations on the down-stream blade row [19] but also up to the throat of the same blade row itself [18,20]. Since the wave length of the vortex street is very small its decay is expected to be very rapid. However, it plays an important role in generating noise.

The propagation of the static pressure fluctuations along the blade surface are best visualized in the form of an $s-t$ diagram. For this purpose the pressure is plotted around its local average and nondimensionalized with the local amplitude $(\tilde{p}-\bar{p})/\hat{p}|_x$. Figures 8($a$) and 8($b$) show the $s-t$ diagram of the measured and calculated pressure fluctuations on stator 1. The local pressure amplitude $\hat{p}_{(x)}$ is shown in black above the contour plot. In Fig. 8(b) the calculated entropy fluctuations, processed in the same way, are added to the graph as line contours. The resolution of the latter is reduced such that only contours of high entropy are shown. The local entropy amplitude is shown in red above Fig. 8(b). Although measurements were only taken at 6 points per surface, the qualitative agreement between experimental data and computation is reasonable. Both diagrams show two propagating pressure variations, that originate from the downstream blade row. The first, and in its amplitude the strongest effect, affects the suction side between 80% of axial chord and the trailing edge. This is the uncovered area of the blade surface which is directly exposed to the potential pressure field of the rotor. In this area, the pressure fluctuations appear to move slowly downstream. In fact, the propagation speed along the surface is equivalent to the rotor passing speed and the fluctuations originate from the rotors potential field moving over the blade surface.

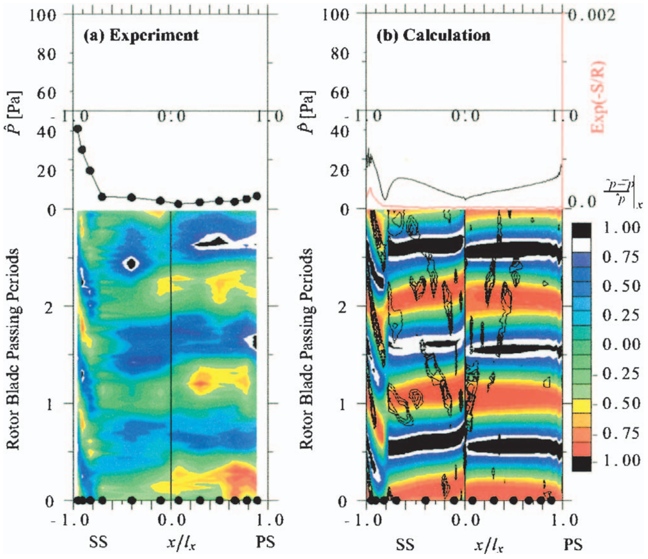

Fig. 8 Propagation of pressure fluctuations on stator 1 surface (midspan); (a) experiment; (b) calculation; SS x/lx PS ×2; rotor blade passing periods ×2 phat [Pa] ($\hat{p}$ [PA]); Exp ($-S/R$); $\tilde{P}-\bar{P}/\hat{P}|_x$

Over the remaining blade surface, pressure fluctuations are propagating upstream with approximately equal magnitude on both sides and decrease slightly towards the leading edge. The reason for the decrease in $\hat{p}$ is explained later. The pressure fluctuations are likely to be due to a one-dimensional pressure wave propagating with the speed of sound in a velocity field. An estimation of their propagation is attempted by the (faint) dashed white line in Fig. 8(b) which represents the path of a disturbance propagating at a speed of $c-u$ along the blade surface s. Over most of the suction surface this compares well with the path of the pressure disturbances. On the pressure surface this estimate is slightly too slow and the propagation speed is nearer to a pressure wave moving axially through the passage at the speed of $c-u_x$ (this is roughly a slope of 0.1 rotor blade passing periods per axial chord). Close to the leading edge the pressure surface is bending into the straight path of such a pressure wave, while the suction side is bending away from it. This explains the reduction of the propagation slope on the pressure side and the increase on the suction side. The fluctuations on the pressure side and suction side in Fig. 8 are taken from two neighboring blades in the same passage. Due to the different axial propagation speed this leads to a phase offset at the leading edge position in the diagram.

On the suction side a distinct phase shift in the propagation lines and a local minimum of $\hat{p}$ exists at about 80% of an axial chord, which is the same point where the propagation speed changes to sonic. This is due to the spatial variation of the rotor potential field and loading with position relative to the stator. As shown earlier in this section (e.g., Fig. 6(a)) $\hat{p}$ increases gradually as the rotor moves from the pressure side of the stator flowfield into the suction side and drops drastically within the wake region. This was accompanied by a phase shift in the time traces of the static pressure relative to the rotor (Fig. 6(b)). The phase shift occurs gradually across the stator pitch and almost instantaneously across the wake, as is also shown in the $s-t$ diagram of Fig. 9. This depicts the static pressure fluctuation $\tilde{p}-\bar{p}$ in the absolute frame of reference measured downstream of stator 1. The position of the wake is clearly visible, due to the high frequency fluctuations within the vortex street. Suction side (SS) and pressure side (PS) are marked on the right-hand side of the graph. The white propagation lines indicate the movement of a point on the rotor. Over the first half of the stator pitch the propagation speed of the pressure lines is much slower than that of a point on a rotor. Thus, the potential field relative to the rotor moves from rotor suction side to rotor pressure side as the rotor moves towards midpitch and the potential field in the absolute frame is almost stationary. After midpitch the potential field relative to the rotor stays stationary with the rotor and its amplitude $\hat{p}$ increases. By the time the rotor has passed over one stator pitch a gradual phase shift of almost 180 deg has occurred. Since the flow is periodic the phase at the beginning of the next pitch must be identical to that at the beginning of the previous stator pitch. Thus, a rapid phase shift must occur as the rotor passes through the stator wake.

Both effects, the change of phase as well as the rapid increase

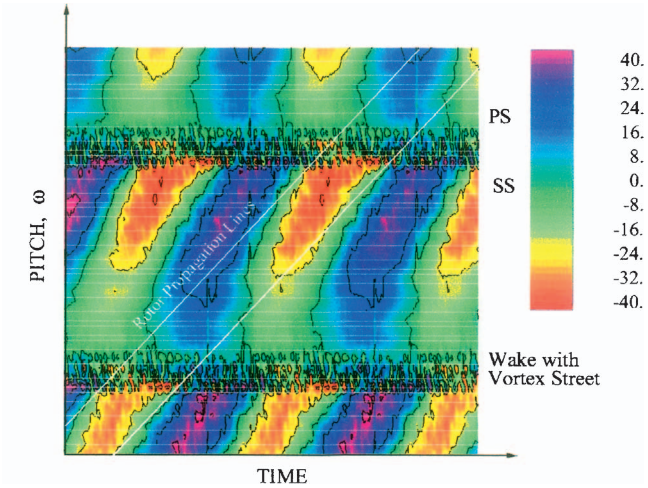

Fig. 9 Time resolved static pressure measurement $\tilde{p}$ in traverse plane 1 (midspan)

in amplitude, can be seen in Fig. 8 at about 80% of an axial chord. The rotor potential field extends axially upstream so that the intersection of the amplitude minimum and the phase shift on the stator surface depends on the stator flow angle and the axial spacing between the blade rows. Since the rotor potential field decays rapidly the amplitude on the stator surface depends on the decay rate of the potential field ($\exp(-2\pi x/S)$) and on the inclination of the suction surface. Thus, the amplitude of the pressure fluctuations in Fig. 8 decreases towards its minimum due to a combination of increased decay with axial distance and reduced front loading of the rotor as it moves towards the pressure side of the wake. The increase in amplitude of the rotor potential field as it moves from pressure side to suction side of the stator flow field is also clearly visible.

The calculated pressure field at one instance in time is presented in Fig. 10. This is taken from the two stage calculation but shows the first two bladerows only. The colored contours represent the difference between the instantaneous static pressure field and the cycle-averaged static pressure field of the stator. The line contours represent the instantaneous pressure field in the rotor passage. For better visualization different contour intervals were selected for both fields. Each of the four stator blade passages shows a different relative rotor blade position, corresponding to one particular instance in time. Since the rotor blade row is moving down the time direction is moving up, i.e., the next instance in time can be seen in the blade passage above.

There are two rapidly decaying concentric pressure fields moving with the rotor. A high pressure field travels in front of the rotor stagnation point (in Fig. 10 red-yellow) which is followed by a low pressure field (green). The spatial and timewise dependency of the pressure field is clearly visible. The line contours in the rotor passage show the changing potential field with rotor position relative to the stator. As the throat of the stator is smaller than one rotor pitch the concentric pressure lines upstream of the rotor extend over the whole stator throat. These move with the rotor and cause small fluctuations in mass flow. This effect can be seen in Fig. 10 (second passage from top) in the form of a pressure wave front moving rapidly upstream. As discussed in Sec. 3 the magnitude of a pressure wave propagating through a duct decreases at a rate of $1/A$. This is the cause of the decline in $\hat{p}$ on the pressure surface and below 80% of axial chord on the suction surface (Fig. 8).

4.2 Numerical Investigation of Isolated Rotor 1-Stator 2-Interaction. After the first stage the flow is highly three-dimensional and unsteady. In order to reduce the multitude of simultaneous interactions from further up- and downstream, an unsteady calculation of the second stator preceded by the first rotor was carried out. The boundary conditions for this calculation, i.e., the pressure drop over the two blade rows as well as the pitchwise-averaged steady flow field in the inlet plane to the rotor were taken from the two stage calculation.

Fig. 10 Instantaneous pressure field at midspan of first stage, taken from 2 stage calculation: colored contours are $p-\bar{p}$ field with contour interval of $\Delta(p-\bar{p})=20$ Pa, line contours of instantaneous pressure field p with contour interval $\Delta p=10$ Pa; stator, rotor

4.2.1 Unsteady Pressure Field Between Rotor 1 and Stator 2. Figure 11 shows contours of $\exp(-S/R)$ (top) and $\tilde{p}-\bar{p}$ (bottom) in the traverse plane between rotor 1 and stator 2. In the calculation there are two coincident planes at this position one fixed relative to the stator and one fixed to the rotor. Figure 11(*a*) shows the variables relative to the rotor and Fig. 11(*b*) relative to the stator. Since $\exp(-S/R)$ is not dependent on the frame of reference there is little difference between the two adjacent quasi-orthogonal planes. Thus, $\exp(-S/R)$ is shown in order to mark the position of the stator flow field in the respective frames of reference. The numbering above the wakes indicates the position of the same blade pitches.

The flow field from rotor 1 is shown to be very three-dimensional with the loss cores having merged at midspan. In comparison, the rotor and stator pressure fields are mainly two-dimensional and do not follow the local blade shape or flow angle.

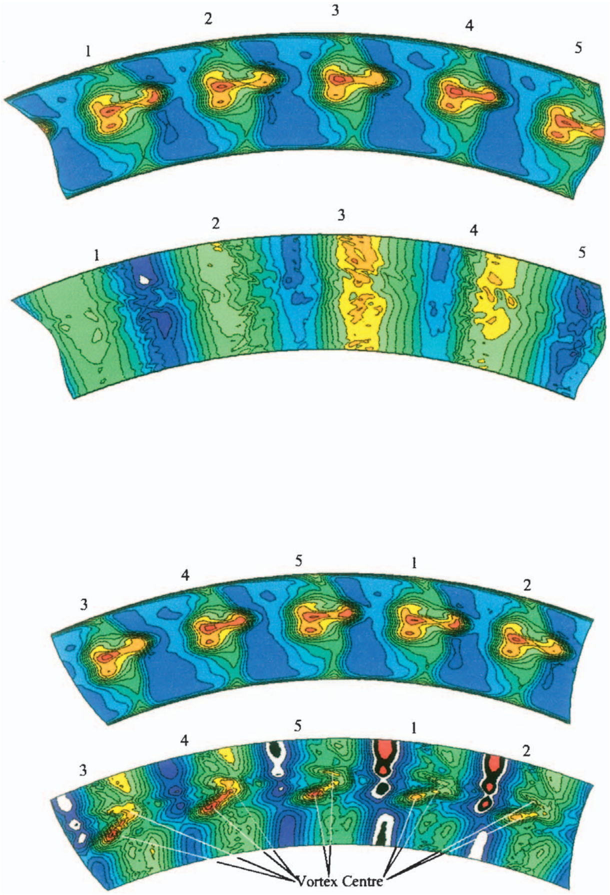

Fig. 11 Unsteady rotor-stator calculation; quasi-orthogonal at traverse plane; top=exp(−S/R); bottom=$\tilde{p}-\bar{p}$; (*a*) last plane of rotor grid, showing pressure field of stator, $\bar{p}$ taken from point fixed to rotor; (*b*) first plane of stator grid, showing pressure field of rotor, $\bar{p}$ taken from point fixed to stator

In both cases a variation of the potential field with relative position of the stator and rotor blade row can be seen. In case of the stator blade row, Fig. 11(*a*), this effect is due to the changing blade loading due to incidence variations. The pressure field in Fig. 11(*a*) is undisturbed by the rotor wake, since the wake is stationary in the rotor frame of reference and since there is little flow acceleration or wake deformation in the passage between the blade rows (see Sec. 3). Similarly the wake does not cause a perturbation of the unsteady pressure field in the absolute frame of reference, Fig. 11(*b*) (bottom). There are, however, two definite regions of low static pressure (yellow/red) at the positions of the loss cores Fig. 11(*b*) (top). These can be identified as the centers of the rotor passage vortices (see also paragraph “Theoretical Analysis”). Additionally, the rotor’s potential field varies circumferentially with its position relative to the stator. However, this is thought to originate from the unsteady variation of the stator front loading rather than being caused by a variation of the rotor’s potential field.

4.2.2 Unsteady Pressure Field in Stator 2 Passage. The unsteady pressure field within the stator passage is affected by the aforementioned effects, namely wake and vortex convection and distortion, potential field interactions and one-dimensional pressure wave propagation. In a low speed facility the convection speed $\bar{u}$ is much smaller than the propagation speed of the pressure wave c, so that the easiest way to differentiate between convective and pressure wave effects is via their propagation speed.

Figure 12 shows an example where a one-dimensional pressure

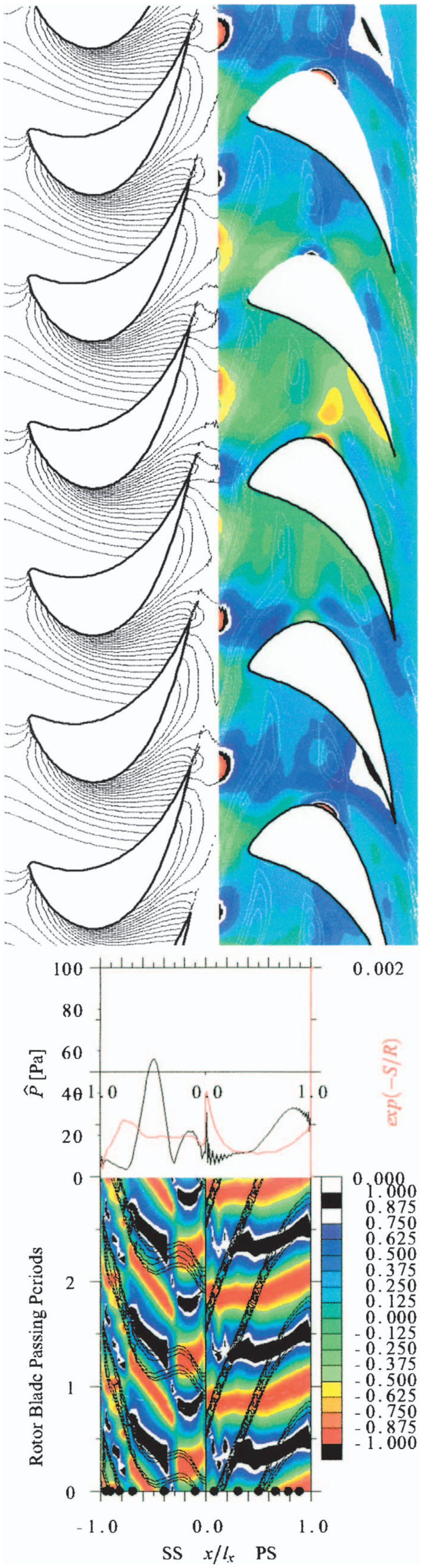

Fig. 12 Unsteady rotor-stator-calculation, 85% span; (*a*) circumferential plane: colored contours of $\tilde{p}-\bar{p}$ with increment of 20 Pa; black contours of $\tilde{p}$; white contours of negative $\hat{u}$; (*b*) s-t diagram of $\hat{p}$ (color) and exp (−S/R) (black lines) on stator 2 surfaces; $\hat{p}$ [Pa]; rotor blade passing periods; SS x/l_x PS; Exp (−S/R)

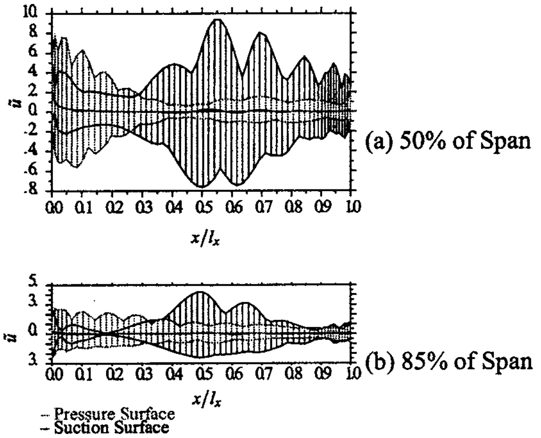

Fig. 13 Envelope of velocity fluctuations $\tilde{u}$ on the surface of four blade passages, taken from unsteady rotor-stator-calculation

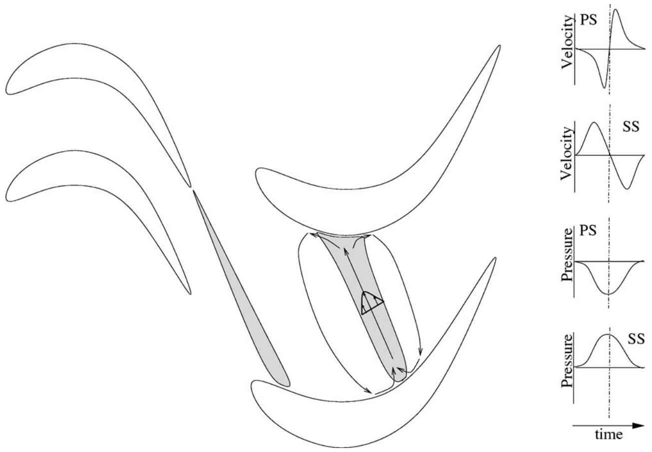

Fig. 14 Representation of a turbine wake as a negative jet [21–23]

wave is clearly visible. The figure is taken at 85% of span, which is away from the convection area of the loss core and at a position where measurements are available. In Fig. 12(a) p is shown as color contours. The white contours are isolines of negative velocity fluctuations $\tilde{u}$ indicating wake positions. The black lines of instantaneous static pressure show the origin of the static pressure waves frozen to the rotor. Initially the potential field frozen to the rotor decays rapidly. However, originating from the same areas of high (red/blue) and low (yellow/green) pressure, pressure fluctuations extend axially into the stator passage. These immediately affect the stator pressure side. The propagation speed of the pressure fluctuations is shown in the $s-t$ diagram in Fig. 12(b). On the pressure side the propagation speed of the calculated pressure fluctuations compares well to the characteristic $c+u$ along the blade surface s, which is depicted by the (faint) dashed white line. The black line contours of negative $\exp(-S/R)$ fluctuation are propagation lines of the wake. The slope of the $\exp(-S/R)$-lines is equivalent to the convection speed $\bar{u}$. On the pressure side, the acceleration towards the trailing edge can be noticed by the decrease in gradient (dt/ds). It is apparent that the pressure fluctuations on the pressure side are caused predominantly by a pressure wave. The amplitude of the unsteady pressure increases towards the trailing edge of the pressure surface. To some extend this can be explained as being similar to a "Cyclic Backpressure Variation," in that the amplitude of a one-dimensional pressure wave is increasing proportional to $1/A$ in a contracting duct. However, since the propagation speed decreases towards trailing edge there must be another, convective mechanism acting on the unsteady pressure field.

As was outlined in the previous paragraph, and can be seen from the unsteady pressure field in the traverse plane, Fig. 11, and in Fig. 12, the wake does not cause unsteady pressure fluctuations unless it is distorted (Sec. 3.1). The envelope of the stator surface velocity fluctuations at 85% of the span is shown in Fig. 13(b). These are not entirely smooth as they are taken from only four blade passages. The red envelope of the pressure side velocity fluctuation decreases in amplitude towards the trailing edge. According to Eq. (7) the amplitude $\hat{p}$ of a pressure perturbation caused by a convecting wake is proportional to $\rho\bar{u}\Delta\hat{u}_L+\rho\hat{u}\Delta\bar{u}_L$. Since both terms are of approximately equal magnitude but opposing sign they largely cancel each other out so that no significant contribution is expected.

A pressure deficit but not a pressure increase could also be induced by a vortex (see Sec. 3.2). In this case, the rotor passage vortices are convected near midspan and the stator secondary vortices are forming near the suction side. Additionally vortices similar to those depicted in Fig. 14 are formed in front of and at the rear of the wake. All of these possibilities have been checked and eliminated as reasons for the observed pressure fluctuations.

The real reason is that as the wake and main stream are convected they are mixed and sheared into a pattern of similarly sized streaks of low and high velocity. The pitchwise pressure gradient of the blade is affected by a velocity fluctuation $u\pm\Delta u$ of the mean velocity according to the radial equilibrium equation by:

$$\frac{\partial p}{\partial n}=\rho\frac{(u+\Delta u)^2}{R_c} \tag{14}$$

If $\Delta u \ll u$ and the unsteady velocity perturbations have little effect on the streamline curvature of the mean stream, the change in pitchwise gradient is

$$\Delta\frac{\partial p}{\partial n}=\rho\frac{u\Delta u}{R_c} \tag{15}$$

Thus, when the mean stream pressure is subtracted the pitchwise gradient of the pressure perturbation is positive or negative dependent on the sign of the instantaneous velocity fluctuation. Furthermore, the local pressure amplitude increases not only according to the magnitude of the local velocity fluctuation but also proportional to the local velocity u, e.g., on the pressure side towards the trailing edge, and inverse proportional to the local streamline curvature. Thus, the maximum pressure fluctuations due to this mechanism are expected to occur at the suction surface crown.

On the suction side the pressure wave dominates only over the first 10% of the blade surface. Here, the waves propagate "upstream" over the suction surface at the circumferential speed of the rotor, Fig. 12(b). Further downstream the variation of pitchwise pressure gradient is increased as the fluid is accelerated, the radius of curvature R_c is reduced and the velocity streaks lie almost perpendicular to the blade surface. As the two mechanisms are not always in phase, their composite pressure fluctuations $\hat{p}$, Fig. 12(b), have a distinct minimum and phase shift at about 30% of the axial chord. As the loading effect becomes dominant the propagation speed is reduced to about convection speed $\bar{u}$. As expected the amplitude peak reaches its maximum at the suction surface crown and abates towards trailing edge.

At 85% of span the velocity streaks were the only convective influence on the unsteady pressure field. According to Fig. 11 their maximum interaction is expected at midspan where the velocity deficit of the wake is largest. Additionally, one of the rotor passage vortices is convected at this spanwise position, so that its influence on the unsteady pressure field can be studied. Figure 15(a) shows the contour plot of $\tilde{p}$ in the circumferential plane at midspan and Fig. 15(b) shows the respective $s-t$ diagram. Figure

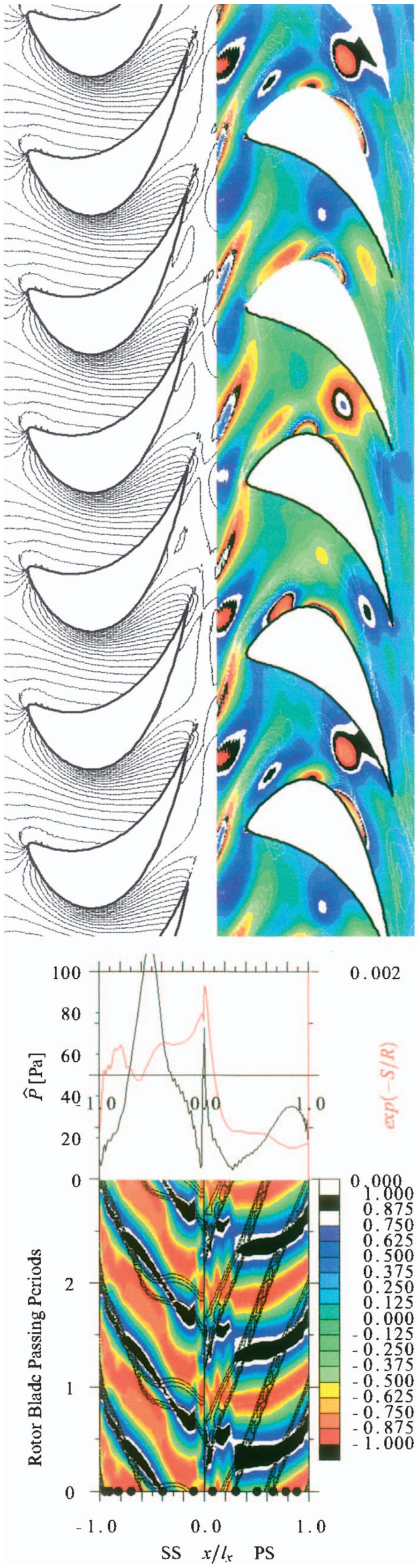

Fig. 15 Unsteady rotor-stator-calculation, at midspan; (*a*) circumferential plane: colored contours of $\tilde{p}-\bar{p}$ with increment of 20 Pa; black contours of $\tilde{p}$; white contours of negative $\hat{u}$; (*b*) s-t diagram of $\hat{p}$ (color) and exp $(-S/R)$ (black lines) on stator 2 surfaces; $\hat{p}$ [Pa]; rotor blade passing periods; SS x/l_x PS; Exp $(-S/R)$

11 showed that the circumferential pressure variations $\tilde{p}$ due to the rotor potential field are radially uniform. The area of low static pressure in the passage vortex core is nearly coincident, but slightly offset to, the low pressure area of the rotor's potential field. The migration of the vortex core can be seen clearly in Fig. 15(*a*) as red–yellow streaks originating from the low pressure area of the rotor's potential field but then distorting it as it is convected with the main stream. The one-dimensional pressure waves, that were observed at the 85% of span position are still present, as can be seen for example in Fig. 15(*b*) by the slope of the pressure fluctuations at the front part of the pressure and suction side

The amplitude characteristic on the stator surface at 50% of the span is similar to that at 85% of the span, Fig. 12(*b*), with the exception of the first 30% of the axial chord on the pressure side. Here a large but rapidly decaying amplitude peak can be observed, that occurs only at midspan of the pressure side. This is where the leading edge cuts through the passage vortex. The vortex is stretched around the leading edge, its streamwise velocity is accelerated and the pressure in the vortex core drops. Figure 13(*b*) shows these increased velocity fluctuations on the pressure surface leading edge which decay rapidly due to the increased viscous dissipation in the accelerated velocity field. The suction side is not affected by this as can be seen by nearly constant velocity amplitudes over the first 40% of the axial chord. Figure 15(*a*) (top) shows the magnitude of the pressure and entropy fluctuations which both have the same sharp but rapidly decaying peak on the pressure side leading edge. It appears that this process causes the generation of additional loss.

In Fig. 15(*b*) some "wiggles" in the pressure fluctuations occur at the pressure side leading edge. These are a numerical feature, which was caused by generating Fig. 15(*b*) with a reduced dataset and are not due to vortex interaction or wake impingement. Plotting the same graph with the full dataset shows that the propagation speed is fairly constant until 60% of chord and almost equal to the characteristic $c+u$ along s. Only a slight variation with chordwise position was observed. Thus, the phase displacement between the one-dimensional pressure wave and the vortex interaction line is small, particularly in the short area of very large pressure amplitudes induced by the vortex, so that the two effects enhance each other. As the phase displacement depends mainly on the wake angle and axial spacing their variation could be used to generate a phase shift large enough for the two effects to cancel one another and so reduce the magnitude of the fluctuations at the leading edge. This would however not necessarily reduce the increased losses due to mixing.

The suction side at 50% of the span is very similar to that at 85% and is almost entirely dominated by convective effects, as can be seen by the nearly parallel propagation lines of the pressure and entropy fluctuations in Fig. 15(*b*). The influence of the pressure field frozen to the rotor can only be seen until about 15% of the axial chord. After that the disturbance amplitude $\hat{p}$ is increasing towards its maximum at about midchord and propagating at about convection speed u. The midspan amplitudes of Δu and $\hat{p}$ (Fig. 13 and Fig. 15(*b*) and Fig. 12(*b*)) are both twice the size of those at 85% of the span, which is consistent with Eq. (15). No distinct phase shift in the pressure propagation lines occurs at 50% of the span as the influence of the convective interactions is stronger and starts earlier.

4.3 Rotor-Stator-Rotor-Interaction on Stator 2 Surface.

The following section shows a comparison of the results from the two-stage unsteady calculation with the measurements on the stator 2 surface. The propagation of the pressure fluctuations along the surface at midspan is shown in the $s-t$ diagram in Fig. 16. Figure 16(*a*) shows the experimental, Fig. 16(*b*) shows the numerical result. As the three-dimensional inlet field of the unsteady calculation did not exactly match that of the measurements, the spanwise position of the computational results was taken slightly off center at 58% of the span. The spatial resolution of the experi-

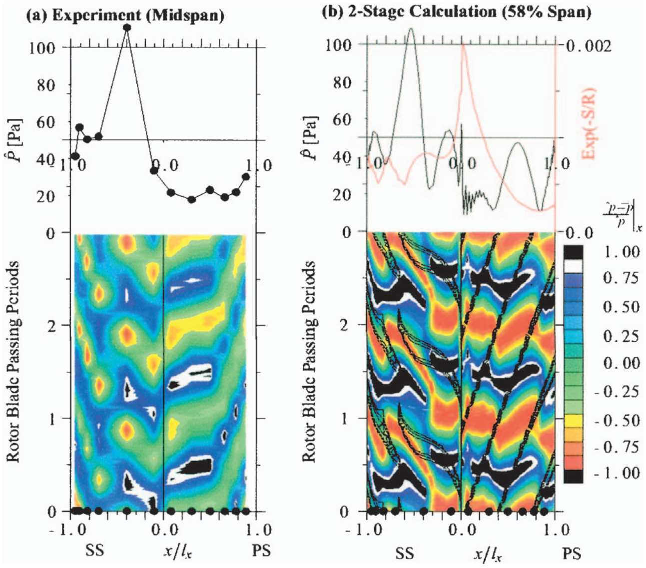

Fig. 16 Propagation of pressure fluctuations on stator 2 surface; (*a*) experimental (midspan); (*b*) 2-stage calculation (58% span); SS x/lx PS ×2; rotor blade passing periods ×2; $\hat{p}$ [Pa] ×2; Exp ($-S/R$); $\tilde{P}-\bar{P}/\hat{P}|_x$

mental data is very low, so that some features, for example phase shifts, are not resolved in the experimental data as well as in the numerical data.

Figure 16(*b*) shows a complex scheme of pressure propagation lines at different speeds and with several phase shifts. The best way to understand these is by superimposing the previous observations for the first and second stator. Although the pressure perturbations originating in the upstream plane are smaller than those in the downstream plane they are more influential at the pressure side. This is first because the pressure side is sheltered from the direct influence of the downstream rotor by the tail of the stator blade and secondly because the amplitude of the downstream propagating pressure waves increases through the blade passage according to $\hat{p} \propto 1/A$ while the upstream propagating pressure waves are reduced in amplitude. The exact influence of the downstream pressure wave is not detectable. Towards the trailing edge the pressure fluctuations due to the unsteady pitchwise pressure gradient are increasing. Since at any moment of time there are at least 3 rotor wakes convecting through the stator and only one pressure wave there are three phase shifts noticeable in the resulting pressure line. The amount of the phase shift depends on the relative size of the two effects. Due to these phase shifts the pressure side propagation line varies around the downstream characteristic $c+u$ of the pressure wave (faint white dashed line) up to 80% of axial chord. Thus, the pressure fluctuations caused by the convected flow field are increasing towards the trailing edge, as described in the previous section. The position at which a phase shift occurs is stationary within the stator. The first position is very close to the leading edge and originates from the short but intense interaction of the rotor passage vortex with the leading edge. Since the first and last phase shifts occur at positions of very large pressure fluctuations of the convected velocity field it can be concluded that the pressure wave is reducing the maximum possible pressure side amplitudes.

On the suction side the upstream and downstream pressure waves dominate the unsteady pressure field in stator 2 upstream of 30% of the axial chord and downstream of 70% of the axial chord, Fig. 16(*b*). In these regions the propagation speed of the pressure field over the blade surface is a function of the rotor wheel speed and the geometry of the suction side surface exposed to the pressure field. The area between 30% and 70% of axial chord is dominated by the convected velocity field and its effect on the local pressure gradient. As on the pressure side there exists a distinct phase shift and amplitude minimum as the mechanisms interact.

The interaction of at least two different wave forms was also confirmed by FFT-analysis on the raw signals of the stator 2 measuring points. These had pronounced frequency peaks at the first and second harmonic of the blade passing frequency (not shown).

5 Summary

The unsteady pressure field in a low speed multistage model turbine was examined computationally and experimentally. In summary, there exists a reassuring agreement between measurement and calculation both quantitatively and qualitatively, although the experimental propagation lines of the pressure waves are only crudely resolved. It was possible to explain the origin of the unsteady pressure fluctuations based on the numerical flow field which matched the experimental results on the surface closely. Four flow features affect the unsteady pressure field in a downstream blade row, namely, the potential field frozen to the upstream blade row, the pressure waves originating from changes to the potential pressure field, the convected unsteady velocity field and the passage vortex of the upstream blade row.

One-dimensional pressure waves and the unsteady variation of the pitchwise pressure gradient due to the changing velocity field were the dominant interaction mechanisms influencing the magnitude of the surface pressure fluctuations. The magnitude of these effects had not been previously anticipated to be more important than other recognized effects such as wake propagation or direct potential field interaction.

All interactions vary in magnitude as they pass through the downstream blade row. The mechanisms act largely independently of one another and their effects can be superimposed. Since they propagate at different speeds the phase between them can shift so that the resulting amplitude can be enhanced or reduced. As they often act simultaneously it can be difficult to determine the magnitude of each effect. The different mechanisms are most easily differentiated by their propagation speed. Since the potential field from the rotor decays quickly it has a limited effect on the flow physics in the stator. The axial pressure wave connected with the potential field induces additional unsteady forces on the blades by increasing and reducing the pressure in neighboring blades, Fig. 12(*a*). The maximum pressure fluctuations induced by the velocity field occur at the suction surface crown and at the rear end of the pressure side.

The maximum pressure fluctuations induced by the one-dimensional pressure wave occur generally at the pressure side. Near the leading edge the surface pressures are mainly influenced by the potential field on the suction side and, if existent, by the convected passage vortex from the upstream blade row.

Acknowledgment

The authors would like to thank Siemens Power Generation and EPSRC for funding this work.

Nomenclature

A = area of blade passage
c = speed of sound
FFT = fast Fourier transformation
h = blade height
h_O = total enthalpy
I, IMR = number of grid notes in circumferential direction, maximum thereof
l, l_x = chord length, axial chord length
L = disturbance wave length
$\dot{m}$ = mass flow
n = normal direction towards center of curvature
p = static pressure
Q = disturbance speed

R, R_c = gas constant, radius of curvature
s = distance along streamline
S = entropy/pitch of a cascade
t = time
u = velocity
U = blade speed
V_x = axial velocity
Δz = blade row spacing along machine axis
Γ = circulation
ρ = density
ϕ = flow coefficient
Φ = $\omega(t-s/Q)$
ω = rotational speed, frequency of disturbance

Accents

˜ = phase locked average
— = time average
ˆ = amplitude

Subscripts

le, te = leading edge, trailing edge
PS, SS = pressure side, suction slide
RMS = root mean square
sb, rb = stator blade, rotor blade

References

[1] Dénos, R., Arts, T., Paniagua, G., Michelassi, V., and Martelli, F., 2000, "Investigation of the Unsteady Rotor Aerodynamics in a Transonic Turbine Stage," ASME Paper No. 2000-GT-435.
[2] Adami, P., Belardini, E., Martelli, F., and Michelassi, V., 2001, "Unsteady Rotor/Stator Interaction: An Improved Unstructured Approach," ASME Paper No. 2001-GT-0356.
[3] Moss, R. W., Ainsworth, R. W., Sheldrake, C. D., and Miller, R., 1997, "The Unsteady Pressure Field Over a Turbine Blade Surface: Visualization and interpretation of Experimental Data," ASME Paper No. 97-GT-474.
[4] Abhari, R., Busby, J., Davis, R., Delaney, R., Dorney, D., Dunn, M., Haldemann, C., and Venable, B., 1998, "Influence of Vane-Blade Spacing on Transonic Turbine Stage Aerodynamics, Part 1: Time Averaged Data and Analysis," ASME Paper No. 98-GT-481.
[5] Abhari, R., Busby, J., Davis, R., Delaney, R., Dorney, D., Dunn, M., Haldemann, C., and Venable, B., 1998, "Influence of Vane-Blade Spacing on Transonic Turbine Stage Aerodynamics, Part II: Time-Resolved Data and Analysis," ASME Paper No. 98-GT-482.
[6] Hilditch, M. A., Smith, G. C., and Singh, U. K., 1998, "Unsteady Flow in a Single Stage Turbine," ASME Paper No. 98-GT-531.
[7] Clark, J. P., Stetson, G. M., Magge, S. S., Ni, R. H., Haldemann, C. W., and Dunn, M. G., 2000, "The Effect of Airfoil Scaling on the Predicted Unsteady Loading on the Blade of a 1 and 1/2 Stage Turbine and a Comparison with Experimental Results," ASME Paper No. 2000-GT-0446.
[8] Dring, R. P., Joslyn, H. D., Hardin, L. W., and Wagner, J. H., 1982, "Turbine Stator-Rotor Interaction," J. Eng. Power, **112**, pp. 729–742.
[9] Rai, M. M., and Madavan, N. K., 1990, "Multi Airfoil Navier–Stokes Simulations of Turbine Rotor-Stator Interaction," J. Turbomach., **112**, pp. 377–384.
[10] Schnell, R., 2001, "Experimental and Numerical Investigation of Blade Pressure Fluctuations on a cfk-Bladed, Counter-Rotating Propfan," ASME Paper No. 2001-GT-0298.
[11] Pullan, G., 2001, "An Experimental and Computational Study of a Shed Vortex in a Turbine Stage," Ph.D. thesis, Cambridge University Engineering Department, Cambridge, UK.
[12] Denton, J. D., 1990, "The Calculation of Three Dimensional Viscous Flow Through Multistage Turbomachines," ASME Paper NO. 90-GT-1990.
[13] Denton, J. D., private communication.
[14] van de Wall, A. G., Kadambi, J. R., and Adamczyk, J. J., 2000, "A Transport Model for the Deterministic Stresses Associated with Turbomachinery Blade Row Interactions," ASME Paper No. 2000-GT-0430.
[15] Roberts, Q. D. H., 1998, "The Trailing Edge Loss of Subsonic Turbine Blades," Ph.D. thesis, Cambridge University Engineering Department, Cambridge, UK.
[16] Parker, R., and Watson, J. F., 1970, "Interaction Effects Between Blade Rows in Turbomachines," Technical Report MR/50/70, University of Wales.
[17] Gostelow, J. P., 1984, *Cascade Aerodynamics*, Pergamon Press, Oxford.
[18] Sondak, D. L., and Dorney, D. J., 1999, "Simulation of Vortex Shedding in a Turbine Stage," J. Propul. Power, **121**, pp. 428–435.
[19] Hummel, F., 2002, "Wake–Wake Interaction and its Potential for Clocking in a Transonic High-Pressure Turbine," J. Turbomach., **124**, pp. 69–75.
[20] Cicatelli, G., and Sieverding, C. H., 1996, "The Effect of Vortex Shedding on the Unsteady Pressure Distribution Around the Trailing Edge of a Turbine Blade," ASME Paper No. 96-GT-359.
[21] Hodson, H. P., 1984, "Measurements of Wake-Generated Unsteadiness in the Rotor Passages of Axial Flow Turbines," ASME Paper No. 84-GT-189.
[22] Hodson, H. P., and Dawes, W. N., 1996, "On the Interpretation of Measured Profile Losses in Unsteady Wake-Turbine Blade Interaction Studies," ASME Paper No. 96-GT-494.
[23] Lefcort, M. D., 1965, "An Investigation into Unsteady Blade Forces in Turbomachines," ASME J. Eng. Power, **87**, pp. 345–354.

M. W. Benner[1]
National Research Council of Canada,
Institute for Aerospace Research,
Ottawa, ON K1A 0R6,
Canada
e-mail: michael.benner@nrc-cnrc.gc.ca

S. A. Sjolander
Department of Mechanical
and Aerospace Engineering,
Carleton University,
Ottawa, ON K1S 5B6
Canada

S. H. Moustapha
Pratt and Whitney Canada, Ltd.,
Longueuil, PQ, J4G 1A1
Canada

An Empirical Prediction Method for Secondary Losses in Turbines—Part I: A New Loss Breakdown Scheme and Penetration Depth Correlation

Despite its wide use in meanline analyses, the conventional loss breakdown scheme is based on a number of assumptions that are known to be physically unsatisfactory. One of these assumptions states that the loss generated in the airfoil surface boundary layers is uniform across the span. The loss results at high positive incidence presented in a previous paper (Benner, M. W., Sjolander, S. A., and Moustapha, S. H., 2004, ASME Paper No. GT2004-53786.) indicate that this assumption causes the conventional scheme to produce erroneous values of the secondary loss component. A new empirical prediction method for secondary losses in turbines has been developed, and it is based on a new loss breakdown scheme. In the first part of this two-part paper, the new loss breakdown scheme is presented. Using data from the current authors' off-design cascade loss measurements, it is shown that the secondary losses obtained with the new scheme produce a trend with incidence that is physically more reasonable. Unlike the conventional loss breakdown scheme, the new scheme requires a correlation for the spanwise penetration depth of the passage vortex separation line at the trailing edge. One such correlation exists (Sharma, O. P., and Butler, T. L., 1987, ASME J. Turbomach., ***109****, pp. 229–236.); however, it was based on a small database. An improved correlation for penetration distance has been developed from a considerably larger database, and it is detailed in this paper.* [DOI: 10.1115/1.2162593]

Introduction

A turbine airfoil is usually designed to produce minimum losses at its design operating condition. Additional losses, often referred to as off-design losses, occur because conditions in the turbine deviate from those at the design point. Such deviations are common and they can occur for several reasons. For instance, in aircraft engines, operation at idle, take-off and cruise all result in changes in the operating conditions for the turbines, particularly the low-pressure stages. Furthermore, any deviation in the compressor and/or turbine efficiency from their target values will result in the turbine operating away from its design point. Uprating an existing engine to produce more power or thrust, by increasing the engine mass flow, for example, can also cause the turbine to operate away from its original design operating condition.

The change in operating conditions can take a number of different forms, including deviations in Reynolds number and Mach number from their design values. Perhaps the most significant effect on losses occurs when the incidence differs from its design value. The present, two-part paper describes a new empirical secondary loss prediction method for use in meanline analyses, and it is the last of a series of papers that have focused on the effects of off-design incidence on profile losses (e.g., Benner et al. [1]) and secondary losses (e.g., Benner et al. [2–4]).

Meanline analysis continues to be an important tool for the turbine aerodynamicist, particularly during the early stages of design when detailed geometries are not known and gas-path, velocity-triangle and airfoil-count optimization studies are being performed. Meanline analysis tools use empirical correlations for loss estimation, and there is an on-going need to review and improve these correlations.

The motivation for developing a new prediction method for secondary losses was based on detailed flow field measurements made in two large-scale, low-speed, linear turbine cascades (Benner et al. [2]). From the measured loss results, problems were identified with the conventional subdivision of the losses into profile and secondary components. In the current paper, these loss results are presented first to highlight the problems that have been observed with the conventional loss breakdown and to provide the necessary background for the subsequent development of the new prediction method. The prediction method is based on a new loss breakdown scheme, and it is described in this paper. With the new breakdown scheme, a correlation is required for the spanwise penetration depth of the passage vortex separation line at the trailing edge. One such correlation exists (Sharma and Butler [5]); however, it was based on a small database. An improved correlation for penetration distance has been developed from a considerably larger database, and it is also detailed in this paper. The recent pertinent references from which data or important findings were obtained are discussed in later sections of the papers.

Part II of this two-part paper presents a modified secondary loss correlation for use with the new loss breakdown scheme. The correlation was based on a substantial database of measurements from Benner [6] and from the open literature. The same database was used to evaluate the new correlation as well as the most recent published secondary loss correlations for design and off-design values of incidence.

---

[1] Author to whom correspondence should be addressed.

Contributed by the International Gas Turbine Institute (IGTI) of ASME for publication in the JOURNAL OF TURBOMACHINERY. Manuscript received October 1, 2004; final manuscript received February 1, 2005. IGTI Review Chair: K. C. Hall. Paper presented at the ASME Turbo Expo 2005: Land, Sea and Air, Reno, NV, June 6–9, 2005, Paper No. GT2005-68637.

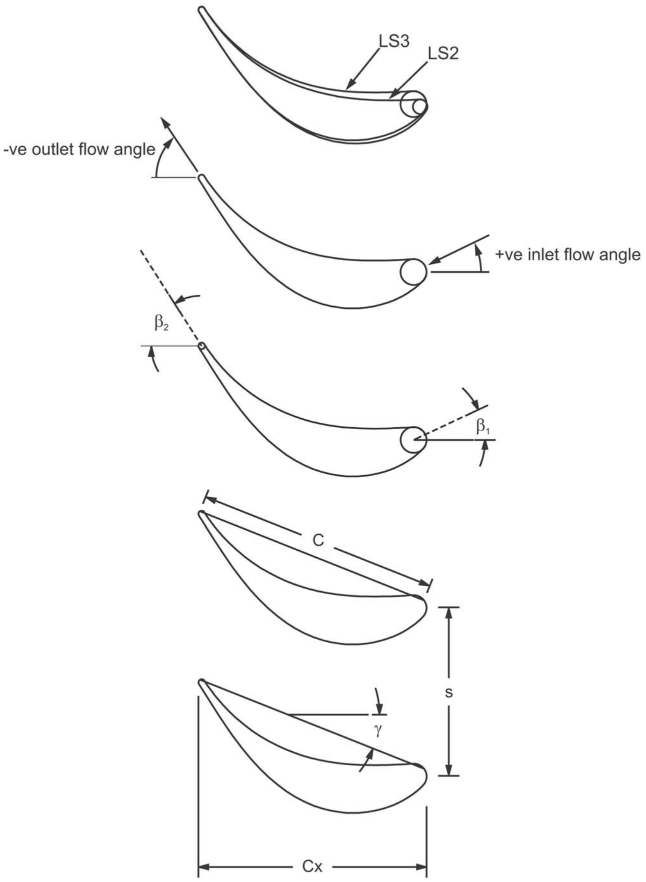

Parameters	LS2	LS3
Blade span, h [mm]	203.7	203.7
Blade spacing, s [mm]	110.7	110.7
True chord, C [mm]	162.8	162.3
Axial chord, Cx [mm]	150.0	149.4
Stagger angle, γ [deg]	23.1	21.6
t_{max}/c [%]	18.0	19.6
Inlet metal angle, β_1 [deg]	29.3	25.5
Outlet metal angle, β_2 [deg]	-57.5	-57.5
Design inlet flow angle, $\alpha_{1,des}$[deg]	28.4	28.4
Design outlet flow angle, $\alpha_{2,des}$[deg]	-57.7	-57.7
Design incidence, $\alpha_{1,des}-\beta_1$ [deg]	-0.9	2.9
Leading-edge diameter, d [mm]	9.4	16.7
Leading-edge wedge angle, We [deg]	52.4	43.0
Trailing-edge thickness, tet [mm]	4.2	4.2

Fig. 1 Cascade geometry and measurement locations

Test Cascades

The off-design loss results presented in the next section were obtained from experimental measurements made in a low-speed, linear cascade test section. The detailed flow field measurements as well as a description of the experimental apparatus, procedures, data acquisition and instrumentation are presented in Benner et al. [2]. As background to the subsequent discussions on the losses, the geometries of the two cascades that were examined are presented here.

The geometries of the two cascades, which are designated LS2 and LS3, are summarized in Fig. 1. LS2 represents the midspan section of a power turbine blade of fairly recent design. After the development of the Moustapha et al. [7] correlation, cascade LS3 was fabricated to examine further the effect of leading-edge geometry on the off-design profile losses. The two airfoils were designed for the same overall loading, as measured by the Zweifel loading parameter (ψ_T=0.89), and lifing requirements. Both airfoils were designed using the same turbine profile design system.

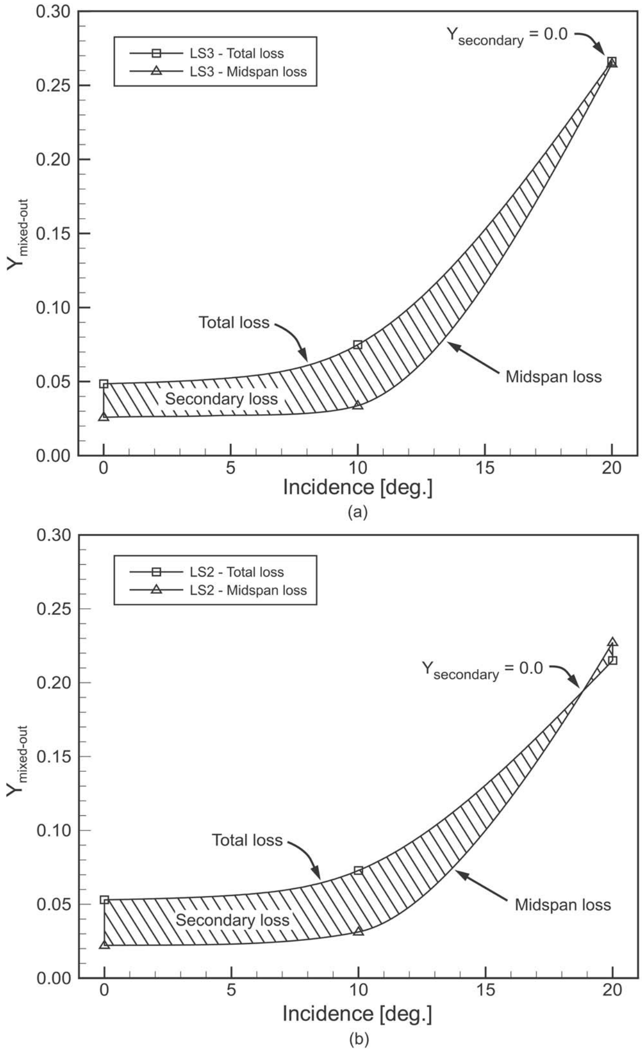

Fig. 2 Loss decomposition using the conventional loss breakdown scheme for (*a*) LS3, (*b*) LS2 (reproduced from Benner et al. [2])

As shown in Fig. 1, the only major geometric differences are in the leading-edge region. LS3 has a leading-edge diameter roughly twice that of LS2. To meet similar lifing requirements, which required similar cross-sectional metal areas, the leading-edge wedge angle for LS3 was reduced to 43.0 deg from the value of 52.4 deg used for LS2. It should be noted that there is a small difference in the stagger angle: The value of 23.1 deg for LS2 was reduced to 21.6 deg for LS3. The difference in stagger angle appears to have an effect on the secondary losses at design incidence, as discussed by Benner et al. [4].

Total-Pressure Losses at Off-Design Incidence

Figures 2(*a*) and 2(*b*) show the influence of incidence on the overall total-pressure loss coefficient, Y_{total}, and the midspan total pressure loss coefficient, Y_{mid}, for LS3 and LS2, respectively.

The measured overall total-pressure loss coefficients are seen to rise gradually from 0 to +10 deg, after which the losses increase more rapidly from +10 to +20 deg for both LS2 and LS3. A similar trend is observed for the midspan losses, and as pointed out in Benner et al. [2], the rapid increase in loss from +10 to +20 deg is largely the result of the onset of trailing-edge separation on the suction side of the airfoil. Because the trailing-edge separation extends over a large percentage of the span (approximately 60% span at the trailing edge), it will have significant influence on the overall losses.

For correlation purposes, the overall losses in Fig. 2 would normally be decomposed into profile and secondary loss components. In a two-dimensional cascade, the profile losses would normally be obtained from the results at midspan where the influence of the secondary flow on the blade surface flow is small. The secondary loss coefficient would then be taken as the difference between the overall loss coefficient and the profile loss coefficient. Thus, it is implicitly assumed that near the endwalls the loss generation on the blade surfaces is essentially the same as that observed at midspan.

Figure 2 shows the effect of this decomposition on the secondary losses for LS3 and LS2, respectively. It is apparent that in these terms the conventional secondary losses decrease for incidence values greater than +10 deg in both cases. In fact, the "secondary losses" are negligible at about +20 deg for LS3, and actually become negative at incidence values above about +19 deg for LS2. Clearly, there are strong secondary flow structures present and generating significant losses at these high-incidence conditions. Therefore, the low or negative loss coefficients resulting from the conventional decomposition are physically misleading. The conventional loss breakdown produces implausible secondary loss results at high values of incidence because the midspan loss no longer provides a good estimate for the losses generated in the blade boundary layers across the full span.

These data indicate that there are inherent problems at large positive values of incidence with the conventional scheme for subdividing the losses. An alternative scheme that is more consistent with the observed physics is described below.

New Loss Breakdown Scheme

As a starting point, the new loss breakdown scheme is developed with the conventional, simplistic notion that the total losses can be subdivided into profile, secondary and tip-leakage loss components. That is,

$$Y_{\text{total}} = Y_{\text{p}} + Y_{\text{sec}} + Y_{\text{tip}} \tag{1}$$

where Y_{total}, Y_{p}, Y_{sec}, and Y_{tip} are the total, profile, secondary and tip-leakage loss components, respectively. The secondary loss component would be obtained at zero tip clearance, as is done in the conventional scheme.

One of the main differences between the conventional and new loss breakdown schemes is the approach that is taken for estimating the profile and secondary loss components: The one proposed here is believed to be more consistent with the observed physics. To assist in the following discussion, Fig. 3 shows a schematic picture of a typical suction surface oil-film pattern.

Based on the flow visualization results presented in Benner et al. [3], there are two regions on the suction surface where the losses generated in the boundary layers are clearly quite different. These two regions are shown in Fig. 3 and are denoted as the primary and secondary regions. From the figure, it can be seen that the primary region is bounded by the passage vortex separation lines (designated as S_4), and the leading and trailing edges. The loss generated in the primary region is determined mainly by the airfoil pressure distribution and Reynolds number (and Mach number for transonic flows). On the other hand, the loss generation in the secondary region is believed to be influenced mainly by the strength of the passage vortex and probably, to a lesser extent, on the chordwise pressure distribution. Therefore, there is no valid justification for assuming similar blade surface losses in the two regions, even at the design incidence.

In the new scheme, the profile loss is defined as the loss generated in surface boundary layers in the primary region; that is, in the region where the blade surface boundary layers are largely uninfluenced by the secondary flows. To obtain the expression for the profile loss it is first assumed that, within the primary region, the average loss per unit airfoil surface area can be represented by the midspan loss per unit suction surface area. This may be expressed mathematically as,

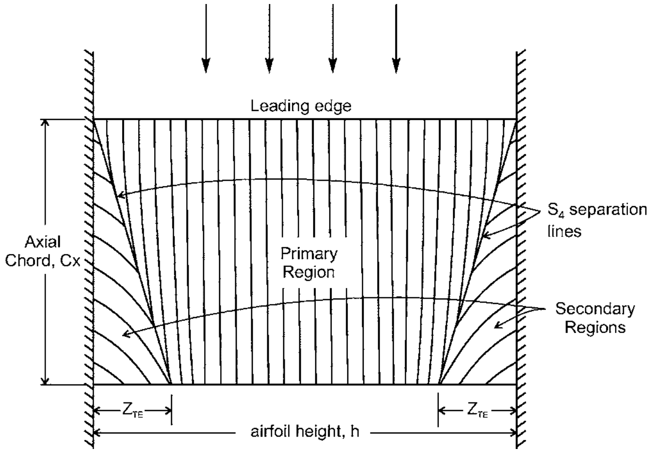

Fig. 3 Suction surface definition for the new loss breakdown scheme

$$\overline{Y_a} \approx \frac{Y_{\text{mid}}}{A_s} \tag{2}$$

where $\overline{Y_a}$ is the average loss per unit airfoil surface area. The suction surface area, A_s, is approximated by $A_s \approx hCx$, where h and Cx are the airfoil span and axial chord, respectively. The profile loss is obtained by simply multiplying Eq. (2) by the surface area of the primary region. Based on the simplified representation of the suction surface flow patterns, the area of the primary region, A_{prim}, is

$$A_{\text{prim}} = hCx - 2(\tfrac{1}{2}Z_{\text{TE}}Cx) \tag{3}$$

where Z_{TE} is the spanwise penetration depth of the S_4 separation line from the endwall at the trailing edge. The profile loss may then be expressed as

$$Y_{\text{p}} = Y_{\text{mid}}\left(\frac{A_{\text{prim}}}{A_s}\right), \tag{4}$$

or

$$Y_{\text{p}} = Y_{\text{mid}}\left(1 - \frac{Z_{\text{TE}}}{h}\right). \tag{5}$$

From Eq. (4), it can be seen that the profile loss is simply the midspan loss weighted by the fraction of suction-surface area occupied by nominally two-dimensional flow. The secondary loss would then be the difference between the overall loss and the profile loss. As a result, the secondary loss includes, not only the endwall loss, but also the loss generated in the airfoil surface boundary layers within the secondary region. Evidently, a benefit of this definition is that it avoids the difficulty of having to separate the airfoil surface boundary layer loss in the secondary region from the overall loss generated in the endwall region.

With the new loss breakdown scheme the overall loss coefficient is written as

$$Y_{\text{total}} = Y_{\text{mid}}\left(1 - \frac{Z_{\text{TE}}}{h}\right) + Y_{\text{sec}}, \tag{6}$$

where the first term on the right-hand side of the equation represents the airfoil profile loss. It is important to note that the maximum realizable value of the nondimensional penetration depth occurs for the case when the passage vortex separation lines from each endwall meet at midspan, that is, when $Z_{\text{TE}}/h = 0.5$.

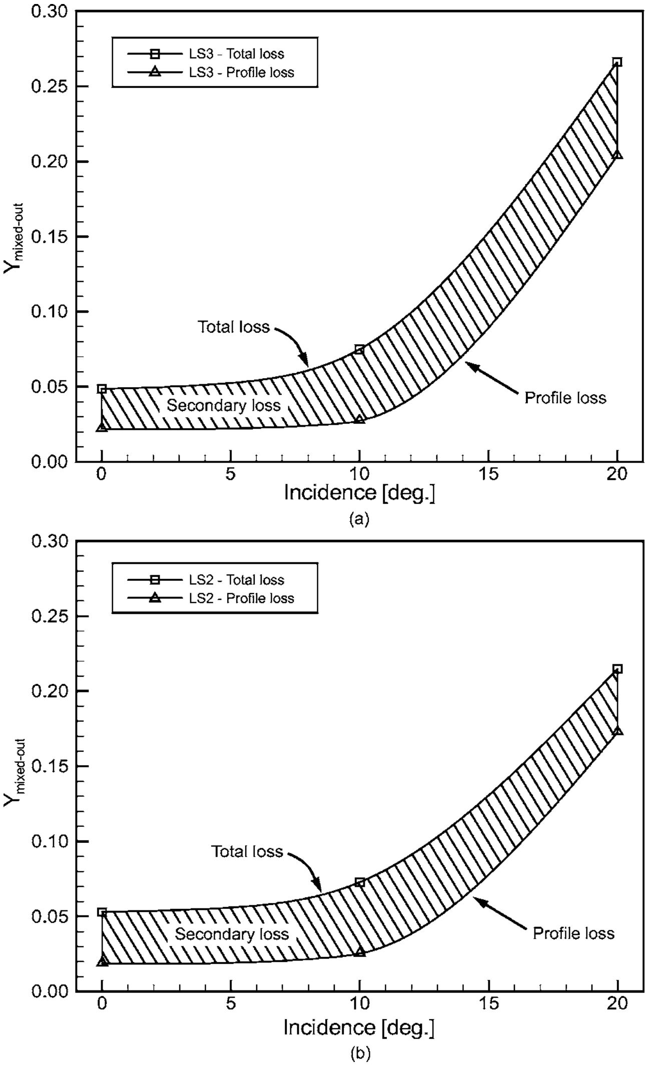

Fig. 4 Loss decomposition using the new loss breakdown scheme for (*a*) LS3, (*b*) LS2

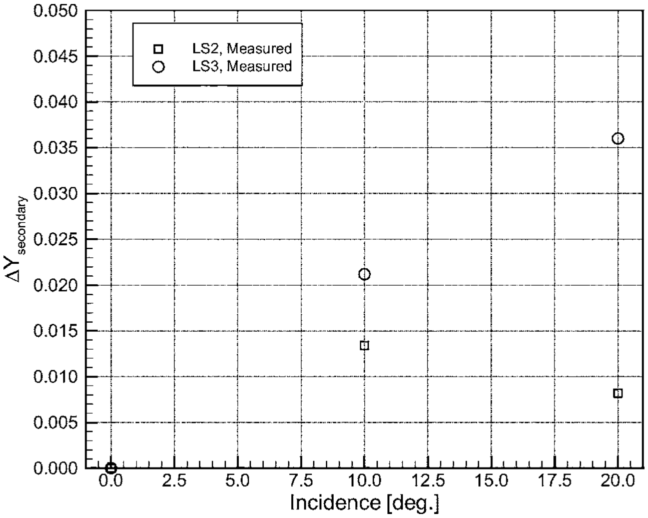

Fig. 5 Comparison of the mixed-out secondary losses at off-design incidence for LS2 and LS3 as obtained from the new loss breakdown scheme

To predict the total loss coefficient with Eq. (6) in the early stages of design, it is necessary to provide a correlation for Y_{mid}, Y_{sec}, and also Z_{TE}/h. It is envisaged that the midspan loss would be obtained from a profile loss correlation such as Kacker and Okapuu [8] at the design point, and Benner et al. [1] at off-design incidence. Correlations for Z_{TE}/h and Y_{sec} have been developed during the course of this work. The new penetration depth correlation is presented later in this paper; the new secondary loss correlation is detailed in Part II.

From the flow visualization results presented in Benner et al. [3], it is clear that the triangular representation of the secondary region presented in Fig. 3 is approximate. In the first place, our experimental results indicate that the point where the S_4 separation first intersects the suction surface varies according to the loading distribution. For the new loss breakdown scheme, the S_4 separation line is assumed to begin at the leading edge, as shown in Fig. 3. Secondly, it is assumed that the boundary of the secondary region is defined by the S_4 separation line. At low values of incidence, a second separation line that is located on the midspan-side and adjacent to the S_4 has been observed by a number of investigators (e.g., Sharma and Butler [5], Benner et al. [4], Hodson and Dominy [9], Jabbari et al. [10]), and this separation line may be a better approximation for the secondary region's boundary. Obviously, there is some room to refine this new loss breakdown scheme; nonetheless, the new scheme, as it has been proposed, is believed to be a significant improvement. Unlike the conventional scheme, it produces physically plausible values of the secondary loss coefficient over a wide range of incidence, as is shown below.

Figure 4 shows the effect of the new loss breakdown scheme on the secondary losses for LS2 and LS3. It is worth noting that the profile loss coefficient was calculated using Eq. (5) with the measured values of the midspan loss coefficient, and with the predicted values of penetration depth from the proposed new correlation (i.e., Eq. (14)), which is described later in the paper. The secondary loss coefficient is then taken as the difference between the overall and profile loss coefficients. By comparison with Fig. 2, it can be seen that the results at design and +10 deg are similar to those obtained with the conventional scheme. However, a significant difference is observed at +20 deg because the midspan flow is separated at this incidence. It is worth noting that the secondary loss values obtained with the new scheme are all higher than the corresponding "conventional" values since they include the boundary layer loss that has been generated in the secondary region. Evidently, the secondary losses obtained with the new scheme now produce a trend with incidence that is physically reasonable.

Figure 5 compares the measured values of the incremental secondary loss as compared to the design inlet flow angle for LS2 and LS3 as obtained using the new loss breakdown scheme. It can be seen that the off-design secondary losses for LS2 are smaller than those of LS3 at both +10 and +20 deg of incidence. This is consistent with the results from the conventional loss breakdown, and it suggests that secondary losses are lower at off-design incidence for an airfoil with a smaller leading-edge diameter, as has been argued by Benner et al. [2].

Correlation for the Penetration Depth of the S_4 Separation Line

Motivation and Sources of Data. To estimate the overall losses with the new loss breakdown scheme, a correlation for the penetration depth of the S_4 line is required, as discussed earlier. Sharma and Butler [5] developed such a correlation for use in their semiempirical model for estimating secondary losses. Due to the scarcity of flow visualization data at the time, their correlation was based on a small database. It consisted of cascade data from 10 test cases, of which 4 were for the same cascade geometry (Langston et al. [11]) but varying inlet boundary layer thicknesses. Since the development of the Sharma and Butler correlation, additional flow visualization data have been published in the open literature. The present authors have compiled data from 19 linear cascade experiments, and these data suggest that important parameters may be missing from the Sharma and Butler correlation. The expanded data set consists of cases from the Sharma and Butler database, recent cases that were available in the open literature, and also those from the present work. The cascade database is summarized in the Appendix (Table 1).

The parameters that are included in the database are those that are believed to be the most important in influencing the penetration depth. A detailed discussion of the relationship between penetration depth and these parameters is presented in the following section. Finally, it should be noted that the database only includes turbine airfoils of modern design.

Factors Influencing Penetration Depth. The starting point for developing a correlation is identifying the geometric and flow parameters that most influence the dependent variable. In this work, the dependent variable is the penetration depth of the S_4 separation line at the trailing edge, Z_{TE}. The passage vortex size is believed to determine this length; as such, the parameters that need to be identified are those that influence the size of the passage vortex. The choice of correlating parameters was based initially on the hypothesis that the passage vortex size was determined by the total airfoil loading, the loading distribution, the channel convergence and the inlet endwall boundary layer thickness. As a basis for discussing the relationship between these parameters and the penetration depth, the Sharma and Butler correlation is presented since it is referred to frequently in this section.

The Sharma and Butler penetration depth correlation is expressed as

$$\frac{Z_{TE}}{Cx} = 0.15\frac{\Delta\alpha}{\sqrt{CR}} + f\left(\frac{\delta_1}{h}\right) \tag{7}$$

where Cx is the airfoil axial chord, δ_1 and h are the inlet boundary layer thickness and airfoil height, respectively. $\Delta\alpha$ is the flow turning in radians and is an approximate measure of the airfoil loading. The convergence ratio, CR, is an approximate measure of the channel acceleration; it is defined as

$$CR = \frac{\cos\alpha_1}{\cos\alpha_2}. \tag{8}$$

The influence of the inlet boundary layer is captured by the function $f(\delta_1/h)$, and it is expressed as

$$f\left(\frac{\delta_1}{h}\right) = 1.4\frac{\delta_1}{h} - 2.73\left(\frac{\delta_1}{h}\right)^2 + 1.77\left(\frac{\delta_1}{h}\right)^3. \tag{9}$$

As noted earlier, one of the parameters that is believed to influence the penetration depth is the total airfoil loading. For axial turbomachines, the total airfoil loading is largely determined by the total flow turning and the pitch-to-chord ratio and as a result, both should appear as correlating parameters. From Eq. (7), it can be seen that Sharma and Butler included flow turning as a correlating parameter, but the effect of pitch-to-chord was not included. Since their work, the influence of pitch-to-chord on the three-dimensionality of the endwall flows has been investigated experimentally by Hodson and Dominy [12] and Perdichizzi and Dossena [13]. Both groups of investigators observed a growth in the passage vortex with increased pitch-to-chord ratio. In the present correlation, the influence of total flow turning and pitch-to-chord ratio are reflected in the tangential loading parameter, F_t, which is defined as

$$F_t = 2\left(\frac{s}{Cx}\right)\cos^2\alpha_m(\tan\alpha_1 - \tan\alpha_2) \tag{10}$$

where α_m is the mean vector angle through the airfoil row and may be expressed as

$$\tan\alpha_m = \tfrac{1}{2}(\tan\alpha_1 + \tan\alpha_2) \tag{11}$$

The parameter, F_t, represents the tangential force per unit length nondimensionalized by dynamic pressure based on the vector-mean velocity. The more familiar Zweifel loading parameter, ψ_T, differs from F_t only in that ψ_T is nondimensionalized by the dynamic pressure based on the outlet dynamic pressure. Mathematically, the two loading parameters are related as follows

$$\psi_T = F_t\left(\frac{\cos^2\alpha_2}{\cos^2\alpha_m}\right). \tag{12}$$

It is worth noting that during the development of the correlation, a few different definitions of loading parameters were evaluated as correlating parameters, including a tangential loading coefficient based on inlet dynamic pressure and the Zweifel loading parameter. The loading coefficient defined in Eq. (10) gave the best agreement between predicted penetration depth and that observed from the data in the current database.

Weiss and Fottner [14] investigated the effect of loading distribution on the endwall flows and observed that the penetration depth was slightly larger for a forward-loaded airfoil. Korakianitis and Papagiannidis [15] argued that the chordwise distribution of the loading is influenced mainly by the stagger angle. They observed that an airfoil tends to become more forward loaded as the stagger angle increases. Although the loading distribution may have a somewhat weak effect on the penetration depth, the stagger angle is retained as a correlating parameter.

To the authors' knowledge, no experiments have been conducted to investigate specifically the influence of channel convergence on secondary flows. Nonetheless, it is argued that increasing channel convergence, which results in increased flow acceleration, will tend to reduce the size of the passage vortex through vortex stretching. Based on these arguments, it is expected that the penetration depth should decrease with increasing channel convergence. Evidently, Sharma and Butler arrived at a similar conclusion as the convergence ratio appears as a parameter in their correlation.

The inlet endwall boundary layer thickness has also been shown to have an influence on the penetration depth of the S_4 separation lines (Graziani et al. [16]). Using data compiled from the open literature, Sharma and Butler found that the variation in penetration depth due to changes in inlet boundary layer thickness was largely independent of cascade geometry. Results obtained during the development of the present correlation seem to be in agreement with their conclusions, as will be discussed later.

An initial attempt was made to correlate the penetration depth based on the parameters described in the preceding paragraphs. The new correlation was somewhat better than the Sharma and Butler correlation; nevertheless, a moderate level of scatter was present suggesting that one or more significant parameters was missing. Subsequently, it was found that the quality of the correlation was improved by including the airfoil aspect ratio as a correlating parameter. The physical relationship between aspect ratio and penetration depth is not immediately evident, notwithstanding that the correlation indicates that it is an important parameter.

The present authors believe that the aspect ratio captures two separate physical effects, each of which influences the penetration depth of the S_4 separation lines. Changing the aspect ratio by either varying airfoil chord length or height produces these different effects. The influence of a reduction in aspect ratio due to an increase in chord length is considered first.

As discussed earlier, the passage vortex strength seems to be influenced mainly by the total loading and the loading distribution. If the chord length is increased while maintaining a given total airfoil loading[2] then the passage vortex strength will remain

---

[2] To maintain a given airfoil loading while increasing the chord requires a proportional increase in the airfoil spacing.

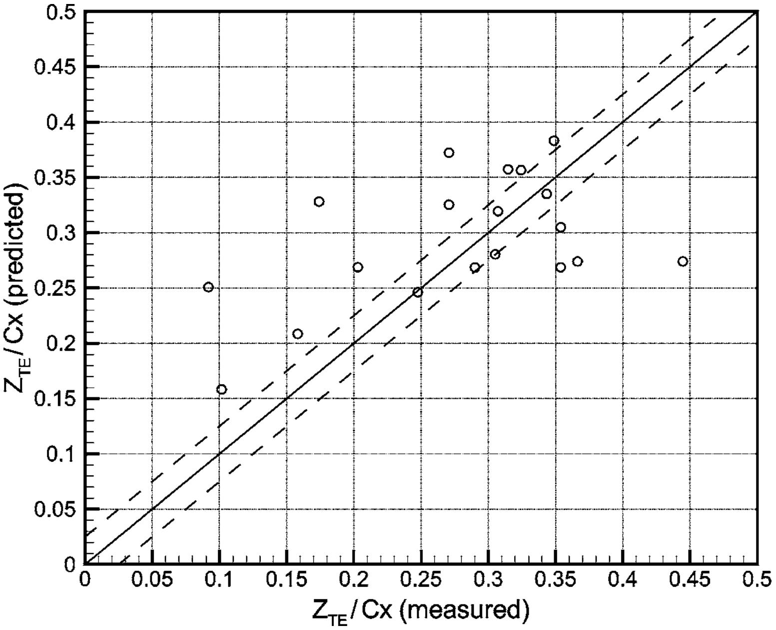

Fig. 6 Evaluation of the penetration depth correlation of Sharma and Butler

invariant. Clearly, increasing the airfoil chord also effects an increase in the channel length. Presumably, the passage vortex becomes larger with increasing chord length since the vortex will tend to entrain more fluid as it evolves through a longer passage. Second, a reduction in aspect ratio due to a decrease in height seems to have a different physical effect on the penetration depth of the S_4 separation lines. As the airfoil height is decreased the blockage produced by the endwall flows becomes a larger proportion of the total flow area. Thus, the effective flow convergence will tend to increase, which as argued earlier, reduces the penetration depth of the S_4 separation lines.

New Correlation. For the new correlation, the penetration depth of the S_4 separation line was assumed to vary as follows:

$$\frac{Z_{\mathrm{TE}}}{h} = a(F_t)^u (CR)^v \left(\frac{h}{c}\right)^w (1 + b \sin^x \gamma) + y\left(\frac{\delta^*}{h}\right)^z . \tag{13}$$

where

Z_{TE}/h = nondimensional penetration depth,
CR = convergence ratio, defined in Eq. (8),
F_t = tangential loading coefficient, defined in Eq. (10),
h/C = airfoil aspect ratio,
δ^*/h = nondimensional inlet endwall boundary layer displacement thickness,
γ = stagger angle in degrees, and
a,b,u,v,w,x,y,z = empirical coefficients.

A few points are noteworthy regarding the form of the new correlation. Like the Sharma and Butler correlation, the influence of the inlet endwall boundary layer displacement thickness on the penetration depth was assumed to be independent of cascade loading and flow convergence. The alternative was to include the boundary layer parameter as a multiplier to the remaining correlating parameters. However, if δ^*/h was a multiplier, it would make $Z_{\mathrm{TE}}/h \rightarrow 0$ as $\delta^*/h \rightarrow 0$ which is clearly incorrect. That is, even for the hypothetical case of zero thickness at the inlet, the endwall boundary layers would continue to develop inside the passage, which in turn, would result in growth of the secondary flows. Finally, the influence of the stagger angle in Eq. (13) was assumed to take the form $(a+b \sin^x \gamma)$ allowing the correlation to apply for impulse turbines (i.e., $\gamma=0.0$ deg).

Having assumed a suitable form for the correlation, the problem then is to determine the values of the eight empirical coefficients in Eq. (13) that give the best agreement between the predicted and measured penetration depths. Establishing the values of these coefficients was treated as a problem in optimization. The process of optimizing was performed with a code written by Sjolander [17], and it is based on a genetic algorithm optimization technique. Islam and Sjolander [18] used this code with apparent success for the development of a correlation for deviation in axial turbines. The fundamentals of the genetic algorithm technique and details of the code are described by Islam [19].

To demonstrate the improvements achieved with the new correlation, the experimental data are compared first with the Sharma and Butler correlation. Figure 6 compares the predicted values of the penetration depth with the measured values for all the cases in Table 1. The solid line represents perfect agreement between the predicted and measured values; the dashed lines represent a ±0.025 error band on the predicted penetration depth. In Fig. 6, it is seen that the agreement between the predicted and measured values is rather poor since a majority of the predictions fall outside the plotted error band. Moreover, a number of the predictions deviate significantly from the measured values indicating that one or more important parameters has probably been omitted.

The expression for the new penetration depth correlation is given in Eq. (14). The empirical coefficients were obtained using the genetic-algorithm optimization code, as mentioned earlier.

$$\frac{Z_{\mathrm{TE}}}{h} = \frac{0.10(F_t)^{0.79}}{\sqrt{CR}\left(\frac{h}{C}\right)^{0.55}} + 32.70\left(\frac{\delta^*}{h}\right)^2 \tag{14}$$

It should be noted that the results from the optimization process indicated that the penetration depth was insensitive to stagger angle, so it was omitted in the final form of the correlation. This result was not completely unexpected given that Weiss and Fottner [14] showed only a 1% change in penetration depth for a fairly significant change in stagger angle (approximately 8 deg).

Figure 7 shows the evaluation diagram for the new penetration depth correlation. As can be seen, the agreement between the measured and predicted values of penetration depth is quite satisfactory. Thus, the new correlation is a significant improvement over the Sharma and Butler correlation (Fig. 6) for the fairly comprehensive data set considered.

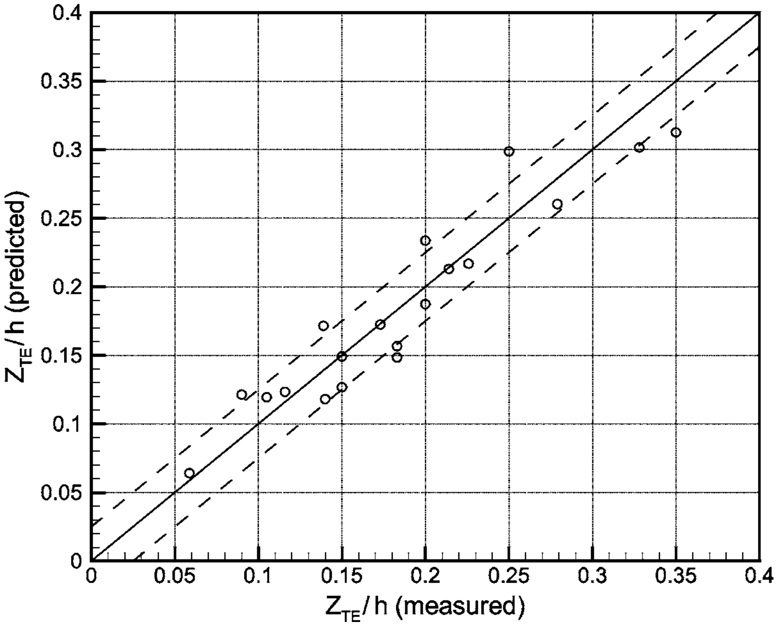

Fig. 7 Evaluation of the new penetration depth correlation

Conclusions

An empirical prediction method for secondary losses has been developed. The method is based on a new loss breakdown scheme that is more consistent with the observed flow physics than the conventional scheme. In the new loss breakdown scheme, the profile loss is defined as the loss generated in the portion of the airfoil surface boundary layers which is largely uninfluenced by the secondary flows. The secondary loss is then simply the difference between the total loss and the profile loss. With the new scheme, the secondary loss component includes the loss generated in the airfoil surface boundary layers where they are affected by the secondary flow.

To use the new breakdown scheme, a correlation for the spanwise location of the passage vortex separation line at the trailing edge is required. Sharma and Butler [5] have developed such a correlation, but it was based on a small database. An improved correlation has been developed from a considerably larger database. By comparison with the Sharma and Butler correlation, the current one includes two additional and important correlating parameters, namely the airfoil aspect ratio and a tangential loading parameter.

Because the secondary loss definition in the new scheme differs from that in the conventional scheme, a new secondary loss correlation for design and off-design values of incidence has been devised. It is detailed in the second part of this two-part paper.

Acknowledgment

Financial support for this study provided by Pratt and Whitney Canada, Inc. and the Natural Sciences and Engineering Research Council of Canada is gratefully acknowledged.

Nomenclature

A_{prim} = area of the primary region (Eq. (3))
A_s = suction surface area
C = airfoil chord length
Cx = airfoil axial chord length
CR = $\cos\alpha_1/\cos\alpha_2$=convergence ratio
F_t = tangential loading nondimensionalized by dynamic pressure based on the vector-mean velocity (Eq. (10))
h = span
i = $\alpha_1-\alpha_{1,\text{design}}$=incidence, in degrees
P = static pressure
P_0 = total pressure
q = P_0-P=dynamic pressure
Re = $\rho V_{CL}C/\mu$=Reynolds number
s = blade pitch or spacing
V = velocity
We = leading-edge wedge angle, in degrees
x = axial coordinate measured from the leading-edge plane
y', z = local pitchwise and spanwise coordinates
Y = $(P_{0,1}-P_{0,2})/(P_{0,2}-P_2)$=mass-averaged total-pressure loss coefficient
Z_{TE} = spanwise distance of the S_4 separation line from the endwall at the trailing edge
α = flow angle measured from the axial direction, in degrees
β = airfoil metal angle measured from the axial direction, in degrees
δ = boundary layer thickness
δ^* = $\int_0^{\delta}(1-V/V_e)dz$=boundary layer displacement thickness
γ = stagger angle measured from the axial direction, in degrees
μ = dynamic viscosity
ρ = density
ψ_T = Zweifel loading parameter

Subscripts

mean = based on vector mean
mid = midspan
p = profile
sec = secondary
TE = trailing edge
tip = tip-leakage
1, 2 = cascade inlet and outlet

Appendix

Table 1 Experimental data for penetration depth correlation

Reference	Actual Z_{TE}/h	Predicted Z_{TE}/h	F_t	CR	h/C	δ^*/h	α_1 (deg)	γ (deg)
Benner [6], LS3	0.15	0.15	2.38	1.45	1.25	0.011	28.4	21.6
Benner [6], LS3	0.20	0.19	2.85	1.25	1.25	0.014	38.4	21.6
Benner [6], LS3	0.20	0.23	3.26	0.98	1.25	0.014	48.4	21.6
Hodson and Dominy [9]	0.15	0.13	2.42	1.33	1.82	0.006	38.8	19.6
Hodson and Dominy [12]	0.18	0.15	2.94	1.32	1.82	0.006	38.8	19.6
Hodson and Dominy [12]	0.18	0.16	2.90	1.15	1.82	0.006	47.4	19.6
Langston et al. [11]	0.33	0.30	4.60	1.61	0.81	0.012	45.3	34.9
Graziani et al. [16]	0.25	0.30	4.64	1.60	0.81	0.003	45.4	34.9
Moore and Adhye [20]	0.35	0.31	4.61	1.61	0.81	0.023	45.3	34.9
Marchal and Sieverding [21]	0.14	0.12	1.93	2.65	0.83	0.011	0.0	42.5
Marchal and Sieverding [21]	0.17	0.17	2.70	2.48	0.79	0.021	30.0	38.5
Jilek [22]	0.06	0.06	1.49	3.86	1.20	0.006	0.0	46.0
Jilek [22]	0.28	0.26	4.67	1.41	1.20	0.009	57.8	12.5
Walsh and Gregory-Smith [23]	0.14	0.17	4.39	2.03	1.79	0.015	42.8	36.1
Harrison [24]	0.23	0.22	4.22	1.94	1.08	0.009	40.0	37.0
Weiss and Fottner [14]	0.12	0.12	3.91	1.75	3.00	0.008	37.7	38.5
Weiss and Fottner [14]	0.11	0.12	3.75	1.75	3.00	0.008	37.7	30.7
Perdichizzi and Dossena [13]	0.21	0.21	2.28	3.88	0.91	0.058	13.9	50.1
Yaras [25]	0.09	0.12	1.27	1.48	0.81	0.018	0.0	37.2

References

[1] Benner, M. W., Sjolander, S. A., and Moustapha, S. H., 1997, “Influence of Leading-Edge Geometry on Profile Losses in Turbines at Off-Design Incidence: Experimental Results and an Improved Correlation,” ASME J. Turbomach., **119**, pp. 193–200.

[2] Benner, M. W., Sjolander, S. A., and Moustapha, S. H., 2004, “Measurements of Secondary Flows Downstream of a Turbine Cascade at Off-Design Incidence,” ASME Paper No. GT2004-53786.

[3] Benner, M. W., Sjolander, S. A., and Moustapha, S. H., 1997, “Measurements of Secondary Flows in a Turbine Cascade at Off-Design Incidence,” ASME Paper No. 97-GT-382.

[4] Benner, M. W., Sjolander, S. A., and Moustapha, S. H., 2004, “The Influence of Leading-Edge Geometry on Secondary Losses in a Turbine Cascade at the Design Incidence,” ASME J. Turbomach., **126**, pp. 277–287.

[5] Sharma, O. P., and Butler, T. L., 1987, “Predictions of Endwall Losses and Secondary Flows in Axial Turbine Cascades,” ASME J. Turbomach., **109**, pp. 229–236.

[6] Benner, M. W., 2003, “The Influence of Leading-Edge Geometry on Profile and Secondary Losses in Turbine Cascades,” Ph.D. thesis, Department of Mechanical and Aerospace Engineering, Carleton University, Ottawa, Canada.

[7] Moustapha, S. H., Kacker, S. C., and Tremblay, B., 1990, “An Improved Incidence Losses Prediction Method for Turbine Airfoils,” ASME J. Turbomach., **112**, pp. 267–276.

[8] Kacker, S. C., and Okapuu, U., 1982, “A Mean Line Prediction Method for Axial Flow Turbine Efficiency,” ASME J. Turbomach., **104**, pp. 111–119.

[9] Hodson, H. P., and Dominy, R. G., 1987a, “Three-Dimensional Flow in a Low-Pressure Turbine Cascade at its Design Condition,” ASME J. Turbomach., **109**, pp. 177–185.

[10] Jabbari, M. Y., Goldstein, R. J., Marston, K. C., and Eckert, E. R. G., 1992, “Three-Dimensional Flow at the Junction between a Turbine Blade and End-Wall,” Waerme- Stoffuebertrag., **27**, pp. 51–59.

[11] Langston, L. S., Nice, M. L., and Hooper, R. M., 1977, “Three-Dimensional Flow Within a Turbine Cascade Passage,” ASME J. Eng. Power, **99**, pp. 21–28.

[12] Hodson, H. P., and Dominy, R. G., 1987b, “The Off-Design Performance of a Low-Pressure Turbine Cascade,” ASME J. Turbomach., **109**, pp. 201–210.

[13] Perdichizzi, A., and Dossena, V., 1993, “Incidence Angle and Pitch-Chord Effects on Secondary Flows Downstream of a Turbine Cascade,” ASME J. Turbomach., **115**, pp. 383–391.

[14] Weiss, A. P., and Fottner, L., 1995, “The Influence of Load Distribution on Secondary Flow in Turbine Cascades,” ASME J. Turbomach., **117**, pp. 133–141.

[15] Korakianitis, T., and Papagiannidis, P., 1993, “Surface-Curvature-Distribution Effects on Turbine-Cascade Performance,” ASME J. Turbomach., **115**, pp. 334–341.

[16] Graziani, R. A., Blair, M. F., Taylor, J. R., and Mayle, R. E., 1980, “An Experimental Study of Endwall and Airfoil Surface Heat Transfer in a Large Scale Turbine Blade Cascade,” ASME J. Eng. Power, **102**, pp. 257–267.

[17] Sjolander, S. A., 2001, “SGA Computer Program,” Private communication.

[18] Islam, A. M. T., and Sjolander, S. A., 1999, “Deviation in Axial Turbines at Subsonic Conditions,” ASME Paper No. 99-GT-26.

[19] Islam, A. M. T., 1999, “An Experimental and Computational Study of the Aerodynamics of Turbine Blades With Damage,” Ph.D. thesis, Department of Mechanical and Aerospace Engineering, Carleton University, Ottawa, Canada.

[20] Moore, J., and Adhye, R. Y., 1985, “Secondary Flows and Losses Downstream of a Turbine Cascade,” ASME J. Turbomach., **107**, pp. 961–968.

[21] Marchal, P., and Sieverding, C. H., 1977, “Secondary Flows within Turbomachinery Bladings,” *Secondary Flows in Turbomachines*, AGARD-CP-214, Paper No. 11, pp. 1–19.

[22] Jilek, J., 1986, “An Experimental Investigation of the Three-Dimensional Flow Within Large Scale Turbine Cascades,” ASME Paper No. 86-GT-170.

[23] Walsh, J. A., and Gregory-Smith, D. G., 1990, “Inlet Skew and the Growth of Secondary Losses and Vorticity in a Turbine Cascade,” ASME J. Turbomach., **112**, pp. 633–642.

[24] Harrison, S., 1990, “Secondary Loss Generation in a Linear Cascade of High-Turning Turbine Blades,” ASME J. Turbomach., **112**, pp. 618–624.

[25] Yaras, M. I., 1990, “Measurements and Prediction of Tip-Clearance Effects in a Linear Turbine Cascade,” Ph.D. thesis, Department of Mechanical and Aerospace Engineering, Carleton University, Ottawa, Canada.

M. W. Benner[1]
National Research Council of Canada,
Institute for Aerospace Research,
Ottawa, ON K1A 0R6,
Canada
e-mail: michael.benner@nrc-cnrc.gc.ca

S. A. Sjolander
Department of Mechanical and Aerospace
Engineering,
Carleton University,
Ottawa, ON K1S 5B6,
Canada

S. H. Moustapha
Pratt and Whitney Canada, Ltd.,
Longueuil, PQ, J4G 1A1
Canada

An Empirical Prediction Method For Secondary Losses In Turbines—Part II: A New Secondary Loss Correlation

A new empirical prediction method for design and off-design secondary losses in turbines has been developed. The empirical prediction method is based on a new loss breakdown scheme, and as discussed in Part I, the secondary loss definition in this new scheme differs from that in the conventional one. Therefore, a new secondary loss correlation for design and off-design incidence values has been developed. It is based on a database of linear cascade measurements from the present authors' experiments as well as cases available in the open literature. The new correlation is based on correlating parameters that are similar to those used in existing correlations. This paper also focuses on providing physical insights into the relationship between these parameters and the loss generation mechanisms in the endwall region. To demonstrate the improvements achieved with the new prediction method, the measured cascade data are compared to predictions from the most recent design and off-design secondary loss correlations (Kacker, S. C. and Okapuu, U., 1982, ASME J. Turbomach., ***104****, pp. 111-119, Moustapha, S. H., Kacker, S. C., and Tremblay, B., 1990, ASME J. Eng. Power,* ***112****, pp. 267–276) using the conventional loss breakdown. The Kacker and Okapuu correlation is based on rotating-rig and engine data, and a scaling factor is needed to make their correlation predictions apply to the linear cascade environment. This suggests that there are additional and significant losses in the engine that are not present in the linear cascade environment.*
[DOI: 10.1115/1.2162594]

Introduction

In the early stages of design, when detailed airfoil geometries are not known, meanline analysis and empirical loss systems continue to be important tools for the turbine aerodynamicist. Therefore, there is an on-going need to review and improve these systems.

Probably the most widely used empirical loss system for axial turbines is that due to Ainley and Mathieson [1]. The Ainley and Mathieson system is a complete system because it includes correlations for all the components of loss, and for both design and off-design conditions. It was subsequently modified by Dunham and Came [2] to reflect the improved understanding of some aspects of the flow, notably the secondary flows. Further improvements to the design-point correlations were presented by Kacker and Okapuu [3]. Craig and Cox [4] and Traupel [5] have also proposed complete loss systems, but these are not as widely used as those based on Ainley and Mathieson's work.

Dunham [6] and Sieverding [7] have performed detailed reviews of the secondary loss correlations from these loss systems as well as others that have been proposed in the past half century. More recently, Moustapha et al. [8] devised new correlations for the profile and secondary losses at off-design conditions. These were significantly more successful at correlating the data than the Ainley and Mathieson correlations. Drawing on the work of Mukhtarov and Krichakin [9], and unlike Ainley and Mathieson, Moustapha et al. included the leading-edge diameter as a correlating parameter. The new off-design correlations were intended for use with the Kacker and Okapuu design-point correlations to form a complete loss system. During the course of the present work, some significant shortcomings in the Moustapha et al. [8] correlations have been identified. An improved correlation for profile losses was presented by Benner et al. [10], and the current paper presents an improved secondary loss correlation.

The current authors have reviewed the previous correlations and together with measurements from the current project (Benner [11]) and data from the open literature have developed a new empirical prediction method for secondary losses in turbines. The motivation for developing a new prediction method for secondary losses was based on the results from detailed flow field measurements made in two large-scale, low-speed, linear turbine cascades (Benner et al. [12]). The prediction method is based on a new loss breakdown scheme that requires a correlation for the spanwise penetration depth of the passage vortex separation line at the trailing edge. Both the new breakdown scheme and penetration depth correlation were detailed in Part I.

Part II of this two-part paper presents a secondary loss correlation for use with the new loss breakdown scheme. The correlation is based on a substantial database of measurements from Benner [11] and from the open literature. The same database is used to evaluate the new correlation as well as the most recent published secondary loss correlations for design and off-design values of incidence.

New Loss Breakdown Scheme and Penetration Depth Correlation

As detailed in Part I, the new prediction method for secondary losses is based on a new loss breakdown scheme. With the new scheme, the overall loss coefficient is written as

---

[1] To whom correspondence should be addressed.

Contributed by the International Gas Turbine Institute (IGTI) of ASME for publication in the JOURNAL OF TURBOMACHINERY. Paper presented at the ASME Turbo Expo 2005: Land, Sea, and Air, Reno, NV, June 6–9, 2005, Paper No. GT2005-68639. Manuscript received October 1, 2004; final manuscript received February 1, 2005. IGTI Review Chair: K. C. Hall.

$$Y_{\text{total}} = Y_{\text{mid}}\left(1 - \frac{Z_{\text{TE}}}{h}\right) + Y_{\text{secondary}}, \quad (1)$$

where Y_{total}, Y_{mid}, and $Y_{\text{secondary}}$ are the overall, midspan and secondary loss coefficients, respectively. Z_{TE}/h is the spanwise penetration depth of the passage vortex separation line from the endwall at the trailing edge nondimensionalized by the airfoil height. The first term on the right-hand side of the equation represents the airfoil profile loss; that is, the loss that is generated in the nominally two-dimensional blade surface boundary layers.

To predict the total loss coefficient with Eq. (1) in the early stages of design, it is necessary to provide a correlation, not only for Y_{mid} and $Y_{\text{secondary}}$, but also Z_{TE}/h. It is envisaged that the midspan loss would be obtained from a profile loss correlation such as Kacker and Okapuu [3] at the design point, and Benner et al. [10] at off-design incidence. The correlation for nondimensional penetration depth has been developed in Part I, and it is expressed as

$$\frac{Z_{\text{TE}}}{h} = \frac{0.10(F_t)^{0.79}}{\sqrt{CR}\left(\frac{h}{C}\right)^{0.55}} + 32.70\left(\frac{\delta^*}{h}\right)^2 \quad (2)$$

The parameters in Eq. (2) are defined as

CR = convergence ratio $= \cos\alpha_1/\cos\alpha_2$

F_t = tangential loading coefficient $= 2(s/Cx)\cos^2\alpha_m\,(\tan\alpha_1 - \tan\alpha_2)$,

h/C = airfoil aspect ratio,

δ^*/h = nondimensional inlet endwall boundary layer displacement thickness,

where α_1 and α_2 are the inlet and outlet flow angles, respectively; α_m is the mean-vector flow angle through the airfoil row and is given by

$$\tan\alpha_m = \tfrac{1}{2}(\tan\alpha_1 + \tan\alpha_2) \quad (3)$$

and s/Cx is the pitch-to-axial chord ratio. The new secondary loss correlation for use in Eq. (1) is detailed in this paper.

Secondary Loss Correlation

Motivation, Sources of Data, and Range of Validity. As discussed in Part I, the definition of secondary loss in the new loss breakdown scheme differs from the one in the conventional scheme. In the new scheme, the losses generated in the thin suction surface boundary layer that develops between the endwall and the passage vortex separation line (S_4) are included as secondary losses. Therefore, a correlation is required for predicting the newly defined secondary loss component. The remaining part of this section details the sources of data that were used for the correlation while the subsequent section describes the parameters that are believed to influence secondary losses. The new correlation is presented in the last section.

The new secondary loss correlation was developed from a database of 34 linear cascade data sets, which are summarized in the Appendix (Table 2). Included in the data set are cases from Benner [11] as well as recent cases from the open literature (within the past several decades) for which sufficient geometric and aerodynamic information were given, or could be estimated with acceptable accuracy. Therefore, the new correlation accounts for recent improvements in airfoil design and incorporates improvements in the understanding of the physics of secondary flows that have been made since the early 1980s.

As can be seen in Table 2, the database consists of cases that cover a wide range of incidence values (−23 to +20 deg), acceleration levels (nozzle to near-impulse airfoils), aspect ratios (0.79–3.0), flow turning (47–110 deg), and inlet endwall boundary layer displacement thickness (from 0.6 to 6.0% of blade height).

The new loss breakdown scheme, like the old one, assumes that the secondary flows from each of the endwalls do not merge at midspan. This limits the range of validity of the correlation to preclude low-aspect ratio geometries; that is, cases where the secondary flows are most likely to merge. Unfortunately, a precise value for the lower limit of aspect ratio cannot be specified since the penetration of the secondary flows is also a function of, amongst other parameters, the airfoil loading. A number of cases from the open literature for which the secondary flows have merged at midspan have been omitted from the database (e.g., Refs. [13,14], all data in Ref. [15] except the case with highest aspect ratio, and Ref. [16] at positive incidence and high negative incidence).

The secondary loss values that appear in Table 2 were evaluated with the new loss breakdown scheme (Eq. (1)) using the penetration depth correlation (Eq. (2)) and the experimental values of mixed-out overall and midspan losses. Unfortunately there were a number of cases in the open literature for which insufficient loss data were given (e.g., Refs. [17–19]). In a number of other cases, the mixing losses were estimated because the mixed-out losses were not quoted. The procedure that was followed to arrive at these estimates is detailed below. It should be noted that the sixth column in Table 2 gives the location of the downstream measurement plane. For cases where measurements were made at multiple axial locations, the furthest downstream location is quoted. If mixed-out loss values have been given, then an asterisk is used to identify the case. Also, the values of nondimensional penetration depth, as predicted using Eq. (2), are included in Table 2.

Based on the results from Benner [11] and the work of Moore and Adhye [18], Hodson and Dominy [20,21] and Harrison [22], an approximate expression for the overall mixing losses has been determined to be

$$\frac{\Delta Y_{\text{total (mixing)}}}{Y_{\text{total (measured)}}} = \begin{cases} (1 - 2x'/Cx) & \text{for } x'/Cx \leq 0.5 \\ 0.0 & \text{for } x'/Cx > 0.5 \end{cases} \quad (4)$$

where x'/Cx is the nondimensional axial location of the measurement plane as measured from the trailing-edge plane. With this approximation, mixing is assumed to be complete at 50% axial chord lengths downstream of the trailing edge. If losses were quoted at multiple measurement planes, then the mixing losses were estimated from the measurements made at the furthest downstream plane, thus minimizing any approximation error.

For the mixing that occurs at midspan, the results of Goobie et al. [23] suggest that the wakes are nearly completely mixed out by 20% axial chord lengths downstream of the trailing edge. Therefore, the measured midspan losses for all cases in the database should provide reasonable estimates of the fully-mixed out losses since all measurement locations were at least 20% axial chord lengths downstream of the trailing edge.

Factors Influencing Secondary Losses. Dunham [6] and Sieverding [7] performed detailed reviews of the twenty or so secondary loss correlations that have been proposed in the past half century. Based on these reviews, there appears to be a number of factors that influence endwall losses: these are total airfoil loading, flow acceleration, size of the endwall surface area and the vorticity in the inlet endwall boundary layer. Moreover, based on the results of Weiss and Fottner [24], Benner et al. [25], and Marchal [26] (as referred to by Sieverding [27]), it also seems that loading distribution is an important factor.

The precise influence that each of these factors has on endwall loss generation is still generally not fully understood—this is undoubtedly an indication of the complexity of the endwall flows.

Consequently, there is very little agreement in the literature concerning the geometric and aerodynamic parameters that are important in capturing the factors that influence loss generation. This is particularly the case for airfoil loading, as will now be discussed.

In his review of secondary loss correlations, Dunham [6] evaluated the quality of some of the more widely used secondary loss correlations by comparing the predictions to a comprehensive set of experimental data. Although the data set was comprised of results from a number of different sources, a majority of the comparisons were made with the results of Wolf [28]. Nonetheless, Dunham concluded that the loading parameter devised by Ainley and Mathieson produced the best agreement between predictions and the then-available experimental data. Therefore, Dunham and Came retained the Ainley and Mathieson loading parameter in their secondary loss correlation, as did Kacker and Okapuu. The Ainley and Mathieson's loading parameter, Z, may be expressed as

$$Z = 4(\tan\alpha_1 - \tan\alpha_2)^2 \frac{\cos^2\alpha_2}{\cos\alpha_m}. \tag{5}$$

As can be seen from Eq. (5), the Ainley and Mathieson loading parameter depends only on the inlet and outlet flow angles and not on the pitch-to-chord ratio. The Craig and Cox correlation, on the other hand, predicts a strong dependence of secondary losses on pitch-to-chord ratio. More recently, Hodson and Dominy [21] and Perdichizzi and Dossena [29] examined the influence of pitch-to-chord ratio on secondary loss behavior. Hodson and Dominy found that the secondary losses increased significantly with increasing pitch-to-chord ratio (i.e., increased airfoil loading) while Perdichizzi and Dossena observed no clear trend. Evidently, more data are necessary to help improve our understanding of the influence of pitch-to-chord ratio. As will be shown in the next section, the correlation developed in this work does not seem to show a pitch-to-chord ratio dependence.

An important source of loss in the endwall region comes from the entropy that is produced in the endwall boundary layers within, upstream and downstream of the airfoil row. For an airfoil with an aspect ratio of unity, Denton [30] estimated that two-thirds of the total secondary loss was generated within the endwall boundary layers. To gain some insight into the parameters that influence the endwall boundary losses it is useful to examine an expression for the total-pressure loss coefficient as derived from the concepts of entropy generation.

To begin, the entropy generation rate for the endwall boundary layer can be expressed as (Denton [30])

$$\dot{S}_{\text{endwall}} = \frac{\rho}{T}\int_0^{Cx}\int_0^{w} C_d V_e^3 \, dy\, dx \tag{6}$$

where C_d is the boundary layer dissipation coefficient, V_e is the velocity at the edge of the boundary layer, x and y are the axial and pitchwise coordinates, respectively. The flow is assumed incompressible with negligible temperature variations. The dissipation coefficient may be interpreted as a dimensionless form of the viscous shear work, and for a two-dimensional boundary layer, it is expressed as

$$C_d = \int_0^{\delta} \frac{\tau}{\rho V_e^2}\frac{d}{dy}\left(\frac{V}{V_e}\right) dy \tag{7}$$

where τ is the shear stress, V is the local flow velocity, and ρ is the fluid density. Based on the work of Harrison [22], it seems that a constant value for the endwall boundary layer dissipation coefficient can be assumed as a rough approximation.

From Eq. (6), it can be seen that the endwall boundary losses are related to the surface area, as one might expect. The parameter that captures the influence of the size of the endwall surface area may be determined by converting Eq. (6) into a mass-averaged loss coefficient. This coefficient may be thought of as the contribution of the endwall losses to the overall secondary pressure loss coefficient and can be expressed as

$$Y_{\text{endwall}} = \frac{T\dot{S}_{\text{endwall}}}{\dot{m}(1/2V_2^2)} \tag{8}$$

for incompressible flows. In Eq. (8), $\dot{m}$ is the mass flow rate through the passage; it may be written as

$$\dot{m} = \rho(hs)(V_2\cos\alpha_2) \tag{9}$$

where V_2 is flow velocity at the exit of the airfoil row. Substituting Eqs. (6) and (9) into (8) and simplifying gives

$$Y_{\text{endwall}} = \frac{2\int_0^{Cx}\int_0^{w} C_d\left(\frac{V_e}{V_2}\right)^3 dy\, dx}{(hs)\cos\alpha_2}. \tag{10}$$

The integrand in Eq. (10) is a nondimensional form of the entropy generation rate per unit surface area, and will be denoted as $\dot{S}_a$. If an average entropy generation rate is assumed over the endwall surface area, then Eq. (10) can be rewritten as

$$Y_{\text{endwall}} = \frac{2\overline{\dot{S}_a}\int_0^{Cx}\int_0^{w} dy\, dx}{(hs)\cos\alpha_2}. \tag{11}$$

If we now make the simplification that the airfoils are infinitely thin, then the suction to pressure surface pitchwise distance, w, can be replaced with the airfoil pitch. Equation (11) then simplifies to

$$Y_{\text{endwall}} = 2\overline{\dot{S}_a}\left(\frac{C_x}{h\cos\alpha_2}\right). \tag{12}$$

From Eq. (12), it can be seen that the influence of the endwall surface area on the loss coefficient is captured by the term in brackets. An important and commonly observed result, at least for cases where the aspect ratio is greater than two, is the inverse dependence of the endwall losses on the airfoil height (e.g., Ref. [3]), and this dependence is also seen to be present in Eq. (12).

The most widely used secondary loss correlations (e.g., Refs. [1–5,9]), show that channel acceleration has a strong influence on secondary losses. In each of these correlations, the losses vary as the inverse of the convergence ratio, a parameter which is an approximate measure of the channel acceleration. To the authors' knowledge, there have been no studies that have examined specifically the influence of channel acceleration on secondary flows.

The influence of inlet endwall boundary layer thickness on secondary losses has been the subject of numerous experimental studies. Evidence from many of these studies (e.g., Ref. [21,31–34]) suggests that the secondary losses are insensitive to the thickness of the inlet endwall layer. In contrast, Dunham [6] reviewed data from ten different studies and concluded that secondary losses were dependent on inlet boundary layer thickness: the largest sensitivity occurred for very thin layers. Others (e.g., [28,35,36]) have reported increasing secondary loss with increasing thickness up to a "critical" thickness beyond which there was no further dependence.

There appear to be a few possible explanations for the differing observed loss behaviors with inlet boundary layer thickness. First, it is possible that the boundary layer thickness (or some measure of it, such as displacement or momentum thickness) is not the most relevant parameter for capturing the relationship between the inlet endwall boundary layer and secondary losses. A second possibility is that there is some other important inlet boundary layer parameter that is changing as the inlet boundary layer thickness is varied. The present authors believe that it is the latter possibility which is the more likely, as will now be discussed.

The following argument is based primarily on the notion that the production of streamwise vorticity from the vorticity contained in the inlet endwall boundary layer has an important role in the production of entropy within and downstream of the airfoil row. This idea seems to be widely accepted since the passage vortex originates from the vorticity contained within the inlet endwall boundary layer. The secondary kinetic energy associated with this vortex as well as the interaction of the vortex with the suction and endwall boundary layers appear to be significant sources of entropy production in the endwall region.

One of the main mechanisms of streamwise vorticity production occurs through the deflection of pre-existing vorticity (i.e., vorticity within the inlet endwall boundary layer). This process is essentially inviscid in nature, and it has been shown that the production of streamwise vorticity at a particular spanwise location is directly proportional to the magnitude of the vorticity and the amount of flow turning (Hawthorne [37]). Therefore, the influence that the inlet endwall boundary layer has on the passage vortex strength is dependent mainly on the distribution of vorticity and the overall circulation in the inlet endwall boundary layer. The circulation per unit streamwise distance is the "jump" in velocity across the boundary layer. It is invariant if the inlet velocity is fixed, as would be the case in experiments that are examining solely the influence of boundary layer thickness. In most turbine cascade experiments, the inlet endwall boundary layers are turbulent (based on quoted values of shape factor) so that most of the streamwise vorticity is produced deep within the layer where the velocity gradients are largest (i.e., within the laminar sublayer and the log-law region). As a result, it is the characteristics of this region that will tend to have an effect on secondary losses. The streamwise vorticity production due to the gradients in the outer layer will be negligible, by comparison. For these reasons the present authors believe that the skin friction coefficient, which is an indicator of the magnitude of the velocity gradients in the inner layer, may be a relevant correlating parameter for secondary losses.

It may also be argued that the inlet boundary layer displacement thickness-to-airfoil height (δ^*/h) should appear as a correlating parameter for secondary losses. This can be best explained if one considers the influence of the secondary kinetic energy on the secondary loss coefficient. The passage vortex generates secondary kinetic energy, and in a linear cascade, it is eventually dissipated through mixing and must be considered as a source of loss. However, from the viewpoint of a mass-averaged secondary loss coefficient, the amount of mass flow associated with this secondary kinetic energy is also important. The contribution of the secondary kinetic energy to the secondary loss coefficient may be expressed as

$$\Delta Y_{\text{secondary}} = \frac{\dot{m}_{pv} C_{\text{SKE}}}{\dot{m}} \tag{13}$$

where $\dot{m}_{pv}$ is the fraction of mass flow through the passage vortex tube that contains fluid of high secondary kinetic energy and $\dot{m}$ is the mass flow through the passage. The nondimensional secondary kinetic energy, C_{SKE}, is defined as the kinetic energy associated with the velocity components in a plane perpendicular to the mass-averaged exit flow angle normalized by the inlet kinetic energy. The mass flow, $\dot{m}_{pv}$, may be expressed in terms of the inlet boundary layer displacement thickness since it is believed that the passage vortex is comprised mainly of fluid from the inlet endwall boundary layer. That is,

$$\dot{m}_{pv} = a\rho V_1 \cos\alpha_1 \delta^* s \tag{14}$$

where a is the fraction of the mass flow through the passage vortex tube that contains fluid of high secondary kinetic energy. The mass flow through the passage may be written as

$$\dot{m} \approx \rho V_1 \cos\alpha_1 (hs). \tag{15}$$

The approximation arises because the displacement thickness is assumed to be small relative to the airfoil height. Substituting Eqs. (14) and (15) into (13) gives

$$\Delta Y_{\text{secondary}} = a\left(\frac{\delta^*}{h}\right) C_{\text{SKE}}. \tag{16}$$

The main conclusion here is that the overall secondary losses may depend, at least to some degree, on the displacement thickness-to-height ratio.

New Correlation

The new secondary loss correlation was assumed to take the following form

$$Y_{\text{secondary}} = (F_{\text{loading}})^a (\cos^b \gamma)(CR)^c \left(\frac{h\cos\alpha_2}{Cx}\right)^d \times \left[w + x(C_f)^e \tanh\left(f\frac{\delta^*}{h}\right)\right] \tag{17}$$

Table 1 defines the parameters in Eq. (17), and it summarizes the physical effect that each parameter is intended to measure. The variables a,b,c,d,e,f,w,x are empirical coefficients, and their values were determined using the same optimization procedure previously described in Part I. Equation (17) is of similar form to the Dunham and Came [2] and Kacker and Okapuu [3] correlations. However, there is one notable difference: The earlier correlations ignore the effect of the inlet endwall boundary layer on the secondary losses. This was done because details of the endwall boundary layer may not be known in the early stages of design. Finally, the effect of the displacement thickness-to-airfoil height ratio in Eq. (17) is expressed in terms of a hyperbolic tangent function because this function produces a similar loss trend to the ones observed by Came [35] and Hultsch and Sauer [38].

The optimization procedure was performed for three cases, each with the same form as Eq. (17) but with different loading parameters. In the first case, the tangential loading coefficient, F_t, was used as the measure of total airfoil loading, and it is defined mathematically in Table 1. This coefficient represents the tangential force per unit length nondimensionalized by dynamic pressure based on the vector-mean velocity. For the second case, the loading parameter in Eq. (17) was taken as

$$F_{\text{loading}} = \frac{F_t}{s/Cx} \tag{18}$$

such that the loading parameter is only a function of the inlet and outlet flow angles. Finally, the optimization was also performed with Ainley and Mathieson's loading coefficient because of its reported success in capturing the influence of total airfoil loading on secondary losses (Dunham and Came [2]). The quality of the correlations was assessed using evaluation diagrams.

Several observations are worth making in connection with the optimization results.

First, the secondary losses were only weakly dependent on the total airfoil loading. Therefore, no particular difference in the quality of the correlation was apparent with any of the three loading parameters, at least to within the uncertainty of the correlation and the scatter in the data. Consequently, the influence of the total

Table 1 List of correlating parameters for new secondary loss correlation

Parameter	Definition	Description
F_{loading}	Tangential loading parameter: $F_t=2(s/Cx)\cos^2\alpha_m(\tan\alpha_1-\tan\alpha_2)$ Tangential loading parameter nondimensionalized by pitch-to-axial chord ratio: $F_t/(s/Cx)=2\cos^2\alpha_m(\tan\alpha_1-\tan\alpha_2)$ Ainley and Mathieson's loading parameter: $Z=4(\tan\alpha_1-\tan\alpha_2)^2\cos^2\alpha_2/\cos\alpha_m$	Measure of total airfoil loading.
$\cos\gamma$	/	Indicator of airfoil loading distribution.
CR	Convergence ratio: $CR=\cos\alpha_1/\cos\alpha_2$	Indicator of flow acceleration.
$Cx/(h\cos\alpha_2)$	/	Captures influence of endwall surface area.
C_f	Skin friction coefficient	Indicator of circulation in the inner layer of inlet endwall boundary layer.
δ^*/h	Displacement thickness-to-airfoil height	Indirect measure of ratio of mass flow in the endwall region to the passage mass flow rate.

airfoil loading was omitted in the final form of the correlation. A tentative explanation for this result is given later.

A second observation concerns the influence of the skin friction coefficient. The initial results from the optimizer indicated that the secondary losses were inversely dependent on the skin friction coefficient. Subsequently, however, the optimizer was run with the skin friction coefficient omitted as a correlating parameter, and no degradation in the quality of the correlation was observed by comparison with the earlier run. With the omission of the skin friction, the expression for the secondary losses is

$$Y_{\text{secondary}}=\frac{0.038+0.41\tanh(1.20\delta^*/h)}{\sqrt{\cos\gamma}(CR)\left(\frac{h\cos\alpha_2}{Cx}\right)^{0.55}}. \qquad (19)$$

To demonstrate the improvements achieved with Eq. (19), the experimental secondary loss data, as obtained using the conventional loss breakdown (i.e., $Y_{\text{secondary}}=Y_{\text{total}}-Y_{\text{mid}}$), were compared first with the predictions of the Kacker and Okapuu [3] (KO) and Moustapha et al. [8] (MKT) correlations. The KO and MKT correlations were used to predict the design incidence and off-design incidence losses, respectively. Figure 1(*a*) compares the KO-MKT secondary loss predictions with the measured values for all the cases in Table 2. Predicted values of $Y_{\text{secondary}}$ that exceeded 0.14 were plotted along the top edge of the figure.

As can be seen in Fig. 1(*a*), the agreement between the predictions and the cascade measurements is poor: the KO-MKT correlations significantly overpredict most of the loss measurements. This result was expected since it is known that the predicted losses from KO are scaled or "calibrated" to reproduce stage efficiencies derived from rotating rig and engine data. The large disparity between the measured cascade losses and the predicted losses indicates that there are additional and significant loss generating mechanisms in the engine environment that are not captured in cascade testing. It is believed that the additional loss generation in the engine environment is caused by a number of factors, which include inlet boundary layer skew, radial pressure gradients and rotor-stator interaction. Disk- and shroud-cavity purge flows undoubtedly have significant effects on the endwall flows, as well. The recent results of McLean et al. [39] have shown that cavity purge flows can seriously degrade the performance of turbine stages. It is envisaged that, once sufficient data becomes available in the open literature, any additional and important parameters that influence secondary loss generation could be included as correlating parameters in the proposed correlation.

Obviously, a more appropriate comparison is to convert the engine-representative losses to cascade-representative losses by an engine-to-cascade scaling factor. Unfortunately, this scaling factor is not normally quoted in published correlations. However, the ratio of the average of the measured losses to the average of the predicted losses for all cases in the cascade database is probably a reasonable estimate. Figure 1(*b*) compares the scaled predicted losses to the measured cascade losses, and as noted in the figure, the value of the engine-to-cascade scaling factor was 0.23. It can be seen that the agreement now is considerably better. However, there are still numerous data points that fall outside the ±0.0075 error band. Furthermore, the shortcomings of the conventional loss breakdown scheme that were described in Part I are evident; that is, a few of the off-design incidence cases have negligible or even negative measured losses.

Figure 2 shows the evaluation diagram for the correlation given by Eq. (19). It is worth noting again that the measured secondary losses were obtained with the new loss breakdown scheme using the experimental values of mixed-out overall and midspan losses and the predicted values of penetration distance. As can be seen, a majority of the predictions lie inside the error band. The largest discrepancies occur for the cases with high values of positive incidence. The appearance of trailing edge flow separation tends to increase the levels of uncertainty for these cases. Nonetheless, with the present prediction method there is considerably less scatter than the combination of conventional loss breakdown and the KO-MKT correlations (Fig. 1(*b*)).

As discussed earlier, the results from the optimizer showed that the secondary losses were essentially independent of the total airfoil loading. This was unexpected since the correlations available in the open literature (e.g., Refs. [3–5]) show the contrary.

The influence of airfoil loading on secondary losses may be examined in more detail with the Wolf [28] secondary loss corre-

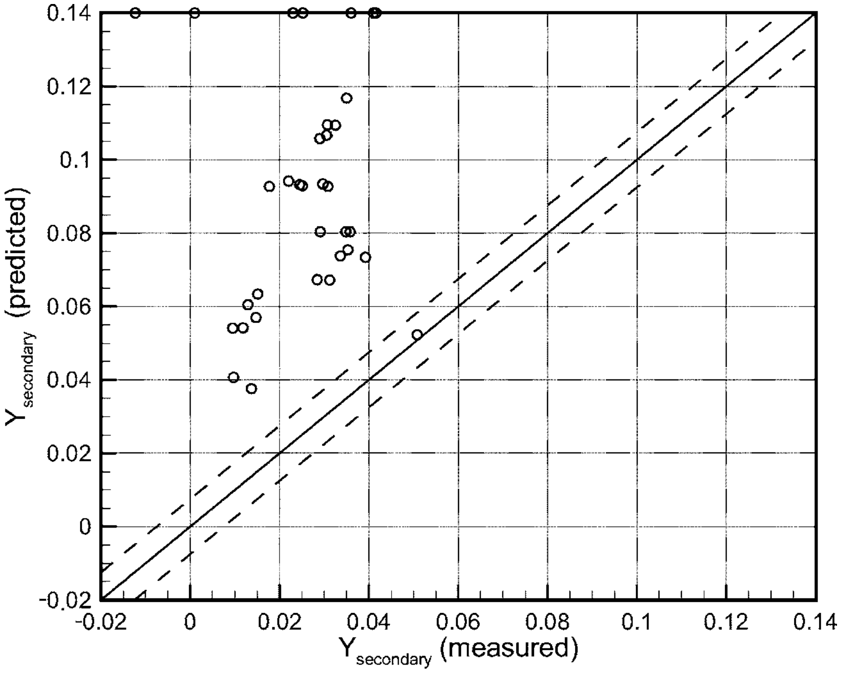

(a)

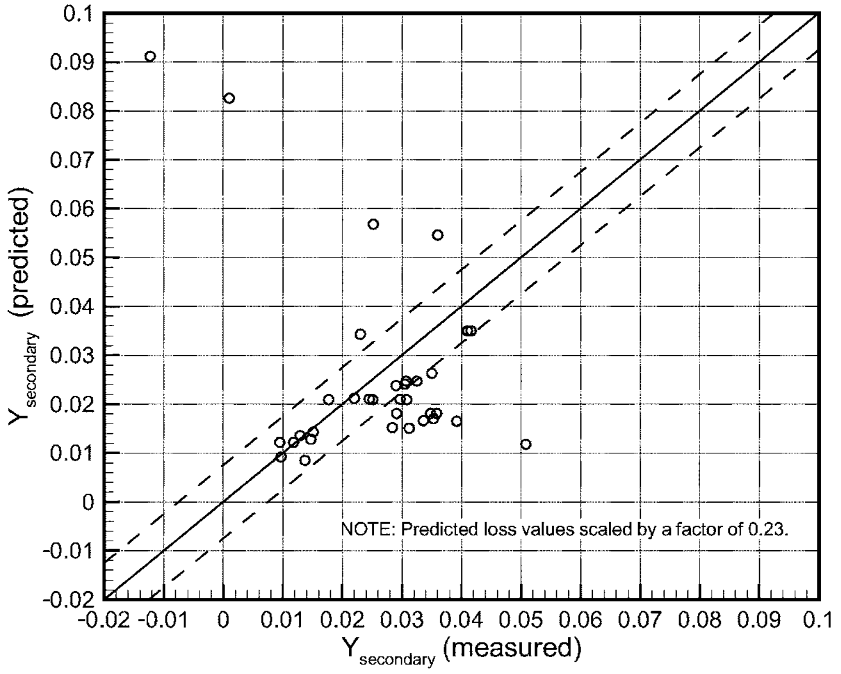

(b)

Fig. 1 Evaluation of the Kacker and Okapuu/Moustapha et al. secondary loss correlations: (*a*) Engine-representative, and (*b*) cascade-representative loss levels

lation. This particular correlation forms the basis for Traupel's correlation, and was chosen because it is based on an extensive set of data from tests that examined solely the influence of airfoil loading and channel acceleration. The cascade geometries that were examined had identical pitch-to-chord ratios, and therefore, the data do not include the influence of this parameter. In the original form of the Wolf correlation, the losses were correlated with the total flow turning and the convergence ratio. The present authors have recast the Wolf correlation in terms of the loading parameter $F_t/(s/Cx)$ and the inverse of the convergence ratio, as shown in Fig. 3.

To gain a better sense of the variation of secondary losses that might be expected for the range of loading values in the database, the cases from the present data set are plotted in Fig. 3, and the grey region shows the area within which most of the data points fall. From Fig. 3, it can be seen that the maximum variation in

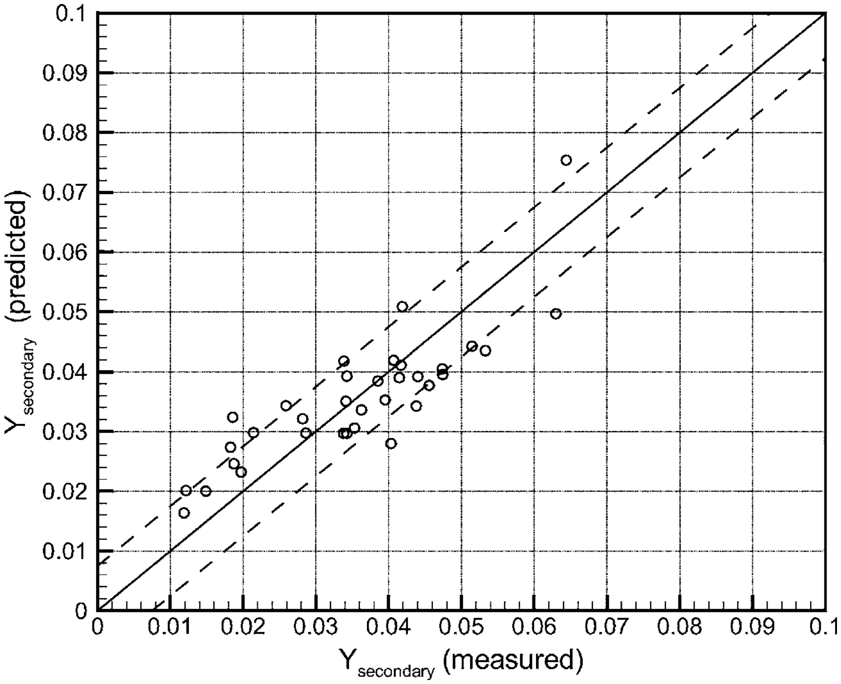

Fig. 2 Evaluation of the secondary loss correlation given by Eq. (19)

losses for the range of loading levels in the current database is $\Delta Y_{\text{secondary}} \approx 0.005$, which is well within the uncertainty of the current loss correlation. Therefore, it is likely that the optimizer has not identified an influence of airfoil loading because the secondary losses are relatively insensitive to loading differences, at least for loading levels that are common in turbines of recent design.

In Benner et al. [25], it was concluded that the loading distribution has an influence on secondary losses and that a more front-loaded airfoil tends to generate higher secondary losses. Furthermore, it was noted that the loading distribution is determined mainly by the stagger angle: An airfoil tends to become more forward-loaded as the stagger angle increases. The new correlation is consistent with these conclusions in that the influence of

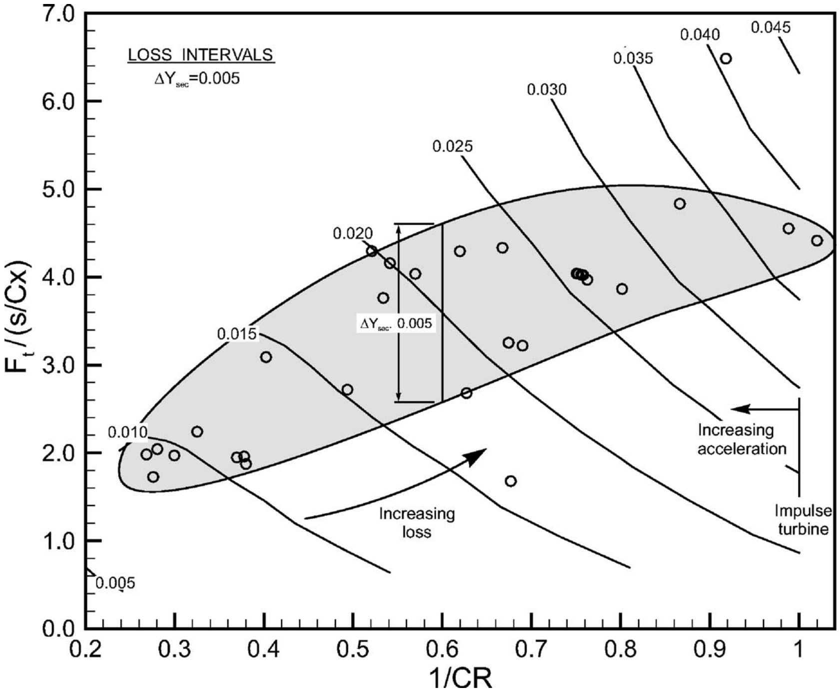

Fig. 3 The influence of convergence ratio and total airfoil loading on secondary losses (based on the secondary loss correlation of Wolf [28])

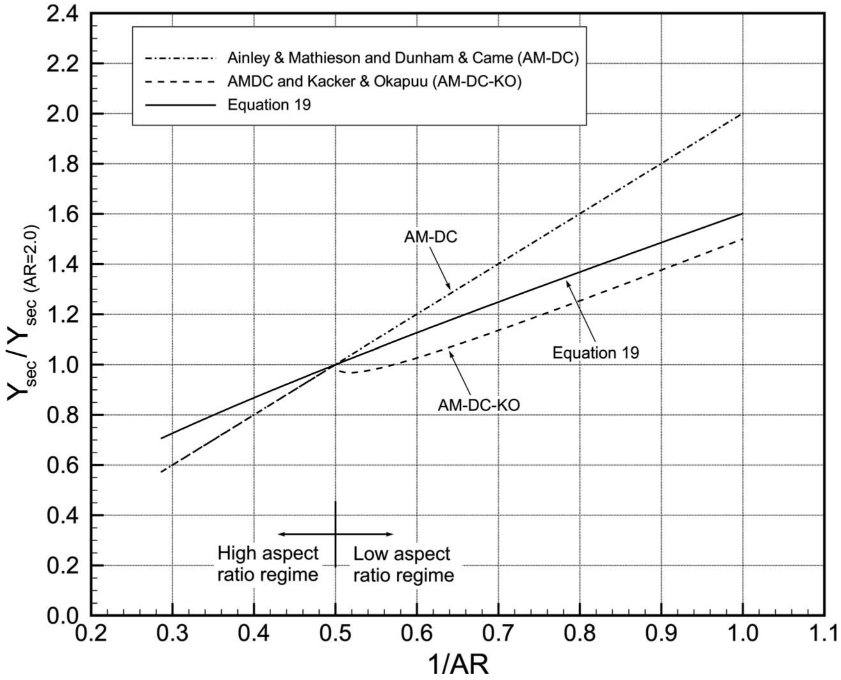

Fig. 4 The influence of aspect ratio on secondary losses

the loading-distribution parameter (cos γ) is significant. The parameter appears in the denominator of Eq. (19) indicating that an increase in stagger angle (more forward loading) produces higher losses.

For the influence of the channel acceleration, the results from the optimizer suggest that the secondary losses vary linearly with the inverse of the convergence ratio. A linear relationship is also used in the Ainley and Mathieson, Dunham and Came, and Kacker and Okapuu correlations.

It was suggested that the dissipation in the endwall boundary layers is a significant contributor to the secondary losses and for this reason, it was postulated that the size of the endwall surface area affects the secondary losses. In the present correlation, the influence of the endwall surface area is a function of the airfoil height-to-axial chord ratio. By comparison, the Dunham and Came, Kacker and Okapuu, and Craig and Cox correlations depend on the airfoil height-to-true-chord ratio.

A number of experimental studies have examined the influence of aspect ratio on secondary losses (e.g., data compiled by Dunham [6] and Atkins [40]). In these studies the aspect ratio variations were achieved exclusively through changes to the airfoil height, and the results strongly suggest that the secondary losses

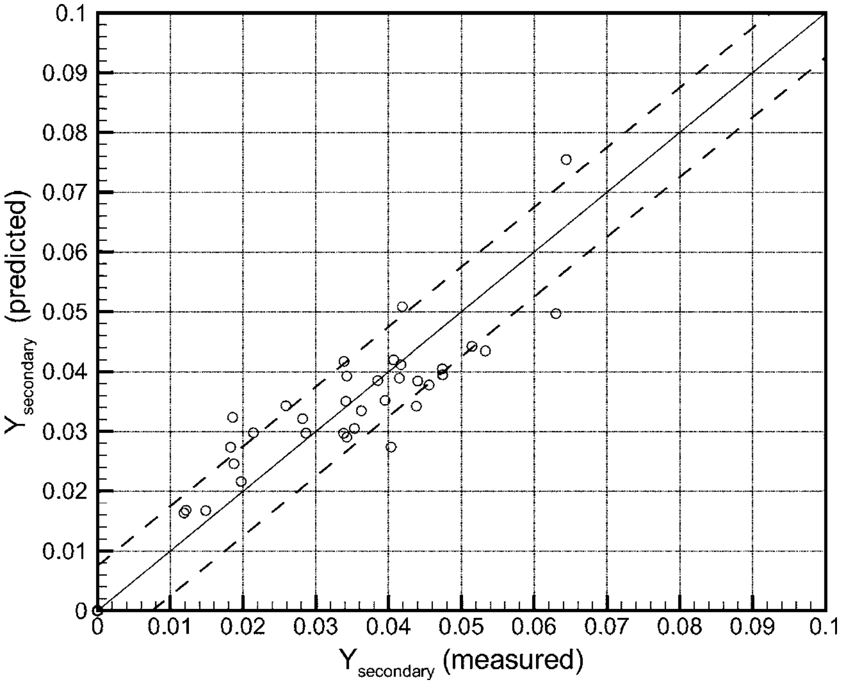

Fig. 5 Evaluation of the new secondary loss correlation (Eq. (20))

vary as the inverse of the airfoil height, at least for large aspect ratios (i.e., $h/C > 2.0$). Based on these results, Dunham and Came correlated the secondary losses with the inverse of the airfoil aspect ratio. This dependence was retained in the Kacker and Okapuu correlation for airfoils with aspect ratios greater than 2.0. For low aspect ratio airfoils (i.e., $h/C < 2.0$), the results of Rogo [41] and Okapuu [42] showed that the secondary losses were less sensitive to aspect ratio, and therefore, Kacker and Okapuu modified the dependence on aspect ratio accordingly.

Figure 4 shows the predicted influence of aspect ratio on secondary losses for one of the cascades examined by Benner [11] using the correlation given by Eq. (19), the Dunham and Came correlation (inverse aspect ratio dependence), and the Kacker and Okapuu correlation (Dunham and Came correlation with modified dependence for low aspect ratios). From the figure, it can be seen that the loss trend with aspect ratio for $h/C < 2.0$ is nearly identical for the new correlation and the Kacker and Okapuu correlation. For aspect ratios greater than 2.0, the loss trend from Eq. (19) differs considerably from the commonly observed inverse aspect ratio dependence. This result was not completely surprising given that the current database consists mostly of low aspect ratio airfoils. For aspect ratios greater than 2.0, an expression for secondary losses has been developed based on Eq. (19) but incorporating the inverse aspect ratio dependence.

The final recommended secondary loss expressions are then

$$Y_{\text{secondary}} = \frac{0.038 + 0.41\tanh(1.20\delta^*/h)}{\sqrt{\cos\gamma}(CR)(h/C)^{0.55}\left(\dfrac{C\cos\alpha_2}{Cx}\right)^{0.55}} \quad \text{for } h/C \leqslant 2.0,$$

$$Y_{\text{secondary}} = \frac{0.052 + 0.56\tanh(1.20\delta^*/h)}{\sqrt{\cos\gamma}(CR)(h/C)\left(\dfrac{C\cos\alpha_2}{Cx}\right)^{0.55}} \quad \text{for } h/C > 2.0. \tag{20}$$

The corresponding evaluation diagram is shown in Fig. 5.

Conclusions

An empirical prediction method for secondary losses has been developed. The method is based on a new loss breakdown scheme that has a different definition of the secondary loss component than the conventional scheme, as described in Part I. As a result, a new secondary loss correlation for design and off-design values of incidence was devised, and it is detailed in this paper. The correlation is based on linear cascade measurements from Benner [11] and from recent cases in the open literature.

To demonstrate the quality of the new empirical prediction method, the predictions from the most recent design and off-design incidence secondary loss correlations (Kacker and Okapuu [3], Moustapha et al. [8]) were compared first to the measured cascade data. The Kacker and Okapuu correlation was intended to reproduce loss data from engines and rotating rigs; therefore, their correlation significantly overpredicted all of the measured cascade data. As found by Kacker and Okapuu, a scaling factor is needed to make their correlation predictions apply to the linear cascade environment. An estimate of the value of their scaling factor has been presented in this paper. There is clearly a need for additional rotating rig/engine tests to better establish the value of that scaling factor, or to otherwise improve the current correlation with additional correlating parameters.

It is recognized that the new secondary loss correlation cannot be used to predict engine-level losses without some general scaling factor, like earlier cascade-derived correlations that have been proposed over the years. We believe that the main value of this correlation is that it is superior in capturing the influence of the various parameters on secondary losses than earlier correlations.

Acknowledgment

Financial support for this study provided by Pratt and Whitney Canada, Inc. and the Natural Sciences and Engineering Research Council of Canada is gratefully acknowledged.

Nomenclature

C = airfoil chord length
C_d = boundary layer dissipation coefficient (Eq. (7))
C_{SKE} = nondimensional secondary kinetic energy
Cx = airfoil axial chord length
CR = $\cos\alpha_1/\cos\alpha_2$=convergence ratio
F_t = tangential loading nondimensionalized by dynamic pressure based on the vector-mean velocity (defined in Table 1)
h = span
i = $\alpha_1 - \alpha_{1,\text{design}}$=incidence, in degrees
IBL = inlet boundary layer
P = static pressure
P_0 = total pressure
q = $P_o - P$=dynamic pressure
s = blade pitch or spacing
$\dot{S}$ = entropy generation rate (Eq. (6))
$\dot{S}_a$ = entropy generation rate per unit surface area
T = temperature
V = velocity
x = axial coordinate measured from the leading-edge plane
x' = axial location of the measurement plane as measured from the trailing-edge plane
y', z = local pitchwise and spanwise co-ordinates
Y = $(P_{0,1} - P_{0,2})/(P_{0,2} - P_2)$=mass-averaged total-pressure loss coefficient
Z = Ainley and Mathieson's loading parameter (Eq. (5))
Z_{TE} = spanwise distance of the passage vortex separation line from the endwall at the trailing edge
α = flow angle measured from the axial direction, in degrees
α_m = vector-mean flow angle (Eq. (3))
β = airfoil metal angle measured from the axial direction, in degrees
δ^* = $\int_0^\delta (1 - V/V_e)dz$=boundary-layer displacement thickness
γ = stagger angle measured from the axial direction, in degrees
ρ = density
τ = shear stress

Subscripts

e = boundary-layer edge value
mid = midspan
pv = passage vortex
TE = trailing edge
1, 2 = cascade inlet and outlet

Appendix

Table 2 Experimental data for new secondary loss correlation

			$Y_{\text{secondary}}$													
Case No.	Reference	Description	Measured	Predicted	Location of Measurement Plane, x'/Cx	Z_{te}/h Predicted	C_f	F_t	Z	s/Cx	$\Delta\alpha$ (deg.)	CR	h/Cx	δ^*/h	α_2 (deg.)	γ (deg.)
1	Benner [11]	LS3, $i=0°$	0.026	0.034	0.40*	0.15	0.0031	2.39	5.40	0.741	81.0	1.45	1.363	0.011	−52.6	21.6
2	Benner [11]	LS3, $i=10°$	0.047	0.040	0.40*	0.19	0.0030	2.86	6.66	0.741	89.4	1.25	1.363	0.014	−51.1	21.6
3	Benner [11]	LS3, $i=20°$	0.063	0.050	0.40*	0.23	0.0030	3.27	8.97	0.741	95.7	0.98	1.363	0.014	−47.3	21.6
4	Benner [11]	LS2, $i=0°$	0.034	0.035	0.40*	0.15	0.0030	2.40	5.48	0.738	82.0	1.48	1.358	0.013	−53.6	23.1
5	Benner [11]	LS2, $i=10°$	0.047	0.040	0.40*	0.19	0.0031	2.93	6.75	0.738	91.7	1.31	1.358	0.013	−53.3	23.1
6	Benner [11]	LS2, $i=20°$	0.042	0.051	0.40*	0.24	0.0029	3.36	8.92	0.738	97.4	1.01	1.358	0.017	−49.0	23.1
7	Hodson and Dominy [20]	Design	0.029	0.030	0.42*	0.13	0.0034	2.42	6.84	0.600	92.9	1.33	1.934	0.006	−54.1	19.6
8	Hodson and Dominy [21]	+22% s/C	0.034	0.030	0.42*	0.15	0.0034	2.94	6.83	0.732	92.6	1.32	1.934	0.006	−53.8	18.2
9	Hodson and Dominy [21]	−18% s/C	0.021	0.030	0.42*	0.11	0.0034	1.99	6.84	0.492	93.0	1.33	1.934	0.006	−54.2	20.6
10	Hodson and Dominy [21]	$i=+8.6°$	0.044	0.034	0.42*	0.16	0.0033	2.90	8.47	0.600	101.5	1.15	1.934	0.006	−54.1	19.6
11	Hodson and Dominy [21]	$i=-20.3°$	0.019	0.025	0.42*	0.08	0.0036	1.61	4.51	0.600	72.0	1.59	1.934	0.006	−53.5	19.6
12	Hodson and Dominy [21]	Thick IBL	0.028	0.032	0.42*	0.13	0.0032	2.42	6.83	0.600	92.7	1.32	1.934	0.013	−53.9	19.6
13	Marchal and Sieverding [31]	Nozzle, thin IBL	0.035	0.031	0.30	0.12	0.0044	1.93	5.42	0.983	67.8	2.65	1.130	0.011	−67.8	42.5
14	Marchal and Sieverding [31]	Nozzle, thick IBL	0.034	0.039	0.30	0.16	0.0036	1.92	5.55	0.983	68.3	2.70	1.130	0.038	−68.3	42.5
15	Marchal and Sieverding [31]	Rotor	0.041	0.039	0.30	0.17	0.0040	2.70	7.54	0.875	99.6	2.48	1.006	0.021	−69.6	38.5
16	Harrison [22]		0.040	0.035	0.23*	0.23	0.0032	4.31	7.65	1.036	105.5	1.85	1.351	0.009	−65.5	37.0
17	Weiss and Fottner [24]	T104 Front-loaded	0.015	0.017	0.50*	0.12	0.0025	3.91	7.20	0.969	100.9	1.75	3.833	0.008	−63.2	38.5
18	Weiss and Fottner [24]	T106 Rear-loaded	0.012	0.017	0.50*	0.12	0.0025	3.75	7.20	0.929	100.9	1.75	3.490	0.008	−63.2	30.7
19	Perdichizzi [43]	M2is=0.3; $i=20°$	0.041	0.042	1.10	0.19	0.0031	2.42	5.38	0.889	79.3	2.03	1.482	0.042	−61.9	45.2
20	Perdichizzi and Dossena [29]	M2is=0.7; s/C=0.58; $i=0°$	0.046	0.038	0.50	0.20	0.0027	1.87	8.48	0.942	88.8	3.73	1.470	0.058	−74.9	50.1
21	Perdichizzi and Dossena [29]	M2is=0.7; s/C=0.73; $i=0°$	0.038	0.039	0.50	0.22	0.0026	2.42	8.16	1.185	88.1	3.57	1.470	0.058	−74.2	50.1
22	Perdichizzi and Dossena [29]	M2is=0.7; s/C=0.87; $i=0°$	0.042	0.041	0.50	0.26	0.0025	3.17	7.19	1.412	85.5	3.08	1.470	0.058	−71.6	50.1
23	DeCecco [44]	LS1	0.053	0.043	0.48*	0.12	0.0038	1.27	2.47	0.754	47.4	1.48	1.020	0.018	−47.4	37.2
24	Gregory-Smith et al. [45]	Thin IBL	0.040	0.027	0.29*	0.18	0.0029	4.69	8.14	1.091	110.3	1.92	2.611	0.021	−67.5	35.9
25	Gregory-Smith et al. [45]	Natural IBL	0.034	0.029	0.29*	0.19	0.0028	4.69	8.14	1.091	110.3	1.92	2.611	0.027	−67.5	35.9
26	Gregory-Smith et al. [45]	Thick IBL	0.044	0.038	0.29*	0.28	0.0018	4.69	8.14	1.091	110.3	1.92	2.611	0.061	−67.5	35.9
27	Yan et al. [46]		0.012	0.016	0.26	0.06	0.0056	1.59	7.42	0.919	74.0	3.62	2.626	0.006	−74.0	47.3
28	Kopper et al. [47]	Planar endwalls	0.036	0.034	0.28	0.18	0.0036	3.25	10.32	2.347	78.7	5.08	1.282	0.025	−78.7	66.4
29	Atkins [40]	Planar endwalls	0.034	0.042	0.50	0.24	0.0033	3.77	7.28	0.870	100.0	1.50	1.206	0.009	−59.5	37.8
30	Chen and Dixon [32]	$\delta^*/C=0.0404$	0.020	0.022	0.91	0.11	0.0034	2.75	7.00	0.732	98.8	1.87	2.654	0.014	−64.0	27.2
31	Mobarak et al. [15]	Cascade No. 3	0.018	0.027	0.86	0.10	0.0030	1.54	7.23	0.780	79.7	3.34	1.489	0.028	−72.7	38.6
32	Yamomoto [48]	Part I—Stator	0.019	0.032	0.28	0.12	0.0033	1.76	5.24	0.942	64.8	2.63	1.230	0.023	−67.7	38.7
33	Yamomoto [49]	Part II—Rotor	0.051	0.044	0.23	0.20	0.0024	3.63	7.35	0.846	101.8	1.61	1.387	0.020	−61.7	44.7
34	Yamomoto and Nouse [16]	$i=7.2°$	0.064	0.075	0.24	0.36	0.0041	5.49	10.75	0.846	117.0	1.09	1.387	0.038	−60.0	44.7

*—Mixed-out losses given.

References

[1] Ainley, D. G., and Mathieson, G. C. R., 1951, "A Method of Performance Estimation for Axial Flow Turbines," British ARC, R&M 2974.

[2] Dunham, J., and Came, P. M., 1970, "Improvements to the Ainley-Mathieson Method of Turbine Performance Prediction," ASME J. Eng. Power, **92**, pp. 252–256.

[3] Kacker, S. C., and Okapuu, U., 1982, "A Mean Line Prediction Method for Axial Flow Turbine Efficiency," ASME J. Eng. Power, **104**, pp. 111–119.

[4] Craig, H. R. M., and Cox, H. J. A., 1971, "Performance Estimation of Axial Flow Turbines," in *Proceedings Institution of Mechanical Engineers 1970–71*, Vol. 185, no. 32/71, pp. 407–424.

[5] Traupel, W., 1977, *Thermische Turbomaschinen*, Springer-Verlag, Berlin.

[6] Dunham, J., 1970, "A Review of Cascade Data on Secondary Losses in Turbines," J. Mech. Eng. Sci., **12**, pp. 48–59.

[7] Sieverding, C. H., 1985, "Axial Turbine Performance Prediction Methods," *Thermodynamics and Fluid Mechanics of Turbomachinery*, Vol. 1, No. 97A of *NATO ASI, Series E*, pp. 737–784.

[8] Moustapha, S. H., Kacker, S. C., and Tremblay, B., 1990, "An Improved Incidence Losses Prediction Method for Turbine Airfoils," ASME J. Turbomach., **112**, pp. 267–276.

[9] Mukhtarov, M. K., and Krichakin, V. I., 1969, "Procedure of Estimating Flow Section Losses in Axial Flow Turbines when Calculating their Characteristics," Teploenergetika, **16**(7), pp. 76–79.

[10] Benner, M. W., Sjolander, S. A., and Moustapha, S. H., 1997, "Influence of Leading-Edge Geometry on Profile Losses in Turbines at Off-Design Incidence: Experimental Results and an Improved Correlation," ASME J. Turbomach., **119**, pp. 193–200.

[11] Benner, M. W., 2003, "The Influence of Leading-Edge Geometry on Profile and Secondary Losses in Turbine Cascades," Ph.D. thesis, Department of Mechanical and Aerospace Engineering, Carleton University, Ottawa, Canada.

[12] Benner, M. W., Sjolander, S. A., and Moustapha, S. H., 2004, "Measurements of Secondary Flows Downstream of a Turbine Cascade at Off-Design Incidence," ASME Paper No. GT2004–53786.

[13] Graziani, R. A., Blair, M. F., Taylor, J. R., and Mayle, R. E., 1980, "An Experimental Study of Endwall and Airfoil Surface Heat Transfer in a Large Scale Turbine Blade Cascade," ASME J. Eng. Power, **102**, pp. 257–267.

[14] Moore, J., and Ransmayr, A., 1984, "Flow in a Turbine Cascade—Part 1: Losses and Leading-Edge Effects," ASME J. Eng. Gas Turbines Power, **106**, pp. 400–408.

[15] Mobarak, A., Khalafallah, M. G., Osman, A. M., and Heikal, H. A., 1988, "Experimental Investigation of Secondary Flow and Mixing Downstream of Straight Cascades," ASME J. Turbomach., **110**, pp. 497–503.

[16] Yamamoto, A., and Nouse, H., 1988, "Effects of Incidence on Three-Dimensional Flows in a Linear Turbine Cascade," ASME J. Turbomach., **110**, pp. 486–496.

[17] Langston, L. S., Nice, M. L., and Hooper, R. M., 1977, "Three-Dimensional Flow Within a Turbine Cascade Passage," ASME J. Eng. Power, **99**, pp. 21–28.

[18] Moore, J., and Adhye, R. Y., 1985, "Secondary Flows and Losses Downstream of a Turbine Cascade," ASME J. Turbomach., **107**, pp. 961–968.

[19] Jilek, J., 1986, "An Experimental Investigation of the Three-Dimensional Flow Within Large Scale Turbine Cascades," ASME Paper No. 86-GT-170.

[20] Hodson, H. P., and Dominy, R. G., 1987a, "Three-Dimensional Flow in a Low-Pressure Turbine Cascade at its Design Condition," ASME J. Turbomach., **109**, pp. 177–185.

[21] Hodson, H. P., and Dominy, R. G., 1987b, "The Off-Design Performance of a Low-Pressure Turbine Cascade," ASME J. Turbomach., **109**, pp. 201—210.

[22] Harrison, S., 1990, "Secondary Loss Generation in a Linear Cascade of High-Turning Turbine Blades," ASME J. Turbomach., **112**, pp. 618–624.

[23] Goobie, S. M., Moustapha, S. H., and Sjolander, S. A., 1989, "An Experimental Investigation of the Effect of Incidence on the Two-Dimensional Performance of an Axial Turbine Cascade," *Proceedings, Ninth International Symposium on Air Breathing Engines*, pp. 197–204.

[24] Weiss, A. P., and Fottner, L., 1995, "The Influence of Load Distribution on Secondary Flow in Turbine Cascades," ASME J. Turbomach., **117**, pp. 133–141.

[25] Benner, M. W., Sjolander, S. A., and Moustapha, S. H., 2004, "The Influence of Leading-Edge Geometry on Secondary Losses in a Turbine Cascade at the Design Incidence," ASME J. Turbomach., **126**, pp. 277–287.

[26] Marchal, P., 1980, "Etude des ecoulements secondaires en grille d'aubes de detente," Ph.D. thesis, Universit Libre de Bruxelles, Brussels, Belgium.

[27] Sieverding, C. H., 1985, "Recent Progress in the Understanding of Basic Aspects of Secondary Flows in Turbine Blade Passages," ASME J. Turbomach., **107**, pp. 249–257.

[28] Wolf, H., 1961, "Die Randverluste in geraden Schaufelgittern," Wiss. Z. Tech. Univ. Dresden, **10**, pp. 353–364.

[29] Perdichizzi, A., and Dossena, V., 1993, "Incidence Angle and Pitch-Chord Effects on Secondary Flows Downstream of a Turbine Cascade," ASME J. Turbomach., **115**, pp. 383–391.

[30] Denton, J. D., 1993, "Loss Mechanisms in Turbomachinery," ASME J. Turbomach., **115**, pp. 621–656.

[31] Marchal, P., and Sieverding, C. H., 1977, "Secondary Flows Within Turbomachinery Bladings," *Secondary Flows in Turbomachines*, AGARD-CP-214, Paper No. 11, pp. 1–19.

[32] Chen, L. D., and Dixon, S. L., 1986, "Growth of Secondary Flow Losses Downstream of a Turbine Blade Cascade," ASME J. Turbomach., **108**, pp. 270–275.

[33] Sharma, O. P., and Butler, T. L., 1987, "Predictions of Endwall Losses and Secondary Flows in Axial Turbine Cascades," ASME J. Turbomach., **109**, pp. 229–236.

[34] Chan, J. K. K., Yaras, M. I., and Sjolander, S. A., 1994, "Interaction between Inlet Boundary Layer, Tip-Leakage and Secondary Flows in a Low-Speed Turbine Cascade," ASME Paper No. 94-GT-250.

[35] Came, P. M., 1973, "Secondary Loss Measurements in a Cascade of Turbine Blades," The Institution of Mechanical Engineering, Paper C33/73, pp. 75–83.

[36] Sauer, H., and Wolf, H., 1994, "The Influence of the Inlet Boundary Layers on the Secondary Losses of Turbine Stages," *Technology Requirements for Small Gas Turbines*, AGARD-CP-537, Paper No. 28, pp. 1–6.

[37] Hawthorne, W. R., 1954, "The Secondary Flow about Struts and Airfoils," J. Aeronaut. Sci., **21**, pp. 588–608 and 648.

[38] Hultsch, M., and Sauer, H., 1979, "Sekundarstromungen in Beschauflungen axialer Turbomaschinen," Maschinenbautechnik, **28**, pp. 32–37.

[39] McLean, C., Camci, C., and Glezer, B., 2001, "Mainstream Aerodynamic Effects Due to Wheelspace Coolant Injection in a High-Pressure Turbine Stage—Part I: Aerodynamic Measurements in the Stationary Frame," ASME J. Turbomach., **123**, pp. 687–696.

[40] Atkins, M. J., 1987, "Secondary Losses and End-Wall Profiling in a Turbine Cascade," The Institution of Mechanical Engineering, Paper No. C255/87, pp. 29–42.

[41] Rogo, C., 1968, "Experimental Aspect Ratio and Tip Clearance Investigation on Small Turbines," SAE Paper No. 680448.

[42] Okapuu, U., 1974, "Some Results from Tests on a High Work Axial Gas Generator Turbine," ASME Paper No. 74-GT-81.

[43] Perdichizzi, A., 1990, "Mach Number Effects on Secondary Flow Development Downstream of a Turbine Cascade," ASME J. Turbomach., **112**, pp. 643–651.

[44] DeCecco, S., 1995, "Behavior of Tip-Leakage Flows at Large Clearances," Master's thesis, Department of Mechanical and Aerospace Engineering, Carleton University, Ottawa, Canada.

[45] Gregory-Smith, D. G., Graves, C. P., and Walsh, J. A., 1988, "Growth of Secondary Losses and Vorticity in an Axial Turbine Cascade," ASME J. Turbomach., **110**, pp. 1–8.

[46] Yan, J., Gregory-Smith, D. G., and Walker, P. J., 1999, "Secondary Flow Reduction in A Nozzle Guide Vane Cascade by Non-Axisymmetric End-wall Profiling," ASME Paper No. 99-GT-339.

[47] Kopper, F. C., Milano, R., and Vanco, M., 1981, "An Experimental Investigation of Endwall Profiling in a Turbine Vane Cascade," AIAA J., **19**, pp. 1033–1040.

[48] Yamamoto, A., 1987a, "Production and Development of Secondary Flows and Losses in Two Types of Straight Turbine Cascades—Part 1: A Stator Case," ASME J. Turbomach., **109**, pp. 186–193.

[49] Yamamoto, A., 1987b, "Production and Development of Secondary Flows and Losses in Two Types of Straight Turbine Cascades—Part II: A Rotor Case," ASME J. Turbomach., **109**, pp. 194–200.

Detached Eddy Simulation of Film Cooling Performance on the Trailing Edge Cutback of Gas Turbine Airfoils

P. Martini

A. Schulz

H. -J. Bauer

Lehrstuhl und Institut für Thermische
Strömungsmaschinen,
Universität Karlsruhe (TH),
Kaiserstr. 12,
76128 Karlsruhe, Germany

C. F. Whitney
ALSTROM Power Technology Centre,
Cambridge Road,
Whetstone, Leicester LE8 6LH, UK

The present study deals with the unsteady flow simulation of trailing edge film cooling on the pressure side cut back of gas turbine airfoils. Before being ejected tangentially on the inclined cut-back surface, the coolant air passes a partly converging passage that is equipped with turbulators such as pin fins and ribs. The film mixing process on the cut back is complicated. In the near slot region, due to the turbulators and the blunt pressure side lip, turbulence is expected to be anisotropic. Furthermore, unsteady flow phenomena like vortex shedding from the pressure side lip might influence the mixing process (i.e., the film cooling effectiveness on the cut-back surface). In the current study, three different internal cooling designs are numerically investigated starting from the steady RaNS *solution, and ending with unsteady detached eddy simulations (DES). Blowing ratios* $M=0.5$*; 0.8; 1.1 are considered. To obtain both, film cooling effectiveness as well as heat transfer coefficients on the cut-back surface, the simulations are performed using adiabatic and diabatic wall boundary conditions. The DES simulations give a detailed insight into the unsteady film mixing process on the trailing edge cut back, which is indeed influenced by vortex shedding from the pressure side lip. Furthermore, the time averaged DES results show very good agreement with the experimental data in terms of film cooling effectiveness and heat transfer coefficients.* [DOI: 10.1115/1.2137739]

Introduction

The thermodynamic cycle efficiency of gas turbines is closely linked to the peak temperature of the working fluid. Advanced gas turbines are operated at peak temperatures that are well beyond the maximum allowable metal temperatures. Currently, temperatures of up to 2000 K are attained at the combustor exit. As a consequence, all hot gas-ducting elements of a gas turbine have to be cooled intensively by compressed air. Since the coolant does not participate in the whole cycle, cooling inherently is a loss. One major developmental effort therefore is, to further reduce the required amount of coolant (i.e., to optimize cooling techniques). For thermally highly loaded blades and vanes, generally a combination of film cooling and internal convective cooling is utilized to guarantee wall temperatures within the limits of the blade material.

Adequate cooling of the blade's trailing edge is especially challenging. From an aerodynamic point of view the trailing edge should be designed as thin as possible, which is in conflict with the cooling design and structural integrity requirements. State-of-the-art cooling concepts often use a pressure side cut back where the pressure sidewall of the trailing edge is shortened with respect to the suction side. Cooling air is ejected through a spanwise slot onto the cut back surface. In order to ensure the structural integrity of the trailing edge, arrays of ribs or pin fins in the coolant passage connect the pressure side and the suction side walls. Additionally, they act as turbulators promoting the internal convective heat transfer in the coolant passage and controlling the blade's coolant mass flux. Figure 1 shows a cross-sectional view of a turbine blade with trailing edge cut back (in this example, the slot is laterally disrupted by stiffening, tapered lands that align flush with the pressure side wall).

A considerable amount of studies exist, dealing with film cooling downstream of holes or slots of various exit geometries. Goldstein [1] gives a detailed review of the most relevant work, done before 1971. However, studies focusing on the complicated film mixing process on the pressure side cut back are relatively rare. The film formed by the slot may be of a complex, three-dimensional structure, especially when turbulators are located close to the ejection slot (i.e., the lip overhang is short). The lip thickness in such configurations is typically about the slot height and the mixing process in the near slot region may be additionally affected by vortex shedding. Taslim et al. [2] experimentally investigate the film cooling effectiveness downstream of trailing edge slots that are spanwise disrupted by wooden lands. They identify the ratio of lip thickness to slot height as being a key parameter for film cooling on the cut-back surfaces. Holloway et al. [3,4] numerically investigate a trailing edge slot, spanwise disrupted by lands for realistic turbine conditions. Their URaNS calculations reveal that an unsteady vortex shedding from the lip ($t/H=0.9$) is responsible for significantly reduced film cooling effectiveness. However, due to the damping caused by the applied k-ϵ turbulence model, it is necessary to excite the process of vortex shedding artificially by means of small, random pressure perturbations. Martini et al. [5] investigate film cooling effectiveness and discharge behavior of a trailing edge slot equipped with an in-line rib array ($s/H=6$). Similar to the results in Ref. [3], steady RaNS computations lead to substantial over-predictions of film cooling effectiveness on the cut-back surface. However, the discharge behavior of the trailing edge slot is predicted reasonably well by steady calculations. Jansson et al. [6] numerically investigate a tangential coolant injection by a clean slot with $t/H=1$ and 0.1 using a two-layer algebraic stress model. Although present for both slots, only for the thick-lipped slot ($t/H=1$) does vortex shedding become dominant on the film mixing process (i.e., film

---

Contributed by the International Gas Turbine Institute (IGTI) of ASME for publication in the JOURNAL OF TURBOMACHINERY. Manuscript received October 1, 2004; final manuscript received February 1, 2005. IGTI Review Chair: K. C. Hall. Paper presented at the ASME Turbo Expo 2005: Land, Sea and Air, Reno, NV, June 6, 2005–June 6, 2005, Paper No. GT2005-68084.

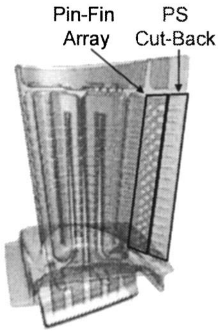

Fig. 1 Cross-sectional view of a turbine blade with pressure side cut back

cooling effectiveness). They also state that the application of the k-ϵ model, which is based on the assumption of isotropic turbulence, produces excessive eddy viscosity and, hence, unduly damps the periodic fluctuations. Although the algebraic stress model yields better results than the k-ϵ model, all computations still show a tendency to overpredict film cooling effectiveness.

Proposed by Spalart et al. [7], detached eddy simulations (DES) is intended to combine the advantages of LES and RaNS models. It was initially developed to predict largely separated flows occurring e.g. behind a stalled wing. So far, only few computational studies in the open literature deal with this relatively new hybrid model (see, e.g., Refs. [7–12]). Numerical simulations of film cooling using DES are particularly rare. The first study, applying DES to a three-dimensional cooling configuration is performed by Roy et al. [13]. They investigate a single row of cooling holes ($z/d=3$) inclined by an angle of 35 deg. The results indicate a highly anisotropic mixing process downstream of the hole. However, the laterally averaged film cooling effectiveness gained from DES provided no clear indication of improved accuracy. The discrepancy in the experiments is partly attributed to the use of a symmetry boundary condition, considering just half of the hole. This might have affected the evolution of unsteady flow downstream of the ejection. A DES simulation for the same configuration but without using the symmetry boundary condition was recently performed by Kapadia et al. [14]. They find a more satisfactory agreement of predicted film cooling effectiveness and experimental results.

The scope of the present work is to extend the application of DES to trailing edge film cooling. The flow on the cut back is characterized by separation zones behind the pressure side lip and the turbulators. Since the DES model is originally intended to predict flows with separation, it might be also suited to capture the complex flow physics, that are involved in the unsteady film mixing process on the trailing edge cut back. To judge this statement critically, various DES analyses are conducted for relevant trailing edge cooling configurations. The numerical predictions are compared to the results gained from a comprehensive experimental study on trailing edge film cooling that is separately reported in a parallel publication [15].

Turbulence Modeling

The following section is intended to provide a very brief overview of the turbulence models applied in the present study. Further details should be taken from the referenced secondary literature.

Shear-Stress Transport k-ω Model. Prior to the unsteady DES calculations, for all numerical test cases (steady) RaNS simulations are performed. As previously stated, the use of RaNS turbulence models, leads to poor predictions in terms of film cooling effectiveness on the cut-back surface. However, the question of how RaNS performs in predicting heat transfer coefficients in that region has not been answered yet.

For this work, the shear-stress transport (SST) k-ω model proposed by Menter et al. [16] is favored. It blends between the standard k-ω formulation in the near wall region and a transformed k-ϵ model away from the walls and accounts for the transport of the turbulent shear stresses. The transport equations for turbulent kinetic energy k and specific dissipation rate ω have the following form [17]:

$$\frac{\partial}{\partial t}(\rho k)+\frac{\partial}{\partial x_i}(\rho k u_i)=\frac{\partial}{\partial x_j}\left(\Gamma_k\frac{\partial k}{\partial x_j}\right)+G_k-Y_k+S_k \tag{1}$$

$$\frac{\partial}{\partial t}(\rho \omega)+\frac{\partial}{\partial x_i}(\rho \omega u_i)=\frac{\partial}{\partial x_j}\left(\Gamma_\omega\frac{\partial \omega}{\partial x_j}\right)+G_\omega-Y_\omega+D_\omega+S_\omega \tag{2}$$

In Eqs. (1) and (2), G symbolizes the generation, Y is the dissipation of k and ω, Γ denotes the effective diffusivity, and S represents user-defined source terms of both turbulence quantities. D_ω is an additional cross-diffusion term for the specific dissipation rate in Eq. (2).

Spalart-Allmaras Model. In this work, DES employs a one-equation RaNS model proposed by Spalart et al. [18]. This relatively new model is designed for aerospace applications including wall bounded flows and boundary layers subjected to adverse pressure gradients [17]. The transport equation for the variable $\tilde{\nu}$, the modified turbulent viscosity, is given as follows:

$$\frac{\partial}{\partial t}(\rho\tilde{\nu})+\frac{\partial}{\partial x_i}(\rho\tilde{\nu}u_i)=G_\nu+\frac{1}{\sigma_{\tilde{\nu}}}\left[\frac{\partial}{\partial x_j}\left\{(\mu+\rho\tilde{\nu})\frac{\partial\tilde{\nu}}{\partial x_j}\right\}+C_{b2}\rho\left(\frac{\partial\tilde{\nu}}{\partial x_j}\right)^2\right]-Y_\nu+S_{\tilde{\nu}} \tag{3}$$

C_{b2} and $\sigma_{\tilde{\nu}}$ are constants and $S_{\tilde{\nu}}$ is a user-defined source term. G_ν and Y_ν, respectively, are terms describing the production and the destruction of turbulent viscosity in the near wall region. Both, production and destruction terms depend on a length scale (d) which is the closest distance to the wall. Based on d, the transport variable $\tilde{\nu}$ becomes identical to the eddy viscosity, ν_t, in the high Reynolds number region, whereas it is zero directly at the wall.

DES Model. DES can be regarded as a RaNS model, which is sensitized to the grid spacing. The result is a hybrid model that selectively adopts either URaNS or LES in appropriate regions of the domain. Wherever the grid is not fine enough for LES (which is usually the case in the viscous near wall region), DES reduces to the unsteady RaNS model on which it is based. In the high Reynolds number region away from the walls, however, DES works in the LES mode. Depending on the grid size, the largest turbulent scales are resolved, whereas the subgrid scales of turbulence are modeled by the same RaNS model.

In the present study, DES is an adapted version of the Spalart-Allmaras formulation. This RaNS model can be easily sensitized to the grid spacing by modifying the length scale (d) which plays a major role in the production and destruction of the turbulent viscosity. In the original Spalart-Allmaras formulation, d denotes the closest distance to the wall whereas in DES it is replaced by

$$\tilde{d}\equiv\min(d,C_{\mathrm{DES}}\Delta) \tag{4}$$

where

$$\Delta\equiv\max(\Delta x,\Delta y,\Delta z) \tag{5}$$

In Eq. (4) C_{DES} is a constant ($C_{\mathrm{DES}}=0.65$) and Δ denotes the scalar grid spacing. From Eq. (4) it becomes clear, that in the near wall region, where $d<C_{\mathrm{DES}}\Delta$, the DES model reduces to the Spalart-Allmaras formulation as $\tilde{d}=d$. However, away from the walls, where $d>C_{\mathrm{DES}}\Delta$, the modified length scale $\tilde{d}$ becomes solely dependant of the local grid size, transforming the Spalart-

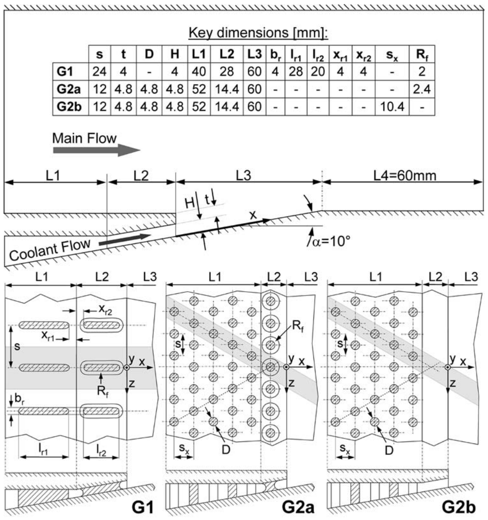
Key dimensions [mm]:

	s	t	D	H	L1	L2	L3	b_r	l_{r1}	l_{r2}	x_{r1}	x_{r2}	s_x	R_f
G1	24	4	-	4	40	28	60	4	28	20	4	4	-	2
G2a	12	4.8	4.8	4.8	52	14.4	60	-	-	-	-	-	-	2.4
G2b	12	4.8	4.8	4.8	52	14.4	60	-	-	-	-	-	10.4	-

Fig. 2 Computational domain and internal design of the trailing edge cooling configurations

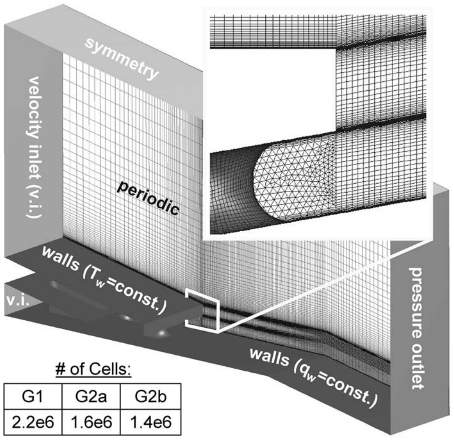

# of Cells:

G1	G2a	G2b
2.2e6	1.6e6	1.4e6

Fig. 3 Computational grid and types of boundary conditions used for the simulations

Allmaras formulation to a one-equation subgrid scale model. Assuming a balance of production and destruction terms, it follows that:

$$\mu_t \sim \rho \Delta^2 S \tag{6}$$

In Eq. (6), S is a resolved deformation rate. In this case, the Spalart-Allmaras formulation reduces to an algebraic mixing-length model for the subgrid range of turbulence, which is similar to the ones used in classical LES formulations [19].

Numerical Considerations

The calculations are performed using the commercial CFD software FLUENT 6.1 (segregated solver). With unsteady frame and mesh sizes of up to 2.2e6 cells, extensive parallelisation is required in the present case. The calculations are conducted on eight CPUs of an IBM RS/6000 SP supercomputer. The overall CPU time required for a single DES calculation is typically 10^3 h.

Computational Grid and Boundary Conditions. The numerical studies concentrate on three relevant trailing edge cooling configurations. They comprise a representative subset of configurations, experimentally investigated in a hot wind tunnel using a generic test setup with enlarged trailing edge models [15]. The measurements cover the discharge behavior of the slot and film cooling performance on the cut back and provide an extensive database for the validation of numerical methods. Figure 2 shows the extension of the computational domain (the shaded area indicates the lateral extension of the numerical grids) and the internal design of the three trailing edge cooling slots considered. All key dimensions are derived from the experiment.

Two pin-fin configurations, an equilaterally staggered array of six rows of cylindrical pins and a five-row configuration with increased lip overhang are considered ($G2a$, $G2b$). In both cases, the equilateral pitch to pin diameter ratio is $s/D=2.5$. Beside these pin-fin configurations, which are often used in the HP turbine, the trailing edge cooling slot is equipped with two rows of long ribs, located in an inline arrangement ($G1$). This design is predominantly found in the LP turbine and results in a significantly lower blockage of the internal passage compared to the pin-fin arrays. The lateral pitch to exit slot height ratio tested for this design is $s/H=6$. The ratio of lip thickness to slot height is unity for all trailing edge slots investigated.

The computational grids are created by Gambit 2.1.2. As indicated by Fig. 2 the lateral extension of the grid is a single pitch (s) and periodic boundary conditions are prescribed on the lateral planes. Figure 3 illustrates the meshing strategy and provides information on the type of boundary conditions used for the simulations. The computational grids are optimized with respect to DES considering the guidelines for grid generation provided by Spalart [20]. The computational meshes are unstructured and consist of a hybrid grid topology using several types of elements. Due to the complex internal design, the coolant cavity is meshed by prisms, tetrahedrals, and pyramidal elements whereas hexahedral elements are used in the external region. By refining the viscous near wall region, an average value of $y^+=1.37$ is achieved for the wall adjacent cells. This allows for the adoption of the turbulence models in their low-Reynolds number formulation, resolving the boundary layer all the way down to the viscous sublayer.

The boundary conditions for the numerical simulations are taken from the experiments. The main flow velocity at the inlet is set to 56 m/s (Ma=0.125) at a hot gas temperature of 500 K. The main flow turbulence intensity is $Tu_{\mathrm{hg}}=7\%$ at a turbulence length scale of 0.01 m. The operating pressure is slightly overatmospheric ($p_{\mathrm{hg}} \approx$ 105,000 Pa). Incompressible ideal gas behavior is assumed, since the Mach numbers are low. In addition, the properties for air are approximated by piecewise linear functions of the temperature.

Coolant air enters the cavity with an ambient temperature of $T_c \approx 293$ K. The coolant flow velocity at the inlet boundary is set to values between 6 and 13 m/s providing the correct coolant mass flux for blowing ratios $M=0.5$; 0.8; 1.1. The blowing ratio is defined as a slot averaged value directly at the exit of the slot

$$M = \frac{\overline{(\rho_c u_c)}_{\mathrm{slot}}}{\rho_{\mathrm{hg}} u_{\mathrm{hg}}} = \frac{m_c}{A_{\mathrm{slot}} \rho_{\mathrm{hg}} u_{\mathrm{hg}}} \tag{7}$$

The turbulence intensity of the coolant is set to be 5% at a length scale of 0.0015 m.

A constant temperature boundary condition is used on the walls (including the pins) upstream of the cut back surface ($L3$), whereas downstream of the cooling slot, a constant heat flux (q_{w}) is imposed on the walls. The heat flux is either an averaged value from the experiment or zero, resulting in adiabatic conditions on the cut-back surface (to comply with the experiment, in that case also the bottom wall of $L2$ is assumed to be adiabatic).

Spatial Discretisation. Second order schemes are applied for the discretisation of convective terms in the transport equations and pressure. For the steady calculations, the second order upwind scheme is chosen for all flow quantities (momentum, energy, turbulence). As recommended for LES applications [17,21], the central differencing scheme is employed for momentum and turbulence in DES, whereas energy transport relies on a second order upwind scheme. For pressure-velocity coupling, the SIMPLEC algorithm is utilized.

Temporal Discretisation and Time Stepping. First order methods in time might be overly diffusive, so a second order implicit formulation is applied for the unsteady DES calculations.

Not only the grid, but also the time step must be small enough to allow for resolution of large-scale turbulent eddies. In the present case, the large-scale turbulence on the cut back is expected to be influenced by vortex shedding from the lip and the wake flow behind the last row of turbulators. Sieverding et al. [22] report a Strouhal number of about 0.21 for vortex shedding downstream of a flat plate with squared trailing edge and turbulent boundary layers

$$\mathrm{Sr} = \frac{f(t + \delta_{1,1} + \delta_{1,2})}{u} \approx 0.21 \tag{8}$$

In Eq. (8), $\delta_{1,1}$ and $\delta_{1,2}$ denote the displacement thickness of the boundary layer on both sides of the plate. Based on Eq. (8), $u_{\mathrm{hg}} = 56$ m/s and an effective lip thickness of 5 mm, the shedding frequency should be about $f = 2.4$ kHz. Since u_{hg} is generally higher than u_c (but of the same order), this value can be regarded as an upper limit for the frequency of periodic fluctuations including those generated by the turbulators.

To guarantee a sufficiently fine temporal resolution of the unsteady effects, a time step of $2.5e\text{-}5s$ is chosen. With respect to vortex shedding from the lip, this would result in approximately 17 time steps per shedding cycle and a local Courant number of $\mathrm{CFL} \approx 1-3$ in the mixing region of $L3$. To assure that the temporal resolution is fine enough, time steps of $1.25e\text{-}5s$ and $5e\text{-}5s$ are tested ($G2a, M = 0.80$). The time averaged film cooling effectiveness on the cut back does not deviate by more than 3% for the different time step sizes and no specific trend is visible.

Fifteen internal iterations per time step are performed causing the residuals to drop by approximately three orders of magnitude, which is the convergence criterion for DES calculations. After reaching a statistically steady state, a period of at least 500 time steps is used to gain time-averaged results.

Results

In this section, the results of the computational studies are presented and compared to the experimental findings. A detailed discussion of the experimental results is given in Ref. [15].

Discharge Coefficients. The discharge behavior of the trailing edge cooling slots is defined by the discharge coefficient (C_D). It relates the actual coolant mass flux to the ideal mass flux resulting from an isentropic expansion from p_{1t} (mass flow averaged total pressure upstream of the turbulators) to p_2 (static pressure of free stream at the ejection slot) in a nozzle having the same exit area A_{slot},

$$C_D = \frac{m_{c,\mathrm{real}}}{m_{c,\mathrm{ideal}}} = \frac{m_{c,\mathrm{real}}}{p_{1t}\left(\frac{p_2}{p_{1t}}\right)^{\frac{\kappa+1}{2\kappa}} A_{\mathrm{slot}} \sqrt{\frac{2\kappa}{(\kappa-1)RT_{1t}}\left[\left(\frac{p_{1t}}{p_2}\right)^{\frac{\kappa-1}{\kappa}} - 1\right]}} \tag{9}$$

Figure 4 shows a comparison of the numerically predicted discharge coefficients and the experimental results for three different blowing ratios M. The predictions of both the steady simulation (k-ω model), as well as the unsteady DES, are in close agreement to the experimental results. With respect to the discharge behavior, there is obviously no need for a costly DES analysis. However, it can be stated that if DES is performed, the resulting discharge coefficients of the trailing edge cooling slots are reliable.

Film Mixing Process and Cooling Effectiveness. As indicated earlier and reported in Refs. [3,5], steady RaNS computations tend to underpredict the film mixing process on the trailing edge cut back. This is exemplarily shown in Fig. 5, where the nondimensional temperature distribution and film cooling effectiveness (laterally averaged) are plotted for a steady computation ($G1, M = 0.80$). The adiabatic film cooling effectiveness is defined as follows:

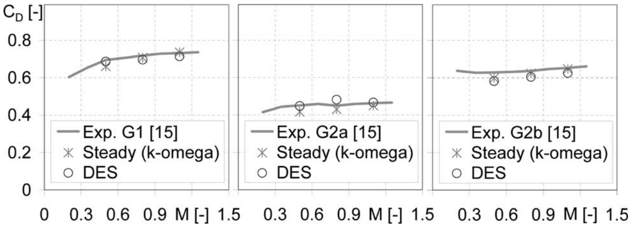

Fig. 4 Discharge behavior of trailing edge coolant slots

$$\eta_{\mathrm{aw}} = \frac{T_{\mathrm{hg}} - T_{\mathrm{aw}}}{T_{\mathrm{hg}} - T_c} \tag{10}$$

In Eq. (10), the static hot gas temperature T_{hg} is utilized which almost equals the stagnation temperature for the present subsonic conditions. T_c is the coolant temperature, measured/predicted at the slot exit in the center between two turbulators.

As illustrated by Fig. 5, at $z/H = 3$ the steady computation predicts a cooling film that protects the cut-back surface almost ideally. In the wake of the rib ($z/H = 0$) turbulent mixing is promoted and locally increases the film temperature. Comparing the laterally averaged film cooling effectiveness of the steady computations with the experimental results, a substantial overprediction becomes visible. While the experiments show a strong decay of film cooling effectiveness for $x/H > 4$, the numerical results remain close to unity over the entire cut-back surface ($L3$ region). Obviously, steady computations are not able to capture the inherent unsteadiness of the flow on the trailing edge cut back.

Consequently, unsteady simulations are conducted with the same turbulence model (SST-k-ω). The unsteady flow is qualitatively revealed in the $L3$ region but the unsteadiness merely appears as a slight wavy structure of the coolant film. Compared to the steady results, the film cooling effectiveness on the cut-back surface ($L3$) remains almost unaltered by this kind of unsteadiness. The unsteady motions seem to be damped out which is not surprising since RaNS models have shown to over-predict eddy viscosity in the separated region downstream of the lip [6].

Since in the LES region DES generally reduces eddy viscosity relative to the RaNS formulation [20], unsteady effects in the flow might be captured more realistically. The instantaneous DES predictions for the double in-line rib array ($G1$) and different blowing ratios are qualitatively shown in Fig. 6. As indicated by the isosurface of constant temperature, vortex shedding from the lip is

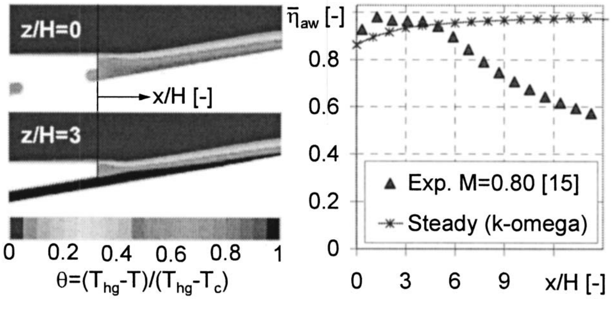

Fig. 5 Nondimensional temperature distribution and laterally averaged film cooling effectiveness ($G1$, $M = 0.80$; steady computation)

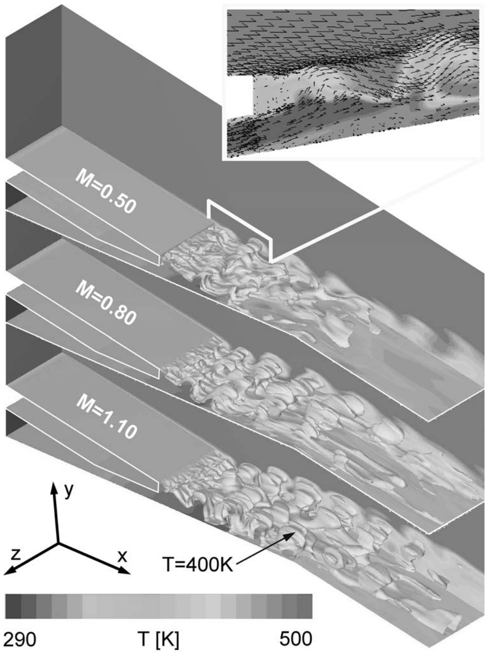

Fig. 6 DES of *G*1: instantaneous contours of static temperature and isosurface ($T=400$ K)

present for all blowing ratios. Superimposed by three-dimensional turbulent eddies, the coherent structures of the shedding can be clearly identified.

In Fig. 7, the nondimensional temperature distribution (instantaneous and time averaged) in the *L*3 region is plotted for the different cooling slots at $M=0.80$. The z coordinate of the planes in Fig. 7 is chosen in such a way that they are located directly between the two turbulators from the last row (closest to the slot exit). The instantaneous results reveal a highly unsteady mixing process, which is influenced by the internal slot design.

Superimposed by turbulent temperature fluctuations, the periodic pattern of vortex shedding from the pressure side lip can be clearly identified for both, the double in-line rib array (*G*1) and the pin-fin configuration with increased lip overhang (*G*2*b*). For *G*2*a*, it seems that the periodic wake flow from the *L*2 turbulators, which are located close to the slot exit, disturbs the generation of vortex shedding behind the blunt lip. In Fig. 7, this is indicated by the more random temperature fluctuations on the cut back. Further on, the instantaneous temperature distribution in the wake of the lip does not indicate the alternate formation of vortices by coolant and hot gas.

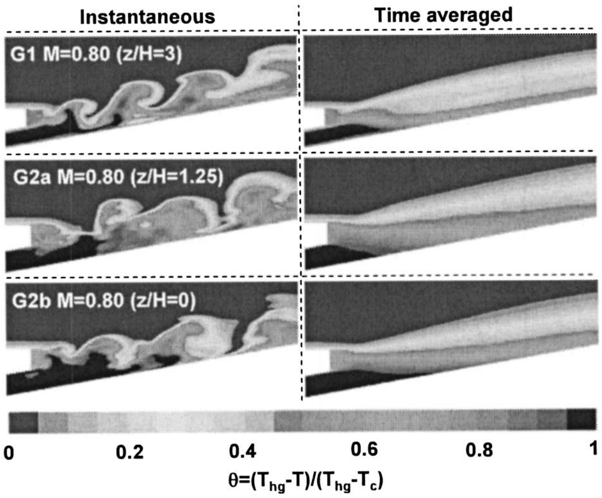

Fig. 7 Instantaneous and time-averaged nondimensional temperature distribution for $M=0.80$ (DES computation)

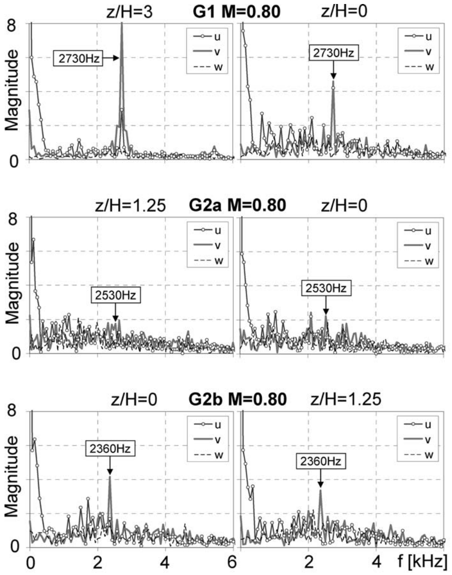

Fig. 8 FFT spectrum of time variant velocity components (u,v,w) at two monitor points ($x/H=4, y/H=1.5$) for $M=0.80$

Compared to the (steady) temperature distribution in Fig. 5, the time-averaged results of Fig. 7 reveal an intensified mixing predicted by the unsteady DES calculations.

To identify the turbulent frequency spectrum of the different configurations, fast Fourier transform (FFT) analyses are conducted using the time variant velocity components (u,v,w) at different locations. There are two monitor points investigated for each configuration. Both have the same nondimensional distance from the slot exit ($x/H=4$) and the *L*3 wall ($y/H=1.5$). The first point is located on the same lateral position as the turbulator from the row closest to the slot exit (*P*1) whereas the second one is laterally shifted by half a pitch relative to the first point (*P*2). Figure 8 shows the FFT frequency spectrum for the velocity components at these two locations for the different cooling slots for $M=0.80$. The three diagrams on the left hand side show the results for *P*2 whereas the diagrams on the right hand side illustrate the frequency spectrum obtained for the points *P*1.

For *G*1 (upper row), caused by vortex shedding from the pressure side lip, distinct peaks of u and v can be observed for $f=2.73$ kHz. Defining a Strouhal number based on the lip thickness and the arithmetic mean value of coolant velocity (mass averaged at slot exit) and hot gas velocity results in a value of $\mathrm{Sr}=0.24$.

The frequency spectrum at the point between the ribs ($G1, z/H=3$) is dominated by vortex shedding from the lip whereas the turbulent noise is quite low (note that the large magnitude of u at low frequencies is caused by the constant component of the signal). Although this seems to be not unrealistic, the periodic boundary condition might also affect the spectrum at $z/H=3$. The situation changes, if the view is focused to the point downstream of the rib ($G1, z/H=0$). Although the peak at 2.73 kHz is still pronounced, the turbulent fluctuations in the wake of the rib cause a broad band of peaks at lower as well as higher frequencies.

Focusing on *G*2*a* (Fig. 8, middle row) a pronounced peak in the frequency spectrum is missing. Assuming $\mathrm{Sr}=0.24$, such a peak would be expected for $f=2525$ Hz. Smaller peaks from the v component can be identified for both monitor points at 2530 Hz.

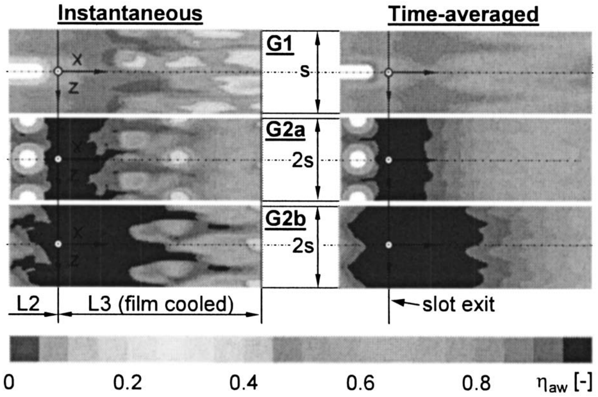

Fig. 9 Distribution of instantaneous and time-averaged film cooling effectiveness for different cooling slots and $M=0.80$

These might be attributed to vortex shedding from the lip. Nevertheless, the frequency spectra support the previous statement that the complex flow situation at the slot exit disturbs the formation of vortex shedding in the present case.

G2b (Fig. 8, lower row) shows a qualitatively similar broadband spectrum than is observed for *G2a*. However, for both monitor points ($z/H=0$ and $z/H=1.25$), vortex shedding causes clear peaks in the v component. The corresponding frequency of $f=2.36$ kHz leads again to the same Strouhal number that is previously detected for *G1a* (Sr=0.24).

The different magnitudes of the velocity components, shown Fig. 8 support the statement of anisotropic turbulence in the near slot region.

Figure 9 shows the instantaneous and time averaged distribution of the adiabatic film cooling effectiveness on the cut-back surface for the three investigated trailing edge cooling slots for $M=0.80$. The instantaneous results reveal how the unsteady flow regime affects cooling on the cut-back surface. Downstream of the core region where wall temperatures are almost unaffected by the main flow, the film is locally broken up. Hot fluid is transported close to the wall, diminishing the adiabatic film cooling effectiveness. Focusing on the time-averaged results, the pin fin arrays (*G2a,b*) show a laterally more uniform film cooling effectiveness than the double in-line rib array (*G1*). This is qualitatively confirmed by the measurements. For *G1*, the experiments reveal a lateral maximum of η_{aw} in the wake of the ribs when M ranges between 0.65 and 1.10. At $M=0.80$, this is not captured by the DES computations. Here, the peaks of η_{aw} are located laterally of the wake but not in the wake itself.

However, as the blowing ratio is increased to $M=1.10$, the predictions show the characteristic peak film cooling effectiveness in the wake of the rib, similar to the experiment.

For a quantitative comparison between numerical predictions and the experiment, the adiabatic film cooling effectiveness is laterally averaged over a single pitch. Figure 10 shows the results for all trailing edge cooling slots and blowing ratios considered in the numerical study. For each blowing ratio, the steady (k-ω) and DES calculations are compared to the corresponding experimental results. The upper row contains the results for the double in-line rib array (*G1*), the middle row for the pin fin array with *L2* pins (*G2a*). Finally, the lower row shows the laterally averaged film cooling effectiveness for the pin-fin configuration without *L2* pins (*G2b*).

As expected, the decay of adiabatic film cooling effectiveness is not correctly captured by the steady simulations, leading to substantial over-predictions of η_{aw} at the end of the cut-back surface (*L3* region).

In contrast to the steady computations, the DES results show significantly better agreement to the experiments. Especially for the pin-fin arrays (*G2a*,*G2b*), the predictions of film cooling effectiveness on the cut-back surface are excellent. For the double in-line rib array (Fig. 10, upper row), however, the adiabatic film cooling effectiveness is underpredicted by DES.

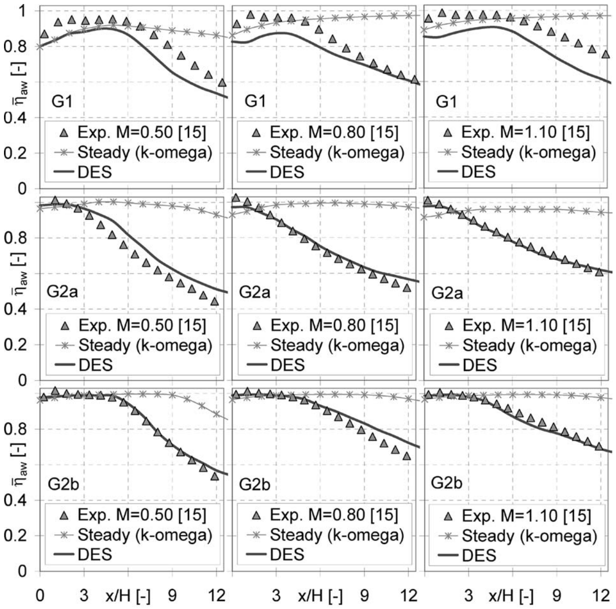

Fig. 10 Laterally averaged film cooling effectiveness for different blowing ratios *M* (upper row: *G1*; middle row: *G2a*; lower row: *G2b*)

This can be partly attributed to the temperature boundary condition used on the bottom wall of *L1*, the converging section of the coolant cavity. As previously stated, a constant wall temperature, the lip temperature of *L2*, is assumed for all metal parts upstream of *L3*. In the experiment, however, the lower wall of *L1* is unheated and, hence, cooler than the lip. In the pin-fin arrays, this plays no major role since the staggered turbulators promote intensive mixing of the coolant. This leads to an almost uniform temperature profile for the coolant at the slot exit hence $\eta_{\mathrm{aw}}\approx 1$ at the beginning of *L3*. As indicated by Fig. 9, for *G1*, the thermal boundary layer imposed on the coolant in *L1* is not fully mixed out on the lower (adiabatic) wall in *L2* since the turbulence between the ribs is relatively low. This explains the underprediction of film cooling effectiveness in the immediate vicinity of the slot exit. Using a lower temperature for the bottom wall in *L1* would increase the film cooling effectiveness in the core region of *G1* where experimental values are close to unity. Whether or not the boundary condition in *L1* accounts for the underpredictions of η_{aw} in the decay region of *L3* for *G1*($M=0.5;1.1$), is an open question that makes further investigations necessary.

Heat Transfer Coefficients. In addition to η_{aw}, a thorough characterisation of film cooling performance includes convective heat transfer on the trailing edge cut back. The heat transfer coefficient, h_f, is defined as follows:

$$h_f=\frac{q_{\mathrm{conv}}}{T_{\mathrm{aw}}-T_w}=\frac{q_{\mathrm{conv}}}{(T_{\mathrm{hg}}-T_w)\left(1-\eta_{\mathrm{aw}}\dfrac{T_{\mathrm{hg}}-T_c}{T_{\mathrm{hg}}-T_w}\right)} \tag{11}$$

For the numerical calculations, the convective wall heat flux, q_{conv}, prescribed downstream of the ejection slot, is an area averaged mean value taken from the experiments.

From Eq. (11) it is clear that for determining the heat transfer coefficients the corresponding computations with an adiabatic cut-back surface (but unchanged flow conditions) are relevant, since

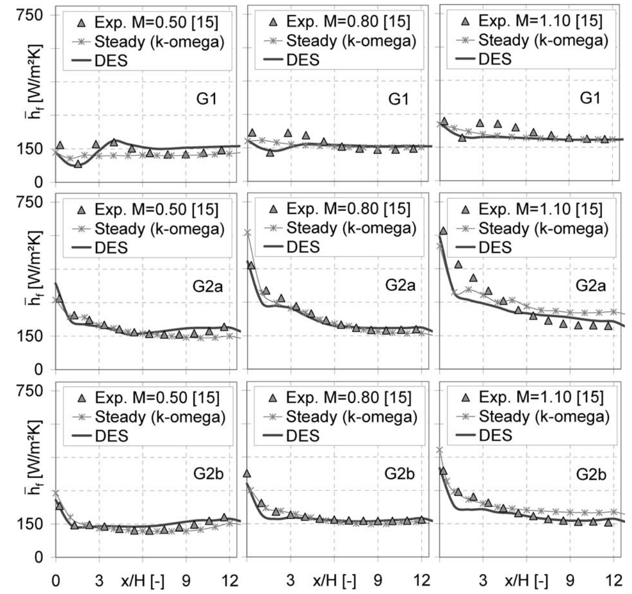

Fig. 11 Laterally averaged heat transfer coefficient for different blowing ratios *M* (upper row: *G*1; middle row: *G2a*; lower row: *G2b*)

the driving temperature difference is $(T_{\mathrm{aw}}-T_w)$.

The quality of steady and DES predictions on heat transfer along the cut-back surface is assessed in Fig. 11. It shows the laterally averaged, heat transfer coefficients downstream of the ejection for all trailing edge cooling slots and blowing ratios considered in the present study. With respect to heat transfer coefficients, the predictions of both, the steady and DES calculations are quite good. Interestingly, for the steady RaNS computations, where adiabatic wall temperatures (i.e., η_{aw}) are poorly predicted, good agreement to the experimentally derived heat transfer coefficients can be stated.

From Fig. 11, one might argue that the heat transfer coefficient on the trailing edge cut-back surface is not significantly affected by the mixing of hot gas and coolant. However, the convective heat transfer (q_{conv}) is, since mixing directly influences the driving temperature difference $(T_{\mathrm{aw}}-T_w)$.

Focusing on the DES predictions, similar levels compared to the steady RaNS results can be observed. In this context, it should be reminded again that in the viscous near wall region, DES functions as an unsteady RaNS model. For the double in-line rib array ($G1$, upper row in Fig. 11) it seems that DES captures the heat transfer near the ejection slot somewhat better since the local minimum of h_f caused by a coolant flow separation is correctly predicted. Not resolved by the steady simulation, vortex shedding affects the pressure distribution near the lip and, hence, directly impacts on the extension of the separation bubble. The following increase of h_f downstream of the separation zone is also captured by DES but for blowing ratios of $M=0.80$ and 1.10 the predictions are too low.

Downstream of the pin-fin arrays (second and third row in Fig. 11) DES and steady k-ω computations provide excellent solutions of h_f with respect to the lower blowing ratios $M=0.50$ and 0.80. For the highest blowing ratio $(M=1.10)$ the steady simulations tend to over-predict heat transfer at $x/H>5$ whereas near the slot exit DES (and partly k-ω) computations of h_f are lower than indicated by the experimental results. In summary, it can be ascertained that even though DES shows slightly improved performance, also steady RaNS computations provide good engineering accuracy in predicting h_f on the trailing edge cut back.

Summary and Conclusions

A comprehensive numerical study has been conducted concentrating on the prediction of film cooling performance downstream of internally ribbed trailing edge cooling slots. In addition to the effects from the internal cooling design, vortex shedding from the blunt pressure side lip may substantially intensify the mixing on the cut back. In the present case, vortex shedding is identified for the rib array $(G1)$ and the pin fin array with increased lip overhang $(G2b)$. In case of $G2a$ (pin-fin array with turbulators close to the slot exit), the evolution of vortex shedding seems to be disturbed by the presence of the $L2$ pins. However, in all three cases, the mixing of the film is an unsteady process being affected by turbulent wake flow instabilities from either the lip and/or the turbulators. That is why steady RaNS computations fail to predict film cooling effectiveness. Although, in the present case, unsteady RaNS calculations capture some of these effects qualitatively, these models tend to damp out unsteady motions and thus over-predict film cooling effectiveness. The main objective of the present work was to investigate whether the relatively new DES model might improve the predictions for film cooling performance on the trailing edge cut back. The key results can be summarized as follows.

DES provides reliable results on the discharge coefficients (C_D) of the different cooling slots. However, also steady RaNS computations perform quite well in this context. So, with respect to the discharge behaviour, time-consuming unsteady calculations do not seem to be mandatory.

Focusing on the adiabatic film cooling effectiveness, the detached eddy simulation shows very good agreement to the experimental results, indicating that the complicated unsteady mixing process between coolant and hot gas is captured more realistically. Superimposed by large turbulent eddies, the coherent structures of vortex shedding can be clearly identified for $G1$ and $G2b$. Confirming former numerical URaNS studies by other authors [4], this flow pattern is involved in the fast decay of adiabatic film cooling effectiveness on the cut back, provided that the coolant flow at the slot exit is not too much disturbed by the internal cooling design.

An advantage of the DES approach is that potential flow instabilities are triggered automatically by resolved turbulent fluctuations. So no artificial excitation (e.g., induced by random pressure perturbations) of the flow is required in the present case.

FFT frequency analyses of the velocity components downstream of the lip reveal a Strouhal number of 0.24 for the shedding process. Furthermore, the FFT analyses underline that the turbulence on the cut back is anisotropic and locally influenced by the internal turbulators.

For a complete characterisation of the film cooling performance on the trailing edge cut-back surface, the in-depth understanding of convective heat transfer is mandatory. In this regard, the detached eddy simulation shows very promising results. For low and intermediate blowing ratios, the predictions of the laterally averaged heat transfer coefficients are in close agreement to the experimental outcomes. For high blowing ratios, DES shows the tendency to under-predict h_f in the direct vicinity of the slot exit $(x/H<3)$ but approaches the experimental results further downstream. However, with respect to the heat transfer coefficients, the results obtained by “simple” steady RaNS computations are good as well. This might be regarded as an indication for a relatively weak influence of unsteady mixing on the heat transfer coefficient. Further studies are necessary to verify this statement. Beyond it, future investigations will also address to the sensitivity of the DES results on grid refinement, which was outside the scope of the present work.

Finally, the present study suggests that DES is well suited for the prediction of trailing edge film cooling. Especially with regard to the film mixing process significant improvements can be stated, which seem to justify the increased amount of computational resources.

Acknowledgment

The reported work was performed within a research project that is part of the European project "AITEB—Aerothermal Investigation of Turbine Endwalls and Blades" (5FP, G4RD-CT-1999-00055). The permission for the publication is gratefully acknowledged by the authors. Finally, the first author would like to thank Dr. Jonas Larsson from Volvo Aero Corporation for his valuable input on the DES solution strategy.

Nomenclature

A_{slot}, m^2 = overall slot area at slot exit ($A_{\mathrm{slot}}=S\times H$)
C_D, - = discharge coefficient
d, m = hole diameter
d, m = length scale (dist. to the closest wall)
$\tilde{d}$, m = modified length scale (Eq. (4))
f, 1/s = frequency
H, m = slot height
h_f, $\mathrm{W/(m^2\,K)}$ = heat transfer coefficient (Eq. (11))
k, $\mathrm{m^2/s^2}$ = turbulent kinetic energy
M, - = blowing ratio ($M=m_c/(A_{\mathrm{slot}}\rho_{\mathrm{hg}}\mathrm{u_{hg}})$)
m_c, kg/s = coolant mass flow rate
p_{1t}, Pa = total pressure of coolant upstream of $L1$
p_2, Pa = static pressure at the slot exit
p_{hg}, Pa = static pressure of hot gas
q_{conv}, $\mathrm{W/m^2}$ = convective heat flux
R, J/(kg K) = ideal gas constant ($R=287.22$ J/(kg K))
s, m = lateral pitch between two ribs or pins
S, m = overall coolant slot width
Sr, - = Strouhal number ($\mathrm{Sr}=f\times l_{\mathrm{char}}/u$)
t, m = lip thickness
T_{1t}, K = total coolant temperature upstream of $L1$
T_{aw}, K = adiabatic wall temperature
T_c, K = coolant temperature at the slot exit
T_{hg}, K = static temperature of hot gas
Tu, - = turbulence intensity
T_w, K = wall temperature
u, m/s = velocity
u_i, m/s = velocity component
x, m = streamwise dist. downstream of slot exit
y, m = coordinate normal to the cut back ($L3$)
z, m = spanwise coordinate

Greek

δ_1, m = displacement thickness
η_{aw}, - = ad. film cooling effectiveness (Eq. (10))
κ, - = ratio of specific heats
μ, Pa s = dynamic viscosity
μ_t, Pa s = turbulent dynamic viscosity
ν, $\mathrm{m^2/s}$ = kinematic viscosity
$\tilde{\nu}$, $\mathrm{m^2/s}$ = modified turbulent kinematic viscosity
ρ, $\mathrm{kg/m^3}$ = density
ω, 1/s = specific dissipation rate

References

[1] Goldstein, R. J., 1971, "Film Cooling," Adv. Heat Transfer, **7**, pp. 321–379.
[2] Taslim, M. E., Spring, S. D., and Mehlmann, B. P., 1990, "An Experimental Investigation of Film Cooling Effectiveness for Slots of Various Exit Geometries," AIAA J.
[3] Holloway, D. S., Leylek, J. H., and Buck, F. A., 2002, "Pressure Side Bleed Film Cooling: Part 1—Steady Framework for Experimental and Computational Results," ASME Paper No. GT-2002-30471.
[4] Holloway, D. S., Leylek, J. H., and Buck, F. A., 2002, "Pressure Side Bleed Film Cooling: Part 2—Unsteady Framework for Experimental and Computational Results," ASME Paper No. GT-2002-30472.
[5] Martini, P., Schulz, A., Whitney, C. F., and Lutum, E., 2003, "Experimental and Numerical Investigation of Trailing Edge Film Cooling Downstream of a Slot With Internal Rib Arrays," Proc. Inst. Mech. Eng., Part A, **217**, pp. 393–401.
[6] Jansson, L. S., Davidson, L., and Olsson, E., 1994, "Calculation of Steady and Unsteady Flows in a Film-Cooling Arrangement Using a Two-Layer Algebraic Stress Model," Numer. Heat Transfer, Part A, Part A, **25**, pp. 237–258.
[7] Spalart, P. R., Jou, W. -H., Strelets, M., and Allmaras, S. R., 1997, "Comments on the Feasibility of LES for Wings, and on a Hybrid RANS/LES Approach," 1st AFOSR Int. Conf. on DNS/LES, 4–8, Aug. 1997, Ruston, LA, *Advances in DNS/LES*, C. Liu, and Z. Liu eds., Greyden Press, Columbus, OH.
[8] Kapadia, S., Roy, S., and Wurtzler, K., 2003, "Detached Eddy Simulation Over a Reference Ahmed Car Model," AIAA Paper.
[9] Viswanathan, A. K., Squires, K. D., and Forsythe, J. R., 2003, "Detached Eddy Simulation of the Flow Over an Axisymmetric Cavity," AIAA Paper.
[10] Kim, S. -E., Cokljat, D., and Liu, F., 2002, "DES of Turbulent Flow Over an Airfoil at High Incidence," AIAA Paper.
[11] Squires, K. D., Forsythe, J. R., and Spalart, P. R., 2001, "Detached-Eddy Simulation of the Separated Flow Around a Forebody Cross-Section," *Direct and Large Eddy Simulation—IV* (ERCOFTAC SERIES 8), B. G. Geurts and R. Friedrich, eds., Kluwer, Dordrecht, December, pp. 481–500.
[12] Pandya, M. J., Frink, N. T., et al., 2004, "Recent Enhancements to USM3D Unstructured Flow Solver for Unsteady Flows," AIAA Paper.
[13] Roy, S., Kapadia, S., and Heidmann, J. D., 2003, "Film Cooling Analysis Using DES Turbulence Model," AIAA Paper.
[14] Kapadia, S., Roy, S., and Heidmann, J. D., 2004, "First Hybrid Turbulence Modeling for Turbine Blade Cooling," Int. J. Thermophys. **18**(4), pp. 154–156.
[15] Martini, P., Schulz, A., and Bauer, H. -J., 2005, "Film Cooling Effectiveness and Heat Transfer on the Trailing Edge Cut-back of Gas Turbine Airfoils With Various Internal Cooling Designs," ASME Paper No. GT2005-68083.
[16] Menter, F. R., 1994, "Two-Equation Eddy-Viscosity Turbulence Models for Engineering Applications," AIAA J., **32**(8), pp. 1598–1605.
[17] FLUENT 6.1 User's Guide, 2003, FLUENT Inc., Chap. 10, pp. 1–82.
[18] Spalart, P., and Allmaras, S., 1992, "A One-Equation Turbulence Model for Aerodynamic Flows," Paper No. AIAA-92-0439.
[19] Lilly, D. K., 1966, "On the Application of the Eddy Viscosity Concept in the Inertial Subrange of Turbulence," NCAR Manuscript 123.
[20] Spalart, P. R., 2001, "Young-Person's Guide to Detached-Eddy Simulation Grids," NASA/CR-2001-211032, pp. 1–23.
[21] ALESSIA Report, 2002, "EP 28189: Application of Large Eddy Simulation to the Solution of Industrial Problems, Best Practice Guide: LES and Acoustics," Issue 1, Internal version 1.4.
[22] Sieverding, C. H., and Heinemann, H., 1990, "The Influence of Boundary Layer State on Vortex Shedding From Flat Plates and Turbine Cascades," ASME J. Turbomach., **112**, pp. 181–187.

P. J. Newton
G. D. Lock
Department of Mechanical Engineering,
University of Bath,
Bath, UK

S. K. Krishnababu
H. P. Hodson
W. N. Dawes
Department of Engineering,
University of Cambridge,
Cambridge, UK

J. Hannis
Siemens Industrial Turbomachinery Ltd.,
Lincoln, UK

C. Whitney
Alstom Power Technology Centre,
Leicester, UK

Heat Transfer and Aerodynamics of Turbine Blade Tips in a Linear Cascade

Local measurements of the heat transfer coefficient and pressure coefficient were conducted on the tip and near tip region of a generic turbine blade in a five-blade linear cascade. Two tip clearance gaps were used: 1.6% and 2.8% chord. Data was obtained at a Reynolds number of 2.3×10^5 *based on exit velocity and chord. Three different tip geometries were investigated: A flat (plain) tip, a suction-side squealer, and a cavity squealer. The experiments reveal that the flow through the plain gap is dominated by flow separation at the pressure-side edge and that the highest levels of heat transfer are located where the flow reattaches on the tip surface. High heat transfer is also measured at locations where the tip-leakage vortex has impinged onto the suction surface of the aerofoil. The experiments are supported by flow visualization computed using the CFX CFD code which has provided insight into the fluid dynamics within the gap. The suction-side and cavity squealers are shown to reduce the heat transfer in the gap but high levels of heat transfer are associated with locations of impingement, identified using the flow visualization and aerodynamic data. Film cooling is introduced on the plain tip at locations near the pressure-side edge within the separated region and a net heat flux reduction analysis is used to quantify the performance of the successful cooling design.* [DOI: 10.1115/1.2137745]

1 Introduction

In a gas turbine a gap between the rotating blade tip and the stationary casing is needed to allow relative motion. In an unshrouded turbine stage this tip gap is nominally of the order 1% of blade height. The difference in pressure between the pressure and suction aerofoil surfaces drives hot mainstream flow through the gap between the tip of the rotating blade and the surrounding casing. The leakage is essentially axial, i.e., orthogonal to the casing motion. The flow separates at the pressure-side edge and, depending on the blade thickness, reattaches downstream. At the exit of the clearance the mixed-out flow meets the mainstream on the suction side and rolls up into a vortex. Geometric changes to the blade tip can be effective in reducing the leakage flow. A current design features a recessed tip, known as a squealer, where the tip gap can be made smaller without risk of significant tip contact with the casing. In addition to mechanical benefits, the recess also acts as a labyrinth seal, increasing resistance to the flow.

This tip leakage has a detrimental effect on the stage efficiency. Aerodynamic losses occur due to viscous effects within the tip gap itself and due to mixing losses when the leakage flow interacts with the passage flow. Furthermore there is a reduction in work output from the stage as the leakage flow exits unturned, though some of this work may be recovered in latter stages of a multistage turbine. Booth et al. [1] estimated that a tip clearance gap of 1% blade height potentially leads to losses of 1%–3% in stage efficiency. Manufacturing tolerances, centrifugal expansion and dissimilarity between the thermal loading of the blade row and casing leads to nonuniform clearance gaps around the annulus. Geometric changes to the tip profile (such as squealers or cavities) are commonly used to improve stage performance.

Another important consequence is the deterioration of the blade tip surface due to regions of high local heat transfer in the narrow gap. The thinning of the pressure-side boundary layer as the leakage flow accelerates into the tip gap causes a rapid rise in heat transfer on entry to the tip gap. Additionally the high velocity mixing within the tip gap itself causes some of the highest heat transfer rates on the blade in what is a very difficult region to cool effectively. The high velocity leakage flow exiting the tip gap creates leakage vortices which impinge onto the suction surface and create further localized regions of elevated heat transfer. All of these factors make the blade tip one of the regions in the engine that limits performance and demands frequent inspection. It is, therefore, important to understand the aerodynamics and heat transfer within the gap in order to introduce new tip designs that might reduce the leakage flow.

This paper presents experiments and computations relating to such flows modeled using generic, blade-tip geometries in an engine-simulated environment. No relative motion between the tip and casing is present in this study and it is assumed that the flow through such clearances is essentially driven by pressure difference. This has been verified by Mayle and Metzger [2] and later Srinivasan and Goldstein [3] who have shown that the shear-stress distribution within such gaps is unaffected by relative motion at 100% engineering equivalent speed and that no measurable change in heat transfer occurred for tip-gap to chord ratios greater than 0.86%.

A review of research quantifying the losses and heat transfer associated with tip clearance flow is provided by Bunker [4]. Much of the early work used idealized models, e.g., Kim and Metzger [5] and Chen et al. [6]. More recently much data has been published using linear cascades: Bunker et al. [7] measured heat transfer for sharp and radiused-edged blades for different clearance gaps; Kwak and Han [8,9] used the transient liquid crystal

---

Contributed by the International Gas Turbine Institute (IGTI) of ASME for publication in the Journal of Turbomachinery. Manuscript received October 1, 2003; final manuscript received March 1, 2004. IGTI Review Chair: A. J. Strazisar. Paper presented at the International Gas Turbine and Aeroengine Congress and Exibition, Vienna, Austria, June 13–17, 2004, Paper No. 2004-GT-69034.

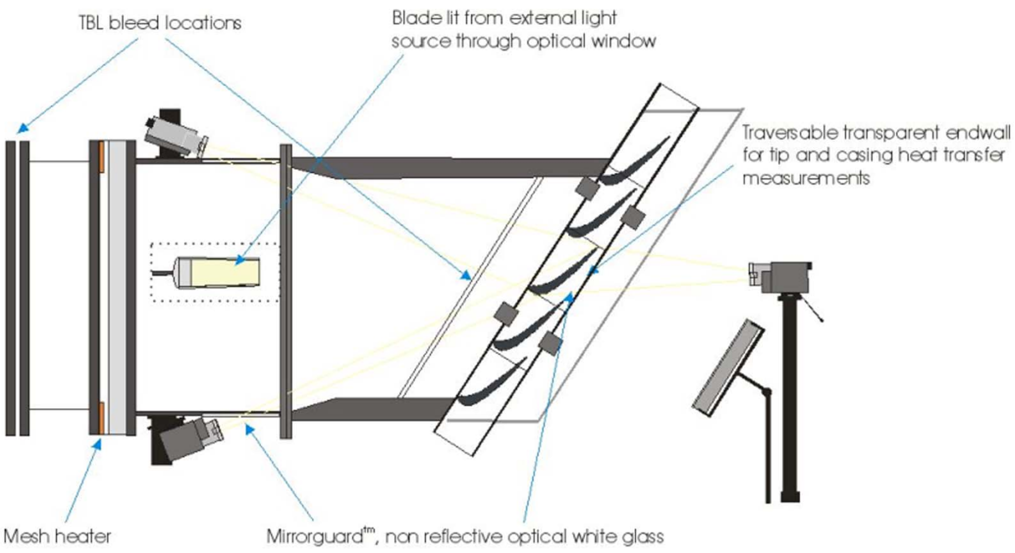

Fig. 1 Low speed cascade modified for heat transfer measurements

technique and Jin and Goldstein [10] the naphthalene technique to determine the effects of clearance gap, turbulence intensity and Reynolds number on the mass/heat transfer from the tip and near-tip surfaces.

This study explores the effects of introducing suction-side and cavity squealers. Film cooling is introduced at locations designed to optimize, in terms of both aerodynamics and heat transfer, the performance of the tip gap. Experimental measurements of heat transfer coefficient and film-cooling effectiveness using the transient liquid crystal technique are described. Pressure measurements, flow visualization and computational results are used to link the aerodynamic and heat transfer characteristics of the flow.

2 Experimental Procedure

The experiments were conducted in the Whittle Laboratory at the University of Cambridge. A schematic of the low-speed linear cascade is shown in Fig. 1. A variable-speed centrifugal fan was used to drive air through a five-blade cascade where it exits to atmosphere. Salient features of the cascade are listed in Table 1 and further detail is available in Heyes et al. [11], who used the same cascade. The blades were cantilevered from the "hub" by a screw arrangement that allows the tip clearance gap to be set. All measurements were made about the central blade in the cascade. The "casing" endwall could be interchanged with transparent windows providing optical access to the blade tip and aerofoil surfaces. The Reynolds number, based on exit velocity and chord, was 2.3×10^5.

The cascade has the same geometry as a two-stage HP version of the Peregrine (Hodson et al. [12]) which itself is based on an actual HP turbine. Three tip-gap geometries were tested: Plain tip, suction-side squealer, and cavity squealer. Referring to Fig. 2, two tip-gap heights, $H = 3.7$ and 6.35 mm (1.6% and 2.8% chord) were used. The cavity and suction-side (SS) squealer geometries were designed in consultation with Siemens and Alstom, and based on the results of Part 1. The SS squealer was defined by offsetting the SS wall by 5 mm. The squealer starts on the chord line and continues until it meets with the pressure surface at the trailing edge. The cavity tip is characterized by offsetting the blade profile internally by 5 mm. At the trailing edge of the blade the cavity

Table 1 Details of low speed cascade

Chord, c	225 mm
Axial chord, C_x	103 mm
Pitch/chord ratio, s/C	0.824
Aspect ratio	2.11
Stage exit Re_c	2.3×10^5
Inlet flow angle, α_1	32.5°
Blade exit angle, α_2	75.6°
Practical tip clearance	3.7–6.35 mm
Mass flow rate	1.6 kg/s
Max thickness/chord	14%

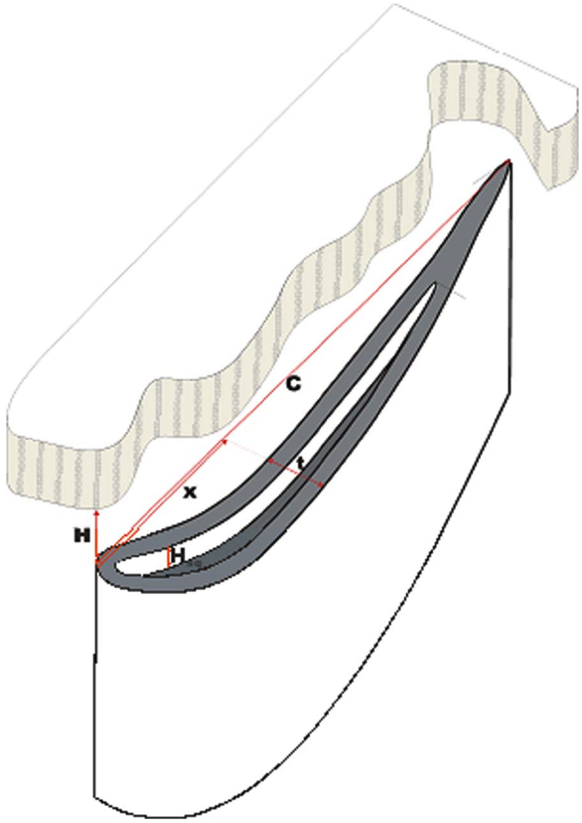

Fig. 2 Definition of blade parameters

closes at $x/C=0.75$ because it was machined using a 1 mm cutting tool. The squealers were sufficiently wide to provide some heat transfer data on their surface but thin enough to prevent reattachment. The cavity depth will affect the aerodynamics and heat transfer in the tip gap. The geometry and dimensions were based on a current Siemens design and on practical considerations. The cavity depth has not been considered as a parameter in this study. Note this is a three-dimensional (3D) study the ratio of cavity depth to gap varies with chord.

Most aerodynamic measurements were made on the casing but tip and aerofoil surface data was also available for the plain-tip geometry. The blade used for aerodynamic measurements was moulded from glass-fiber reinforced-epoxy in a CNC machined aluminium mould. During the moulding process a nylon string of 1 mm diameter was placed radially on the gel coat of the central blade. Once the epoxy set these strings were withdrawn and the resulting holes acted as pressure conduits for 16 subsequently drilled rows of chord-wise pressure tappings about the blade surface. Twenty-one cross-chord slots of 1 mm width were then milled into the tip interface, interfacing with the pressure-side conduits. These were used to gain tip pressure data using the micro tapping technique described by Bindon [13].

Static pressure data was also gathered using a traversing endwall. The endwall was traversed in a pitchwise direction using a computer-controlled stepper motor. Two rows of 21 pressure tapping holes located one blade pitch apart were used to measure endwall static pressure over the tip of the central blade and adjacent passages. All aerodynamic measurements were carried out using two cross-calibrated Scanivalve units.

The heat transfer experiments were performed on a polycarbonate replica of the cascade blades. Two replicas were made, a solid plain tip blade and a hollow blade with interchangeable tips for the film cooling and squealer investigations. Tip pieces were also constructed from Rhoacell, a low-conductivity machinable foam used to create an adiabatic surface. Heat transfer was measured using thermochromic liquid crystal (TLC). The method of analysis is described in the next section. Both narrow-band and wide-band liquid crystal were used. The color-play of the TLC was recorded with three digital video cameras. The traversing endwall used for pressure measurements was replaced with a similar polycarbonate endwall with an optical window. Optical access was also gained to the pressure and suction aerofoil surfaces as well as the leading edge. The use of a single narrow band crystal negated the potential errors associated with the viewing of TLC color-play under oblique lighting upon curved surfaces. To accurately remodel the blade surface from the three video feeds, the blade was marked with a radial grid which was used in an automated program to calculate camera angle. Due to the relatively large range of heat transfer rates measured, a number of experiments were performed at various nondimensional temperatures ($0.3<\theta<0.6$—see next section) to alleviate time errors at high heat transfer coefficients and conduction errors at low heat transfer coefficients.

There have been many published references regarding the effect of viewing angle on the calibration of both wide and narrow band TLC. Ireland and Jones [14] and Farina et al. [15] are good examples. The crystals used here were calibrated both in situ and using an isothermal copper-block calibration apparatus where the lighting and illumination angles were varied between 0 and 30 deg. This calibration method and apparatus is described in detail in Syson et al. [16]. Small uncertainties in the temperature obtained from the calibration were ±0.2 C. This amplifies to an uncertainty in heat transfer coefficient of approximately 3%, as explained by Owen et al. [17].

Fig. 3 The mesh heater

A hot mainstream flow was generated using an upstream wire mesh (Gillespie et al. [18]) powered by a 15 kW welder, shown in Fig. 3. Due to the large mass flow through the cascade (~ 2.8 kg/s), only the flow entering the tip gap was heated, the remaining flow passing through a cold mesh adjacent to the heater mesh. The heater mesh had a high aspect ratio of 6 and a thicker than typical wire diameter was employed in order to reduce the mesh resistance such that the welder could deliver maximum power at 50 V DC. An aerofoil profile within the mesh assembly was used to help prevent the hot flow from mixing with the unheated flow. Traverse profiles indicated minimal mixing between the heated and unheated flows and a homogenous temperature profile entering the blade row. Boundary layer bleeds were implemented on the endwall to eliminate the thermal boundary layer. Area traverses upstream of the blade row have shown temperature field distortion within the region of interest to be less than 0.1°C with the heater mesh on.

The mesh heater created an effective step-change in the air temperature immediately downstream, but at the cascade an exponential-type rise in air temperature was measured using a high-frequency thermocouple. A light emitting diode (LED) was used as a visual trigger to indicate the initialization of the welder, and hence the mesh, in the experiment. The distance between the mesh and the leading edge of the central blade divided by the flow velocity synchronised the thermocouple data and TLC color-play video. The time taken for the surface to locally reach a predetermined hue, corresponding to the maximum intensity of green light, was recorded and the thermocouple temperature history was resolved as a series of exponentials as described in the next section.

Film cooling experiments were performed using a single reservoir inside the blade. The temperature of the pressurised coolant flow was controlled carefully. Thermocouples and a total pressure probe were located inside the blade and three tubes insulated with Rhoacell, running through the length of the blade to holes in the hub, supplied coolant to the tip. A flow meter was used to gauge

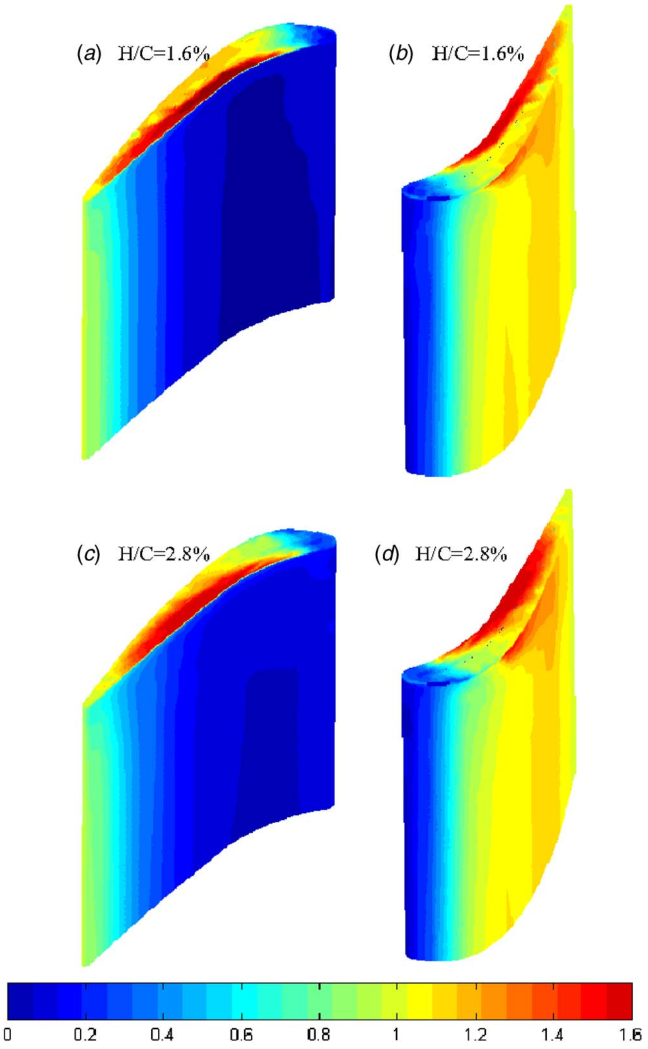

Fig. 4 C_p Contours as measured on the blade and tip

the coolant flow rate. Each film-cooling hole was lined with 1 mm of Rhoacell to reduce two-dimensional (2D) conduction effects around the holes.

3 Transient Heat Transfer Technique

This section describes the experimental technique used to measure the heat transfer coefficient using themochromic liquid crystals. Further details of the theory are available in Shultz and Jones [19], Ireland and Jones [14] and Newton et al. [20].

The heat transfer coefficient, h, is defined as

$$q_w = h(T_{aw} - T_w) \tag{1}$$

where q_w is the surface heat flux from the air to the wall, T_w is the surface temperature of the wall, and T_{aw} is the adiabatic-wall temperature. T_{aw} depends on the total-temperature of the air, T_a, and, in cases where compressibility is an issue, on the fluid dynamics.

In a typical transient test, an abrupt change in air temperature is generated, and narrow-band TLC is used to determine the surface temperature, T_w, of the test piece. Knowing the time, t, at which the surface reaches T_w, h (assumed time-invariant) can be calculated from the solution of Fourier's one-dimensional conduction equation for the case of a semi-infinite plate.

In the tests reported here, the mesh heater created an effective step-change in the air temperature, but at the test section an exponential-type rise in air temperature was produced. Newton et al. [20] show that the adiabatic wall temperature, T_{aw}, could be fitted by an exponential series of m terms, such that

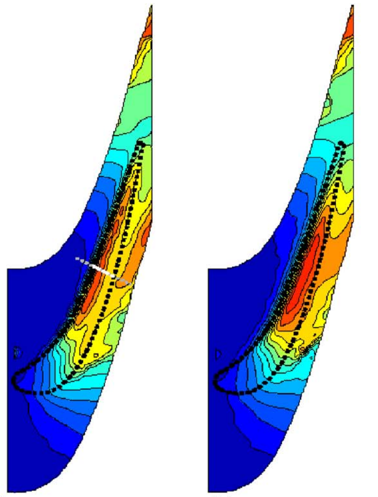

(a) Plain Tip H/C=1.6% (b) Plain Tip H/C=2.8%

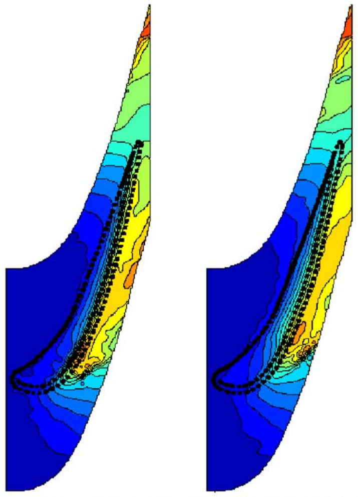

(c) SSS Tip H/C=1.6% (d) SSS Tip H/C=2.8%

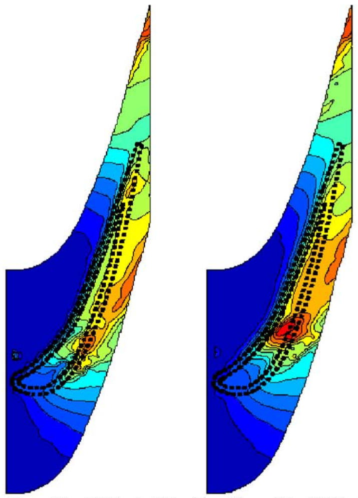

(e) Cav. Tip H/C=1.6% (f) Cav. Tip H/C=2.8%

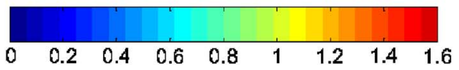

Fig. 5 C_p Contours as measured on the casing

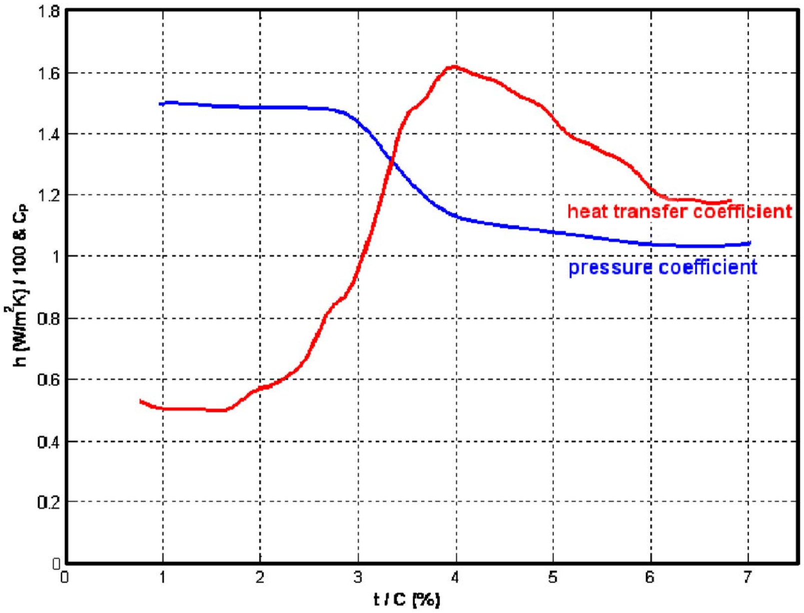

Fig. 6 Cross-chord measurements of C_p and h at $x/C=50\%$ $H/C=1.6\%$

$$T_{aw}(t)=T_{a,0}+\sum_{j=1}^{m}T_{a,j}(1-e^{-t/\tau_j}) \quad (2)$$

where $T_{a,0}$ is the air temperature at $t=0$, $T_{a,j}$, and τ_j are the constant amplitudes and time-constants, respectively. As $t\rightarrow\infty$,

$$T_{aw,\infty}=T_0+\sum_{j=1}^{m}T_{a,j} \quad (3)$$

where T_0 is the initial temperature of the wall, such that

$$T_0=T_{a,0} \quad (4)$$

Fourier's conduction equation for a semi-infinite slab has been solved by Gillespie et al. [21] for the case where there is a simple exponential increase in the air temperature, corresponding to the case where $m=1$ in Eq. (3). The solution is

$$\theta=\frac{T_w-T_0}{T_{aw,\infty}-T_0}=g(\beta,\beta_\tau) \quad (5)$$

where

$$g(\beta,\beta_\tau)=1-\frac{1}{1+\beta_\tau^2}e^{\beta^2}\operatorname{erfc}(\beta)-e^{-t/\tau}\frac{\beta_\tau^2}{1+\beta_\tau^2}\times\left\{1+\frac{1}{\beta_\tau}\left[\frac{1}{\pi}\sqrt{\frac{t}{\tau}}+\frac{2}{\pi}\sum_{n=1}^{\infty}\frac{1}{n}e^{-n^2/4}\sinh\left(n\sqrt{\frac{t}{\tau}}\right)\right]\right\} \quad (6)$$

$$\beta=\frac{h\sqrt{t}}{\sqrt{\rho ck}} \quad (7)$$

and

$$\beta_\tau=\frac{h\sqrt{\tau}}{\sqrt{\rho ck}} \quad (8)$$

For the case where $\tau=0$, Eq. (5) simplifies to

$$\theta=f(\beta) \quad (9)$$

where, from Eq. (6)

$$f(\beta)=1-e^{\beta^2}\operatorname{erfc}(\beta) \quad (10)$$

which is the well-known solution of Fourier's equation for a step-change in the air temperature.

The general solution for an exponential series, corresponding to Eq. (3), is given by Newton et al. [20] as

$$\theta=\sum_{j=1}^{m}\frac{T_{a,j}}{T_{aw,\infty}-T_0}g(\beta,\beta_{\tau j}) \quad (11)$$

For the special case where $m=1$, $T_{a,1}=T_{aw,\infty}-T_0$ and Eq. (11) reduces to (6).

The presence of cooling, i.e., injected air at a second temperature T_c, introduces the film cooling effectiveness, $\eta=(T_{aw}-T_c)/(T_a-T_c)$ as a variable in addition to h. Like h, it is assumed that η is only a function of the aerodynamics and time invariant.

The cooled heat transfer measurements were performed in two stages. Film cooling effectiveness was measured on a Rhoacell tip with the wide-band TLC. Heat transfer coefficient was then obtained by a separate experiment using a narrow-band crystal and polycarbonate tip. The heat transfer coefficient was deduced using the local measured η.

In order to evaluate the influence of the coolant in an engine environment a net heat flux reduction (NHFR) similar to that used by Sen et al. [22] is used. The NHRF is the ratio of the reduction in heat flux due to film cooling to the heat flux without cooling:

$$\Theta_E=\frac{T_a-T_c}{T_r-T_w} \quad (12)$$

$$\text{NHFR}=\frac{q_w-q_{w,c}}{q_w}=1-\frac{h_c}{\overline{h_{uc}}}(1-\eta\Theta_E) \quad (13)$$

Here $\overline{h_{uc}}$ is the mean uncooled heat transfer coefficient. The objective of film cooling is to increase NHFR by reducing heat transfer coefficient and increasing η. The NHFR is most meaningful at engine-representative conditions. The value of θ_E was selected as 1.5, comparable to that of Sargison et al. [23] and based on an air total temperature $T_a=1900$ K, a blade metal temperature $T_w=1200$ K, a coolant total temperature $T_c=880$ K, and a transonic air recovery temperature $T_r=1880$ K. An integrated average of the NHFR may be used to determine the overall performance of

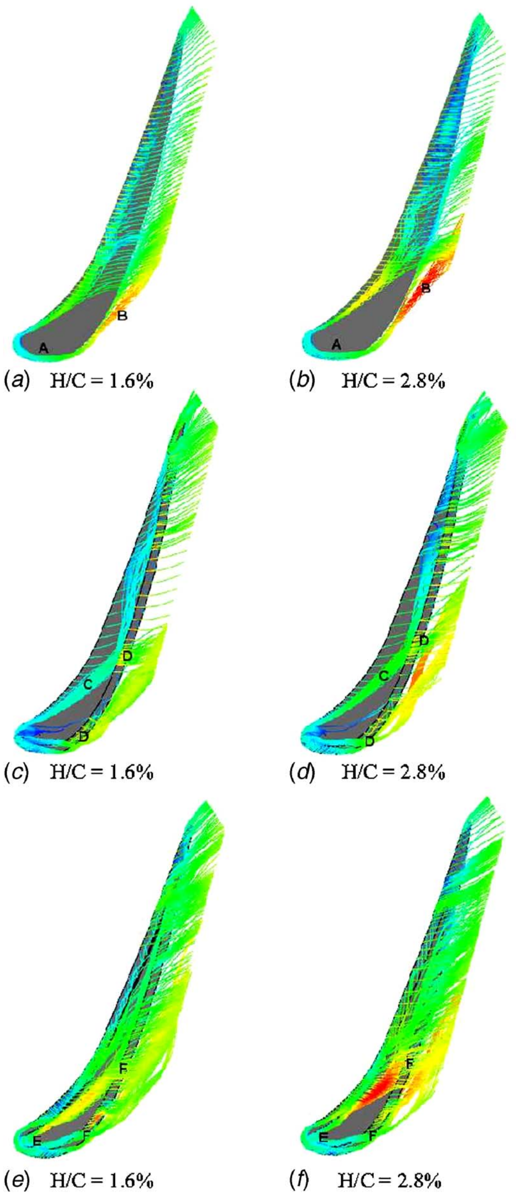

(*a*) H/C = 1.6% (*b*) H/C = 2.8%

(*c*) H/C = 1.6% (*d*) H/C = 2.8%

(*e*) H/C = 1.6% (*f*) H/C = 2.8%

Fig. 7 CFX flow visualization

a cooled geometry by means of a summation over all $i=1$ to n pixels:

$$\overline{\mathrm{NHFR}} = 1 - \frac{1}{n \, . \, \overline{h_{uc}}} \sum_{i=1}^{n} h_{c,i}(1 - \eta \Theta_E) \tag{14}$$

4 Experimental Results

The experimental results are divided into two main sections: Aerodynamic (pressure) and heat transfer (temperature) results. Three geometries, at two gap heights, were tested: Plain tip, suction-side squealer, and cavity. Most aerodynamic measurements are made on the casing—tip and aerofoil surface data is only available for the plain-tip geometry. In contrast, the heat transfer data has only been gathered on the tip, with aerofoil data only presented for the plain-tip case. The experiments are supported by flow visualization information computed using the CFX code.

Aerodynamic Measurements for the Plain Tip. Figures 4(*a*)–4(*d*) show measurements of the pressure coefficient, C_p, on the plain tip blade as well as data on the suction and pressure aerofoil surfaces at clearance heights of 3.7 and 6.35 mm ($H/C=1.6\%$ and 2.8%, respectively). Note that only 33% of the blade span is shown. These figures clearly illustrate that between $0.2<x/C<0.9$ there is a region of high velocity associated with the flow separating from the pressure-side edge of the tip gap. The flow subsequently decelerates as it reattaches to the tip surface before reaching the suction surface. Figures 5(*a*) and 5(*b*) show the corresponding C_p measured on the casing, indicating similar features. A region of relatively low leakage velocity is observed near the leading edge of the blade tip, $x/C<0.2$, where there is less pressure differential to drive flow across the gap.

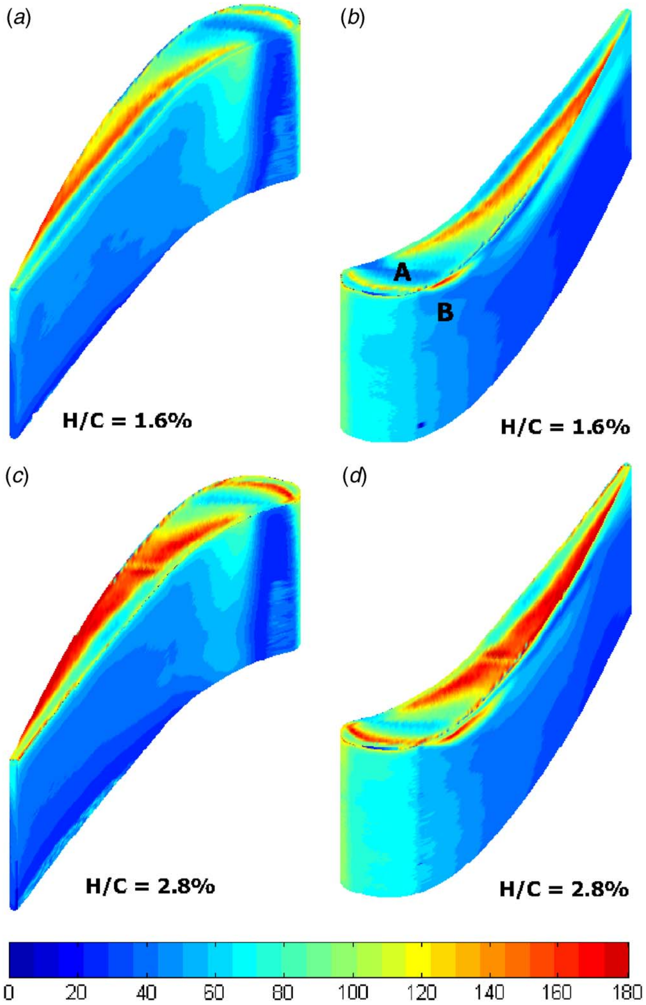

Fig. 8 Heat transfer coefficients for plain tip geometry: Top H/C 1.6%, bottom $H/C=2.8\%$

Figure 6 shows C_p plotted on the tip along a line perpendicular to the chord, which is approximately along the line of leakage trajectory, at $x/C=50\%$. The blade tip is approximately 9% of chord thickness at this location. The pressure data illustrates the presence of a separation bubble with reattachment approximately a third of the distance along the cross-chord line following the acceleration-deceleration through the vena contracta. High heat transfer coefficient is observed where the flow reattaches.

Flow reattachment is indicated by an abrupt decrease in the rate of deceleration on the tip. The red-yellow contour divides in Fig. 4 provide an approximate indication of the reattachment line.

It is evident that with the larger clearance gap, the region of separation increases, as reported widely (for example, Heyes et al., [11]). The leakage flow is accompanied by a small acceleration on the pressure-side aerofoil surface in the immediate vicinity

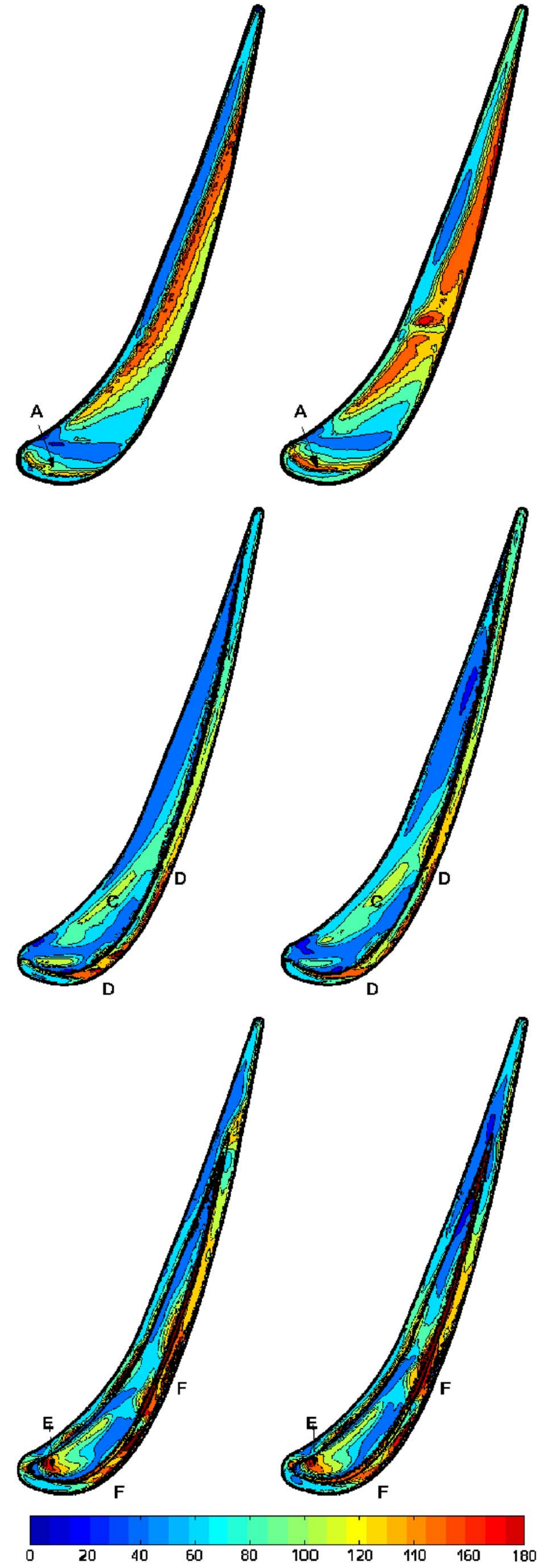

Fig. 9 Heat transfer coefficient for plain (top pair), squealer (middle) and cavity (bottom) geometries (W/m^2K)

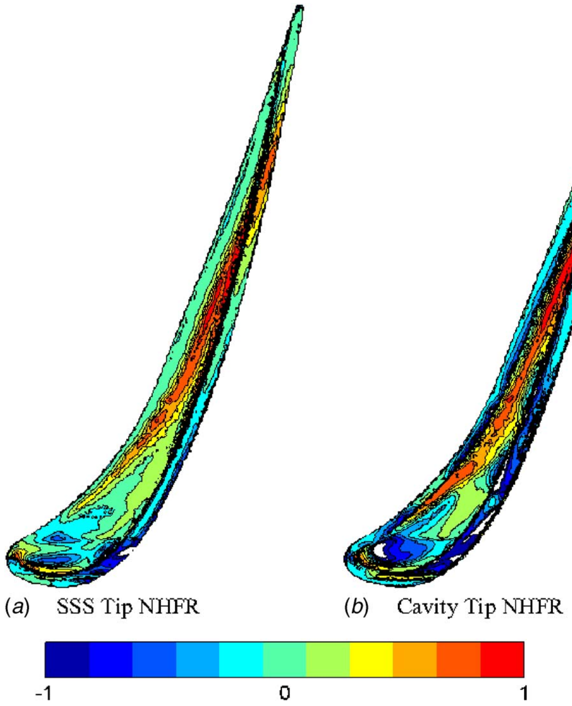
(*a*) SSS Tip NHFR (*b*) Cavity Tip NHFR

Fig. 10 Uncooled tip NHFR for H/C=1.6%

of the gap, which is accentuated in the larger tip gap. The impingement of the leakage vortex is visible on the suction-side aerofoil surface. The intensity of the leakage vortex is observed to increase in intensity as clearance gap increases.

Figures 7(*a*) and 7(*b*) illustrate the trajectory of leading-edge streamlines, obtained by CFX, for the case of the plain tip. The streamlines are color-coded to mark velocity. The flow visualization predictions support the experimental data, indicating high leakage velocities in the regions of high C_p. The CFD has captured the pressure-side separation discussed above and also reveals a similar separation near the leading edge of the blade ($x/c=0$), marked A where flow is driven into the tip gap by high pressure near the stagnation point of the blade. The highest velocities are calculated in the tip-leakage vortex on the suction side of the tip, marked B in the two figures. The strength of this vortex is observed to increase as the gap width increases.

Aerodynamic Measurements for SS-Squealer and Cavity Tip. Figures 5(*c*) and 5(*d*) show measurements of C_p on the casing for flow through the gap with suction-side squealer. The corresponding CFD streamlines are shown in Figs. 7(*c*) and 7(*d*). High C_p at and downstream of the squealer ridge is observed where the reduced area at the squealer causes an abrupt acceleration. Although the flow again separates off the pressure-side corner of the tip, the CFD streamlines indicate that reattachment is mainly associated with a swirling vortical flow within the pressure-side separation bubble. This flow, driven along its axis by the chordwise pressure gradient, impinges on the foremost, thicker portion of the tip (marked C) and on the squealer at two positions marked D in Figs. 7(*c*) and 7(*d*). Enhanced heat transfer is expected at these locations. The first position is near the leading edge of the blade while the second is at $x/C\approx 0.30$. The vortical flow is more intense for the larger gap and the second point of impingement is further along the chord line at $x/C\approx 0.35$.

Heat Transfer Measurements for Plain Tip. Figures 8(*a*)–8(*d*) show measurements of the heat transfer coefficient on the plain tip blade as well as data on the suction and pressure aerofoil surfaces at clearance heights of 3.7 and 6.35 mm ($H/C=1.6\%$ and 2.8%, respectively). Note that only 25% of the blade

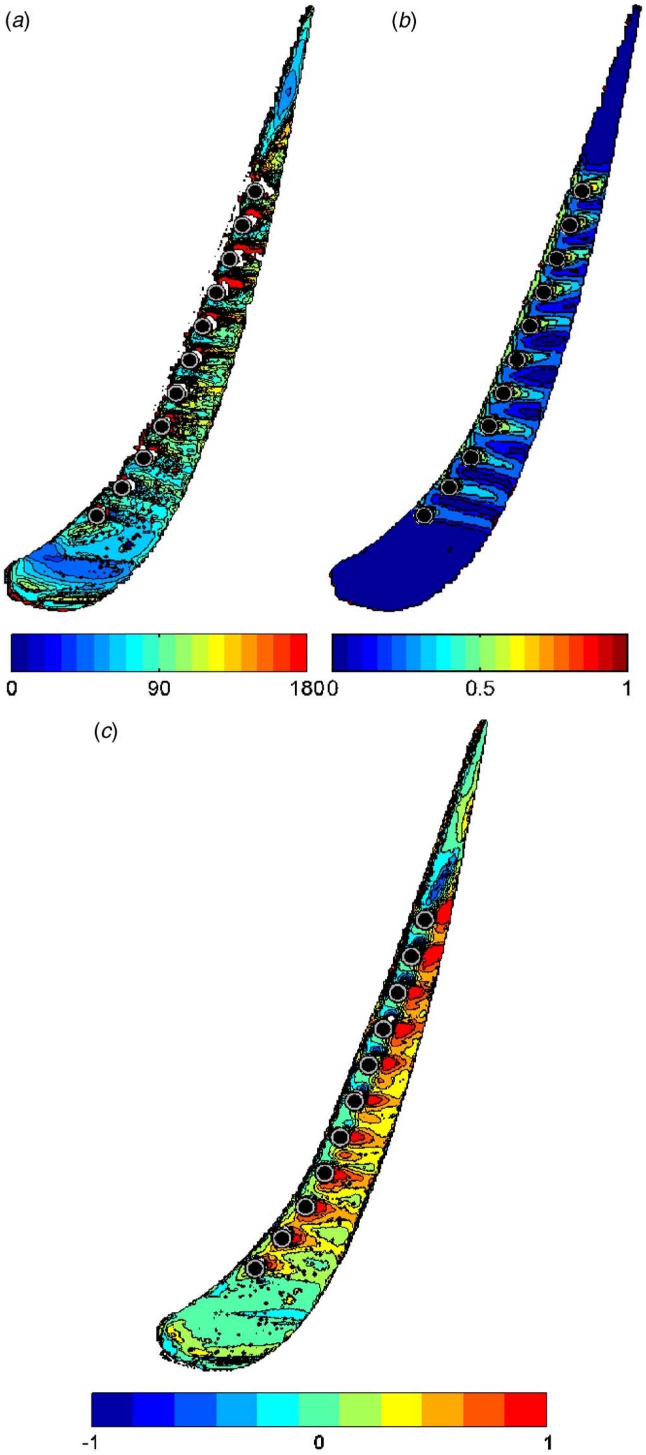

Fig. 11 (*a*)–(*c*). Cooled Tip *h*, η and NHFR

span is shown. The most striking observation is that the highest heat transfer coefficient on any surface (including the stagnation region on the pressure and suction aerofoil surfaces) is observed on the tip of the blade!

The associated pressure field and CFD flow visualization are shown in Figs. 4(*a*)–4(*d*), 7(*a*), and 7(*b*). It is observed that the maximum heat transfer coefficient occurs in the region of reattachment on the blade tip essentially along a line parallel to the pressure-side rim. This region is more extensive for the larger tip gap, though the peak values of h are similar. Figure 6(*b*) shows h plotted on the tip along a line perpendicular to the chord, which is approximately along the line of leakage trajectory, at $x/c=50\%$. The blade tip is approximately 9% of chord thickness at this location. Comparison with Fig. 6(*a*) does indeed indicate that the high heat transfer coefficient is located where the flow reattaches.

A ridge of high heat transfer is also observed near the leading-edge of the blade (marked A in Figs. 8(*b*) and 8(*d*)) where flow which is driven into the tip gap by high pressure near the stagnation point of the blade, separates and then reattaches (see A in Figs. 7(*a*) and 7(*b*)). Generally there is low heat transfer in this leading edge region where there is less pressure differential to drive flow across the gap.

The impingement of the tip-leakage vortex (marked B in Figs. 7(*a*), 7(*b*), and 8(*b*)–8(*d*)) is visible on the suction-side aerofoil surface where high heat transfer is observed. The area of the region influenced the leakage vortex is observed to increase as the intensity of the vortex increases with the increase in clearance gap. It is interesting to note that the origin of the leakage vortex appears to be the flow over the leading edge of the suction surface.

Heat Transfer Measurements for SS-Squealer and Cavity Tip. Figures 9(*c*)–9(*f*) show contours of heat transfer coefficient on the blade tip for the suction-side squealer and cavity geometries, respectively. Note Figs. 9(*a*) and 9(*b*) shows the heat transfer for the plain tip again for comparison. It is immediately evident that both the suction-side squealer and cavity squealer have eliminated the peak in heat transfer associated with the intense fluid-dynamic effect of flow reattachment exhibited by the plain tip. However, the suction-side squealer features locations of high local heat transfer at positions marked C and D. The corresponding CFD streamlines are shown in Figs. 7(*c*) and 7(*d*) and the locations where flow is observed to impinge on the tip and squealer (also marked C and D) correlate well with these positions of high heat transfer. The cavity squealer also features local spots of high heat transfer (marked F), which correspond well to the flow impingement marked in the flow visualization, Figs. 7(*e*) and 7(*f*). In addition, high heat transfer is observed at the base of the squealer at position E, possibly associated with the vortical flow drawing fluid into the cavity. The heat transfer in both the suction-side squealer and cavity squealer are relatively insensitive to the tip-gap clearance.

Figures 10(*a*) and 10(*b*) show the NHFR for the suction-side and cavity squealer for the case of a $H/C=1.6\%$. No film cooling is present and so here the NHFR is based on the local heat transfer coefficient compared with that measured using the plain tip, i.e., $\mathrm{NHFR}=1-h/h_{\text{plain-tip}}$. Regions of positive NHFR in Figs. 11(*a*) and 11(*b*) indicate a beneficial influence of the squealer geometry while regions of negative NHFR indicate an increase in heat transfer. An integrated average of the NHFR for the suction-side squealer was calculated as 0.15, suggesting a reduction of 15% in heat flux. The integrated NHFR for the cavity squealer was 0.0, indicating no net overall benefit at this tip-gap height.

Cooled Heat Transfer Measurements on Plain Tip. The squealer geometries are one method that can be used to reduce the heat transfer on the tip of the blade. An alternate method is to use film cooling. A coolant configuration was designed, based on the data collected on the uncooled tip. The coolant holes were located at 5 mm from the pressure-side corner in a cross chord direction, in order to inject coolant into the separation bubble. The holes spanned from 15% to 70% chord to coincide with the regions of heightened heat transfer. This had the secondary benefit of avoiding the regions of high static pressure at the leading edge of the blade which would have resulted in coolant ingestion at low blowing rates. The coolant hole diameter was 4 mm which scales to engine representative film cooling geometries, as suggested by Siemens and Alstom. Note that a coolant mass flow equal to 1% of the mainstream flow is typically used in the turbine.

Figures 11(*a*)–11(*c*) illustrate cooling data for a plain tip for the case of $H/C=1.6\%$. The average coolant blowing rate was 0.9,

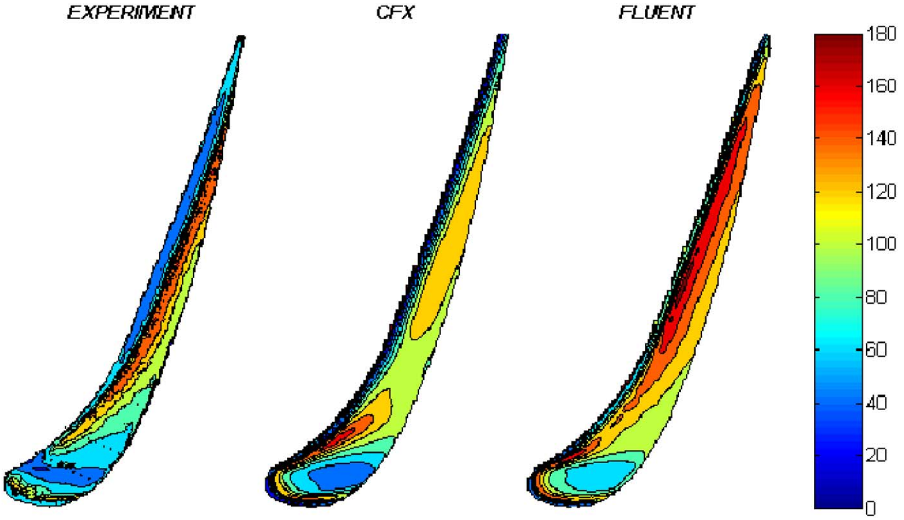

Fig. 12 CFD predictions of h (W/m^{2}K) for plain tip, H/C=1.6%

which corresponded to a coolant mass flow equal to 0.5% of the mainstream flow—a percentage not untypical of that used in engineering practice. Note Fig. 9(*a*) is the equivalent map for the uncooled tip. These figures show contours of heat transfer coefficient, film cooling effectiveness and local NHFR on the cooled tip. The holes have been positioned to inject coolant into the separation bubble and this has successfully avoided the high heat transfer associated with reattachment present in the uncooled case. There are, however, some regions of high local heat transfer coefficient near the holes due to the fluid-interaction between the coolant and mainstream. The cooling footprints shown in the effectiveness plot indicate that the flow is essentially perpendicular to the chord and that the coolant remains attached.

The NHFR provides a quantification of the reduction in heat transfer to the tip with film cooling compared to that heat transfer without cooling. The objective of film cooling is to increase NHFR by reducing heat transfer coefficient and increasing effectiveness. Regions of positive NHFR in Fig. 10(*c*) indicate a beneficial influence of the coolant and these are predominantly located in the cooling footprints. Some regions of negative NHFR are observed in areas where the effectiveness is low but the heat transfer coefficient has been elevated due to increased turbulent mixing with the cooling present. Away from the cooling holes the NHFR is near zero. An integrated average of the NHFR, defined by Eq. (14), was calculated as 0.33, indicating an effective cooling design. For a given blade tip geometry and mainstream flow conditions, the NHFR is a function of the cooling-hole locations as well as the coolant blowing rate. Only one case has been reported here but a positive integrated NHFR resulted for all cases where the coolant was injected into the separation bubble on the tip.

Predicted heat transfer coefficients for the uncooled plain tip for the case of $H/C=1.6\%$ are shown in Fig. 12. These calculations were performed using two commercial codes: FLUENT and CFX. These calculations are shown to be in good qualitative agreement with the experiments and have captured all of the flow features described in the above discussion.

5 Conclusions

Contours of heat transfer coefficient have been measured on the tip of a generic turbine blade as well as on the aerofoil suction and pressure surfaces near the tip. The experiments were conducted at an exit Reynolds number$=2.3\times10^5$ in a five-blade linear cascade using the transient liquid crystal technique. Tip clearances of 1.6% and 2.8% chord and three different tip geometries were used. These measurements were supported by pressure measurements on the tip and casing and by flow visualization calculated using CFX.

The highest heat transfer coefficients on any surface (including the stagnation region on the pressure and suction aerofoil surfaces) were observed on the tip of the blade. The pressure and flow visualization revealed that the flow through the plain tip gap was governed by a separation bubble near the pressure-side entrance to the gap. The leakage flow separated from the tip surface and reattached in a region parallel to the pressure-side rim. The highest heat transfer coefficients were located in this region. A ridge of high heat transfer was also observed near the leading edge where flow which is driven into the tip gap by high pressure near the stagnation point of the blade, separates and then reattaches. Generally there is low heat transfer in this region where there is less pressure difference to drive flow across the gap. The impingement of the leakage vortex is visible on the suction-side aerofoil surface where high heat transfer is also observed. This feature was also captured clearly by the flow visualization. The area of the region influenced by the leakage vortex was observed to increase as the vortex became more intense with an increase in clearance gap.

Both squealer geometries eliminated the peak in heat transfer associated with flow reattachment from the pressure-side rim which dominated the case of the plain tip. However, high local heat transfer was observed at positions on the squealers which corresponded to areas of impingement. The cavity squealer also featured local spots of high heat transfer at the base of the squealer near the leading edge, possibly associated with vortical flow drawing fluid into the cavity. The areas of high measured heat transfer correlated well with the locations of impingement determined by the calculated flow visualization. The suction-side squealer featured an integrated net heat flux reduction (NHFR) of 0.15 while the cavity squealer revealed no net heat flux reduction.

Film cooling holes were introduced on the plain tip along a line 5 mm from the pressure-side corner in a cross chord direction in order to inject coolant into the separation bubble. This successfully eliminated the high heat transfer associated with reattachment present in the uncooled case. Measurements of heat transfer coefficient and cooling effectiveness led to a calculation of the NHRF on the blade tip. An integrated average of the NHFR, calculated that the net heat flux to the tip at engine-level temperatures would be reduced by 33% (for a coolant mass flow equivalent to 0.5% of the mainstream), indicating an effective cooling design.

Nomenclature

B = blowing rate, $B=\rho_c v_c/\rho_a v_a$
C = specific heat of wall
C = chord, 225 mm
C_p = pressure coefficient, $C_p=(P_t-P)/(P_t-P_e)$
$f(\beta)$ = step-change solution of Fourier's equation
$g(\beta,\beta_\tau)$ = exponential solution of Fourier's equation
h = heat transfer coefficient $(q_w/(T_{aw}-T_w))$
H = tip clearance gap
H_{sq} = squealer height
k = thermal conductivity of wall
m = number of terms in exponential series
NHRF = net heat flux reduction, $\text{NHFR}=(q_w-q_{w,c})/q_w$
P = pressure
q_w = heat flux from air to wall
t = time, blade thickness
T = temperature
v = free-stream velocity
x = distance along chord
β = parameter in step-change solution $\beta=(h\sqrt{t/\rho ck})$
β_τ = parameter in exponential solution $\beta_\tau=(h\sqrt{\tau/\rho ck})$
ρ = density
η = film cooling effectiveness, $\eta=(T_{aw}-T_c)/(T_a-T_c)$
θ = nondimensional temp. $\theta=(T_w-T_0)/(T_{aw,\infty}-T_{w0})$
Θ_E = ND engine. temp $\Theta_E=(T_a-T_c)/(T_r-T_w)$
τ = time constant

Subscripts

0 = value at $t=0$
∞ = value as $t\rightarrow\infty$
a = mainstream air
aw = adiabatic wall
c = coolant, cooled
e = cascade exit
j = jth term in series
r = recovery
t = upstream stagnation condition
uc = uncooled

References

[1] Booth, T. C., Dodge, P. R., and Hepworth, H. K., 1982, "Rotor Tip Leakage: Part 1; Basic Methodology," ASME J. Eng. Power, **104**, pp. 154–161.

[2] Mayle, R. E., and Metzger, D. E., 1986, "Heat Transfer at the Tip of an Unshrouded Turbine Blade," *Proceedings, Seventh International Heat Transfer Conference*, Vol. 3, pp. 87–92.

[3] Srinivasan, V., and Goldstein, R. J., 2003, "Effect of Endwall Motion on Blade Tip Heat Transfer," ASME J. Turbomach., **125**, pp. 267–273.

[4] Bunker, R. S., 2001, "A Review of Turbine Blade Tip Heat Transfer, Heat Transfer in Gas Turbine Systems," Ann. N.Y. Acad. Sci., **934**, pp. 64–79.

[5] Kim, Y. W., and Metzger, D. E., 1993, "Heat Transfer and Effectiveness on Film Cooled Turbine Blade Tip Models," ASME Paper No. 93-GT–208.

[6] Chen, G., Dawes, W. N., and Hodson, 1993, "A Numerical and Experimental Investigation of Turbine Tip Gap Flow," 29th Joint Propulsion Conference and Exhibit, AIAA Paper No. 93-2253.

[7] Bunker, R. S., Bailey, J. C., and Ameri, A. A., 1999, "Heat Transfer and Flow on the First Stage Blade Tip of a Power Generation Gas Turbine. Part I: Experimental Results," ASME Paper No. 99-GT-169.

[8] Kwak, J. S., and Han, J. C., 2002, "Heat Transfer Coefficient and Film-Cooling Effectiveness on a Gas Turbine Blade Tip," ASME Paper No. GT-2002-30194.

[9] Kwak, J. S., and Han, J. C., 2002, "Heat Transfer Coefficient and Film-Cooling Effectiveness on the Squealer Tip of a Gas Turbine Blade," ASME Paper No. GT-2002-30555.

[10] Jin, P., and Goldstein, R. J., 2002, "Local Mass/Heat Transfer on Turbine Blade Near-Tip Surfaces," ASME Paper No. GT-2002-30556.

[11] Heyes, F. J. G., Hodson, H. P., and Dailey, G. M., 1991, "The Effect of Blade Tip Geometry on the Tip Leakage Flow in Axial Turbine Cascades," ASME Paper No. 91-GT-135.

[12] Hodson, H. P., Banieghbal, M. R., and Dailey, G. M., 1995, "Three-Dimensional Interactions in the Rotor of an Axial Turbine," AIAA J. Propul. Power, **11**(2), pp. 196–204.

[13] Bindon, J. P., 1989, "The Measurement and Formation of Tip Clearance Loss," ASME J. Turbomach., **111**, pp. 257–263.

[14] Ireland, P. T., and Jones, T. V., 2000, "Liquid Crystal measurements of Heat Transfer and Surface Shear Stress," Meas. Sci. Technol., **11**, pp. 969–986.

[15] Farina, D. J., Hacker, J. M., Moffat, R. J., and Eaton, K., 1993, "Illuminant Invariant Calibration of Thermochromic Liquid Crystals," *Visualization of Heat Transfer Processes*, American Society of Mechanical Engineers, Heat Transfer Division, Vol. 252, pp. 1–11.

[16] Syson, B. J., Pilbrow, R. G., and Owen, J. M., 1996, "Effect of Rotation on Temperature Response of Thermochromic Liquid Crystal," Int. J. Heat Fluid Flow, **17**, pp. 491–499.

[17] Owen, J. M., Newton, P. J., and Lock, G. D., 2003, "Transient Heat Transfer Measurements Using Thermochromic Liquid Crystal. Part 2: Experimental Uncertainties," Int. J. Heat Fluid Flow, **24**, pp. 23–28.

[18] Gillespie, D. R. H., Wang, Z., and Ireland, P. T., 2001, "Heater element," European Patent No. 0847679.

[19] Schultz, D. L., and Jones, T. V., 1973, "Heat Transfer Measurements in Short Duration Hypersonic Facilities," Paper No. AGARD-AG-165.

[20] Newton, P. J., Yan, Y., Stevens, N. E., Evatt, S. T., Lock, G. D., and Owen, J. M., 2003, "Transient Heat Transfer Measurements Using Thermochromic Liquid Crystal. Part 1: An Improved Technique," Int. J. Heat Fluid Flow, **24**, pp. 14–22.

[21] Gillespie, D. R. H., Wang, Z., Ireland, P. T., and Kohler, S. T., 1998, "Full Surface Local Heat Transfer Measurements in a Model of an Integrally Cast Impingement Cooling Geometry," ASME J. Turbomach., **120**, pp. 92–99.

[22] Sen, B., Schmidt, D. L., and Bogard, D. G., 1994, "Film Cooling with Compound Angle Holes: Heat Transfer," ASME Paper No. 94-GT-311.

[23] Sargison, J. E., Guo, S. M., Oldfield, M. L. G., Lock, G. D., and Rawlinson, A. J., 2002, "A Converging Slot-Hole Film-Cooling Geometry—Part 2: Transonic Nozzle Guide Vane Heat Transfer and Loss," ASME J. Turbomach., **124**, pp. 461–471.

M. E. Taslim

A. Khanicheh

Mechanical and Industrial Engineering
Department,
Northeastern University,
360 Huntington Avenue,
Boston, MA 02115

Experimental and Numerical Study of Impingement on an Airfoil Leading Edge With and Without Showerhead and Gill Film Holes

This experimental investigation deals with impingement on the leading edge of an airfoil with and without showerhead film holes and its effects on heat transfer coefficients on the airfoil nose area as well as the pressure and suction side areas. a comparison between the experimental and numerical results are also made. the tests were run for a range of flow conditions pertinent to common practice and at an elevated range of jet Reynolds numbers (8000–48,000). The major conclusions of this study were: (a) The presence of showerhead film holes along the leading edge enhances the internal impingement heat transfer coefficients significantly, and (b) while the numerical predictions of impingement heat transfer coefficients for the no-showerhead case were in good agreement with the measured values, the case with showerhead flow was under-predicted by as much as 30% indicating a need for a more elaborate turbulence modeling. [DOI: 10.1115/1.2137742]

Introduction

Leading edge cooling cavities in modern gas turbine airfoils play an important role in maintaining the leading edge temperature at levels consistent with airfoil design life. These cavities often have a complex cross-sectional shape to be compatible with the external contour of the blade at the leading edge. Furthermore, to enhance the heat transfer coefficient in these cavities, they are often roughened on three walls with ribs of different geometries. The cooling flow for these geometries usually enters the cavity from one end of the airfoil flows radially to the other side or, in the most recent designs, enters the leading edge cavity from the adjacent cavity through a series of cross-over holes on the partition wall between the two cavities. In the latter case, the cross-over jets impinge on a smooth leading-edge wall and exit through the showerhead film holes, gill film holes on the pressure and suction sides, and, in some cases, forms a cross flow in the leading-edge cavity and moves toward the end of the cavity.

Various methods have been developed over the years to keep the turbine airfoils temperatures below critical levels consistent with the required life for each component. Parallel with advances in airfoil material properties, advances in airfoil cooling schemes have also been remarkable. A main objective in turbine airfoil cooling design is to achieve maximum heat removal from the airfoil metal while minimizing the required coolant flow rate. One such method is to route coolant air through serpentine passages within the airfoil and convectively remove heat from the airfoil. The coolant is then ejected either at the tip of the airfoil, through the cooling slots along the trailing edge or the film holes on the airfoil surface at critical locations. To further enhance the heat transfer, the cooling channel walls are often roughened with ribs. Extensive research has been conducted on various aspects of the rib-roughened channels and it is concluded that geometric parameters such as passage aspect ratio, rib height to passage hydraulic diameter or blockage ratio, rib angle of attack, the manner in which the ribs are positioned relative to one another (in-line, staggered, crisscross, etc.), rib pitch-to-height ratio and rib shape (round versus sharp corners, fillets, rib aspect ratio, and skewness towards the flow direction) have pronounced effects on both local and overall heat transfer coefficients. The interested reader is referred to the work of investigators such as Burggraf [1], Chandra and Han [2], El-Husayni et al. [3], Han [4], Han et al. [5–7], Metzger et al. [8–10], Taslim and Spring [11,12], Taslim et al. [13–15], Webb et al. [16] and Zhang et al. [17].

Airfoil leading-edge surface, being exposed to very high gas temperatures, is often a life-limiting region and requires more complex cooling schemes especially in modern gas turbines with elevated turbine inlet temperatures. A combination of convective and film cooling is used in conventional designs to maintain the leading-edge metal temperature at levels consistent with airfoil design life. This study focuses on the leading-edge jet impingement and effects that showerhead film holes have on the impingement heat transfer coefficient. In this flow arrangement, the coolant enters the leading-edge cooling cavity as jets from the adjacent cavity through a series of crossover holes on the partition wall between the two cavities. The cross-over jets impinge on the leading-edge wall and exit through the leading-edge film holes on the pressure and suction sides, or form a crossflow in the leading-edge cavity and move toward the airfoil tip. A survey of many existing gas turbine airfoil geometries show that, for analytical as well as experimental analyses, such cavities can be simplified by simulating the shape as a four-sided polygon with one curved side that simulates the leading edge curvature, a rectangle with one curved side (often the smaller side) or a trapezoid, the smaller base of which is replaced with a curved wall. The available data in open literature is mostly for the jet impingement on flat surfaces that are smooth or rib-roughened and a few cases of impingement on concave but smooth surfaces. These studies include the work of Chupp et al. [18], Metzger et al. [19], Kercher and Tabakoff [20], Florschetz et al. [21–23], Metzger and Bunker [24], Bunker and Metzger [25], Van Treuren et al. [26], Chang et al. [27], Huang et al. [28], and Akella and Han [29]. However, as dictated by the external shape of an airfoil leading edge, the test section in this investigation was a symmetric channel with a circular nose,

---

Contributed by the International Gas Turbine Institute (IGTI) of ASME for publication in the JOURNAL OF TURBOMACHINERY. Manuscript received October 1, 2004; final manuscript received February 1, 2005. IGTI Review Chair: K. C. Hall. Paper presented at the ASME Turbo Expo 2005: Land, Sea and Air, Reno, NV, June 6–9, 2005, Paper No. GT2005-68037.

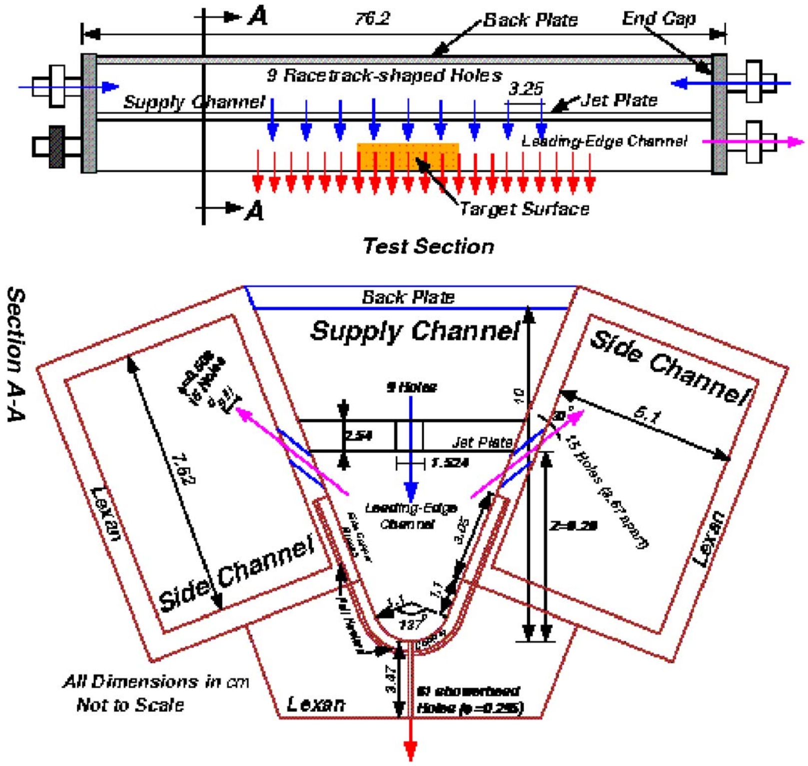

Fig. 1 Schematic of the test apparatus

two tapered sidewalls and a flat fourth wall on which the crossover jets were positioned. Experimental results for this setup with circular as well as racetrack-shaped crossover holes and for a variety of target surface geometries have already been reported by Taslim et al. [30–33]. The present study, however, deals with the impingement of jets issued from racetrack-shaped crossover holes on a concave target surface with and without the presence of showerhead film holes. Depending on the flow arrangement, the impingement air was ejected entirely through a row of holes on the target surface along the leading edge simulating the airfoil showerhead film holes, or split through the showerhead holes and two rows of holes on the side walls representing the pressure and suction side "gill" film holes, or partially (76%) through the showerhead holes and the balance (24%) through one end of the channel representing an airfoil tip. Data were gathered for a range of jet Reynolds number up to 48,000 and were compared with those numerically calculated.

Test Sections

Figures 1 and 2 show schematically the rig layout and its cross-sectional area, the target surface, and the cross-over hole geometry. A conventional technique of heated walls in conjunction with thermocouples was used to measure the heat transfer coefficient. The test wall, where all measurements were taken, consisted of nine removable machined copper pieces which were heated by

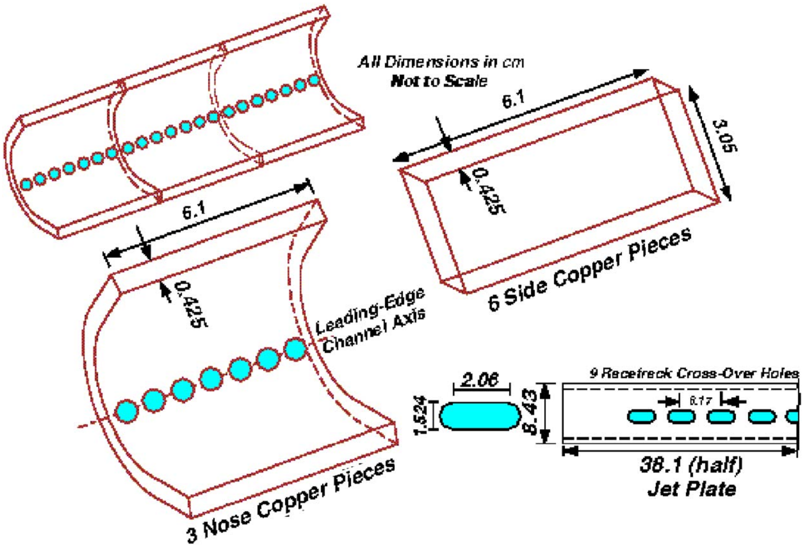

Fig. 2 Target surface and crossover jet geometries

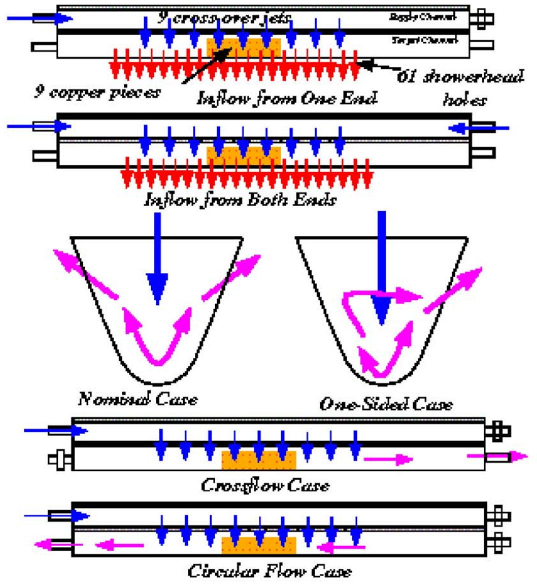

3b) Outflow arrangements for no showerhead flow tests.

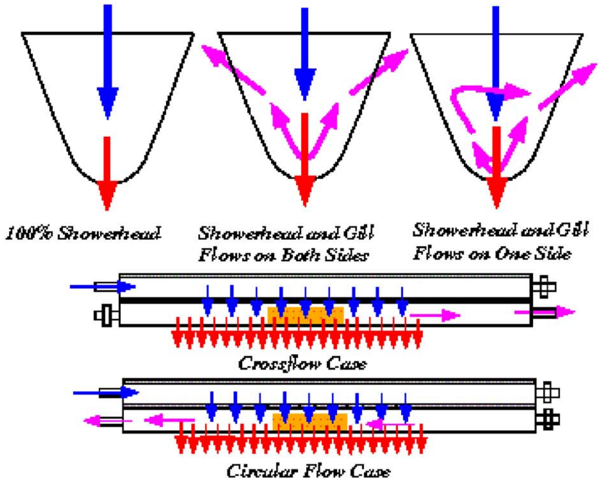

3c) Outflow arrangements for no showerhead flow tests.

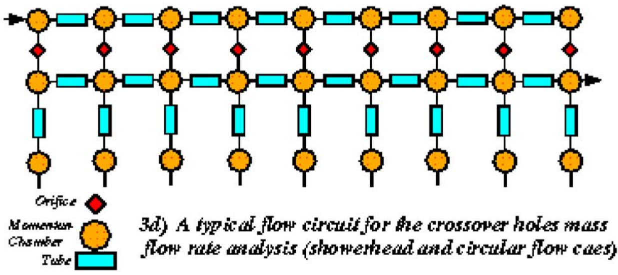

3d) A typical flow circuit for the crossover holes mass flow rate analysis (showerhead and circular flow caes).

Fig. 3 Inflow and outflow arrangements

foil heaters attached on the back of the pieces (see Fig. 3). By proper adjustment of the Ohmic power to the foil heater immediately underneath the copper pieces, the desirable surface temperature was obtained. The test rig was 85.5 cm long. The circular wall simulating the leading-edge nose with an inner radius of 1.1 cm and an arc angle of 137 deg was made of acrylic plastic with a 9.9 cm long recess in the middle to house the nine copper pieces. For the showerhead flow cases, 61 0.595 cm diameter holes at a center-to-center distance of 0.87 cm were drilled along the leading edge nose at a 90 deg angle with the channel longitudinal axis. Seven of these holes passed through each copper piece on the leading edge (a total of 21 holes on the copper pieces). The remaining 41 holes were drilled symmetrically on both sides of the copper pieces on the Lexan® nose piece. This single row of holes, with properly scaled flow area, simulated an airfoil showerhead hole design that is typically configured as two rows. This test rig, however, was limited to one row of holes because the copper pieces were covered with etched-foil heaters through which could not be drilled. A flange on each side of the leading-edge piece facilitated the connection of the side walls to this piece. A circular recess along the inner radius with a depth of 3.2 mm and a length of 18.5 cm allowed the copper pieces to be fitted into the Lexan® shell flush with the channel surface. The two identical side channels with cross-sectional areas of 271 cm^2 (15.24 cm by 17.78 cm) and the same length as the leading-edge piece were also made of clear acrylic plastic. The side channels' main function was to maintain the dump pressure to consequently control the amount of flow through the "gill" holes on the airfoil suction and pressure sides. Eight angled cylindrical holes with a diameter of 5.08 mm and a center-to-center distance of 3.658 cm were drilled on each side channel wall at an angle of 30 deg with the sidewall to simulate gill holes on the suction and pressure sides of an airfoil. These holes were staggered along the length of the test section with respect to the crossover jet holes on the jet plate. A valve at the exit of each side channel controls the amount of gill hole flow on each side. A removable 2.54 cm thick jet plate corresponding to a Z/d_{jet} value of 2.8 was made of acrylic plastic to produce the impinging jets. Nine racetrack-shaped holes with a cross section shown in Fig. 2 (made of two half circles of 1.524 cm diameter and a rectangle of 1.524 by 2.06 cm) were drilled at a distance of 6.17 cm from each other (center-to-center) on the jet plate. The jet plate was attached and sealed to the side channel walls to simulate the partition wall between the leading-edge and its adjacent cooling cavity in an airfoil. The crossover holes were centered with respect to both the length and width of the jet plate. For the nominal position of the jet plate, a jet impinged at the center of each copper piece. The removable copper pieces, installed in the acrylic nose piece, provided the ability to change the impingement surface geometries in the test rig. Two sets of nose copper piece geometries were manufactured and tested: (1) A set with no showerhead holes and (2) a set of three with showerhead holes. On each piece seven 0.596 cm diameter holes were drilled. Custom-made thin etched-foil heaters with a thickness of about 0.2 mm were glued around the outer surface of each copper piece to provide the necessary heat flux. For each geometry, three identical copper pieces, separated by a 1 mm thick rubber insulator, were mounted next to each other. Heat transfer coefficients were measured on the middle piece while the other two pieces acted as guard heaters to minimize the heat losses to the adjacent walls. The test section wall temperature was adjusted to a desirable level by varying the Ohmic power to these heaters. Six thermocouples were embedded in each of the three middle copper pieces with their beads close to the exposed surface. Three thermocouples were embedded in each guard copper piece. The average of the six thermocouple readings in the middle copper pieces, which, if different, only differed by a fraction of a degree, was used as the surface temperature in the data reduction software for the average heat transfer coefficient. A nominal surface temperature of 45°C was selected so that with a jet temperature of about 20°C, a reasonable 25°C temperature difference existed between the wall surface and air. AC power was supplied to individual heaters through an existing power panel with individual Variacs for each heater. Heat flux for each heater was calculated using the measured voltage and amperage, and the surface area of each heater. Typical amperage and voltage levels for each heater varied from 0.23 to 0.4 amps and 20–45 V, respectively. Air properties were evaluated at jet temperature.

The trapezoidal supply channel was formed by the exterior walls of the side channels, the jet plate and a 1.27 cm thick aluminum back plate as shown in Fig. 1. The end caps were fixed

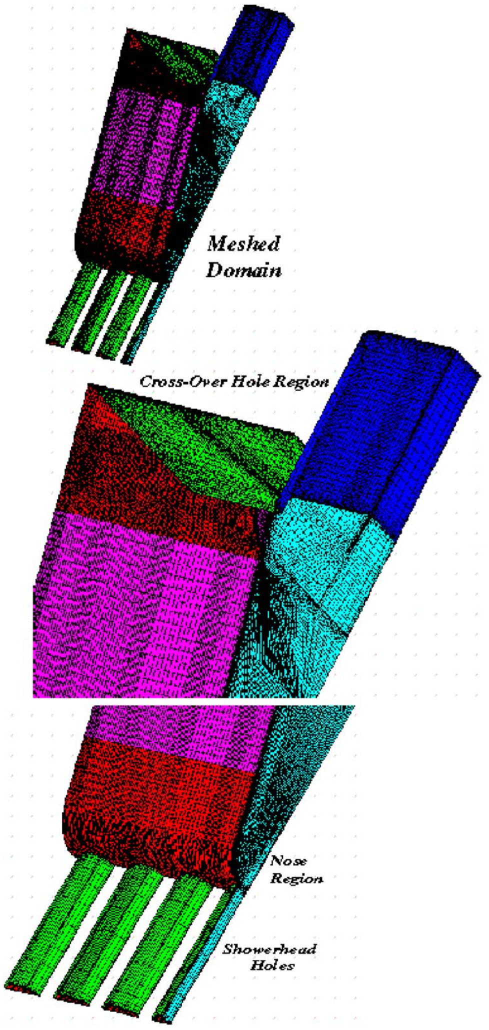

Fig. 4 Typical mesh arrangement around the computational domain periphery

such that it was possible to control the flow and pressure in each channel, thus simulating many variations that may occur in actual airfoil environments. Static pressure taps and thermocouples in each channel measured the pressure and temperature at different locations. The test sections were covered on all sides, by 5 cm thick glasswool insulation to minimize heat losses to the environment. Radiational heat loss from the heated wall to the unheated walls, heat losses from the copper piece in the entrance region of the showerhead holes, and losses to ambient air were taken into consideration when heat transfer coefficients were calculated. A contact micro-manometer with an accuracy of 0.025 mm of water column as well as a series of oil and mercury manometers measured the pressures and pressure differences between the static pressure taps mounted on both sides of the roughened section for each geometry. For all cases, a critical venturimeter was used to measure the total air mass flow rate entering the supply channel.

Computational Models

The computational models were constructed for a representative repeated domain with two symmetric planes in each case. Figure 4 shows this representative domain for the target geometry with showerhead holes and details of the mesh distribution on the surface of the domain. The computational domain size for the no-showerhead geometry was the same. The CFD analysis was performed using FLUENT/UNS solver by Fluent, Inc., a pressure-correction based, multiblock, multigrid, unstructured/adaptive solver. Standard high Reynolds number k-ε turbulence model in conjunction with the generalized wall function was used for turbulence closure. The average y^+ for the first layer of cells was calculated to vary between 4.5 and 10 for all cases. Other available turbulence models in this commercial code, short of two-layer model which required a change in mesh arrangement for each geometry and was beyond the scope of this investigation, were also tested and did not produce results significantly different from those of k-ε model. Mesh independence was achieved at about 700,000 cells for a typical model. Cells in all models were entirely hexagonal, a preferred choice for CFD analyses, and were varied in size bi-geometrically from the boundaries to the center of the computational domain in order to have finer mesh close to the boundaries. Figure 4 shows the mesh distribution around the periphery of a typical model.

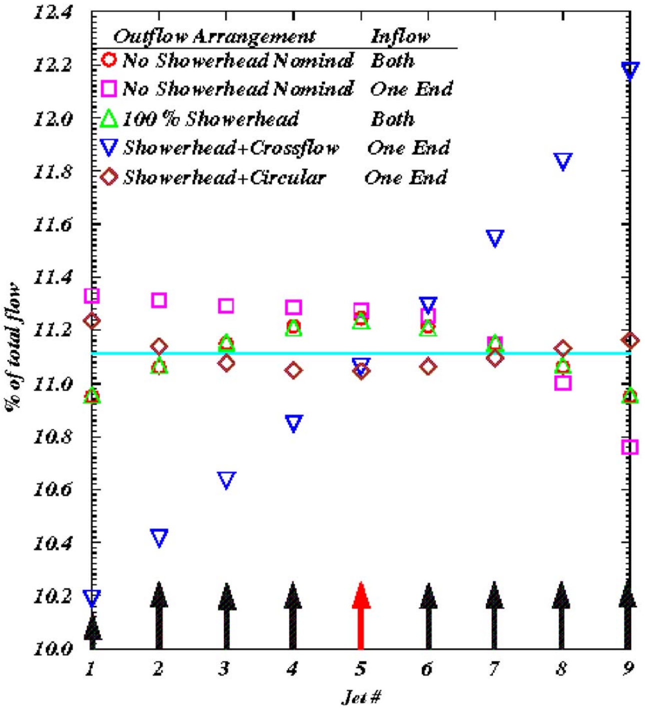

Fig. 5 Percentage of air flow rate through each crossover hole for some fow arrangements

Results and Discussion

A total of 112 tests were run in this investigation. All tests had several common features. There were always nine impinging jets issuing from the jet plate. The middle jet (fifth) always impinged on the copper leading-edge test piece in the middle of the test section and the reported heat transfer results are always for the copper test pieces in the middle (one leading-edge piece and two side pieces). Heat losses from the middle copper pieces to the ambient by conduction and convection as well as the heat losses by radiation to the unheated walls were taken into consideration when the impingement heat transfer coefficient was calculated. When showerhead holes were active, the heat loss in the entrance regions of the showerhead holes, drilled through the copper, were taken into consideration as well. The fourth and sixth jets impinged on the side copper pieces that acted as guard heaters. The remaining six jets impinged on the acrylic leading-edge wall to simulate the flow field in a typical leading-edge cooling channel. The jet Reynolds number is based on the total measured mass flow rate and the total area of the nine impingement holes. This choice of Reynolds number was based on the airfoil thermal circuit designers' common practice. However, Fig. 5 shows that the fifth jet for which the results are presented here, has mass flow

Table 1 Outflow arrangements

	Outflow arrangements (Fig. 3)				
NO SHOWERHEAD	Outflow from gill holes on one side (no cross flow)	Outflow equally from gill holes on both sides (no cross flow)	Outflow from the opposite end of channel inlet (no gill flow)	Outflow from the same end of channel inlet (no gill flow)	
WITH SHOWERHEAD	100% showerhead (no gill or cross flow)	73.5% Showerhead, 26.5% from gill holes on both sides (no cross flow)	85% Showerhead, 15% from gill holes on one side (no cross flow)	85% Showerhead, 15% cross flow from the opposite end of channel inlet (no gill flow)	85% Showerhead, 15% cross flow from the same end of channel inlet (no gill flow)

rates of 11.245%, 11.275%, 11.236%, 11.063%, and 11.047% of the total flow for the tested geometries and flow arrangements. Given that the average flow for each hole is 11.111%, if one wishes to find the jet Reynolds number based on the mass flow rate through the fifth hole, one can use the multipliers 1.012, 1.015, 1.011, 0.996, and 0.994 for different cases, respectively, which corresponds to a maximum increase of 1.5% and a maximum decrease of 0.6%. Two inflow arrangements to the supply channel, as shown in Fig. 3(*a*), where air either entered from one end or both ends, were tested. Static pressure taps, installed in the middle and at each end of the supply and leading-edge channels, measured no significant difference between different locations along each channel (about 1 cm of water column for a supply pressure ranging from 110 to 172 Kpa). Experimental uncertainty in heat transfer coefficient, following the method of Kline and McClintock [34] was determined to be 6%. For clarity, we will discuss the results of no-showerhead flow and showerhead flow separately and then compare them.

No Showerhead Flow

Four outflow arrangements for the exiting cooling air, shown in Fig. 3(*b*) and Table 1, were tested the "nominal flow" case was the case in which the air, after impinging on the leading-edge wall, was ejected equally through the side channel holes which simulate the gill holes on the pressure and suction sides of an airfoil. The "one-sided" case was the case in which the air, after impinging on the leading-edge wall, was ejected through the gill holes on one side only. The "crossflow" case was the case in which the air, after impinging on the leading-edge wall, was ejected from one end of the leading-edge channel simulating the blade tip. The "circular flow" case was the case in which the air, after impinging on the leading-edge wall, was ejected from the end of the leading-edge channel on the same side of the test rig as it entered thus producing a circular pattern. In the last two outflow arrangements, all side channel valves were closed and gill holes were plugged so that the only way out for the cooling air after impingement was through the end of the leading-edge channel.

Figure 6 shows the heat transfer coefficients for the nominal outflow case and for flow entering from one end and both ends of the supply channel. It is seen that for the entire range of the jet Reynolds number, flow entering from one end of the supply channel produces higher heat transfer coefficient than the case of flow entering from both ends. This behavior can be explained by Fig. 5 that shows a slightly higher share of coolant mass flow rate through the fifth cross-over hole for the case of flow entering from one end of supply channel. Leading-edge heat transfer results are shown for the two jet Reynolds number calculations—one based on the average flow through the nine crossover holes and the other based on the flow through the fifth crossover hole. As was explained in the previous section, there is a shift of about 1.5% increase in the jet Reynolds number. For other geometries and flow arrangements, this shift is less than 1.5% as was explained in the previous section. It is also observed that sidewall heat transfer coefficient specially at the lower range of the jet Reynolds number are slightly higher than those on the leading-edge wall. This behavior is due to the fact that cooling air, on its way to the sidewall gill holes comes in good contact with the sidewall thus producing high levels of heat transfer coefficients.

Figure 7 shows the heat transfer results for the case in which flow exited from one row of side holes. As expected, the heat transfer coefficient on the side with open gill holes increased significantly. On the opposite side, however, there was an equally significant drop in heat transfer coefficient because the cooling jets on their way out of the leading-edge channel did not have much interaction with a good portion of the side wall with plugged gill holes. The heat transfer coefficient levels on the leading-edge wall fell in between the two sidewall values. Again, for the reason mentioned above, flow entering from one side of the supply channel produced higher heat transfer coefficients. The maximum difference was measured on the leading-edge wall, at the higher end of the Reynolds number range, to be about 10%.

Figure 8 compares the results of two other outflow conditions of circular and crossflow. The axial flow was caused by the four upstream jets in each case. It is seen that the circular outflow case, in general, produced lower heat transfer coefficients than cross-

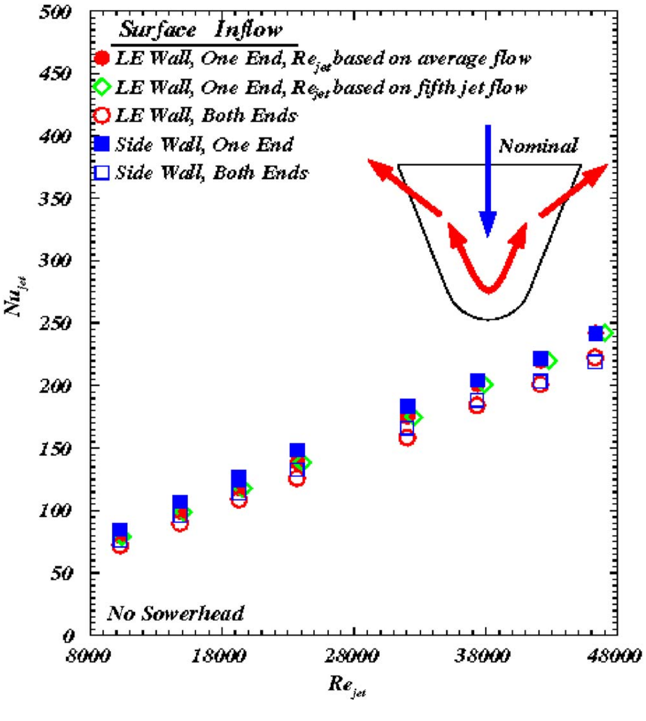

Fig. 6 Nusselt number variation with Reynolds number for the nominal case of no showerhead flow

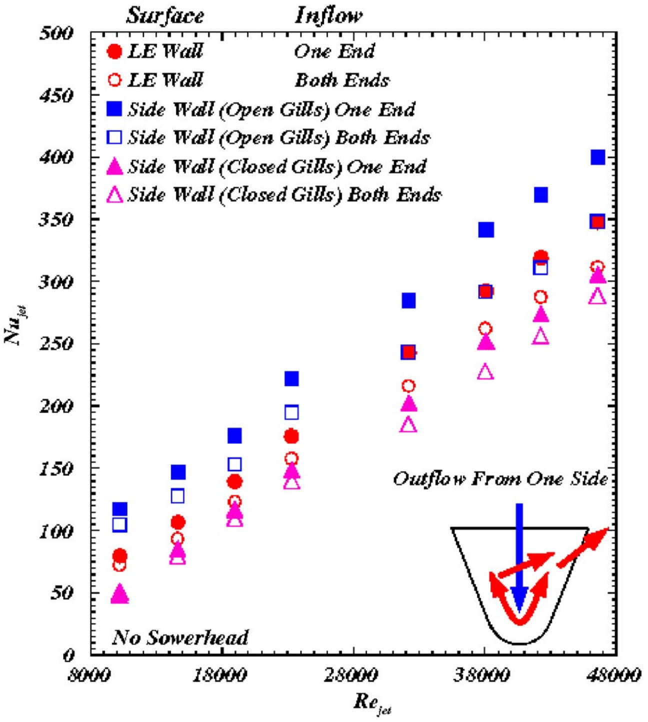

Fig. 7 Nusselt number variation with Reynolds number for the one-sided case of no showerhead flow

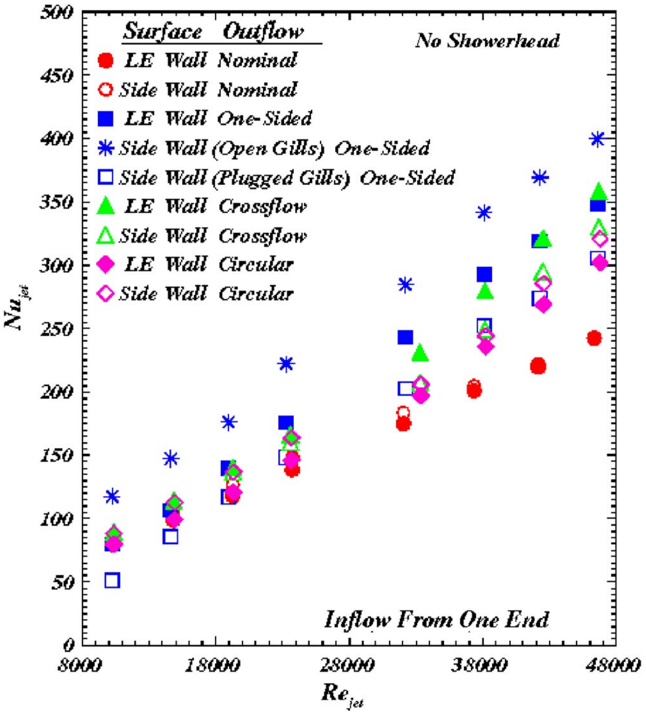

Fig. 9 Comparison between the heat transfer results of different outflow arrangements in no-showerhead cases

flow case especially on the leading-edge wall. The reason for this behavior is that, based on our flow circuit analysis, the sum of mass flow rates for the four upstream jets in the circular outflow case was less than that for the crossflow case. It is also seen that the leading-edge wall heat transfer coefficients in the crossflow case are higher than those on the side walls indication that directing the jets towards the side gills holes on their way out of the leading edge channel is a more effective way to produce higher heat transfer coefficients on the side walls.

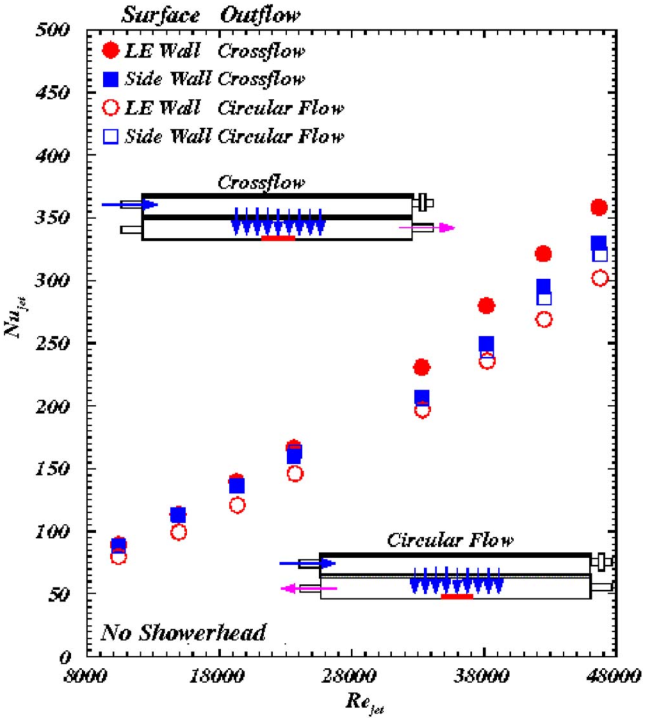

Fig. 8 Nusselt number variation with Reynolds number for the cross and circular flow cases of no showerhead flow

A comparison is made between the test results of all outflow arrangements in Fig. 9. For clarity, this comparison is for the case of inflow from one end of the supply channel. The case of outflow from both ends produces the same pattern thus not shown here due to space limitations. The highest heat transfer coefficient both on the leading edge and side wall corresponds to the case outflow from the row of gill holes on one side of the channel. As was discussed earlier, the returning coolant, after impingement on the leading-edge wall, produces a great deal of mixing around the nose area and comes into a very effective contact with the side wall on its way to the gill holes. This combination produces high levels of heat transfer coefficients both on the leading edge and side wall.

Showerhead Flow

Three outflow arrangements for the exiting cooling air, shown in Fig. 3(*c*) and Table 1, were tested. The "100% showerhead flow" case was the case in which all cooling air, after impinging on the leading-edge wall, was ejected through a row of holes on the target surface. The "symmetric flow" case was the case in which 73.5% of the cooling air, after impinging on the leading-edge wall, was ejected through the leading-edge holes and the remaining 26.5% through the side holes simulating the "gill" holes on the pressure and suction sides of an airfoil. The "one-sided flow" case was the case in which 85% of the cooling air, after impinging on the leading-edge wall, was ejected through the leading-edge holes and the remaining 15% through the side holes on one side of the leading-edge channel. The "crossflow" case was the case in which 85% of the cooling air, after impinging on the leading-edge wall, was ejected through the leading-edge holes while the remaining 15% was ejected from one end of the leading-edge channel simulating the air foil tip flow. The "circular flow" case was similar to the crossflow case except that the axial flow was ejected from the same end of the rig it entered the supply channel thus creating a circular flow. In the latter two flow ar-

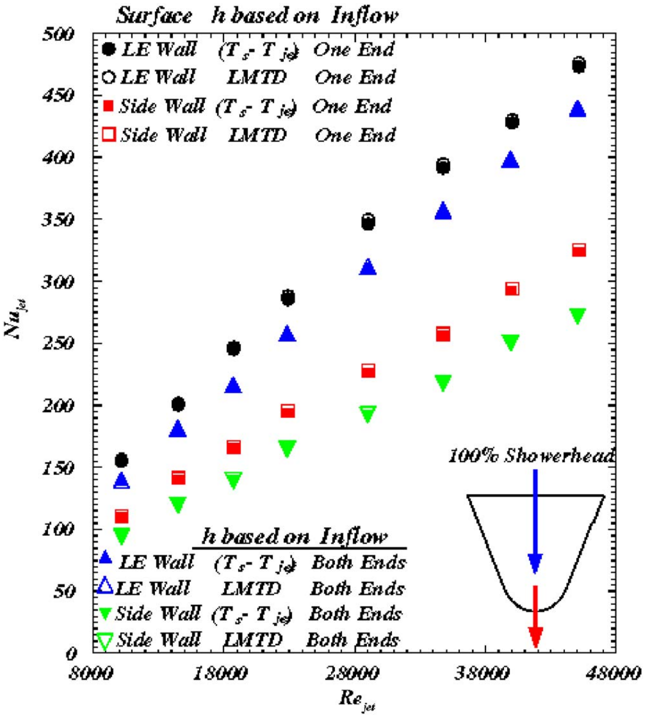

Fig. 10 Nusselt number variation with Reynolds number for the 100% showerhead flow case

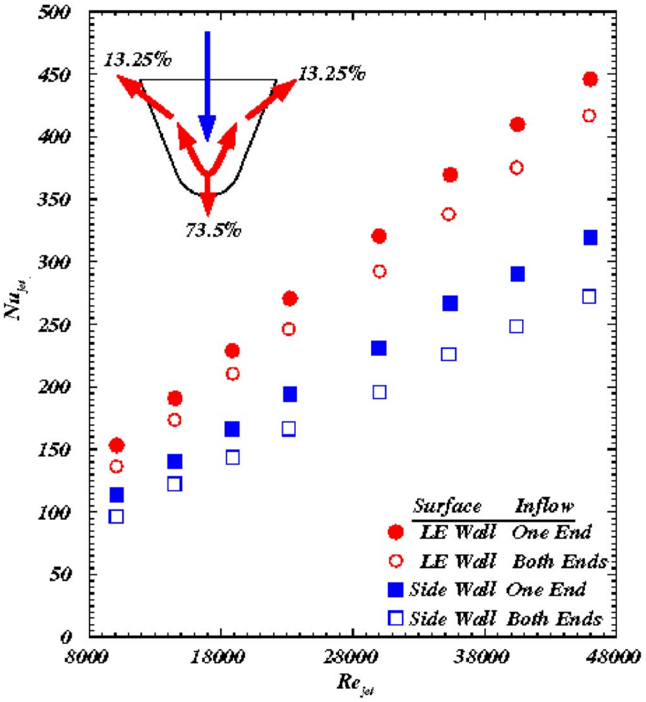

Fig. 11 Nusselt number variation with Reynolds number for the combined case of showerhead and gill (symmetric) flows

rangements, portion of the four jets upstream of the middle jet that was not ejected through the leading-edge holes (spent air) formed a crossflow that affected the impingement heat transfer coefficient.

Heat transfer results for the case of 100% showerhead flow are shown in Fig. 10. Unlike the no-showerhead cases discussed previously, a big difference is noticed between the heat transfer coefficients on the leading-edge wall and on the sidewalls. This was expected because the only way out for the impinging jets is through the leading-edge holes. Thus their cooling effects are mostly felt by the leading-edge wall. Only a small portion of the cooling jets, after impingement, will have interactions with the sidewalls. As a result, a lower heat transfer coefficient was measured on the sidewall. For the same reason given for the no-showerhead case, the inflow from one end of the supply channel produced higher heat transfer coefficients than when flow entered from both ends of the supply channel. It is, furthermore, noticed that the heat transfer coefficient levels are in general higher than those for the no showerhead cases. This behavior was continuously observed in our previous studies [30,31] as well. The mere presence of showerhead holes draws the impinging jets more effectively towards the leading-edge walls thus producing higher heat transfer coefficients. Data reduction was also performed using the logarithmic meat temperature difference for the calculation of the impingement heat transfer coefficients and the film temperature for the evaluation of air properties. The LMTD-based results for the entire 112 tests showed a reduction of less than 1% in the Nusselt numbers for the no-showerhead flow cases and an increase of less than 1% for the showerhead flow cases. Figure 10 shows the results of the two methods for the showerhead flow cases. The LMTD results for the no showerhead cases are not shown since the data points were practically on top of each other.

Figure 11 shows the heat transfer results of a combined showerhead and gill hole flows (symmetric flow). Percentages of outflow from the showerhead and gill holes were 73.5% and 26.5%, respectively. Compared with the 100% showerhead case, a slight decrease and a slight increase in heat transfer coefficients on the leading-edge and side walls were measured, respectively. These changes go along with the changes of mass flow rates through the showerhead and gill holes. Again, for the same reason given for the no-showerhead case, the inflow from one end of the supply channel produced higher heat transfer coefficients than when flow entered from both ends of the supply channel.

Figure 12 shows the heat transfer results of a combined showerhead and gill hole flows. In this outflow arrangement, the gill holes were open only on one side. Percentages of outflow from the

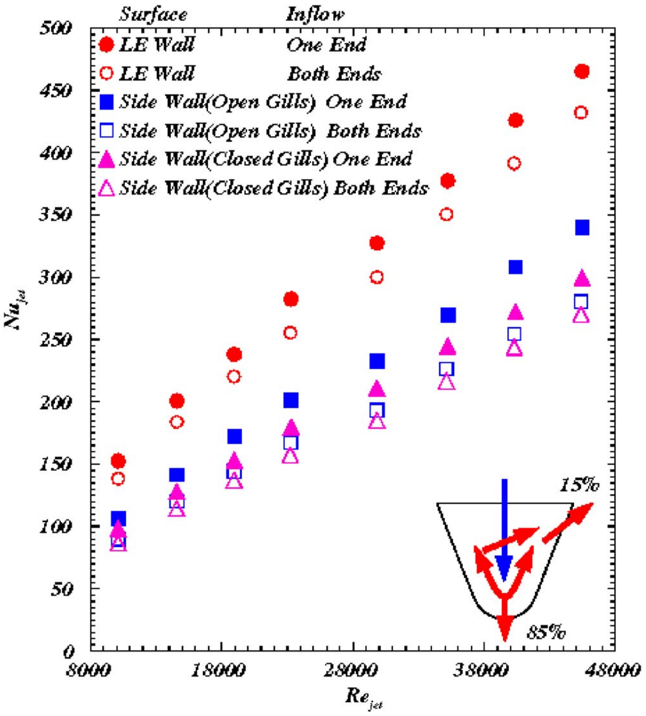

Fig. 12 Nusselt number variation with Reynolds number for the combined case of showerhead and gill (one side) flows

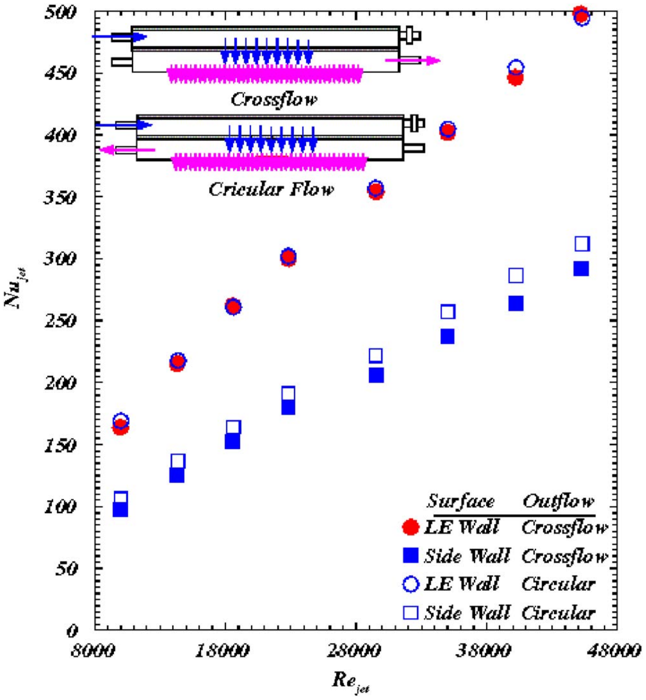

Fig. 13 Nusselt number variation with Reynolds number for the combined case of showerhead and cross or circular flows

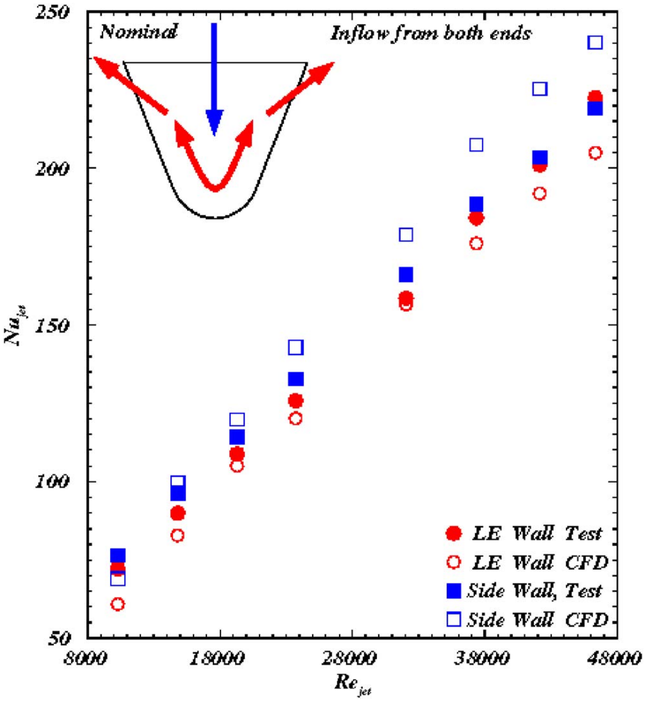

Fig. 14 Comparison between the experimental and numerical heat transfer results for the nominal case of no-showerhead flow

showerhead and gill holes were 85% and 15%, respectively. Compared with the case of gill holes on both sides, a maximum increase of 6.5% in heat transfer coefficient on the side with open gill holes and a decrease of 6% on the side with plugged gill holes were measured. A slight increase of about 4% in heat transfer coefficient was measured on the leading-edge wall. These changes go along with the changes of mass flow rates through the showerhead and gill holes. Again, for the same reason given for the no-showerhead case, the inflow from one end of the supply channel produced higher heat transfer coefficients than when flow entered from both ends of the supply channel.

Figure 13 shows the heat transfer results of a combined showerhead and axial flows. Similar to the no-showerhead cases discussed before, both cross and circular outflows were tested. Leading-edge wall heat transfer coefficients were almost identical because the showerhead flow was dominant and relatively small axial mass flow rate was not able to deter the impinging jets. The sidewall heat transfer coefficients were slightly higher for the circular outflow case. This difference which at its maximum level was about 6% is due to a variation in axial flow rate in the two cases.

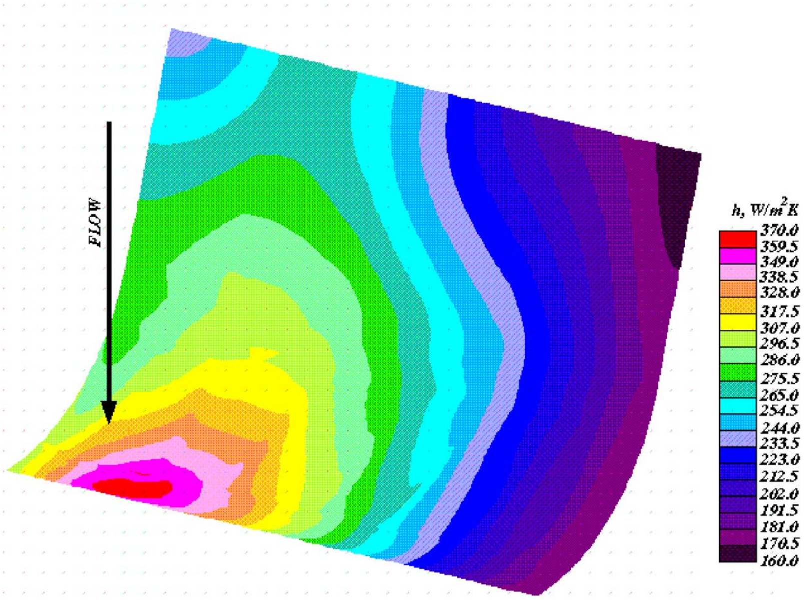

Fig. 15 Representative numerical heat transfer coefficient variation on the leading-edge wall

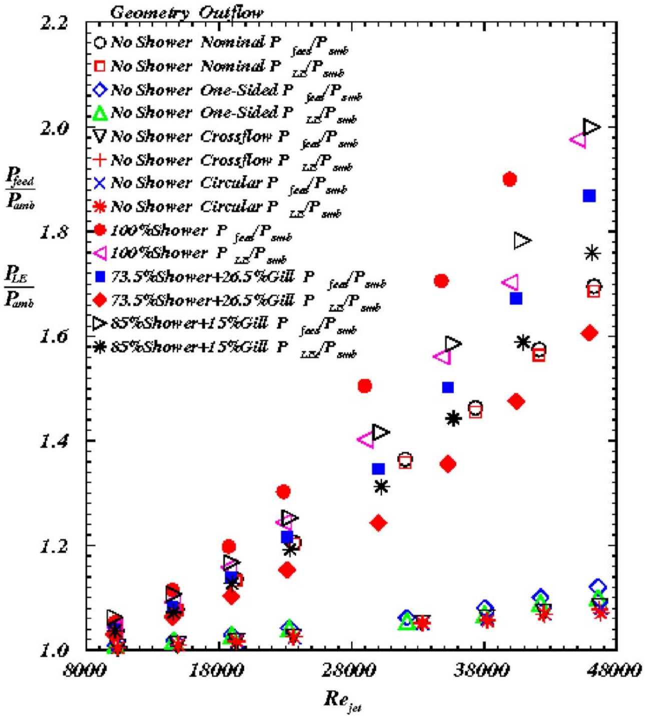

Fig. 16 Pressure ratios across the crossover holes and the leading-edge channel for different flow arrangements

Static pressures in the feed and leading-edge channels, normalized with the lab pressure, for all outflow arrangements are shown in Fig. 16. Those cases with no showerhead holes show lower pressure ratios across the crossover and gill holes and different outflow arrangements show very close pressure ratios. The showerhead cases, however, show much higher pressure ratios due to lower showerhead holes exit area compared to those of the gill holes. For this reason, the case of 100% showerhead outflow represents the maximum pressure ratio while the no showerhead case with the crossflow arrangement showed the lowest pressure ratio since the flow exited from the open end of the leading-edge channel.

Numerical Results

Representative CFD results are compared with the experimental data in Figs. 14–18. CFD models with constant heat flux boundary conditions identical to the tested geometry for each case were run on PC Pentium 4, 1.6 GHZ machines with 512 MB memory. A typical case took about 1000 iterations and about four to five hours to converge. Good agreement between the measured and numerically calculated impingement heat transfer coefficients are observed for the no-showehead case. The CFD results for the leading-edge heat transfer coefficients are underpredicted with a maximum difference of about 16% for smallest Reynolds number and a minimum of about 1.3% in the middle range of the Reynolds number. The CFD results for the sidewall heat transfer coefficients, however, are generally overpredicted with an average difference of about 10%. Typical heat transfer coefficient variations on the leading-edge and side walls for the no-showerhead case are shown in Figs. 15 and 17. Since, taking advantage of symmetry, only half of the domain was modeled, the high heat transfer coefficient regions in these figures correspond to the impingement location in Fig. 15 and gill hole location in Fig. 17. An area-weighted Nusselt number is reported in these two figures. Finally, a comparison is made between the test and CFD results for the 100% showerhead case in Fig. 18. A remarkable underestimation is observed by the CFD both on the leading edge and side walls. It is speculated that the mixing effects of jet after impingements and their interaction with the leading edge and side walls were not captured by the CFD. A more dense mesh, combined with a different turbulence model, including a two-layer, could improve the CFD results. That effort is underway and results will be reported later.

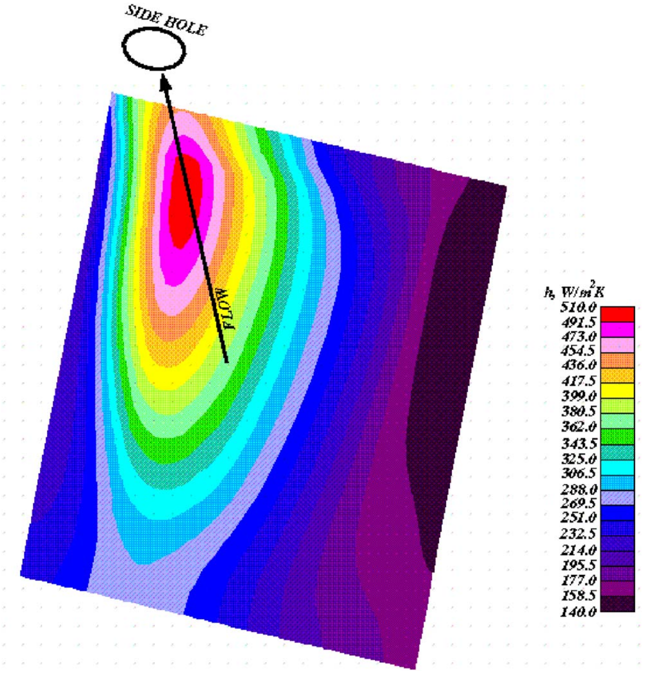

Fig. 17 Representative numerical heat transfer coefficient variation on the side wall

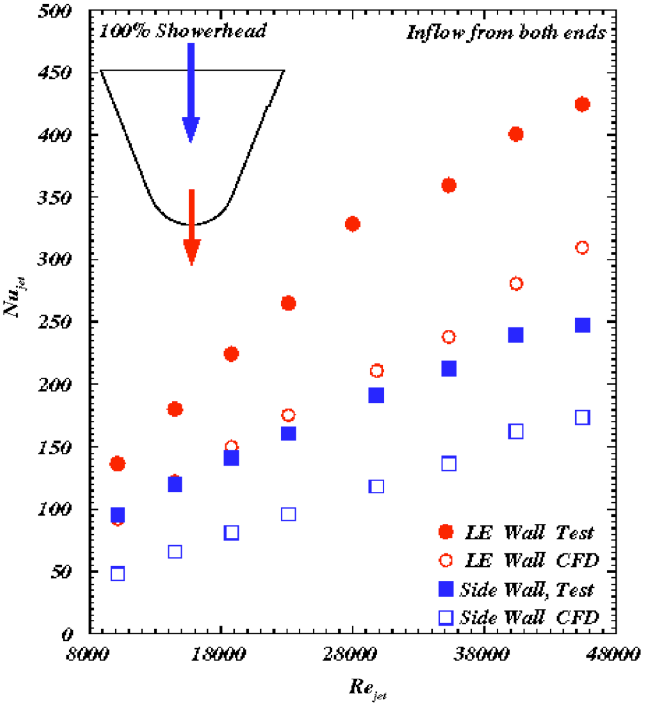

Fig. 18 Comparison between the experimental and numerical heat transfer results for the 100% showerhead flow case

Conclusions

Leading-edge impingement heat transfer coefficients with and without the presence of showerhead holes were measured for a variety of outflow arrangements. Heat transfer results on the leading-edge nose and on the side walls were measured and reported separately. Representative CFD results were also presented. Major conclusions of this study were:

(a) For the same coolant flow, the heat transfer coefficients were higher for those cases with the showerhead flow;

(b) The no-showerhead cases produced its highest heat transfer coefficient levels when coolant was ejected from the gill holes on one side of the channel;

(c) The agreement between the numerical and experimental results for the no-showerhead flow case was reasonable with an average difference of about 10%. However, the CFD results were underpredicted up to 30% when impingement with showerhead flow was modeled.

Nomenclature

A_{hole} = total area of all nine cross-over holes
A_{HT} = heat transfer area
AR = cooling channel aspect ratio
d_{gill} = gill hole diameter (0.508 cm)
d_{jet} = racetrack hole hydraulic diameter (2.228 cm)
d_{shower} = showerhead hole diameter (0.594 cm)
D_h = cooling channel hydraulic diameter
h = average heat transfer coefficient on the leading edge or side walls, $[(vi/A_{\text{HT}})-q_{\text{loss}}]/(T_s-T_{\text{jet}})$
i = current through the foil heater on the middle copper piece
k = air thermal conductivity
LMTD = logarithmic mean temperature difference, $[(T_s-T_m)-(T_s-T_{\text{jet}})]/\log[(T_s-T_m)/(T_s-T_{\text{jet}})]$
m = total mass flow rate through all nine crossover holes
Nu_{jet} = average Nusselt number based on the jet diameter, hd_{jet}/k
P = channel perimeter without ribs
P_{amb} = ambient (lab) pressure
P_{feed} = supply channel pressure (upstream of crossover holes)
P_{LE} = leading edge channel pressure
q_{loss} = heat losses from the middle copper piece to the ambient by conduction and convection as well as the heat losses by radiation to the unheated walls
R_{nose} = channel radius at the leading edge
Re_{jet} = Reynolds number based on the jet diameter $(\rho U_{\text{jet}}d_{\text{jet}}/\mu)$
T_f = film temperature, $(T_s+T_m)/2$
T_{jet} = air jet temperature
T_m = air mixed mean temperature
T_s = surface temperature
U_{jet} = jet mean velocity, $m/(\rho A_{\text{hole}})$
Z = jet place distance to the target surface (Fig. 1)
v = voltage drop across the foil heater on the middle copper piece
β = showerhead hole angle with the channel axial direction (30 deg, Fig. 1)
μ = air dynamic viscosity at jet temperature
ρ = air density at jet temperature and pressure

References

[1] Burggraf, F., 1970, "Experimental Heat Transfer and Pressure Drop With Two-Dimensional Turbulence Promoters Applied to Two Opposite Walls of a Square Tube," *Augmentation of Convective Heat and Mass Transfer*, A. E. Bergles and R. L. Webb, eds. ASME, New York, pp. 70–79.

[2] Chandra, P. R., and Han, J. C., 1989, "Pressure Drop and Mass Transfer in Two-Pass Ribbed Channels," J. Thermophys. Heat Transfer, **3**(3), pp. 315–319.

[3] El-Husayni, H. A., Taslim, M. E., and Kercher, D. M., 1994, "An Experimental Investigation of Heat Transfer Coefficients in a Spanwise Rotating Channel With Two Opposite Rib-Roughened Walls," ASME J. Turbomach., **113**, pp. 75–82.

[4] Han, J. C., 1984, "Heat Transfer and Friction in Channels With Two Opposite Rib-Roughened Walls," ASME J. Heat Transfer, **106**(4), pp. 774–781.

[5] Han, J. C., Glicksman, L. R., and Rohsenow, W. M., 1978, "An Investigation of Heat Transfer and Friction for Rib Roughened Surfaces," Int. J. Heat Mass Transfer, **21**, pp. 1143–1156.

[6] Han, J. C., Park, J. S., and Lei, C. K., 1985, "Heat Transfer Enhancement in Channels With Turbulence Promoters," ASME J. Eng. Gas Turbines Power, **107**(1), pp. 628–635.

[7] Han, J. C., Zhang, Y. M., and Lee, C. P., 1992, "Influence of Surface Heat Flux Ratio on Heat Transfer Augmentation in Square Channels With Parallel, Crossed, and V-Shaped Angled Ribs," ASME J. Turbomach., **114**, pp. 872–880.

[8] Metzger, D. E., Vedula, R. P., and Breen, D. D., 1987, "The Effect of Rib Angle and Length on Convection Heat Transfer in Rib-Roughened Triangular Ducts," *Proceedings of the ASME-JSME Thermal Engineering Joint Conference*, Vol. 3, pp. 327–333.

[9] Metzger, D. E., Chyu, M. K., and Bunker, R. S., 1988, "The Contribution of On-Rib Heat Transfer Coefficients to Total Heat Transfer from Rib-Roughened Surfaces," *Transport Phenomena in Rotating Machinery*, J. H. Kim, ed., Hemisphere, Washington, DC.

[10] Metzger, D. E., Fan, C. S., and Yu, Y., 1990, "Effects of Rib Angle and Orientation on Local Heat Transfer in Square Channels With Angled Roughness Ribs," *Compact Heat Exchangers: A Festschrift for A. L. London*, Hemisphere, Washington, DC, pp. 151–167.

[11] Taslim, M. E., and Spring, S. D., 1988, "An Experimental Investigation of Heat Transfer Coefficients and Friction Factors in Passages of Different Aspect Ratios Roughened With 45° Turbulators," *Proc. National Heat Conference*, Houston, TX.

[12] Taslim, M. E., and Spring, S. D., 1988, "Experimental Heat Transfer and Friction Factors in Turbulated Cooling Passages of Different Aspect Ratios, Where Turbulators are Staggered," Paper No. AIAA-88–3014.

[13] Taslim, M. E., Bondi, L. A., and Kercher, D. M., 1991, "An Experimental Investigation of Heat Transfer in an Orthogonally Rotating Channel Roughened 45 Degree Criss-Cross Ribs on Two Opposite Walls," ASME J. Turbomach., **113**, pp. 346–353.

[14] Taslim, M. E., and Spring, S. D., 1991, "An Experimental Investigation Into the Effects Turbulator Profile and Spacing Have on Heat Transfer Coefficients and Friction Factors in Small Cooled Turbine Airfoils," Paper No. AIAA-91–2033.

[15] Taslim, M. E., Rahman, A., and Spring, S. D., 1991, "An Experimental Investigation of Heat Transfer Coefficients in a Spanwise Rotating Channel With Two Opposite Rib-Roughened Walls," ASME J. Turbomach., **113**, pp. 75–82.

[16] Webb, R. L., Eckert, E. R. G., and Goldstein, R. J., 1971, "Heat Transfer and Friction in Tubes With Repeated-Rib-Roughness," Int. J. Heat Mass Transfer, **14**, pp. 601–617.

[17] Zhang, Y. M., Gu, W. Z., and Han, J. C., 1994, "Heat Transfer and Friction in Rectangular Channels With Ribbed or Ribbed-Grooved Walls," ASME J. Heat Transfer, **116**(1), pp. 58–65.

[18] Chupp, R. E., Helms, H. E., McFadden, P. W., and Brown, T. R., 1969, "Evaluation of Internal Heat Transfer Coefficients for Impingement Cooled Turbine Blades," J. Aircr., **6**(1), pp. 203–208.

[19] Metzger, D. E., Yamashita, T., and Jenkins, C. W., 1969, "Impingement Cooling of Concave Surfaces With Lines of Circular Air Jets," J. Eng. Power, **93**(3), pp. 149–155.

[20] Kercher, D. M., and Tabakoff, W., 1970, "Heat Transfer by a Square Array of Round Air Jets Impinging Perpendicular to a Flat Surface Including the Effect of Spent Air," J. Eng. Power, **92**(1), pp. 73–82.

[21] Florschetz, L. W., Berry, R. A., and Metzger, D. E., 1980, "Periodic Streamwise Variation of Heat Transfer Coefficients for Inline and Staggered of Circular Jets With Crossflow of Spent Air," ASME J. Heat Transfer, **102**(1), pp. 132–137.

[22] Florschetz, L. W., Truman, C. R., and Metzger, D. E., 1981, "Streamwise Flow and Heat Transfer Distribution for Jet Impingement with Crossflow," ASME J. Heat Transfer, **103**(2), pp. 337–342.

[23] Florschetz, L. W., Metzger, D. E., Su, C. C., Isoda, Y., and Tseng, H. H., 1984, "Heat Transfer Characteristics for Jet Arrays Impingement With Initial Crossflow," ASME J. Heat Transfer, **106**(1), pp. 34–41.

[24] Metzger, D. E., and Bunker, R. S., 1990, "Local Heat Transfer in Internally Cooled Turbine Airfoil Leading Edge Regions—Part I: Impingement Cooling Without Film Coolant Extraction," ASME J. Turbomach., **112**(3), pp. 451–458.

[25] Bunker, R. S., and Metzger, D. E., 1990, "Local Heat Transfer in Internally Cooled Turbine Airfoil Leading Edge Regions—Part II: Impingement Cooling With Film Coolant Extraction," ASME J. Turbomach., **112**(3), pp. 459–466.

[26] Van Treuren, K. W., Wang, Z., Ireland, P. T., and Jones, T. V., 1994, "Detailed Measurements of Local Heat Transfer Coefficient and Adiabatic Wall Temperature Beneath an Array of Impinging Jets," ASME J. Turbomach., **116**(2), pp. 269–374.

[27] Chang, H., Zhang, D., and Huang, T., 1997, "Impingement Heat Transfer From Rib Roughened Surface Within Arrays of Circular Jet: The Effect of the Rela-

tive Position of the Jet Hole to the Ribs," ASME Paper No. 97-GT-331.
[28] Huang, Y., Ekkad, S. V., and Han, J. C., 1998, "Detailed Heat Transfer Distributions Under an Array of Orthogonal Impinging Jets," J. Thermophys. Heat Transfer, **12**(1), pp. 73–79.
[29] Akella, K. V., and Han, J. C., 1999, "Impingement Cooling in Rotating Two-Pass Rectangular Channels With Ribbed Walls," J. Thermophys. Heat Transfer, **13**(3), pp. 364–371.
[30] Taslim, M. E., Pan, Y., and Spring, S. D., 2001, "An Experimental Study of Impingement on Roughened Airfoil Leading-Walls With Film Holes," ASME J. Turbomach., **123**(4), pp. 766–773.
[31] Taslim, M. E., Pan, Y., and Bakhtari, K., 2002, "Experimental Racetrack Shaped Jet Impingement on a Roughened Leading-Edge Wall With Film Holes," ASME Paper No. GT-2002–30477.
[32] Taslim, M. E., Setayeshgar, L., and Spring, S. D., 2001, "An Experimental Evaluation of Advanced Leading Edge Impingement Cooling Concepts," ASME J. Turbomach., **123**(2), pp. 147–153.
[33] Taslim, M. E., Bakhtari, K., and Liu, H., 2003, "Experimental and Numerical Investigation of Impingement on a Rib-Roughened Leading-Edge Wall," ASME J. Turbomach., **125**, pp. 1–10.
[34] Kline, S. J., and McClintock, F. A., 1953, "Describing Uncertainty in Single-Sample Experiments," Mech. Eng. (Am. Soc. Mech. Eng.), **75**, pp. 3–8.

G. E. Andrews

R. A. A. Abdul Hussain

M. C. Mkpadi

Energy and Resources Research Institute,
School of Process, Environment
and Materials Engineering,
The University of Leeds,
Leeds LS2 9JT, UK

Enhanced Impingement Heat Transfer: The Influence of Impingement X/D for Interrupted Rib Obstacles (Rectangular Pin Fins)

Impingement flat wall cooling, with 15.2 mm pitch square hole arrays, was investigated in the presence of an array of interrupted rib obstacles. These ribs took the form of rectangular pin-fins with a 50% blockage to the cross flow. One side exit of the air was used, and there was no initial cross flow. Three hole diameters were investigated, which allowed the impingement wall pressure loss to be varied at constant coolant mass flow rate. Combustor wall cooling was the main application of the work, where a low wall cooling pressure loss is required if the air is subsequently to be fed to a low NO_x *combustor. The results showed that the increase in surface average impingement heat transfer, relative to that for a smooth wall, was small and greatest for an X/D of 3.06 at 15%. The main effect of the interrupted ribs was to change the influence of cross flow, which produced a deterioration in the heat transfer with distance compared to a smooth impingement wall. With the interrupted ribs the heat transfer increased with distance. If the heat transfer was compared at the trailing edge of the test section, where the upstream cross flow was at a maximum, then at high coolant flow rates the increase in heat transfer was 21%, 47%, and 25% for X/D of 4.66, 3.06, and 1.86, respectively.*

[DOI: 10.1115/1.1860574]

1 Introduction

Impingement cooling is used in gas turbine blade internal cooling for platform and airfoil surfaces in the midvane region. Impingement cooling is also used in combustor wall cooling for low $\mathrm{NO_x}$ gas turbine combustion, where no film cooling is desirable due to the adverse increase in $\mathrm{NO_x}$ and CO [1]. The present work set out to investigate whether low pressure loss small X/D impingement jet cooling, using high air mass flow rates in a regenerative cooling configuration, was worthwhile. The aim of the regenerative cooling is to use all of the low $\mathrm{NO_x}$ burner combustion air for wall cooling prior to injection of that air through the low $\mathrm{NO_x}$ burner.

For larger X/D the pressure loss increases and, if this is to be kept low, then the mass flow rate has to be lower. This then limits high X/D impingement cooling to using only a portion of the combustion air flow and discharging this air through wall film cooling jets in the transition duct or through dilution holes. This is the procedure currently used in most low $\mathrm{NO_x}$ combustor cooling applications of this technique. In future low $\mathrm{NO_x}$ combustors all the compressor air will be required for combustion, and the use of this type of impingement cooling is likely to be replaced by regenerative cooling with a low pressure loss, small X/D high mass flow design requirement.

For turbine vane cooling it is normally the midpassage and the tip region that is impingement cooled [2]. The midvane region has a geometry that can be represented by flat plate impingement heat transfer, sometimes with an upstream cross flow in the impingement gap. This upstream flow is the flow from the tip cooling region, which in many cases is an impingement-cooled region. Some recent investigators of enhanced impingement cooling have used experimental configurations with imposed upstream cross flow [3,4]. However, if the turbine tip area is cooled with impingement air jets, which are subsequently used for tip film cooling, then the midpassage region has no upstream cross flow. Some recent investigators of impingement cooling with obstacles in the gap have used this configuration [5,6].

Impingement cooling, with several rows of holes with a single direction of discharge flow, self generates a cross flow for the downstream rows of holes from the discharge from the upstream rows. For smooth walls this cross flow results in a decrease in the impingement heat transfer with axial distance [7–10]. However, with obstacles in the gap it is anticipated that their prime effect may be to interact with the cross flow to enhance the heat transfer and hence have the greatest influence on the downstream portion of the test sections. This was first shown by Trabolt and Obot [11] for small transverse ribs and by Abdul Hussain and Andrews [12] for large transverse ribs, interrupted ribs, and ribs with circular holes.

A problem with impingement cooling and cross-flow interactions is that as the impingement wall pressure loss is reduced and then the pressure loss due to the cross flow becomes a greater proportion of the overall pressure loss. This can then lead to a flow maldistribution between the rows of impingement holes [9]. The geometries for which flow maldistribution was important was shown by Andrews and Hussain [13,14] to be predicted by the parameter W in Eq(1), for a constant density between the jet and cross flow. If the jet velocity ratio U_j/U_c was less then 2 or W less then 6, then flow maldistribution was significant and increased as W decreased or Uj/Uc decreased.

$$W=[U_j/(U_cC_d)]^2=[(1/C_dNA)Z/D]^2 \tag{1}$$

In the present work with obstacles in the gap the increase in

---

Contributed by the International Gas Turbine Institute (IGTI) of ASME for publication in the JOURNAL OF TURBOMACHINERY. Manuscript received October 1, 2003; final manuscript received March 1, 2004. IGTI Review Chair: A. J. Strazisar. Paper presented at the International Gas Turbine and Aeroengine Congress and Exhibition, Vienna, Austria, June 13–17, 2004, Paper No. 2004-GT-54184.

pressure loss due to the cross flow caused by the obstacles will increase the flow maldistribution. However, the effect of flow maldistribution is to divert cooling air from the leading edge to the trailing edge of the impingement-cooled gap, and this enhances heat transfer in the trailing-edge region, but reduces the upstream cross flow. These effects will be shown to be a strong influence in the present results.

2 Rib Enhanced Impingement Heat Transfer Literature Review

In the present work a high rib blockage of the impingement gap of 50% was investigated. This blockage had previously been investigated by Abdul Hussain and Andrews [12], for three rib designs termed Rough A, B, and C. These were a plane rib (Rough A), an interrupted rib or rectangular pin-fin array (Rough B), and a rib with holes drilled for the cross flow to pass (Rough C). Their results showed some of the highest enhancement in impingement heat transfer in the literature. This high cross-flow blockage of 50% is larger than has been studied by most other workers. The rectangular pin-fin array (Rough B) was investigated further in the present work using a range of impingement jet X/D.

The reason for the significance of large blockage obstacles, rather than small boundary layer trip obstacles, is the generation of large-scale recirculation zones in the impingement gap with associated turbulence generation. These aerodynamics are generated by the interaction of the induced cross flow in the downstream portion of the impingement gap with the large obstacles. The review of previous work below shows that the highest enhancements of impingement heat transfer due to obstacles in the gap are for geometries with a high cross-flow blockage.

The internal aerodynamics of impingement jet arrays in a closed duct with Z/D less than about 10 were investigated using CFD by Abdul Hussain and Andrews [12] and A1 Dabagh et al. [15]. These CFD studies have been experimentally confirmed in the studies of Son et al. [2,16] for triangular impingement hole arrays. The impingement jet flows interact to generate a reverse flow on the centerline between adjacent holes, and in the present work the rib was located so that each side of the rib was scrubbed by this reverse flow. The intention was to increase the convective heat transfer with the ribs and also to increase the surface area available for heat transfer (by 79.8%). The action of the cross flow would create additional turbulent wake interactions with the ribs.

It has not previously been recognized that the obstacle blockage to the cross flow is an important parameter in the enhanced heat transfer, as it is rarely given in the papers. The blockages have been evaluated from the geometries given in the papers. Kercher and Tabakoff [8] studied very narrow gaps with between 11% and 34% blockage by the ribs. Trabold and Obot [11] investigated small ribs in large gaps with a blockage range from 1.6% to 12.8% for $X/D=3.15$ and 1.78. Shizuya and Kawaike [17] investigated a single rib blockage of 12.5% and pin-fin obstacles with blockages of 16% and 40% for an X/D of 4 and 8. Chang et al. [18,19] investigated continuous cross-flow ribs with blockages of 25%, 38%, and 50% in the presence of upstream cross flow and for $X/D=5$, 7.5, and 10 with square hole arrays. These geometries would give higher impingement wall pressure loss than in the present work, and there would be no significant flow maldistribution. They showed that for the same impingement jet Reynolds number, the higher the blockage of the ribs the higher the Nusselt number, and that the influence of the ribs increased as the cross-flow velocity increased relative to the impingement jet velocity.

The circular pin-fin obstacle array in the impingement gap used by Hoecker et al. [5] was of a diameter larger than the impingement jet diameter. The pin height-to-diameter ratio was 1. The blockage used by Hoecker et al. [5] was varied by increasing the impingement gap. Blockages of 10%, 20%, and 30% were investigated for $X/D=4.35$, 6.5, and 13. However, the pin-fin blockage was not varied as an independent parameter, as X/D was decreased as the blockage was increased, and hence the impact of the pin-fin blockage was not determined. For an X/D of 6.5 and a 20% blockage the heat transfer enhancement was between 10% and 35%. For an X/D of 4.35 and a blockage of 30% the effect of the pin-fins varied from an enhancement of less than 5% to a deterioration of up to 5%.

The earliest investigation of enhanced impingement heat transfer using pin-fins was by Shizuya and Kawaike [17] for a constant Z of 8 mm and D of 2.5 mm. Roughness elements of repeated rectangular ribs, pin-fins, and combinations of ribs and pin-fins were investigated on flat and concave surfaces. Transverse ribs alone, with a blockage of 12.5%, had negligible influence on the heat transfer, but the addition of pin-fins with a blockage of 40% increased the heat transfer by 50% for an X/D of 4 and by 16% for an X/D of 8. This is the highest reported influence of surface roughness on impingement heat transfer, and the best geometry had two pin-fins for each impingement hole. The results showed that the greatest influence of the pin-fin obstacles was for the highest cross-flow blockage, although this was not directly stated. There was no comparison of the various surface roughness elements at constant cross-flow blockage, as in the present work.

Annerfeldt et al. [6] investigated enhanced impingement heat transfer using various pin-fin arrays, including round, triangular, V gutter, and rectangular pin-fin shapes. The rectangular pin-fin geometry was aligned with the shortest width into the flow, giving the lowest blockage. In the present work the rectangular pin-fins have the longest side into the cross flow, giving the 50% blockage. In previous work [20], the authors compared this geometry with the lower blockage of the ribs parallel to the cross flow (co-flow) with the impingement jets aligned with the centerline of the pin-fin, similar to the work of Annerfeldt et al. [6]. This showed a slightly inferior heat transfer coefficient for co-flow for the pin-fin ribs, but an slight enhancement for the plain ribs.

The cross-flow blockages studied by Annerfeldt et al. [6] were 13–39% for triangular and V gutter pins, 8–24% for cylindrical pins, and 4–14% for rectangular pins. An X/D of 5 was used in the study, similar to the present work X/D of 4.66. The results showed the greatest enhancement of heat transfer for the geometries with the highest blockage, for the same impingement X/D. The maximum enhancement for the triangular pins was 30%.

3 Impingement Jet Array Geometries

The impingement wall and attached ribs were the same throughout the present work and the same as the Rough B geometry investigated for one X/D by Abdul Hussain and Andrews [12]. The geometry was a rib height e of 8 mm, in an impingement gap Z of 9 mm. The rib was not attached to the outer wall to avoid the thermal stresses that would occur in combustor cooling with a hot inner wall and cool outer wall.

The rib was transverse to the cross flow and was a slotted rib with 50% of the total cross-flow area blocked. The comparison of cross flow with co-flow orientation of the ribs for one X/D and Rough A and Rough B ribs has been made by Andrews et al. [20]. This showed only small differences from the smooth wall heat transfer, but for the present interrupted ribs (Rough B) there was a significantly better heat transfer than for plane ribs (Rough A). The major advantage of the co-flow was the lower pressure loss due to lower blockage of the ribs.

The ribs had 10 gaps of 6.6 mm width so that there was one rib for each impingement hole, which was directed on the centerline between the ribs in all the present tests. Offset impingement jets have also been investigated by the authors; the impingement jets then scrubbed one of the faces of a rib. There was no improvement of the heat transfer, as any enhancement of the rib heat transfer on one side was offset by the deterioration on the other side.

The rib thickness was 3 mm, and this geometry left a flat plate obstacle, 3 mm thick, 8.59 mm wide, and 8 mm high for each impingement jet. The distance from the rear face of rib to the front

Table 1 Impingement square jet array geometries

X/D	4.66	3.06	1.86
Z/D	2.75	1.81	1.10
e/D	2.45	1.61	0.98
N holes/m^2	4306	4306	4306
X (mm)	15.2	15.2	15.2
Z (mm)	9.0	9.0	9.0
D (mm)	3.27	4.98	8.19
L/D	1.94	1.28	0.78
N	10	10	10
E (mm)	8	8	8
$DP/P\%$ $G=1$ kg/s m^2	0.40	0.07	0.01
Uj/Uc $N=9$	1.8	0.77	0.29

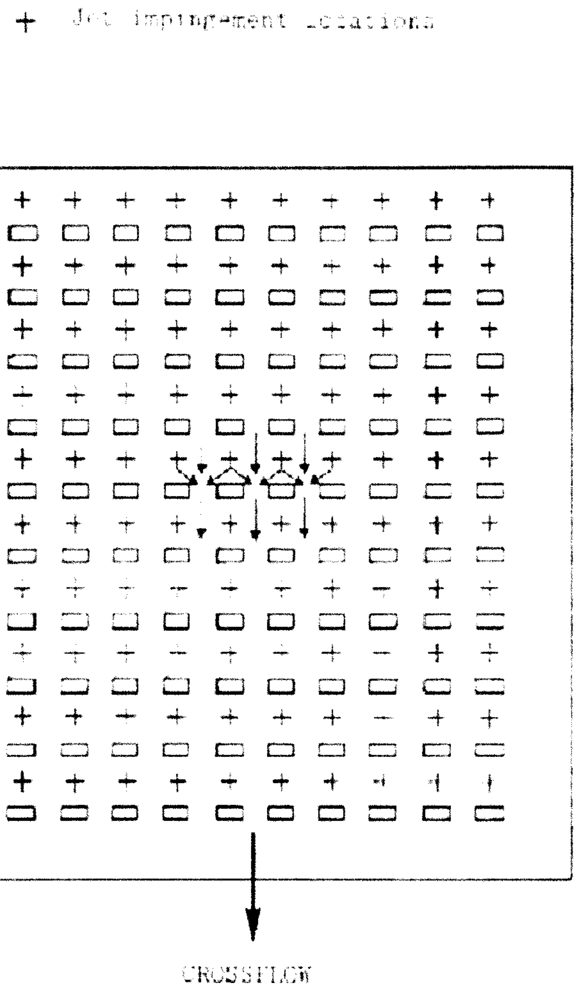

Fig. 1 Rectangular pin-fin obstacle configuration

face of the downstream rib was 12.2 mm, and this was bigger than the largest impingement hole investigated of 8.19 mm dia.

The variation of X/D was undertaken so that high coolant mass flow rates could be investigated without excessive pressure loss. The three geometries investigated are detailed in Table 1. Each test plate was 152.4 mm^2, and all heat transfer measurements were taken on the plate centerline between the central two rows of impingement holes. All of the impingement jet walls were 6.3 mm thick stainless steel, and the impingement-cooled target plate was 6.3 mm thick stainless steel. The pin-fin array was also stainless steel, and the whole geometry was machined from solid, so that there were no joints between the plate and the pins.

The test walls with $X/D=4.66$ and 1.86 were also manufactured with the impingement holes moved half a hole pitch in a transverse direction relative to the rectangular pin-fins. This enabled the impingement jets to be directed between the pin-fins instead of in-line with them. This then gave a direct interaction between the impingement jets and the high cross-flow velocity flowing between the pin-fins.

The change in Z/D in the present work was a necessary result of the requirement to investigate the influence of the pin-fin obstacles at a constant cross-flow velocity. However, Andrews and Hussain [14] and Andrews et al. [21] have shown that over a range of Z/D from 0.5 to 5, there was no major influence of Z/D on the mean surface average heat transfer, and several investigators have also found this [7–9].

The surface area of the rib gave a 79.8% increase in the heat transfer surface area of the impingement wall per impingement jet. The rib was positioned so that the impingement jet was aligned with the centerline of the flat obstacle and midway between two consecutive obstacles, as shown in Fig. 1. The alternative arrangement of the impingement jet in line with the gap between the pin-fins was also investigated. This enabled the impingement jets to be directed between the pin-fins instead of in-line with them.

In between the ribs, the cross-flow mean velocity was increased locally by 100% because of the 50% overall blockage of the ribs. However, with the continuous ribs the peak ross-flow velocity was displaced from the impingement-cooled surface to the impingement jet plate surface. Any influence on enhanced heat transfer was then only due to enhanced turbulence by the cross flow on the impingement-cooled surface. The rectangular pin-fin obstacles had both increased cross-flow velocity and enhanced cross-flow turbulence on the impingement surface.

The measured impingement plate pressure losses in Table 1 are those for the impingement plate with a free discharge with no impingement wall, cross flow, or obstacles. The pressure loss in Fig. 2 was measured as the static pressure difference between the impingement air supply plenum chamber upstream of the impingement test wall and the impingement gap discharge pressure, which was atmospheric.

The overall pressure loss was dominated by the pressure loss of the cross flow in the duct. The presence of the smooth impingement wall had no influence on the overall pressure loss for $Z/D > 1$, as the one dynamic head hole exit loss for a free discharge is replaced by the one dynamic head loss for a 90 deg bend [22]. If Z/D is <1, then the smooth wall restricts the outlet hole area and the pressure loss increases. These considerations are valid for all X/D.

Figure 2 shows that for an X/D of 1.86 with the impingement wall in place and cross flow established, the overall pressure loss for $G=1$ kg/s m^2 was 0.25%. This may be taken as the pressure loss of the smooth duct flow as the impingement wall pressure loss for an X/D of 1.86 was negligible, as shown in Table 1. For an X/D of 4.66 at the same coolant flow rate, the overall pressure loss was 0.65%, consisting of the 0.25% duct flow pressure loss plus the 0.4% impingement wall pressure loss from Table 1. The addition to the 50% blockage pin-fin ribs in the cross-flow gap increased the cross-flow duct pressure loss by only 0.15% at the same flow rate. Hence, the use of a 50% obstacle blockage in the impingement gap is only of minor importance from an overall pressure-loss point of view, and there is no reason for these types of large-scale pin-fins not to be used for heat transfer enhancement.

The 0.15% cross-flow duct pressure loss was significant relative to the very low pressure loss of the impingement walls for $X/D=3.06$ and 1.86. This would produce a flow maldistribution between the rows of impingement jets with a greater flow in the downstream jets and a reduced flow in the upstream leading-edge region [13,14]. Table 1 also shows that the impingement jet velocity to cross-flow velocity ratio Uj/Uc was well below unity.

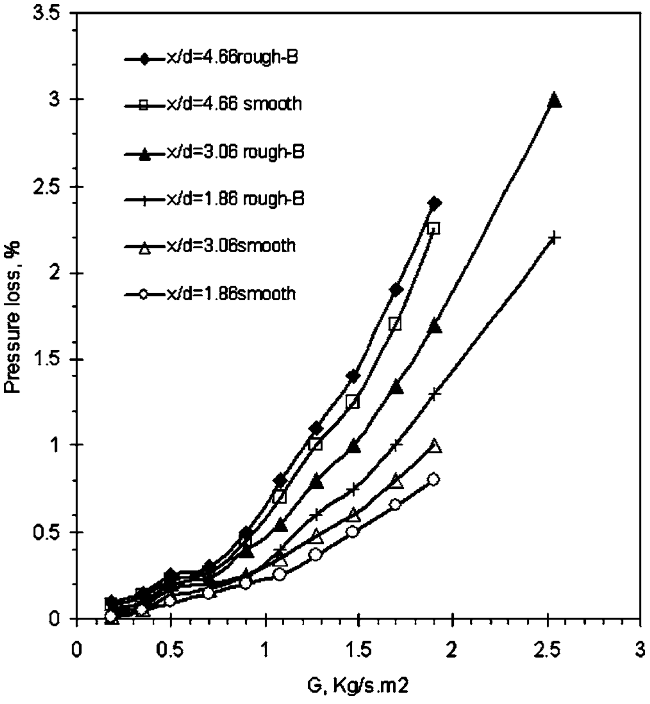

Fig. 2 Pressure loss as a function of *G* for the smooth and rectangular pin-fin impingement flow for *X*/*D*=1.86, 3.06, and 4.66

Equation (1) shows that W is then less than 1, which indicates that there was significant flow maldistribution between the impingement holes. This would be greater for $X/D=1.86$ than 3.06.

For an X/D of 4.66 with Uj/Uc of 1.8, the flow maldistribution between the leading-edge impingement hole and the trailing-edge hole can be shown to be approximately 24%. For an X/D of 3.06 and 1.86, this flow maldistribution increases substantially, but it is difficult to estimate as the flow maldistribution increases the impingement wall pressure loss and this increases the flow maldistribution.

Abdul Hussain and Andrews [10] have shown that for a smooth wall the influence of the flow maldistribution is to increase the impingement heat transfer in the trailing-edge region, whereas there is a decrease in heat transfer coefficient in the trailing-edge region in the absence of flow maldistribution [7].

4 Experimental Techniques

The experimental techniques have been fully detailed previously [10,12,23] and shown to have excellent repeatability and to give good agreement with the mean surface averaged heat transfer coefficient measurements using alternative techniques [7,8]. A 152 mm^2 test section was mounted on the base of an internally insulated plenum chamber for the coolant supply. The impingement gap was made using a stainless-steel spacer with a flow discharge from the downstream edge of the gap. For measurements on the test plate centerline, the conduction heat transfer between the target and the impingement wall at the flanges was shown to be small.

The impingement gap Z was set by a metal spacer flange and compared to an insulating spacer. This showed no significant difference except for the thermocouple closest to the leading-edge flange. This thermocouple was not used in the present analysis.

Both the 6.3 mm thick stainless-steel impingement target plates with roughness elements and the impingement jet plates were instrumented with brazed embedded mineral insulated Type K thermocouples. The thermocouple leads were fed along the surface of the impingement wall on the electrical heater side. This side was well insulated, and there was negligible heat loss through the thermocouple leads. Sufficient transverse thermocouples on the centerline were used to establish that the central axial region was not influenced by any sidewall effects. The axial variation of the temperatures along the centerline in the direction of the cross flow of impingement air was determined.

The thermocouples were spaced every 15.2 mm on the centerline of the target wall midway between the center two rows of impingement jets. The thermocouples were also midway between the ribs and hence 7.6 mm from the centreline of the impingement jets and the ribs. Conduction within the wall would give a locally near-uniform temperature, but if there was any small local temperature gradient then the thermocouple was at the lowest temperature location and hence the derived values of h would be conservative. The low Biot number (<0.2 for all tests and <0.1 for most of the data) gave a locally averaged temperature so that the values of h were locally surface averaged. However, over the larger distances of the 25 mm between thermocouples and the 152 mm length of the test wall, the axial variations in h resulted in differences in the temperatures between thermocouples. These enabled the axial variation of the surface-averaged heat transfer coefficient to be determined. This method has been shown in previous work to give good agreement for the axial variation of impingement heat transfer with the work of Chance [7], Kercher and Tabakoff [8], and Florschuetz et al. [9] who used different measurement techniques.

The test wall was electrically heated in the absence of any impingement coolant flow to a temperature of approximately 80°C. The electrical power was switched off, the coolant flow initiated at a preset flow rate, and the plate temperature monitored as a function of the time. The transient cooling is governed by a first-order response, and the time constant τ was determined from the results.

$$\tau = mC/hAp \tag{2}$$

The mass of the ribs was included in the thermal mass of the wall. The heat transfer surface area Ap was taken as the same as that of the smooth wall, ignoring the increase in surface area due to the ribs. This procedure has also been used by other workers investigating the influence of ribs on convective heat transfer [11,24,25]. Hoecker et al. [5] are the only investigators to include the area of the pins in the impingement heat transfer surface area. The use of the same heat transfer surface area for the smooth and rough surfaces essentially allows any effect of the increased surface area of the pins to be included in the overall effect of the pins on the heat transfer.

Error analysis shows that the main error in the determination of the heat transfer coefficient is the determination of the time constant in Eq. (2) from the transient temperature data using Type K thermocouples. The time constant was derived as the slope of the line plotting the impingement wall-temperature-to-coolant-temperature difference as a function of the rate of change of the wall temperature [15]. A least-squares fit to the line was used. The maximum temperature difference from ambient was 60°C at the start of the cooling process, and this was determined with a resolution of 0.1°C. The wall-temperature-to-coolant-temperature difference was determined with 0.2°C resolution, and the resolution was 0.3% of the temperature difference at the start of the cooling and 4% at the end of the cooling, when the temperature difference was 5°C.

The rate of temperature change was determined by differentiation of the cooling temperature versus time records for each thermocouple. This then avoids any calibration errors of the thermocouples. The rate of cooling was determined for 5°C temperature drop intervals with a 2% resolution. At least 12 rates of cooling were determined for each thermocouple, and these were plotted against the temperature difference. All the data fell within 3% of the best fit line. The coolant mass flow rate was determined using calibrated variable area flow meters to an accuracy of 2% of reading.

The error analysis indicates a maximum possible error of 5% in the time constant and hence in h, when the flow and τ errors are combined. Agreement with the results of other workers has been shown to be within 5% for the same geometries. Repeat tests, with a test rig rebuild of the test geometry, have shown that the measurement of h can be repeated to better than 5%.

The range of G investigated was that appropriate for gas turbine combustor wall cooling. A G of 2 kg/(s m^2 bar) represents approximately all of the combustor air flow being used to regeneratively impingement cool the combustor wall. Lower values of G represent part of the combustor airflow used for impingement cooling.

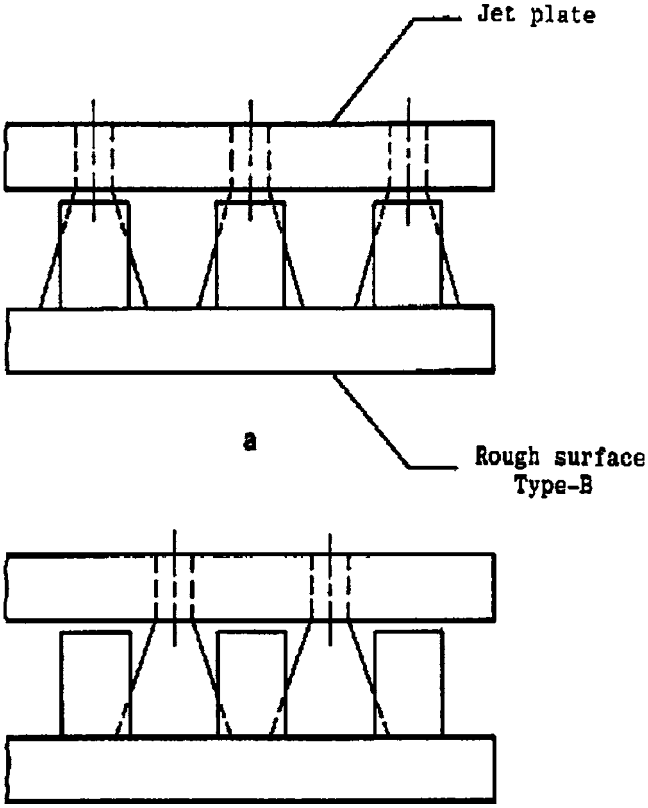

Fig. 3 In-line and offset impingement jet

5 Influence of Impingement Jet Alignment With the Pin-Fin on Surface-Averaged Heat Transfer

With a pin-fin obstacle array the impingement jet can be aligned with the pins (in-line) or between the pins (offset), as shown in Fig. 3. The in-line arrangement is designed to use the rectangular pin to shelter the impingement jet from the cross-flow velocity so that it is not deflected by the cross flow with a consequent reduction in the heat transfer. Also the maximum effect of the cross flow cooling between the pins would be gained.

Abdul Hussain and Andrews [12] have previously shown for one X/D that in-line jets and ribs in the upstream area of the test wall, where there is minimal cross flow, results in a deterioration in the impingement heat transfer. It was postulated that this was because the rectangular pin prevented the impingement mixing of the surface jets resulting from two adjacent impingement jets. However, since then Son et al. [26] have shown that the flow structure where the wall jets from adjacent holes meet are a region where flow separates turning toward the holed impingement surface, and there is a band of low heat transfer coefficient in this region. They also showed that the imposition of a low blockage surface roughness element in this region caused an enhancement in heat transfer coefficient due to the surface impingement of the wall jet with the roughness element. This is directly the opposite of the findings in this work with large blockage ribs.

An explanation of this difference is that the low blockage roughness had negligible impact on the flow distribution, as the cross-flow pressure loss was not enhanced as it is with the large blockage ribs used in the present work. It is thus possible that the reduction in the upstream impingement flow in the present work dominates the lack of enhancement of the heat transfer. Son et al. [26] also noted that the region of enhanced heat transfer on the roughness element was confined to a small region at the base of the roughness element, which may explain why there was little additional benefit observed with the larger ribs in the present work.

In an attempt to investigate the impingement flow and rib interactions further, the offset impingement jet configuration was investigated. This would permit the aerodynamic interaction of the impingement jets on the surface, as in conventional smooth wall impingement heat transfer, and this may reduce the deterioration in the heat transfer with in-line jets. However, in this location these jets will experience the high cross-flow velocity through the gap between the pin-fins; that is twice the level of cross flow with no pin-fins.

The surface-averaged heat transfer coefficients are shown as a function of G in Figs. 4 and 5 for $X/D=1.86$ and 4.66, respectively. These results show for both X/D a very small influence of the impingement jet alignment on the overall heat transfer. The in-line impingement jets had a slightly superior performance for both test geometries and this was greatest for an X/D of 1.86. It is shown in Sec. 6 that the greatest influence of the pin-fin array on heat transfer was in the downstream region and that this effect was larger for an X/D of 1.86 than 4.66.

This was considered to be due to the higher flow maldistribution for an X/D of 1.86, which increased the heat transfer in the

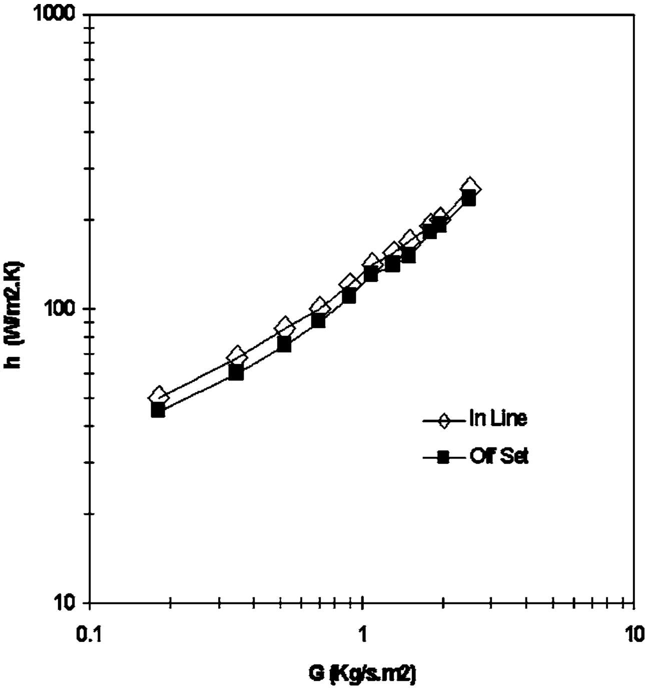

Fig. 4 Influence of G on the surface-averaged impingement heat transfer coefficient for $X/D=1.86$. Comparison of in-line and offset jets.

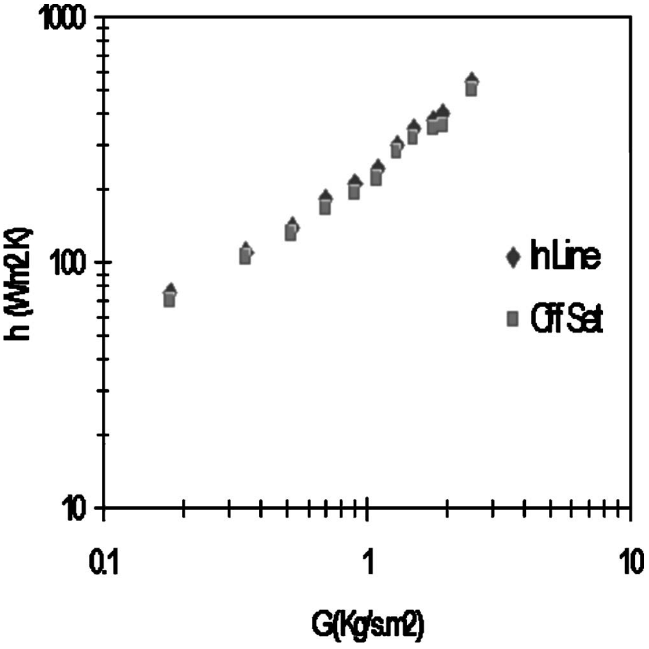

Fig. 5 The influence of *G* on the surface-averaged impingement heat transfer coefficient for *X*/*D*=4.66, *Z*/*D*=2.75, *Uj*/*Uc* =1.8. Comparison of in-line and offset jets relative to the rectangular pin obstacles.

trailing-edge region due to higher local impingement jet mass flow rates. These results show that the aerodynamic interaction of the impingement jets with the pins results in slightly better heat transfer for in-line jets compared to offset. However, the effect is small and only slightly greater than the measurement uncertainty for an individual measurement of h. The results thus show little benefit of the high cross velocity in the offset jet configuration.

One of the reasons the in-line jets has a slightly better heat transfer is that there is a region of high blockage between the two rows of ribs that the wall jet must impinge into and then flow out of, in order to make use of the heat transfer surface between the ribs. This is a highly tortuous path, which is unlike the case of offset jets that are unlikely to effectively cool the surface between the fins. Also, as discussed above, the higher local cross-flow velocity for the offset jets will cause a greater impingement jet deflection and associated deterioration in impingement heat transfer.

The difference between in-line and offset jets is greater for the low X/D of 1.86 than for an X/D of 4.66, where the results are identical at low G. This is because the jet velocities are much lower and hence the cross-flow velocity will create a greater impingement jet deflection. For in-line jets the impingement jets are protected from the cross flow by the pin-fins.

The ratio of the heat transfer coefficient for a rough wall to that for a smooth impingement wall is shown in Fig. 6 as a function of G. This shows that the in-line impingement jets gave about a 10% increase in heat transfer relative to the offset jets for an X/D of 1.86 and about 6% for an X/D of 4.66. The enhancement was variable with G, and this was due to the differences in the variation of h with distance for the smooth and rough walls, as shown in Section 6.

The results in Fig. 6 show that at all values of G the rectangular pin-fins arrays for both X/D had inferior surface-averaged heat transfer coefficients to those for a smooth wall. This is considered to be due to the action of the fins in increasing the cross-flow pressure loss. This induces a flow maldistribution so that the upstream impingement jets have a reduced air mass flow with the downstream jets enhanced, as discussed above.

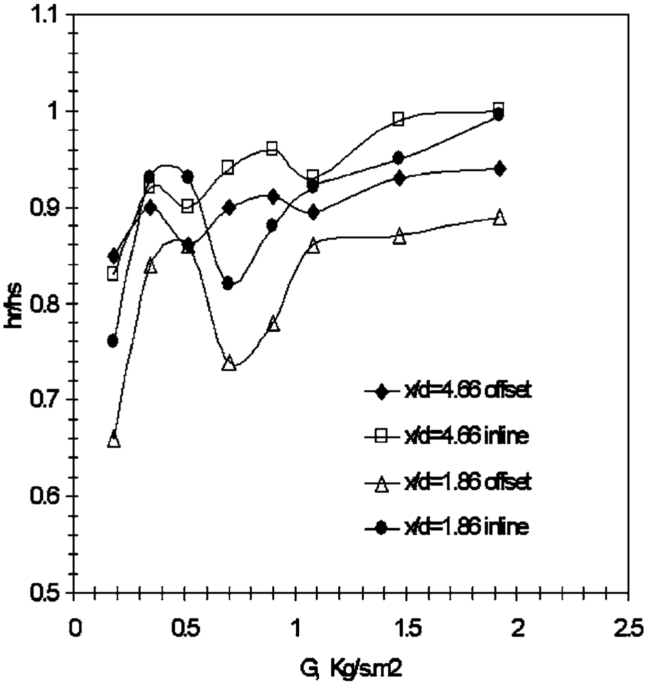

Fig. 6 *hr*/*hs* as a function of *G* for *X*/*D* 1.86, 3.06, and 4.66

These results are similar to those of Hoecker et al. [5] for an X/D of 4.3, Z/D of 2.5, and a cross-flow blockage of 30%. They also found that the presence of an array of cylindrical pin-fins in the impingement jet aerodynamics decreased the heat transfer compared to a smooth plate at high jet Reynolds numbers. This geometry is quite close to that of the present work, although they used a triangular array of impingement jets and pin-fins, which gave a mixed in-line and offset jet configuration relative to the pins. The main direction of the impingement jets was on the centerline between the holes, which would expose the impingement jets to the maximum cross local flow and, therefore, would not be expected to be a good configuration.

Annerfeldt et al. [6] investigated various pin-fin shapes for an X/D of 5. For Z/D values similar to the present work, all the geometries showed a deterioration in the mean surface-averaged heat transfer relative to a flat wall. For 30% blockage pin-fins the deterioration was around 30%, depending on the jet Re. Their results were for impingement jets in-line with the pin-fins. For larger impingement gaps with reduced cross-flow velocities the effect of the pins was to enhance the mean heat transfer, but the maximum effect was 10% at high impingement jet flow rates.

6 Influence of *X*/*D* and Impingement Wall Pressure Loss on Surface-Averaged Heat Transfer

The influence of the coolant mass flow rate on the heat transfer coefficient is shown in Figs. 7–9 for $X/D=1.86$, 3.06, and 4.66, respectively. The ratios of the jet-to-coolant velocity at the last hole of the crossflow were 0.29, 0.78, and 1.8, respectively. All three results were with in-line jets and are compared with the smooth wall results. For an X/D of 1.86 and 4.66, the influence of the rectangular pin-fins was to decrease slightly the overall heat transfer coefficient. For an X/D of 3.06 at high mass flow rates, there was a small increase in the surface-averaged heat transfer. At the maximum flow rate this increase was 20%.

Figures 7–9 show that there was a difference in the dependence of the heat transfer coefficient on the mass flow rate, which is the same as the dependence on the impingement hole Reynolds number. Table 2 shows the values of y for the smooth and rough walls, which were obtained from a least-squares fit to the data in Figs.

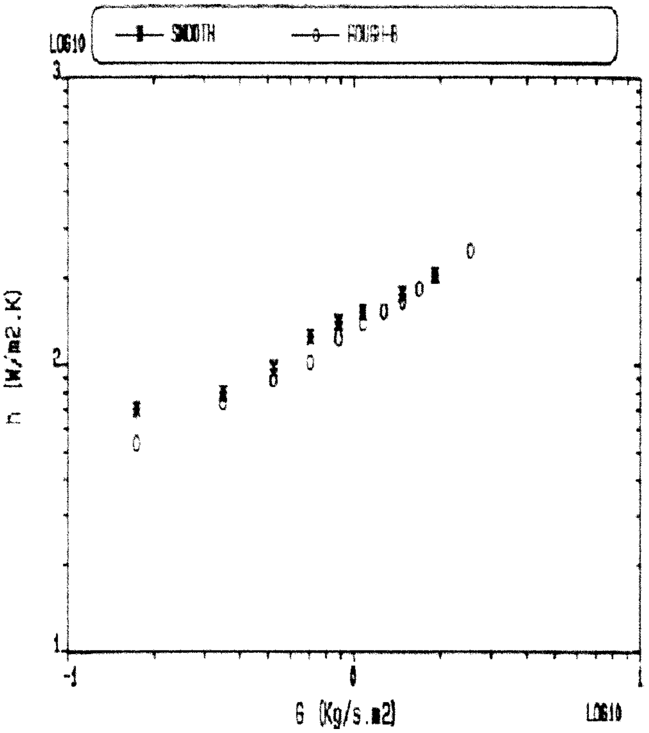

Fig. 7 Comparison of the surface-averaged impingement heat transfer coefficient as a function of *G* for smooth and rectangular pin-fin surface roughness, $X/D=1.86$, $Uj/Uc=0.29$

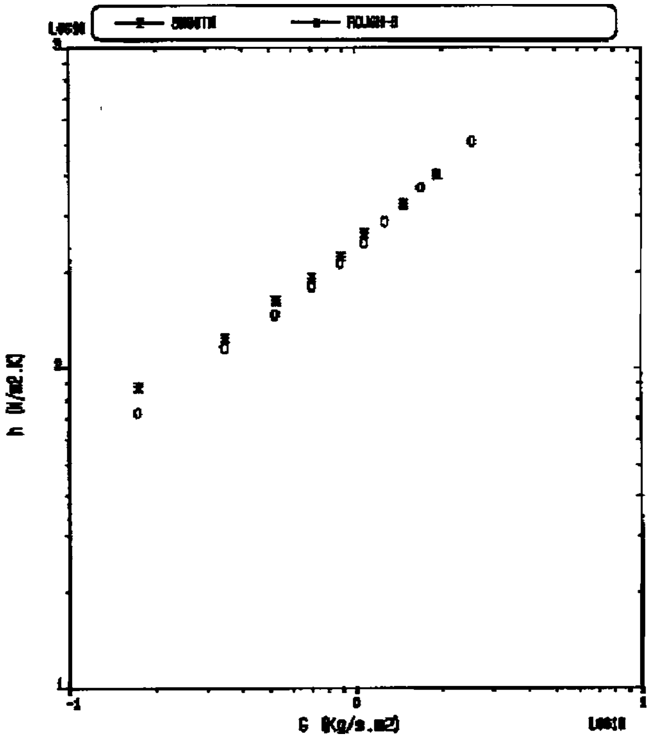

Fig. 9 Surface-averaged impingement heat transfer for smooth and rectangular pin-fin rough surfaces, as a function of *G* for $X/D=4.66$

7–9. This exponent has been fitted to the higher coolant mass flow data. The reason for this is that at low mass flow rates the impingement jet hole Reynolds numbers are in the laminar regime, as shown in Fig. 12 below. The *G* and Re exponent *y* in Table 2 is valid only for the turbulent flow regime. This is one of the problems of undertaking the tests at atmospheric pressure. At atmospheric pressure, *G* becomes the mass flow rate per unit surface area per bar and the jet Reynolds numbers are turbulent at low impingement velocities through the density term in Re.

The influence of the array of pin-fins was to increase the dependence of *h* on *G*. This was due to the increase in the cross-flow velocity as *G* was increased. This causes more interaction of the cross flow with the pin-fin array so that wake turbulence behind the rectangular pin-fins is created, which increases the heat transfer coefficient.

Figure 10 shows the comparison of the surface-averaged heat transfer coefficient for the three X/D as a function of *G* for the rectangular pin-fin arrays. This shows, as expected, that at constant mass flow rate a higher heat transfer coefficient results as the X/D is increased. This is because the impingement jet velocity and jet Re is increased, and this increases the heat transfer. However, the impingement wall pressure loss is also increased as X/D is increased at constant mass flow rate. This increase in pressure loss for an X/D of 4.66 compared to 1.86 is a factor of 40, as shown in Table 1.

Most of the pressure loss at low X/D was in the cross flow over the pin-fin array and not at the impingement wall. The aim of reducing the X/D in the present work was to achieve a high cool-

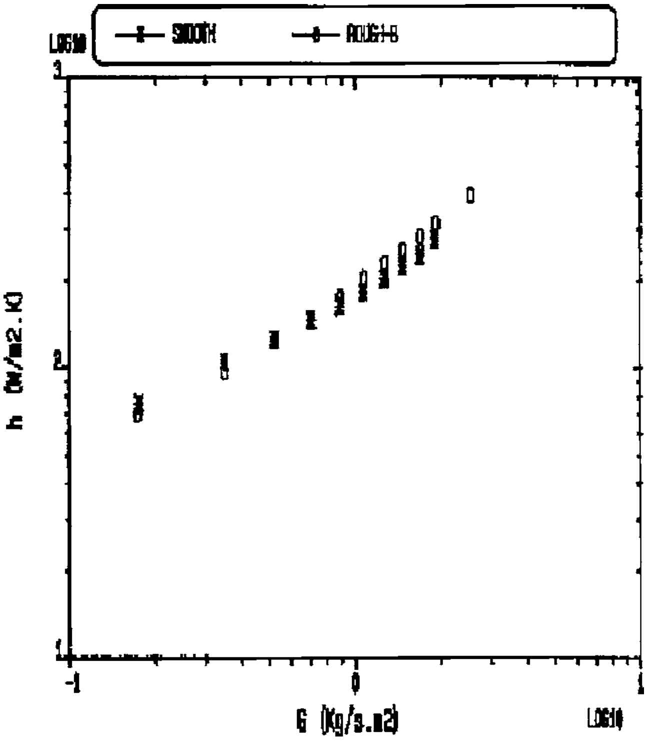

Fig. 8 Comparison of the surface-averaged impingement heat transfer coefficient as a function of *G* for smooth and rectangular pin-fin roughness for in-line jets, $X/D=3.06$, $Z/D=1.8$, $Uj/Uc=0.78$

Table 2 Exponent *y* for $h=\text{const } G^y$

X/D	1.86	3.06	4.66
Smooth	0.51	0.63	0.70
Pin-fin	0.69	0.77	0.79

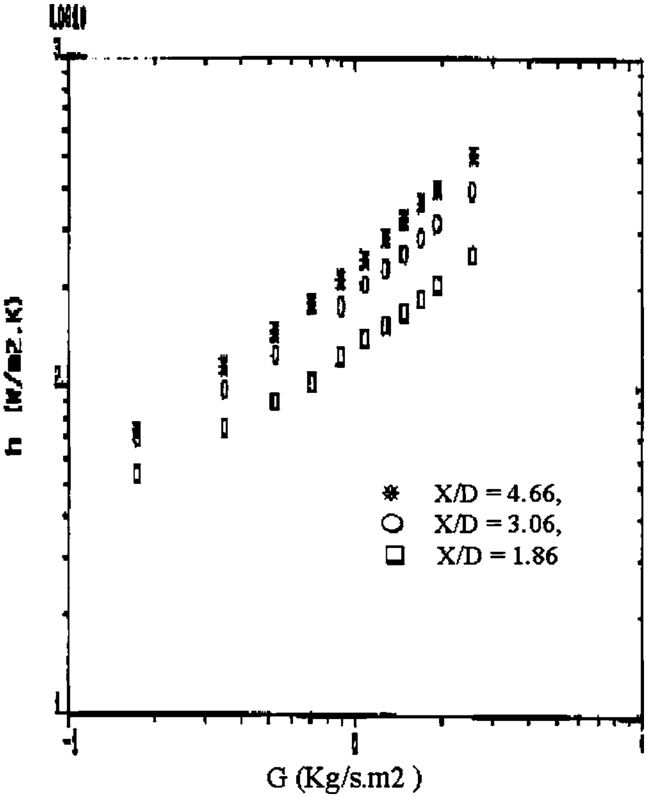

Fig. 10 Influence of *X*/*D* on surface-averaged impingement heat transfer as a function of *G*

ant mass flow rate at an acceptable pressure loss so that the coolant air could still be used for the main combustor with, say, a 3% pressure loss. A maximum impingement cooling pressure loss of 1% is desirable. Using the pressure loss data in Fig. 2 it can be shown, for a constant pressure loss, that a higher coolant flow rate can be used with an X/D of 3.06 and a G of 1.45 instead of a G of 1.2 $\mathrm{kg/sm^2}$ for an X/D of 4.66 to achieve the same value of h.

For an X/D of 1.86 at the same pressure loss there was only a 10% reduction in the achievable h at a 1% pressure loss, as the mass flow can be increased to a G of 1.85 $\mathrm{kg/sm^2}$. This compares with the 50% reduction in h when the comparison is made at constant mass flow rate of coolant. If the same comparison is made in Figs. 7–9 for a smooth wall, then at 1% pressure loss higher values of h can be achieved, as for each X/D a higher mass flow rate can be used. This is due to the lower pressure loss characteristics of the smooth walls. This is the problem in many enhanced heat transfer situations using rough surfaces, the increase in pressure loss reduces the mass flow rate and this reduces h. This trend was seen in the present work.

The hr/hs ratios as a function of G is shown in Fig. 11. This shows that only for an X/D of 3.06 was there a consistent increase in the heat transfer coefficient and then only for high coolant mass flow rates, where cross-flow velocities were maximized. At the highest mass flow rates investigated, the increase in surface-averaged heat transfer was 15%. For an X/D of 1.86 and 4.66, the results show that the rectangular pin-fin array caused a reduction in heat transfer for most coolant flow rates. It will be shown in Sec. 6 that the reason for the greater impact of the pin-fin array on heat transfer for an $X/D=3.06$ was because of differences in the axial variation of heat transfer between smooth and rough surfaces.

The impingement plate geometry for $X/D=3.06$ and $Z/D=1.81$ with 10 rows of impingement jets is close to that of the recent work of Bailey and Bunker [27]. They presented results for square arrays of impingement holes with an X/D of 3 and Z/D of 1.25 for 12 rows of holes. They used higher jet Reynolds numbers than in the present work because of the use of larger diameter holes. They found a value for the exponent y for the exponential dependence of Nu on Re for this geometry of 0.68. This is only 8% different from the present value for the smooth wall of 0.63 in Table 2. They measured the flow maldistribution between the rows of holes and showed that at this value of X/D there was a severe flow maldistribution, as predicted above. The final row of holes had three times the flow rate of the leading edge holes. This produced a maldistribution in the heat transfer distribution with higher heat transfer at the trailing edge than the leading edge.

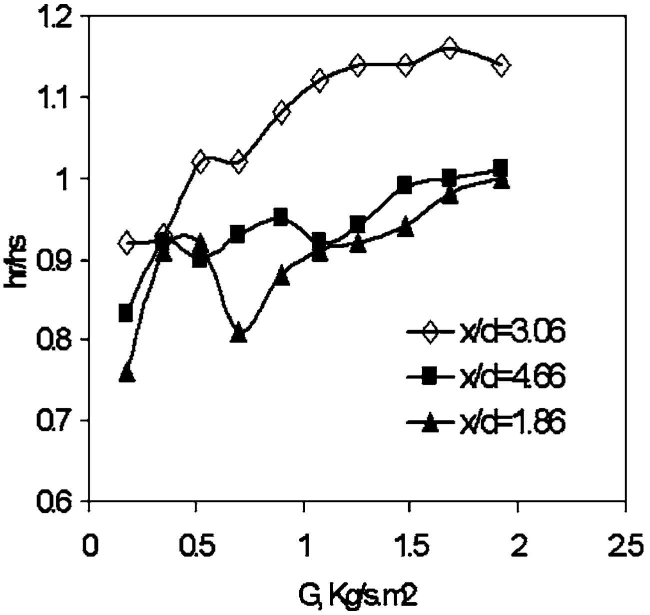

Fig. 11 Ratio of rough rectangular pin-fin surface to smooth surface-averaged impingement heat transfer coefficient as a function of *G*. Comparison of the influence of square array impingement hole *X*/*D*.

The present results are presented in Fig. 12 as a conventional

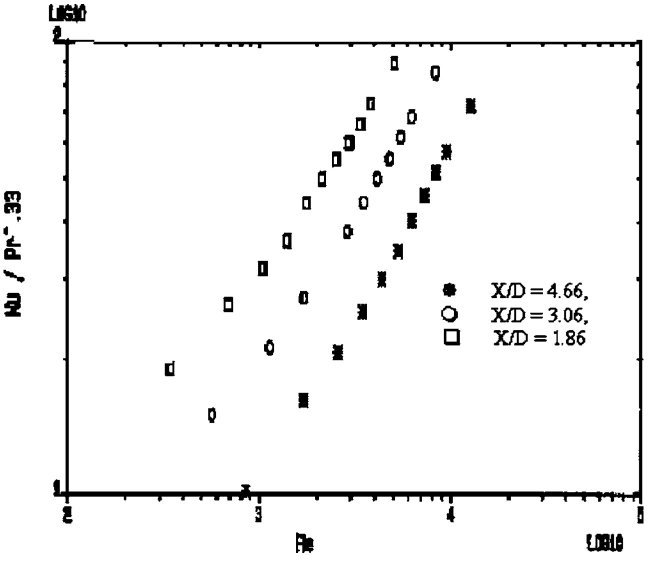

Fig. 12 Influence of square array impingement jet *X*/*D* on Nusselt versus impingement jet Reynolds number plot, *X* =15.2 mm and *Z*=9 mm. Impingement surface with rectangular pin-fin array with one fin in-line with each impingement jet and offset midway between the jets.

Nusselt number divided by Prandtl number to the one-third power as a function of the impingement jet Reynolds number. The geometrical variable is the impingement hole diameter, which at constant mass flow rate reduces Re as D is increased and increases Nu as D is increased for a constant h. The net result is that Fig. 12 appears to suggest that at constant impingement jet Reynolds number, the heat transfer increases as X/D is reduced, whereas the reverse is the case when comparison is made at the more practical constant coolant mass flow rate.

For the $X/D=3.06$ geometry, direct comparison to the smooth wall results of Bailey and Bunker [27] can be made. For a Re of 10,000 the present results extrapolate to a Nu of 90 and their results for a local impingement jet Re of 10,000 was a Nu of 80. The difference is the small influence of the pin-fin array.

7 Influence of X/D on Axial Variation of the Heat Transfer Coefficient

The flow maldistribution that is large for $X/D=3.06$ and 1.86 means that surface-averaged heat transfer data can mask trends that are different at the upstream leading and downstream trailing edges. The axial variation in the heat transfer coefficients are shown in Figs. 13–15 for a G of 1.9 kg/sm^2. For an X/D of 1.86 there was a severe flow maldistribution caused by the pressure loss in the cross-flow duct being greater than that at the impingement wall. The duct flow pressure loss was increased by the rectangular pin-fin array, and hence the maldistribution was greater than for the smooth wall. The trailing edge thus has a locally higher impingement jet flow that increases the heat transfer coefficient. Coupled with this is the increase in h because of the turbulence in the cross-flow wake flow behind the slotted rib obstacles. At the leading edge the presence of the pin-fin array decreases the heat transfer. This is due to the reduced mass flow rate to the upstream jets because of flow maldistribution induced by the crossflow pressure loss.

For an X/D of 3.06, Fig. 14 shows that the axial variation of h is quite different for the smooth and rough walls, and after 50 mm the rough wall has an increasingly higher value of h for all axial distances. This is why the surface average h shows the greatest benefit of the surface roughness for this X/D. For the smooth wall the leading-edge region shows a deterioration in h with distance, as expected for cross-flow heat transfer. However, the impact of flow maldistribution is to increase the jet mass flow rate in the trailing-edge region and this causes h to increase. The higher pressure loss with the rectangular pin-fin array in the cross-flow gap causes a higher pressure loss and a greater flow maldistribution. The result is a steady increase in h with axial distance.

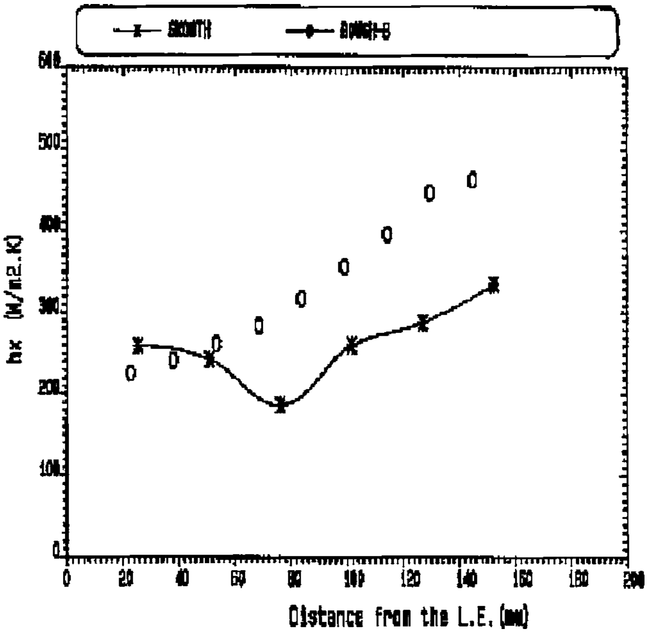

Fig. 14 Impingement heat transfer coefficient as a function of axial distance from the leading edge. Comparison between smooth wall and rough wall rectangular pin-fin array impingement heat transfer, $X/D=3.06$, $G=1.9$ kg/sm^2.

For an X/D of 4.66 Fig. 15 shows that for a smooth wall, h decreases with distance, as found in all investigation of impingement heat transfer where flow maldistribution is not large [14]. The small increase in h in the trailing-edge region (120 mm) was

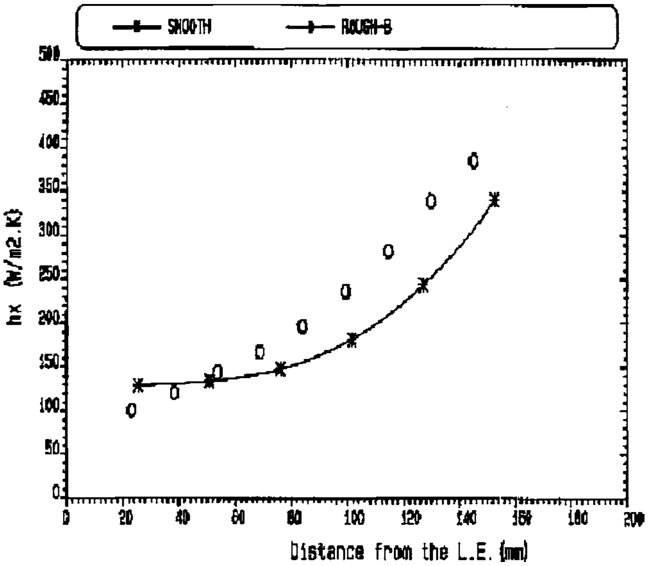

Fig. 13 Variation of the impingement heat transfer coefficient with axial distance from the leading edge. Comparison of smooth surface impingement heat transfer with a rectangular pin-fin rough surface, $X/D=1.86$, $G=1.91$ kg/sm^2.

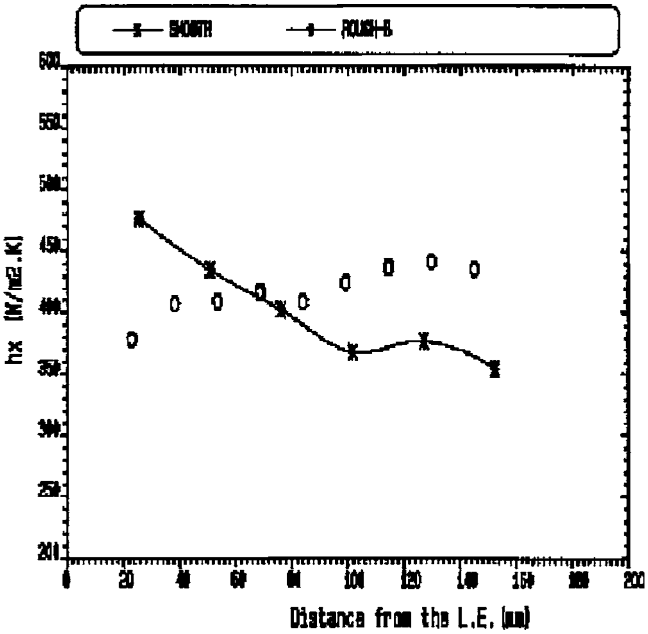

Fig. 15 Impingement heat transfer coefficient as a function of the axial distance from the leading edge. Comparison of smooth surface and rough rectangular pin-fin arrays with square array impingement jets, $X/D=4.66$, $G=1.92$ kg/sm^2.

Table 3 Summary of the rough/smooth ratio of h for $G = 1.9$ kg/sm^2

X/D	Surface averaged	Trailing edge
4.66	1.0	1.19
3.06	1.15	1.40
1.86	1.0	1.20

due to the small flow maldistribution (approximately 24% determined from the pressure loss). However, in the presence of the rectangular pin-fin array, h has a small increase with axial distance. This is because of the interaction of the cross flow with the pin-fin array, which creates turbulent wakes behind each rectangular pin-fin.

The influence of the rectangular pin-fin array on h is summarized in Table 3 for the surface-averaged heat transfer at a G of 1.9 kg/sm^2 and for the trailing-edge region for each X/D. Similar trends were found at lower values of G. These results demonstrate that the main advantage of the rectangular pin-fin array was in the trailing-edge region. This trailing-edge enhancement of h was partially because of interaction of the cross flow with the pin-fins to create locally higher cross-flow velocities offset from the impingement jets and wake turbulence behind the pin-fins. Also the downstream heat transfer was enhanced by the flow maldistribution caused by the pressure loss of the pin-fin array. Both of these effects would locally increase the convective heat transfer in the trailing-edge region. The flow maldistribution contributed to the reduced heat transfer in the leading-edge region.

8 Discussion

The present results show that obstacles of the present rectangular pin-fin type with 50% flow blockage are only worth using in situations where there is significant cross flow. This may be self-generated cross flow in impingement cooling with many rows of holes and a flow exit in a single direction, or it may be the outflow of cooling air from, say, vane tip cooling. In the leading-edge region in the absence of cross flow, obstacles degrade impingement heat transfer possibly because of the increased pressure loss in the impingement gap, which increases the flow maldistribution, starving the leading edge of air. However, in previous work [20,28] it has been shown that if the present obstacles are aligned with the cross flow so that only the small width of the obstacles is the blockage, then there is still only a small influence of the obstacles on the heat transfer compared to a smooth wall.

For the geometries investigated, the high coolant mass flow rate, small X/D geometry had a 10% lower heat transfer coefficient than for the lower coolant mass flow rate larger X/D geometry. Thus, cooling combustors using all the combustion air with low pressure loss regenerative cooling is likely to result in a deterioration in wall cooling; this is when compared to the used of a higher X/D and a lower coolant mass flow rate. In this case the impingement air would be discharged as downstream film cooling air and not be used for lean combustion. This is the main use of impingement cooling in gas turbine low NO$_x$ combustors today.

For turbine blade impingement cooling, high coolant mass flow rates cannot be used. The aim is to minimize the coolant mass flow rate at a pressure loss of typically 4%. The present results show that a large impingement X/D is preferable for this application, as this involves higher impingement jet velocities. Future work will investigate values of X/D up to 21, and the influence of the use of several pin-fins per impingement jet will be investigated as well.

9 Conclusions

1. Obstacles of the pin-fin type investigated in this work are only worth using with impingement cooling in situations where there is significant cross flow, such as in the trailing-edge region of an array of impingement jets with no initial cross flow. This applies for the rectangular pin-fins with a 50% blockage and Andrews et al. [20] showed that it is also true if the pins are turned to be aligned with the cross flow and, hence, with a lower blockage.
2. For the best enhancement of heat transfer in the presence of cross flow, the roughness element blockage should be large. The present use of a 50% blockage resulted in higher enhancement of impingement heat transfer in the trailing-edge region of the test wall than has been found by most other investigators. However, the present results are also influenced by the change in pressure loss in the cross-flow passage due to the high blockage, which diverts air to the trailing edge.
3. In the absence of cross flow in the leading-edge region, heat transfer deteriorated relative to a smooth surface. This is postulated to be due to the change in impingement jet flow distribution caused by the increase in impingement gap cross-flow pressure loss with the high blockage ribs.
4. The addition of surface area by the use of large pin-fin obstacles was not a significant feature in the enhancement of the heat transfer. The main influence of the pins was to interact with the cross flow to generate locally higher surface cross-flow velocities and turbulence in the wake region behind the rectangular pins. If the surface area increase was significant, then this would result in increased heat transfer in the leading-edge region, where cross flow is zero
5. The in-line jets had a significantly better heat transfer than offset jets because of the better surface coverage of the impingement flow with inline jets and the greater cross-flow deflection of the impingement jets in the offset alignment.

Acknowledgment

We would like to thank the EPSRC for a research grant that provided the equipment used. We would like to thank the Iraq Government for a research scholarship to R. A. A. Abdul Husain. The test facility was constructed, commissioned, and operated by R. A. Boreham. We would like to thank one of the reviewers for comments on the cause of the reduced heat transfer with the ribs used in this work and on the reasons for the differences between in-line and offset jets, which have been included in the revised paper.

Nomenclature

A = impingement hole area per unit surface area ($A = \pi/4(X/D)^2$)
Ap = impingement surface area
C = specific heat of the test wall
C_d = Discharge Coefficient ($G = Cd\,A(2\rho DP)^{0.5}$)
DP = pressure loss from upstream of the impingement wall to the atmospheric impingement discharge
e = rib height, m
h = heat transfer coefficient
hr/hs = ratio of the rough to smooth surface heat transfer coefficients.
L = Impingement hole length, m
m = mass of the test wall, kg
N = number of upstream rows of holes
D = impingement hole diameter, m
G = mass flow rate per unit surface area per bar Kg/(s m^{2}bar) (pressure=1 bar in this work)
Nu = impingement Nusselt number
Re = impingement jet Reynolds number
U_j = impingement jet velocity, m/s
U_c = cross-flow velocity, m/s
τ = time constant, Eq. (2)

W = flow maldistribution parameter, Eq. (1)
X = hole pitch, m
y = exponent for the dependence of h on G and U_j
Z = impingement gap, m

References

[1] Andrews, G. E., and Kim, M. N., 2001, "The Influence of Film Cooling on Emission for a Low NO_x Radial Swirler Gas Turbine Combustor," ASME Paper No. 2001-GT-0071.
[2] Son, C. Gillespie, D., Ireland, P., and Dailey G. M., 2001, "Heat Transfer Characteristics of an Impingement Plate Used in a Turbine Vane Cooling System," ASME Paper No. 2001-GT-154.
[3] Haiping, C., Dalin, Z., and Taiping H., 1997, "Impingement Heat Transfer From Rib Roughened Surface Within Arrays of Circular Jets: The Effect of the Relative Position of the Jet Hole to the Rib," ASME Paper No. 97-GT-331.
[4] Haiping, C., Jingyu, Z., and Taipping, H., 1998, "Experimental Investigation on Impingement Heat Transfer From Rib Roughened Surface Within Arrays of Circular Jets: Effect of Geometric Parameters," ASME Paper No. 98-GT-208.
[5] Hoecker, R., Johnson, B. V., Hausladen, J., Rothbrust, M., and Weigand, B., 1999, "Impingement Cooling Experiments With Flat and Pin Plate Target Surfaces," ASME Paper No. 99-GT-252.
[6] Annerfeldt, M. O., Persson, J. L., and Torisson, T., 2001, "Experimental Investigation of Impingement Cooling With Turbulators or Surface Enlarging Elements," ASME Paper No. 2001-GT-149.
[7] Chance, J. T., 1974, "Experimental Investigations of Air Impingement Heat Transfer Under an Array of Thermal Jets," Tappi J. **57**, pp. 108–112.
[8] Kercher, D. M., and Tabakoff, W., 1970, "Heat Transfer by a Square Array of Round Air Jets Impinging Perpendicular to a Flat Surface," ASME J. Eng. Power, **92**, pp. 73–82.
[9] Florschuetz, L. W., Truman, C. R., and Metzger, D. E., 1981, "Streamwise Flow and Heat Transfer Distribution for Jet Array Impingement With Initial Crossflow," ASME J. Heat Transfer **103**, pp. 337–342.
[10] Abdul Hussain, R. A. A., and Andrews, G. E., 1990, "Full Coverage Impingement Heat Transfer at High Temperatures," ASME Paper No. 90-GT-285.
[11] Trabold, T. A., and Obot, N. T., 1987, "Impingement Heat Transfer Within Arrays of Circular Jets, Part II: Effects of Crossflow in the Presence of Roughness Elements," ASME Paper No. 87-GT-200.
[12] Abdul Hussain, R. A. A., and Andrews, G. E., 1991, "Enhanced Full Coverage Impingement Heat Transfer With Obstacles in the Gap," ASME Paper No. 91-GT-346.
[13] Andrews, G. E., and Hussain, C. I., 1986, "Full Coverage Impingement Heat Transfer: The Influence of Channel Height," *Proc. of 8th Int. Heat Transfer Conference*, Hemisphere, Washington, DC, pp. 1205–1211.
[14] Andrews, G. E., and Hussain, C. I., 1987, "Full Coverage Impingement Heat Transfer: The Influence of Crossflow," AIAA Paper 87-2010.
[15] Al Dabagh, A. M., Andrews, G. E., Abdul Husain, R. A. A., Husain, C. I., Nazari, A., and Wu, J., 1989, Impingement/Effusion Cooling: The Influence of the Number of Impingement Holes and Pressure Loss on the Heat Transfer coefficient, ASME Paper No. 89-GT-188.
[16] Son, C. M., Gillespie, D. R. H., Ireland, P. T., and Dailey, G. M., 2000, "Heat Transfer and Flow Characteristics of an Engine Representative Impingement Cooling System," ASME Paper No. 2000-GT-219.
[17] Shizuya, M., and Kawaike, K., 1987, "Experimental Investigation of Blade Internal Cooling Methods Using Ribs and Fins," *Tokyo International Gas Turbine Congress*, Paper 87-Tokyo-IGTC-65, Vol. **III**, pp. 159–166.
[18] Chang, H. et al., 1997.
[19] Chang, H., Jingyu, Z., and Taiping, H., 1998, "Experimental Investigation on Impingement Heat Transfer From Rib Roughened Surface Within Arrays of Circular Jet: Effect of Geometric Parameters," ASME Paper No. 98-GT-208.
[20] Andrews, G. E., Abdul Hussain, R. A. A., and Mkpadi, M. C., 2003, "Enhanced Impingement Heat Transfer: Comparison of Co-flow and Cross-flow With Rib Turbulators," *Proc. of Int. Gas Turbine Congress 2003 Tokyo*, IGTC2003Tokyo TS-075.
[21] Andrews, G. E., Asere, A. A., Hussain, C. I., and Mkpadi, M. C., 1985, "Full Coverage Impingement Heat Transfer: The Variation in Pitch to Diameter Ratio at Constant Gap," *Heat Transfer and Cooling in Gas Turbines*, AGARD CP 390 Paper No. 26, pp. 26-1–26-13.
[22] Andrews, G. E., and Mkpadi, M. C., 1983, "Full Coverage Discrete Hole Wall Cooling: Discharge Coefficients," ASME Paper No. 83-GT-79.
[23] Andrews, G. E., and Hussain, C. I., 1984, "Full Coverage Impingement Heat Transfer: The Influence of Impingement Jet Size," *Proc. of 1st UK National Heat Transfer Conference*, IChemE Symp. Ser. No. 86, pp. 1115–1124.
[24] Tabakoff, W., and McFarlane, E. R., 1975, "Gas Turbine Blade Heat Transfer With Rough Surfaces," ASME Paper No. 75-WA/HT-107.
[25] Han, J. C., 1984, "Heat Transfer and Friction in Channels With Two Opposite Rib-Roughened Walls," ASME J. Heat Transfer **106**, pp. 774–781.
[26] Son, C. M., Gillespie, D. R. H., Ireland, P. T., and Dailey, G. M., 2000, "Heat Transfer Enhancement Strategy for an Impingement Cooling System," *Proc. of 8th Int. Symp. Tranport Phenomena and Dynamics of Rotating Machinery*.
[27] Bailey, J. C., and Bunker, R. S., 2002, "Local Heat Transfer and Flow Distributions for Impinging Jet Arrays of Dense and Sparse Extent," ASME Paper No. GT-2002-30473.
[28] Andrews, G. E., Al Dabagh, A. M., Asere, A. A. A., Bazdidi-Tehrani, F., Mkpadi, M. C., and Nazari, A., 1992, "Impingement/Effusion Cooling," *Heat Transfer and Cooling in Gas Turbines*, Antalya, Turkey, AGARD CP 527, pp. 30-1–30-10.

Effectiveness of a Serpentine Inlet Duct Flow Control Technique at Design and Off-Design Simulated Flight Conditions

Angie Rabe Scribben[1]

Wing Ng

Ricardo Burdisso

Mechanical Engineering Department,
Virginia Tech,
Blacksburg, VA 24061

An experimental investigation was conducted in a static ground test facility to determine the effectiveness of a serpentine inlet duct active flow control technique for two simulated flight conditions. The experiments used a scaled model of a compact, diffusing, serpentine, engine inlet duct developed by Lockheed Martin with a flow control technique using air injection through microjets at 1% of the inlet mass flow rate. The experimental results, in the form of total pressure measurements at the exit of the inlet, were used to predict the stability of a compression system through a parallel compressor model. The inlet duct was tested at cruise condition and angle of attack flight cases to determine the change in inlet performance due to flow control at different flight conditions. The experiments were run at an inlet throat Mach number of 0.55 and a resulting Reynolds number, based on the hydraulic diameter at the inlet throat, of $1.76^{*}10^{5}$. *For both of the flight conditions tested, the flow control technique was found to reduce inlet distortion at the exit of the inlet by as much as 70% while increasing total pressure recovery by as much as 2%. The inlet total pressure profile was input in a parallel compressor model to predict the changes in stability margin of a compression system due to flow control for design and off-design flight conditions. Without flow control, both cases show a reduction in stability margin of 70%. With the addition of flow control, each case was able to recover a significant portion (up to 55%) of the undistorted stability margin. This flow control technique has improved the operating range of a compression system as compared to the same inlet duct without flow control.* [DOI: 10.1115/1.2098787]

Introduction

The recent emphasis on unmanned aerial vehicles (UAVs) includes the ability to take new risks in enhancing aircraft abilities and performance. One way to increase performance is to reduce aircraft weight, which can be accomplished through a reduction in length. Serpentine or S-shaped inlet ducts have been introduced into UAVs to meet a variety of design requirements. By designing more compact serpentine inlet ducts, the length of the aircraft can be reduced, improving the aircraft thrust-to-weight ratio.

While these inlet ducts achieve certain design goals, they also pose design challenges such as reducing the stability margin of the propulsion system. More aggressive inlet ducts result in increased turning, which produces boundary layer separation and secondary flow within the duct as shown in Fig. 1. The compact nature of the duct limits the length for diffusion and dissipation of these secondary flows, and leads to greater distortion levels at the engine fan face. This inlet distortion, or nonuniform flow, can produce a reduction in stability margin for the compressor or fan of the turbine engine.

In many cases, the flow from the inlet duct is not of an acceptable flow quality for the engine airflow. The flow must be controlled or corrected to improve the flow quality entering the turbine engine. Additionally, the secondary flow generated within the serpentine duct will be more severe at off-design conditions, such as angle of attack, for these more aggressive serpentine ducts. Because the effect of off-design conditions is not yet well understood for these ducts, design revisions may be required to ensure acceptable flow quality at any condition that may occur during a flight mission.

In this research the inlet duct was tested in a static facility at two simulated flight conditions: cruise condition and angle of attack. The angle of attack case matched a computational fluid dynamics (CFD)-predicted total pressure profile at the inlet throat. In this way, a realistic flight condition was simulated. Both flight conditions were tested with and without flow control at a throat Mach number of 0.55 to determine the effect of flow control on each test case. The flow control, in the form of mass injection through microjets, used 1% of the inlet mass flow rate.

Total pressure measurements were taken at the aerodynamic interface plane (AIP). From these detailed measurements, total pressure contours were generated showing pressure deficiencies in the flow. The total pressure measurements were also used to describe the flow through multiple descriptors including circumferential distortion and pressure recovery. These distortion descriptors are used to evaluate the flow quality at the AIP.

Finally, a compression system model was used to evaluate the impact of the flow field on the stability margin of a compression system. The total pressure distortion was used to determine the change in stability margin based on variations in the total pressure recovery for the different flight conditions tested and the addition of flow control. In this way the impact of inlet total pressure distortion can be evaluated as it affects the stability of the gas turbine engine.

Previous Work

The flow development within a serpentine duct has been examined in addition to the effect of geometric design factors such as centerline curvature, diffusing cross-sectional area, and transition-

---

[1] Currently at the Air Force Research Laboratory, Wright-Patterson Air Force Base, OH.

Contributed by the International Gas Turbine Institute (IGTI) of ASME for the publication in the JOURNAL OF TURBOMACHINERY. Manuscript received October 1, 2003; final manuscript received March 1, 2004. IGTI Review Chair: A. J. Strazisar. Paper presented at the International Gas Turbine and Aeroengine Congress and Exhibition, Vienna, Austria, June 13–17, 2004, Paper No. 2004-GT-53475.

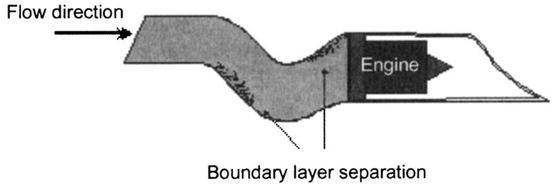

Fig. 1 Schematic of serpentine inlet duct flow separation

ing cross-sectional area. These geometric design factors will impact the amount of distortion at the exit of the inlet. This distortion results in a reduction in operability range for the gas turbine engine directly downstream of the inlet duct. The distortion leads to blockage in certain sections of the fan. The incoming flow then reacts to this slow-moving air by avoiding that section of the fan [1]. Attempts to reduce the impact of the serpentine inlet duct on a gas turbine engine through flow control have also been made.

Several studies [2–7] have been conducted to investigate the flow behavior within serpentine ducts. Each of the ducts in these studies had a circular cross-section and a centerline curvature with two turns of equal magnitude to give the duct the shape of an ‘S.’ These studies revealed flow separation, in the form of two counter-rotating vortices, at the first turn of the serpentine inlet duct. In some cases the flow reattached later in the duct, while in other cases, the flow separated again, at the second turn. Differences in the severity of the centerline curvature and the magnitude of the cross-sectional area diffusion influenced the degree of separation in the duct as well as the amount of distortion created by the duct.

Povinelli and Towne [8] tested several geometric design factors to determine which factors caused the most distortion at the exit of the inlet. They tested ducts with centerline curvature only, transitioning cross section only, centerline curvature and transitioning cross section, and diffusing cross-sectional area. The diffusing cross-sectional area duct demonstrated the largest increase in distortion with respect to a straight circular duct. The duct with centerline curvature showed the second largest increase. These tests indicate that the degree of cross-sectional area diffusion and the severity of centerline curvature have the largest impact on the amount of distortion created by a particular inlet duct.

Efforts have been made to control the flow within serpentine and S-shaped inlet ducts and to decrease the amount of distortion created. Different categories of flow control include active, passive, open-loop, and closed-loop flow control. Active flow control requires an actuator to change the flow, such as air injection through microjets, while passive flow control is a fixed modification to the flow, such as vane or fin-type vortex generators. Closed-loop flow control requires that the flow control system be able to respond to changes in the flow through a feedback loop, which provides information on the flow in real time. Closed-loop flow control in a serpentine duct has only recently been examined [9]. Sensing technology that would enable closed-loop flow control to be available for a serpentine inlet duct application is still in the research and development stage. Open-loop flow control has no feedback loop; however, open-loop flow control can involve different prescribed settings based on engine speed, for example, with no real-time corrections.

Two different approaches to open-loop flow control have been tested in serpentine inlet ducts. The boundary layer energizing approach attempts to fill the low-pressure region present during flow separation, while the vortex generator approach seeks to cancel the net secondary flow in the duct by producing a secondary flow opposite to the flow formed in the duct. The flow within a serpentine duct is characterized by two distinct counter-rotating vortices at each separation point. For a circular cross-section duct, both pairs of vortices will form in the center of the duct laterally and either the top or bottom of the duct, whichever is the inside of the turn. An example of the location of the vortices is shown in Fig. 2, where the bottom of the duct is the inside of the first turn and the top of the duct is the inside of the second turn. The vortices from the earlier turns should be weaker because they have had more time to dissipate over the length of the duct. With more aggressive serpentine inlets, the vortex generating approach to flow control has found more success in reducing the distortion produced by the serpentine duct. Passive flow control techniques met with initial success; however, active flow control techniques are more desirable. For example, active flow control allows optimized flow control efforts for different portions of the mission. Also, providing flow control through the addition of pressurized air eliminates the risk of damage to the engine from flow control hardware. As compared to vane vortex generators, microjets are also easier to alter based on flight condition through changing the amount of air delivered.

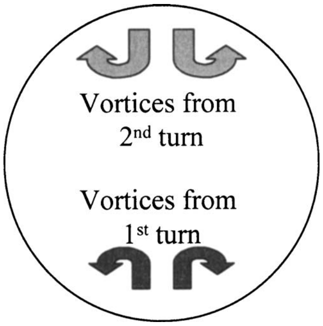

Fig. 2 Direction of vortices formed within a serpentine duct

In vortex generator flow control there are several design factors such as geometry, position, and, in the case of microjets, the total mass flow through the jets. Several studies [10–15] have been performed to determine the critical design factors. The axial position of the vortex generators is critical. The vortex generators must be upstream of the point of separation to be effective. The geometry of the vortex generators is also critical in order to orient the vortices from the vortex generators so that they cancel the vortices formed at the turns in the duct.

Open-loop flow control has been successfully demonstrated for both active and passive flow control designs. The flow control has successfully reduced the distortion at the exit of the inlet while increasing total pressure recovery. However, in each case the flow control was designed for one operation point. The next step is to determine how well the flow control works at off-design points and how effective the flow control is in regaining engine operability range.

Excessive inlet distortion could result in an inability to complete mission requirements because inlet distortion can reduce engine operability range. The distortion will decrease the stability limit of the compression system and reduce the operability range through a reduction in stability margin. A compression system model can predict the effect of inlet distortion on the stability limit of a compression system. In addition, the model can help determine how useful flow control will be in regaining operability range.

Figure 3 shows a compressor map with the total pressure ratio versus corrected mass flow including constant corrected speed lines, an operating line, and a stability limit line. The stability margin can be defined for a constant speed line as

$$SM = \frac{PR_{SL} - PR_{OP}}{PR_{OP}} \times 100$$

This stability margin definition will be used throughout this work.

To determine the change in stability margin due to inlet distortion through a computational approach, the variation in incoming total pressure must be accounted for. This variation defines the distortion and creates the nonuniform flow coming into the en-

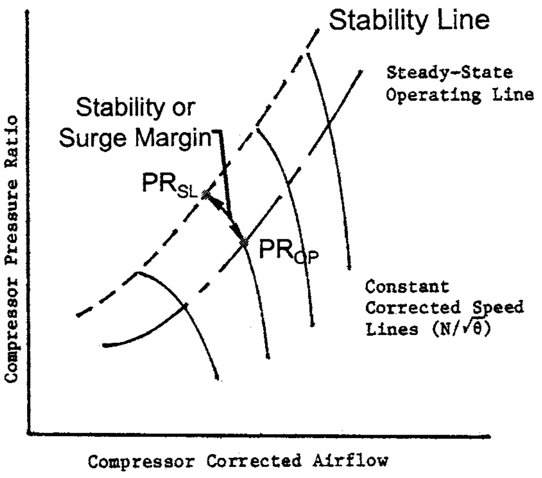

Fig. 3 Compressor map with stability margin definition

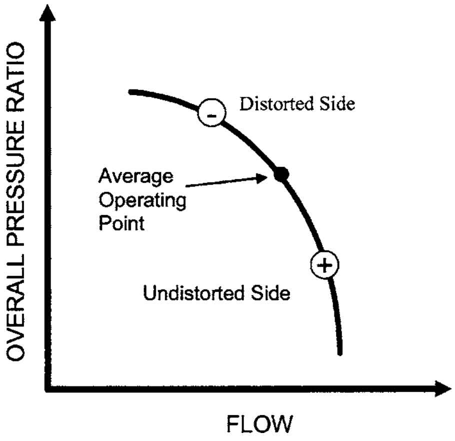

Fig. 5 Parallel compressor operating point analysis

gine. The parallel compressor model is a one-dimensional approach to inlet distortion. Parallel compressor theory [16] models the compressor by circumferentially dividing it into several equal-area segments (typically up to 6 segments can be used before circumferential cross flow between segments becomes too significant to ignore) as seen in Fig. 4. Each division is treated as a separate compressor with individual inlet boundary conditions and a common exit boundary condition. The model can be modified to include some circumferential mass redistribution based on static pressure differences between adjacent sections, which will lead to cross flow. The compressor model is said to stall when one of the parallel compressors reaches the stability limit of the original compressor. The stall point is then calculated by averaging the operating points for the segments at the point where one of the segments has stalled as shown in Fig. 5. In this way circumferential distortion can be modeled as the inlet boundary condition. A parallel compressor model, used in combination with total pressure distributions at the exit of the inlet duct, could be used to predict the stability margin for a compression system where the flow can be naturally divided circumferentially. For flow fields with large differences in the radial profile, the parallel compressor approach is not valid.

Motivation

The present research developed a method to examine the effect of an off-design flight condition, angle of attack, in the static ground testing phase. A flow control technique, consisting of open-loop mass flow injection, applied to an ultracompact, highly offset inlet duct is evaluated at design (cruise) and at off-design (angle of attack) flight conditions. The experimental results are used in a parallel compressor code to predict the change in stability margin of a compression system with flow control for the design and off-design flight conditions. In this way vehicle design can be verified through ground testing and improved computational analysis tools at an earlier design stage.

Inlet Duct Static Ground Test Facility

A static ground test facility was developed to simulate the flow behavior in a serpentine inlet duct at different flight conditions. The flight conditions examined were cruise flight (design) and angle of attack (off-design). The flow field is defined in terms of total pressure distribution at the exit of the inlet duct.

The experimental facility is shown in Fig. 6. From left to right, the front plenum chamber and bellmouth, located in front of the inlet, are used to bring air into the inlet isentropically. The inlet test article is attached to the bellmouth upstream and the measurement rig downstream. At each connection the cross-sectional areas are matched. The measurement rig holds the traverses and probes to measure the total pressure at the exit of the inlet. The aft plenum chamber allows the air to expand from the 10 in. (25.4 cm) diameter jet exiting the measurement rig to the 22 in. (55.9 cm) diameter of the engine. The gas turbine engine at the rear of the setup is used to pull air through the system. Protective screens are located at the entrance to the system and in front of the engine to prevent foreign objects from entering the system and causing damage to the engine.

Figure 7 shows a drawing of the inlet duct used throughout this research. The first section of the duct is level for about 10 in. This is known as the constant area section and is used for the flight simulation. The flow control is located at the second turn of the duct because the secondary flow at this point produces a severe total pressure distortion at the aerodynamic interface plane, AIP. Finally, the AIP is the plane at the exit of the inlet duct. In the final

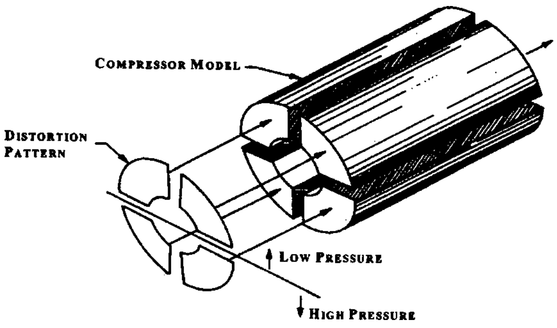

Fig. 4 Parallel compressor concept

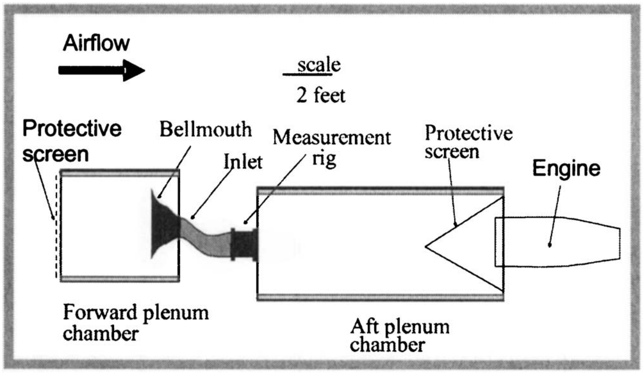

Fig. 6 Schematic of inlet static ground test facility

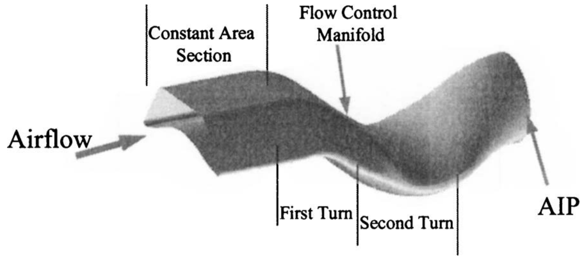

Fig. 7 Experimental inlet duct

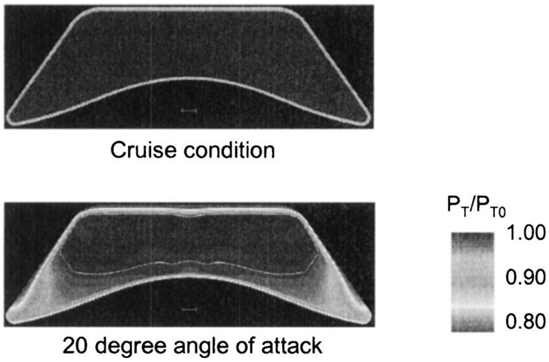

Fig. 8 Inlet throat total pressure CFD predictions ©Lockheed Martin. Used with permission.

application, this plane will be just upstream of the engine fan face. In the current work, the engine is used only to pull air through the system due to differences in scale between the inlet duct (10 in.(25.4 cm) exit diameter) and the engine fan face (22 in.(55.9 cm) diameter].

Throttling the engine until the desired Mach number is achieved at the throat of the inlet sets the test condition. The throat of the inlet occurs in the constant area section (see Fig. 7). The throat Mach number was set to 0.55±0.01 for all experimental tests. Four static pressure measurements around the circumference of the inlet duct at the throat are averaged to obtain the throat static pressure. Isentropic flow is assumed within the constant area section of the inlet; therefore, the ambient total pressure is used to calculate the Mach number. The throat Mach number is calculated by

$$M = \sqrt{\left[\left(\frac{P_0}{P}\right)^{(\gamma-1)/\gamma} - 1\right]\left(\frac{2}{\gamma-1}\right)}$$

where γ is 1.4 for ambient air.

The facility was used to experimentally determine the total pressure recovery at the AIP for different conditions imposed on the serpentine duct. The two conditions that varied were the flight condition being simulated and the presence of flow control. The goal of the research was to determine how effective the flow control was in improving the flow conditions at design and off-design simulated flight conditions.

Measurements

A 20 Kiel probe total pressure rake was used with two traversing units, one radial and one circumferential, to obtain steady-state total pressure measurements at the AIP. The Kiel probe rake reduces the effect of flow angularity allowing total pressure to be measured for flow within ±12 deg of the Kiel-head axis. The probes have a head to head spacing of 1/2 in. (1.27 cm) except for the 20th probe, which is only 1/4 in. (0.635 cm) from the 19th probe. This spacing arrangement allows all the probes to fit within the duct area. The desired radial measurement density was 1/4 in.(0.635 cm) so that one radial traverse is required. There is then one duplicate point obtained which is used to verify measurement repeatability. Because the probe rake covered the diameter of the exit plane, the rake was traversed 180 deg circumferentially. Measurements were taken every 10 deg to obtain a total pressure grid at the exit of the inlet consisting of 702 unique data points.

For each measurement, the probe was held stationary for 30 s, following which 30 s worth of data were acquired. At each measurement point, the 30 s worth of data (1000 total data points) were averaged to acquire a single average total pressure for that point. These time-averaged total pressures were then used to describe the steady-state flow qualities. The transducers used for the measurements were two Scanivalve DSA units with a measurement range of 0–5 Δpsi (0–34.5 kPa) (differential pressure between the measured total pressure and the ambient total pressure). The accuracy of the transducers is reported as 0.05% full scale, or 0.0025 psid (17 Pa). A total of 24 channels was used, consisting of 20 total pressure measurements at the AIP to define the flow quality and four static pressure measurements for the throat Mach number measurement. Static pressure measurements were collected and processed through a LABVIEW code to define the throat Mach number for each measurement station in real time. Using propagation of uncertainty, the Mach number uncertainty is 0.0005. However, since a gas turbine engine was used to set the airflow through the system, the Mach number for each experimental test is only accurate to the repeatability or sustainability of a run condition. In this case the uncertainty of the Mach number is ±0.01.

Additional measurements were required for the mass flow injection rate of the flow control system. Because the mass flow injection rate was controlled using a closed-loop control system, the uncertainty based on experimental repeatability results is greater than the uncertainty propagation due to measurement devices. The experimental repeatability yields an uncertainty of 0.056 lbm/s (0.025 kg/s), or 3.4%.

Flight Condition Simulation

The constant area section is also used in the flight condition simulation to produce a boundary layer to approximate the boundary layer from the forebody of the air vehicle. In this way the facility simulates a cruise flight condition. In a cruise condition, the aircraft is moving through stagnant air, creating a constant angle of flight relative to the incoming flow direction. In order to simulate angle of attack, additional boundary layer growth was required and an additional constant area section was installed ahead of the existing constant area section.

Computational fluid dynamic (CFD) results, supplied by Lockheed Martin, determined the desired total pressure profiles at the inlet throat for an angle of attack of 20 deg. The total pressure contours are shown in Fig. 8 for cruise (0 deg angle of attack) and 20 deg angle of attack. For cruise condition, the throat total pressure profile shows uniform high total pressure recovery. The angle of attack case shows increased boundary layer growth along the walls and additional total pressure deficits in the corner regions of the cross section. CFD studies showed that an additional constant area section 6 in. long would create the desired boundary layer growth along the walls. This section was installed between the bellmouth and the inlet duct.

To produce the total pressure deficits in the corner regions, screen material was used. The screen that most closely matched an angle of attack of 15–20 deg is shown in Fig. 9. The screen material covers almost the same area as the desired area of pressure deficit. The screens were located in between the additional 6 in. (15.24 cm) constant area section and the existing 10 in. (25.4 cm) constant area section. Two total pressure probes were installed in one corner of the cross section, 10 in. (25.4 cm)

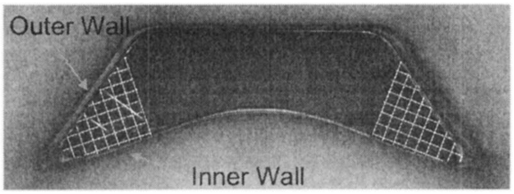

a). Angle of Attack Simulation Setup

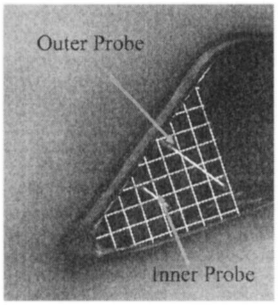

b). Close-up of Total Pressure Probes

Fig. 9 Angle of attack simulation setup

downstream of the screens. These probes were manually traversed to obtain data to compare with the desired throat total pressure profile for simulated angle of attack. This comparison is shown in the results and discussion section.

Distortion Descriptors

The total pressure data were evaluated using the guidelines in ARP 1420 [17]. Each of the distortion descriptors relies on the recommended data grid, consisting of 40 points. This grid is considered to be the minimum number of data points required to describe a flow field. The data plane to be measured is divided into 40 sections of equal area, and the 40 points are the centroids of these sections. The descriptors use the data in terms of five circumferential rings. Ring 1 represents the hub region, while ring 5 lies in the tip region.

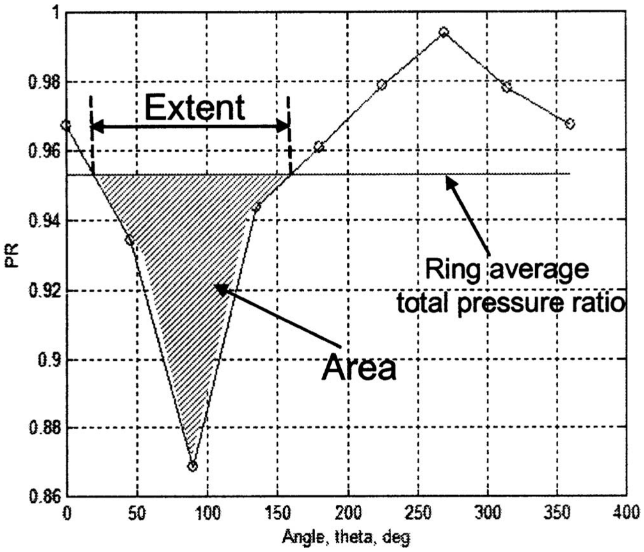

Fig. 10 Ring total pressure recovery example

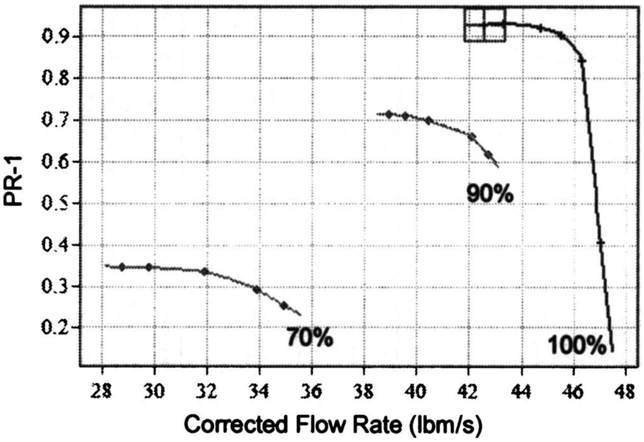

Fig. 11 Stage 35 compressor map

The two most common inlet flow parameters are the circumferential distortion and the total pressure recovery. The area-averaged total pressure recovery was calculated for each case to determine how much total pressure is lost through the inlet duct. Figure 10 shows an example of the total pressure recovery versus circumferential location for one ring in the 40-point grid. The circumferential distortion is calculated from these data as

$$\frac{\Delta PC}{P} = \frac{\text{Area}}{\text{Extent}}$$

Therefore, the circumferential distortion accounts for both the area of the low total pressure region and the extent of the low total pressure region. This value is calculated for each of the five rings. The engine will be limited by its response to the most severe distortion, so the values reported are the maximum circumferential distortion for each case.

Compression Stage Simulation

The total pressure values at the exit were then used in a parallel compressor code, DYNamic Turbine Engine Compressor Code (DYNTECC) [18]. The DYNTECC model is a one-dimensional compression system model to evaluate the performance and stability of compression systems. A finite difference technique is used to solve the conservation of mass, conservation of momentum, and energy equations in the axial direction. Shaft work and blade forces are included as source terms in the equations. These source terms are determined from the pressure and temperature stage characteristics, which are input into the program. DYNTECC uses a control volume approach, with each rotor-stator pair forming a control volume [18]. The model has been modified to include circumferential mass redistribution [19]. In this way the individual parallel compressors are no longer isolated from one another, and cross-flow between adjacent segments based on static pressure differences is accounted for.

This research took advantage of data already available within DYNTECC for NASA Stage 35. This is a single, axial flow, inlet stage for an 8-stage compressor. Stage 35 data are available for three corrected speed lines [20] as seen in Fig. 11. In order to provide continuity between the inlet total pressure distortion data and the compression system model, the mass flow rate was normalized by the flow area and matched for the two cases. This matching occurs at the 70% speed line. The mass flow through the compressor changes as the operating points move along the speed line; however, these changes in mass flow rate ($<10\%$) are believed to be small enough not to change the qualitative results from the simulation. The code was run with a constant exit static pressure to obtain the operating point for each inlet condition, simulating a compressor component level test. The stability limit for each case is obtained by increasing the exit static pressure, or backpressure, in the simulation until the code indicates stall. Stall will occur when one of the parallel compressors reaches the un-

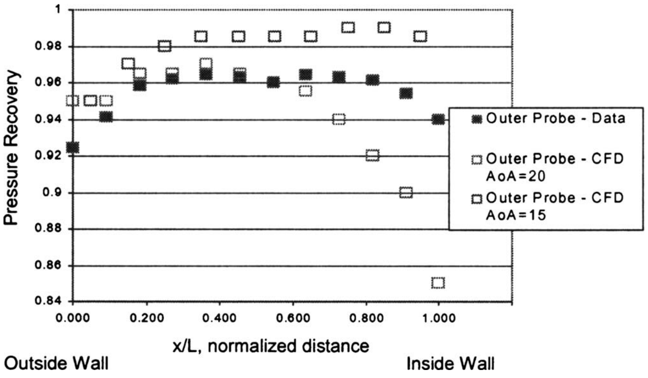

Fig. 12 Angle of attack simulation throat total pressure profile

distorted stability limit. The operating points for each of the parallel compressors at that moment are averaged to obtain the stability limit for the compressor. The stability margins are then calculated using the pressure ratio at the operating points and stability limits for each case. These are compared to the stability margin for the same compressor stage with uniform inflow and no total pressure loss at the entrance. The effectiveness of the flow control technique was evaluated by improvements in total pressure recovery and stability margin and reduction in circumferential distortion.

Results and Discussion

Experimental tests were first run to verify the angle of attack simulation by comparing throat total pressure measurements to the CFD results. The data show an experimental condition in between the CFD results for 15 deg angle of attack and 20 deg angle of attack. The results for the outer probe location from two CFD-generated angles of attack and the experimental data (configuration in Fig. 9) are shown in Fig. 12. Figure 12 shows the pressure recovery (total pressure at a point normalized by ambient total pressure) versus the distance from the outside wall (see Fig. 9) normalized by total distance between the inside and outside wall. Near the outside wall, the agreement between the experimental results and the predicted results is very close. From the middle of the passage area to the inside wall, the experimental results lie in between the predicted profiles for 15- and 20 deg angle of attack. Therefore, the flow field generated experimentally was consistent with expected flight conditions. It was felt that this could determine the affect of a realistic angle of attack flight condition on the flow exiting the duct. In addition, the flow control technique designed for cruise flight could be evaluated at angle of attack.

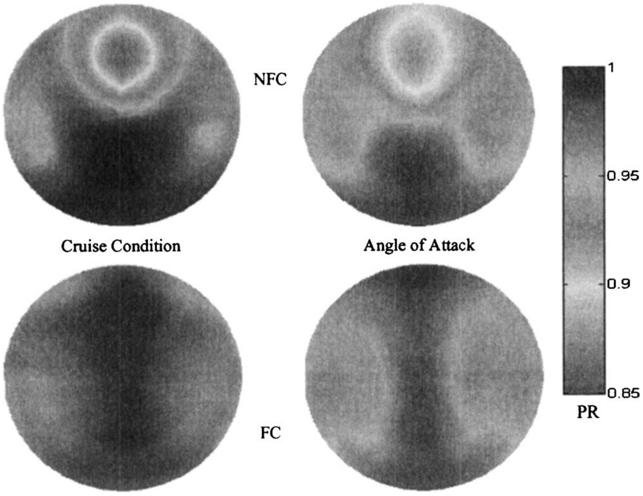

Fig. 13 AIP total pressure contours

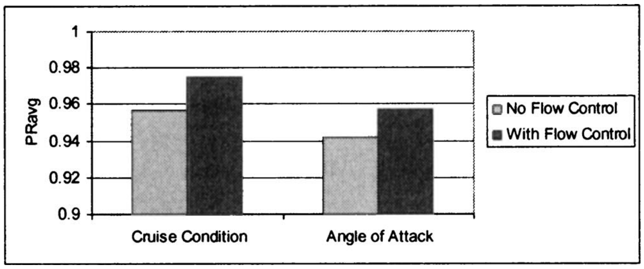

Fig. 14 Effect of flow control of average pressure recovery for design and off-design points

Detailed total pressure measurements were taken at the AIP to determine the quality of the flow exiting the inlet duct. The total pressure contours are shown in Fig. 13. The cases without flow control are shown in the top row, while the cases with flow control are shown in the bottom row. Comparing the contours on top to the corresponding contours on the bottom, the effect of flow control was to eliminate the severe total pressure deficit in the top central region of the AIP. According to CFD studies, as well as previous research, this severe total pressure deficit is due to the second turn in the duct, where flow separation occurs through the formation of two counter-rotating vortices. The side regions of total pressure loss do not change with the addition of flow control.

The total pressure data were used to determine the average pressure recovery for each case. These results are shown in Fig. 14. A 2% increase in pressure recovery was achieved with the addition of flow control. Because the pressure recovery for the angle of attack case without flow control is ~2% lower than the cruise case without flow control, the pressure recovery achievable with flow control also differs based on flight condition. Looking at Fig. 13, the flow control, even at off-design, eliminated the top central pressure deficit, resulting in a ~2% increase in total pressure recovery. The cruise condition had minor pressure loss along the sides with and without flow control. The corresponding region in the angle of attack case shows more significant pressure losses due to the off-design condition. This difference in pressure loss results in the lower pressure recovery with angle of attack.

While the pressure recovery indicates losses through the duct, the circumferential distortion shows the uniformity of those losses. High circumferential distortion indicates a total pressure loss concentrated in one area, while lower circumferential distortion indicates a more uniform flow field. Figure 15 shows the maximum circumferential distortion for each flight condition. The cruise condition has higher circumferential distortion than the angle of attack case without flow control. This trend differs from that for total pressure recovery because the circumferential distortion term relies on the average total pressure recovery and the area of low pressure regions (regions below the average pressure recovery) weighted by the extent of the region of low total pressure.

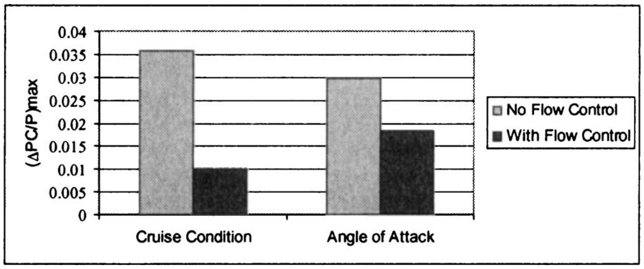

Fig. 15 Effect of flow control on circumferential distortion for design and off-design points

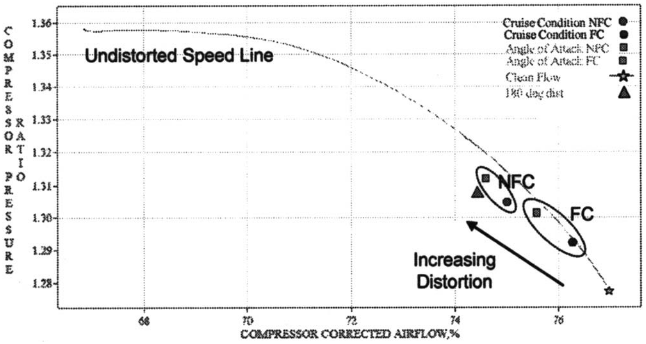

Fig. 16 Effect of flow control on operating points for design and off-design conditions

The circumferential distortion will be low even if the total pressure recovery is low as long as the total pressure loss is uniform throughout the AIP. For this reason, the total pressure recovery must be balanced with the circumferential distortion.

The addition of flow control reduces the circumferential distortion for both cases, with the largest reduction occurring for the cruise condition case. The cruise condition distortion is reduced by ~70% with the addition of flow control. This significant reduction occurs because the cruise condition case represents the design point for the flow control system. There is still a reduction in circumferential distortion for the angle of attack case, but the effect is not as substantial. The reason for this is the additional distortion in the off-design case in the form of stronger corner vortices from the first turn of the duct which are unaffected by the flow control technique. Therefore, the flow control is still effective in reducing the circumferential distortion at off-design conditions but to a lesser degree than for the design point, as expected.

The total pressure distribution was used in DYNTECC to determine how these improvements in total pressure recovery and reductions in circumferential distortion would affect the stability margin of a compressor stage. The parallel compressor divisions were based on total pressure trends. From Fig. 13, each case shows four distinct regions of total pressure recovery. The cases without flow control show one region of high total pressure loss at the top center, two regions of moderate total pressure loss along the sides, and one region with low total pressure loss at the bottom. With the addition of flow control, only the top region changes significantly from a region of high total pressure loss to a region of low total pressure loss. These divisions were used to break the area into four parallel compressors. The simulation was run with a constant exit static pressure, simulating a compressor rig test; therefore, the operating points move up the speed line with increased distortion as seen in Fig. 16. The averaging of the points for the four parallel compressors moves the operating and stability limit points off the speed line. An additional point is shown for a classical 180 deg distortion pattern, which includes a 10% total pressure loss over half of the inlet area [21]. The 180 deg distortion shows a distorted operating point similar to the experimental distortion cases without flow control.

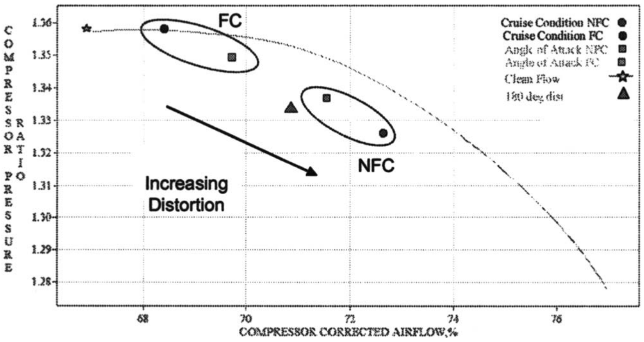

Fig. 17 Effect of flow control on stability limits for design and off-design conditions

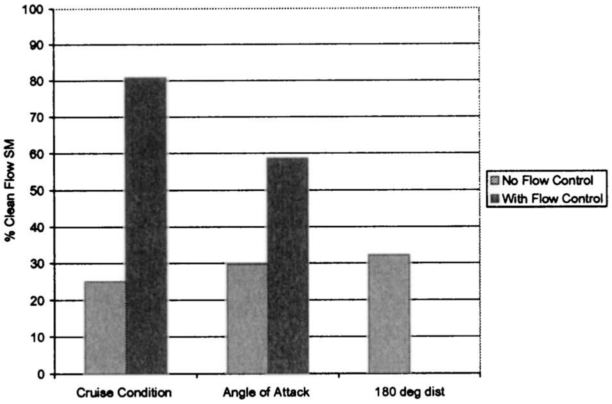

Fig. 18 Effect of flow control on stability margin for design and off-design points

The change in stability limit due to increased distortion is shown in Fig. 17. The stability limit is calculated by ramping the exit static pressure until one of the parallel compressors reaches the undistorted stability limit. At this point the entire compressor is said to stall and the operating points are averaged to obtain the stability limit. The cruise condition with flow control shows almost no change in pressure ratio with a ~2% increase in corrected airflow with respect to the ideal, clean flow, case. Without flow control, the cruise condition shows a lower stability limit than the angle of attack. This is due to the higher circumferential distortion with the cruise condition no-flow control case. The additional point of 180 deg distortion falls in between the flow control and no-flow control test cases.

The points in Fig. 16 and Fig. 17 were used to calculate a stability margin for each case. Figure 18 shows the stability margin for each test case as a percentage of the maximum possible stability margin, or the clean flow stability margin. Without flow control, less than 30% of the original stability margin remains. This stability margin would affect the ability to carry out mission requirements. With the addition of flow control, the stability margin for the design case improves to 80% of the clean flow stability margin and just under 60% for the off-design case. The flow control technique has allowed a significant improvement in operability range for the same inlet duct without flow control.

The above experimental results were obtained using steady-state, time-averaged total pressures. Inlet-engine test methodology for compressor aerodynamic stability is based on engine tests showing that distortion patterns lasting for a time on the order of one engine revolution are felt by the engine as if they were steady-state conditions. This methodology does not address vibration issues or cyclic fatigue. Thus, inlet tests must be conducted using high-response total pressure probes in order to determine the worst-case distortion pattern that the engine sees as a steady-state pattern. The use of high-response instrumentation (minimum of 40 pressures, time correlated) is difficult and expensive. We have elected to use steady-state inlet total pressures, recognizing that the high-response distortion levels would be higher but the trends observed using the steady-state total pressures are valid.

Conclusions

A serpentine inlet duct was tested experimentally at two simulated flight conditions to determine the flow quality produced at the AIP. The flight conditions consisted of a cruise condition and an angle of attack. The angle of attack case was produced by matching CFD predictions of the total pressure field at the throat of the inlet duct. The inlet duct was tested with and without a flow control technique at each flight condition to determine the effectiveness of the flow control technique at both design and off-design conditions. Finally, these data were used to predict the gain in stability margin of a compression stage with the addition of flow control.

The experimental testing for the flight conditions without flow control revealed high total pressure losses at the top center of the AIP, and moderate total pressure losses in the side regions of the AIP. The total pressure loss is in the form of secondary flow created at each turn in the serpentine duct. Flow separation occurs in the uncontrolled case in the form of counter-rotating vortices, which result in total pressure losses at the AIP. The first turn in the duct produces flow separation in the uncontrolled case, but some dissipation occurs prior to the AIP. This results in the moderate total pressure loss in the side regions of the AIP. Flow separation also occurs in the second turn of the serpentine duct, producing additional secondary flow. There is very little dissipation of the secondary flow from the second turn of the inlet duct. This flow distortion is seen in the large total pressure deficit at the top center of the AIP in the uncontrolled cases.

The flow control technique developed by Lockheed Martin eliminated the large total pressure deficit at the AIP for both cases. The angle of attack flight condition resulted in moderate total pressure loss in the side regions, which were not affected by the addition of flow control. This moderate total pressure loss provided lower total pressure recovery for the angle of attack case. Because of the lower area-averaged total pressure recovery, the off-design condition without flow control actually shows more uniform flow, or less circumferential distortion. With flow control, the off-design condition shows reduced circumferential distortion.

A parallel compressor model within DYNTECC was used to predict the change in stability margin for a compressor stage subjected to the experimentally determined total pressure losses at the AIP. The flight conditions without flow control showed a loss in stability range of ~70% of the clean flow stability margin. With the addition of flow control, the stability margin was improved to 80% of the clean flow stability margin for the cruise condition and 60% for angle of attack.

Finally, this research has provided the ability to simulate off-design flight conditions at an earlier design stage than was previously available. In addition, the conclusions regarding the gains in stability margin due to flow control emphasize the importance of a successful flow control technique. In the case studied throughout this research, the flow control improves the flow dramatically and allows the serpentine inlet duct to be used without compromising the flow quality at the engine fan face. These results encourage additional use of flow control, since 1% of the inlet mass flow rate was used to create a 55% improvement in stability margin for the design case.

Acknowledgment

The authors would like to acknowledge the collaboration that went into this research including significant contributions from Daniel Miller and Phil Truax from Lockheed Martin, and Skip Gridley from the Air Force Research Laboratory. This research was supported through an SBIR award to Techsburg, Inc.

Nomenclature

AIP = aerodynamic interface plane
AoA = angle of attack
CFD = computational fluid dynamics
FC = flow control
M = mach number
NFC = no flow control
P = static pressure
P_o = total pressure
PR = total pressure ratio
$\mathrm{PR}_{\mathrm{OP}}$ = pressure ratio at the operating point
$\mathrm{PR}_{\mathrm{SL}}$ = pressure ratio at the stability limit
SM = stability margin
γ = specific heat ratio
$\Delta PC/P$ = circumferential distortion intensity

References

[1] Hill, P., and Peterson, C., 1992, *Mechanics and Thermodynamics of Propulsion*, Addison-Wesley Publishing Co., Reading, MA.
[2] Bansod, P., and Bradshaw, P., 1972, "The Flow in S-Shaped Ducts," Aeronaut. Q., **23**, pp. 131–140.
[3] Rowe, M., 1970, "Measurements and Computations of Flow in Pipe Bends," J. Fluid Mech., **43**, Part 4, pp. 771–783.
[4] Sullivan, J. P., Murthy, S. N. B., Davis, R., and Hong, S., 1982, "S-Shaped Duct Flows," Office of Naval Research Contract Number N-78-C-0710.
[5] Vakili, A., Wu, J. M., Liver, P., and Bhat, M. K., 1983, "An Experimental Investigation of Secondary Flows in an S-Shaped Circular Duct," NASA Final Report NAG3–233.
[6] Vakili, A., Wu, J. M., Liver, P., and Bhat, M. K., 1983, "Measurements of Compressible Secondary Flow in a Circular S-Duct," AIAA, Fluid and Plasma Dynamics Conference, 16th, Danvers, MA, July 12–14, 1983.
[7] Wellborn, S. R., Reichert, B. A., and Okiishi, T. H., 1992, "An Experimental Investigation of the Flow in a Diffusing S-Duct," *AIAA/SAE/ASME/ASEE 28th Joint Propulsion Conference and Exhibit*, AIAA-92-3622.
[8] Povinelli, L. A., and Towne, C. E., 1986, "Viscous Analyses for Flow Through Subsonic and Supersonic Intakes," *AGARD Propulsion and Energetics Panel Meeting on Engine Response to Distorted Inflow Conditions*.
[9] Anderson, J. M., 2003, "Non-Intrusive Sensing and Feedback Control of Serpentine Inlet Flow Distortion," Ph.D. Thesis, Virginia Tech, Blacksburg, VA.
[10] Anderson, B. H., and Gibb, J., 1992, "Study on Vortex Generator Flow Control for the Management of Inlet Distortion," *AIAA/SAE/ASME/ASEE 28th Joint Propulsion Conference and Exhibit*, AIAA-92-3177.
[11] Hamstra, J. W., Miller, D. N., Truax, P. P., Anderson, B. A., and Wendt, B. J., 2000, "Active Inlet Flow Control Technology Demonstration," *22nd International Council of the Aeronautical Sciences*, ICA-6112.
[12] Jaw, L. C., Cousins, W. T., Wu, D. N., and Bryg, D. J., 2001, "Design and Test of a Semi-Passive Flow Control Device for Inlet Distortion Suppression," ASME J. Turbomach., **123**, pp. 9–13.
[13] Reichert, B. A., and Wendt, B. J., 1994, "Improving Diffusing S-Duct Performance by Secondary Flow Control," AIAA 94-0365, *AIAA 32nd Aerospace Sciences Meeting and Exhibit*, Reno, NV.
[14] Reichert, B. A., and Wendt, B. J., 1993, "An Experimental Investigation of S-Duct Flow Control Using Arrays of Low-Profile Vortex Generators," AIAA 93-0018.
[15] Vakili, A. D., Wu, J. M., Liver, P., and Bhat, M. K., 1985, "Flow Control in a Diffusing S-Duct," *AIAA Shear Flow Control Conference*, AIAA-85–0524.
[16] Mazzawy, R. S., 1977, "Multiple Segment Parallel Compressor Model for Circumferential Flow Distortion," J. Eng. Power, **99**, pp. 288–296.
[17] SAE S-16 Committee, 1978, ARP 1420, "Gas Turbine Engine Inlet Flow Distortion Guidelines," Society of Automotive Engineers.
[18] Hale, A. A., and Davis, M. W., Jr., 1992, "DYNamic Turbine Engine Compressor Code, DYNTECC—Theory and Capabilities," AIAA-92-3190.
[19] Shahrokhi, K. A., and Davis, M. W., 1995, "Application of a Modified Dynamic Compression System Model to a Low-Aspect Ratio Fan: Effects of Inlet Distortion," AIAA 95-0301, *AIAA 33rd Aerospace Sciences Meeting and Exhibit*, Reno, NV.
[20] Reid, L., and Moore, R. D., 1978, "Performance of Single-Stage Axial-Flow Transonic Compressor With Rotor and Stator Aspect Ratios of 1.19 and 1.26, Respectively, and With Design Pressure Ratio of 1.82," NASA Technical Paper 1338, Lewis Research Center, Cleveland, OH.
[21] SAE S-16 Committee, 1983, AIR 1419, "Inlet Total-Pressure-Distortion Considerations for Gas-Turbine Engines," Society of Automotive Engineers.

Flowfield and Pressure Measurements in a Rotating Two-Pass Duct With Staggered Rounded Ribs Skewed 45 Degrees to the Flow

Tong-Miin Liou
e-mail: tmliou@pme.nthu.edu.tw

Y. Sian Hwang

Yi-Chen Li

Department of Power Mechanical Engineering,
National Tsing Hua University,
Hsinchu, Taiwan, ROC

Laser-Doppler velocimetry and pressure measurements are presented of the local velocity and wall pressure distributions in a rotating two-pass square duct with staggered ribs placed on the leading and trailing walls at an angle of 45 deg *to the main stream. The ribs were square in cross section with the radii of rounds and fillets to rib height ratios of 0.33. The rib-height/duct-height ratio and the pitch/rib-height ratio were 0.136 and 10, respectively. The duct Reynolds number was* 1×10^4 *and rotation number Ro ranged from 0 to 0.2. Results are documented in terms of the evolutions of both main flow and cross-stream secondary flow, the distributions of the pressure coefficient, and the variation of friction factor with Ro. For CFD reference, the periodic fully developed flow condition is absent for the present length of the rotating passage roughened with staggered* 45 deg *ribs. In addition, the relationships between the regional averaged Nusselt number, transverse and convective mean velocity component, and turbulent kinetic energy are addressed. Using these relationships the general superiority of heat transfer enhancement of the staggered* 45 deg *ribs arrangement over the in-line one can be reasonably illustrated. Simple expressions are obtained to correlate the friction factor with Ro, which are lacking in the published literature for passages ribbed with staggered* 45 deg *ribs. The staggered* 45 deg *ribs are found to reduce the friction loss to about* 88% ± 1% *of the in-line* 45 deg *ribs for the rotating passage under the same operating conditions. The respective contributions of the angled ribs and passage rotation on the passage friction loss are identified.* [DOI: 10.1115/1.2162180]

Introduction

Augmented internal cooling for metal blades of a gas turbine engine is the main theme of the present study. In existing turbine blade designs staggered and skewed ribs are more commonly arranged on the leading and trailing wall of one or several radial internal passages connected by 180 deg sharp turns to induce lasting vortices, trip boundary layer, disturb core flow, and enhance turbulence level. In general, surface heat transfer is augmented with the penalty of increased pressure loss. Thus, efforts should be given for a better understanding of the associated local fluid flow and friction loss such that a better compromise between the heat transfer enhancement and pressure loss can be attained. However, most previous studies only emphasized the heat transfer outcome partly because measuring fluid flow in a rotating coolant duct is relatively difficult. This fact motivates the complementary investigations of flow field and pressure distribution in the present study.

Table 1 lists flowfield measurements in ribbed rotating ducts relevant to the present study. For coolant passage orientation $\theta=0$ deg (Fig. 1), Iacovides et al. [1–3] reported laser-Doppler velocimetry (LDV) and wall pressure measurements in a two-pass passage for assessment of turbulence models used in the computation of blade-cooling flows. In the up and down passes, the leading and trailing walls were roughened with 90 deg angled ribs of square cross section in a staggered arrangement. Their study focused on the effects of the location of the first outer-wall rib, after the bend exit, on the development of the downstream turbulence level and three-dimensionality (3-D) of the flow. Hsieh et al. [4] performed LDV measurements in a two-pass passage operating at a very low rotating number, $\mathrm{Ro}=0.06$. The ribs had a square cross section. Their measurements were made only along the longitudinal symmetry plane and beyond the rib height. Note that all the above investigations did not measure the cross-stream secondary flow development.

For $\theta=90$ deg, Tse and Steuber [5] studied mean flow characteristics in a rotating four-pass coolant passage using LDV. Their ribs having a semi-circular cross section were skewed −45 and +45 deg respectively, to the radially outward and inward main stream and arranged in a staggered mode. Reynolds number (Re) and rotating number (Ro) were fixed at 25,000 and 0.24, respectively. In the first passage within 5 D_H upstream of the turn the secondary flow was found to be characterized by a counterclockwise swirl on the trailing side and a corner recirculation at the inner corner of the leading side. Within 3 D_H after the first turn the secondary flow was featured by a clockwise swirl on the leading side and a corner recirculation zone at the inner corner of the trailing side. Turbulence quantities were not reported. Liou et al. [6] studied fluid flow in a rotating two-pass duct with in-line 90 deg ribs. The ribs were square in cross section. Their LDV data were presented with Re fixed at 1×10^4 and Ro varied from 0 to 0.2. The rotating ribbed duct flow was found to produce higher $U_{\max}/U_b$ and $u'_{\max}/U_b$, stronger total averaged secondary flow, and higher heat transfer enhancement. Keeping the same operating conditions, they further performed LDV and pressure mea-

---

Contributed by the International Gas Turbine Institute (IGTI) of ASME for publication in the Journal of Turbomachinery. Paper presented at the International Gas Turbine and Aeroengine Congress and Exhibition, Vienna, Austria, June 13–17, 2004, Paper No. 2004-GT-53173. Manuscript received October 1, 2003; final manuscript received March 1, 2004. IGTI Review Chair: A. J. Strazisar.

Table 1 A list of flow field measurements in rotating rib-roughened square ducts by various research groups [*S*: Staggered; *P*: Parallel (In-line); *E*(*f*): power spectral density ($m^2 s^{-1}$)]

Lead author	Year	Exp. tech	θ (deg)	Pass no.	Rib	H/D_H	Pi/H	Re$\times 10^{-4}$	Ro	$\Delta\rho/\rho$	Measured Quantity	Measured Stations
Iacovides	1996	LDV									$U,W,u',w',\overline{uw}$	27
	1998		0	2	90 deg *S*	0.1	10	10.0	0–0.2	0	$U,W,u',w',\overline{uw}$, P_s	21
	1999										$U,W,u',w',\overline{uw}$	12
Tse	1997		90	4	45 deg *S*	0.1	5	2.5	0.24	0	U,V,W	10
Hsieh	1997		0	2	90 deg *P*	0.2	5	0.5–1.0	0, 0.06	NA	U,W	20
Liou	2002										U,V,u',v',P	80
	2003a										$U,V,u',v',P,E(f)$	
	2003b		90	2	90 deg *P*	0.136	10	1.0	0–0.2	0	U,V,u',v',P	
	2003c				45 deg *P*						U,V,u',v',P	
Servouze	2003	PIV	90	2	60 deg *P*	0.1	10	0.5	0,0.66	0	U,W	78
								2.5	0,0.33			
Present	2004	LDV	90	2	45 deg *S*	0.136	10	1.0	0–0.2	0	U,V,u',v',P	80

surements for in-line detached 90 deg ribs [7,8] and in-line 45 deg ribs [9]. Among these studies, spectrum analysis was reported in [7] and the absence of a fully developed flow condition in the rotating ribbed passage was concluded in [9]. In recent years measurements of flow structure in two-pass square ducts with 45 deg rib turbulators were also performed by Schabacker et al. [10] and Chanteloup et al. [11] using particle image velocimetry (PIV), but the ducts were all stationary. Servouze and Sturgis [12] presented flow field measurements in one branch of a two-pass coolant passage with seven pairs of in-line 60 deg ribs under adiabatic conditions using 2-D PIV. The ribs had square cross section. They presented average velocity fields at Ro=0, 0.06 for Re=25,000 and Ro=0, 0.33 for Re=5000. There were no measurements of the cross-stream secondary flow development. Similar to that made by Liou et al. in [6], no separation bubble immediately downstream of the bend was observed.

Numerically, Prakash and Zerkle [13] showed that Coriolis effects (Ro=0.12) are less pronounced in a 90 deg ribbed passage compared to a smooth wall passage. Iacovides and Raisee [14] found that the isotropic eddy viscosity model and the widely used wall function approach are unable to capture physically reasonable heat transfer and flow field features in serpentine cooling ducts with 90 deg ribs. This is because the turn and ribs usually generate flow separation and anisotropic turbulence. Jang et al. [15] computed flow and heat transfer in a one-pass rotating square duct with 45 deg ribs using a Reynolds stress turbulence model. The ribs had rounded cross section and were staggered relative to each other. Their results revealed that the Coriolis force, centrifugal buoyancy, and 45 deg ribs generate strong anisotropic turbulent stresses and heat fluxes. Obviously, the computational studies cited above all suggest the necessity of detailed fluid flow measurements in a rotating multi-pass ribbed duct with 180 deg sharp turning. Recently, Tafti [16] and Saha and Acharya [17] performed large eddy simulations (LES) of flow and heat transfer in a single-pass rotating passage roughened with in-line and staggered 90 deg ribs, respectively. In their simulations fully developed flow and heat transfer conditions were assumed.

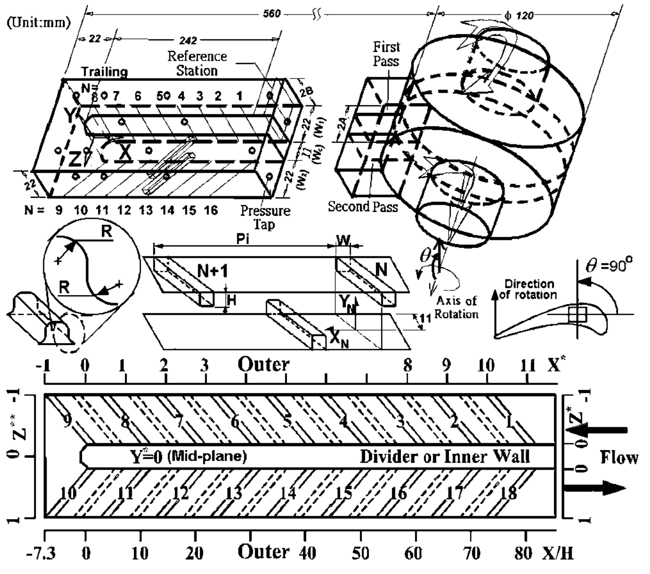

Fig. 1 Sketch of configuration, coordinate system, and dimension of test section

In contrast to the fluid flow measurements, heat transfer measurements in rotating serpentine ribbed passages [6,18–24] are more abundant. Taslim et al. [18] studied heat transfer characteristics in rotating one-pass passage with 45 deg angled ribs arranged in a criss-cross mode on the leading and trailing walls. They found that rotational effects were more pronounced in ribbed passages with a higher aspect ratio and a lower rib blockage ratio. Fann et al. [23] made local heat transfer measurements in a rotating four-pass passage with ribbed surfaces. They concluded that both rotation and ribs improved the local heat transfer, and 45 deg ribs performed the best in both the stationary and rotating cases. Recently, Azad et al. [24] performed experimental heat transfer studies in a two-pass rectangular passage. Their results showed that 45 deg parallel ribs produced a better heat transfer augmentation than 45 deg cross ribs.

Although aforementioned studies have provided valuable information, most of them were focused only on the heat transfer part. In addition, most of the previous velocity results reported from measuring these difficult-to-measure flows were with square-sectioned ribs. Studies with square ribs are generally related to more academic interest in the use in CFD validation and the help in understanding the embedded flow physics. Hence, the present investigation aims at exploring local velocity distributions with rounded ribs which take account of casting constraints. Moreover, all the above-mentioned studies with staggered 45 deg ribs and passage orientation θ=90 deg did not provide turbulence data and local wall pressure relevant to the friction loss. The pressure distribution data bank will thus be presented in the present work. It is believed that the information gathered would provide a more useful reference to the turbine cooling designer.

Experimental Apparatus and Conditions

Test Section and Conditions. The configuration, coordinate system, and dimensions of the test section, made of 20 mm thick

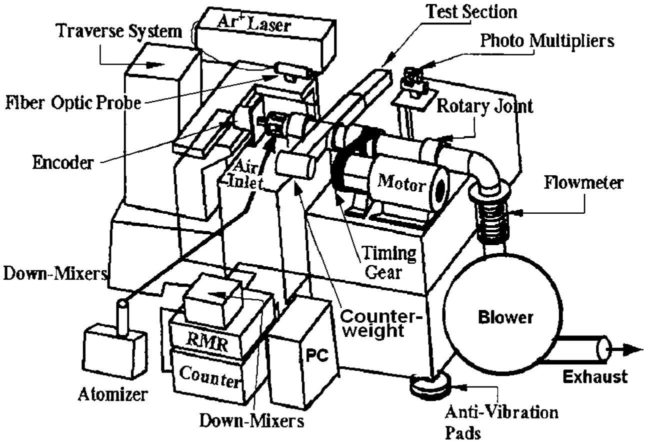

Fig. 2 Schematic drawing of flow system and LDV apparatus

acrylic sheets for optical access, are schematically shown in Fig. 1. The flow passages had square cross section with a hydraulic diameter D_H=22 mm and the divider-wall thickness was 0.5 D_H. At the turn, the clearance between the tip of the divider wall and the duct outer wall was fixed at 1 D_H. The 45 deg transverse Plexiglas ribs were mounted on the leading and trailing walls and staggered relative to each other. The cross section of the ribs had rounded edges and corners with the rib-tip and rib-root radius to rib height ratio R/H of 0.33. In each pass eight and nine ribs were equally spaced on the leading and trailing walls, respectively. The tips of the first rib pair were located at 13.8 mm downstream of the front edge of the test section. H/D_H and Pi/H were 0.136 and 10, respectively, in each pass. The Reynolds number, based on the bulk mean air velocity of 7.58 m/s and D_H, was fixed at 1.0×10^4. The rotation number varied from 0 to 0.20, corresponding to rotational speeds from 0 to 660 rpm.

The velocity measurements were undertaken at the entrance reference station and in the region 1.5 rib pitches upstream to 1.5 rib pitches downstream of the turn along the longitudinal central plane of each pass, i.e., $Z^* = \pm 0.5$. At each X station the LDV measurements were made at 9 to 14 locations. Additional measurements at four selected X stations were also made for checking periodic fully developed flow condition. Cross-stream transverse velocity component measurements were performed in four selected cross-sections to reveal the secondary flow structures. In each cross-section plane the LDV measurements were made at 72 locations. The wall pressures were measured at the 16 locations indicated in Fig. 1 along the leading and trailing walls.

Experimental Apparatus. The experimental apparatus consisting of flow system and optical system is depicted in Fig. 2. For the optical system, the principle of LDV has been described in detail in the authors' previous studies [6–9]. For the flow system, the inlet air firstly flowed radially outward in the first pass, made a 180 deg sharp turn, and flowed radially inward in the second pass. A 2.2 KW turbo-blower controlled by a frequency converter was used to drive the air from the test section to ambient. A micro-differential pressure transducer (Kyowa PDL-40GB) connected to 16 pressure taps on the leading and trailing walls (Fig. 1) measured the wall pressures. The pressure transducer was located on the wall of the hollow shaft (Fig. 1), i.e., at a radius of 60 mm. These signals were subsequently amplified and fed via the slip ring to the PC for storage. Note that the microdifferential pressure transducer was referenced to a pressure tap located at the inlet reference station, X^*=11.6 or X/H=85 in Fig. 1. It used a foil strain gage as its detector element and permits high precision measurement of very small differential pressure. Its accuracy is within ±0.1% of the 400 mmAq (3922 N/m^2) full-scale value.

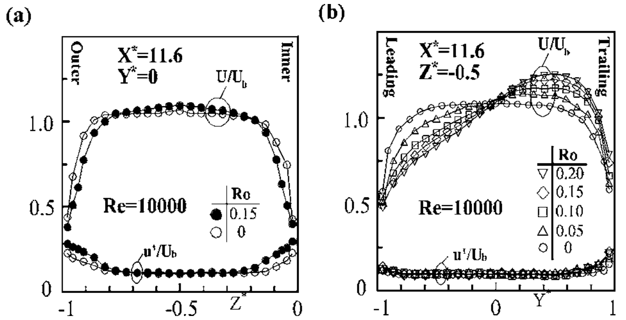

Fig. 3 Longitudinal mean velocity and turbulence intensity profiles at inlet reference station X^*=11.6 of the first pass in (*a*) Y^*=0 (mid-plane) and (*b*) Z^*=–0.5 planes.

Data Uncertainty

The uncertainties in the pressure loss measurements are ±0.1%, ±0.5%, and ±0.1% associated with the pressure transducer temperature effect on output, the slip ring noise, and the amplifier noise, respectively. A resultant uncertainty of ±0.52% is thus estimated for the pressure loss data. The corresponding uncertainty in C_p is ±0.64%. For a 95% confidence level, the statistical errors in the mean velocity and turbulence intensity are less than 1.8% and 3.1%, respectively. More detailed uncertainty estimates and velocity bias correlations are included in Liou et al. [6–9].

Results and Discussion

Fluid Flow at Inlet Reference Station. In the first outward passage the inlet reference station was selected at X^*=11.6 (or X/H=85), which is located at 5H distance upstream of the first rib on the trailing wall (N=1 in Fig. 1). Figures 3(*a*) and 3(*b*) depict the variation of streamwise mean X-component velocity and turbulence intensity profiles with Ro at inlet reference station in two orthogonal lines Y^*=0 and Z^*=–0.5, respectively. Because the span line Y^*=0 is perpendicular to the Coriolis force, all the U/U_b and u'/U_b profiles in Y^*=0 line (Fig. 3(*a*)) are very symmetric to the central line Z^*=–0.5. The peaks U and u' respectively increase from 1.07U_b and 0.18U_b at Ro=0 to 1.12U_b and 0.23U_b at Ro=0.15. For CFD reference, the boundary layer thickness defined at 95% $U_{\max}$ is δ_{95}/H=1.2/1.1 and 1.5/1.5 along the inner/outer wall for Ro=0 and 0.15, respectively.

On the Z^*=–0.5 line, the U/U_b and u'/U_b profiles (Fig. 3(*b*)) are rather symmetric for Ro=0. As Ro is increased from 0 to 0.2, the skewness of U/U_b and u'/U_b increases monotonically due to the increase of the Coriolis force directed toward the trailing wall (Y^*=1) and, in turn, the steeper mean velocity gradient near the trailing wall. The U and u' peaks can be as high as 1.25U_b and 0.22U_b, respectively, for Ro=0.2. The uniform parts of u'/U_b profiles extend to (with respect to Y^*=0) 70% of the channel height and have values of 10.0%±0.5%. The boundary layer thickness is δ_{95}/H=1.4/1.3, 3.1/1.2, 3.7/1.2, 4.0/0.9, 4.4/1.0 along the leading/trailing wall for Ro=0, 0.05, 0.10, 0.15, and 0.2, respectively.

Spatial Periodicity of U/U$_b$. The fully developed flow condition is often assumed by researchers in performing LES simulations of fluid flow and/or heat transfer in a rotating ribbed passage for internal cooling of turbine blades [16,17]. Figure 4 provides an example to examine this assumption in terms of a comparison of the longitudinal mean velocity profiles at a fixed station X_N/H =3.5 but in different pitches ($X_{N+1}-X_N$), N=4 to 7 in the first passage. The data shown are away from the entrance of the first passage and the 180 deg turn. It is seen that the maximum differences between any two consecutive profiles are from 15% U_b to 51% U_b in the first passage. Thus, a fully developed flow condi-

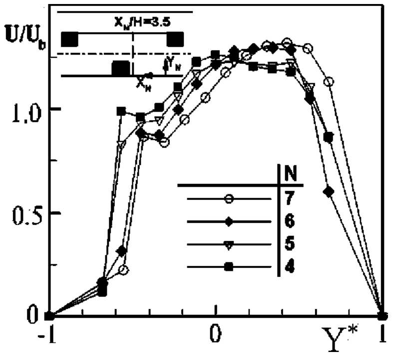

Fig. 4 Examination of periodic fully developed condition by comparing U/U_b profiles at $X_N/H=3.5$ in various pitches for $\mathrm{Ro}=0.15$

tion is never attained in the rotating duct investigated. This result is contrary to that found in a similar two-pass duct under stationary condition [25]. Bonhoff et al. [25] in their PIV measurements in the upstream leg (radially outward passage) of stationary ribbed duct flows reported that a fully developed flow condition in terms of mean velocity and turbulent kinetic energy was achieved after three and ten rib pitches, respectively, for staggered 90 deg ribs. The corresponding development lengths required approximately 8 and 12 rib pitches, respectively, for staggered 45 deg rib arrangement. The above differences pose a challenge to the CFD predictions on the rotating ribbed passage flow since a turbine blade has a finite length.

Evolution of Streamwise Mean Flow. Figure 5 depicts the evolution of the streamwise mean velocity profile along the $Z^*=-0.5$ and $Z^*=+0.5$ plane for the case of $\mathrm{Ro}=0.15$. As the fluid flows radially outward over the first 45 deg angled rib mounted on the trailing wall, the U/U_b at $X^*=10$ station decreases in the region $|Y^*|\geqq 0.5$ due to rib's blockage but must increase in the region $|Y^*|<0.5$ due to mass conservation. The profiles is still skewed toward the trailing wall as a result of the Coriolis force. The peak U is $1.81U_b$ while $U_{\max}=1.85U_b$ for the case of in-line 45 deg ribs at the same Ro [9]. It is obvious that an in-line rib arrangement has a slightly larger nozzle or contraction effect than the staggered one and, therefore, a slightly higher $U_{\max}$.

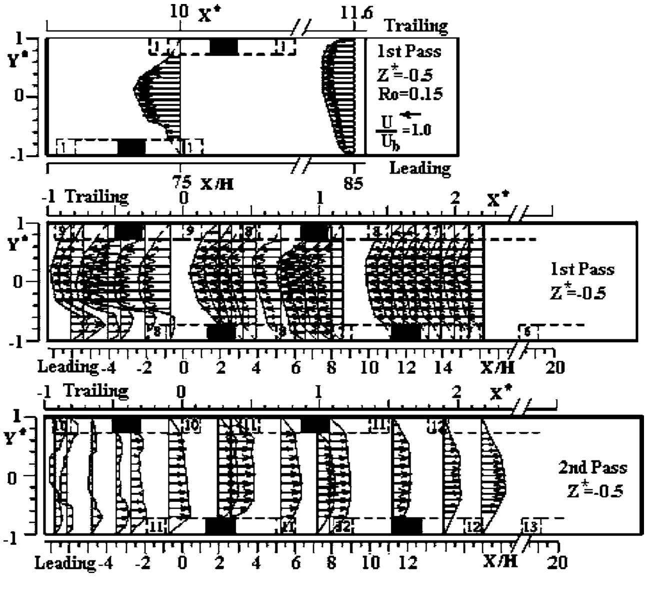

Fig. 5 Evolution of longitudinal mean velocity component in $Z^*=-0.5$ and $Z^*=0.5$ planes

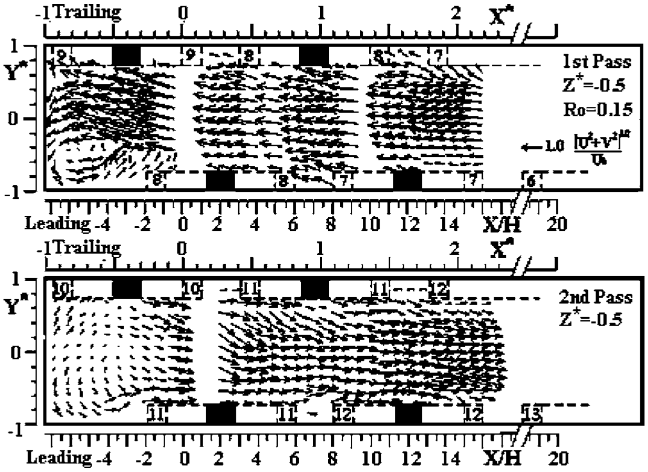

Fig. 6 Mean velocity vector plots around the turn for $\mathrm{Re}=1.0\times 104$ and $\mathrm{Ro}=0.15$ in X-Y plane of the (*a*) first and (*b*) second passages

Figure 6 depicts the longitudinal mean velocity profiles in-between $X^*=2.2$ to -1 ($N=7-9$) along $Z^*=-0.5$ plane and $X^*=-1-2.2$ ($N=10-12$) along $Z^*=+0.5$ plane to demonstrate the flow characteristics around the turn. The mean velocity vector plots unveil the slant impingement of fluid flow upon the first-pass trailing wall and second-pass leading wall directed by the Coriolis force. Specific examples are the slant velocity vectors in the region $1.5<X^*<1.8$ adjacent to the trailing wall of the first pass. The corresponding heat transfer on this wall is to be enhanced. Note that LDV measurements within a rib height (3 mm) distance to the wall were generally not attainable due to rib's blockage of laser beams. Exceptions are the two rib-height gaps between the consecutive 45 deg angled ribs on the leading or trailing walls. Within the 180 deg sharp turn ($-1<X^*<0$ or $-7.3<X/H<0$) and in the $Z^*=-0.5$ plane of the first pass (Figs. 5 and 6), the curvature and rotation make the flow pattern form a strongly skewed Dean-type vortex flow. More specifically, the Dean vortices degenerate into a single vortex located near the passage tip and leading wall. The velocity components normal to the passage tip as well as normal to the leading or trailing wall play an important role in augmenting heat transfer. Inside the turn ($-1X^*<0$) on the first outward duct side, the near wall mean velocity vectors in the region ($Y^*=1$ and $-1<X^*<-0.5$) have larger Y component and are directed toward the trailing wall ($Y^*=1$). The downwash effect is expected to markedly increase the heat transfer rate. In contrast, the near-wall mean velocity vectors in the region ($Y^*=-1$ and $-0.5X^*<0$) have larger Y component but are directed away from the leading wall. The upwash effect is not expected to contribute to the heat transfer enhancement. Inside the turn ($-1<X^*<0$) on the second pass side (in the $Z^*=0.5$ plane), the U/U_b profiles in Fig. 5 clearly indicate the presence of a pair of counter-rotating skewed Dean-type vortices. In addition, one expects that heat transfer enhancement inside the turn on the second pass side is higher on the leading wall than on the trailing wall since the velocity vectors in Fig. 6 are more inclined toward the leading wall.

Evolution of Cross-Stream Secondary Flow. A 180 deg turn can induce cross-stream secondary flow as shown in Fig. 7 in terms of mean velocity vectors pattern on the mid-turn cross-sectional plane. The counter-rotating Dean-type vortices pair is skewed by duct rotation as mentioned above. Core flow impingements on the top half of the passage tip ($X^*=-1$) and on the major portion of leading wall ($Y^*=-1$) are clearly unveiled.

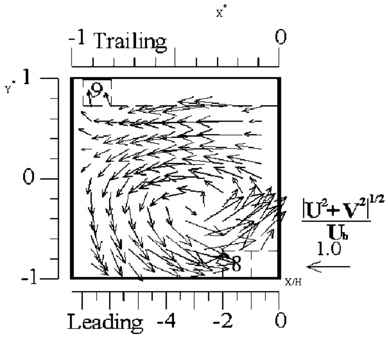

Fig. 7 Mean velocity vector plot on the mid-turn cross-section ($Z^*=0$) for $Re=1.0\times10^4$ and $Ro=0.15$

Angled ribs can generate cross-stream secondary flow in the two radial passages as well. A 45 deg angled rib generates an angled vortex with a vorticity vector $\vec{\Omega}$ that parallels the rib. The $\vec{\Omega}$ has a longitudinal component $\vec{\Omega}_x$, as schematically shown in the middle portion of Fig. 8, giving the secondary flow pattern on the cross-sectional plane. The $\vec{\Omega}_x$ is directed towards the upstream and downstream direction for ribs mounted on the leading and trailing wall, respectively, in the radially outward passage. The trend is reversed in the radially inward passage. In the following discussion, all the secondary flow patterns are viewed from the downstream towards upstream direction and, hence, the divider or inner wall ($Z^*=0$) is always on the right-hand side. Before examining the secondary flow patterns depicted in Fig. 8, one should first understand that they are actually the resultants of the two structures generated by the angled ribs and duct rotation. In the first radially outward passage, the 45 deg rib generates the secondary flow consisting of two counter-rotating vortices that drive fluid from the duct center towards the inner (or divider) wall ($Z^*=0$) along the center plane and to the outer wall ($Z^*=-1$) along the ribbed trailing ($Y^*=1$) and leading ($Y^*=-1$) walls. However, duct rotation also induces secondary flow consisting of two counter-rotating vortices that steer fluid from the duct center towards the trailing wall along the center plane and to the leading wall along the inner and outer wall. Hence, the double-cell longitudinal counter-rotating vortex structures respectively induced by the angled rib pair and duct rotation are perpendicular to one another. Each structure has a counter-clockwise circulating vortex and a clockwise circulating vortex. The two structures will interact. The degree of interaction depends on the value of Ro.

The resultants of the combined effect of the staggered 45 deg ribs and duct rotation on the secondary flows in the first and second passages are depicted in the upper and lower parts of Fig. 8, respectively. For $Ro=0.2$, the Coriolis force is large enough to make the above-mentioned two counter-clockwise vortices (from each structure) and two clockwise vortices reinforce each other and merge into a single counter-clockwise vortex and a single clockwise vortex, respectively. It is seen that at $X^*=9.81$ between $N=1$ and $N=2$, i.e., the front portion of the ribbed first passage, the left and the upper half of the cross-section is dominated by the single counter-clockwise vortex whereas the forth quadrant of the cross section is predominated by the single clockwise vortex. At the rear portion of the ribbed first pass, $X^*=1.64$ between $N=7$ and $N=8$, the subsonic flow senses the presence of the geometric turn and makes some adjustments. It responds with an upward compression of the counter-clockwise vortex and, in turn, a leftward expansion of the clockwise vortex. Inside the turn (between $N=9$ and $N=10$) the angled ribs and geometry curvature have similar effects on the secondary flow pattern: directing the central core flow towards the outer wall ($X^*=-1$). Thus, the secondary flow has the familiar pattern of Dean-type double vortex with the upper vortex cell squeezed by the rotation effect, as has been shown in Fig. 7.

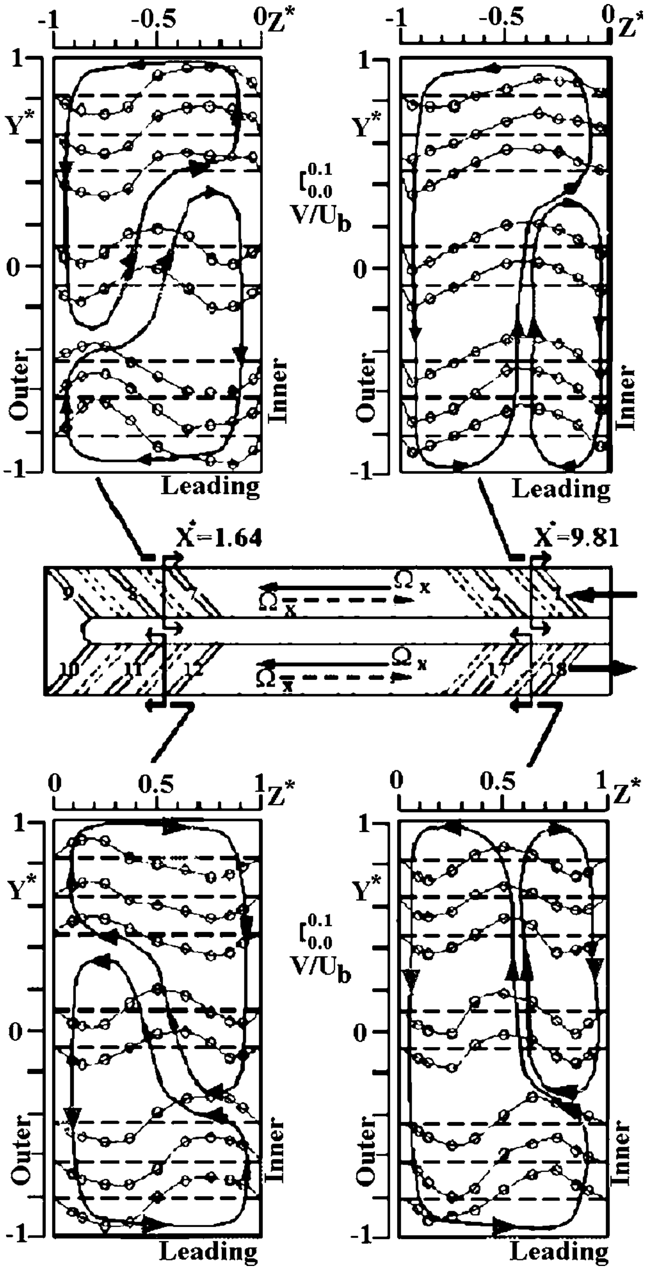

Fig. 8 Distributions of transverse mean velocity on the cross-sectional planes near the entrance, around the 180 deg turn, and near the exit for $Ro=0.2$ (dotted and solid arrows stand for Ω_x generated by the ribs on the leading and trailing wall, respectively)

Immediately after the turn at $X^*=1.64$ between $N=11$ and $N=12$, Fig. 8 depicts that the secondary flow still keeps the Dean-vortices pattern with, however, the lower counter-clockwise vortex (Fig. 7) squeezed and the upper clockwise vortex extended by the reversed Coriolis force due to the radially inward flow in the second passage. Far downstream near the outlet at $X^*=9.81$ between $N=17$ and $N=18$ of the second passage, the secondary flow pattern assumes a mirror image of that at the corresponding X^* station of the first passage. The same observation can be applied to the secondary flow patterns at the aforementioned $X^*=1.64$ of the first and second passages, as well. Nevertheless, all the vor-

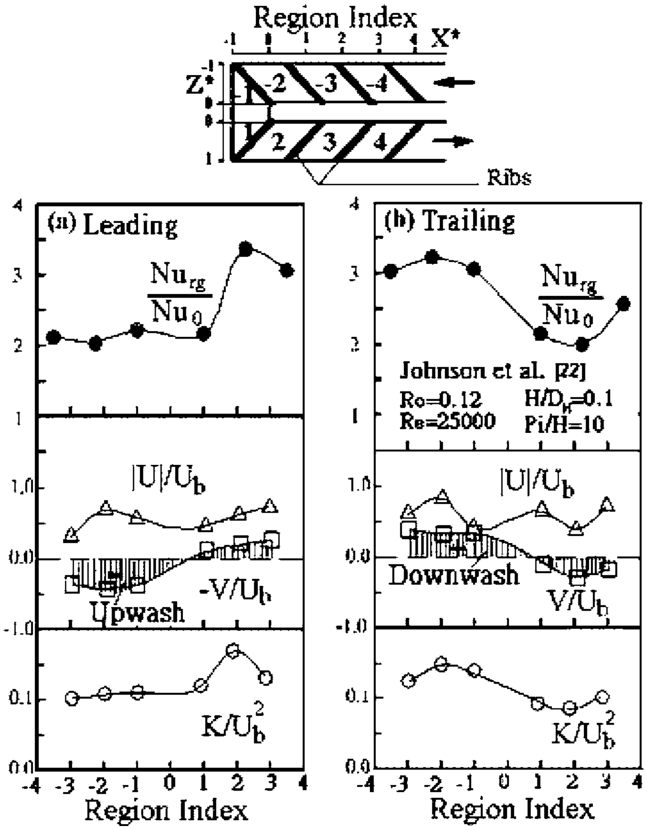

Fig. 9 Relationships between mean velocity components, turbulent kinetic energy, and regional averaged surface heat transfer coefficient

texes rotate in opposite directions due to reversed Coriolis force. Similar mirror image observation can also be found in the rotating four-pass square duct flow with 45 deg staggered ribs studied by Tse and Steuber [5]. Their rib-to-duct height ratio, $H/2B=0.1$, and rotation number, $\mathrm{Ro}=0.24$, are respectively lower and higher than those ($H/2B=0.136$ and $\mathrm{Ro}=0.20$) of the present case. With a higher value of Ro, their secondary flow on the mid-turn cross section was predominated by a single vortex only, instead of that shown in Fig. 7. Quantitatively, the maximum positive/negative transverse mean velocities of the secondary flow on the cross-sectional planes examined reach $+0.16U_b/-0.13U_b$ and $+0.18U_b/-0.18U_b$ at $X^*=9.81$ and $X^*=1.64$ of the first passage, respectively. They attain the values of $+0.15U_b/-0.16U_b$ and $+0.16U_b/-0.20U_b$ at $X^*=1.64$ and $X^*=9.81$ of the second passage, respectively.

Surface Heat Transfer and Fluid Flow. The upper part of Fig. 9 shows the region averaged Nusselt number ratio distributions reported by Johnson et al. [22] in their thermocouple measurements of surface heat transfer in a three-pass rotating square channel roughened with staggered 45 deg semi-circular ribs at $\mathrm{Ro}=0.12$. The heat transfer coefficient distributions in the first and second passages show different dependences on rotation, primarily due to the reversal of the Coriolis forces acting on the moving fluid in radially outward and inward rotating flow. It is well worth relating the present flowfield results to their heat transfer results. The X and Y mean velocity components ($U/U_b, V/U_b$) and turbulent kinetic energy K/U_b^2 at 1.5 mm away from the leading and trailing wall measured in the present study ($\mathrm{Ro}=0.15$) are respectively depicted in the middle and lower parts of Fig. 9. The present fluid flow results further reveal that the distributions of K/U_b^2 (Fig. 9, lower part) are approximately correlated with those of $\mathrm{Nu_{rg}/Nu_0}$ (Fig. 9, upper part) within measurement uncertainties. In other words, turbulence enhances the heat transfer, as expected. The magnitude and direction of the mean transverse velocity component V are also essential to the heat transfer enhancement on the leading and trailing wall. In the middle part of Fig. 9 the positive values of $-V/U_b$ and V/U_b near the leading and trailing wall, respectively, denote the downwash (or impingement) effect on the heat transfer surface whereas the negative values indicate the upwash effect, as a result of the secondary flow induced by the Coriolis force, 45 deg angled ribs, and geometric turn (for flow inside the turn and in the second passage). Near the first-pass (region indices: −3, −2, −1) leading wall and the second-pass trailing wall (region indices: 1, 2, 3), the upwash effect of the secondary flow lowers the heat transfer enhancement on the corresponding walls. In contrast, the downwash effect of the secondary flow increases the heat transfer enhancement on the first-pass trailing wall and second-pass leading wall. Thus, the shapes of K/U_b^2 curves once modulated by the downwash and upwash effects of the secondary flow tend to correlate very well with those of the $\mathrm{Nu_{rg}/Nu_0}$ curves. As for the convective effect denoted by U/U_b, Fig. 9 shows it uniformly contributes to the heat transfer enhancement on both the leading and trailing wall.

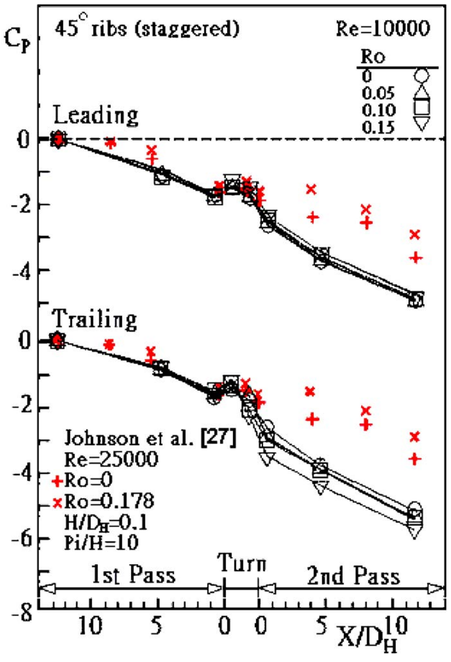

Fig. 10 Variation of dimensionless wall pressure with X/D_H at various rotation numbers (+ and ×: measured along the outer and inner side walls of the up and down passes, respectively)

Local Pressure Coefficient and Average Friction Factor. Measurements of streamwise wall pressure distributions along the leading and trailing wall were performed since knowledge of the coolant passage pressure loss will help in designing an efficient rotating cooling system. In addition, the data of local pressure distributions along rotating two-pass coolant ducts is scarce in open literature to date. The results are plotted in Fig. 10. It is seen that the trend is similar to the familiar pressure distribution along the "outer" wall of a stationary curved smooth passage because the locations of the two pressure taps inside the turn are closer to the "outer" wall (Fig. 1) [9,26]. The pressure loss results measured by Johnson et al. [26] in a rotating square passage ribbed by staggered 45° semi-circular ribs are also included in Fig. 10 for comparison. Their data (cross in Fig. 10) show a pressure loss smaller than the present case since their pressure taps were respectively arranged on the smooth outer and inner side wall of the first

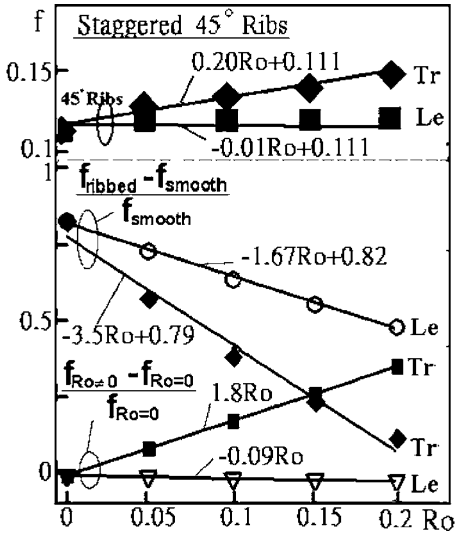

Fig. 11 Friction factor versus rotation number (Re=10,000, Tr=trailing, Le=leading)

and second passage. Moreover, since the side wall is perpendicular to the Coriolis force, their data [27] indicate a different response to the rotation rate.

Figure 11 depicts the rotation number dependence of average friction factor f in the staggered 45 deg ribbed passage flow. The maximum deviations of the measured data from the f correlations are 5.5%. The results show an increase of f (positive slop) with increasing Ro on the trailing wall but a slight decrease (negative slop) of f with increasing Ro on the leading wall, respectively. The above trend on the trailing wall is because of the decrease of C_p with increasing Ro on the trailing wall of the second inward duct (Fig. 10). In contrast, the decrease of f with increasing Ro on the leading wall is due to the increase of C_p with increasing Ro on the leading wall of second inward duct toward which the Coriolis force is directed (Fig. 10).

It is interesting to examine the respective effect of ribs and passage rotation on f, as depicted in Fig. 11. It turns out that with ribs and passage rotation the passage f on the leading/trailing walls increase 49%/12% of f_{smooth} and −2%/36% of $f_{\text{Ro}=0}$, respectively, at Ro=0.2. The maximum deviations of the measured data from the $f_{\text{ribbed}}-f_{\text{smoothed}}/f_{\text{smoothed}}$ correlations on the leading/trailing walls are 2.1%/4.8%. One more aspect worthy of attention is that a replacement of in-line 45 deg ribs [9] with staggered 45 deg angled ribs diminishes the friction losses to about 88%±1% of the in-line 45 deg ribbed case under the same operating conditions (Ro=0 to 0.2). The reason is that the staggered 45 deg angled ribs have blockage ratio only half of that generated by the in-line 45 deg angled ribs and, in turn, less resistance to the main stream.

Comparisons Between Staggered and In-Line 45 deg Rib Arrangements. One of the major differences in the flow fields between the staggered and in-line 45 deg angled rib arrangements is shown in Fig. 12 in terms of the transverse mean velocity distribution along the passage centerline. For the case of in-line 45 deg ribs (Fig. 12(*a*)), it is observed that the transverse mean velocities are all positive (towards the trailing wall) in the first passage and negative (towards the leading wall) in the second passage. That is, the fluid flow faithfully responds to the Coriolis force. Nevertheless, when one replaces the 45 deg angled ribs from the in-line arrangement to the staggered one [Fig. 12(*b*)], the alternate positive and negative V/U_b indicate that the geometric stagger leads to a wavy flow pattern in the radially outward and inward passages.

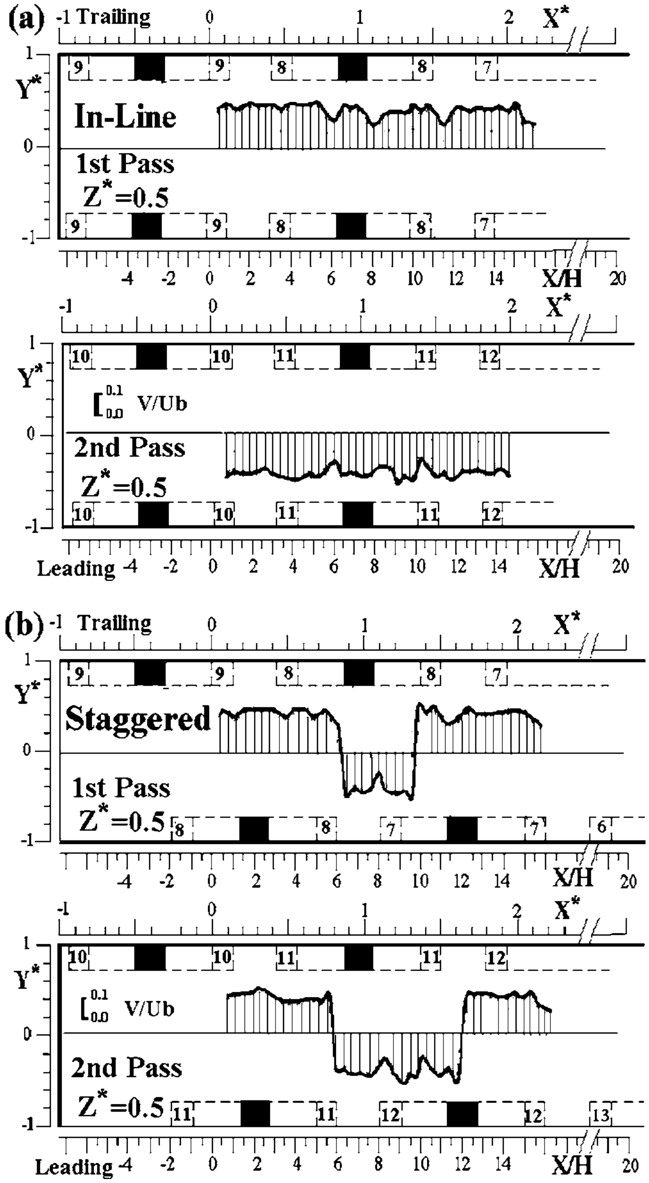

Fig. 12 Distribution of centerline transverse mean velocity near the 180 deg turn for the cases (*a*) in-line 45 deg ribs and (*b*) staggered 45 deg ribs at Ro=0.15

Table 2 shows comparisons of passage-averaged ratios of Nusselt number, convective mean velocity, impingement mean velocity, and turbulent kinetic energy between the in-line and staggered 45 deg angled rib arrangements for Ro=0.15. In general, the magnitudes of these flow dynamic data provide the rationale for the superiority of heat transfer enhancement of the staggered case over that of the in-line one on the first-passage leading and trailing walls and on the second-passage leading wall; similarly for the inferiority of heat transfer enhancement of the staggered case on the second-passage trailing wall. It is worth pointing out from Table 2 that the downwash effect plays a major role in the superior heat transfer augmentation attained by the staggered 45 deg ribs on the first-passage trailing wall and second-passage leading wall. Table 2 also indicates the reduction of the average friction factor f to 88% and 89% on the leading and trailing walls, respectively, when the in-line 45 deg angled ribs [9] are replaced by the staggered 45 deg angled ribs.

Table 2 Comparisons of passage averaged $\mathrm{Nu}_{rg}/\mathrm{Nu}_0$, $|U|/U_b$, downwash ($-V/U_b$ or V/U_b), and K/U_b^2 between in-line and staggered 45□rib arrangements for Ro=0.15.

	1st Pass				2nd Pass			
	Leading		Trailing		Leading		Trailing	
	In-Line	Staggered	In-Line	Staggered	In-Line	Staggered	In-Line	Staggered
$\mathrm{Nu}_{rg}/\mathrm{Nu}_0$	2.02	3.65	2.99	3.13	2.84	3.27	2.36	2.18
$\lvert U\rvert/U_b$	0.44	0.54	0.59	0.59	0.59	0.59	0.62	0.57
Downwash	⋯	⋯	0.26	0.34	0.14	0.20	⋯	⋯
K/U_b^2	0.06	0.11	0.12	0.14	0.13	0.14	0.10	0.10

	Leading		Trailing	
	In-Line	Staggered	In-Line	Staggered
f	0.1235	0.1095	0.1610	0.1410

Concluding Remarks

1. The streamwise distributions of region averaged Nussult number ratio on the leading and trailing wall roughened with staggered 45 deg ribs reported previously by other researchers can be reasonably illustrated by the corresponding distributions of region-averaged convective mean velocity, magnitude and direction of the transverse mean velocity, and turbulent kinetic energy obtained in the present study.
2. Similarly, the superiority of heat transfer augmentation of the staggered 45 deg ribs over that of in-line 45 deg ribs can be explained by comparing the corresponding values of the aforementioned flow dynamic parameters.
3. The measured evolution of main flow indicates the absence of a periodic fully developed flow condition in the rotating ribbed (45 deg, staggered) two-pass square duct of 12.8 hydraulic diameters in length investigated in the present study. This finding is opposite to the results previously reported from the stationary ribbed (45 and 90 deg, staggered) passage flows.
4. For Ro=0.2 the cross-stream secondary flow patterns in the radially outward passage are featured by two counter-rotating vortices. Their sizes are generally not equal but gradually approach the same as the flow progresses from the front to rear portion of the passage. Inside the turn the secondary flow patterns consist of a large and a squeezed vortex. Immediately after the turn in the radially inward passage, the secondary flow patterns are simply the mirror images of the corresponding secondary flow patterns in the radially outward passage except the reverse of rotating directions.
5. Simple expressions are developed to linearly correlate the friction factor with rotation number for engineering reference. A replacement of in-line 45 deg angled ribs with staggered ones diminishes the friction losses to about 88%±1% of the in-line one under the range of Ro examined.
6. It is found that the staggered 45 deg ribs and the passage rotation respectively contribute to 49%/12% of f_{smooth} and −2%/36% of $f_{\mathrm{Ro}=0}$ friction increases on the leading/trailing wall of the two-pass internal coolant passage at Ro=0.2.

Acknowledgment

Support for this work was partially provided by the National Science Council of the Republic of China under Contract No. NSC 92-2212-E-007-047.

Nomenclature

A = half width of duct, m
B = half height of duct, m
C_p = pressure coefficient, $(P-P_0)/0.5\rho U_b^2$
D_H = hydraulic diameter, $4AB/(A+B)$, m
f = friction factor, $(\Delta P/\Delta X)\cdot D_H/(\rho U_b^2/2)$
h = heat transfer coefficient, $\mathrm{Wm}^{-2}\,\mathrm{K}^{-1}$
H = rib height, m
k = turbulent kinetic energy, $(\overline{u^2}+\overline{v^2})/2$, $\mathrm{m}^2\,\mathrm{s}^{-2}$
k_a = thermal conductivity of air, $\mathrm{Wm}^{-1}\,\mathrm{K}^{-1}$
Nu = local Nusselt number, $h\cdot D_H/k_a$
Nu_0 = Nusselt number in fully developed tube flow, $0.023\cdot\mathrm{Re}^{0.8}\cdot\mathrm{Pr}^{0.4}$
$\mathrm{Nu}_{\mathrm{rg}}$ = regional averaged Nu
P = wall static pressure, Nm^{-2}
P_0 = pressure at $X/H=88$ in first pass, Nm^{-2}
Pi = rib pitch, m
Pr = Prandtl number of air, ν/α
R = radii of rib's rounds and fillets, m
Re = Reynolds number, U_bD_H/ν
Ro = rotation number, $\omega D_H/U_b$
U = streamwise mean velocity, ms^{-1}
U_b = duct bulk mean velocity, ms^{-1}
u = streamwise velocity fluctuation, ms^{-1}
u' = rms value of streamwise velocity fluctuation, $\sqrt{\overline{u^2}}$, ms^{-1}
V = transverse mean velocity, ms^{-1}
v = transverse velocity fluctuation, ms^{-1}
v' = rms value of transverse velocity fluctuation, $\sqrt{\overline{v^2}}$, ms^{-1}
W = rib width, m
W_d = divider thickness, m
X = streamwise coordinate, Fig. 1, m
X^* = normalized streamwise coordinate, X/D_H
X_N = streamwise coordinate in a pitch, Fig. 9, m
Y = transverse coordinate, Fig. 1, m
Y^* = normalized transverse coordinate, Y/B
Y_N = transverse coordinate in a pitch, Fig. 9, m
Z = spanwise coordinate, Fig. 1, m
Z^*, Z^{**} = normalized spanwise coordinate, (i) $X<0$, $Z^{**}=Z/(2A+W_d/2)$ (in the turn) (ii) X□0, $Z<0$, $Z^*=(Z+W_d/2)/2A$ (in the first pass) (iii) X□0, $Z>0$, $Z^*=(Z-W_d/2)/2A$ (in the second pass)

Greek Symbols

θ = coolant passage orientation, Fig. 1, deg
ρ = air density, $\mathrm{kg/m}^3$
ν = kinematic viscosity of air, m^2/s

α = thermal diffusivity of air, m^2/s
Ω = vorticity, s^{-1}
ω = rotating speed, rad s^{-1}

Subscripts

b = bulk
max = maximum value
x = streamwise component

References

[1] Iacovides, H., Jackson, D. C., Kelemenis, G., Launder, B. E., and Yuan, Y. M., 1996, "LDA Study of the Flow Development Through an Orthogonally Rotating U-Bend of Strong Curvature and Rib Roughened Walls," Eng. Turbulence Model Exp., **3**, pp. 561–570.
[2] Iacovides, H., Jackson, D. C., Ji, H., Kelemenis, G., Launder, B. E., and Nikas, K., 1998, "LDA Study of the Flow Development Through an Orthogonally Rotating U-Bend of Strong Curvature and Rib Roughened Walls," ASME J. Turbomach., **120**, pp. 386–391.
[3] Iacovides, H., Jackson, D. C., Launder, B. E., and Yuan, Y. M., 1999, "An Experimental Study of a Rib-Roughened Rotating U-Bend Flow," Exp. Therm. Fluid Sci., **19**, pp. 151–159.
[4] Hsieh, S. S., Chiang, M. H., and Chen, P. J., 1997, "Velocity Measurements and Local Heat Transfer in a Rotating Ribbed Two-Pass Square Channel With Uneven Wall Heat Flux," ASME Paper No. 97-GT-160.
[5] Tse, G. N., and Steuber, G. D., 1997, "Flow in a Rotating Square Serpentine Coolant Passage With Skewed Trips," ASME Paper No. 97-GT-529.
[6] Liou, T. M., Chen, M. Y., and Tsai, M. H., 2002, "Fluid Flow and Heat Transfer in a Rotating Two-Pass Square Duct With In-Line 90-deg Ribs," ASME Paper No. 2001-GT-0185, ASME J. Turbomach., **124**, pp. 260–268.
[7] Liou, T. M., Chen, M. Y., and Chang, K. H., 2003, "Spectrum Analysis of Fluid Flow in a Rotating Two-Pass Duct With Detached 90° Ribs," J. Exp. Thermal Fluid Sci., **27**(3), pp. 313–321.
[8] Liou, T. M., Chen, M. Y., and Wang, Y. M., 2003, "Heat Transfer, Fluid Flow, and Pressure Measurements Inside a Rotating Two-Pass Duct With Detached 90 Deg Ribs," ASME J. Turbomach., **125**(3), pp. 565–574.
[9] Liou, T. M., and Dai, G. Y., 2003, "Pressure and Flow Characteristics in a Rotating Two-Pass Duct With 45° Angled Ribs," ASME Paper No. 2003-GT-38346.
[10] Schabacker, J., Bolcs, A., and Johnson, B. V., 1999, "PIV Investigation of the Flow Characteristics in an Internal Coolant Passage With 45° Rib Arrangement," ASME Paper No. 99-GT-120.
[11] Chanteloup, D., Juaneda, Y., and Bolcs, A., 2002, "Combined 3D Flow and Heat Transfer Measurements in a Two-Pass Internal Coolant Passage of Gas Turbine Airfoil," ASME Paper No. GT-2002–30214.
[12] Servouze, Y., and Sturgis, J. C., 2003, "Heat Transfer and Flowfield Measurements in a Rib-Roughened Branch of a Rotating Two-Pass Duct," ASME Paper No. GT2003-38048.
[13] Prakash, C., and Zerkle, R., 1995, "Prediction of Turbulent Flow and Heat Transfer in a Ribbed Rectangular Duct With and Without Rotation," ASME J. Turbomach., **177**, pp. 255–264.
[14] Iacovides, H., and Raisee, M., 1999, "Recent Progress in the Computation of Flow and Heat Transfer in Internal Cooling Passages of Turbine Blades," Int. J. Heat Fluid Flow, **20**, pp. 320–328.
[15] Jang, Y. J., Chen, H. C., and Han, J. C., 2000, "Flow and Heat Transfer in a Rotating Square Channel With 45° Angled Ribs by Reynolds Stress Turbulence Model," ASME Paper 2000-GT-0229.
[16] Tafti, D. K., 2003, "Large-Eddy Simulations of Heat Transfer in a Ribbed Channel for Internal Cooling of Turbine Blades," ASME Paper No. GT-2003–38122.
[17] Saha, A. K., and Acharya, Sumanta, 2003, "Flow and Heat Transfer in an Internally Ribbed Duct With Rotation: An Assessment of LES and URANS," ASME Paper No. GT-2003-38619.
[18] Taslim, M. E., Rahman, A., and Spring, S. D., 1991, "An Experimental Investigation of Heat Transfer Coefficients in a Spanwise Rotating Channel With Two Opposite Rib-Roughened Walls," ASME J. Turbomach., **113**, pp. 75–82.
[19] Taslim, M. E., Bondi, L. A., and Kercher, D. M., 1991, "An Experimental Investigation of Heat Transfer in an Orthogonally Rotating Channel Roughened With 45° Criss-Cross Ribs on Two Opposite Walls," ASME J. Turbomach., **113**, pp. 346–353.
[20] Wagner, J. H., Johnson, B. V., Graziani, R. A., and Yeh, F. C., 1992, "Heat Transfer in Rotating Serpentine Passages With Trips Normal to the Flow," ASME J. Turbomach., **114**, pp. 847–857.
[21] Parsons, J. A., Han, J. C., and Zhang, Y. M., 1994, "Wall Heating Effect on Local Heat Transfer in a Rotating Two-Pass Square Channel With 90° Rib Turbulators," Int. J. Heat Mass Transfer, **37**(9), pp. 1411–1420.
[22] Johnson, B. V., Wagner, J. H., Steuber, G. D., and Yeh, F. C., 1994, "Heat Transfer in Rotating Serpentine Passage With Trips Skewed to the Flow," ASME J. Turbomach., **116**, pp. 113–123.
[23] Fann, S., Yang, W. J., and Zhang, N., 1994, "Local Heat Transfer in a Rotating Serpentine Passage With Rib-Roughened Surfaces," Int. J. Heat Mass Transfer, **37**(2), pp. 217–228.
[24] Azad, G. S., Uddin, M. J., and Han, J. C., 2001, "Heat Transfer in a Two-Pass Rectangular Channel With 45° Angled Rib Turbulators," ASME Paper No. 2001-GT-186.
[25] Bonhoff, B., Schabacker, J., Parneix, S., Leusch, J., Johnson, B. V., and Bolcs, A., 1999, "Experimental and Numerical Study of Developed Flow and Heat Transfer in Coolant Channels With 45° and 90° Ribs," ASME Paper No. 99-GT-123.
[26] Liou, T. M., Chen, C. C., and Chen, M. Y., 2003, "Rotating Effect on Fluid Flow in Two Smooth Ducts Connected by a 180-Degree Bend," ASME Paper 2000-GT-228, ASME J. Fluids Eng., **125**, pp. 327–335.
[27] Johnson, B. V., Wagner, J. H., and Steuber, G. D., 1991, "Effects of Rotation on Coolant Passage Heat Transfer—Vol. II Coolant Passages With Trips Normal and Skewed to the Flow," NASA Contract Report 4396, pp. 103–108.

Effects of Surface-Roughness Geometry on Separation-Bubble Transition

Stephen K. Roberts
e-mail: skrobert@connect.carleton.ca

Metin I. Yaras
e-mail: metin-yaras@carleton.ca

Department of Mechanical
and Aerospace Engineering,
Carleton University,
Ottawa K1S 5B6, Canada

This paper presents measurements of separation-bubble transition over a range of surfaces with randomly distributed roughness elements. The tested roughness patterns represent the typical range of roughness conditions encountered on in-service turbine blades. Through these measurements, the effects of size and spacing of the roughness elements, and the tendency of the roughness pattern toward protrusions or depressions (skewness), on the inception location and rate of transition are evaluated. Increased roughness height, increased spacing of the roughness elements, and a tendency of the roughness pattern toward depressions (negative skewness) are observed to promote earlier transition inception. The observed effects of roughness spacing and skewness are found to be small in comparison to that of the roughness height. Variation in the dominant mode of instability in the separated shear layer is achieved through adjustment of the streamwise pressure distribution. The results provide examples for the extent of interaction between viscous and inviscid stability mechanisms. [DOI: 10.1115/1.2101852]

Introduction

Surface imperfections on in-service gas-turbine blade rows can have a significant effect on the blade-passage flow (e.g., Leipold et al.; Bons and McClain [1,2]). The main causes of roughness on turbine blades are hydrocarbon deposits and erosion due to impact with small particles. The level of surface roughness on a gas-turbine blade, which can vary in height from 2 to 160 μm (Bons et al., Taylor [3,4]), depends on the location of the blade within the engine, and the length of time it has been in service. The distribution of roughness over the blade surface is typically nonuniform, with significant variations in both the streamwise and spanwise directions (e.g., Bons et al.; Taylor [3,4]).

For example, the roughness level at the leading edge of a high-pressure-turbine stator blade (Fig. 1(*a*)) is noted to be of larger scale than that observed near the suction peak of a low-pressure turbine rotor blade (Fig. 1(*b*)) from the same engine. Closer proximity to the combustor and more rapid accumulation of roughness in stagnation regions are responsible for the rougher surface conditions noted near the leading edge of the stator blade.

Modification of the blade-surface boundary layer by surface roughness has been shown to reduce turbine aerodynamic efficiency (e.g., Kind et al.; Boynton et al.; Suder et al. [5–7]), and increase the surface heat-transfer rate (e.g., Bons and McClain; Blair, Pinson, and Wang; Wang and Rice [2,8–10]). Blade-surface heat transfer rates may also be affected by changes in the surface material properties when the roughness is due to hydrocarbon deposits, or when a protective coating is eroded.

Understanding the effects of surface roughness is essential for predicting in-service aerodynamic performance, and thus optimizing blade designs for maximum operational efficiency and life. One means by which surface roughness may affect the flow field is through its influence on the transition of the blade-surface boundary layer from a laminar to a turbulent state. Sufficiently large surface roughness is known to "trip" the laminar boundary layer, after which a very rapid transition process takes place (e.g., Gibbings et al. [11–13], Klebanoff and Tidstrom [14]). If the roughness level is insufficient to trigger immediate transition inception, as is often the case with low-pressure turbine blades, the location of transition inception in an attached boundary layer moves progressively upstream with increases in surface roughness (e.g., Pinson and Wang; Gibbings and Al Shukri; Kerho and Bragg [9,15,16]). Similar trends have also recently been observed in separation-bubble transition (Roberts and Yaras; Volino and Bohl [17,18]).

For a given surface roughness height, the geometry of the roughness pattern may have a significant effect on how the boundary-layer development is affected by the surface conditions. It was suggested by Morris [19] that the effect of roughness on the boundary layer occurs primarily through vorticity and turbulence shed in the wakes of roughness elements. The influence of this wake turbulence on the surrounding flow, and the extent by which neighboring wakes interact, are affected by the shape, size, and spacing of the roughness elements. The effects of these features of roughness patterns on turbulent boundary layers have been studied extensively for both deterministic (e.g., Waigh and Kind; Dirling Dvorak [20–22]), and random (e.g., Bons; Belnap et al.; Sigal and Danberg [23–25]) roughness. The recent experiments of Stripf et al. [26] over deterministically rough surfaces suggest the roughness geometry to be less influential in transitional flows than in fully turbulent boundary layers. Nonetheless, movement of the location of transition inception with variations in roughness spacing is evident in their experimental data, with the effect of spacing becoming less pronounced at the highest Reynolds numbers and turbulence levels tested. In a recent study on the effects of stochastic roughness on separation-bubble transition conducted by the present authors [17], transition inception generally occurred further upstream with increased roughness height. However, a reversal of this trend was observed for two of the surfaces included in the study, which was attributed to differences in the spacing of the roughness elements.

The above-noted effects of surface roughness on the location of transition inception in separation bubbles must occur through modification of the mechanism causing instability. In small separation bubbles, where the shear layer is located relatively close to the surface, a significant effect of wall damping on the shear layer remains. In these instances, transition inception is preceded by the growth of Tollmien-Schlichting (T-S) instability waves (e.g., Roberts and Yaras; Volino and Bohl; Volino [17,18,27]), which may break down and form turbulent spots characteristic of natural tran-

---

Contributed by the International Gas Turbine Institute (IGTI) of ASME for publication in the Journal of Turbomachinery. Manuscript received October 1, 2004; final manuscript received February 1, 2005. IGTI Review Chair: K. C. Hall. Paper presented at the ASME Turbo Expo 2005: Land, Sea, and Air, Reno, NV, June 6–9, 2005, Paper No. GT2005-68664.

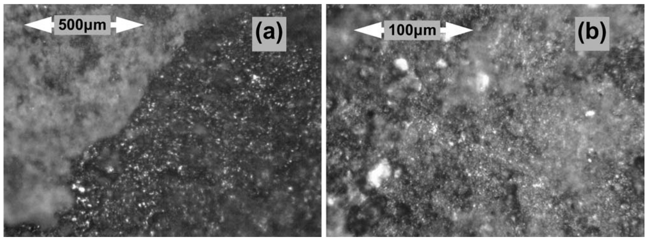

Fig. 1 Surface roughness at the leading edge of a HP turbine nozzle (*a*), and near the suction peak of a LP turbine blade (*b*). Note: magnification is higher in (*b*).

sition in attached boundary layers. The Λ vortices normally associated with natural attached-flow transition have also been observed in separated shear layers (Bao and Dallmann [28]). As the separated shear layer moves away from the surface, the damping of the wall becomes less pronounced, and the flow begins to more closely resemble a free shear layer, in which the inviscid Kelvin-Helmholtz (K-H) instability mechanism is expected to dominate (e.g., Malkiel and Mayle; Watmuff; Yang and Voke; Spalart and Strelets [29–32]). Computational studies of separated boundary layers have shown that the distance of the shear layer from the surface, the thickness of the shear layer, and the flow Reynolds number are all factors affecting the dominant instability mode (e.g., Rist and Maucher; Chandrasekhar [33,34]).

Published studies on boundary-layer transition do not provide information from which the effects of roughness geometry on the transition process in separation bubbles may be derived for the stochastically rough surfaces typical of turbomachinery blades. In the present paper, the location of inception and rate of transition are documented for seven surfaces with different roughness geometries. The study encompasses ranges of roughness height of 0.7 to 185 μm, skewness of -0.6 to $+0.4$, and spacing of 490 to 2720 μm. Results are presented for three flow Reynolds numbers and two streamwise pressure distributions representative of the suction-side pressure distribution of low-pressure turbines. In addition to shedding light on the effects of roughness geometry in separation-bubble transition, the study allows further evaluation of a model recently proposed by the authors [35] for predicting transition inception in separation bubbles.

Experimental Setup

The experiments are performed in a closed-circuit wind tunnel on a flat test surface upon which streamwise pressure gradients are imposed using a contoured wall forming the ceiling of the test section (Fig. 2). The boundary layer developing over the 1220 mm long test surface is measured using a hot-wire anemometer with a single tungsten sensor of 5 μm diameter and 1.3 mm length. The probe is traversed at multiple streamwise positions along the centerline of the test plate, spaced 25 mm apart in the transition zone and 50 mm elsewhere. The number of measurement locations in each boundary layer traverse varies between 25 near the test plate leading edge and 80 in the fully turbulent boundary layer. Additionally, streamwise traverses are performed in 2.0 mm increments, at a distance of 1.25 mm from the test surface, providing streamwise intermittency distributions and growth rates of instabilities with high resolution.

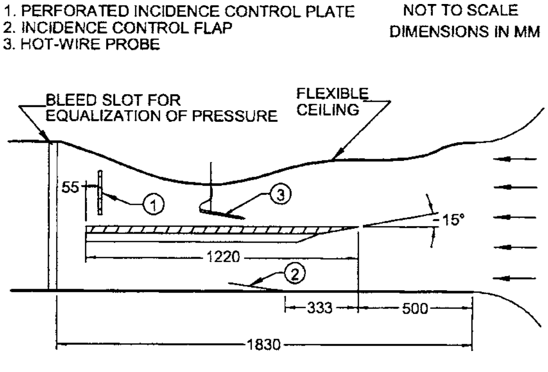

Fig. 2 Schematic of the wind tunnel test section

Table 1 Measured surface roughness parameters

Surface	k_{rms} (μm) ±7%	R_z (μm) ±7%	R_t (μm) ±7%	W (μm) ±7%	S_{sk} ±0.1
Smooth	0.7[a]	⋯	⋯	⋯	⋯
Blue laminate	31	164	184	2720	+0.4
White laminate	33	151	166	2270	−0.1
Vinyl	48	173	194	3500	+0.2
Tar paper	53	306	340	490	+0.4
Fine shingle	107	1140	1350	540	+0.0
Coarse shingle	185	1150	1320	1610	−0.6

[a] Roughness height specified by the manufacturer

The analog output of the hot-wire anemometer is sampled at 8 kHz over 20 measurement cycles, with each containing 8192 samples. The signal is low-pass filtered with a cutoff frequency of 3.8 kHz prior to digitization.

Test Surfaces. The smoothest surface ($k_{\mathrm{rms}}=0.7$ μm) of the present study is a 25 mm thick CHART-MIC-6 aluminum plate with an elliptic leading edge of 15.9 mm and 3.2 mm axis dimensions located at the tip of the 15 deg knife-edge shown in Fig. 2. The remaining test plates were constructed by bonding materials of desired roughness patterns onto a 25.4 mm thick medium density fiber (MDF) board. These roughness layers consist of two countertop laminates ($k_{\mathrm{rms}}=31$ μm, $k_{\mathrm{rms}}=33$ μm), vinyl floor material ($k_{\mathrm{rms}}=48$ μm), tar paper ($k_{\mathrm{rms}}=53$ μm), fine asphalt shingle ($k_{\mathrm{rms}}=107$ μm), and coarse asphalt shingle ($k_{\mathrm{rms}}=185$ μm) surfaces. The leading edge of these rough-surface test plates consists of a 50.8 mm long aluminum section with a smooth surface, mounted onto the test plates such that its top surface is aligned with the peaks of the roughness elements. This leading edge attachment is also machined to a 15 deg knife edge, and its tip is elliptic with the same axis dimensions as the smooth plate.

The roughness geometries were measured through 3D laser triangulation scans. The statistical roughness parameters deemed to have the strongest influence on the flow are summarized in Table 1. The height of the roughness elements is quantified by the root-mean-square (rms) of the roughness height distribution, computed as

$$k_{\mathrm{rms}} = \sqrt{\frac{1}{N}\sum_{i=1}^{N}(y_i-\mu)^2} \tag{1}$$

where μ is the mean surface elevation and N is the number of samples included in the surface scan. The roughness height is also often quantified by its maximum range ($R_t=y_{\max}-y_{\min}$), or by the average range of the ten (typically) highest peaks and deepest depressions (R_z). For reference, these quantities are also included in Table 1. However, the authors prefer to use k_{rms} to describe the average height of roughness elements, since the values of R_z and R_t are sensitive to the size of the sample from which they are computed.

The average spacing of roughness elements is quantified by

$$W = \frac{2N\Delta x}{n} \tag{2}$$

where Δx is the scanning resolution, and n is the number of times

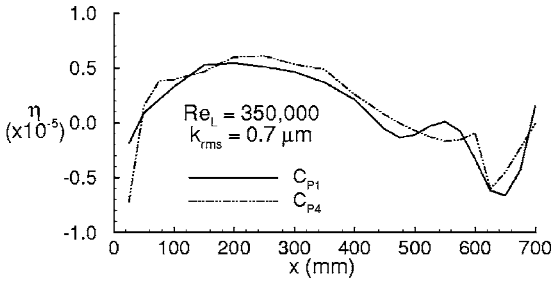

Fig. 3 Streamwise distribution of the acceleration parameter

the roughness distribution crosses the mean surface elevation.

The effects of protrusions and depressions on the boundary layer development are expected to be different. The tendency of the roughness pattern toward protrusions or depressions is identified by the skewness of the roughness height distribution

$$S_{\mathrm{sk}} = \frac{1}{k_{\mathrm{rms}}^3 N} \sum_{i=1}^{N} (y_i - \mu)^3 \tag{3}$$

For positive values of S_{sk}, the peaks of the roughness elements are on average located further from the mean elevation compared to the depths of the indentations, and negative values indicate the inverse.

The kurtosis of the roughness height distribution (Ku) is also frequently documented in roughness studies. This parameter is a measure of the agreement between the roughness height distribution and a Gaussian distribution. Values of $\mathrm{Ku} > 3$ indicate a greater than normal number of peaks and valleys, and $\mathrm{Ku} < 3$ indicates the inverse. With the exception of the fine shingle surface ($\mathrm{Ku} = 5.1$), the values of Ku for the surfaces were all similar ($2.8 < \mathrm{Ku} < 3.3$). Since no noteworthy trends with Ku could be observed in the current data, these values are not included in Table 1.

The chosen range of roughness conditions is consistent with the roughness patterns typically observed on turbine blades of in-service gas turbine engines. This is based on comparison of the values of k_{rms} documented by Bons et al. ranging between 2.4 and 8.8 μm for the midspan/midchord region of turbine blades. Assuming typical chord lengths for low-pressure turbines between 3 and 15 cm, the maximum range of k_{rms}/c implied by the measurements of Bons et al. is between 15×10^{-6} and 300×10^{-6}. This compares reasonably well to the present values of k_{rms}/L ranging from 25×10^{-6} to 150×10^{-6} (excluding the smooth surface). The corresponding range of skewness measured by Bons et al. is $-0.11 < S_{\mathrm{sk}} < +0.72$, and the range of spacing is estimated from their data to be $40 < W/k_{\mathrm{rms}} < 150$. These also compare reasonably well with the ranges of the present study of $-0.6 < S_{\mathrm{sk}} < +0.4$, and $9 < W/k_{\mathrm{rms}} < 90$.

Test Conditions. Streamwise distributions of the free-stream acceleration parameter $[\eta = (\nu/U_e^2) dU_e/dx]$ are shown in Fig. 3. These results are for the smooth-surface test cases at $\mathrm{Re}_L = 350{,}000$, and are similar for the remainder of the test cases. All of the surfaces were tested with the C_{P1} pressure distribution. This pressure distribution has been used in earlier experimental studies by the authors, upon which the development of a transition model was based [35]. The distribution designated as C_{P4} has an initial acceleration similar to the C_{P1} distribution, which is followed by a milder adverse pressure gradient. The milder adverse pressure gradient results in a smaller separation bubble, as seen in Fig. 4. Measurements with the C_{P4} pressure distribution were limited to the $k_{\mathrm{rms}} = 0.7$, 31, and 185 μm surfaces.

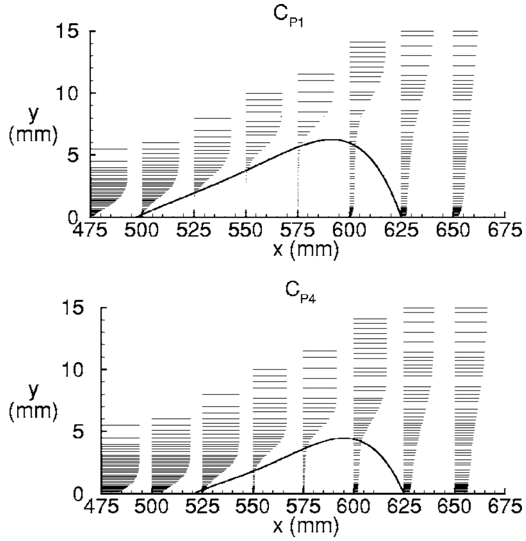

Fig. 4 Time-averaged streamwise velocity field—the separation-bubble contour is shown with the dividing streamline. $\mathrm{Re}_L = 35{,}000$, $k_{\mathrm{rms}} = 0.7$ μm

Measurements for all surfaces were performed for flow Reynolds numbers of 350,000 and 470,000, based on the plate length of $L = 1220$ mm, and reference velocities of about 4.5 and 6.0 m/s measured at $x = 25$ mm, $y = 25$ mm. For the $k_{\mathrm{rms}} = 0.7$ and 185 μm surfaces, measurements were also obtained at a flow Reynolds number of 145,000, for the C_{P4} pressure distribution. All of the experiments were conducted under low free-stream turbulence conditions, with the turbulence intensity at the leading edge of the test surface ranging between 0.5% and 0.7%.

Results and Discussion

Location of Transition Onset. For reference, the experimental results for the C_{P1} and C_{P4} pressure distributions are summarized in Tables 2 and 3, respectively. In each of the tables, the results are presented in order of increasing Reynolds number, followed by increasing roughness height. It is most effective to study these results in the context of a transition-inception correlation recently proposed by the authors on the basis of a subset of the present data, limited to the C_{P1} pressure distribution and fewer roughness patterns, and additional measurements performed at elevated levels of free-stream turbulence [35]

$$\mathrm{Re}_{s-ts} = \left(835 - 36TF - (1400 - 25e^{0.45TF})\frac{k_{\mathrm{rms}}}{\theta_s}\right)\mathrm{Re}_{\theta_s}^{0.7} \tag{4}$$

This formulation is more comprehensive than published alternatives (e.g., Mayle [36]) in that it accounts for the effects on transition onset of both surface roughness and free-stream turbulence, quantified by Taylor's [37] turbulence factor $[\mathrm{TF} = Tu_{\mathrm{ref}}(L/\lambda_s)^{0.2}]$, where TF is expressed in percent for use in Eq. (4).

Predictions based on Eq. (4) are compared to the experimental results in Fig. 5. The slightly smaller symbols filled in gray represent the data points previously used to develop Eq. (4). The extent of agreement between these data points and the predictions is similar to what is observed for the new data points shown by the larger hollow (C_{P4} pressure distribution) and black-colored (C_{P1} pressure distribution) symbols. With these new results, a slightly better fit to the experimental data is given by

$$\mathrm{Re}_{s-ts} = \left(785 - 30TF - (1400 - 25e^{0.45TF})\frac{k_{\mathrm{rms}}}{\theta_s}\right)\mathrm{Re}_{\theta_s}^{0.7} \tag{5}$$

This formulation remains consistent with previous measurements at elevated free-stream turbulence levels, not shown in Fig. 5.

The choice of roughness height to correlate the effect of surface roughness on the location of transition inception in Eq. (4) is supported by the strong sensitivity of Re_{s-ts} to k_{rms}, as is evident

Table 2 Separation-bubble flow and surface conditions-C_{P1} pressure distribution

Re_L ±5% $\times 10^3$	k_{rms} ±7% (μm)	k_{rms}/θ_s ±10% $\times 10^{-3}$	S_{sk} ±0.1	W/k_{rms} ±10%	x_s ±5 (mm)	$x_{ts}-x_s$ ±6 (mm)	η_s ±15% $\times 10^{-7}$	λ_{θ_s} ±15% $\times 10^{-2}$	Re_{θ_s} ±10	Re_{s-ts} ±3 $\times 10^3$	H_{ts} ±0.1	log(N) ±0.2	f_{MA} ±10% (Hz)	zf_{MA} [Eq. (10)]
350	0.7	1.4	⋯	⋯	498	69	−9.6	−6.4	258	36	8.7	0.14	200	204
350	31	62	+0.4	88	500	59	−22.5	−13.8	257	30	4.2	0.87	160	258
350	33	70	−0.1	69	500	55	−9.4	−7.0	273	32	5.3	0.72	180	341
350	48	110	+0.2	73	503	46	−28.7	−18.8	258	27	6.1	0.54	180	152
350	53	110	+0.4	9	495	66	−15.4	−10.2	257	35	5.6	0.51	170	192
350	107	206	0.0	5	505	40	−11.9	−9.9	286	22	5.6	0.51	200	239
350	185	347	−0.6	9	505	32	−16.7	−13.8	286	17	4.7	0.21	210	145
470	0.7	1.6	⋯	⋯	500	67	−8.2	−7.7	305	47	7.3	0.52	270	300
470	31	78	+0.4	88	507	48	−13.5	−13.4	316	38	5.8	0.95	410	355
470	33	76	−0.1	69	504	43	−11.3	−12.5	333	33	5.5	0.63	180	153
470	48	119	+0.2	73	505	43	−10.8	−10.5	310	33	5.6	0.72	215	187
470	53	98	+0.4	9	505	50	−11.3	−16.2	376	35	5.3	0.35	200	262
470	107	228	0.0	5	510	25	−9.1	−10.9	343	18	5.0	0.21	270	169
470	185	405	−0.6	9	510	11	−13.7	−15.8	338	8	4.2	−0.09	250	208

in Fig. 5. One can argue that the spacing and skewness of the roughness pattern should be included in such a correlation, for these roughness parameters are expected to influence the disturbances introduced into the boundary layer.

In the case of very close spacing of the roughness elements, the regions between the elements are unlikely to exchange significant mass and momentum with the exterior flow passing over the crests of the roughness elements. This situation of limited disturbance would also be present in the case of very large spacing owing to the relatively small number of roughness elements. Thus, there exists an element spacing between these two extremes for which the extent of disturbances experienced by the boundary layer is maximized.

Protrusions affect the local boundary layer flow by displacing the oncoming fluid and shedding vorticity. In the case of depressions, disturbance of the local flow field is dependent on mass and momentum exchange between the fluid inside the depressions and the exterior boundary layer flow. In either case, the extent of the disturbance is expected to depend on the sharpness of the roughness feature. For a given roughness height and spacing, a tendency towards sharper protrusions would bias the skewness of the roughness distribution towards larger positive values, whereas a tendency towards sharper depressions would yield a larger negative skewness value. The differences in the way the boundary layer flow is disturbed by protrusions and depressions, and the expected dependency of the disturbance magnitude on the sharpness of the roughness feature, justify the consideration of the skewness of the roughness pattern in the context of the transition process.

Two of the test surfaces with similar values of roughness height and skewness ($k_{rms}=48$ μm, $S_{sk}=+0.2$ versus $k_{rms}=53$ μm, $S_{sk}=+0.4$) provide an opportunity for establishing the effect of changing the roughness element spacing from $W/k_{rms}=73$ to $W/k_{rms}=9$ on the inception of transition in separation bubbles. Based on the $x_{ts}-x_s$ values tabulated in Table 2 for both flow Reynolds numbers tested, a slight upstream movement of the transition inception location with increased spacing of roughness elements is evident. This trend is also supported by comparison of the results for the surfaces with $k_{rms}=31$ μm ($W/k_{rms}=88, S_{sk}=+0.4$) and $k_{rms}=53$ μm ($W/k_{rms}=9, S_{sk}=+0.4$). In these two cases, the tendency of upstream movement of the transition inception location with increased roughness height appears to have been more than offset by the opposing effect of increased spacing of the roughness elements.

It is noted that the effect of varying the spacing of roughness elements over the $W/k_{rms}=9$ to 88 range results in considerably less movement of the transition onset location than that caused by varying k_{rms} from 0.7 to 185 μm. Since the ranges for W/k_{rms} and k_{rms}/θ_s represent typical conditions encountered on low-pressure gas turbine blades, absence of W/k_{rms} in the correlation of Eq. (5) is justified.

The surfaces with $k_{rms}=31$ and 33 μm have similar roughness spacing ($W/k_{rms}=88$ versus 69), while their skewness is of opposite sign ($S_{sk}+0.4$ versus −0.1). For both of the tested flow Reynolds numbers, the location of transition onset ($x_{ts}-x_s$) is slightly further upstream for the surface with negative skew. Again, this effect is secondary compared to the sensitivity of transition inception to the height of the roughness elements.

These results suggest that for the type of surface roughness typical of turbomachinery blades, the effect of roughness on transition inception in a separated shear layer is adequately quantified through k_{rms}/θ_s.

Rate of Transition. Streamwise distributions of boundary-layer intermittency were computed for the test cases with the C_{P1} pres-

Table 3 Separation-bubble flow and surface conditions-C_{P4} pressure distribution

Re_L ±5% $\times 10^3$	k_{rms} ±7% (μm)	k_{rms}/θ_s ±10% $\times 10^{-3}$	S_{sk} ±0.1	W/k_{rms} ±10%	x_s ±5 (mm)	$x_{ts}-x_s$ ±6 (mm)	η_s ±15% $\times 10^{-7}$	λ_{θ_s} ±15% $\times 10^{-2}$	Re_{θ_s} ±10	Re_{s-ts} ±3 $\times 10^3$	f_{MA} ±10% (Hz)	f_{MA} [Eq. (10)]
145	0.7	1.0	⋯	⋯	521	106	−36.8	−10.6	169	24	30	62
145	185	231	−0.6	9	533	61	−10.4	−4.0	196	15	30	57
350	0.7	1.4	⋯	⋯	525	62	−22.2	−20.6	309	38	200	120
350	31	62	+0.4	88	540	59	−15.2	−12.1	283	34	175	197
350	185	388	−0.6	9	528	39	−19.6	−14.6	271	22	200	197
470	0.7	1.8	⋯	⋯	520	51	−13.2	−14.4	329	43	320	340
470	31	67	+0.4	88	550	39	−12.4	−14.7	345	31	300	233

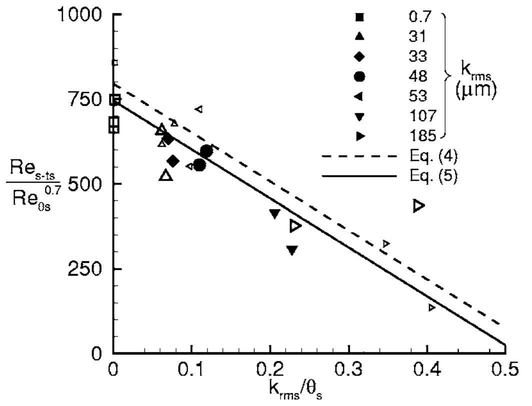

Fig. 5 Measured and predicted locations of transition inception

sure distribution using a conditional sampling algorithm [38]. In Fig. 6, these experimental values are compared to the predictions obtained through the following expression:

$$\gamma = 1 - e^{-n\int_{x_{ts}}^{x}\{\sigma/[\tan(\alpha)U]\}dx\int_{x_{ts}}^{x}\tan(\alpha)dx} \tag{6}$$

proposed by Solomon et al. [39] on the basis of Emmons' [40] original work. The integrals appearing in the exponent represent the streamwise and spanwise spreading rates of turbulent spots. The spanwise spreading angle, α, is estimated through a correlation proposed by Gostelow et al. [41]

$$\alpha = 4 + \frac{22.14}{0.79 + 2.72e^{47.63\lambda_\theta}} \tag{7}$$

while the parameter σ is obtained from a correlation proposed by D'Ovidio et al. [42]

$$\sigma = 0.024 + \frac{0.604}{1 + 5e^{66\lambda_\theta}} \tag{8}$$

The spot production rate, n, is obtained using the following expression recently proposed by the present authors [35]:

$$N = \frac{0.55H_{ts} - 2.2}{1 - 0.63H_{ts} + 0.14H_{ts}^2} \tag{9}$$

where $N = n\sigma\theta_{ts}^3/\nu$ is a nondimensional spot production parameter.

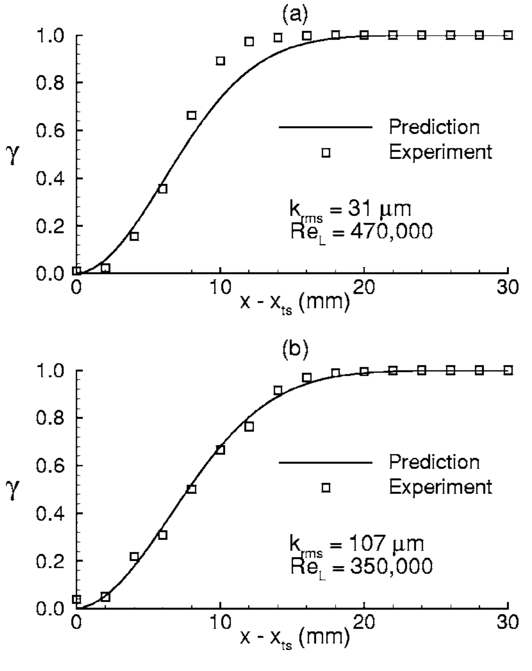

Fig. 6 Streamwise intermittency distributions for selected test cases

The good agreement between the measured and predicted intermittency distributions in Fig. 6 is representative of all the present test cases with the C_{P1} pressure distribution. The roughness elements can potentially alter the transition rate by affecting the production rate of turbulent spots at the transition inception location and/or the rate at which these spots spread as they are convected downstream. The present model predicts the rough surface cases with the same accuracy as the smooth surface case. This suggests that any effects of surface roughness on transition in the separated shear layer are already accounted for by the independent variables appearing in Eqs. (6)–(9). For example, in Eq. (9), the spot production parameter depends solely on the shape factor at transition inception, which implies that surface roughness affects the formation rate of turbulent spots by modifying the local velocity profile. This is an intuitive result as long as the instability mechanism leading to transition inception remains the same. For the present test cases, the region of the separated shear layer in which the transition process occurs is located well above the roughness peaks. Absence of a direct effect of roughness elements on the spreading rate of turbulent spots, as implied by Eqs. (7) and (8), is therefore not surprising.

Pretransitional Growth of Disturbances. Upstream movement of the transition inception location with increasing surface roughness may be the result of changes in the frequency, initial amplitude, and/or amplification rate of disturbances at the most unstable frequencies. Spectral analysis of the present experimental results was performed to establish the relative importance of these factors.

In Fig. 7, Fourier spectra of u'/U_{ref} are shown at various stages of development of the boundary layer for the $k_{rms}=0.7$ μm and $k_{rms}=107$ μm surfaces with the C_{P1} pressure distribution and $Re_L=350{,}000$. It is noted that the frequency at which the highest amplification rate of instability waves occurs (f_{MA}) does not vary significantly between the two surface conditions. This result applies to the remainder of the tested surfaces and flow conditions as well (Tables 2 and 3). In the majority of cases, the measured value of f_{MA} agrees closely with the prediction based on Walker's [43] correlation developed for the growth of Tollmien Schlichting (T-S) waves in attached-flow boundary-layer transition

$$f_{MA} = \frac{3.2U_e^2}{2\pi\nu Re_{\delta^*}^{3/2}} \tag{10}$$

shown by a dashed vertical line in Fig. 7.

The streamwise growth of the energy of disturbances at the measured value of f_{MA} is shown for several cases in Fig. 8 for $Re_L=350{,}000$. The trends in this figure were confirmed to be consistent with those for the remaining flow Reynolds numbers and surface roughness conditions. The power spectral density shown in this figure was determined by averaging the power spectrum of u'/U_{ref} within a frequency range of ±15% of f_{MA}. Measurements for some of the surfaces are omitted from the figure for clarity. From the trends in this figure, the rate of exponential growth shortly before transition onset is seen to be largely insensitive to the level of surface roughness. It is evident, however, that the initial magnitude of the disturbance at f_{MA} is notably larger for the rough surfaces than for the smooth surface. This result suggests that the larger initial amplitude of the disturbances at the frequency of maximum amplification rate is a significant factor in promoting earlier transition inception on rough surfaces.

In the cases with the C_{P1} pressure distribution, the intermittent turbulence activity observed in the hot-wire velocity traces in the transition zone (Fig. 9(*a*)) closely resembles the velocity traces previously observed by the authors in attached-flow transition. This, together with the presence of instability waves of dominant

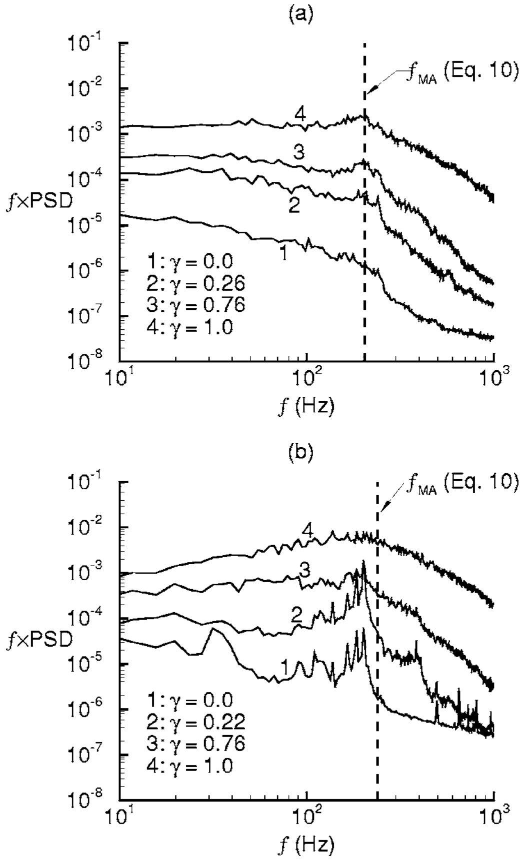

Fig. 7 Fourier power spectrum of u'/U_{ref} for Re_L=350,000, C_{P1} pressure distribution-(*a*) k_{rms}=0.7 μm; (*b*) k_{rms}=107 μm

frequency and growth rate patterns typical of Tollmien-Schlichting waves, suggests that the transition process in these test cases is driven by viscous instability. For the test cases with the C_{P4} pressure distribution, no structures resembling turbulent spots could be identified in the hot-wire velocity traces. Instead, the transition process was characterized by large-amplitude velocity fluctuations near f_{MA} just before transition (Fig. 9(*b*)), and the breakdown to full turbulence was sudden (Fig. 9(*c*)).

It is suggested that in these test cases viscous T-S instability is accompanied by the inviscid Kelvin-Helmholtz instability, and that the latter is responsible for the ultimate breakdown to turbulence. K-H instability is characterized by the formation, and often pairing, of large, two-dimensional vortices in the separated shear layer (e.g., Estevadoral and Kleis [44]). The regular shedding of these vortical structures would likely result in large-amplitude velocity fluctuations such as those seen in Fig. 9(*b*). The fact that the vorticity shedding occurs at the dominant frequency of the T-S waves in the separated shear layer demonstrates the interaction between the two instability mechanisms in these instances.

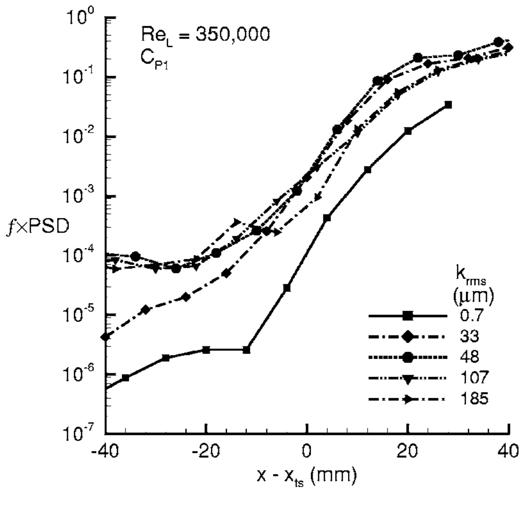

Fig. 8 Growth rate of disturbance energy in the u'/U_{ref} spectrum at f_{MA} (Re_L=350,000, C_{P1} pressure distribution)

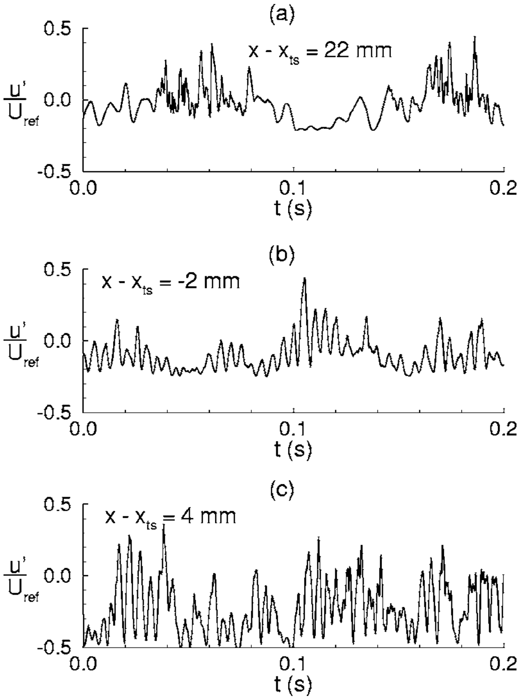

Fig. 9 Sample hot-wire signals in the separation bubble for the C_{P1} (*a*) and C_{P4} (*b*), (*c*) pressure distributions

The observed differences between the transition patterns of the C_{P1} and C_{P4} cases is consistent with the stability bounds for the K-H mechanism determined by Chandrasekhar [34]. Chandrasekhar established the conditions for K-H instability to be $0 < \kappa d < 1$, where κ is the wave number of the dominant disturbance frequency, and d is a shear layer thickness parameter that arises from the hyperbolic-tangent curve fit to the local velocity profile. For the test cases with the C_{P4} pressure distribution, the parameter κd just upstream of transition varies between 0.4 and 0.5. This is nearer to the value of 0.44, for which Michalke [45] computed the maximum amplification rate to occur, than the values between 0.6 and 0.7 for the C_{P1} pressure distribution. The greater inviscid instability of the velocity profiles for the C_{P4} pressure distribution is consistent with the more dominant role of the K-H mechanism observed in the transition process of these test cases.

Conclusions

This paper has presented measurements of separation-bubble transition over a range of surfaces with randomly distributed roughness elements, for the purpose of quantifying the effects of size and spacing of the roughness elements, and the tendency of the roughness pattern toward protrusions or depressions on the transition process.

For surface roughness conditions typical of in-service turbomachinery blades, the spacing and skewness of the roughness pattern is found to have a secondary effect on the location of transition inception, as compared to the effect of roughness height.

The experimental results are used to further evaluate semi-empirical models recently proposed by the authors for predicting the inception location and rate of transition. A slight adjustment to the constants of the transition inception model is proposed to achieve similar prediction accuracy for the recent experimental results as for the original data set upon which the model was based. The transition rate model is shown to yield accurate predictions of the current results without the need for an explicit roughness-related term in the model. The transition rate is predicted well only for one of the two streamwise pressure distributions tested. Evidence is provided to suggest that the transition process for this pressure distribution is driven by the viscous Tollmien-Schlichting mechanism. In the test cases with the second pressure distribution, the inviscid Kelvin-Helmholtz instability mechanism is shown to dominate. The very sudden transition process and large-amplitude pretransitional disturbances are consistent with the periodic shedding of vortical structures typical of this transition process. This shedding frequency matches the dominant frequency of the Tollmien-Schlichting waves prevailing in the separated shear layer.

Acknowledgment

The authors wish to acknowledge the financial support of Pratt & Whitney Canada in this project.

Nomenclature

C_{P1}, C_{P4} = identifiers for the type of pressure distribution
f = frequency (Hz)
H = boundary layer shape factor
k_{rms} = rms roughness height (Eq. (1))
L = length of test plates=1220 mm
N = number of surface measurement samples (Eqs. (1)–(3))
= spot production rate parameter (Eq. (9))
n = number of times the roughness distribution crosses the mean elevation (Eq. (2))
= turbulent spot production rate $(ms)^{-1}$ (Eq. (6))
PSD = power spectral density of u'/U_{ref}
R_t = maximum roughness height range
R_z = ten-point roughness height range
Re_L = reference Reynolds number based on L and U_{ref}
Re_s = Reynolds number based on x_s and U_{e_s}
Re_{s-ts} = Reynolds number based on $(x_{ts}-x_s)$ and U_{e_s}
Re_θ = Reynolds number based on θ and U_e
Re_{δ^*} = Reynolds number based on δ^* and U_e
S_{sk} = skewness of the roughness height distribution (Eq. (3))
TF = Taylor's turbulence factor $TF=Tu_{ref}(L/\lambda_s)^{0.2}$
Tu = free-stream turbulence intensity (%)
Tu_{ref} = reference turbulence intensity (%), measured 10 mm upstream of the test surface leading edge
U_e = local free-stream velocity
U_{ref} = reference streamwise velocity measured at
= $x=25$ nm, $y=25$ mm, $z=382$ mm
u' = fluctuating component of velocity
W = average spacing of roughness elements (Eq. (2))
x, y = streamwise and surface-normal spatial coordinates
δ^* = boundary layer displacement thickness
Δx = surface scan lateral resolution
α = spot spreading angle (Eq. (7))
γ = boundary layer intermittency
η = acceleration parameter $\eta=(\nu/U_e^2)(dU_e/dx)$
κ = wave number of the dominant disturbance (m^{-1})
λ_θ = Thwaites' pressure-gradient parameter $\lambda_\theta=(\theta^2/\nu)(dU_e/dx)$
λ_s = integral length scale of free-stream turbulence
μ = mean elevation of rough surfaces $\mu=\Sigma y_i/N$
σ = spot propagation parameter (Eq. (8))
θ = boundary layer momentum thickness
ν = kinematic viscosity

Subscripts

MA = maximum amplification rate of T-S waves
s = separation
ts = start of transition

References

[1] Leipold, R., Boese, M., and Fottner, L., 2000, "The Influence of Technical Surface Roughness Caused by Precision Forging on the Flow Around a Highly Loaded Compressor Cascade," ASME J. Turbomach., **122**, pp. 416–425.

[2] Bons, J. P., and McClain, S. T., 2003, "The Effect of Real Turbine Roughness With Pressure Gradient on Heat Transfer," ASME J. Turbomach., **126**, pp. 333–441.

[3] Bons, J. P., McClain, S. T., Taylor, R. P., and Rivir, R. B., 2001, "The Many Faces of Turbine Surface Roughness," ASME J. Turbomach., **123**, pp. 739–748.

[4] Taylor, R. P., 1990, "Surface Roughness Measurements on Gas Turbine Blades," ASME J. Turbomach., **112**, pp. 175–180.

[5] Kind, R. J., Serjak, P. J., and Abbott, M. W. P., 1998, "Measurements and Prediction of the Effects of Surface Roughness on Profile Losses and Deviation in a Turbine Cascade," ASME J. Turbomach., **120**, pp. 20–27.

[6] Boynton, J. L., Tabibzadeh, R., and Hudson, S. T., 1992, "Investigation of Rotor Blade Roughness Effects on Turbine Performance," ASME J. Turbomach., **115**, pp. 614–620.

[7] Suder, K. L., Chima, R. V., Strazisar, A. J., and Roberts, W. B., 1995, "The Effect of Adding Roughness and Thickness to a Transonic Axial Compressor Rotor," ASME J. Turbomach., **117**, pp. 491–505.

[8] Blair, M. F., 1994, "An Experimental Study of Heat Transfer in a Large Scale Turbine Rotor Passage," ASME J. Turbomach., **116**, pp. 1–13.

[9] Pinson, M. W., and Want, T., 1997, "Effects of Leading-Edge Roughness on Fluid Flow and Heat Transfer in the Transitional Boundary Layer Over a Flat Plate," Int. J. Heat Mass Transfer, **40**, pp. 2813–2823.

[10] Wang, T., and Rice, M. C., 2003, "Effect of Elevated Free-Stream Turbulence on Transitional Heat Transfer Over Dual-Scaled Rough Surfaces," ASME GT2003-38835.

[11] Gibbings, J. C., Goksel, O. T., and Hall, D. J., 1986, "The Influence of Roughness Trips Upon Boundary-Layer Transition—Part 1 Characteristics of Wire Trips," Aeronaut. J., **90**, pp. 289–301.

[12] Gibbings, J. C., Goksel, O. T., and Hall, D. J., 1986, "The Influence of Roughness Trips Upon Boundary-Layer Transition—Part 2 Characteristics of Single Spherical Trips," Aeronaut. J., **90**, pp. 357–367.

[13] Gibbings, J. C., Goksel, O. T., and Hall, D. J., 1986, "The Influence of Roughness Trips Upon Boundary-Layer Transition—Part 3 Characteristics of Rows of Spherical Transition Strips," Aeronaut. J., **90**, pp. 393–398.

[14] Klebanoff, P. S., and Tidstrom, K. D., 1982, "Mechanism by Which a Two-Dimensional Roughness Element Induces Boundary-Layer Transition," Phys. Fluids, **15**, pp. 1173–1188.

[15] Gibbings, J. C., and Al-Shukri, S. M., 1997, "Effect of Sandpaper Roughness and Stream Turbulence on the Laminar Layer and its Transition," Aeronaut. J., **101**, pp. 17–24.

[16] Kerho, M. F., and Bragg, M. B., 1997, "Airfoil Boundary-Layer Development and Transition With Large Leading-Edge Roughness," AIAA J., **35**, pp. 75–84.

[17] Roberts, S. K., and Yaras, M. I., 2005, "Boundary Layer Transition Affected by Surface Roughness and Free-Stream Turbulence," ASME J. Fluids Eng., **127**, pp. 449–457.

[18] Volino, R. J., and Bohl, D. G., 2004, "Separated Flow Transition Mechanism and Prediction With High and Low Freestream Turbulence Under Low Pressure Turbine Conditions," ASME GT2004-53360.

[19] Morris, H. M., 1955, "A New Concept of Flow in Rough Conduits," Trans. Am. Soc. Civ. Eng., **120**, pp. 373–398.

[20] Waigh, D. R., and Kind, R. J., 1998, "Improved Aerodynamic Characterization of Regular Three-Dimensional Roughness," AIAA J., **36**, pp. 1117–1119.

[21] Dirling, R. B. J., 1973, "A Method for Computing Rough Wall Heat Transfer Rates on Reentry Nosetips," AIAA J., 73–763.

[22] Dvorak, F. A., 1969, "Calculation of Turbulent Boundary Layers on Rough Surfaces in Pressure Gradient," AIAA J., **7**, pp. 1752–1759.

[23] Bons, J. P., 2002, "St and cf Augmentation for Real Turbine Roughness With Elevated Freestream Turbulence," ASME GT2002-30198.

[24] Belnap, B. J., van Rij, J. A., and Ligrani, P. M., 2002, "A Reynolds Analogy for Real Component Surface Roughness," Int. J. Heat Mass Transfer, **45**, pp. 3089–3099.

[25] Sigal, A., and Danberg, J. E., 1990, "New Correlation of the Roughness Den-

sity Effect on the Turbulent Boundary Layer," AIAA J., **20**, pp. 554–556.

[26] Stripf, M., Schulz, A., and Wittig, S., 2005, "Surface Roughness Effects on External Heat Transfer of a HP Turbine Vane," ASME J. Turbomach., **127**, pp. 200–208.

[27] Volino, R. J., 2002, "Separated Flow Transition under Simulated Low-Pressure Turbine Airfoil Conditions: Part 2-Turbulence Spectra," ASME J. Turbomach., **124**, pp. 656–664.

[28] Bao, F., and Dallmann, U. C., 2004, "Some Physical Aspects of Separation Bubble on a Rounded Backward-Facing Step," Aerosol Sci. Technol., **8**, pp. 83–91.

[29] Malkiel, E., and Mayle, R. E., 1996, "Transition in a Separation Bubble," ASME J. Turbomach., **118**, pp. 752–759.

[30] Watmuff, J. H., 1999, "Evolution of a Wave Packet Into Vortex Loops in a Laminar Separation Bubble," J. Fluid Mech., **397**, pp. 119–139.

[31] Yang, Z., and Voke, P. R., 2001, "Large-Eddy Simulation of Boundary-Layer Separation and Transition at a Change of Surface Curvature," J. Fluid Mech., **493**, pp. 305–333.

[32] Spalart, P. R., and Strelets, M. K., 2000, "Mechanisms of Transition and Heat Transfer in a Separation Bubble," J. Fluid Mech., **403**, pp. 329–349.

[33] Rist, U., and Maucher, U., 2002, "Investigations of Time-Growing Instabilities in Laminar Separation Bubbles," Eur. J. Mech. B/Fluids, **21**, pp. 495–509.

[34] Chandrasekhar, S., 1961, *Hydrodynamic and Hydromagnetic Stability* Clarendon Press, Oxford.

[35] Roberts, S. K., and Yaras, M. I., 2005, "Modeling Transition in Attached and Separated Boundary Layers," ASME J. Turbomach., **127**, pp. 402–411.

[36] Mayle, R. E., 1991, "The Role of Laminar-Turbulent Transition in Gas Turbine Engine," ASME J. Turbomach., **113**, pp. 509–537.

[37] Taylor, G. I., 1939, "Some Recent Development in the Study of Turbulence," *Proc. 5th Intl. Cong. Appl. Mech*, J. P. den Hartog, and H. Peters, eds., Wiley, New York, pp. 294–310.

[38] Roberts, S. K., and Yaras, M. I., 2003, "Measurements and Prediction of Free-Stream Turbulence and Pressure Gradient Effects on Attached Flow Boundary Layer Transition," ASME GT2003-38261.

[39] Solomon, W. J., Walker, G. J., and Gostelow, J. P., 1996, "Transition Length Prediction for Flows With Rapidly Changing Pressure Gradients," ASME J. Turbomach., **118**, pp. 744–751.

[40] Emmons, H. W., 1951, "The Laminar-Turbulent Transition in a Boundary Layer—Part 1," J. Aeronaut. Sci., **18**, pp. 490–498.

[41] Gostelow, J. P., Melwani, N., and Walker, G. J., 1996, "Effects of Streamwise Pressure Gradient on Turbulent Spot Development," ASME J. Turbomach., **118**, pp. 737–743.

[42] D'Ovidio, A., Harkins, J. A., and Gostelow, J. P., 2001, "Turbulent Spots in Strong Adverse Pressure Gradients—Part 2: Spot Propagation and Spreading Rates," ASME 2001–GT–0406.

[43] Walker, G. J., 1989, "Transitional Flow on Axial Compressor Blading," AIAA J., **27**, pp. 595–602.

[44] Estevadoral, J., and Kleis, S. J., 1999, "High-Resolution Measurements of Two-Dimensional Instabilities and Turbulence Transition in Plane Mixing Layers," Exp. Fluids, **27**, pp. 378–390.

[45] Michalke, A., 1964, "On the Inviscid Instability of the Hyperbolic-Tangent Velocity Profile," J. Fluid Mech., **19**, pp. 543–556.

A Numerical Investigation of Boundary Layer Suction in Compound Lean Compressor Cascades

Yanping Song
e-mail: songyanping@hit.edu.cn

Fu Chen

Jun Yang

Zhongqi Wang

School of Energy Science and Engineering,
Harbin Institute of Technology,
Harbin 150001, China

This paper is focused on the numerical investigation of boundary layer suction (BLS) via a slot on the suction surfaces of two compound lean compressor cascades with large camber angles as well as a conventional straight compressor cascade for comparison. The objective of the investigation is to study the influence of boundary layer suction on the performance of compound lean compressor cascades, thus to discuss the possibility of the application of boundary layer suction to improve their performance. An extensive numerical study has been carried out under different spanwise lengths, different axial positions of the slots, and different suction flow rates. The results show that the total loss of all three cascades is reduced significantly by boundary layer suction, and the largest reduction occurs at the highest suction flow rate. The axial locations of the slot have little effect on the total loss of the three cascades, which means the slots are opened within the optimal axial range in this case. The slot opened along the full span is the best one to obtain the largest reduction in total loss for all three cascades due to the alleviation of flow separation in the corner between the endwall and the suction surface. Moreover, the flow turning is increased, and pressure rise at the rear of the passage is recovered along the whole blade height via boundary layer suction along the full span, enhancing the working range of the highly loaded compressor cascades. [DOI: 10.1115/1.2162181]

Introduction

The trend to reduce compressor size and weight by reducing the number of stages leads to higher amounts of diffusion per stage, which will cause large loss in the compressor. Since the improvement in the aerodynamic performance of aero-engines depends on further increases in the efficiency of each component, especially the compressor and turbine, many researchers are addressing this issue through the use of varying flow control techniques. Boundary layer suction (BLS) and compound lean blade are two of the techniques.

Kerrebrock et al. discussed the concept of aspirated compressors, addressing that boundary layer suction at the shock impingement location on the suction surface of transonic compressor blades could increase flow turning, flow capacity, and efficiency [1]. Removal of low-energy fluid at critical locations could produce approximately twice the work realizable without boundary layer suction [2]. Schuler et al. [3] designed and tested a fan stage with a pressure ratio of 1.6 at a tip Mach number of 0.7. The measured adiabatic efficiency of the rotor for the throughflow was 96% at the design point and that for the stage was 90% by means of boundary layer suction. Merchant et al. [4] validated and demonstrated this concept of boundary layer suction through the design and analysis of a unique aspirated compressor stage which achieved a total pressure ratio of 3.5 at a tip speed of 1500 ft/s. The experimentally determined stage performance of this aspirated fan stage was in good agreement with the 3D viscous computation prediction, and in turn close to the design intent [5]. Also in this paper, the authors recommend opportunities to enhance the performance of future designs, particularly with respect to managing the endwall flows through three-dimensional design features and developing more effective endwall flow control schemes.

Many attempts have been made to control endwall flows and reduce endwall losses such as Breugelmans et al. [6] and Sasaki et al. [7] who clarified the positive effect of the dihedral (compound lean) in a linear compressor cascade when the suction/endwall corner laid on the obtuse side. Weingold et al. [8] investigated compound lean stators in a three-stage compressor, which had dihedral on both endwalls, and reported a 1% increase in overall efficiency and an elimination of corner stall.

The focus of the present investigation is to study numerically the application of boundary layer suction to the compound lean compressor cascades with large camber angles, to discuss the possibility of further performance improvement of compound lean compressor cascade via boundary layer suction, and to prepare for the future experiments which will be carried out in a low-speed wind tunnel.

Investigated Compressor Cascades and BLS Implementation

To obtain a large diffusion within a stator passage, a compressor cascade with NACA65 profile and 60 deg camber angles was designed as the baseline to study BLS effect on the performance improvement of a highly loaded compressor cascade. The geometric parameters of the cascade are listed in Table 1.

The compound lean was introduced to the baseline by shifting the blade profile towards the circumferential direction to create a curved stacking line which is different from the straight stacking line of the baseline as shown in Fig. 1. The stacking line of the compound lean blade consisted of five parts, two straight-line segments at the two endwalls and one at the midspan, and two circular arcs used to connect the middle straight-line segment to the two straight-line segments at the two endwalls. The portion of the blade height by the straight-line segment at the endwall was defined as the lean length (L_B), which was 15% of the blade height

---

Contributed by the International Gas Turbine Institute of ASME for publication in the JOURNAL OF TURBOMACHINERY. Manuscript received October 1, 2004; final manuscript received February 1, 2005. IGTI Review Chair: K. C. Hall. Paper presented at the ASME Turbo Expo 2005: Land, Sea and Air, Reno, NV, June 6–9, 2005, Paper No. GT2005-68441.

Table 1 Parameters of the cascade

chord (m)	0.1	aspect ratio	1
solidity	1.364	stagger angle (degree)	18.18
inlet metal angle (degree)	48.19	outlet metal angle (degree)	−11.81

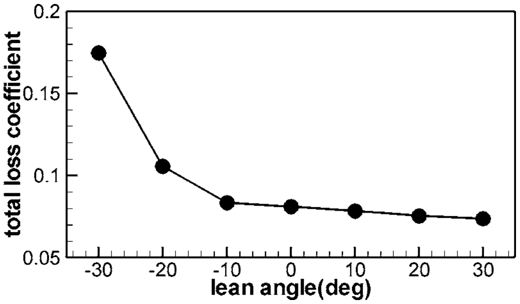

Fig. 2 Comparison of total loss of the cascades

at the two endwalls in this case. The angle between the straight-line segment of the curved stacking line and the straight stacking line was defined as the lean angle (Λ_B), which was positive if the angle between the pressure surface and the endwall was acute. Otherwise, the lean angle was negative if the angle between the pressure surface and the endwall was obtuse, that is, an acute angle was between the suction surface and the endwall.

The 30 deg lean angle and −10 deg lean angle were finally selected in this study after analyzing the total loss of the two cascades with that of the baseline before BLS application. The total pressure loss coefficient is defined as (upstream-local)/inlet dynamic head. The 25% of the axial chord downstream of the blade trailing edge is chosen as the location for the comparison of the exit properties, such as total loss coefficient, pitch-averaged loss coefficient, and exit flow angle throughout the paper. The weighting factor of local mass flow rates is included to get the pitch-averaged loss coefficient and the total loss coefficient.

As shown in Fig. 2, the cascades with 30 deg and −10 deg lean angle have nearly the same amount of total loss as the baseline which corresponds to 0 deg lean angle, thus the effect of boundary layer suction on the performance of the cascades with different geometries could be evaluated based on the same original total loss level. Another intent of such selection was due to the question of how much performance improvement could be further obtained for the compound lean cascades through boundary layer suction since the two cascades have the minimum total loss among the designed positive and negative compound lean cascades, respectively.

Boundary layer suction in compressor cascade was implemented by sucking low-energy fluid from the slot on the suction surface. The slot was 1.5 mm wide and the radial length was selected as 100% of the blade height (configuration A) and 50% of the blade height, which included configuration B (from the hub to 25% of the blade height plus from the tip to 75% of the blade height) and configuration C (from 25% to 75% of the blade height). The axial positions of the slot were at 65%, 70%, and 75% of the axial chord. The suction flow rates were 0.5% and 1.0% of the cascade inlet mass flow, which were realized by adjusting the pressure inside the slot.

Numerical Procedure

The geometry of the cascade with the details of the slot shown in Fig. 3 was simulated using FLUENT, a commercial CFD package. Unstructured hexahedral grid was created by GAMBIT within the blade passage with a total grid number of 790,000. The k-epsilon turbulence and wall function were used to model the boundary layer.

The inlet conditions for this cascade were a Mach number of 0.2 with an inlet air angle of 48.19 deg. The atmospheric pressure was the exit condition. The inlet and exit boundary conditions were chosen to meet the real conditions of the future cascade test, which will be carried out in a low speed wind tunnel at HIT. The

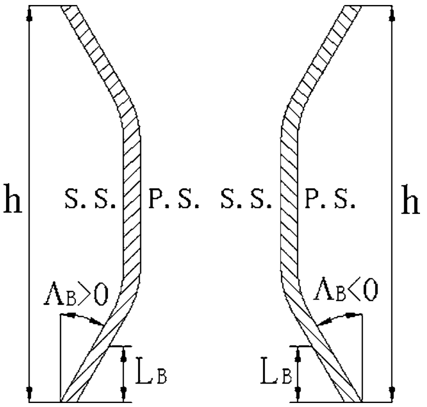

Fig. 1 Stacking lines of compound lean cascades

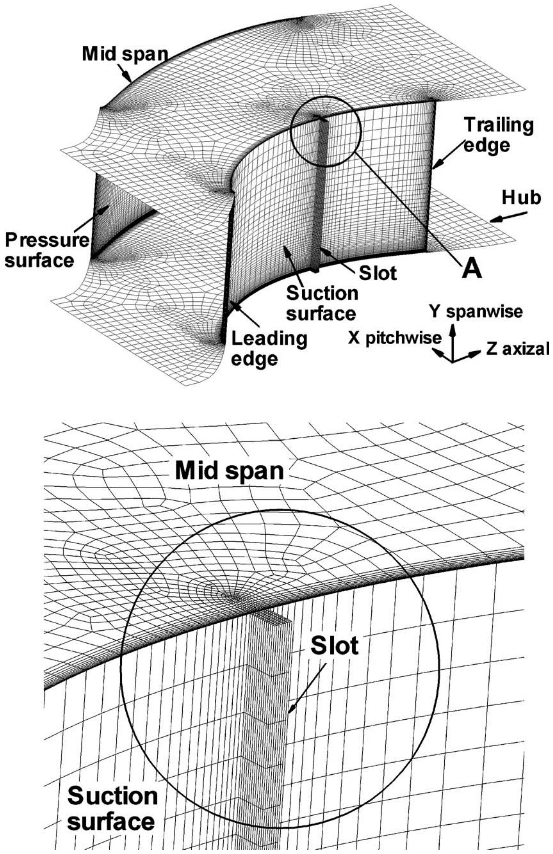

Fig. 3 Grid for cascade and slot

flow details inside the slot were not given in this paper although different static pressures inside the slot were set to get the desired suction flow rates.

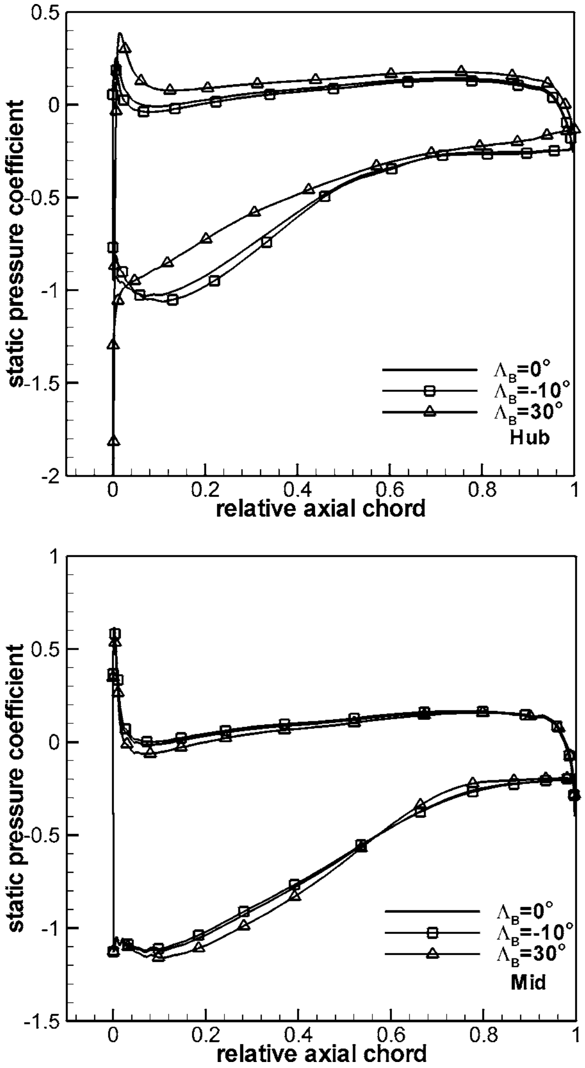

Fig. 4 Static pressure distribution on the blade surfaces

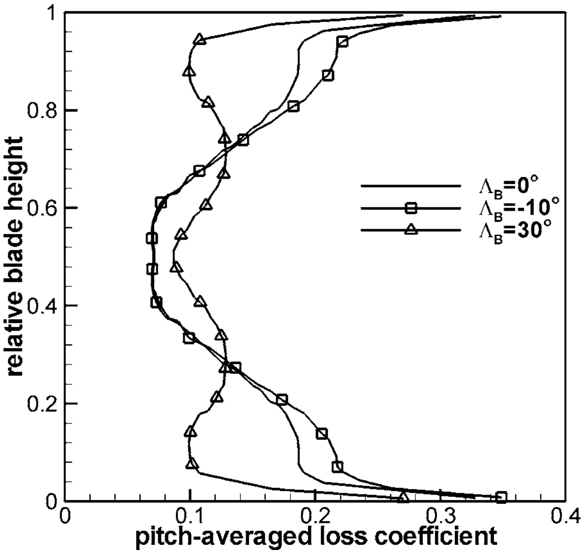

Fig. 5 Radial distribution of pitch-averaged loss coefficient

Results and Discussion

In the following figures, Λ_B and β represent the lean angle and the suction flow rate, respectively.

The distribution of the static pressure coefficient along the blade surfaces is shown in Fig. 4. The static pressure coefficient is defined as (local-exit)/inlet dynamic head. Compared to the conventional straight blade, the blade loading decreases at the endwalls and increases at the midspan for the positive compound lean blade, whereas the opposite distribution of the blade loading occurs for the negative compound lean blade. The variation of the blade loading after introducing compound lean also changes the radial distribution of the pitch-averaged cascade loss (Fig. 5). Compared to the conventional straight cascade, the total pressure loss increases at the midspan of the positive compound lean cascade and at the two endwalls of the negative compound lean cascade. Configuration C, therefore, was used in the positive compound lean blade to reduce the increased loss at the midspan. For the same reason, configuration B was applied to the negative compound lean blade to reduce the high loss at the endwalls. Another reason for the applications of configurations C and B comes from the mechanical consideration; after all, the blade with a whole spanwise slot will reduce the mechanical stability significantly provided in use. Configuration A is also studied for all three cascades for comparison with configurations B and C.

Figure 6 shows the loss reduction of the investigated cascades when the boundary layer is sucked at different axial positions. The ordinate, the total loss reduction via BLS, is defined as (total loss of cascade with BLS-total loss of the straight cascade without BLS)/total loss of the straight cascade without BLS. As shown in Fig. 6, the total loss of all three cascades is reduced significantly by boundary layer suction, and the largest reduction occurs at higher suction flow rate.

For the conventional straight cascade, the loss is reduced by 30% via configuration A, 25% via configuration B, and 10% via configuration C by sucking 1.0% of the flow away at 70% of the axial chord, which proves that configuration A is better than configurations B and C in reducing total loss. Similarly, for the positive and the negative compound lean cascades, configuration A is also the choice to obtain the largest amount of total loss reduction. The axial locations of the slot have little effect on the total loss of the three cascades, especially at higher suction flow rate, which means the slots were opened within the optimal axial range in this case. Thus, the distribution of the flow parameters for all three cascades in the following sections is derived from the flow field simulated when 1% of the flow rate is sucked away from the slot at 70% of the axial chord. It is interesting to note that configuration A with higher suction flow rate is the one to get the largest total loss reduction for all three cascades. As shown in Fig. 7, although configurations B and C reduce the loss furthest at the endwalls and at the midspan, respectively, configuration A reduces the loss evenly along the whole span, corresponding to the largest total loss reduction.

Figure 8 shows the distribution of the static pressure coefficient on the blade surfaces. The existence of the slot disturbs the pressure distribution around it. Flow suction accelerates the flow near the suction surface before the slot from the leading edge, thus increases the blade loading. The exit static pressure also gets higher, especially in the region where a severe flow separation occurs before suction, which means that the static pressure rise is recovered after the slot due to the alleviation of the flow separation via boundary layer suction.

The comparison of the exit flow angle is shown in Fig. 9. Boundary layer suction apparently increases the flow turning.

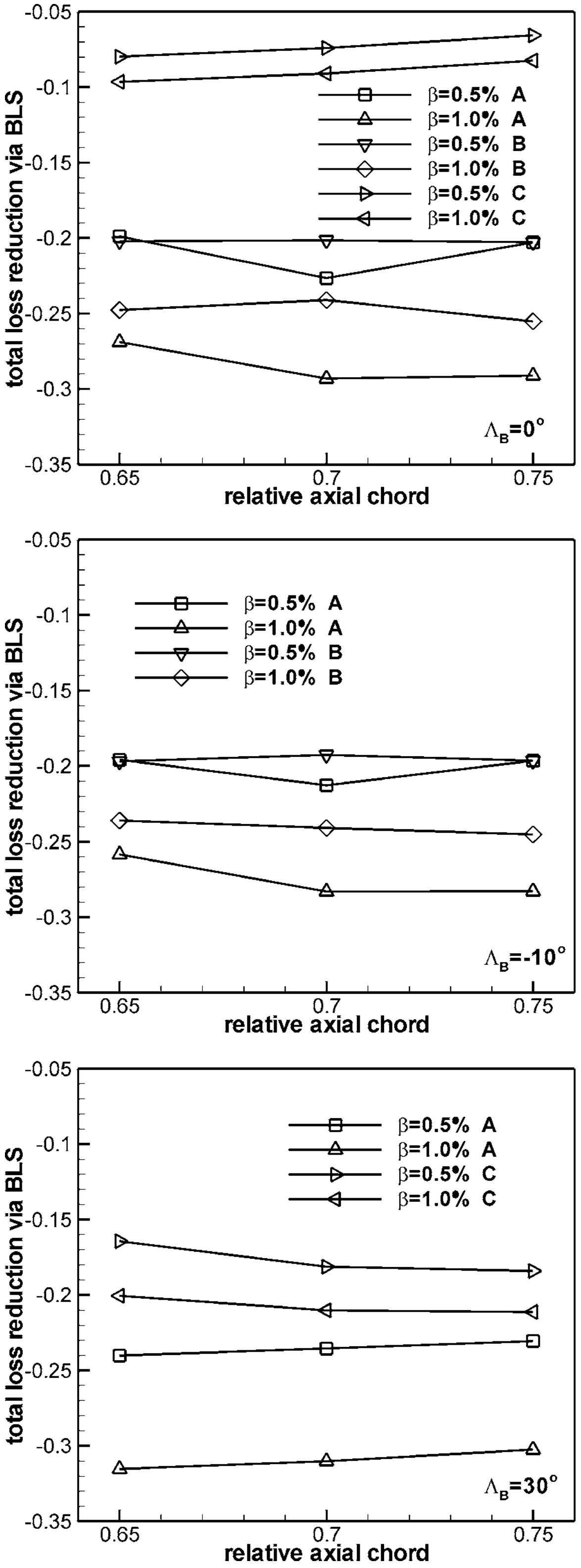

Fig. 6 Reduction in total loss with boundary layer suction

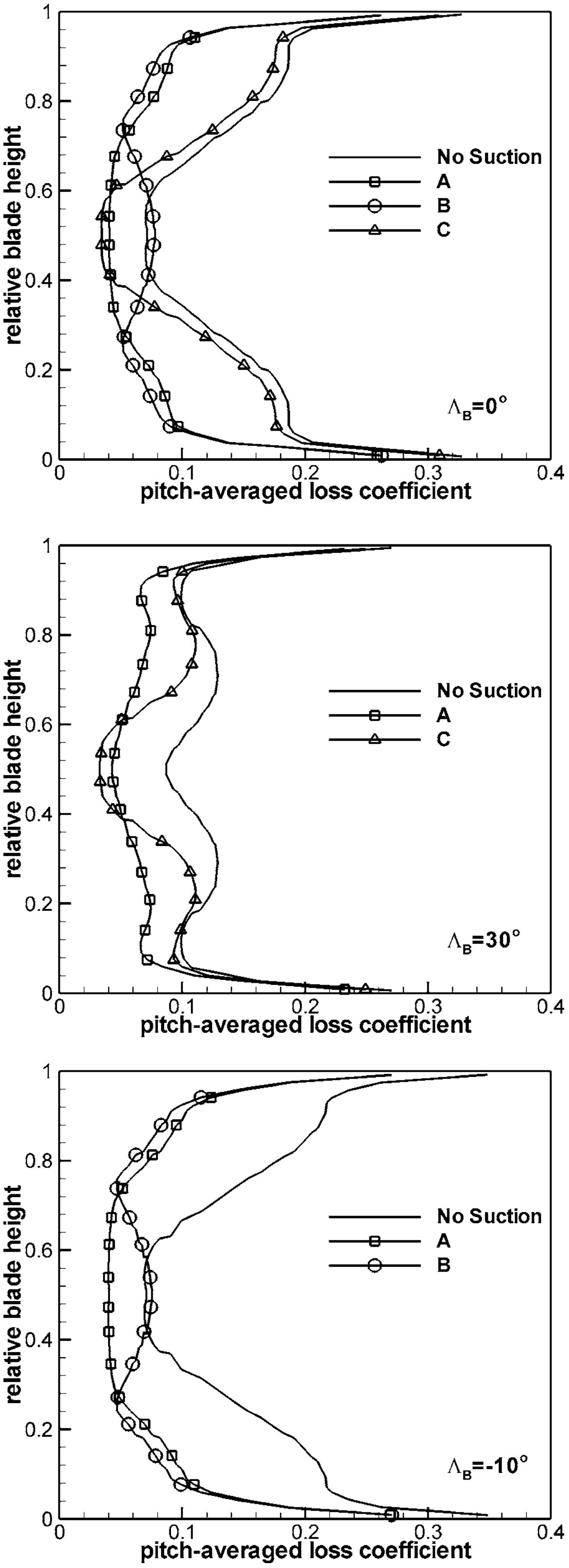

Fig. 7 Radial distribution of pitch-averaged loss coefficient

Flow suction on the suction surface causes the fluid flowing towards the suction side, thus increasing the turning angle; in other words, since the low-energy fluid is sucked away, the passage blockage is reduced and the deviation angle decreases. An increase in turning angle along the whole blade height is only obtained in configuration A for all three cascades, representing a uniform distribution of the exit angle along the blade height.

Compared to the contours of the static pressure coefficient on the suction surface of the conventional straight blade without BLS in Fig. 10, boundary layer suction recovers the static pressure rise

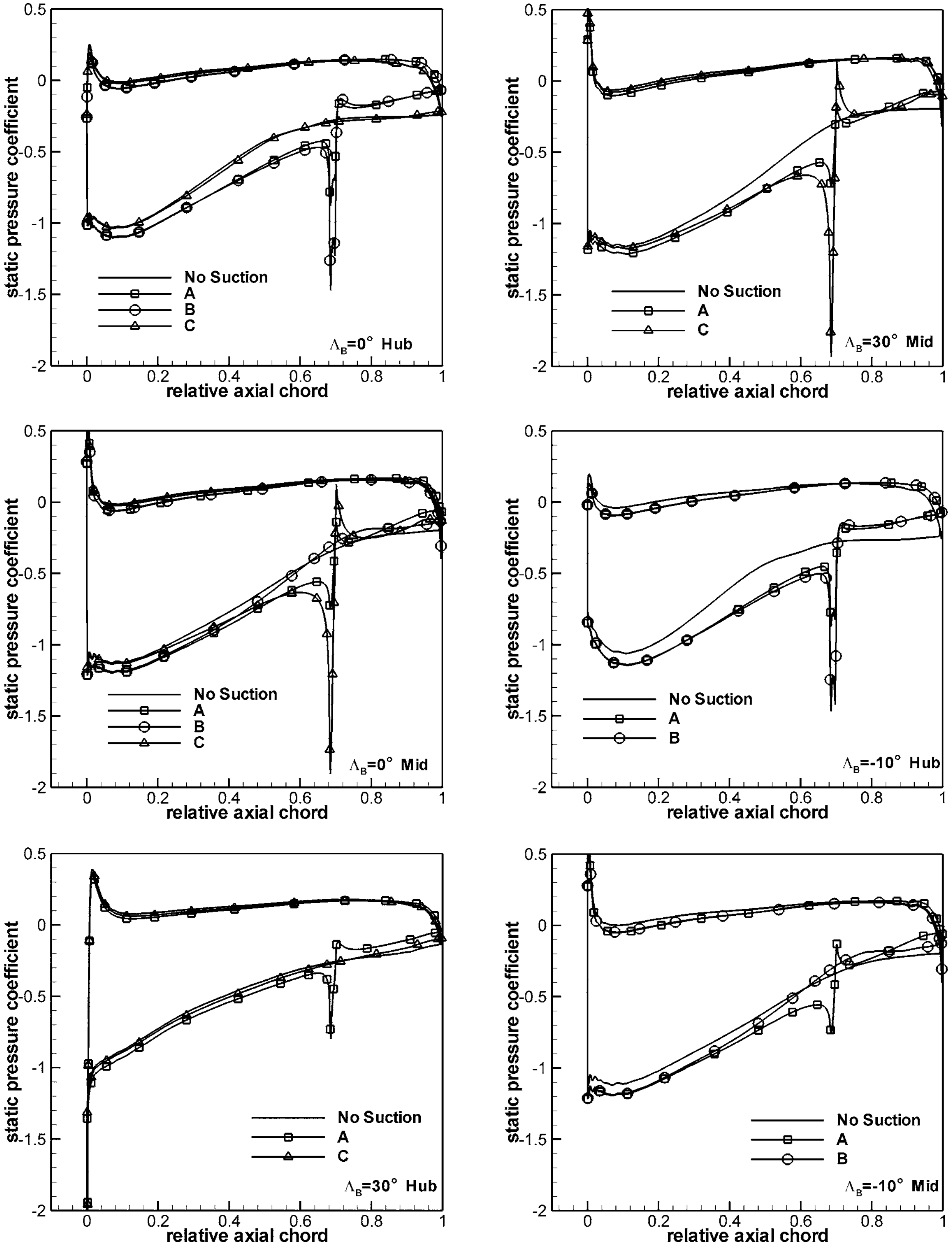

Fig. 8 Static pressure distribution on the blade surfaces

after the slot significantly, especially for configurations A and B. The thick black region in the figures represents the slot on the suction surface. As shown in Fig. 11, the positive compound lean blade gets higher static pressure rise with configuration A than that with configuration C. Moreover, the larger curvature of the static pressure contours shows higher static pressure at the two endwalls than the midspan. Figure 12 represents the static pressure contours on the suction surface of the negative compound lean blade. Similarly, the recovery of the static pressure rise after the slot is more obvious with configuration A than configuration B. It concludes

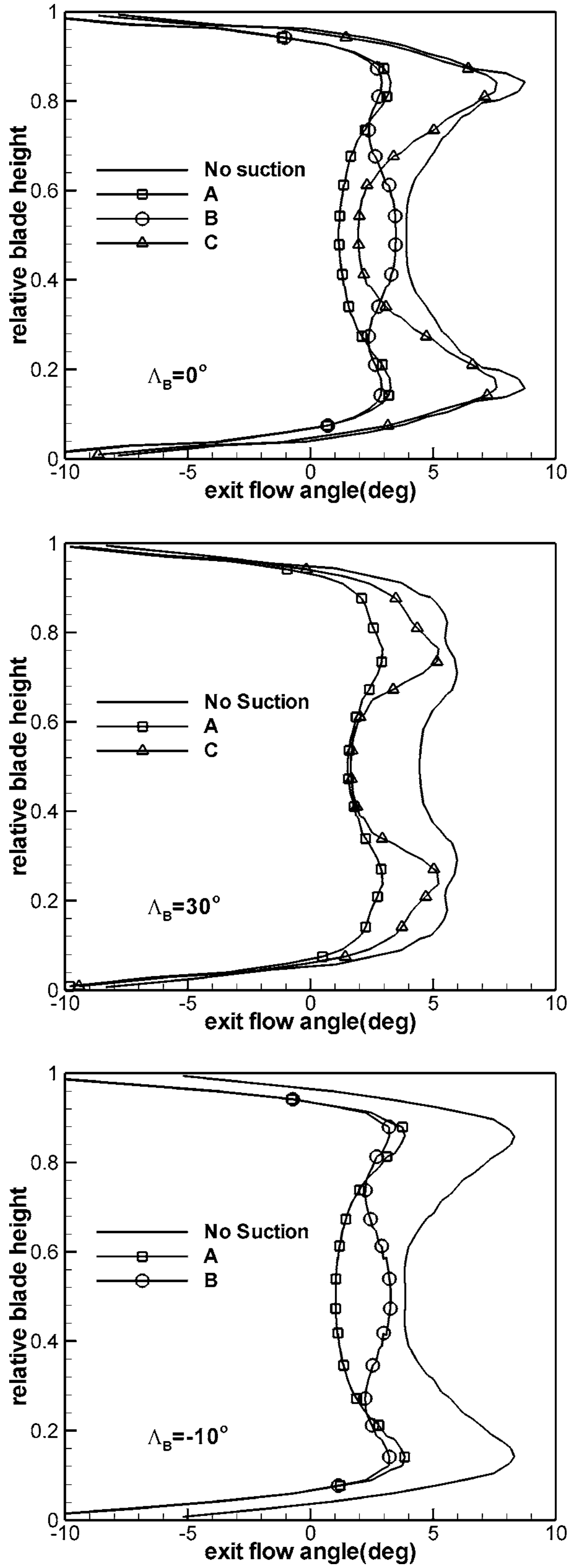

Fig. 9 Radial distribution of exit flow angle

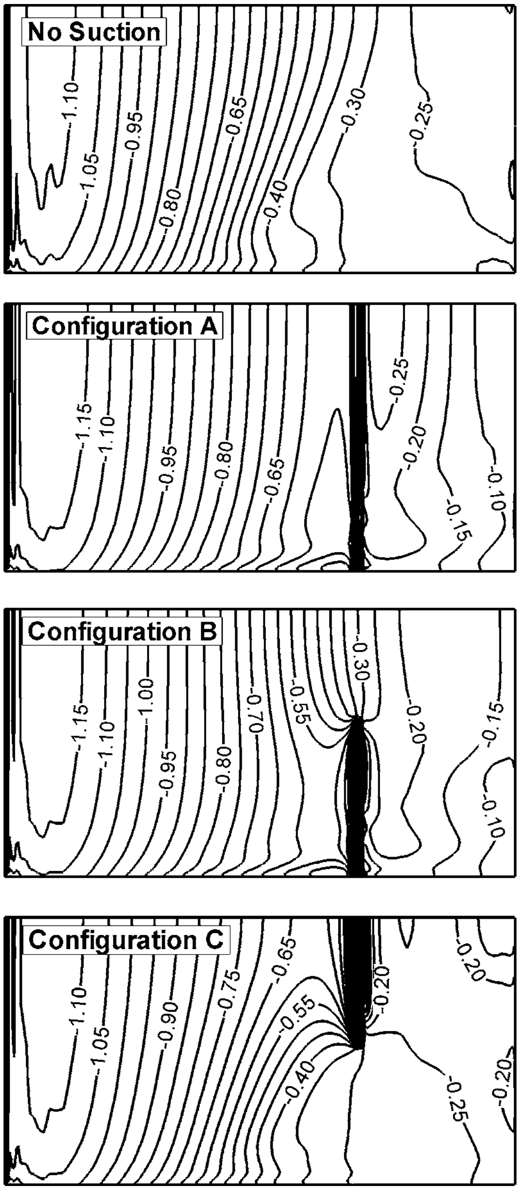

Fig. 10 Static pressure contours on suction surface of the conventional straight blade (left side: L.E., right side: T.E.)

that BLS with configuration A increases the static pressure along the whole blade height, while configurations B and C can only take effect at the local spanwise positions.

Since the static pressure coefficient contours in the upper and lower halves of the cascade are symmetrical with respect to the midspan, only contours in the lower half are illustrated in the figures.

Figure 13 shows the comparison of the total loss reduction of the investigated cascades with the same slot configuration when the boundary layer is sucked at the different axial positions. Similar to Fig. 6, the ordinate represents the level of reduction in total loss compared to the conventional straight cascade without BLS.

When the boundary layer is sucked from the whole blade height, the positive compound lean cascade has the largest loss reduction, while the negative compound lean cascade has the least, and the conventional straight cascade is in the middle. When the boundary layer is sucked from local spanwise positions, i.e., from the midspan or the endwall, however, the effect of configuration B on reducing the total loss is better than configuration C since, as shown in Fig. 5, the endwall loss of the negative compound lean cascade is much larger than the loss of the positive compound lean cascade at the midspan.

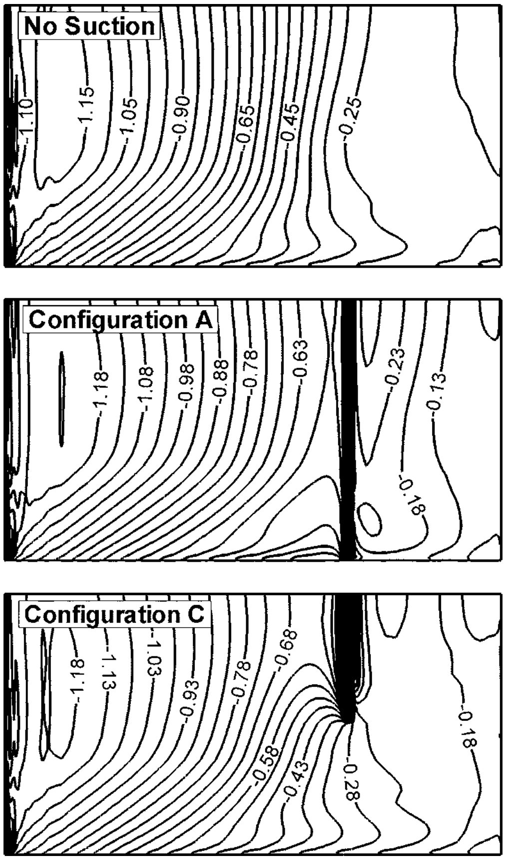

Fig. 11 Static pressure contours on suction surface of positive compound lean blade (left side: L.E., right side: T.E.)

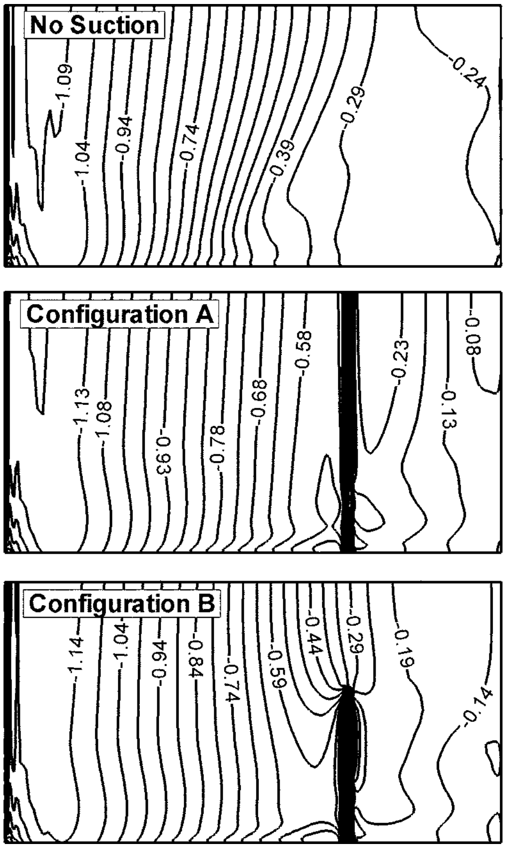

Fig. 12 Static pressure contours on suction surface of negative compound lean blade (left side: L.E., right side: T.E.)

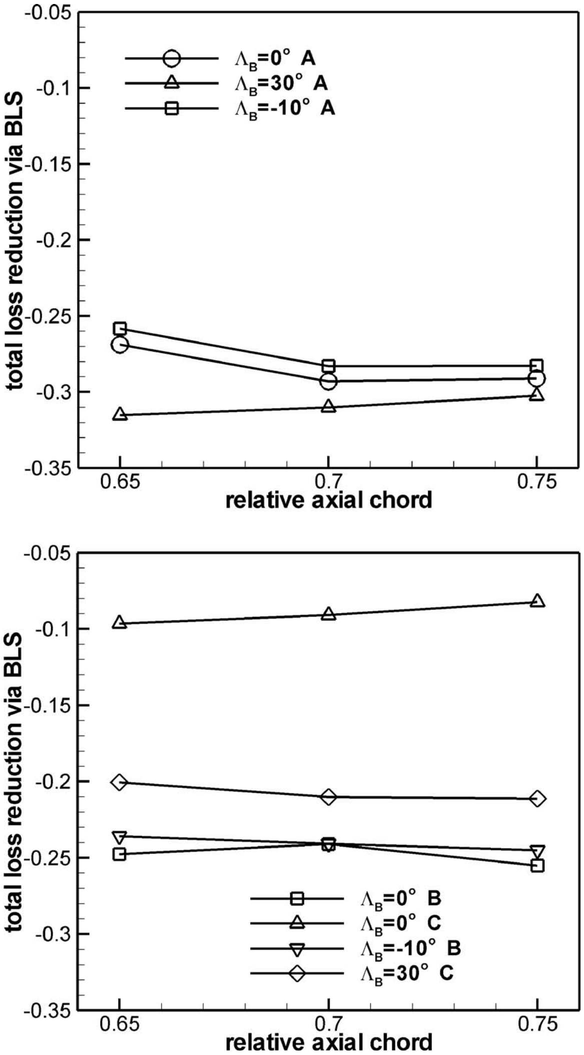

Fig. 13 Reduction in total loss with boundary layer suction

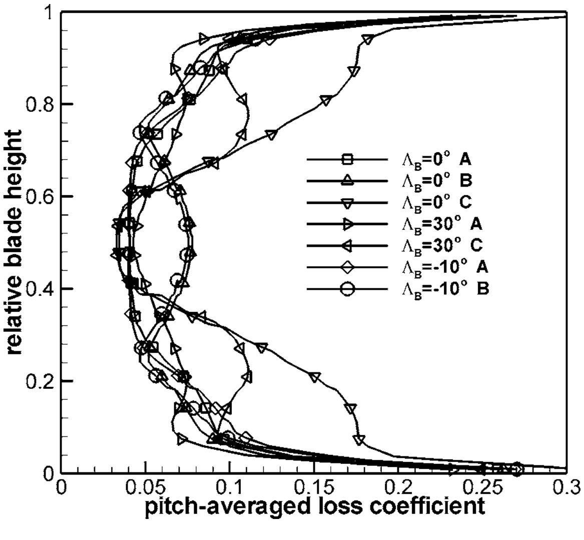

Fig. 14 Radial distribution of loss with boundary layer suction

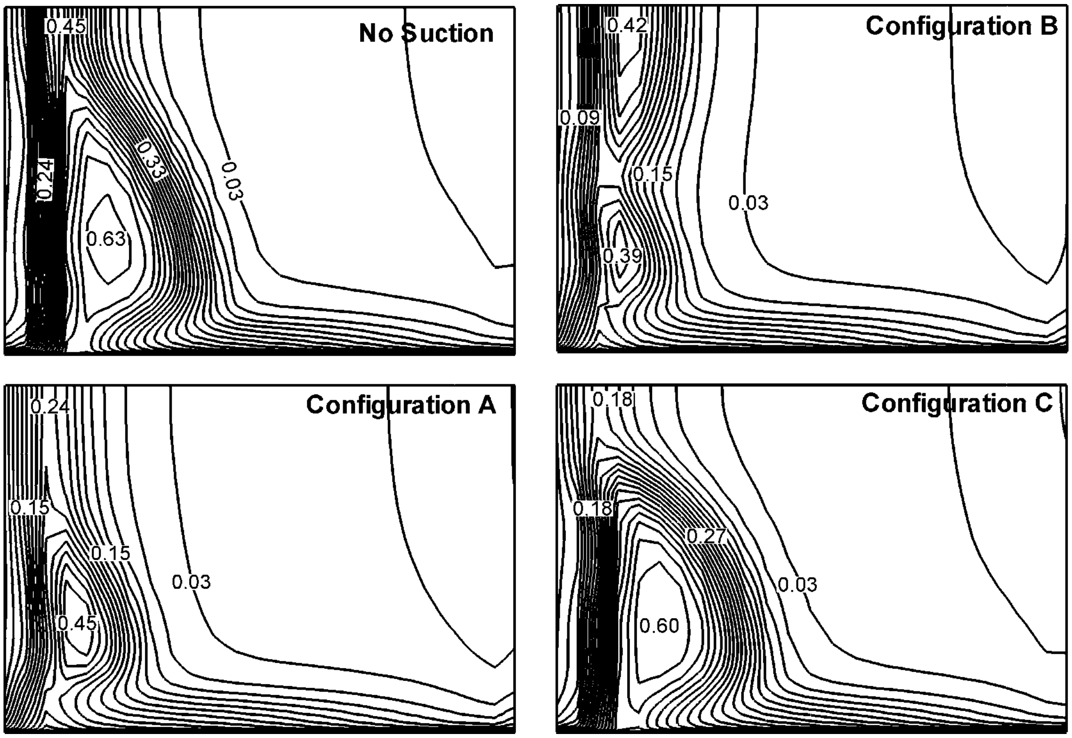

Fig. 15 Loss contours at the exit of the straight cascade (left side: SS, right side: PS)

Figure 14 shows the distribution of the pitch-averaged loss along the blade height. Compared to Fig. 5, boundary layer suction along the whole blade height does not change the relationship of the spanwise distribution of the loss among the three cascades, but the difference of the loss among the three cascades, however, decreases significantly. The spanwise distribution of the loss is nearly the same for both the conventional straight cascade and the negative compound lean cascade when configuration B is applied, most likely due to the similar loss distribution of the two cascades without boundary layer suction as shown in Fig. 5. Boundary layer suction at the midspan (configuration C) reduces more loss at the midspan of the positive compound lean cascade than the conventional straight cascade, which means that the effect of boundary layer suction on the loss reduction is, to some extent, dependent on the loss level before boundary layer suction is applied; the higher the previous loss level, the larger the loss reduction obtained. The combination of the positive compound lean cascade and boundary layer suction can reduce the endwall loss significantly.

Figures 15–17 illustrate the contours of the total pressure loss coefficient at the cascade exit, which show that only configuration A can reduce the loss uniformly along the blade height, representing the most effective way for loss reduction. Similar to Figs. 10–12, only contours in the lower half are illustrated in the figures.

Figures 18–20 show the limiting streamline on the suction surfaces of the three cascades. For the same reason as for Figs. 10–12, only the distribution of the limiting streamline on the lower half of the blade suction surface is illustrated in the figures. When configuration B or C is applied, although the flow condition near the suction surface is improved after the slot due to the removal of the low-energy fluid, little fundamental change occurs at the spanwise positions where no slot is placed, thus representing a

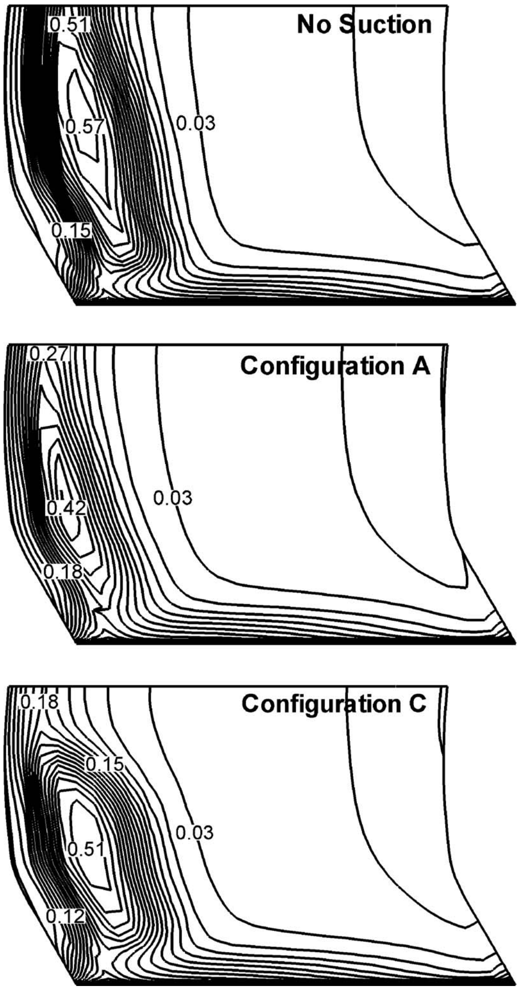

Fig. 16 Loss contours at the exit of the positive compound lean cascade (left side: SS, right side: PS)

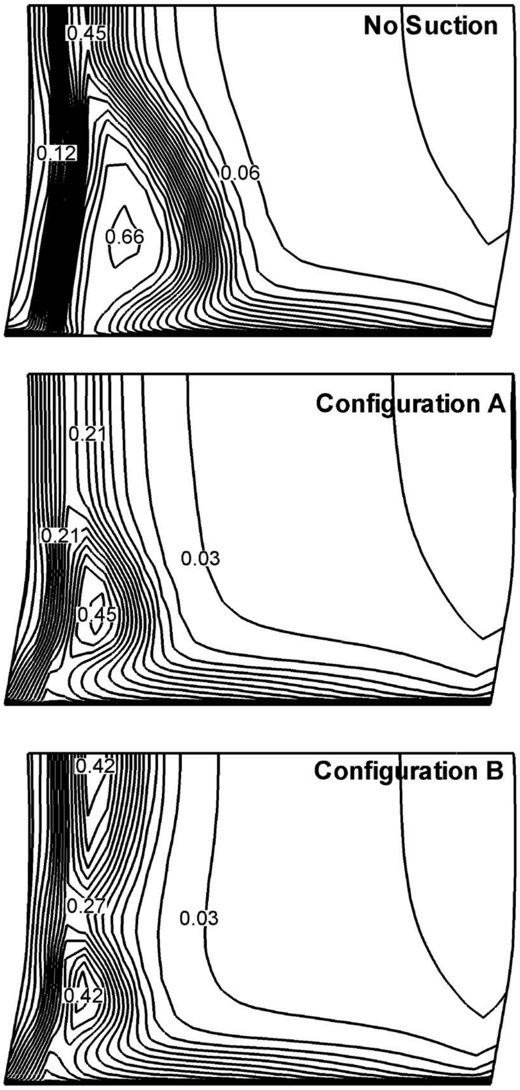

Fig. 17 Loss contours at the exit of the negative compound lean cascade (left side: SS, right side: PS)

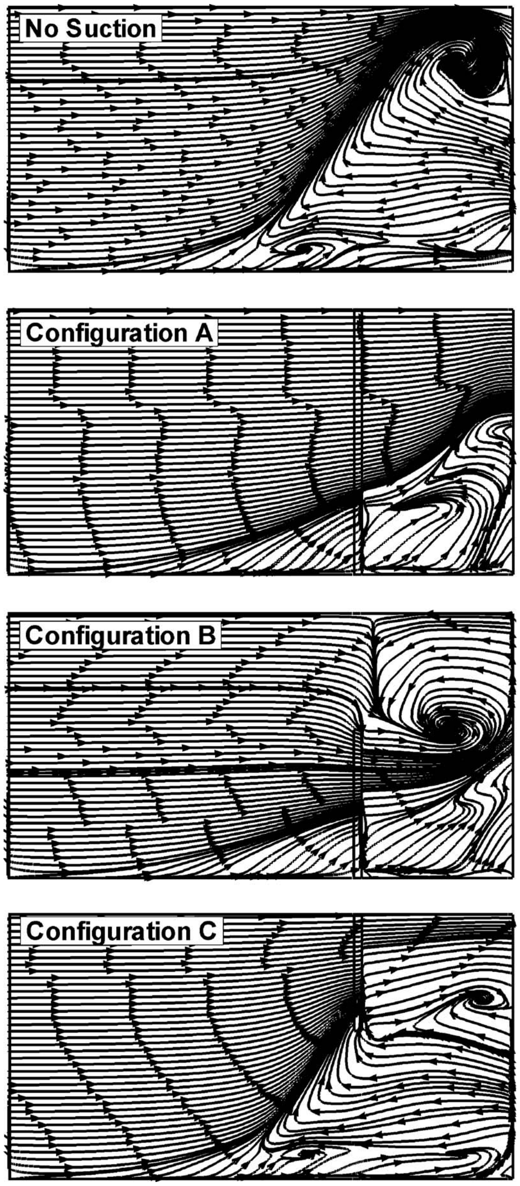

Fig. 18 Limiting streamline on suction surface of the straight cascade (left side: L.E., right side: T.E.)

more complex flow pattern in comparison with that of the conventional straight cascade without boundary layer suction. The limiting streamline distribution also proves that only configuration A can reduce corner stall by sucking the boundary layer away evenly along the blade height.

Although the limiting streamline pattern of configuration A for the positive compound lean cascade is worse, compared to that of the conventional straight cascade and the negative compound lean cascade, this configuration reduces the value and the size of the loss core most near the suction surface in the flow passage of the positive compound lean cascade in comparison with the other two cascades as shown in Figs. 15–17, which contributes the most to the total loss reduction of the cascade. This contribution, however, cannot be seen from the distribution of the limiting streamline on the suction surface.

Conclusion

Boundary layer suction changes the static pressure distribution on the blade surface, which is beneficial for the flow behavior improvement. First, it accelerates the flow near the suction surface before the slot from the leading edge, which avoids the increase in loss caused by the early separation of low-energy fluid, thus improving the performance. Second, a longer region of static pressure diffusion compared to the conventional straight blade is built up in the flow passage, further increasing the static pressure ratio. Third, it increases blade loading significantly. Therefore, boundary layer suction is an effective way to reduce loss and further increase the static pressure ratio and blade loading in the highly loaded compressor cascade.

Boundary layer suction can further improve the performance of the compound lean compressor cascade. The combination of the positive compound lean cascade and boundary layer suction can be used together to reduce endwall loss when endwall loss is the major part of the total loss of the compressor cascade, especially in the rear stage of highly loaded compressors.

Based on the mechanical consideration, the proposed boundary layer suction at local spanwise locations where local loss is much higher than the rest of the blade height is not successful from the

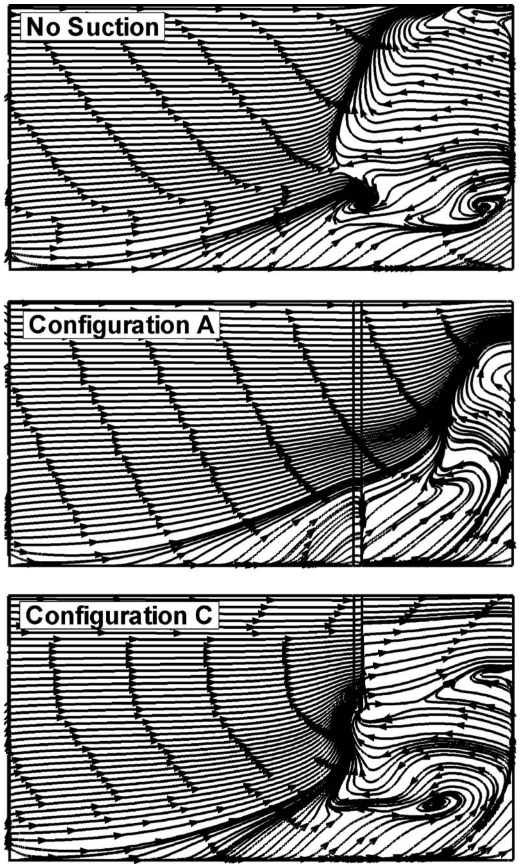

Fig. 19 Limiting streamline on suction surface of the positive compound lean cascade (left side: L.E., right side: T.E.)

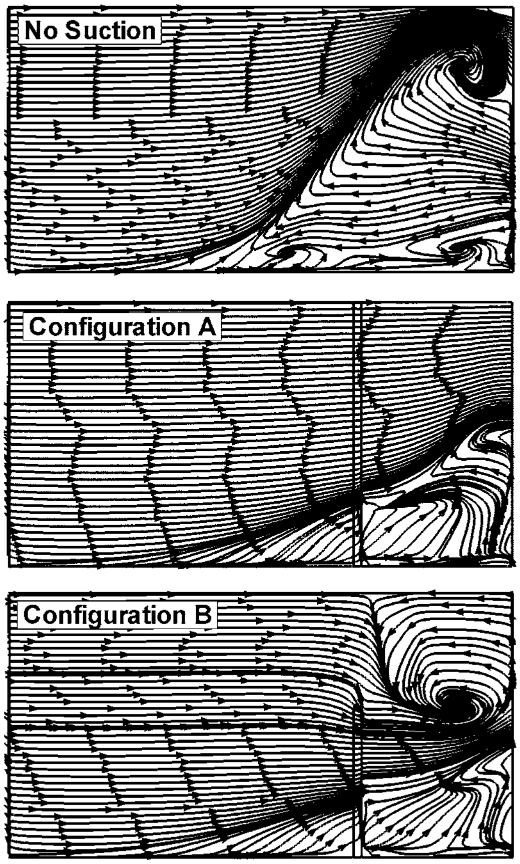

Fig. 20 Limiting streamline on suction surface of the negative compound lean cascade (left side: L.E., right side: T.E.)

viewpoint of total loss reduction. The slot opened along the full span is the best one to obtain the largest reduction in total loss for all three cascades due to the alleviation of flow separation in the corner between the endwall and the suction surface, in which the largest improvement in performance is obtained for the positive compound lean compressor cascade.

Acknowledgment

The authors would like to acknowledge the support of National Natural Science Foundation of China, Grant No. 50236020.

References

[1] Kerrebrock, J. L., Reijnen, D. P., Ziminsky, W. S., and Smilg, L. M., 1997, "Aspirated Compressors," ASME Paper No. 97-GT-525.
[2] Kerrebrock, J. L., Drela, M. A., Merchant, A., and Schuler, B. J., 1998, "A Family of Designs for Aspirated Compressors," ASME Paper No. 98-GT-196.
[3] Schuler, B. J., Kerrebrock, J. L., Merchant, A. A., Drela, M., and Adamczyk, J., 2000, "Design, Analysis, Fabrication and Test of an Aspirated Fan Stage," ASME Paper No. 2000-GT-618.
[4] Merchant, A. A., Drela, M., Kerrebrock, J. L., Adamczyk, J. J., and Celestina, M., 2000, "Aerodynamic Design and Analysis of a High Pressure Ratio Aspirated Compressor Stage," ASME Paper No. 2000-GT-619.
[5] Merchant, A., Kerrebrock, J. L., Adamczyk, J. J., and Braunscheidel, E., 2004, "Experimental Investigation of a High Pressure Ratio Aspirated Fan Stage," ASME Paper No. GT2004-53679.
[6] Breugelmans, F. A. H., and Carels, Y., 1984, "Influence of Dihedral on the Secondary Flow in a Two-Dimensional Compressor Cascade," ASME J. Eng. Gas Turbines Power, **106**, pp. 578–584.
[7] Sasaki, T., and Breugelmans, F. A. E., 1997, "Comparison of Sweep and Dihedral Effects on Compressors Cascade Performance," ASME Paper No. 97-GT-2.
[8] Weingold, H. D., and Neubert, R. J., 1995, "Reduction of Compressor Stator Endwall Losses through the Use of Bowed Stators," ASME Paper No. 95-GT-380.

Effects of Geometry on Brush Seal Pressure and Flow Fields—Part I: Front Plate Configurations

Yahya Dogu[1]
Department of Mechanical Engineering,
Kirikkale University,
Yahsihan, Kirikkale 71451, Turkey
e-mail: ydogu@kku.edu.tr

Mahmut F. Aksit
Faculty of Engineering and Natural Sciences,
Sabanci University,
Tuzla, Istanbul 34956, Turkey
e-mail: aksit@sabanciuniv.edu

Pressure and flow fields lay at the basis of such common phenomena affecting brush seal performance as bristle flutter, blow-down, hang-up, hysteresis, pressure stiffening, wear, and leakage. Over the past two decades of brush seal evolution, manufacturers and researchers have applied many geometric configurations to the front and backing plates of a standard brush seal in order to control the flow field and consequent seal performance. The number of studies evaluating the effect of geometric configurations on the brush seal flow field remains limited in spite of the high number of filed patent disclosures. This study presents a numerical analysis of brush seal pressure and flow fields with regard to common conceptual front plate configurations. A CFD model has been employed to calculate pressure and flow fields in the seal domain. The model incorporates a bulk porous medium approach for the bristle pack. The effectiveness of various conceptual geometries has been outlined in terms of flow field formation. Results disclose unique effects of geometry on pressure and flow fields such that a longer front plate drives outward radial flow while playing a protective role against upstream cavity disturbances. Findings also indicate that variations in front plate geometry do not directly affect leakage performance. A long front plate or damper shim considerably changes the flow field while at the same time having limited effect on the pressure field. Moreover, a strong suction towards the clearance enhances inward radial flow in clearance operation.
[DOI: 10.1115/1.2101857]

1 Introduction

Developments in brush seal design have demonstrated the significance of the flow field dictating seal dynamics and performance. As illustrated in Fig. 1, early designs utilized short front plate configuration. Welded at the outer periphery, front and backing plates clamp the bristle pack. The straight backing plate is extended to provide mechanical support for tiny bristles. This geometry is referred to as the standard or conventional brush seal. The bristle pack is divided radially into two distinct regions, which are labeled the fence height and upper regions (Fig. 1). The fence height is the radial height between bristle tips and backing plate inner diameter. The upper region, on the other hand, is the rest of the bristle height out to the bristle pinch point.

The aim of brush seal evolution and continued efforts at development have been to raise brush seal performance, benefits, and usage. A review of the literature reveals that most of the improvements and disclosures to date have focused on the geometry of front and backing plates. The number of issued patents dealing with brush seal geometry is considerably high. However, there is a clear lack of literature on front and backing plate configurations in terms of pressure and flow fields. This study investigates the effect of front plate geometry on brush seal pressure and flow fields. The impact of backing plate geometry on seal flow field is intended to be the subject of another study.

1.1 Importance of Flow Field on Brush Seal Dynamics. Flow analyses of the standard brush seal [1] show that the accumulated flow diffusion into the bristle pack governs a strong inward radial flow over the backing plate for contact operation. The inward flow peaks around the backing plate corner, joining the axial flow in the fence height region before escaping into the downstream cavity. For a clearance seal, however, flow predominantly occurs through clearance in addition to the contact seal flow patterns. Overall, pressure and flow fields within both the pack and the vicinity of the seal control the seal performance and dynamic behavior. This is what constitutes the focus of this study.

In addition to the brush seal geometry, the geometries of upstream and downstream cavities have a considerable impact on seal flow field development. The geometry of the upstream cavity, for instance, is not always favorable with respect to streamlining the incoming flow and minimizing flow disturbances including recirculation, turbulence, and impingement. In some applications, the brush seal is located between the labyrinth teeth, rotor steps, or near turning points that cause jet impingements or recirculations in the approaching flow [2]. In order to prevent undesired effects of such flow disturbances, various protective front plate geometries have been applied.

Brush seal dynamic issues including blow-down, hang-up, and pressure stiffening are related to one another. Blow-down is driven by inward radial flow as a result of the radial pressure gradient within the bristle pack. Blow-down helps close seal clearance, leading to an increase in leakage performance. If the seal is already in contact, however, blow-down increases contact loads and frictional heat reducing wear performance. Under operational pressure load, bristles may blow-down or remain hung-up depending on the balance of frictional and radial flow drag forces. Bristle hang-up occurs primarily when the seal is subjected to rotor excursions under large pressure loads.

Bristle flutter and the resulting uneven wear are also related to pressure and flow fields. The flutter is driven by the interaction of upstream flow with the first row of bristles in the form of flow momentum, attack angle, turbulence level, and swirl. Flow-

---

[1] To whom correspondence should be addressed.

Contributed by the Aeromechanics Committee of ASME for publication in the JOURNAL OF TURBOMACHINERY. Manuscript received January 14, 2005, final manuscript received July 15, 2005. Review conducted by D. Prasad.

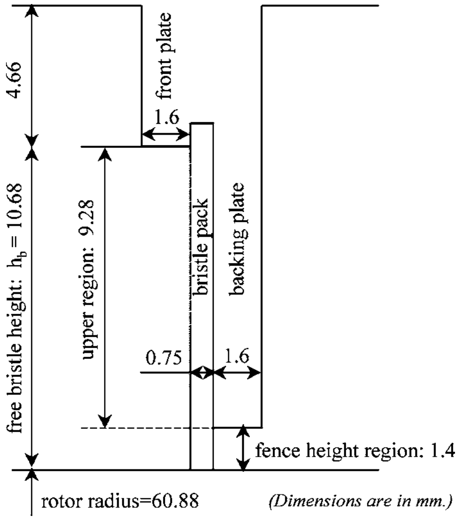

Fig. 1 Schematic of brush seal

induced flutter leads to instability and failure of upstream bristles. Subsequent exposure of other bristle rows to the same unsettling excitation may result in overall seal degradation and failure.

While seal dynamic issues are related, they may have counteracting effects on seal performance. The complex relation and balance between the dynamic issues cannot be understood without a thorough understanding of how underlying pressure and flow fields operate. Improving brush seal performance requires the control of pressure and flow fields.

1.2 Studies on Front Plate Configurations. For the most part, focused research on front plate configurations appears to be limited. Other than a few articles [3–6], the majority of available literature is in the form of patent disclosures. The few existing articles focus only on seal stiffness in relation to various front and backing plate configurations. For example, Short et al. [4] experimentally studied seal stiffness by incorporating a damper shim in combination with a backing plate relief. They measured reduction in both bristle blow-down and hysteresis using the combination. Berard and Short [5] tested another combination with relief in both the backing and long front plates. Providing relief at the long front plate reduced seal stiffness. The front plate relief contribution on overall bristle stiffness was negligible beyond a relief depth of 0.508 mm (0.020 in.). O'Neil et al. [6] applied a perforated shield in front of the bristle pack for dual stage seals. The shields worked well to prevent bristle flutter and instability.

1.2.1 Overview of Patents on Long Front Plate Configurations. A review of patent databases reveals the existence of several disclosures that suggest various forms of long front plate configurations. For instance, with regard to dual stage sealing applications, Tseng et al. [7] proposed placing a honeycomb type of baffle plate between two seals to reduce such flow disturbances as recirculation, turbulence, and swirl, in approaching flow to downstream seal. In their study, they also applied bypass holes and an extending flange on the backing plate of upstream seal to eliminate flow disturbances degrading the downstream seal. Their goal was to reduce bristle wear associated with flow disturbances and outward radial flow. At the same time, they related excessive wear of front bristles to such flow disturbances. They also attempted to use an inlet flow guide on a long front plate to streamline the flow approaching the seal [8].

Similar to what Tseng et al. did in their application [7], Millener and Edmunds [9] introduced a porous front plate. They argued that the porous front plate reduced disturbing forces on the bristles by modifying flow patterns to minimize lift off. They presented numerical flow visualization data indicating that an inward radial flow could be induced in front of bristle packs through the application of a porous front plate.

Hoffelner [10] and Gail et al. [11,12] presented a generalized long front plate with a covering ring in contact with bristles. They claimed that the ring would maintain bristle stability and compensate excitations by eccentric rotor motion. Gail et al. [11,12] also tried various porous shields upstream of the front plate to reduce flow swirl.

Another proposal regarding long front plates was made by Dinc et al. [13,14]. They suggested using a long front plate with holes and an extended ledge. The aim of this configuration was the prevention of bristle flutter ordinarily caused by outward radial flow by purging relief between the bristle pack and front plate. Holes on the front plate were placed near the fence height region to channel and streamline the flow so as to minimize turbulence.

Albers et al. [15] applied an annular ring touching upstream bristles. They proposed to damp bristle flutter due to pressure pulsations or rotor excitations.

Similarly, Kono [16] placed a ring in the gap between the long front plate and the upstream seal face. However, in contrast to previous applications [15], Kono's aim was to increase sealing performance by preventing fluid from entering the gap, and to minimize radial pressure drop over bristle pack.

1.2.2 Overview of Patents with Damper Shim Applications. Unlike a long front plate with relief, a damper shim maintains contact with upstream bristles. Tseng et al. [17] utilized different damper shims to reduce upstream bristle chamfering by absorbing the bristle vibration. Basu and Short [18] applied damper shims with a recessed backing plate. They aimed at reducing the uneven wear of front bristles by minimizing the inward radial flow. Carter [19] introduced overlapping damper shim combinations in contact with upstream bristles. Carter suggested that the arrangement would dampen bristle vibrations resulting from movement of pressurized fluid and circumferential velocity.

1.3 The Scope of the Present Work. Although related literature indicates the importance of front plate configuration and resulting flow field, apart from Millener and Edmunds [9], published studies have not provided sufficient evidence demonstrating the effect of front plate geometry on flow field. The goal of geometric modifications is to increase seal performance through the control of flow field and consequent brush seal dynamics. This study presents a comparative CFD analysis of pressure and flow fields on conceptual front plate configurations. Detailed evaluation is performed for different flow properties by scanning the entire brush seal domain. The effectiveness of modifications is also discussed by evaluating pressure and flow fields.

2 CFD Model

A two-dimensional axisymmetric CFD model is employed for the flow field investigation. The model domain consists of upstream and downstream cavities and a bristle pack as shown in Fig. 2. Front and backing plates are included as solid boundaries. The bristle pack is treated as a bulk porous medium through application of a non-Darcian transport equation. Details of the present bulk porous medium approach and utilized CFD model are given by Dogu [1] and will be summarized here for completeness.

The flow is assumed to be compressible, complying with the ideal gas law, and turbulent, following the k-ε turbulence model. The Navier-Stokes equations for flow through up- and downstream cavities can be written in Cartesian tensor notations as

$$\frac{\partial \rho u_i}{\partial x_i} = 0 \tag{1}$$

$$u_j \frac{\partial \rho u_i}{\partial x_j} = -\frac{\partial P}{\partial x_i} + \mu \frac{\partial^2 u_i}{\partial x_j \partial x_j} \tag{2}$$

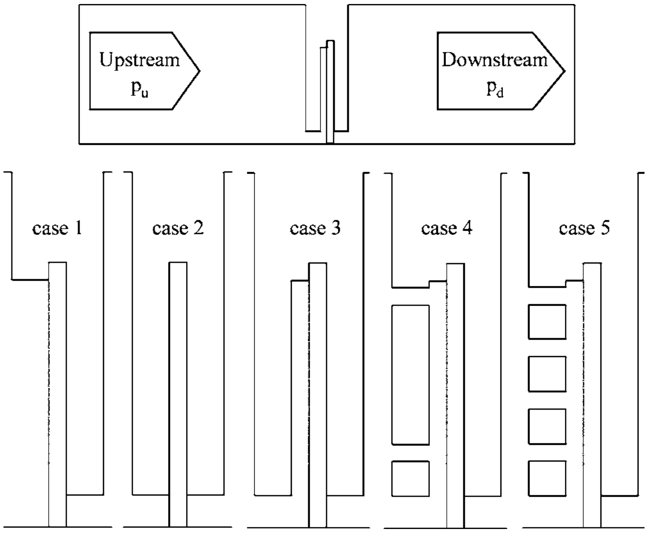

Fig. 2 Front plate configurations

In addition to inertial and viscous forces (as in Eq. (2)), flow through a porous bristle pack is subject to additional resistance forces due to fluid friction at solid bristle surfaces. Among the many transport models for the porous media, the transport equation for the porous bristle pack is represented with the following non-Darcian porous media resistance equation:

$$-\frac{dP}{dx_i} = (\alpha_i|\bar{u}_i| + \beta_i)\bar{u}_i \qquad (3)$$

where x_i represents the orthographic flow directions and $\bar{u}_i$ is the superficial velocity in the direction of x_i. The superficial velocity refers to the velocity that would exist for the same volumetric rate of flow in the absence of porous medium. As in the present work, this bulk porous medium approach has been selected as the best fit to the flow within the porous bristle pack and is the one employed and validated by many researchers [1,20–27]. The equation has a nonlinear form defining a balance equation between pressure gradient and effective flow resistance terms. The coefficients of α and β represent spatially anisotropic effective inertial and viscous flow resistance terms, respectively. In general, frictional forces within the porous bristle pack (described on the right-hand side of Eq. (3)) are added to the right-hand side of the momentum equation (Eq. (2)) to represent additional flow resistance forces. However, as in the case for the compact bristle pack under pressure load, inertial and viscous forces in Eq. (2) for the highly resistive porous medium become negligibly small relative to frictional forces due to fluid-solid interaction. Therefore, Eq. (3) stands alone for flow transport in porous bristle pack for the present bulk porous medium approach.

The aim in the bulk porous medium approach is to replace the flow through voids among randomly distributed bristles with a flow through a resistive porous medium that will represent real life pressure and flow fields within the bristle pack and transmit the measured flow rate. In the analysis, the pressure and flow fields within the bristle pack are determined by solving the porous medium transport equation that is a function of algebraic flow resistance coefficients, α and β. The resistance coefficients are functions of many parameters: geometric configuration, operating conditions, and bristle pack dynamic issues. To account for all these parameters in a balanced manner, the flow resistance coefficients are calculated using experimental data. From the beginning of brush seal research, typically three physical quantities have been measured: flow rate, radial pressure distribution on the backing plate, and axial pressure distribution on the rotor. For a comprehensive calibration, the present bulk porous medium approach incorporates all three measured experimental data. After an extensive effort at calibration, radial pressure on the backing plate, axial pressure on the rotor, and leakage are all compared well with experimental data and other porous medium analyses. Details of the calibration data will be discussed in the results and discussion section.

2.1 Front Plate Configurations.

In order to cover common concepts while keeping the number of analyses manageable, five different front plate configurations, as illustrated in Fig. 2, have been selected. The standard seal geometry, which is referred to as case 1, has a short front plate and straight backing plate, as given by Bayley and Long [20] and Turner et al. [21] (Fig. 1). This configuration is set as the baseline. The model uses a bristle pack thickness of 0.75 mm (0.0295 in.). The thickness of the front and backing plates is 1.6 mm (0.0630 in.). The fence height is set at 1.4 mm (0.0551 in.) with a free bristle height of 10.68 mm (0.4205 in.).

In the second configuration, a long front plate in contact with the bristle pack is employed. In terms of flow formation, this case represents a damper shim application. Case 3 is a typical long front plate configuration with a relief. Relief depth is set at 0.75 mm (0.0295 in.), which is comparable to the thickness of the bristle pack. The last two cases (4 and 5) are variations of case 3, with two and four holes on the long front plate, respectively. The reason for making a distinction between cases 4 and 5 is to illustrate the effect of front plate hole configuration. Hole size is set at 0.75 mm (0.0295 in.). In case 4, two holes are placed at the outer and inner ends of the front plate to visualize the stabilizing effect of flow injection at the extreme ends. Case 5 has equally spaced multiple holes to represent porous or perforated front plate applications. All of the front plate holes are treated as circumferential slots in the two-dimensional axisymmetric CFD model. The effects of front plate holes are indeed three-dimensional. If there are limited holes set far apart, the two-dimensional analysis locally investigates the flow around the holes. When the number of holes over the circumference is large, as in the case of perforated porous shields [7,9,13], a two-dimensional analysis would be sufficient to capture their effects. Meanwhile, in some applications, these holes are applied as a set of circumferential slots that are also suitable for a two-dimensional treatment. Overall, the two-dimensional analysis sufficiently captures the flow behavior in the effected region around the holes.

2.2 Analysis Parameters and Boundary Conditions.

Brush seals applications have been expanding and have come to include a wide variety of geometry and operating conditions. The effects of front plate configurations would differ depending on a number of parameters, including geometry (bristle diameter and arrangement, dimensions of brush seal and assembly region, etc.) and operating conditions (pressure load, temperature, bristle tip to rotor clearance, working fluid, rotor speed, etc.). When accompanied by the five configurations specified above (Fig. 2), the large number of analyses required to investigate all the parameters would be beyond the scope of a single paper. Indeed, the aim of the present study is to investigate the fundamental effects of front plate configurations relative to each other for a certain set of operating conditions and baseline seal geometry. In order to provide a comparison, the geometry and operating conditions have been determined to represent seals for which test results are widely reported in the literature.

Besides geometric configurations, seal-operating clearance is a significant parameter affecting the shape of flow field. Contact and clearance operating modes develop distinct flow fields. Therefore, both operating modes have been included in the analyses. All clearance analyses are performed introducing a typical 0.1 mm (0.0039 in.) gap between rotor and bristle tips.

In addition to a bristle pack, the model includes up- and downstream cavities that are axially extended to ensure fully developed

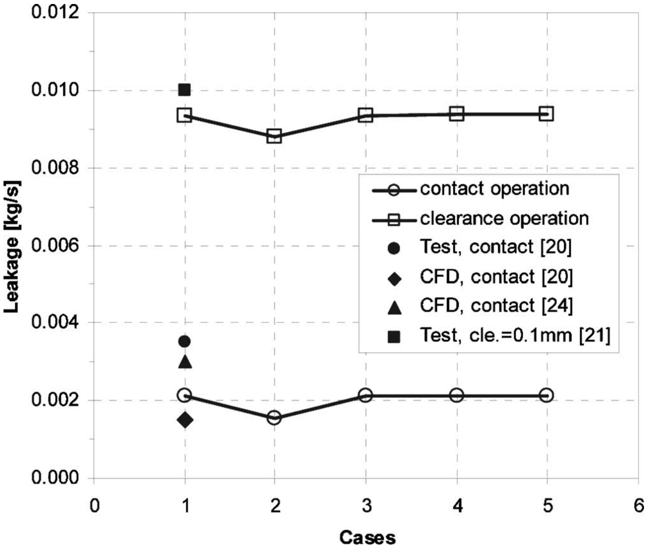

Fig. 3 Leakage evaluation for front plate configurations

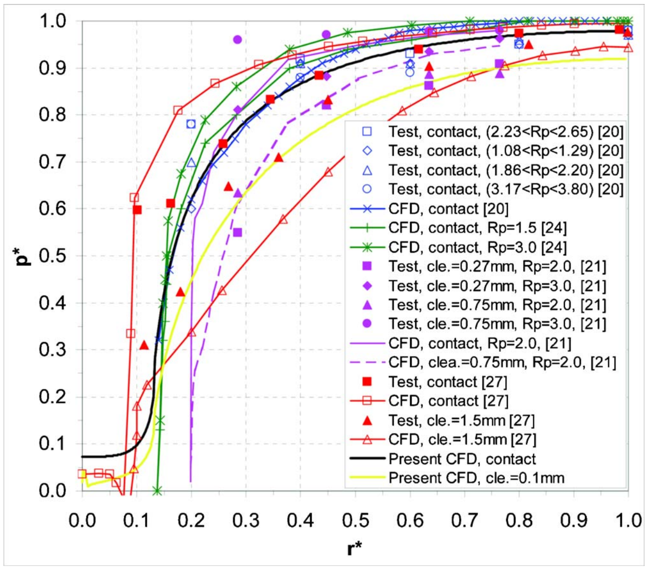

Fig. 5 Radial pressure distribution on backing plate

flow conditions, as shown in Fig. 2. The domain is finely meshed to ensure a mesh-independent solution. The typical mesh size is on the order of 1×10^{-5} mm in brush seal region. Pressure conditions are prescribed at upstream and downstream boundaries as 150 and 100 kPa. Air properties are taken as constant at inlet temperature of 20°C. In fact, brush seals typically operate at higher temperatures. With increasing temperature, a leakage reduction is observed due to a decrease in density with temperature. When the ideal gas law is applied, preserving the continuity, density reduction yields a smaller mass flow rate for the same volumetric flow. As the effect of increasing temperature on flow velocities and patterns is minimal, the present study provides a basic comparison for front plate geometries. The bristle pack is defined as a porous medium whose flow resistance coefficients are prescribed through a calibration procedure [1]. Rotation is not included in the current analyses. Rotor rotation drives a tangential flow, which impedes the overall leakage rate. However, its effect on axial and radial flow formations remains limited within the seal beyond the fence height region. Typical clearance operation would involve strong axial flow patterns with higher flow speeds than that of rotation-induced tangential flow speeds. When flow patterns around and within the brush pack are considered, the disturbance of swirl generated by rotation remains localized near the rotor surface without affecting the axial and radial flow patterns beyond the fence height region. Considering the numerous characterization data collected through static room-temperature seal tests, though ignoring the rotation, the current analysis provides a basic yet meaningful comparison of front plate configurations in controlling the flow patterns within and around the brush pack. Detailed sensitivity analyses with dimensional variations on plate thickness, gaps, diameters of holes, etc. are beyond the scope of this work, and hence will be avoided. The present work aims to evaluate overall pressure and flow fields for different front plate configurations.

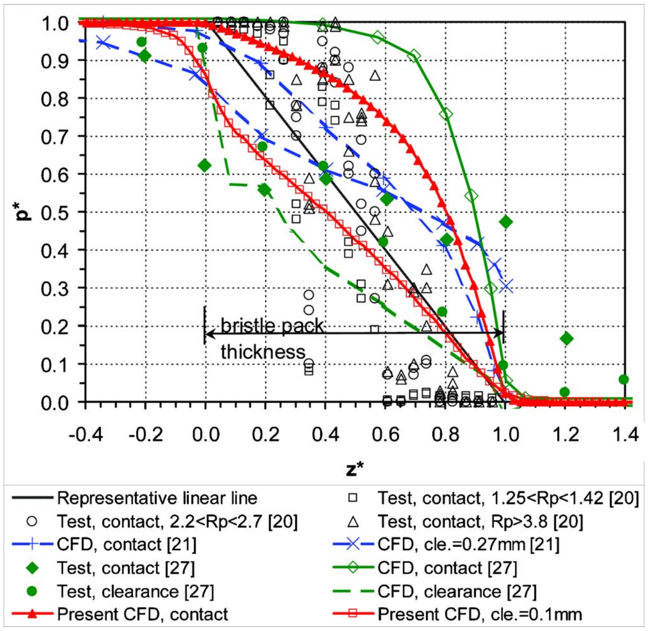

Fig. 4 Axial pressure distribution on rotor surface

3 Results and Discussion

The importance of the flow field in the vicinity and within the bristle pack requires a thorough evaluation of model results. To reveal hidden details that may not be apparent in overall pressure and flow field maps, different flow properties are plotted upstream of the bristle pack. Results for contact and clearance operations are separately evaluated for all five configurations.

3.1 Leakage Evaluation and Verification. The first criterion to be evaluated is the effect of geometric variations on overall leakage performance (Fig. 3). Results indicate that front plate modifications do not affect seal leakage. For example, except for case 2, leakage for all contact operations is around 0.0021 kg/s while clearance operation results in a more than four times greater increase, reaching 0.0094 kg/s. Leakage results for the calibrated set of flow resistance coefficients compare well with published experimental data and other CFD models [20,21,24], as illustrated in Fig. 3.

For case 2, the calculated leakage of 0.0016 kg/s for contact operation and 0.0088 kg/s for clearance operation is less than that in other cases. The representative damper shim prevents flow penetration above the fence height. This eliminates leakage contribution by inward radial flow from the upper region, leaving the fence height region as the only leakage path.

Before analyzing pressure and flow fields further, verification of the model is done by comparing radial pressure on the backing plate and axial pressure on the rotor with experimental and other

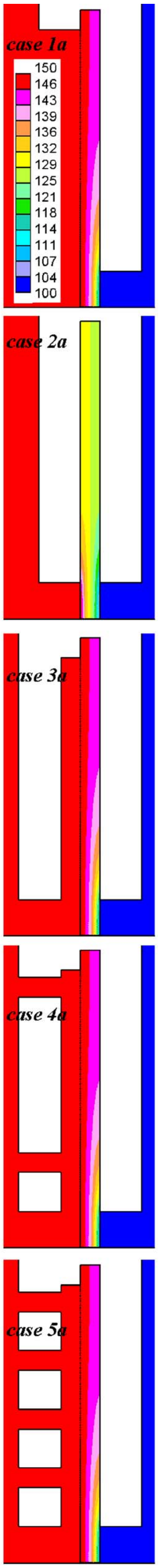

Fig. 6 Pressure (kPa) for contact operation

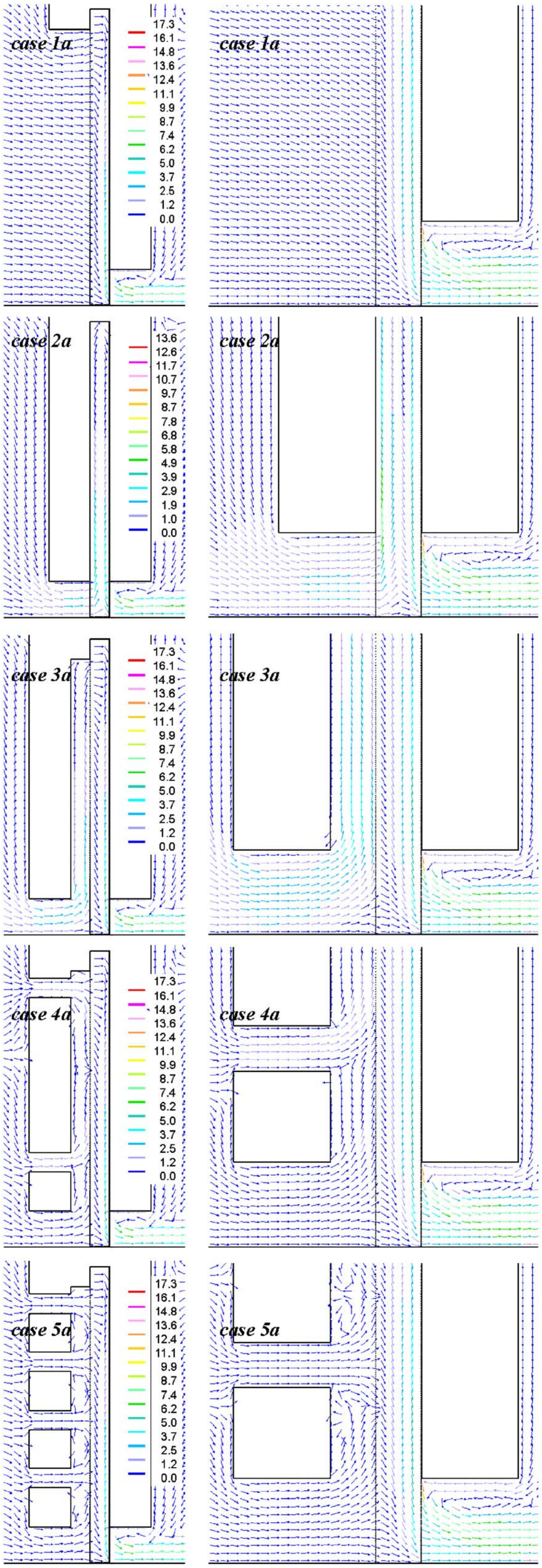

Fig. 7 Velocity vectors (m/s) for contact operation

porous medium model data [1,20,21,24,27]. The comparison is performed for the baseline configuration of case 1, which is similar to those available in published studies. During the course of calibration, considering physical backing plate support, the brush seal is divided into two permeable regions: fence height and upper regions. Flow resistance for the upper region was found to be 20% higher than for the fence height region, which matched the experimental data. This was expected, as bristles compact over the back-

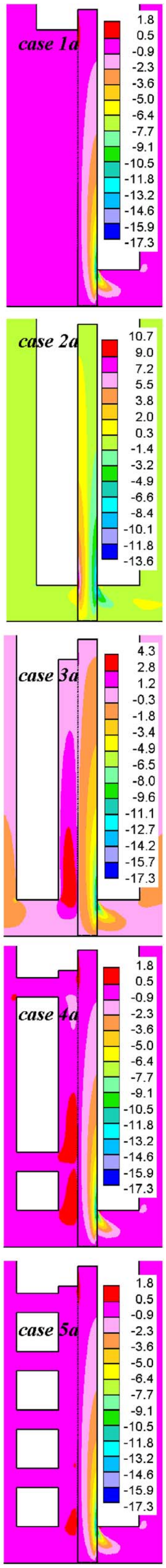

Fig. 8 Radial velocity (m/s) for contact operation

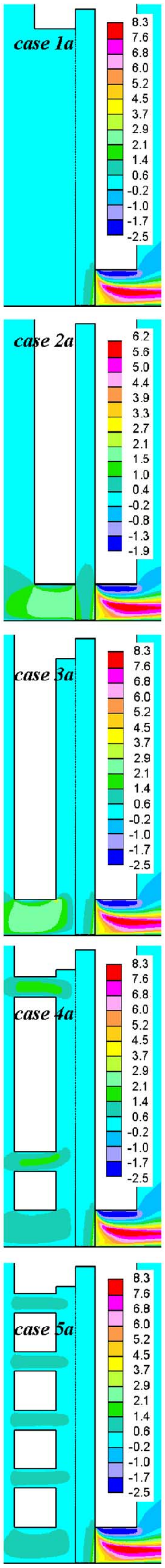

Fig. 9 Axial velocity (m/s) for contact operation

ing plate under axial pressure load. The calibrated set of flow resistance coefficients for the fence height region are inertial resistances, $\alpha_i=1\times10^5$ kg/m^4 and $\alpha_k=7.5\times10^6$ kg/m^4, and viscous resistances, $\beta_i=1\times10^5$ kg/m^3-s and $\beta_k=4.5\times10^7$ kg/m^3-s. The subscripts, i and k, denote the radial and axial directions, respectively.

3.1.1 Axial Pressure on Rotor Surface. Figure 4 shows the axial variation of pressure on the rotor surface. Comprehensive data have been compiled from previous tests and analyses

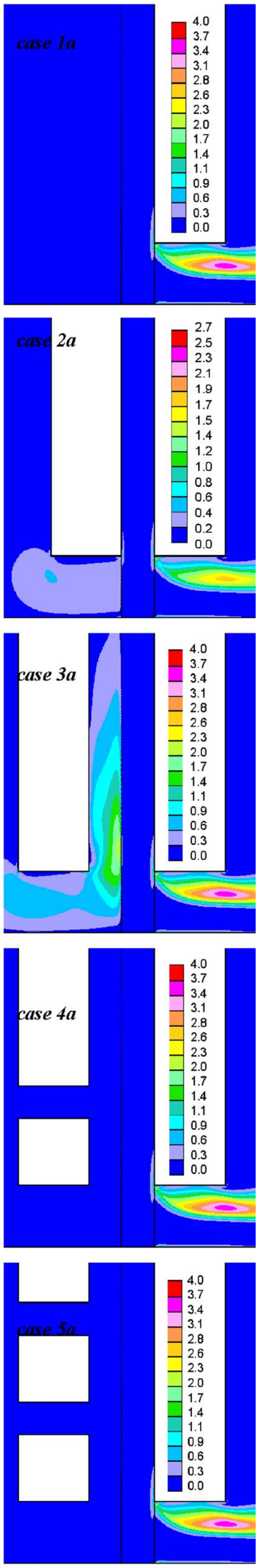

Fig. 10 Turbulent kinetic energy $(\mathrm{m}^2/\mathrm{s}^2)$ for contact operation

[20,21,27] for contact and clearance operations. The pressure is measured using pressure taps embedded in the rotor. In order to show all the data on the same scale, dimensionless pressure is defined with respect to upstream and downstream pressures, $p^* = (p-p_d)/(p_u-p_d)$. The axial distance is measured from upstream face of the bristle pack and normalized by dividing by the pack thickness. The normalized locations at $z^*=0$ and $z^*=1$ respectively correspond to the upstream and downstream face of bristle pack. The pressure drops from upstream to downstream through the bristle pack thickness. The data vary widely as seen in Fig. 4. The overall pressure variation trend for contact operation is such that a small drop in pressure is observed at the upstream half of the pack thickness. Most of the pressure drop occurs over the last one-third of the pack thickness through the downstream face. As expected, the downstream bristle rows are subject to higher-pressure loads. For the clearance operation, the pressure drop starts in front of the bristle pack due to the suction effect of clearance, roughly following a linear line. The present CFD analysis has a trend that is similar to that of the test data and other CFD results.

3.1.2 Radial Pressure on Backing Plate. Radial pressure on the backing plate is depicted in Fig. 5, which includes a wide range of data [20,21,24,27] concerning contact and clearance operations. In addition to dimensionless pressure, normalized radial distance from the rotor surface is utilized to allow comparison of all the data on the same scale. The radial distance is normalized by dividing that distance by the bristle free height between the rotor surface and the bristle pinch point: $r^*=y/h_b$. The data are distributed widely (Fig. 5). For contact operation, both test and CFD results show that the pressure on the backing plate for the upper half of the upper region is constant and nearly equal to the upstream pressure. The pressure gradually drops to the downstream pressure level near the backing plate corner. This distribution shows that there is a pressure gradient that extends from the upper to the fence height regions, which directs the flow radially inward. This flow pulls the bristles towards the rotor surface, resulting in blow-down effect. For clearance operation, the pressure drop is likely to spread towards the bristle root. The results from the current CFD analysis follow the trend similar to others.

Overall, as plotted in Figs. 3–5, the present bulk porous medium approach represents the pressure fields and leakage well when compared to experimental and other porous medium data.

3.2 Pressure and Flow Field Evaluation. Considering the high number of cases analyzed, the results for contact operation are grouped in Figs. 6–10 while clearance results are illustrated in Figs. 11–15. Results for contact and clearance operations are identified with notations "*a*" and "*b*," respectively. To reveal the details of flow properties, Fig. 16 presents a summary of different flow properties in front of the bristle pack. Pressure, radial velocity, axial velocity, and turbulent kinetic energy are separately studied at an axial section placed one-fourth of bristle pack thickness (0.1875 mm (0.0074 in.)) away from upstream bristles. Since the flow momentum hitting the bristle pack is the primary concern in brush seal dynamics, this axial section is to be located in such a way that flow properties are not affected by diffusion into the resistive bristle pack barrier, yet are sufficiently close to capture flow momentum. For all line plots presented in Fig. 16, radial distance from the rotor surface, y, is normalized with respect to total free bristle height, h_b, as $r^*=y/h_b$. The fence height corresponds to value of $r^*=0.13$.

3.2.1 Pressure Field. The pressure field drives flow and velocity vectors. Pressure contours indicate similar trends for all cases with contact (Fig. 6) and clearance operation (Fig. 11) except for case 2. Generally, most pressure drop occurs on the downstream side of the bristle pack in the fence height region. Around the bristle root region, pressure within the bristle pack is close to that of the upstream pressure; therefore, the axial pressure gradient is small. For case 2, more evenly distributed axial pressure contours are observed. Unlike other cases, pressure at the upper bristle pack region is close to the average of upstream and downstream pressures.

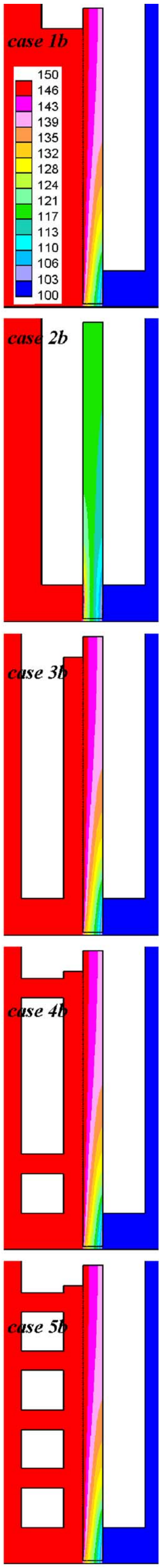

Fig. 11 Pressure (kPa) for clearance operation

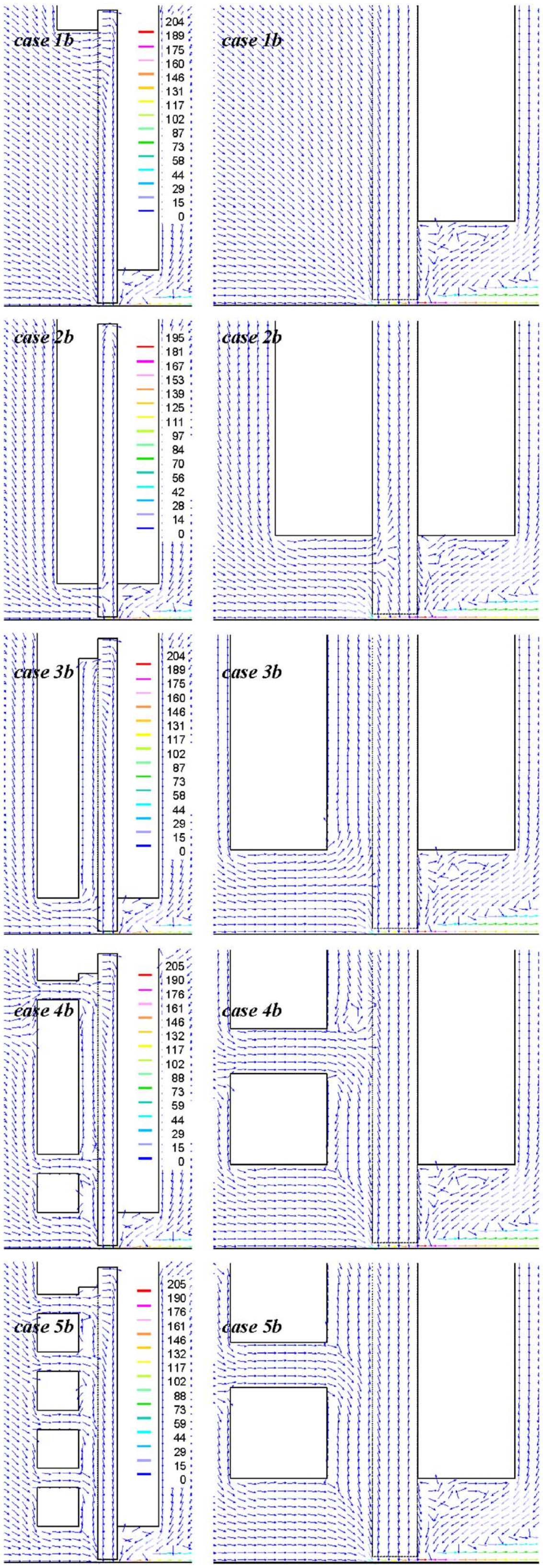

Fig. 12 Velocity vectors (m/s) for clearance operation

For all clearance operations, pressure contours have similar profiles (Fig. 11). At fence height, pressure drop is more evenly distributed axially over the bristle pack than is contact operation.

Radial pressure distribution in front of the bristle pack is plotted in Fig. 16(*a*). Pressure is normalized with respect to upstream and downstream pressures as defined $p^{*}=(p-p_d)/(p_u-p_d)$. For all contact operations, radial pressure in front of the bristle pack is constant and equal to upstream pressure with negligible deviations closer to the rotor surface. However, the clearance operation gen-

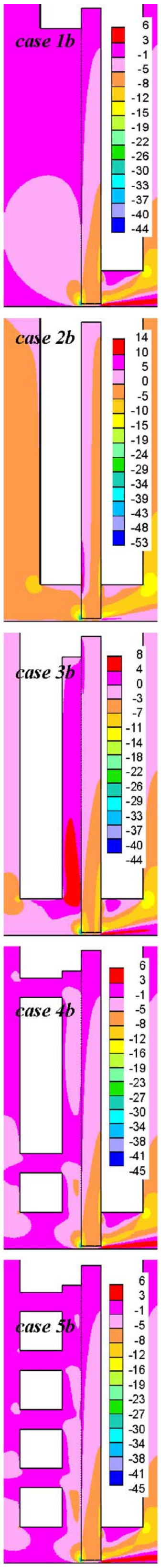

Fig. 13 Radial velocity (m/s) for clearance operation

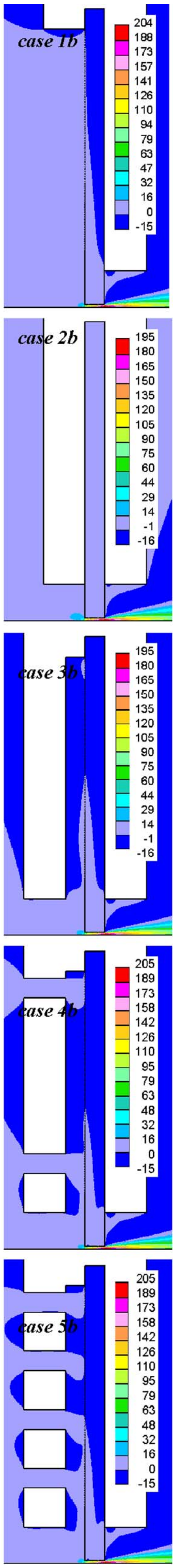

Fig. 14 Axial velocity (m/s) for clearance operation

erates a slight drop in upstream pressure in the clearance region.

Overall, all front plate configurations produce similar pressure fields except for case 2. Unlike other cases, pressure drop is not confined to fence height, but rather spreads throughout the entire seal height.

3.2.2 Velocity Vectors. Velocity vectors show overall flow patterns. Contact and clearance operations are illustrated in Figs. 7 and 12, respectively. For each case, two vector plots are produced, one for the overall seal flow field and the other for flow details

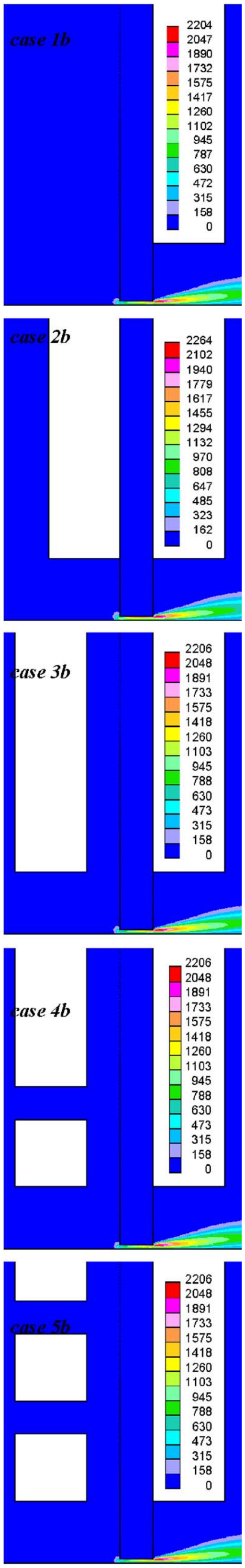

Fig. 15 Turbulent kinetic energy (m^2/s^2) for clearance operation

around the critical fence height region.

What is immediately clear with respect to velocity vectors is that the long front plate acts as a barrier to upstream cavity disturbances. This has the consequence of directing the approaching flow towards the fence height region. The other observation is that excessive flow through clearance dominates the entire flow field in all clearance operations.

3.2.3 Radial Velocity. Radial velocity is one of the main drivers affecting the onset of bristle lift and flutter. It is plotted in Fig. 8 for contact and Fig. 13 for clearance operations. Positive values represent radially outward flow direction. The standard short front plate yields inward radial flow along the upstream bristle face. Outward radial flow is observed for all long front plate configurations at the inner edge of the front plate. For cases 2 and 3, the front plate inner edge region is the only opening through which flow into the relief cavity and the bristle pack is possible. For case 2, a representative damper shim prevents flow penetration above the fence height. As also observed by Millener and Edmunds [9], a strong outward radial flow forms at the inner edge of the damper shim. Even with additional flow through front plate holes in cases 4 and 5, a small outward radial flow may persist.

In contact operation, the outward radial velocity upstream bristle face at the front plate edge level is about 1.8 m/s for cases 4a and 5a, while reaching 4.3 m/s for case 3a (Fig. 8). Maximum outward velocity among all cases occurs for case 2a at 10.7 m/s. The increasing number of front plate holes enhances inward radial flow in front plate relief promoting blow-down. Flow entering through holes locally separates into inward and outward directions, resulting in fluctuations in radial velocity as seen in Fig. 16(*b*).

For all contact operations, flow velocity peaks at the backing plate inner edge (Figs. 7 and 8). Accumulated flow penetration into bristle pack forms a strong inward radial flow over the backing plate. Following the trend in leakage rates, maximum inward radial flow reaches −14 m/s in case 2a, while all other cases it peaks around −17 m/s.

In addition to the flow patterns developed in contact operations, a strong axial flow is superimposed for clearance operation (Fig. 12). Suction towards clearance enhances inward radial flow for the entire brush seal (Fig. 13). However, a small outward flow in the front relief region remains in case 3b. Overall, the location of maximum inward flow shifts from the backing plate inner edge to the upstream inner edge of the bristle pack for all clearance operations. The maximum inward radial velocity upstream bristle face at clearance inlet is −53 m/s for case 2b, and −44 m/s for all other cases.

Detailed evaluation of flow field over upstream face of the bristles reveals that the clearance operation enhances the inward radial flow (Fig. 16(*b*)). For contact operations, in case 1a, a slight inward radial flow is distributed over the entire bristle face since the bristle face is open to the large upstream cavity. Cases 2a and 3a yield only outward radial flow. Case 3a has the maximum outward radial flow since the relief gap and bristle pack is filled with fluid through the front plate inner edge region as discussed above. However, cases 4a and 5a have both radial outward and inward flow due to impingement through front plate holes. The fluctuations are more pronounced for four holes, e.g., case 5a. Meanwhile, for clearance operations, inward radial flow is dominant for all cases except case 3b. The inward radial velocity exceeds −12 m/s for all clearance operations at the inner edge of the bristles. For case 3b, the bristle upstream face is subject to both inward and outward radial flows. Beyond the observed stagnation point at $r^*=0.075$, radial flow turns outward. This flow formation can be enhanced with the effects of turbulence and could trigger bristle flutter, depending on the balance of inward and outward aerodynamic forces. Radial flow fluctuations for cases 4b and 5b remain entirely negative.

3.2.4 Axial Velocity. Axial velocity is known to determine overall leakage rates. Driven by axial flow and strong turbulence cells, the balance of axial pull and push forces on the upstream bristle rows contributes to bristle dynamics.

For contact operation, maximum axial velocity is reached when

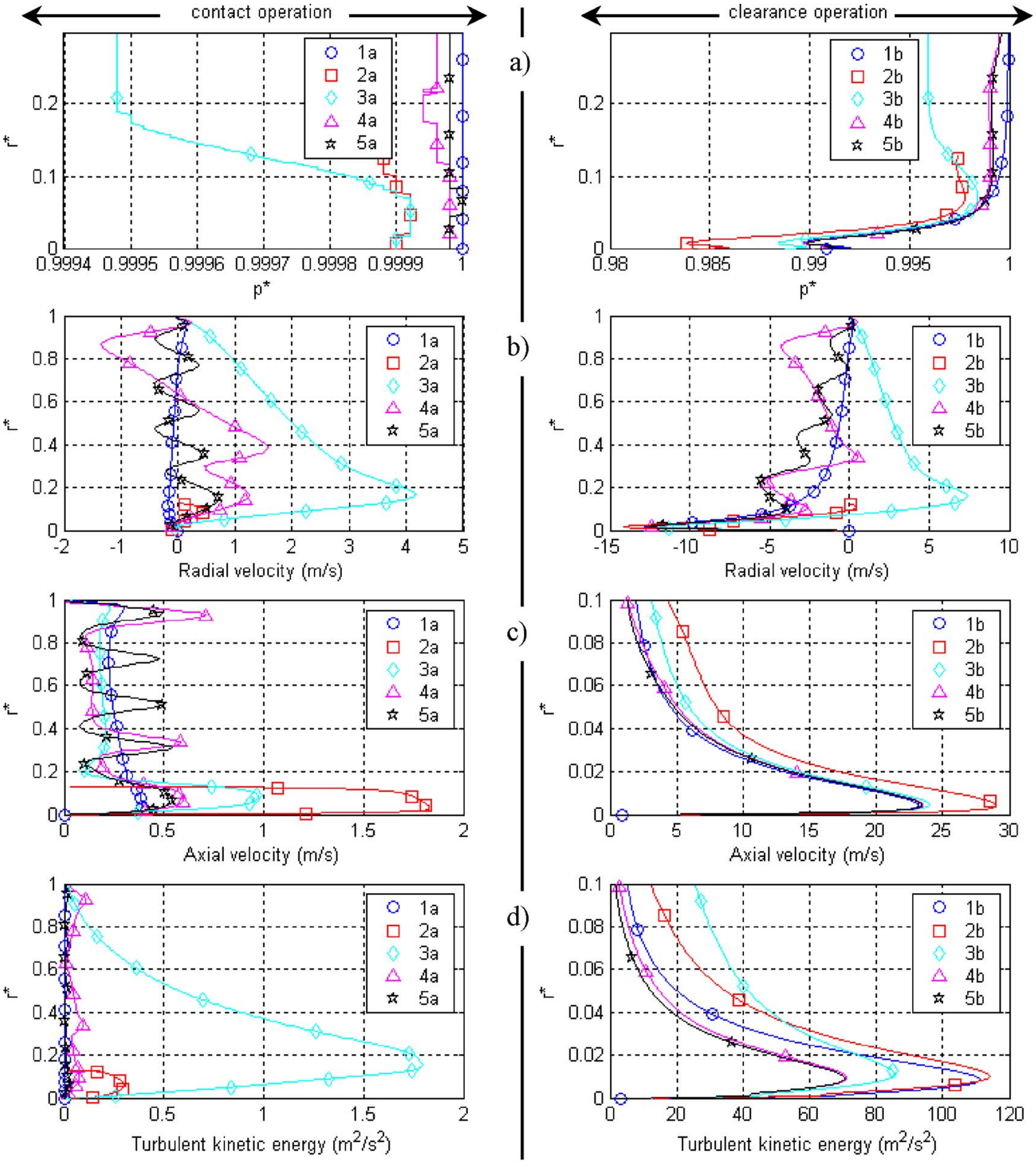

Fig. 16 Flow properties in front of bristle pack: (*a*) pressure, (*b*) radial velocity, (*c*) axial velocity, and (*d*) turbulent kinetic energy

inward radial flow turns axial around the backing plate inner edge and merges with the main axial flow through the fence height (Fig. 9). The merging radial flow drives recirculation underneath the backing plate edge. Maximum axial velocity is around 8 m/s for all front plate cases (except for case 2a, where it is around 6 m/s), with positive value representing downstream flow direction. As plotted in Fig. 16(*c*), axial velocity is uniform around 0.3 m/s throughout the bristle height for case 1a. The long front plate channels the entire flow to the fence height region, thereby increasing axial velocity. Front plate holes form local flow impingements (Fig. 16(*c*)).

Unlike contact operation, maximum axial velocity forms at the clearance outlet at around 205 m/s (except for cases 2b and 3b at 195 m/s) for all clearance operation (Fig. 14). The effect of accelerated flow due to clearance is evident with the excessive increase in axial velocity. Front plate configurations do not considerably affect axial flow for clearance operation. The large variations near the fence height are evident in Fig. 16(*c*), which presents a close up for radial distribution in front of the bristle pack. The maximum axial velocity exceeds 20 m/s at the clearance gap. Radially further out, axial velocity decreases exponentially to 2 m/s at $r^*=0.1$.

3.2.5 Turbulent Kinetic Energy. Seal stability is affected by the level of upstream turbulence, which is defined as the energy of fluctuating flow velocity, $k=\overline{u_i'^2}/2$. Turbulent energy peaks at maximum velocity locations under the backing plate and clearance for contact and clearance operation, respectively.

As illustrated in Fig. 10, turbulent kinetic energy is relatively small (up to 4 $\mathrm{m^2/s^2}$) for contact operation. Higher outward radial velocity results in higher energy levels at the upstream face of the bristle pack for case 3a. Due to outward radial flow, the long front plate produces more turbulence in front of the bristle pack. Front plate holes, however, help minimize this turbulence level. On the other hand, turbulent kinetic energy peaks at a much higher value for clearance operation, exceeding 2200 $\mathrm{m^2/s^2}$ at the downstream side of the clearance (Fig. 15).

Radial distribution of turbulent energy is examined in front of the bristle pack. This distribution is plotted in Fig. 16(*d*). Case 3a shows maximum turbulence levels within other contact operations. However, energy remains rather limited compared to any of the clearance operations. To illustrate steep changes near fence height, Fig. 16(*d*) presents a close-up of radial distribution. High flow rates at clearance drive energy levels to the maximum, while it decreases exponentially further out. The long front plate with holes (cases 4b and 5b) reduces the maximum value of turbulence at the clearance inlet region from 120 to 70 $\mathrm{m^2/s^2}$.

4 Conclusions

Understanding seal pressure and flow fields is necessary for advanced brush seal designs. Using a CFD analysis, pressure and flow fields have been investigated for common conceptual front plate configurations. A detailed literature survey including comprehensive-up-to date patent disclosures on front plate geometries has been presented. Similarly, the effects of backing plate geometries have been studied in the companion paper [28].

The following conclusions have been reached from the results of analyses of both contact and clearance operations.

- The use of a long front plate or damper shim considerably changes the flow field when compared to standard brush seal configuration, while having a limited effect on pressure field.
- Distinct flow field variations are observed between damper shim and other front plate applications.
- When used with a relief, the effect of long front plates on leakage is negligible. The use of a damper shim reduces leakage by preventing diffusion in the upper region. However, this benefit diminishes for clearance operations. A typical clearance of 0.1 mm (0.0039 in.) increases leakage rates over four times that of contact operation.
- Although a long front plate plays a role in preventing such upstream cavity flow disturbances as jets or recirculations, it generates outward radial flow within the axial relief between the front plate and bristles. Front plate holes suppress this outward flow. For clearance operations, a strong suction towards the clearance enhances inward radial flow over the entire seal region.
- Dominant flow patterns are different for contact and clearance operations. The location of maximum inward flow shifts from the backing plate inner edge for contact operation to the upstream inner edge of the brush pack for clearance operation.

Observed flow formations provide insight into seal dynamic issues in relation to pressure and flow fields. For instance, excessive inward radial flow in front of the bristle pack may lead to higher blow-down yielding uneven seal wear. Outward radial flow generated by front plate applications may combine with turbulent excitation to push seal to instability. Overall, inclusion of other significant parameters such as rotor rotation and heat generation will facilitate better understanding of brush seal dynamic behavior.

Acknowledgment

The authors would like to thank Dr. Raymond Chupp of General Electric Global Research Center for his valuable evaluation, discussions, and insightful comments.

Nomenclature

h_b = free bristle height, m
k = turbulent kinetic energy, $\mathrm{m^2/s^2}$
p = static pressure, Pa
p^* = normalized pressure, $p^*=(p-p_d)/(p_u-p_d)$
r^* = normalized radial coordinate, $r^*=y/h_b$
u = spatial velocity component, m/s
u' = fluctuating velocity component, m/s
$\bar{u}$ = superficial velocity, m/s
x = spatial coordinate direction, m
y = radial distance from rotor surface, m
z^* = normalized axial coordinate
α = inertial flow resistance coefficient, $\mathrm{kg/m^4}$
β = viscous flow resistance coefficient, $\mathrm{kg/(m^3\text{-}s)}$
μ = dynamic viscosity, Pa-s
ρ = density, $\mathrm{kg/m^3}$

Subscripts

d = downstream
i = spatial coordinate and radial direction
j = spatial coordinate and tangential direction
k = spatial coordinate and axial direction
u = upstream

References

[1] Dogu, Y., 2005, “Investigation of Brush Seal Flow Characteristics Using Bulk Porous Medium Approach,” ASME J. Eng. Gas Turbines Power, **127**(1), pp. 136–144.
[2] Dinc, S., Demiroglu, M., Turnquist, N., Mortzheim, J., Goetze, G., Maupin, J., Hopkins, J., Wolfe, C., and Florin, M., 2002, “Fundamental Design Issues of Brush Seals for Industrial Applications,” ASME J. Turbomach., **124**(2), pp. 293–300.
[3] Basu, P., Datta, A., Loewenthal, R., Short, J., and Johnson, R., 1994, “Hysteresis and Bristle Stiffening Effects in Brush Seals,” J. Propul. Power, **10**(4), pp. 569–575.
[4] Short, J. F., Basu, P., Datta, A., Loewenthal, R. G., and Prior, R. J., 1996, “Advanced Brush Seal Development,” AIAA paper no. 96–2907.
[5] Berard, G., and Short, J., 1999, “Influence of Design Features on Brush Seal Performance,” AIAA paper no. 99–2685.
[6] O’Neil, A. T., Hogg, S. I., Withers, P. A., Turner, M. T., and Jones, T. V., 1997, “Multiple Brush Seals in Series,” ASME paper no. 97-GT-194.
[7] Tseng, W.-Y., Glynn, C. C., Bristol, B. L., and Hetico, R. R., 1994, “Brush Seal,” US patent no. 5,318,309.
[8] Tseng, W.-Y., Bristol, B. L., Hetico, R. R., and Glynn, C. C., 1994, “Brush Seal,” US patent no. 5,335,920.
[9] Millener, P. J., and Edmunds, T. M., 1996, “Brush Seal with Porous Upstream Side-Plate,” US patent no. 5,496,045.
[10] Hoffelner, H., 1997, “Brush Seal for Turbo-Engines,” US patent no. 5,688,105.
[11] Gail, A., Michel, U., Pfister, E., Reisinger, L., and Miller, T., 1998, “Brush Seal for Turbo-Engines,” US patent no. 5,752,805.
[12] Gail, A., Michel, U., Pfister, E., Reisinger, L., and Miller, T., 2000, “Brush Seal for Turbo Engines,” US patent no. 6,077,038.
[13] Dinc, O. S., Dogu, Y., Battle, M. E., Albers, R. J., and Proctor, R., 2001, “Brush Seal Segment Having Bristle Damping,” US patent no. 6,293,554.
[14] Dinc, O. S., Albers, R. J., Dogu, Y., and Zhou, M., 2001, “Rotary Machine Containing a Brush Seal,” US patent no. 6,302,646.
[15] Albers, R. J., Bauer, R. C., Brauer, J. C., Schmid, S. J., and Lewis, K. M., 2003, “Brush Seal Support,” US patent no. 6,644,668.
[16] Kono, T., 2003, “Brush Seal Device,” US patent no. 6,655,692.
[17] Tseng, W.-Y., Bristol, B. L., Hetico, R. R., and Glynn, C. C., 1996, “Brush Seal,” US patent no. 5,568,931.
[18] Basu, P., and Short, J. F., 1999, “Brush Seal with a Flexible Front Plate,” US patent no. 5,884,918.
[19] Carter, B. A., 2000, “Shingle Damper Brush Seal,” US patent no. 6,032,959.
[20] Bayley, F. J., and Long, C. A., 1993, “A Combined Experimental and Theoretical Study of Flow and Pressure Distributions in a Brush Seal,” ASME J. Eng. Gas Turbines Power, **115**(2), pp. 404–410.
[21] Turner, M. T., Chew, J. W., and Long, C. A., 1998, “Experimental Investigation and Mathematical Modeling of Clearance Brush Seals,” ASME J. Eng. Gas Turbines Power, **120**(3), pp. 573–579.
[22] Ergun, S., 1952, “Fluid Flow through Packed Columns,” Chem. Eng. Prog., **19**, pp. 89–94.
[23] Hendricks, R. C., Flower, R., and Howe, H., 1996, “A Brush Seal Program Modeling and Developments,” NASA Technical Memorandum 107158.
[24] Chew, J. W., Lapworth, B. L., and Millener, P. J., 1995, “Mathematical Modeling of Brush Seals,” Int. J. Heat Fluid Flow, **16**(2), pp. 493–500.
[25] Chew, J. W., and Hogg, S. I., 1997, “Porosity Modeling of Brush Seals,” ASME J. Tribol., **119**, pp. 769–775.
[26] Chen, L. H., Wood, P. E., Jones, T. V., and Chew, J. W., 1999, “An Iterative CFD and Mechanical Brush Seal Model and Comparison with Experimental Results,” ASME J. Eng. Gas Turbines Power, **121**(4), pp. 656–661.
[27] Chen, L. H., Wood, P. E., Jones, T. V., and Chew, J. W., 2000, “Detailed Experimental Studies of Flow in Large Scale Brush Seal Model and a Comparison with CFD Predictions,” ASME J. Eng. Gas Turbines Power, **122**, pp. 672–679.
[28] Dogu, Y., and Aksit, M. F., 2006, “Effects of Geometry on Brush Seal Pressure and Flow Fields—II. Backing Plate Configurations,” ASME J. Turbomach., **128**, pp. 379–389.

Yahya Dogu[1]
Department of Mechanical Engineering,
Kirikkale University,
Yahsihan, Kirikkale 71451, Turkey
e-mail: ydogu@kku.edu.tr

Mahmut F. Aksit
Faculty of Engineering and Natural Sciences,
Sabanci University,
Tuzla, Istanbul 34956, Turkey
e-mail: aksit@sabanciuniv.edu

Effects of Geometry on Brush Seal Pressure and Flow Fields—Part II: Backing Plate Configurations

Brush seal dynamic behavior is strongly related to pressure and flow fields. Developments in brush seal design have led to geometric modifications to control flow field and consequent brush seal issues including blow-down, hang-up, and pressure stiffening. Some of the geometric enhancements have been found to have common use as backing plate modifications. Over the two decades of brush seal evolution, many backing plate configurations have been suggested in numerous patent disclosures. Even so, literature on the effects of geometric modifications on pressure and flow fields remains limited. This study numerically investigates brush seal pressure and flow fields for such common conceptual backing plate configurations as single and multiple grooves, with and without by-pass passages. The CFD analysis presented employs a bulk porous medium approach for the bristle pack. The effectiveness of various backing plate configurations outlining important flow features is discussed. Results indicate that backing plate configurations have a decisive role in shaping seal pressure fields. In general, it has been found that all cases having bypass configuration leak more. Moreover, the major portion of the seal leakage through fence height is fed from the backing plate cavity. The single backing plate groove forms a constant pressure behind the bristle pack. In contrast, multiple grooves form multiple constant pressure regions. [DOI: 10.1115/1.2101858]

1 Introduction

The brush seal has been successfully applied to rotating machinery since the 1980s. Numerous investigations have focused on extending brush seal performance for challenging applications. Over the years, structural and flow models have been developed utilizing accumulated theoretical knowledge and experimental findings. Common brush seal terminology involves many inherent brush seal dynamic issues, including bristle flutter, blow-down, hang-up, stiffness, instability, tip wear, pressure-carrying capacity, effective clearance, and leakage. Dinc et al. [1] have recently outlined a robust design procedure containing many complex design parameters. Developments in brush seal design indicate the significance of pressure and flow fields in dictating seal dynamics and performance.

Early brush seal applications utilized a short front plate and a straight backing plate, which are illustrated in Fig. 1. Bristles are clamped between the front and backing plates with a lay angle to the rotor for flexibility. The backing plate is extended towards the rotor surface up to maximum radial rotor-stator closure in order to provide mechanical support. This typical configuration is referred to as the standard brush seal design. The bristle pack is divided radially into two distinct regions, labeled as fence height and upper regions (Fig. 1). The radial height between the bristle tips and the backing plate inner diameter is called the fence height. The rest of the bristle height out to the bristle pinch point is called the upper region.

Governed predominantly by the flow field, bristles are mainly subject to three types of force: elastic, frictional, and aerodynamic. The balance of these forces dictates bristle equilibrium and brush seal dynamic behavior. Elastic forces are set by bristle mechanical properties and geometry. Frictional forces among bristles and between bristles and the backing plate depend on the friction coefficient as well as the fluid-solid interaction. The brush seal flow field driven by pressure load not only sets aerodynamic forces but also interbristle interaction by moving and compacting the bristle pack.

Inherent flexibility allows bristles to compact under pressure load. Frictional forces keep bristles hung-up on the backing plate while drag forces, due to inward radial flow, pull them towards the rotor. The balance of compacting and blow-down forces dictates whether the seal closes under pressure or remains hung-up. Determining this delicate balance requires detailed knowledge of pressure and flow fields and the resulting force equilibrium. The emphasis of this study is to investigate the effect of various conceptual backing plate configurations on pressure and flow fields.

1.1 Studies on Backing Plate Configurations.

A survey of the literature on brush seals reveals a limited number of experimental studies evaluating the effect of backing plate configuration on seal stiffening and blow-down [2–5]. Of the few studies done on the subject is one done by Short et al. [3], who, in their measurements of bristle stiffness, placed an axial relief between the bristle pack and the backing plate. Their findings indicated significant reductions in seal stiffness for backing plate relief depths up to 0.508 mm(0.020 in.). Their configuration also incorporated a flow deflector (damper shim) combined with a backing plate relief. The combined arrangement yielded important reductions for both blow-down and hysteresis. In a study conducted by Berard and Short [4], another combination with a relief in both backing and long front plates was tested. Results of these tests indicated that the introduction of front plate relief reduced seal stiffness. It was also reported that the front plate relief contribution to overall bristle stiffness was negligible beyond a relief depth of 0.508 mm(0.020 in.). In a different study, Crudgington and Bowsher [5] examined the effect of backing plate grooves on blow-

---

[1] To whom correspondence should be addressed.

Contributed by the Aeromechanics Committee of ASME for publication in the JOURNAL OF TURBOMACHINERY. Manuscript received January 14, 2005, final manuscript received July 15, 2005. Review conducted by M. Montgomery.

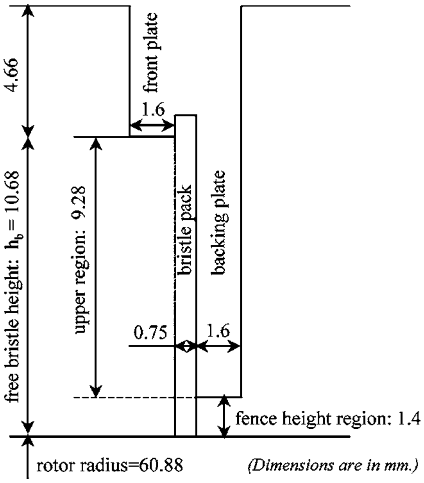

Fig. 1 Schematic of brush seal

down. The unexpected findings indicated a higher blow-down for the standard backing plate than for the grooved plate. This behavior was attributed to higher axial compression.

Overview of Patents on Backing Plate Configurations. Various forms of backing plate configurations have been proposed through several disclosures. For instance, Basu [6] and Basu and Short [7] have suggested various geometries of backing plate recess. Their aim was to reduce friction in order to control bristle hang-up and pressure stiffening. Morrison et al. [8,9] proposed balancing axial forces by pressurizing various backing plate cavities. This would result in the bristles having more freedom to move radially, thereby increasing flexibility and reducing the risk of hang-up. In a study of dual seal configuration, Tseng et al. [10] applied bypass holes on the backing plate of an upstream seal to streamline the flow approaching the downstream seal. They aimed at reducing the downstream seal wear associated with flow disturbances and outward radial flow. A variation of this was carried out by Fellenstein et al. [11], who placed backing plate holes to connect grooves to the downstream cavity. Their purpose was to relax bristles and decrease drag force resulting from excessive inward flow at the inner edge of the backing plate. Dhar et al. [12], on the other hand, used a flexible member between the bristle pack and backing plate. Their aim was to reduce bristle stresses by absorbing some portion of the bending force.

1.2 The Scope of the Present Work. Advanced brush seal designs for higher performance and severe applications require a standard straight backing plate to be replaced by modified plates. These modifications change pressure and flow field formations and control brush seal dynamics. Published studies have lacked evidence outlining the effects of conceptual geometric modifications. This study numerically investigates pressure and flow fields for common backing plate configurations. The CFD model presented is based on a bulk porous medium approach [13]. In this study, the effects of backing plate modifications are presented in a comparative manner with a detailed evaluation being performed for different flow properties by scanning the entire brush seal domain. Finally, the effectiveness of modifications on forming seal flow field is discussed.

2 The CFD Model

The brush seal is located between the high- and low-pressure cavities around rotating shafts. A two-dimensional axisymmetric CFD model is employed to solve the governing fluid flow equations. In addition to front and backing plate boundaries, the model domain includes upstream and downstream cavities surrounded by a stator and a rotor. A porous bristle pack is defined with flow resistance coefficients to which a simplified form of a non-Darcian transport equation is applied. Details of the bulk porous medium approach are presented by Dogu [13] and summarized here for completeness.

The model assumes a compressible and turbulent flow based on the ideal gas law and the k-ε turbulence model. Governing Navier-Stokes equations for flow through upstream and downstream cavities can be written in Cartesian tensor notations as follows:

$$\frac{\partial \rho u_i}{\partial x_i} = 0 \tag{1}$$

$$u_j \frac{\partial \rho u_i}{\partial x_j} = -\frac{\partial P}{\partial x_i} + \mu \frac{\partial^2 u_i}{\partial x_j \partial x_j} \tag{2}$$

This equation expresses the balance of inertial, pressure, and viscous forces in a free fluid flow stream. In addition to these three forces, frictional forces at the fluid-solid interface should be included for flow in a porous bristle pack. Among the many transport models for porous media, the following non-Darcian equation has been employed:

$$-\frac{dP}{dx_i} = (\alpha_i |\bar{u}_i| + \beta_i)\bar{u}_i \tag{3}$$

where α and β, respectively, represent spatially anisotropic effective inertial and viscous flow resistance coefficients throughout the bristle pack. This nonlinear transport equation for porous bristle pack, which is employed and validated by many researchers, has been selected as the best fit [13–22]. In the equation, x_i represents the orthographic flow directions and $\bar{u}_i$ is the superficial velocity in the direction of x_i. The superficial velocity refers to the velocity that would exist for the same volumetric rate of flow in the absence of porous medium. The equation mainly defines a balance between the pressure gradient and effective flow resistance terms within the porous bristle pack.

In general, frictional forces for the porous bristle pack, described on the right-hand side of Eq. (3), are added to the right-hand side of the momentum equation, Eq. (2). Under pressure load, the bristle pack tightly compacts and forms a stiff structure acting as a highly resistive porous medium. An order of magnitude analysis for Eqs. (2) and (3) reveals that inertial and viscous forces in Eq. (2) are negligibly small compared to fluid-solid frictional forces [Eq. (3)]. Therefore, Eq. (3) stands alone for flow transport in the porous bristle pack for the present bulk porous medium model.

The model relies on a careful determination of the flow resistance coefficients α and β. These coefficients are a function of geometric configuration, operating conditions, and bristle dynamic behavior. They are determined through a calibration procedure that utilizes all available experimental measurements for leakage, radial pressure on backing plate, and axial pressure on the rotor [14,15]. This bulk porous medium approach resolves incorporation of all the parameters in a balanced manner matching experimental data. Further details on the model and the calibration are presented in the companion paper [22].

2.1 Backing Plate Configurations. Over the years, various geometric modifications, e.g., pressure relief grooves, have been suggested to reduce frictional lock at the backing plate. Friction between the bristles and the backing plate is one of the main parameters determining whether the seal blows-down or remains hung-up. Based on a review of previous work, five common backing plate concepts are chosen in the scope of present study (Fig. 2). Standard configuration with straight backing plate (case 1) is selected as the baseline. As shown in Fig. 1, the standard seal typically has a 0.75 mm(0.0295 in.) thick bristle pack, 1.6 mm(0.0630 in.) thick front and backing plates, a fence height of 1.4 mm(0.0551 in.), and a free bristle height of

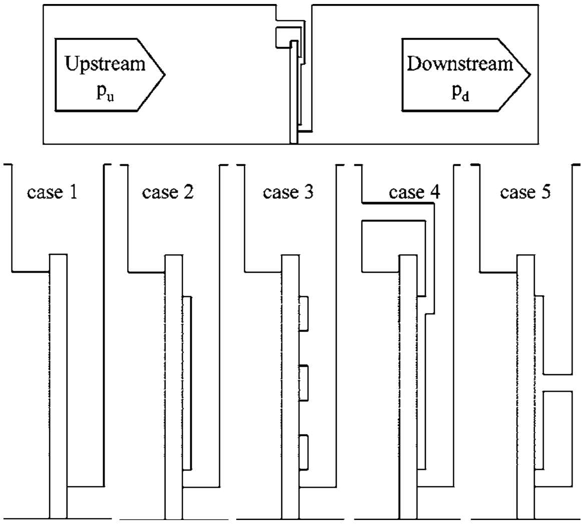

Fig. 2 Backing plate configurations

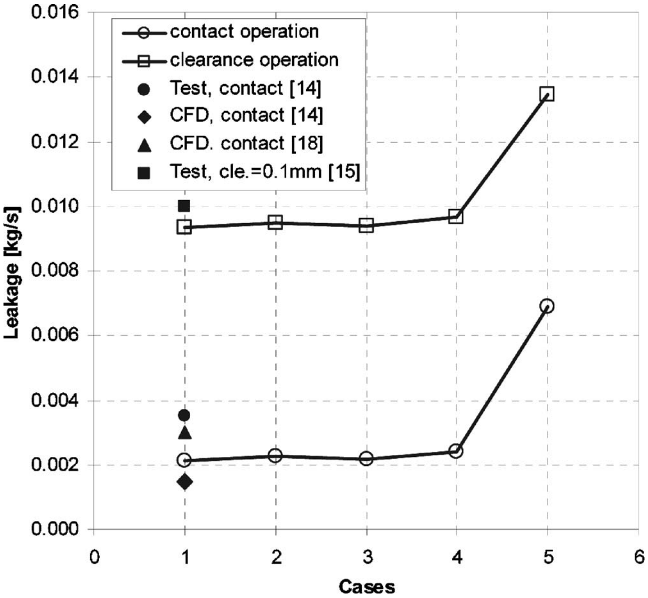

Fig. 3 Leakage evaluation for backing plate configurations

10.68 mm(0.4205 in.) [14,15].

Case 2 defines a single longitudinal groove in the backing plate (Fig. 2). A representative axial groove depth of 0.375 mm(0.0148 in.) is selected. The radial groove height covers the entire bristle pack by leaving a small space at the bristle root region and backing plate inner edge to provide support for bristles. In terms of flow formation, this case also represents one of the backing plate relief suggestions in the literature [3,4,6,7]. Under pressure, load bristles axially deflect and contact the backing plate corner, thus forming a closed cavity.

In case 3, the single groove of case 2 is divided into three parts. This configuration aims at passively controlling radial pressure distribution on the backing plate by forming local constant pressure regions.

In case 4, the single groove of case 2 is connected to the upstream cavity through a bypass passage. In some applications, a bypass flow is fed through an actively controlled pressure supply. Supply pressure can be adjusted to control axial pressure load over the bristle pack and to minimize backing plate friction.

The backing plate hole of case 5 connects the single grove of case 2 straight to the downstream cavity. The aim is to generate an evenly distributed axial pressure load over the entire bristle pack to prevent excessive bristle bending at fence height. Bypass size is selected as 0.75 mm(0.0295 in.) for a representative analysis. All of the grooves and holes are treated as circumferential slots in the two-dimensional axisymmetric CFD model. Most backing plate grooves are in the form of circumferential slots [6–9], allowing a reliable representation in the two-dimensional axisymmetric model. The number of bypass holes on the backing plate is so large [11] as in case 5 that is also suitable for the axisymmetric model.

2.2 Analysis Parameters and Boundary Conditions. Analysis parameters are defined to represent common brush seal application. The aim of the present study is to investigate the fundamental effects of backing plate configurations relative to each other for a certain set of operating conditions and the standard baseline brush geometry. When comparing the effect of backing plate configurations, many parameters, such as geometry (bristle diameter and arrangement, dimensions of brush seal and assembly region, etc.) and operating conditions (pressure load, temperature, bristle tip to rotor clearance, working fluid, rotor speed, etc.) should be considered. However, considering the five different cases with the number of operating parameters would require such a large number of combinations as to exceed the scope of this paper. Use of a representative case with available data is a more practical approach.

To study differences in flow fields for contact and clearance operations, all five configurations have been analyzed for both operating modes. A representative 0.1 mm(0.0039 in.) gap is used for all clearance runs. Upstream and downstream cavities are axially extended for fully developed flow conditions approaching and leaving the brush seal. To obtain a mesh-independent solution, a fine mesh is employed with typical cell size down to 1×10^{-5} mm. One set of pressure boundary conditions is prescribed for all configurations. Pressure is defined at upstream and downstream boundaries as 150 and 100 kPa. Air properties are assumed constant at inlet room temperature. Higher practical temperatures mean lower mass flow rate as density decreases with temperature. However, the volumetric flow rate, velocities, and flow patterns remain similar, thereby allowing simple comparisons to be made through the current analysis. Present analysis does not include rotor rotation. Rotor rotation drives a tangential flow, which impedes the overall leakage rate. However, its effect on axial and radial flow formations remains limited within the seal beyond the fence height region. Typical clearance operation would involve strong axial flow patterns with higher flow speeds than that of rotation-induced tangential flow speeds. When flow patterns around and within the brush pack are considered, the disturbance of swirl generated by rotation remains localized near the rotor surface without affecting the axial and radial flow patterns beyond the fence height region. Considering the numerous characterization data collected through static room-temperature seal tests, though ignoring the rotation, the current analysis provides a basic yet meaningful comparison of backing plate configurations in controlling the flow patterns within and around the brush pack. Finally, the effect of dimensional variations on pressure and flow field formations is also excluded from the scope of the present work.

3 Results and Discussion

The results of analyses of all cases are studied in a comparative manner. Brush seal dynamic behavior is related to pressure and flow fields in the vicinity of and within the bristle pack. Sectional details are also provided to reveal flow properties at critical locations.

3.1 Leakage Evaluation. As presented in Fig. 3, the effect of backing plate geometry on overall leakage performance is studied first. In general, all cases having the bypass configuration leak more. Other cases have a performance similar to that of the standard seal configuration. Calculated leakage values for a standard seal reasonably compare to experimental measurements and other CFD models [14,15,18]. The porous medium approach is further validated by making comparison of radial pressure on the backing plate and axial pressure on the rotor with experimental and other porous medium models. A detailed discussion on validation and verification is included in the companion paper [22].

For contact operation, cases 1–3 yield 0.0021 kg/s of leakage. In case 4, additional flow through the bypass passage from upstream to the backing plate cavity increases leakage to 0.0024 kg/s. The flow rate through the bypass passage is calculated as 0.0015 kg/s. The large bypass passage flow rate indicates that a major portion of seal leakage through fence height is fed from the backing plate cavity. In case 5, the backing plate bypass hole degrades leakage performance to 0.0069 kg/s. An additional leak path formed by the bypass hole means a larger porous opening, resulting in greater leakage. Leakage through the bypass hole is calculated as 0.0057 kg/s. A comparison of leakage rates indicates an absence of leakage contribution from the backing plate groove to the fence height flow in contrast to all other cases.

For clearance operation, additional leakage through the seal clearance is superimposed on the existing leakage trend outlined for the contact operation. Except for case 5, all other configurations show similar leakage performance at around 0.0094 kg/s. A representative 0.1 mm(0.0039 in.) of clearance increases leakage rate more than four times that of contact operation. In case 4, the bypass passage flow rate increases to 0.0021 kg/s. On the other hand, for case 5, leakage is calculated as 0.0135 kg/s, of which 0.047 kg/s leaks through the bypass hole on the backing plate.

3.2 Pressure and Flow Field Evaluation.

Flow fields for various configurations are evaluated using radial and axial velocity vectors, pressure, and turbulent kinetic energy distributions. For easy comparison, results for contact and clearance operations are labeled as “a” and “b” and grouped in Figs. 4–8 and Figs. 9–13 respectively.

The presence of a flow field over the backing plate is of primary concern in terms of seal dynamic issues including blow-down, hang-up, and stiffening. Since the effect of backing plate configurations on flow field is being investigated, important flow details are studied at an axial section near the backing plate. The results of this examination are presented in Fig. 14. The axial section is located through the center of adjoining mesh to the backing plate. Radial distance from rotor surface, y, is normalized with respect to the total free bristle height, h_b, as $r^*=y/h_b$. The fence height corresponds to a value of $r^*=0.13$.

Pressure Field. For contact operation, a drop in pressure mainly occurs around the inner edge of the backing plate in all configurations except for case 5a (Fig. 4). For the standard seal (case 1a), pressure within the bristle pack is close to the upstream pressure beyond the fence height. In contrast to the standard case, the use of a single groove (case 2a) introduces a constant pressure region on the backing plate while increasing axial pressure drop beyond the fence height. When multiple grooves are used (case 3a), each groove has a constant pressure with increasing magnitude as it moves from the innermost to outer pockets. For case 4a, the bypass passage flow from upstream removes the axial pressure gradient along the backing plate groove. Only the fence height region faces the axial pressure load. The radial pressure gradient within the bristle pack is concentrated on the inner edge of the backing plate. Case 5a is unique in that all radial seal sections face the same axial pressure drop. The uniform pressure distribution within the pack eliminates any local overloading and bending. The even distribution of pressure load may also lead to controlled pressure stiffening and blow-down.

For clearance operation, pressure is more evenly distributed over the axial pack thickness at the fence height (Fig. 9). Various configurations operating at clearance yield similar pressure profiles. The general difference in clearance operation is that pressure on the backing plate is closer to downstream pressure.

Radial pressure distribution on the backing plate is plotted in Fig. 14(*a*) for the fence height region. Pressure is normalized with respect to up/downstream pressures as $p^*=(p-p_d)/(p_u-p_d)$. For all cases, pressure is almost equal to downstream pressure at the fence height region. Previous discussions of pressure contours can also be visualized in Fig. 14(*a*).

Velocity Vectors. Velocity vectors define flow field for contact and clearance operations, as presented in Figs. 5 and 10, respectively. In addition to overall velocity maps for the entire seal, close-ups for critical fence height region are presented to visualize flow formations. Generally, flow penetrates the bristle pack along the upstream face. Diffused air flows radially inward over the backing plate, eventually turning axially and merging with the main leakage flow at fence height. As expected, changes in the backing plate configuration do not directly affect the velocity vectors upstream of the bristle pack. Backing plate grooves accelerate velocity and introduce local recirculations in pockets. Bypass passages involve notably high velocities. For all clearance operations (Fig. 10), the dominant flow occurs through the gap while maintaining a velocity vector field similar to that found in contact operation (Fig. 5). Suction generated by clearance enhances inward radial flow within the entire seal.

Radial Velocity. Radial velocity contours help in understanding the inherent dynamic problems leading to blow-down or lift off. Figures 6 and 11 present radial velocity contours for contact and clearance operations. Negative values represent radially inward flow direction.

For contact operation, flow over the backing plate accelerates as it moves inward. If backing plate grooves are used (cases 2a and 3a), inward flow fills each groove at the outer end and leaves at the inner end, resulting in higher radial flow velocity behind the bristle pack. Except for case 5a, maximum inward velocity exceeds 17 m/s on the inner edge of the backing plate. On the other hand, in case 4a, bypass flow from upstream pressurizes the entire groove, thereby minimizing diffusion through the bristle pack. When the backing plate groove is connected to the downstream cavity through a bypass hole (case 5a), diffusing flow above the fence height is diverted towards the groove. Unlike any of the other cases, this creates a radial outward flow around the inner edge of the backing plate towards the bypass hole. While an inward flow exists beyond the bypass hole, an outward flow is generated below.

As pointed out in the discussion on velocity vectors, clearance operation drives a dominating inward suction while preserving the flow trends observed for contact operation (Fig. 11). The inward radial velocity peaks towards the clearance inlet at innermost edge of the bristle pack, reaching a value of −44 m/s except for case 5b.

Overall, upstream bristles are subject to excessive inward radial flow for clearance operation while downstream bristles face the maximum inward flow for contact operation. The addition of grooves on the backing plate opens free flow regions for inward radial flow behind the porous bristle pack.

As illustrated in Fig. 14(*b*), radial velocity over the backing plate ranges from −17 to 1 m/s for both of the contact and clearance operations, except for case 5. Inward radial flow increases from the bristle root to the inner edge of the backing plate. Fluctuations form at the starting and ending points of the groove while the overall trend is similar to that of other cases. It should be noted that fluctuations through grooves will be higher than those presented in Fig. 14(*b*) since the radial profile presented is derived at the center of adjoining porous mesh to the backing plate rather than through the grooves.

Axial Velocity. Axial velocity contours are presented in Figs. 7

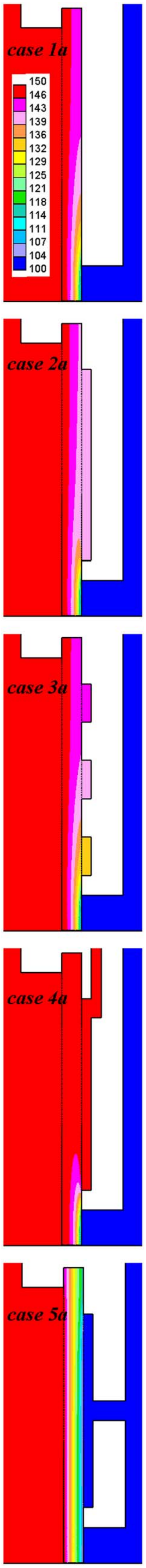

Fig. 4 Pressure (kPa) for contact operation

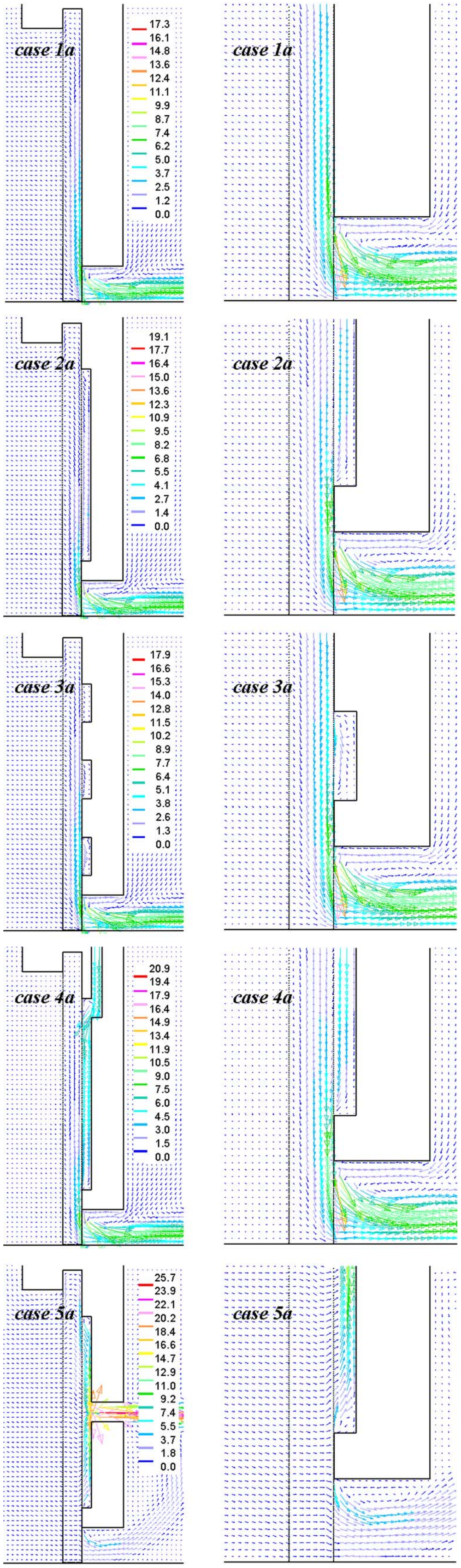

Fig. 5 Velocity vectors (m/s) for contact operation

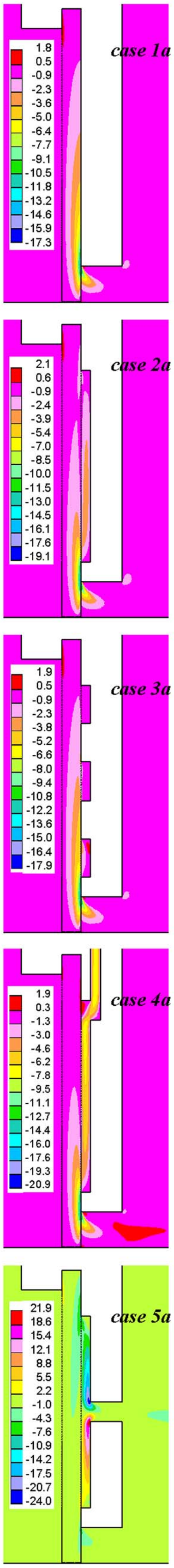

Fig. 6 Radial velocity (m/s) for contact operation

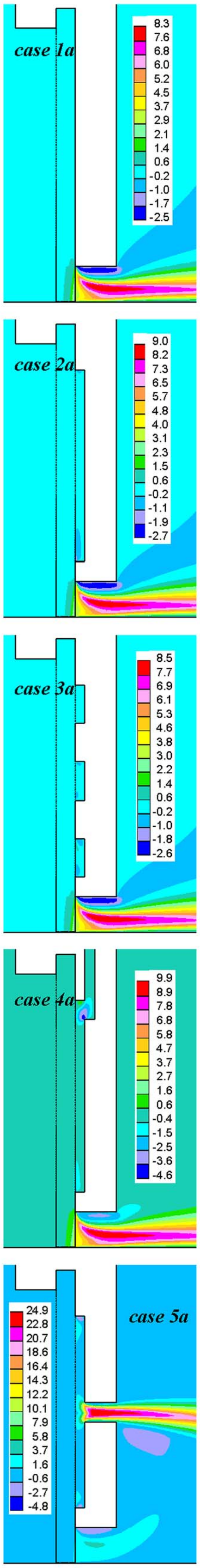

Fig. 7 Axial velocity (m/s) for contact operation

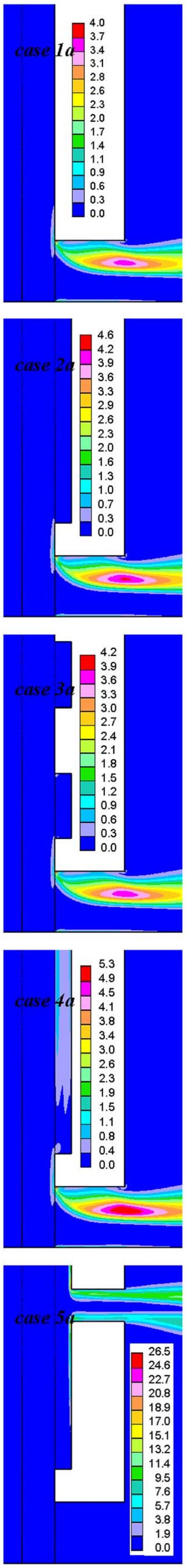

Fig. 8 Turbulent kinetic energy (m^2/s^2) for contact operation

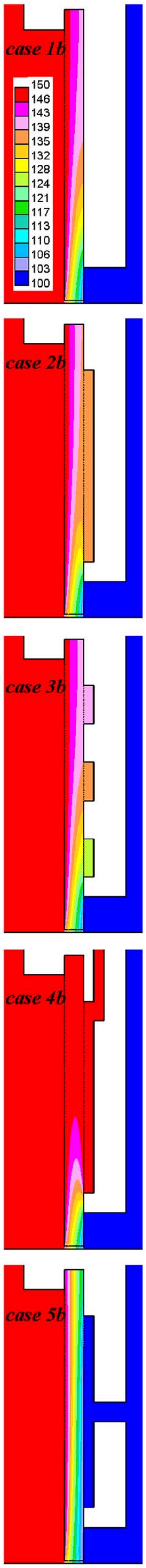

Fig. 9 Pressure (kPa) for clearance operation

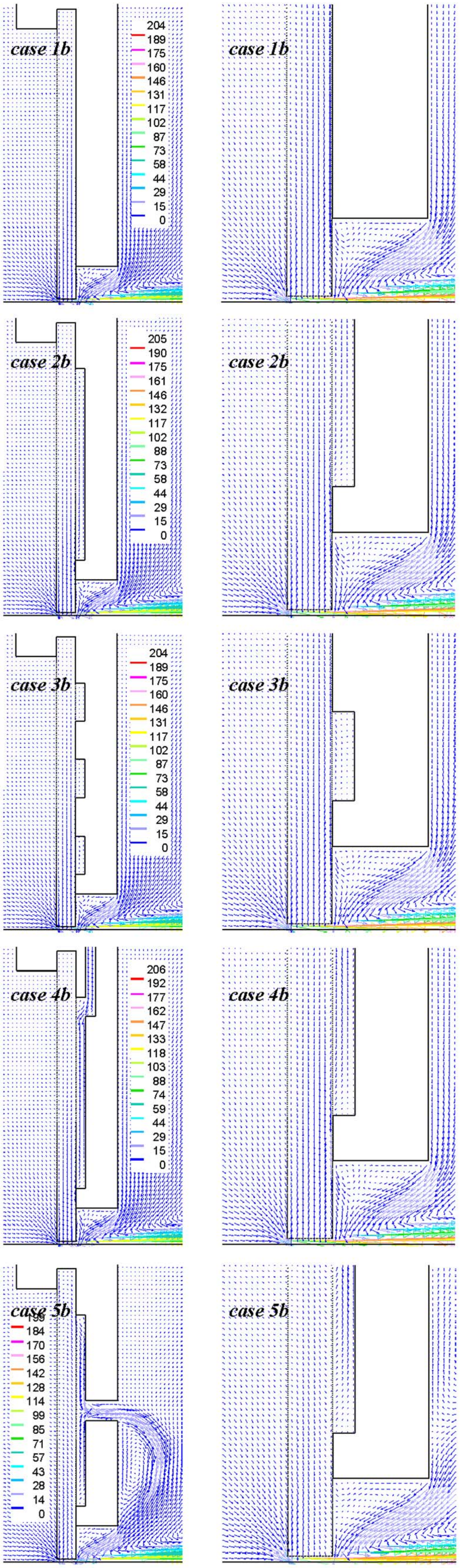

Fig. 10 Velocity vectors (m/s) for clearance operation

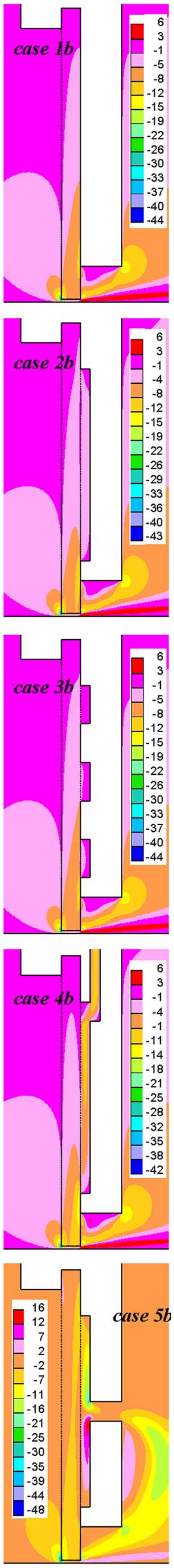

Fig. 11 Radial velocity (m/s) for clearance operation

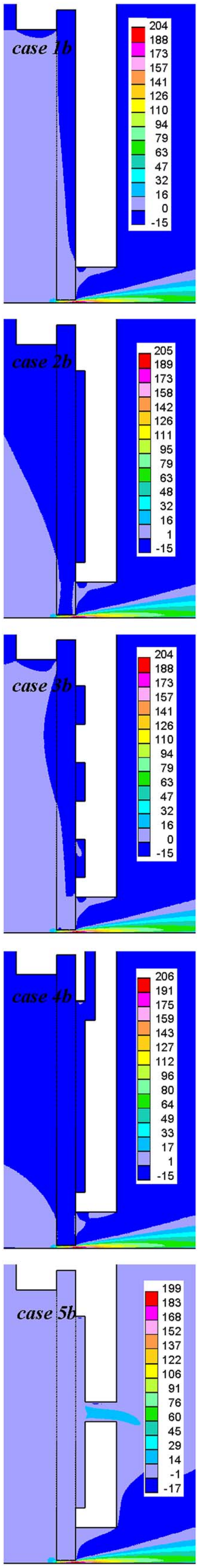

Fig. 12 Axial velocity (m/s) for clearance operation

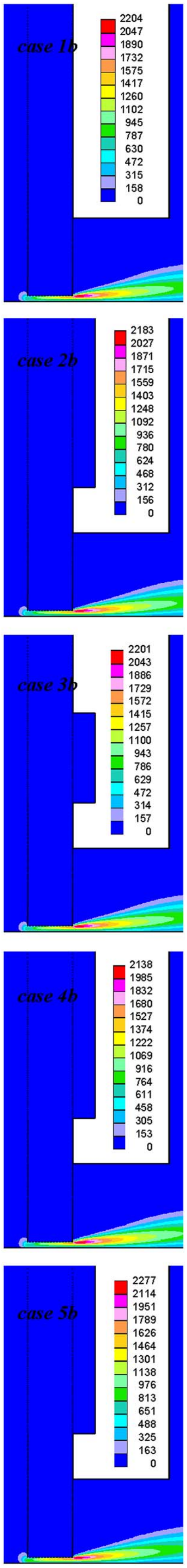

Fig. 13 Turbulent kinetic energy (m^2/s^2) for clearance operation

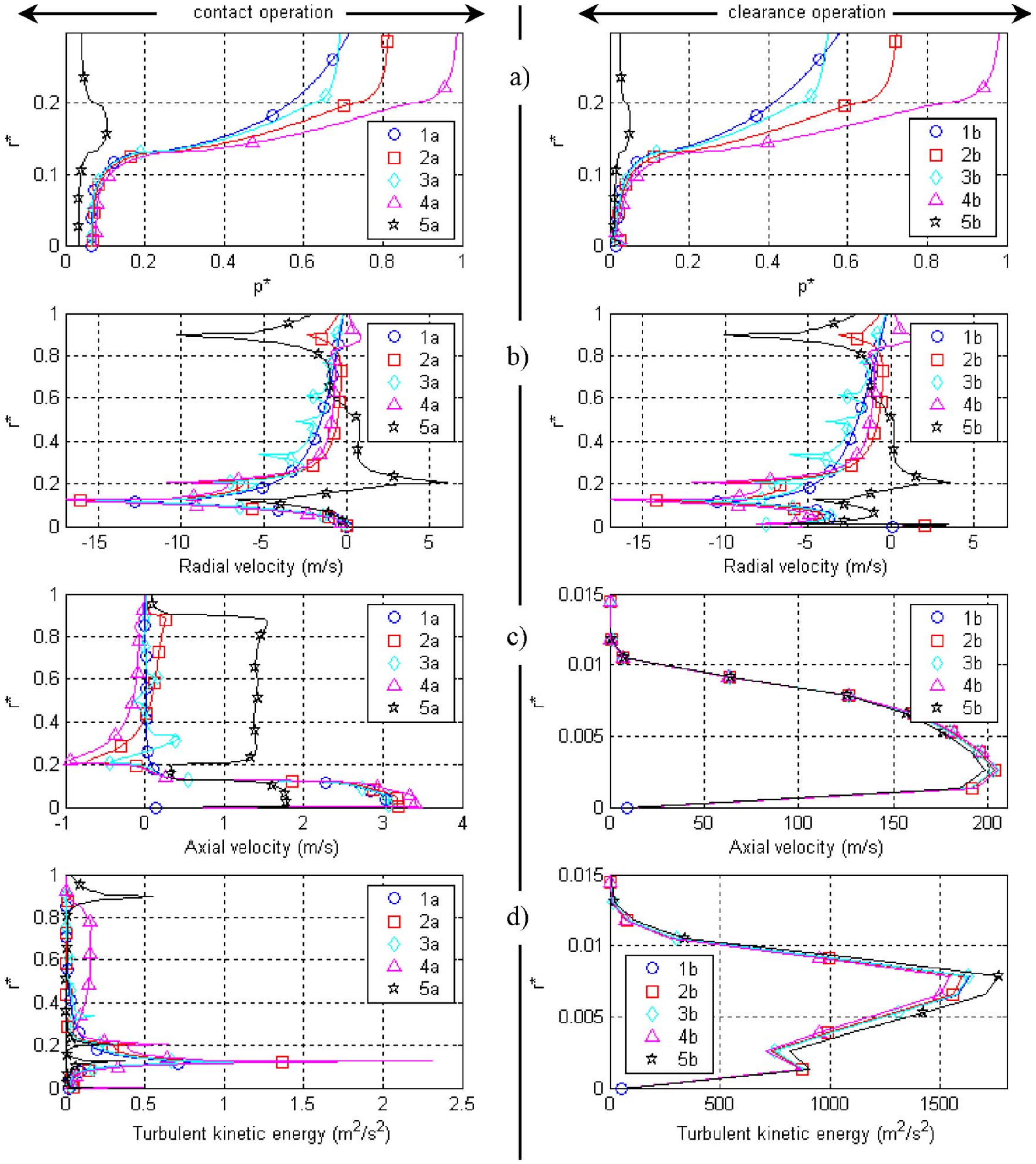

Fig. 14 Flow properties on backing plate: (*a*) pressure, (*b*) radial velocity, (*c*) axial velocity, and (*d*) turbulent kinetic energy

and 12 for contact and clearance operations. Positive values represent downstream flow direction. Except for case 5, backing plate modifications do not appear to affect axial flow.

For contact operation, maximum axial velocity is around 9 m/s and is located below the backing plate where inward radial flow merges with axial leakage. A recirculation forms as the flow turns under the backing plate. For case 5a, the maximum values are observed at the bypass hole, reaching 25 m/s. On the other hand, maximum axial velocity reaches 200 m/s at the clearance exit for all clearance operations.

Similar to the radial velocity case, the study of radial profile near the backing plate shows small fluctuations as the flow enters and exits the grooves [Fig. 14(*c*)]. As before, the clearance operation dominates and diminishes the effects of grooves on the axial velocity profile.

Turbulent Kinetic Energy. Turbulent kinetic energy is one of the mechanisms that triggers bristle flutter. Derived from fluctuating flow velocity, kinetic energy, $k=\overline{u_i'^2}/2$, can be used to evaluate the level of turbulence with respect to backing plate modifications. Turbulent kinetic energy contours for contact and clearance operations are plotted in Figs. 8 and 13. Maximum turbulent energy is located at high velocity points, as discussed above. For contact operation, it is relatively small, being 4 m^2/s^2 under the backing plate, while reaching 26 m^2/s^2 at the bypass hole for case 5a. High inward radial flow within the groove generates high energy levels in case 4a. Regardless of the backing plate geometry, turbulent energy is much higher for the clearance operation, reaching 2200 m^2/s^2 at clearance.

The radial distribution of turbulent kinetic energy behind the bristle pack is plotted in Fig. 14(*d*). In the contact operation, no significant turbulence is detected due to a highly resistive porous bristle pack. Turbulent energy peaks at the inner corner of the backing plate. For the clearance operation, just as is the case in the contact operation, turbulent energy has a similar profile in the upper bristle pack region. Nevertheless, it is very high at clearance due to higher velocities.

4 Conclusions

Advances in brush seal technology have led to the development of various backing plate design features. Seal pressure and flow fields have been numerically investigated for different conceptual backing plate configurations. Identified effects of backing plate configurations can be summarized as follows:

- Overall backing plate modifications shape the seal pressure field while their effect on the flow field formation remains limited.
- Leakage does not considerably change with backing plate modifications except for bypass arrangements. Bypass from upstream (case 4) introduces a small increase in leakage, while bypass to downstream (case 5) causes a drastic increase. Overall, leakage significantly increases with clearance.
- Except for downstream bypass (case 5), the major portion of the seal leakage through fence height is fed from the backing plate cavity.
- Introduction of a groove (case 2) generates a constant pressure across the backing plate, thereby increasing overall axial pressure drop beyond fence height.
- Multiple grooves control the radial pressure gradient on the backing plate by forming multiple constant pressure domains with increasing magnitude as moved from inner to outer pockets.
- Bypass from upstream (case 4) removes the pressure gradient along the groove. Only the fence height region faces the axial pressure load.
- Bypass to downstream (case 5) generates the same axial pressure drop at all radial seal sections, eliminating the radial pressure gradient. This may boost the seal pressure load capacity at the expense of some additional leakage.

Overall results from various configurations indicate that backing plate modifications have the potential to control the seal pressure field. Proper selection of backing plate configuration for different challenging tasks may hold the key to success. Better understanding of pressure and flow fields may enable designers to minimize undesired seal dynamic behavior. Advanced analysis tools, including other significant parameters such as rotor rotation and heat generation, may guide future applications.

Acknowledgment

The authors would like to thank Dr. Raymond Chupp of General Electric Global Research Center for his valuable evaluation, discussions, and insightful comments.

Nomenclature

h_b = free bristle height, m
k = turbulent kinetic energy, $\mathrm{m^2/s^2}$
p = static pressure, Pa
p^* = normalized pressure, $p^*=(p-p_d)/(p_u-p_d)$
r^* = normalized radial coordinate, $r^*=y/h_b$
u = spatial velocity component, m/s
u' = fluctuating velocity component, m/s
$\bar{u}$ = superficial velocity, m/s
x = spatial coordinate direction, m
y = radial distance from rotor surface, m
α = inertial flow resistance coefficient, $\mathrm{kg/m^4}$
β = viscous flow resistance coefficient, $\mathrm{kg/(m^3\text{-}s)}$
μ = dynamic viscosity, Pa-s
ρ = density, $\mathrm{kg/m^3}$

Subscripts

d = downstream
i = spatial coordinate and radial direction
j = spatial coordinate
u = upstream

References

[1] Dinc, S., Demiroglu, M., Turnquist, N., Mortzheim, J., Goetze, G., Maupin, J., Hopkins, J., Wolfe, C., and Florin, M., 2002, "Fundamental Design Issues of Brush Seals for Industrial Applications," ASME J. Turbomach., **124**(2), pp. 293–300.
[2] Basu, P., Datta, A., Loewenthal, R., Short, J., and Johnson, R., 1994, "Hysteresis and Bristle Stiffening Effects in Brush Seals," J. Propul. Power, **10**(4), pp. 569–575.
[3] Short, J. F., Basu, P., Datta, A., Loewenthal, R. G., and Prior, R. J., 1996, "Advanced Brush Seal Development," AIAA paper no. 96-2907.
[4] Berard, G., and Short, J., 1999, "Influence of Design Features on Brush Seal Performance," AIAA paper no. 99-2685.
[5] Crudgington, P. F., and Bowsher, A., 2003, "Brush Seal Blow Down," AIAA paper no. 2003-4697.
[6] Basu, P., 1995, "Brush Seal Device Having a Recessed Back Plate," US patent no. 5,401,036.
[7] Basu, P., and Short, J. F., 1999, "Brush Seal With a Flexible Front Plate," US patent no. 5,884,918.
[8] Morrison, M. K., Withers, P. A., Jones, T. V., and Wood, P. E., 1998, "Brush Seal," US patent no. 5,799,952.
[9] Morrison, M. K., Withers, P. A., Jones, T. V., and Wood, P. E., 2001, "Brush Seal," US patent no. 6,173,962.
[10] Tseng, W.-Y., Glynn, C. C., Bristol, B. L., and Hetico, R. R., 1994, "Brush Seal," US patent no. 5,318,309.
[11] Fellenstein, J., McCutchan, S. P., Hyland, J., and Van Duyn, K. G., 2002, "Brush Seal," US patent no. 6,457,719.
[12] Dhar, V. B., Turnquist, N. A., Venkatesh, R. G., and Agrawal, L., 2004, "Brush Seal for a Rotary Machine and Method of Retrofitting," US patent no. 6,685,427.
[13] Dogu, Y., 2005, "Investigation of Brush Seal Flow Characteristics Using Bulk Porous Medium Approach," ASME J. Eng. Gas Turbines Power, **127**(1), pp. 136–144.
[14] Bayley, F. J., and Long, C. A., 1993, "A Combined Experimental and Theoretical Study of Flow and Pressure Distributions in a Brush Seal," ASME J. Eng. Gas Turbines Power, **115**(2), pp. 404–410.
[15] Turner, M. T., Chew, J. W., and Long, C. A., 1998, "Experimental Investigation and Mathematical Modeling of Clearance Brush Seals," ASME J. Eng. Gas Turbines Power, **120**(3), pp. 573–579.
[16] Ergun, S., 1952, "Fluid Flow Through Packed Columns," Chem. Eng. Prog., **19**, pp. 89–94.
[17] Hendricks, R. C., Flower, R., and Howe, H., 1996, "A Brush Seal Program Modeling and Developments," NASA Technical Memorandum 107158.
[18] Chew, J. W., Lapworth, B. L., and Millener, P. J., 1995, "Mathematical Modeling of Brush Seals," Int. J. Heat Fluid Flow, **16**(2), pp. 493–500.
[19] Chew, J. W., and Hogg, S. I., 1997, "Porosity Modeling of Brush Seals," ASME J. Tribol., **119**, pp. 769–775.
[20] Chen, L. H., Wood, P. E., Jones, T. V., and Chew, J. W., 1999, "An Iterative CFD and Mechanical Brush Seal Model and Comparison With Experimental Results," ASME J. Eng. Gas Turbines Power, **121**(4), pp. 656–661.
[21] Chen, L. H., Wood, P. E., Jones, T. V., and Chew, J. W., 2000, "Detailed Experimental Studies of Flow in Large Scale Brush Seal Model and a Comparison With CFD Predictions," ASME J. Eng. Gas Turbines Power, **122**, pp. 672–679.
[22] Dogu, Y., and Aksit, M. F., 2006, "Effects of Geometry on Brush Seal Pressure and Flow Fields: I. Front Plate Configurations," ASME J. Turbomach., **128**, pp. 367–378.

Hong Yang
Dirk Nuernberger
Institute of Propulsion Technology,
German Aerospace Center (DLR),
Linder Hoehe,
51147 Cologne, Germany

Hans-Peter Kersken
Simulation and Software Technology,
German Aerospace Center (DLR),
Linder Hoehe,
51147 Cologne, Germany

Toward Excellence in Turbomachinery Computational Fluid Dynamics: A Hybrid Structured-Unstructured Reynolds-Averaged Navier-Stokes Solver

A three-dimensional hybrid structured-unstructured Reynolds-averaged Navier-Stokes (RANS) solver has been developed to simulate flows in complex turbomachinery geometries. It is built by coupling an existing structured computational fluid dynamics (CFD) solver with a newly developed unstructured-grid module via a conservative hybrid-grid interfacing algorithm, so that it can get benefits from the both structured and unstructured grids. The unstructured-grid module has been developed with consistent numerical algorithms, data structure, user interface and parallelization to those of the structured one. The numerical features of the hybrid RANS solver are its second-order accurate upwind scheme in space, its SGS implicit formulation of time integration, and its accurate modeling of steady/unsteady boundary conditions for multistage turbomachinery flows. The hybrid-grid interfacing algorithm is essentially an extension of the conservative zonal approach that has been previously applied on the mismatched zonal interface of the structured grids, and it is fully conservative and also second-order accurate. Due to the mismatched grids allowed at the block interface, users would have great flexibility to build the hybrid grids even with different structured and unstructured grid generators. The performance of the hybrid RANS solver is assessed with a variety of validation and application examples, through which the hybrid RANS solver has been demonstrated to be able to cope with the flows in complex turbomachinery geometries and to be promising for the future industrial applications. [DOI: 10.1115/1.2162182]

1 Introduction

Computational fluid dynamics (CFD) has become a major element in the aero-design of turbomachines, and its applicability to more and more complex numerical models is in great demand from the industry. In the literature, both structured and unstructured grid concepts have been used for the CFD simulations. In principle, both the concepts show contrary properties, the advantage of one often corresponds to the drawbacks of the other, and vice versa. At present for turbomachinery applications, most components in regular shape can be meshed with high-quality structured grids. However, in some components or local area, such as casing treatments, coolant channels, or tip clearance, very often it is not easy to generate structured grids even with a multi-block topology. To combine the geometric flexibility of the unstructured-grid methods with the numerical accuracy and efficiency of the structured-grid methods, a hybrid structured-unstructured CFD solver would be desired if it can support both structured- and unstructured-grid topologies in the same modeling.

Nowadays the structured CFD solvers are still popular within the design loop of turbomachines although they are restricted in their geometric flexibility. Nevertheless, during the past decade the unstructured-grid methods have also shown that they are promising in turbomachinery applications (e.g., Dawes [1], Contreras, et al. [2], Sheng [3]). In parallel to the separate development of structured and unstructured CFD solvers, a combination of structured and unstructured solvers was naturally conceived when dealing with complex geometries. Soetrisno et al. [4] built up a 2-D hybrid structured-unstructured approach associating triangular and quadrilateral grids at a 1-to-1 abutting grid interface. They have shown successful applications to some 2-D external flow cases, such as flapped wings, but their approach is hard to extend to 3-D space due to its coherent restrictions of grid node distributions at the structured-unstructured grid interface, and additionally it is not fully conservative at the interface. In a similar way, Contreras et al. [2] also reported their so-called semi-unstructured-grid method with a 1-to-1 abutting hybrid-grid interface which only allows performing 2-D blade-to-blade analyses.

This paper presents recent progress about development of a 3-D hybrid structured-unstructured RANS solver which consists of a structured-grid module and an unstructured-grid module together with a conservative coupling interface to associate patched structured and unstructured grids. Within this hybrid RANS solver, the structured-grid part comes from an existing structured CFD solver TRACE [5–7], while the unstructured one is of our new development employing consistent numerical algorithms and sharing same data structure with the structured one. The distinguished features of this hybrid structured-unstructured RANS solver are the following:

1. Applicable to three-dimensional, steady or unsteady flow simulations on block-structured or block-unstructured

---

Contributed by the International Gas Turbine Institute of ASME for publication in the JOURNAL OF TURBOMACHINERY. Manuscript received October 1, 2004; final manuscript received February 1, 2005. IGTI Review Chair: K. C. Hall. Paper presented at the ASME Turbo Expo 2005; Land, Sea, and Air, Reno, NV, June 6–9, 2005, Paper No. GT2005-68735.

grids, or hybrid structured-unstructured grids with stationary or sliding block interfaces;
2. Flexible at the hybrid-grid interface which does not require the 1-to-1 abutting connections between the structured and unstructured grid blocks;
3. Fully conservative and second-order accurate at the hybrid-grid interface;
4. Consistent numerical algorithms employed on the both structured and unstructured grids;
5. Same data structure, I/O, user interface, and parallel distributed processing shared by the structured and unstructured grid modules.

An overview of the existing numerical simulation system TRACE is briefed in the next section, which is followed by details of the new development of the unstructured-grid module and the hybrid-grid interfacing algorithm. Afterwards five validation examples are presented, including (1) flat plate boundary layer; (2) circular bump channel; (3) 1.5-stage compressor; (4) unsteady interaction of wake and turbine cascade; and (5) real industrial configuration of intake and IGV combination which also serves as an application example of the hybrid grids in complex geometries. At the end, conclusions are provided.

2 Numerical Simulation System TRACE

The hybrid structured-unstructured RANS solver is developed under the framework of the Turbomachinery Numerical Simulation System TRACE [5–7], in which the structured-grid solver has been developed for more than a decade and it is being applied by a growing user community in both research and industry. Thanks to a close cooperation with MTU Aero Engines, the industrial requirements have helped to shape TRACE into a highly efficient and accurate CFD tool well suited to both time-accurate (unsteady) and steady-state (stationary) simulations of turbomachinery flows.

The structured-grid solver allows using the block-structured grid topology and in particular the mismatched abutting block interface which is managed by the conservative zonal approach [8,9]. Under the relative frame of reference, the 3-D Reynolds-averaged Navier-Stokes equations are integrated in time by a fully implicit formulation of the first- or second-order accurate scheme for the compressible ideal gas or real gas in conjunction with the Spalart-Allmaras one-equation turbulence model [10] or alternatively the Wilcox k-ω two-equation turbulence model [11]. The convective fluxes are discretized using the Roe's TVD upwind scheme which is combined with the van Leer's MUSCL extrapolation to obtain second-order accuracy in space. The derivatives of the viscous fluxes are approximated by central differences. The laminar-turbulent transition is predicted by Drela's formulation of Abu-Ghanam/Shaw (AGS) transition criterion [12]. For a stationary multistage calculation, the nonreflecting formulation according to Giles [13] is applied at inlet and outlet boundaries, whereas the coupling of different stages is realized by the so-called mixing-plane approach. The time-accurate calculation through dual time stepping applies the nonreflecting boundary conditions of Acton and Cargill [14] at the inlet and outlet, while at the interface of sliding grids, the conservative zonal interface algorithm of Yang et al. [8,9] is employed. The solver has been parallelized based on domain decomposition using communication libraries MPI/PVM, and therefore it can be run on a wide variety of distributed or shared memory computer systems. For more details about the structured solver, please refer to Refs. [5–7].

3 Unstructured-Grid Module

In this section, basic numerical features of the new unstructured-grid module are to be presented. The unstructured-grid module has been developed using numerical algorithms consistent to those of the structured one. Built within the existing framework of the structured solver, the unstructured-grid module also employs the cell-centered scheme for storage of data and facilitates the I/O with standard CGNS format [15] as well. However, because there are no I/J/K indices or curvilinear coordinates available on the unstructured grid, the element connectivity in terms of cell-to-cell and face-to-cell has to be supplied from the input and then stored in the memory. This connectivity in addition to general block-to-block grid connectivity is generated by a preprocessing tool and recorded in the CGNS format. For details of the unstructured CGNS data structure, please refer to the CGNS website at http://www.cgns.org. Furthermore, all known element types such as hexahedron, tetrahedron, prism, and pyramid are supported by the unstructured-grid module.

The nondimensional RANS equation system to be solved reads in integral form for a bounded domain V with a boundary ∂V in a rotating frame of reference

$$\frac{\partial}{\partial t}\iiint_V \hat{Q}\,\mathrm{d}V + \iint_{\partial V} \hat{F}(\hat{Q})\vec{n}\,\mathrm{d}S = \frac{1}{\mathrm{Re}_0}\iint_{\partial V} \hat{F}_v(\hat{Q})\vec{n}\,\mathrm{d}S + \iiint_V \hat{\Omega}\,\mathrm{d}V \tag{1}$$

where Re_0 is reference Reynolds number, $\hat{Q}$ is the state vector, $\hat{F}(\hat{Q})$ is the convective flux vector, $\hat{F}_v(\hat{Q})$ is the diffusive flux vector, and $\hat{\Omega}$ is the rotating source term. The dimensionless low-Reynolds formulation of the Spalart-Allmaras turbulence model reads in integral form

$$\frac{\partial}{\partial t}\int_V \tilde{\nu}\,\mathrm{d}V = -\int_V \vec{V}\cdot\nabla\tilde{\nu}\,\mathrm{d}V + \frac{1}{\sigma \mathrm{Re}_0}\int_V \nabla\cdot[(\nu+\tilde{\nu})\nabla\tilde{\nu} + c_{b2}\nabla\tilde{\nu}]\mathrm{d}V + P + D \tag{2}$$

where $\tilde{\nu}$ is a working variable relating to the eddy viscosity ν_t, P and D are abbreviations for the production and destruction terms, respectively, and σ and c_{b2} are model's constants given by Spalart and Allmaras [10].

3.1 Spatial Discretization. A finite-volume discretization is applied to Eq. (1) which results in a consistent approximation to the conservation law where the time rate of change of the state vector $\hat{Q}$ within the domain V is balanced by the net fluxes of $\hat{F}(\hat{Q})$ and $\hat{F}_v(\hat{Q})$ across the boundary surface ∂V. The convective fluxes are discretized using Roe's upwind scheme [16] at a cell interface (ij) which is shared by cell i and cell j:

$$[\hat{F}(\hat{Q})\cdot\vec{n}]_{(ij)} = \tfrac{1}{2}\vec{n}_{(ij)}\cdot[\hat{F}(\hat{Q}^L) + \hat{F}(\hat{Q}^R) - |\hat{A}(\bar{Q})|(\hat{Q}^R - \hat{Q}^L)]_{(ij)} \tag{3}$$

where $\hat{Q}^L$ and $\hat{Q}^R$ are left and right states at cell interface (ij), $\bar{Q}$ is the Roe averaged state from $\hat{Q}^L$ and $\hat{Q}^R$, and $\hat{A}(\bar{Q})$ is the Jacobian of the flux vector $\hat{F}(\bar{Q})$, which can be decomposed into

$$\hat{A}(\bar{Q}) = \hat{R}\hat{\Lambda}\hat{R}^{-1} \tag{4}$$

where the right eigenvector matrix is evaluated via Roe's averaging of the states $\hat{Q}^L$ and $\hat{Q}^R$, and $\hat{\Lambda}$ is a diagonal matrix containing the entropy-corrected eigenvalues of the inviscid part of Eq. (1). The linear reconstruction is used at cell interface to reach second-order accurate formulation:

$$\hat{Q}^L = \hat{Q}_i + \vec{d}_i\,.\,(\nabla\hat{Q})_i\cdot\Theta_i \tag{5}$$

$$\hat{Q}^R = \hat{Q}_j + \vec{d}_j\cdot(\nabla\hat{Q})_j\cdot\Theta_j \tag{6}$$

where the subscripts i and j denote cell centered value, $\nabla\hat{Q}$ is the gradient, $\vec{d}$ is a distance vector pointing from the cell centroid to the face center, and Θ is the limiting factor which is used to enforce a monotone behavior of the reconstructed values. The Green-Gauss formula is used to calculate the gradient [17]

$$(\nabla \hat{Q})_i = \frac{1}{V_i} \cdot \sum_{j=1}^{N_F} [\hat{Q}_{(ij)} \cdot \Delta \vec{S}_{(ij)}] \tag{7}$$

where V_i is the volume of cell i, N_F is the number of faces belonging to cell i, the subscript (ij) denotes face values, and $\Delta \vec{S}_{(ij)}$ is the area vector of face (ij). The limiting factor according to Venkatakrishnan [18] is applied on primitive variables.

3.2 Time Integration. Both the multistage Runge-Kutta explicit scheme and Euler implicit scheme have been implemented in the unstructured-grid module. However, only the implicit scheme is to be tackled herein. For steady problems, time accuracy is of no importance, therefore the robust first-order accurate Euler backward time integration scheme has been implemented, whereas for unsteady problems, the second-order-accurate Crank-Nicolson scheme has been incorporated into the dual time stepping approach.

To derive the Euler backward scheme, Eq. (1) can be written in semi-discrete form as

$$\frac{d}{dt}\hat{Q} = \hat{R} \tag{8}$$

and in discrete form as

$$V_i \frac{\Delta \hat{Q}_i^n}{\Delta t} = \hat{R}_i^{n+1} \tag{9}$$

where Δt is the time increment, V is cell volume, $\hat{R}$ is the right-hand-side residual, and $\Delta \hat{Q}^n$ is the difference of an unknown vector between time levels n and $n+1$: $\Delta \hat{Q}^n = \hat{Q}^{n+1} - \hat{Q}^n$. The right-hand-side (RHS) of Eq. (9) can be linearized in time, then writing linearized Eq. (9) for all cells leads to a delta form of backward Euler scheme:

$$\hat{A} \Delta \hat{Q}^n = \hat{R}^n \tag{10}$$

where matrix

$$\hat{A} = \frac{V}{\Delta t} I - \frac{\partial \hat{R}^n}{\partial \hat{Q}} \tag{11}$$

and I is the identity matrix. In order to reduce the number of nonzero entries in the matrix and to simplify the linearization, only a first-order representation of numerical fluxes is linearized. This results in the graph of the sparse matrix $\partial \hat{R} / \partial \hat{Q}$ being identical to the graph of the supporting unstructured grid (i.e., every cell in the matrix is connected only to its nearest neighbors). When taking similar finite-volume formulation of Jacobian matrices on the left-hand-side (LHS) to that of Nuernberger et al. [19] on structured grids, we may rewrite Eq. (10) in the following form

$$(L + U + D) \Delta \hat{Q}^n = \hat{R}^n \tag{12}$$

where L consists only of terms in the strictly lower triangular matrix, U of terms in the strictly upper triangular matrix, and D of diagonal terms, and they can be expressed as

$$L = \sum_{j \in L(i)} [\mp |\hat{A}|_{(ij)}^{\pm} - \hat{A}_{\nu_j}] \cdot \Delta S_{(ij)} \tag{13}$$

$$U = \sum_{j \in U(i)} [\mp |\hat{A}|_{(ij)}^{\pm} - \hat{A}_{\nu_j}] \cdot \Delta S_{(ij)} \tag{14}$$

$$D = \frac{V_i}{\Delta t_i} I + \sum_{j=1}^{N_F} [\pm |\hat{A}|_{(ij)}^{\pm} + \hat{A}_{\nu_j}] \cdot \Delta S_{(ij)} - \frac{\partial (V_i \hat{\Omega}_i)}{\partial \hat{Q}} \tag{15}$$

where under the sign of summation, $L(i)$ and $U(i)$ denote the nearest neighbors of cell i which belong to the lower (upper) matrix, $\hat{A}_\nu$ stands for the Jacobian matrix of viscous fluxes, $|\hat{A}|^{\pm}$ is the split Jacobian matrix of convective fluxes corresponding to positive and negative eigenvalues,

$$|\hat{A}|^{\pm} = R \hat{\Lambda}^{\pm} R^{-1} \tag{16}$$

and the sign in front of $|\hat{A}|^{\pm}$ depends on if cell i is on the right or left of cell face (ij). The symmetric Gauss-Seidel (SGS) relaxation scheme is employed to iteratively solve Eq. (12) with first a forward sweep

$$(D + L) \Delta \hat{Q}^{k+1/2} = \hat{R} - U \Delta \hat{Q}^k \tag{17}$$

and then a backward sweep

$$(D + U) \Delta \hat{Q}^{k+1} = \hat{R} - L \Delta \hat{Q}^{k+1/2} \tag{18}$$

where the superscript k is a subiteration index. If only one subiteration is performed, the SGS method will be equivalent to the lower-upper symmetric Gauss-Seidel (LU-SGS) scheme of Yoon and Jameson [20].

To speed up the convergence rate of time-accurate simulations, an implicit formulation of dual time stepping is developed based on the implicit time integration technique outlined in the above paragraphs. Introducing a derivative of $\hat{Q}$ over a pseudo time τ in Eq. (8)

$$\frac{\partial \hat{Q}}{\partial \tau} = - \frac{\partial \hat{Q}}{\partial t} - \hat{F}(\hat{Q}) = \hat{R}^*(\hat{Q}) \tag{19}$$

where $\hat{F}(\hat{Q})$ stands for the flux vector consisting of both convective and viscous contributions. First of all we may formulate Eq. (19) as a nonlinear implicit scheme, i.e.,

$$\frac{\partial \hat{Q}^*}{\partial \tau} = \hat{R}^*[(\hat{Q}^*)^{m+1}] \tag{20}$$

with $(m+1)$ being the new pseudo-time level and $\hat{Q}^*$ an approximation to $\hat{Q}^{n+1}$. Then the new residual $\hat{R}^*$ defined in Eq. (19) can be linearized in the pseudo time, and the derivative $\partial \hat{Q}^* / \partial t$ can be discretized by the second-order-accurate Crank-Nicolson scheme, resulting in the following second-order accurate dual time stepping formulation

$$\left(1 + \frac{\Delta \tau}{\Delta t} + \frac{\Delta \tau}{2} \hat{A}^m\right) \cdot \Delta \hat{Q}^* = - \frac{\Delta \tau}{\Delta t} (\hat{Q}^*)^m + \frac{\Delta \tau}{\Delta t} \hat{Q}^n - \frac{\hat{F}^m}{2} \Delta \tau - \frac{\hat{F}^n}{2} \Delta \tau \tag{21}$$

where $\hat{A}^m$ is the flux Jacobian $\hat{A}^m = (\partial \hat{F} / \partial \hat{Q}^*)|_m$. To have efficient time-accurate computations, the LU-SGS method with one relaxation step is chosen to solve Eq. (21). Like the structured-grid module, the local time stepping is also employed in the unstructured-grid module for both the steady-state flow simulation and the pseudo-time iteration of the unsteady flow.

3.3 Boundary Conditions. All boundary conditions are specified via so-called ghost or dummy cells beside the boundaries. Only one layer of ghosts has been employed for the second-order accurate spatial discretization. For an interior block interface or a periodic/shadow interface, the ghost cells can be copied/rotated from the partner side, while for other boundaries, the ghost cells are created by a simple extrapolation from the interior cells at the boundaries. For the implicit time integration, an implicit treatment of boundary conditions on the LHS is performed by modifying the matrix terms in Eq. (12) to appropriately reflect the desired boundary conditions:

$$\Delta \hat{Q}_{\text{ghost}} = M \cdot \Delta \hat{Q}_{\text{interior}} \tag{22}$$

where M is the matrix to fulfill the relations between ghost cells and their neighboring interior cells. In addition to the implicit treatment of boundary conditions on the LHS, for the RHS of the implicit scheme the boundary conditions have to be enforced explicitly at every time step.

The Riemann invariant boundary conditions are used at the inflow and outflow boundaries, and the slip and no-slip boundary conditions are applied at inviscid and viscous walls, respectively. At the 1-to-1 abutting block interface, the whole vector $\hat{Q}$ of the conservative variables and gradients of primitive variables are specified in every ghost cell based on the values from the partner side, i.e., values at each corresponding interior cell. At the ghost cells of a rotational periodic boundary, the velocity vector and the gradients of pressure, density, turbulence viscosity, and cylindrical components of velocity are specified by rotating their shadow cells to one pitch angle. At mismatched zonal or block interface, a conservative zonal approach was implemented according to Yang et al. [8,9], which is to be presented in a later section.

3.4 Turbulence Model. The Spalart-Allmaras turbulence transport equation in integral from Eq. (2) has been solved with similar numerical algorithms to the aforementioned solutions of the Navier-Stokes equations. The convection term of Eq. (2) is formulated at cell i with volume V_i

$$\int_{V_i} \vec{V} \cdot \nabla \tilde{\nu} \mathrm{d}V = \vec{V}_i \cdot \sum_{j=1}^{N_F} [\tilde{\nu}_{(ij)} \cdot \Delta \vec{S}_{(ij)} \cdot \text{sign}] \tag{23}$$

where $\vec{V}_i$ is the velocity vector at the centroid of cell i, and sign takes "+" if cell i is on the left of cell face (ij), otherwise "−" if cell i is on the right. If the convection of the eddy viscosity is to be resolved properly, the upwind scheme has to be taken in calculation of face value $\tilde{\nu}_{(ij)}$. A similar linear reconstruction approach to Eqs. (5) and (6) is used to formulate the second-order-accurate upwind scheme for the calculation of $\tilde{\nu}_{(ij)}$. To discretize the diffusion term in Eq. (2) which consists of two parts $\int_V \nabla \cdot [(\nu + \tilde{\nu}) \nabla \tilde{\nu}] \mathrm{d}V$ and $\int_V \nabla^2 \tilde{\nu} \mathrm{d}V$ (the constants in front are omitted), the Green-Gauss formula of Eq. (7) is applied again to calculate the derivatives $\partial \tilde{\nu} / \partial x$, $\partial \tilde{\nu} / \partial y$, and $\partial \tilde{\nu} / \partial z$.

The same time integration schemes as those to Eq. (1) have also been developed for the time-marching computation of Eq. (2). To have an efficient and stable computation on the turbulence model, it is necessary to develop an implicit formulation of time integration to solve Eq. (2). Applying the Euler backward scheme to the discrete form of Eq. (2) $\partial \tilde{\nu} / \partial t = R_{\tilde{\nu}}^{n+1}$ leads to the following linear system of equations

$$(I - \Delta t M) \Delta \tilde{\nu} = \Delta t R_{\tilde{\nu}}^{n} \tag{24}$$

where $\Delta \tilde{\nu} = \tilde{\nu}^{n+1} - \tilde{\nu}^{n}$, $R_{\tilde{\nu}}$ is residual, and M is a Jacobian matrix which is defined as $M_{ij} = \partial (R_{\tilde{\nu}}^{n})_i / \partial \tilde{\nu}_j$. We have applied the same SGS iterative method as the one formulated in Eqs. (17) and (18) to iteratively solve Eq. (24). Furthermore, a similar implicit formulation of the dual time stepping approach as the one in Eq. (21) has been adopted in the time-accurate computation of Eq. (2).

The boundary conditions for Eq. (2) are also realized with one layer of ghost cells beside the boundaries. The implicit operator at boundary cells also needs to be modified in a similar way to the one expressed by Eq. (22) if an implicit treatment of boundary conditions is to be performed. For the RHS, at inflow boundary, the $\tilde{\nu}$ is prescribed with the freestream value, while at outflow boundary, the $\tilde{\nu}$ is extrapolated from the interior. At a solid wall, the no-slip wall condition for $\tilde{\nu}$ is enforced by setting

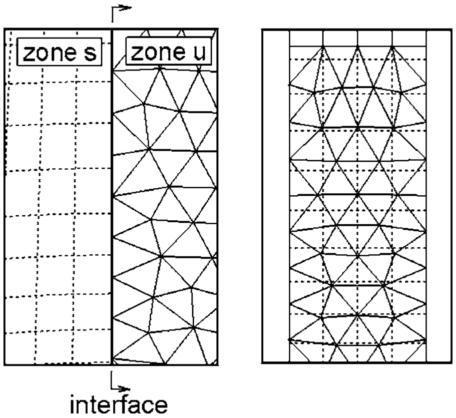

Fig. 1 Schematic of hybrid-grid interface

$$\tilde{\nu}_{\text{ghost}} = - \tilde{\nu}_{\text{interior}} \tag{25}$$

where the subscript interior denotes an interior cell neighboring to the ghost cell. The gradient $\nabla \tilde{\nu}$ also needs to be set properly at the ghost cells. For instance, at a solid wall, the no-slip condition requires

$$(\nabla \tilde{\nu})_{\text{ghost}} = - (\nabla \tilde{\nu})_{\text{interior}} + 2 \frac{\vec{n}}{|\vec{n}|^2} \vec{n} \cdot (\nabla \tilde{\nu})_{\text{interior}} \tag{26}$$

For coarse grid computations (with $y^+ > 1$ near wall), the Spalding wall function [21] is applied, so that the entire turbulent boundary layer need not be resolved, and a large grid spacing may be used at wall.

4 Hybrid-Grid Interfacing Algorithm

One of the key techniques developed for the hybrid structured-unstructured RANS solver is an association of the structured grid with the unstructured grid. At the hybrid structured-unstructured-grid interface, generally the nodal points are not necessarily matched between the two sides and the interface may be in any shape. A fully conservative and second-order-accurate coupling algorithm has been developed for the hybrid grid interface based on the conservative zonal approach of the authors, which was previously applied on the structured grids [8,9]. Thus, the structured and the unstructured grids need to be patched at their common boundary surface. Figure 1 shows an example of the hybrid-grid interface between patched structured grid (zone s) and unstructured grid (zone u). Consistent with the numerical schemes on the interior cells, the same Roe's upwind and central differencing formulations are applied to evaluate the convective fluxes and the viscous fluxes, respectively, at only one side of the hybrid-grid interface (e.g., at side of zone s), while for the other side of the interface (e.g., at side of zone u), a conservative rezoning is performed based on the known fluxes from its partner side and the grid overlapping relations between the two sides.

To reach second-order accurate coupling at the hybrid-grid interface, only one layer of ghost cells is needed for computing the left and right states at the interface boundaries. Herein the ghost cells are created by a simple extrapolation from the interior cells in both patched zones, and the conserved variables at the ghost cells are interpolated from those of the interface cells pertaining to the partner side. Furthermore, the unknown states at one side of the interface can be also interpolated from the known states at the other side. For instance, the left states at the interface boundary of zone s in Fig. 1 can be MUSCL extrapolated based on states of the interior cells and of the one-layer ghost cells from its own side, whereas its unknown right states can be interpolated from the known states at the interface boundary of the unstructured zone u. With the correct left and right states, the convective fluxes at the interface boundary can be calculated via the Roe's approximate Riemann solver [16]. If the viscous fluxes are also obtained with the central differencing scheme at the interface boundary of zone *s*, the total numerical flux vector can be calculated in zone *s* as follows

$$(\hat{F}_t^s)_{1/2,j,k} = (\hat{F}^s)_{1/2,j,k} - (\hat{F}_\nu^s)_{1/2,j,k}/\mathrm{Re}_0 \tag{27}$$

where the superscript *s* denotes the zone *s*, and the subscripts $(1/2,j,k)$ are indices of cell interfaces. To have the conservation across the hybrid-grid interface, the numerical fluxes at the interface boundary of zone *u* are formulated with a conservative rezoning calculation based on the known fluxes from the side of zone *s*

$$(\hat{F}_t^u)_i = \sum_{j^+}\sum_{k^+} (\hat{F}_t^s)_{1/2,j^+,k^+} \frac{(\Delta\bar{S})^i_{1/2,j^+,k^+}}{(\Delta S^s)_{1/2,j^+,k^+}} \tag{28}$$

where $(\Delta S^s)_{1/2,j^+,k^+}$ is the face area of the interface cells of zone *s* which overlap the cell face *i* of zone *u*, $(\Delta\bar{S})^i_{1/2,j^+,k^+}$ is the overlapped area between the cell face *i* of zone *u* and the cell face $(1/2,j^+,k^+)$ of zone *s*, and j^+,k^+ denote relative indices of zonal cell faces in zone *s* which are in contact with the cell face *i* pertaining to zone *u*. Equation (28) is derived by assuming the fluxes are piecewise constant within a cell face at the interface boundary.

To calculate the overlapped area $(\Delta\bar{S})^i_{1/2,j^+,k^+}$, a modified Sutherland-Hodgman clipping algorithm [22], borrowed from the computer graphics field, is used to remove or clip that part of the quadrilateral cell faces in zone *s* that falls outside of the boundary of the polygon cell face *i* in zone *u* at the interface. Additionally the overlapping relations of two patched grids determined by the clipping algorithm are also used in the area-weighted interpolation of conserved variables at the ghost cells and of the unknown states at the cell interfaces. To handle the curved zonal interface which may have gap or clearance, uniqueness to the zonal boundaries is made in the rezoning calculation through a transformation to a local coordinates system defined on each cell face of donor grid, e.g., zone *s* in the aforementioned example. Due to the rezoning calculation being executed in absolute frame of reference herein, one should also notice that if two adjoining zones are discretized in different frames of reference, the rezoning fluxes on the LHS of Eq. (28) need to be transformed to the appropriate frame of reference under which zone *u* is discretized.

For simulations about multi-components in turbomachines, very often at the hybrid-grid interface the so-called mixed cells may also show up, the faces of which are not fully covered by fluid, namely a portion of their faces belongs to solid [9]. For such case with the mixed cells, special treatments are performed at the interface: first figuring out the mixed cells, and then combining both contributions of the fluxes from the fluid part and the solid part with conservative rezoning calculation and the no-slip solid boundary conditions, respectively. For more details about the mixed-cell approach, please refer to Yang et al. [9].

The generalized hybrid-grid interfacing algorithm has no restrictions of grid topology at the interface, i.e., all possible patterns of the grid topologies at the interface are supported, no matter in which combinations: structured-unstructured, structured-structured, or unstructured-unstructured. To make the hybrid-grid interfacing algorithm efficient and robust, a sophisticated search algorithm is developed on the basis of computational geometry and the clipping algorithm [22]. In addition, the hybrid-grid interfacing algorithm has been parallelized as well with the help of MPI/PVM communication libraries, and an asymmetric communication has been designed for sending and receiving data between two patched zones.

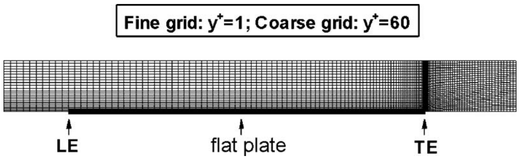

Fig. 2 Hexahedral grid around flat plate

5 Validation Examples

The hybrid structured-unstructured RANS solver has been validated by a variety of test cases with respect to steady/unsteady internal flows. In the following five validation examples are to be presented, and the last one also serves as an application example of the hybrid RANS solver to deal with complex geometries in turbomachines.

5.1 Flat Plate Boundary Layer. The flat plate boundary layer simulation is used to assess the capability of the newly developed unstructured-grid module and to compare with the existing structured-grid module on identical hexahedral grids. The computations of fully turbulent boundary layer were made on quasi-3D hexahedral "channel" grids around the flat plate for $\mathrm{Ma}_{\mathrm{inflow}}=0.5$ and $\mathrm{Re}_L=2\times 10^6$ where "*L*" is the length of the plate. Two resolutions of the H-type hexahedral grids were used in the computations (see Fig. 2), one with 45 grid lines in normal direction to the plate which corresponds to an averaged $y^+\approx 1$ at near-wall cells, while the other one has 27 grid lines in the same direction which corresponds to an averaged $y^+\approx 60$ near wall, so that on the coarser grid, the wall function has to be applied in the computations. For the both structured- and unstructured-grid computations, the CFL number of 20 was always chosen.

With the identical hexahedral grid, one may find from Fig. 3 that in terms of time steps, the unstructured-grid module can reach the same convergence speed as that of the structured-grid module, and their convergence behavior looks similar to each other. However, with respect to CPU time consumption per cell and per time step, the structured-grid module and the unstructured-grid module would require about 0.1 and 0.13 ms, respectively, if computing on a single UltraSPARC-III processor of the Sun Blade-1000 workstation with 750 MHz clock rate and 2.5 GB RAM. Thus the unstructured-grid module would be 30% slower than the structured one when working on the aforementioned computer. Figure 4 compares the contours of eddy viscosity in the boundary layer of the flat plate predicted by the unstructured- and the structured-grid modules on the finer grid, from which one may observe that

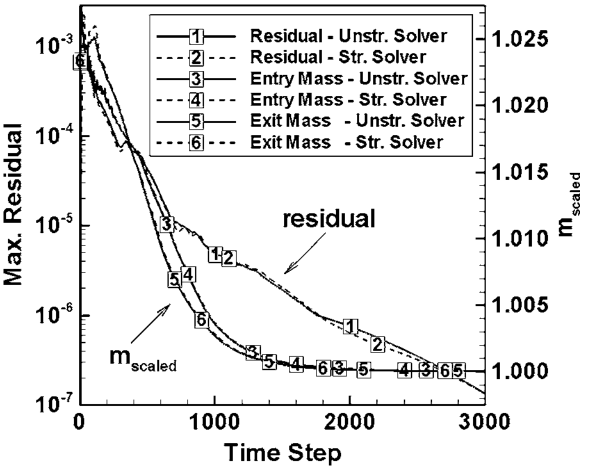

Fig. 3 Comparison of convergence for flat plate computations ($y^+=1$, CFL No. =20)

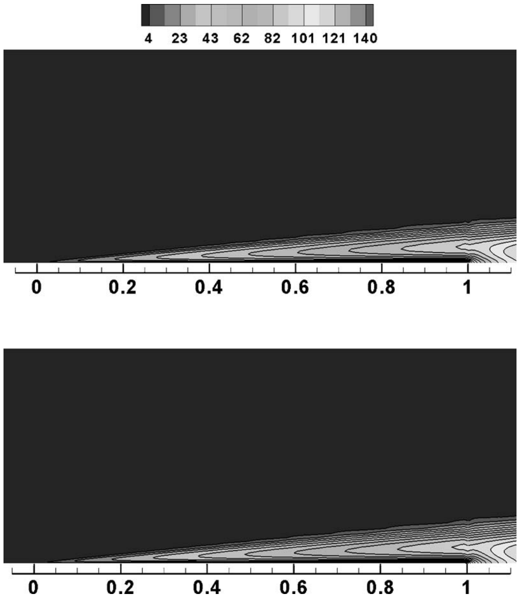

Fig. 4 Comparison of nondimensional eddy viscosity ν_T/ν_0 contours in the boundary layer of flat plate ($y^+=1$, scaling factor $x:y=1:5$). (top) Unstructured solver and (bottom) structured solver.

the same eddy viscosity distribution has been achieved by the unstructured-grid module as that by the structured one. Similarly the computations on the coarser grid also show well agreed boundary-layer solutions and well comparable performance of the unstructured- and the structured-grid modules (omitted herein).

Figures 5 and 6 illustrate the agreement of computed results with the theoretical correlations [23] in the skin friction along the plate and the velocity profile at the middle of the plate. These two figures also portray the effect of normal grid density on the skin friction factor and law-of-the-wall behavior at $x/L=0.5$. Basically these two figures can demonstrate that the predicted results are in good agreement with the theoretical correlations on both the grids and with both the solver modules, except that on the coarser grid the skin friction factor was overpredicted in the forward 20% of the flat plate due to that, in that region, there are too few grid cells located in the thin boundary layer. Nevertheless, the principal interest for this test case is in the remaining region of the plate where the calculated results even on the coarser grid agree well with the theoretical correlations.

Furthermore, we also used the flat plate case to assess the performance of the hybrid solver, especially the CPU-time penalty associated with the hybrid-grid interface computation. Maintaining both the topology and the size of the finer hexahedral grid shown in Fig. 2, we split it into two blocks at position $x/L=0.56$, in which the upstream block containing 51.2% of the total cells is handled in the structured way while the other one with 48.8% of the total cells is solved by the unstructured-grid module (Fig. 7). To have a mismatched grid interface between the two blocks, we adjusted the structured grid by increasing 4% of its first spacing in vertical direction to the flat plate. Figure 7 illustrates the boundary-layer development across the interface, from which together with Fig. 8, i.e., a plot of skin friction along the flat plate, one may get an impression that the calculated boundary layer can go through the hybrid-grid interface continuously and smoothly, and therefore the hybrid-grid interface can be applied in the viscous-dominant region. For this hybrid-grid simulation, we found in total it requires 16.5% more CPU time than that of the purely structured grid computation, and at the interface the coupling process does not require much CPU time which is actually equal to about 1.8% of the CPU time spent by the purely structured grid simulation on the aforementioned computer.

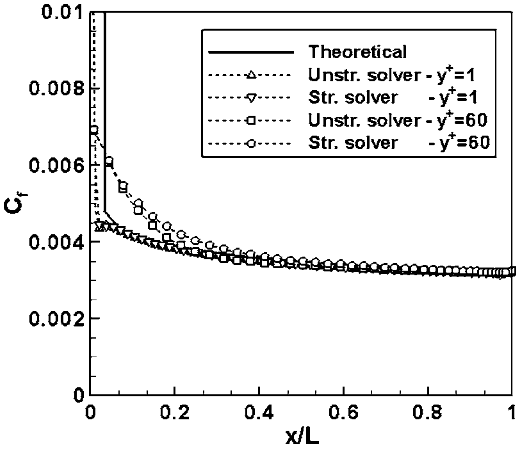

Fig. 5 Comparison of skin friction factor on flat plate

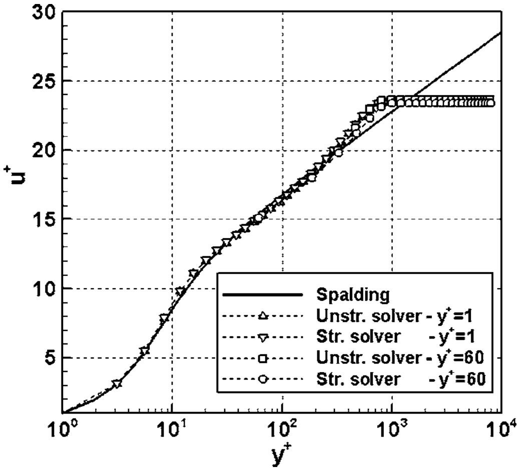

Fig. 6 Comparison of velocity profile at the middle of flat plate

5.2 Bump Channel. The inviscid flow through the Ni's circular bump channel [24] was computed with purely structured grids and with hybrid structured-unstructured grids, respectively. This test case is good and strict for checking the accuracy and conservation properties of the hybrid RANS solver. The computed results on the hybrid grids can be validated with those of the structured-grid module and some theoretical knowledge about the flow through the bump channel. Two flow states are considered herein, namely the subsonic flow with inflow Mach number 0.5 and the supersonic flow with inflow Mach number 1.4. For the

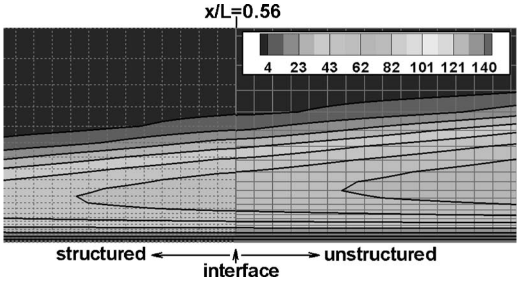

Fig. 7 The simulated flat-plate boundary layer across the hybrid-grid interface (contours of the eddy viscosity ν_T/ν_0, $y^+=1$, scaling factor $x:y=1:5$)

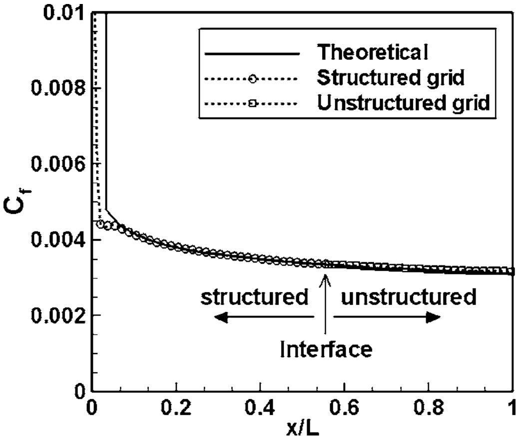

Fig. 8 The skin friction factor on flat plate from the hybrid-grid simulation ($y^+=1$ case)

subsonic case, the bump height is equal to 10% of the channel width, while for the supersonic case, the bump height is only 4% of the channel width. The hybrid structured-unstructured grid was generated in such a way that the half of the channel was meshed with the structured grid and the other half the unstructured grid with a structured- and an unstructured-grid generator, respectively, and a hybrid-grid interface was formed by adjoining the structured and unstructured grids together in the middle of the channel (see Fig. 9). Actually the structured-grid part in the hybrid-grid modeling in Fig. 9(*a*) is identical to the left half of the purely structured one in Fig. 9(*b*), and in the unstructured grid a couple of prism layers fill the near-wall region. To resolve the shock waves precisely the grids used for the supersonic case are much finer than those of the subsonic case (Fig. 10).

For the subsonic flow case, Fig. 9 shows the structured and hybrid grids, the predicted Mach number contours in the channel, and the predicted Mach number distributions at the lower and upper walls of the channel. From Fig. 9 one may observe that the computed Mach number of the hybrid-grid modeling has a similar distribution to that of the structured-grid computation in the bump channel, and the Mach number on the walls also shows a quite symmetric distribution to the middle of the bump. Most important for this validation is that the computed Mach number contour lines are going smoothly and continuously across the hybrid-grid interface (see Fig. 9(*a*)), and the computed inflow and outflow mass flowrates are identical even at the fourth digit after the decimal point. Figure 11 compares the convergence history of hybrid-grid computation to that of the structured one, from which one may find that using CFL number 20, the computations on both the grids can reach convergence within less than 1000 time steps, and although the hybrid-grid computation converged a little bit slower than the one of the structured-grid computation, it can finally reach a three order less magnitude of the maximal residual than the structured-grid computation.

For the supersonic flow case, Fig. 12 gives the computed Mach number contours on the hybrid and structured grids as shown in Fig. 10. From Fig. 12, one may observe that the hybrid RANS solver has no problem computing the flow with discontinuities across the hybrid-grid interface, and the shock wave reflection and interaction can be captured very well by the hybrid-grid computation, which are even better than those obtained on the structured grid. The better resolution of shock waves on the hybrid grid is due to the finer unstructured grid being generated in the region where the reflection and the interaction of the shock waves would occur. This result manifests that a hybrid-grid simulation can benefit from a better local control and adaptation in its unstructured grid.

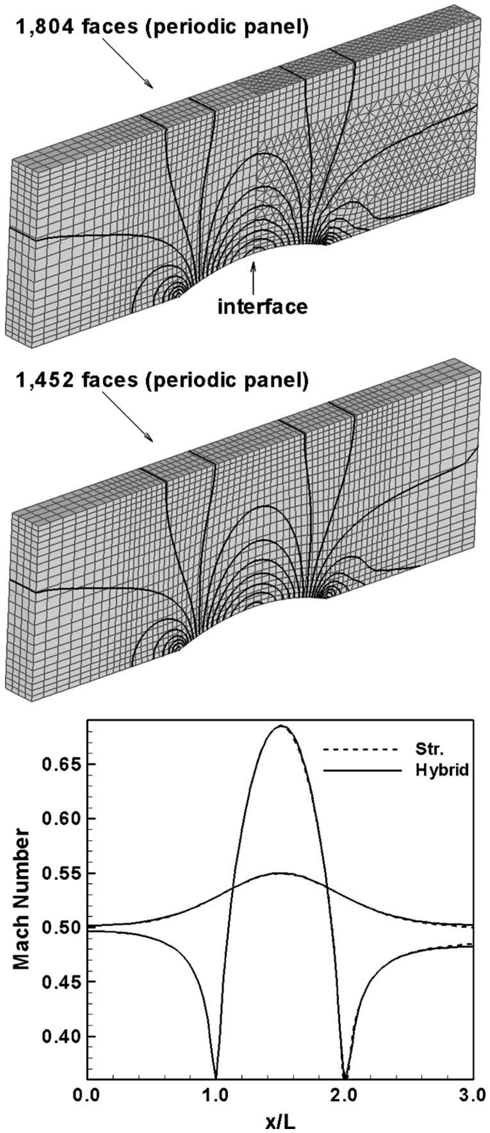

Fig. 9 Subsonic flow in the bump channel – grids, Mach number contours, and Mach number at walls ($Ma_{inflow}=0.5$). (top) Hybrid grid, (middle) structured grid, and (bottom) Mach number at walls.

5.3 1.5-Stage Compressor. This test case was built by extracting the first three blade rows out of a 3.5-stage Aachen compressor test case [25], so that only stator 0, rotor 1, and stator 1 were considered in this validation work (see Fig. 13). In the modeling, most of computational domain has been meshed with the block-structured grids, except the tip clearance gap (0.33 mm high or 0.4% of span at the rotor mid-chord) of the rotor which was meshed with three-block unstructured grids. The clustered unstructured grids near the blade leading edge and trailing edge are due to coupling of the structured and unstructured grids at the hybrid-grid interface. In total there are 165,504 cells in the structured grids (35 nodal points in the radial direction), whereas there are 8102 cells in the unstructured tip clearance. In addition, Fig. 13 also shows two measuring planes *I,1* and *I,2*, which are in the axial gaps between the rotor and the two stators. Both flows under the design and off-design operating conditions were simulated, in which the measured static pressure behind stator 1 was used as our outflow boundary condition. Under the design operating condition, the computed total pressure ratio Π_t of the stage 1 is 1.308, which agrees very well with the measured value 1.31, and the computed relative mass error between the entry and exit of the

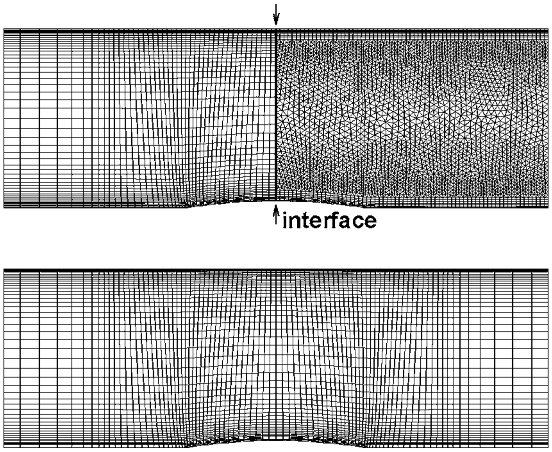

Fig. 10 Grids in the bump channel, supersonic case. (top) Hybrid grid (6957 faces on viewing plane) and (bottom) structured grid (4400 faces on viewing plane).

computational domain is about 0.001%, which means the hybrid-grid interfacing algorithm can handle the curved zonal interface conservatively. To check the effect of the unstructured tip clearance, Fig. 14 compares the measurement and the computation at the design point with the radial distributions of circumferentially averaged absolute total pressure, Mach number, and flow angles at measuring planes *I,1* and *I,2*, and Fig. 15 compares the pressure distributions along stator blade profiles at 90% span. Furthermore, to validate if the curved interface can handle severe flow conditions, we also computed the so-called BP2 off-design operating point [25], which is actually a near-stall point at the rotating speed of 84%*N*. For this operating condition, the computed total pressure ratio Π_t is 1.266, which also matches the measured value 1.27 well, and Fig. 16 gives the radial distribution of the absolute total pressure at the rotor entry and exit, and the isentropic Mach number along the stator-1 blade profile at 90% span. Figures 14–16 are used to demonstrate that the computed results by the hybrid RANS solver are in good agreement with the measurement data at both design and off-design operating conditions.

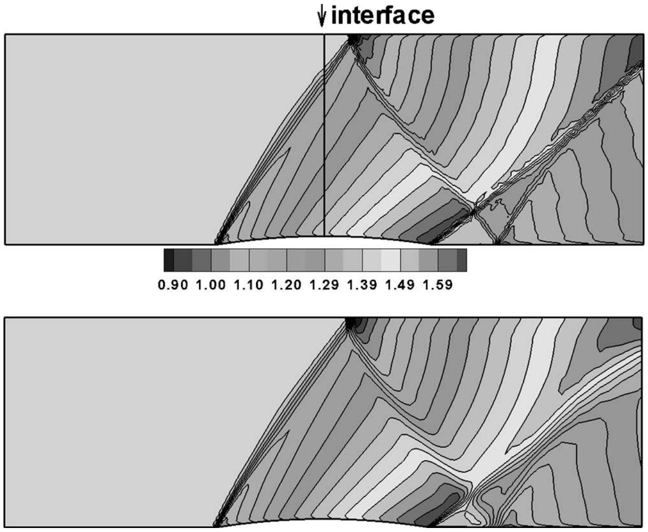

Fig. 12 Mach number contours for the supersonic flow in the bump channel ($Ma_{inflow}=1.4$) (top) with hybrid grid and (bottom) with structured grid

5.4 Unsteady Interaction of Wake and Turbine Cascade. This test case is a low-pressure turbine cascade subject to the unsteady wake of a moving bar from Acton and Fottner [26,27]. It was used to validate the capability of the time-accurate calculation with the hybrid structured-unstructured RANS solver. Herein only the flow with Reynolds number $Re_{2th}=2\times10^5$ is of our concern. The quasi-3D numerical modeling of the experiment is shown in Fig. 17, where only one slicing plane of the cascade and the bar was modeled with the hybrid grids, i.e., the unstructured grid was used around the bar (7513 cells), and the rest was meshed with structured grids (23,216 cells). From Fig. 17, one may notice that the hybrid-grid interface is in shape of a cylinder. To adequately resolve the boundary-layer flow at the solid walls, highly condensed grids were generated around the solid walls, and all first cells of the walls have been set within a distance $y^+<1.5$ in inner wall coordinates. To resolve the wake on its way through the turbine passage, the grid was made rather fine in circumferential direction at the interface of the moving bar and the turbine cascade mesh blocks (with 71 nodal points). The conditions of the bar are diameter $D=2$ mm, moving speed $\nu_{bar}=30$ m/s, and pitch $P=80$ mm. In addition, for this case, a laminar-turbulence transition appears on the suction surface of the turbine blade, which was modeled by the transition correlation of Drela [12] in the computation.

First, a steady-state calculation without any wake perturbation

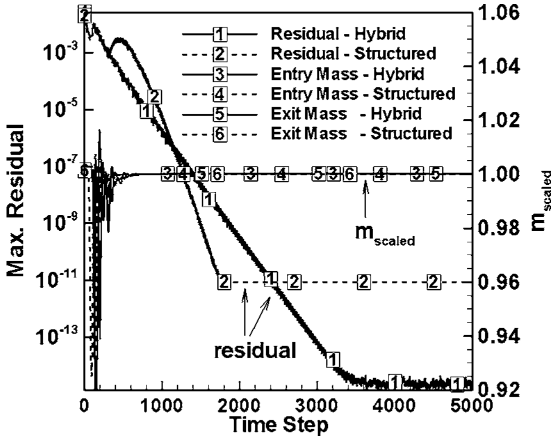

Fig. 11 Comparison of convergence on the structured and hybrid grids for the subsonic flow in the bump channel (CFL No. =20)

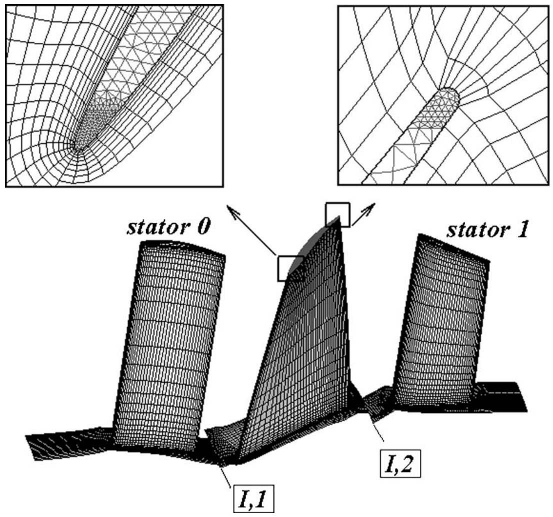

Fig. 13 Numerical model of the 1.5-stage compressor using hybrid grid in rotor tip clearance gap

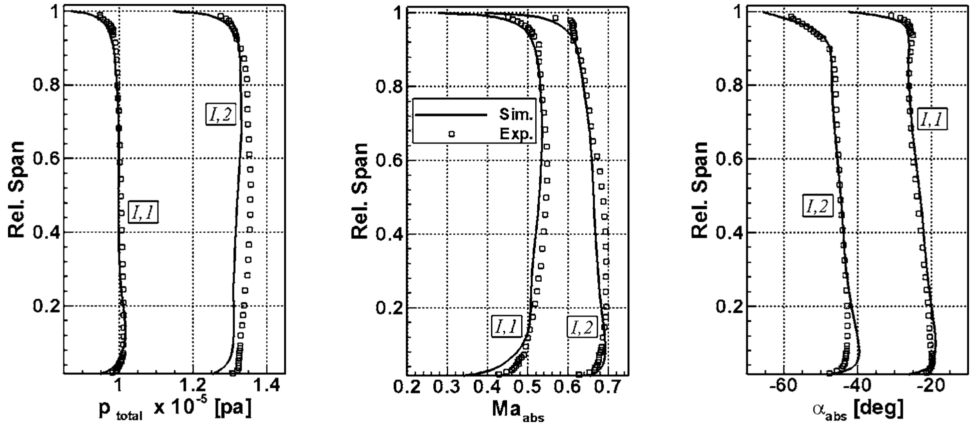

Fig. 14 Radial distributions of circumferentially averaged total pressure, Mach number, and flow angle at the entry and exit of the rotor (design point)

was performed in order to initialize the flow field and to check if the hybrid RANS solver is capable of handling transitional flows with a laminar separation bubble. In Fig. 18, the measured and predicted pressure coefficient distributions are compared for the two Reynolds numbers 2×10^5 and 3×10^5, which can also be used to illustrate the Reynolds number effect in the transitional flows. One can observe excellent agreement between the experimental and numerical data, and at the lower Reynolds number, the pressure gradient levels off in a more pronounced way before it recovers again in the transitional zone near the rearward suction side.

In the unsteady case, the bar is moving with a speed of 30 m/s, giving rise to a wake passing frequency of 375 Hz, and 256 time steps were used to resolve one wake passing period in the computation. Within every physical time step, 60 subiterations of the dual time stepping were performed. As expected from the Reynolds number of the cylinder $\mathrm{Re}_D=2840$, a von Karman vortex street forms in the wake of the moving bar. Figure 19 shows instantaneous distribution of the eddy viscosity, in which a close-up view at the hybrid-grid interface is presented to show the shedding vortices can be resolved adequately with the curved interface. Further, the wake-induced transition is also visualized in Fig. 19 (the beginning of which is marked by an arrow). The computed inflow/outflow mass flowrate versus time steps is given in Fig. 20, from which one may find that there are higher perturbation frequencies added onto the wake passing frequency, which are mainly due to the shedding von Karman vortex street and the wandering of the start location of the transition on the rearward suction surface of the blade. Nevertheless, Fig. 20 has shown that within less than ten wake passing periods, the time periodicity can be achieved for the unsteady wake-blade interaction simulation.

In Fig. 21, a fast Fourier transform (FFT) analysis of an unsteady mass flow signal in the moving wakes reveals frequencies of higher amplitude in the range of 8.6 to 10.5 kHz. This corresponds to an average Strouhal number of 0.20 which agrees well with the measurement data in [23]. Finally, for the unsteady case, a "semi-quantitative" comparison with the hot film measurement by Acton and Fottner [26,27] is given in Fig. 22, a space-time plot of the wall shear stress of the suction-side boundary layer. The comparison is semi-quantitative since the hot film data are in a raw form, i.e., in terms of the hot film anemometer output voltage $(E-E_0)$ normalized by the zero flow signal E_0. Having the proportionality $\sqrt[3]{\tau_w}\propto(E^2-E_0^2)/E_0^2$ in mind, one may find it is still meaningful to compare the measured $(E-E_0)/E_0$ with the computed wall shear stress since the variation of these quantities is of prime interest in the validation of the hybrid RANS solver. In Fig. 22, the temporal variation of the transition start location "T" has been marked as a solid black line by assuming that the transition start is always associated with a pronounced increase of the wall shear stress. From Fig. 22, one may observe that the computed and measured temporal variations of the transition start location on the blade suction surface are qualitatively comparable to each other. Furthermore, the calculated plot also presents two peaks (i.e., two extreme upstream positions) instead of a single one during a wake passing period, which can also be found in the measured plot in Fig. 22. The same phenomenon has been observed and investigated by Eulitz [28] who once computed the case of $\nu_{\mathrm{bar}}=40$ m/s on a 2-D structured grid.

5.5 Combination of Intake and IGV.

Finally, the hybrid-

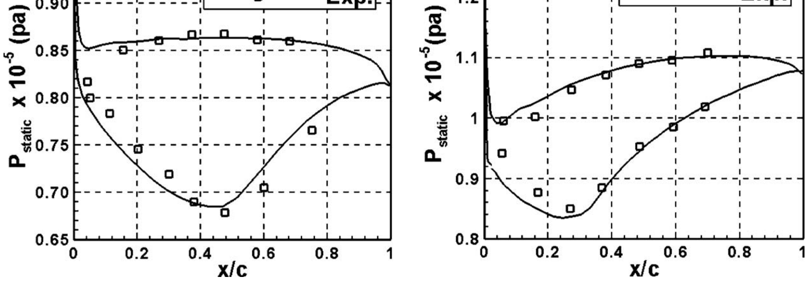

Fig. 15 Comparison of predicted and measured pressure distributions on stator blade surfaces at 90% span (design point). (left) Stator 0 and (right) stator 1.

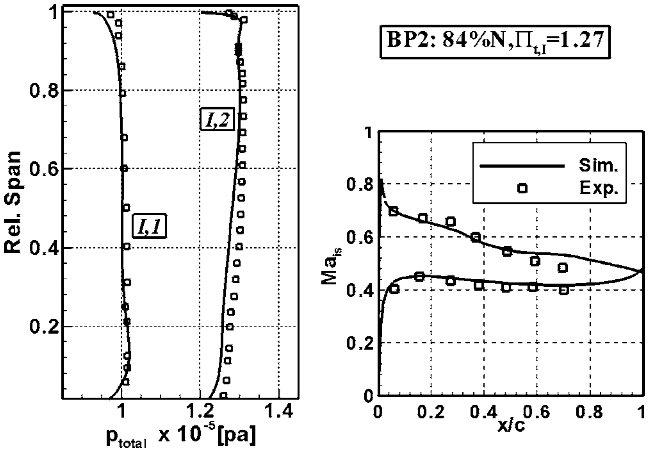

Fig. 16 Comparison of the simulated results with the experimental data at operating point BP2. (left) Total pressure at rotor entry and exit and (right) isentropic Mach number on stator-1 blade surfaces at 90% span.

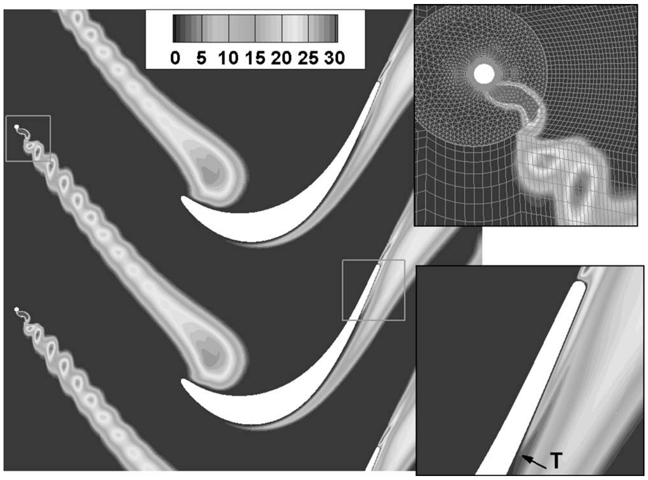

Fig. 19 Instantaneous distribution of nondimensional eddy viscosity ν_T/ν_0

grid topology was applied to a real industrial configuration which is a combination of two turbo-components, i.e., an intake and an IGV (see Fig. 23). In this case, the geometry of the intake is so complex that it is thought to be a very good example for being meshed with unstructured topology, whereas the geometry of the IGV is quite simple so that it can readily be meshed with regular block-structured grids. To facilitate a parallel computation and to control grid density at different positions, we have partitioned the intake into 10 blocks while the whole annulus of IGV was split into 82 grid blocks. Figure 23 shows the hybrid grid generated for the whole configuration and a close-up of the grid around the

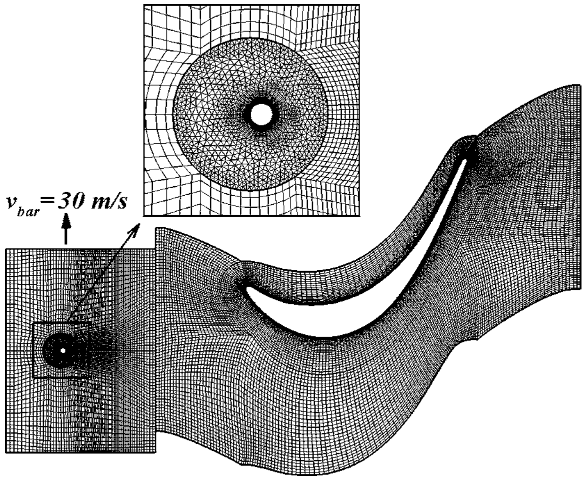

Fig. 17 Numerical model of moving-bar experiment using hybrid grids

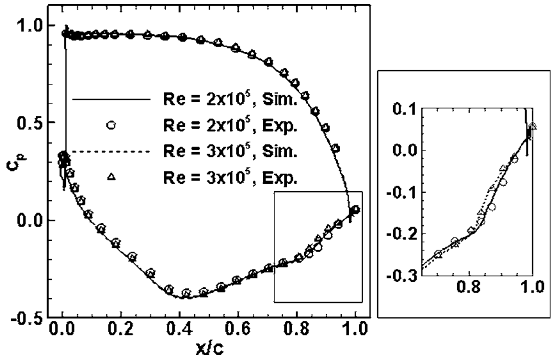

Fig. 18 Pressure coefficient distributions along blade surfaces

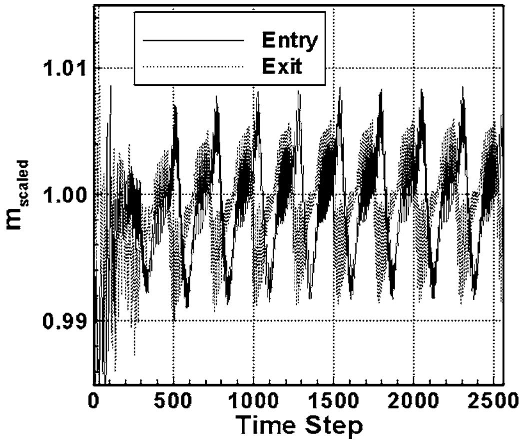

Fig. 20 Scaled mass flowrate versus time step at entry and exit boundaries

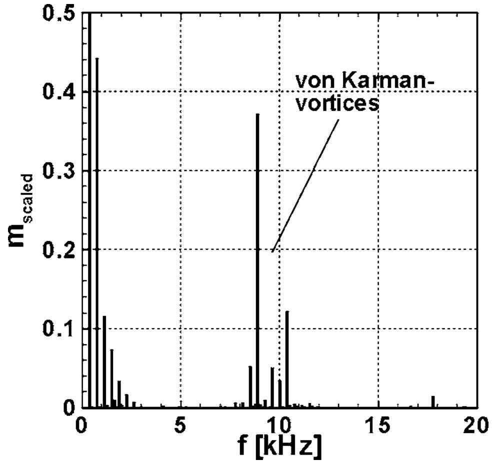

Fig. 21 FFT spectrum of unsteady mass flow signal in the wake of the moving bar

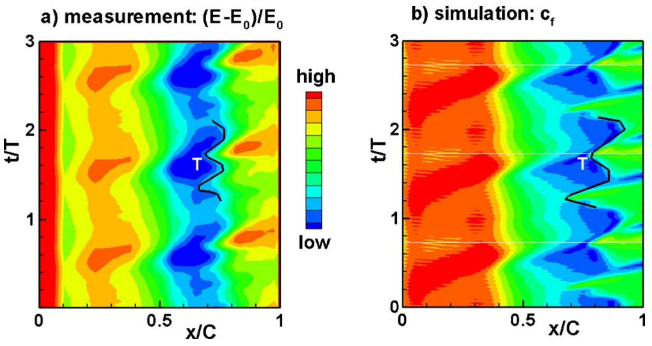

Fig. 22 Comparison of unsteady hot-film signals (left) and predicted suction-side skin friction (right) over three wake passing periods

hybrid-grid interface. The size of the hybrid grid is 2.73 million cells in total which are a summation of 1.15 million cells in the unstructured grid of the intake and 1.58 million cells in the structured grid of the IGV. To validate the hybrid-grid computation, a multi-block structured grid was also generated for the intake such that a purely structured-grid model has also been set up for the validation purpose, in which the grid of the IGV is identical to that of the hybrid-grid model, whereas the structured grid for the intake contains 26 blocks with 1.03 million cells (see Fig. 24). For visual clarity, the structured grids in the IGV are neglected from the global view in Figs. 23 and 24, and only one of every four structured grid lines is shown for the intake in Fig. 24. Certainly the structured-grid generation for the intake needs much more man power than the unstructured-grid generation.

Figure 25 gives the convergence history of inflow and outflow mass flowrates for the hybrid-grid computation with a CFL number of 15, from which one may observe that at about 4500 time steps the computation becomes converged. Furthermore, the relative mass error of the hybrid-grid computation is only 0.0068% between the inflow and outflow boundaries. This means even for such complex geometry with a large grid size, the conservation of the hybrid-grid computation is still satisfactory.

The computed results between the hybrid and structured grid solutions are compared through Figs. 26–28. Figure 26 gives a global view of the pressure distributions computed on the hybrid and structured grids, from which one may observe that nearly the same overall distributions of pressure have been obtained by both computations. Figure 27 plots a close-up of pressure distributions around the interface between the intake and the IGV, which shows good agreement of the computed results on the hybrid and structured grids. Finally Fig. 28 gives the computed pressure distributions on the main exit of the intake that is connected to the IGV, from which one may notice that the computed result on the unstructured grid looks similar to that on the structured grid. Therefore, this test case can also serve as an application example to

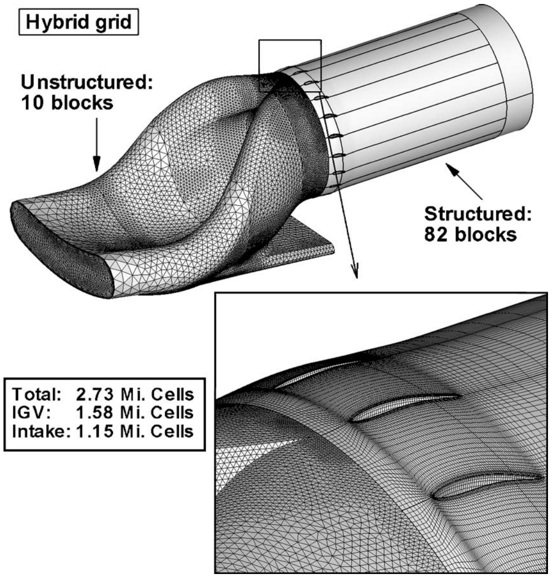

Fig. 23 Hybrid grid model of the intake and IGV

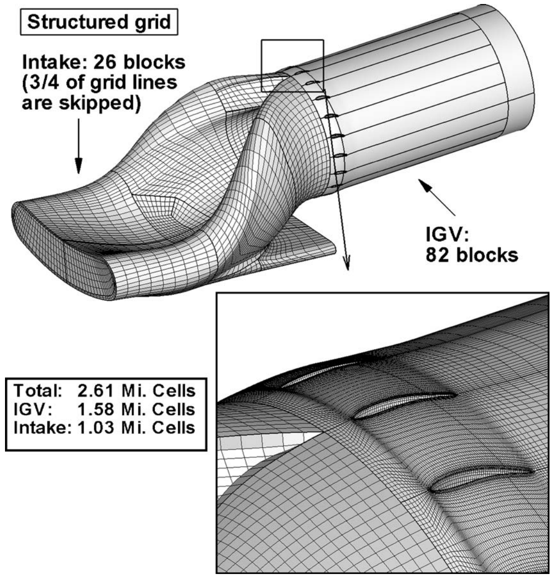

Fig. 24 Structured grid model of the intake and IGV

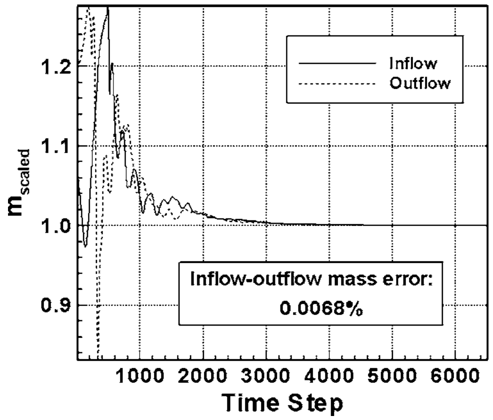

Fig. 25 Mass flowrate versus time step for the hybrid grid simulation of the intake and IGV

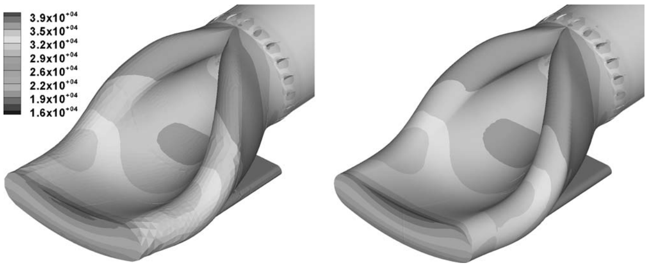

Fig. 26 Comparison of pressure flooded contours at outer boundaries—a global view for overall. (left) Hybrid and (right) structured.

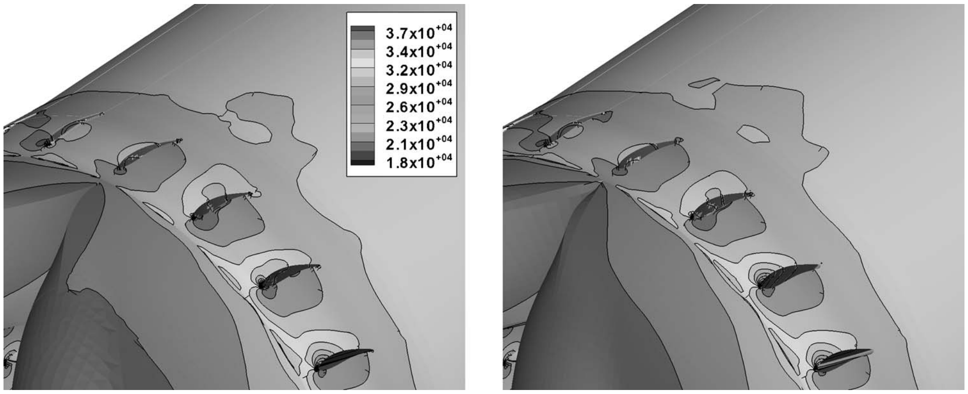

Fig. 27 Comparison of computed pressure contour distributions—close-up around the interface of the intake and the IGV. (left) Hybrid and (right) structured.

demonstrate that our hybrid structured-unstructured RANS solver is indeed capable of solving the flows in complex turbomachinery geometries.

6 Summary and Conclusions

A 3-D hybrid structured-unstructured RANS solver is presented and validated by a variety of test cases. The newly developed unstructured-grid module is consistent with the existing structured one in numerical algorithms, data structure, I/O, user interface, and parallelization. The numerical features of the unstructured-grid module are its second-order-accurate spatial discretization with the linear reconstruction approach, and its SGS implicit formulation of time integration that allows using a rather big CFL number. The structured- and unstructured-grid modules are coupled via the second-order-accurate conservative zonal approach, leading to a powerful hybrid structured-unstructured RANS solver. The validation and application examples have demonstrated that our hybrid RANS solver is accurate and conservative for both steady- and unsteady-state simulations, and it is applicable to the flows in complex turbomachinery geometries.

One advantage of the hybrid RANS solver is its flexibility at the hybrid-grid interface, which means to some extent users are allowed to generate the structured and unstructured grids independently even with different structured- and unstructured-grid generators. Furthermore, users can mesh any part of the space with unstructured topology and the rest still remains structured so that all sophisticated numerical algorithms specially developed for the structured grids are still valuable to the hybrid-grid simulation. Therefore, with the hybrid-grid approach, we have drastically extended the applicability of the existing structured CFD solver, and the ongoing development of the hybrid RANS solver is marching towards excellence in turbomachinery CFD.

Currently more sophisticated numerical models, such as the k-ω two-equation turbulence model and nonreflecting boundary conditions, are being developed for the unstructured-grid module. These will be reported together with other improvements on the hybrid RANS solver in the near future.

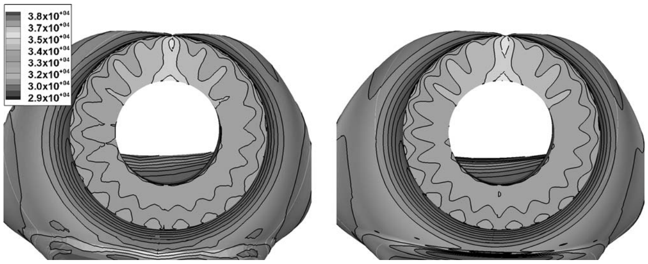

Fig. 28 Comparison of pressure contours at the main exit of the intake—a rear view. (left) Hybrid and (right) structured.

Acknowledgment

The authors are very grateful to MTU Aero Engines, especially Dr. Karl Engel for their cooperation on the development of the hybrid RANS solver and for their supply of some test cases. The authors also would like to thank their colleagues Dr. Edmund Kügeler, Anton Weber, Thomas Röber, and Dragan Kozulovic for their support in the validation process of the hybrid RANS solver.

Nomenclature

C = chord
C_f = skin friction factor, $2\tau_w/(\rho_0 a_0^2)$
C_p = pressure coefficient, $(p-p_2)/(p_0-p_2)$
e = specific total energy
IGV = inlet guide vane
I/O = input/output
LHS/RHS = left hand side/right hand side
m_{scaled} = mass flowrate relative to reference value
Ma = Mach number
$\vec{n}$ = unit normal vector
N = rotating speed at design operating condition
p = pressure
$\hat{Q}$ = state vector, $(\rho,\rho u,\rho v,\rho w,e)^T$
Re = Reynolds number
u^+ = non-dimensional velocity, V/u_τ
$\vec{V}$ = velocity vector, $(u,v,w)^T$
V = control volume
x,y,z = Cartesian coordinates
y^+ = non-dimensional wall distance, $\Delta y\cdot u_\tau/\nu$
RANS = Reynolds-averaged Navier-Stokes equations
ρ = density
τ = pseudo time step of dual time stepping
τ_w = wall shear stress
ν = kinematic viscosity
ν_t = eddy viscosity

Subscripts

0 = stagnation flow conditions
2 = exit flow conditions
$2th$ = isentropic exit flow conditions
(ij) = cell interface shared by cell i and cell j
i = cell index
L = flat-plate length or bump-channel width

t = total value
abs = absolute value

References

[1] Dawes, W. N., 1992 "The Simulation of Three-Dimensional Viscous Flow in Turbomachinery Geometries Using a Solution-Adaptive Unstructured Mesh Methodology", ASME J. Turbomach. **114**, pp. 528–537.

[2] Contreras, J., et al., 2002, "Semi-Unstructured Grid Methods for Turbomachinery Applications," ASME Paper No. GT-2002-30572.

[3] Sheng, C., 2004, "Full Annulus Simulation of a High-Speed Centrifugal Compressor Using an Unstructured RANS Flow Solver," ASME Paper No. GT2004-53657.

[4] Soetrisno, M., Imlay, S. T., and Roberts, D. W., 1994, "A Zonal Implicit Procedure for Hybrid Structured-Unstructured Grids," AIAA Paper No. AIAA-94-0645.

[5] Nuernberger, D., Eulitz, F., Schmitt, S., and Zachcial, A., 2001, "Recent Progress in the Numerical Simulation of Unsteady Viscous Multistage Turbomachinery Flows," ISABE-2001-1081.

[6] Eulitz, F., Engel, K., Nuernberger, D., Schmitt, S., and Yamamoto, K., 1998, "On Recent Advances of a Parallel Time-Advanced Navier-Stokes Solver for Unsteady Turbomachinery Flow," *Proceedings of Computational Fluid Dynamics '98, Proceedings, ECCOMAS*, K. D. Papailiou, D. Tsachalis, J. Periaux, C. Hirsch, and M. Pandolfi, eds., John Wiley & Sons, New York, Vol. 1, pp. 252–258.

[7] Engel, K., Eulitz, F., Pokorny, S., and Faden, M., 1996, "3D Navier-Stokes Solver for the Simulation of the Unsteady Turbomachinery Flow on a Massively Parallel Hardware Architecture," Notes on Numerical Fluid Dynamics, Vieweg, **52**, pp. 1–17.

[8] Yang, H., Nuernberger, D., and Weber, A., 2002, "A Conservative Zonal Approach with Applications to Unsteady Turbomachinery Flows," Deutscher Luft- und Raumfahrt Kongress 2002, DGLR-JT2002-073, Sept. 23–26, Stuttgart, Germany.

[9] Yang, H., Nuernberger, D., Nicke, E., and Weber, A., 2003, "Numerical Investigation of Casing Treatment Mechanisms With Conservative Mixed-Cell Approach," Atlanta, ASME Paper No. GT2003-38483.

[10] Spalart, P., and Allmaras, S., 1992, "A One-Equation Turbulence Model for Aerodynamic Flows," AIAA Paper No. AIAA-92-0439.

[11] Wilcox, D. C., 1998, "*Turbulence Modelling for CFD*," 2nd ed., DCW Industries, Anaheim, CA.

[12] Drela, M., 1995, "MISES Implementation of Modified Abu-Ghannam/Shaw Criterion (Revision)," MIT Aero-Astro.

[13] Giles, M. B., 1988, "Non-Reflecting Boundary Conditions for the Euler Equations," CFDL-TR-88-1, CFD Lab., MIT.

[14] Acton, E., and Cargill, M., 1988, "Non-Reflecting Boundary Conditions for Computations of Unsteady Turbomachinery Flow," *Proceedings, 4th Int. Symp. Unsteady Aerodynamics and Aeroelasticity of Turbomachines and Propellers*, pp. 211–228.

[15] Poirier, D., Allmaras, S. R., McCarthy, D. R., et al., 1998, "The CGNS System – Standard for Aerodynamic Data," AIAA Paper No. AIAA-98-3007.

[16] Roe, P. L., 1981, "Approximate Riemann Solvers, Parameter Vectors and Difference Schemes," J. Comput. Phys., **43**, pp. 357–372.

[17] Barth, T. J., and Jesperson, D. C., 1989, "The Design and Application of Upwind Schemes on Unstructured Meshes," AIAA Paper No. AIAA-89-0366.

[18] Venkatakrishnan, V., 1995, "Convergence to Steady State Solutions of the Euler Equations on Unstructured Grids with Limiters," J. Comput. Phys., **118**, pp. 120–130.

[19] Nuernberger, D., Eulitz, F., and Schmitt, S., 1999, "Effiziente Berechnung der instationären Strömung in Turbomaschinen mittels impliziter Zeitintegration," *Proc. DGLR-Jahrestagung*, Berlin (in German).

[20] Yoon, S., and Jameson, A., 1988, "Lower-Upper Symmetric-Gauss-Seidel Method for the Euler and Navier-Stokes Equations," AIAA J., **26**, pp. 1025–1026.

[21] Spalding, D. B., 1961, "A Single Formula for the Law of the Wall," ASME J. Appl. Mech., **28**, pp. 455–457.

[22] Newman, W. M., and Sproull, R. F., 1979, *Principles of Interactive Computer Graphics*, McGraw-Hill, New York, pp. 69–72.

[23] White, F. M., 1991, *Viscous Fluid Flow*, 2nd ed., McGraw-Hill, New York, pp. 415–435; pp. 9–12.

[24] Ni, R. H., 1982, "A Multiple-Grid Scheme for Solving the Euler Equations," AIAA J., **20**, pp. 1565–1571.

[25] Hoynacki, A., 1999, "Einfluß von instationärer Strömung und Turbulenz auf die Grenzschichten und auf die Druckverteilung von Beschaufelungen moderner mehrstufiger Axialverdichter," final report of FVV, Heft 679 (in German).

[26] Acton, P., and Fottner, L., 1997, "Investigation of the Boundary-Layer Development on a Highly Loaded Low-Pressure Turbine Cascade under the Influence of Instationary Inlet Flow Conditions,"*Proceedings 8th ISUAAT*.

[27] Acton, P., 1998, "Untersuchung des Grenzschichtum-schlages an einem hochbelasteten Turbinengitter unter inhomogenen und instationären Zuströmbedingungen," dissertation, Universität BW München (in German).

[28] Eulitz, F., 1999, "A RANS Method for the Time-Accurate Simulation of Wake-Induced Boundary-Layer Transition in Turbine Flows," ISABE 99-7275.

E. P. Petrov

D. J. Ewins

Centre of Vibration Engineering,
Mechanical Engineering Department,
Imperial College London,
South Kensington Campus,
London SW7 2AZ, UK

Effects of Damping and Varying Contact Area at Blade-Disk Joints in Forced Response Analysis of Bladed Disk Assemblies

An approach is developed to analyze the multiharmonic forced response of large-scale finite element models of bladed disks taking account of the nonlinear forces acting at the contact interfaces of blade roots. Area contact interaction is modeled by area friction contact elements which allow for friction stresses under variable normal load, unilateral contacts, clearances, and interferences. Examples of application of the new approach to the analysis of root damping and forced response levels are given and numerical investigations of effects of contact conditions at root joints and excitation levels are explored for practical bladed disks. [DOI: 10.1115/1.2181998]

1 Introduction

Bladed disks are subjected to high levels of vibration amplitudes excited under service conditions by aerodynamics forces. Such forces can have a very dense frequency spectrum and, similarly, the spectrum of the natural frequencies of practical structures is also customarily very dense. These dense excitation and natural frequency spectra combine to make the task of avoiding all resonance regimes almost impossible. Because of that the problem of developing methods in order to provide accurate, fast, and robust predictive tools for the analysis of forced vibration response levels of bladed disks under operating conditions is a problem of major practical importance.

Accuracy of prediction of forced response levels is dependent on the modelling of bladed disk components (i.e., blades, disk, shroud, damping devices, etc.) and on the modeling of the interaction forces at the contact interfaces between these components.

Demands made by the gas-turbine industry to increase the accuracy of predictive analysis methods for forced response of bladed disks require development of advanced models and methods describing in detail all components of the bladed disk including the interaction of these components at the joints of the assembly. Friction at blade-disk joints is an important source of damping in bladed disk assemblies. It results from the action of friction forces caused by usually small relative motions between blades and the disk at the contacting surfaces of the blade roots. The contact interaction forces have a strongly nonlinear character due to: (i) slip-stick transitions, (ii) the unilateral character of the interaction force acting along a normal to the contact surface, (iii) the influence of normal force on slip-stick transitions and the magnitude of the friction force, (iv) variation of contact area where slip occurs during each cycle of vibration, and others.

Moreover, variation of the contact area at the blade roots induced by the blade vibration also causes variation of the elasticity and stiffness properties of blade-disk joints over each vibration cycle and hence can affect resonance frequencies of a bladed disk.

Methods for forced response analysis of bladed disk assemblies must allow calculations to be performed which include all these nonlinear effects, i.e., they are to be representative.

Bladed disks are structures of complex geometric shape and dynamical properties. Numerical analysis of forced response levels of bladed disks commonly requires the application of detailed finite element (FE) models in order to describe realistic design features and to achieve practically acceptable accuracy. The number of degrees of freedom in realistic finite element models can reach 10^5–10^7 (see, for example, Ref. [13]) which makes the numerical cost of forced response calculations large, even in linear forced response calculations. For the case of bladed disks with friction contacts at the blade roots, a nonlinear vibration analysis is essential. The nonlinear forced response analysis requires solution of nonlinear equations of motion, which is much numerically more expensive than the conventional analysis methods used for linear vibrations. Because of this, special reduction techniques are necessary to make the use of large-scale models feasible in the analysis of nonlinear vibrations of bladed disks.

There are several reported theoretical and experiments studies of blade-disk joints (see, e.g., Refs. [1–4]) where static loading and deformations are considered. These studies are focused mostly on the analysis of contact stresses and stresses in areas close to the contact interfaces. Detailed FE models are often developed only for small areas adjacent to the contact interface itself to make the calculations feasible and cost effective. Solutions of nonlinear dynamic problems in bladed disks (see Refs. [5–14]) have been performed for localized contacts in special devices, such as friction dampers, or for localized contacts of blade shrouds. The main problem for the dynamic analysis of bladed disks with root joints, and the effects of root damping, on forced response of bladed disks has not been investigated to date.

In this paper, a new method for the analysis of nonlinear forced response of bladed disks with blade-disk joints in frequency domain is proposed. Special friction area contact elements are developed to the model nonlinear interaction phenomena which occur at the friction contact interfaces in the blade roots. These contact elements take account of any time variation of the actual contact area during vibration, the unilateral character of interaction of mating surfaces along normal direction to the contact interface and the stick-slip transitions for friction contacts. Large-scale FE models describing design features in detail are implemented. The method includes the multiharmonic balance formulation of the equations of motion for steady response and a technique developed for efficient reduction of the number of degrees of freedom in resolving nonlinear equations which preserves the necessary accuracy and completeness of the initial large scale finite element models. Numerical investigations of multiharmonic

---

Contributed by the International Gas Turbine Institute (IGTI) of ASME for publication in the JOURNAL OF TURBOMACHINERY. Manuscript received August 25, 2005; final manuscript received September 28, 2005. IGTI Review Chair: K. C. Hall. Paper presented at the ASME Turbo Expo 2005: Land, Sea, and Air, Reno, NV, June 6–9, 2005, Paper No. GT2005-68936.

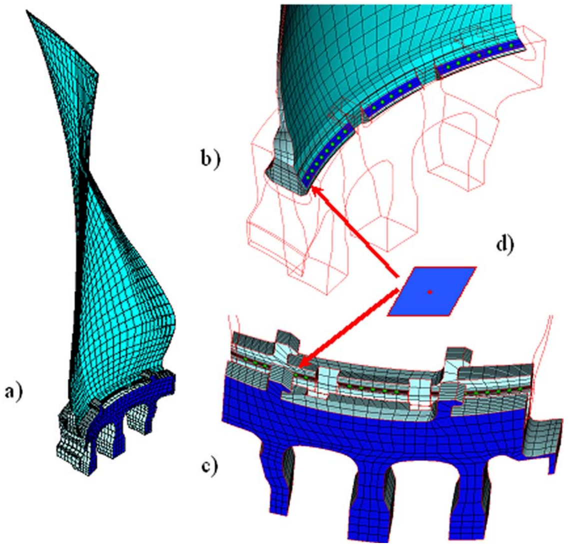

Fig. 1 Bladed disk models: (*a*) a bladed disk sector; (*b*) master nodes of the reduced model at blade contact surfaces; (*c*) master nodes at disk contact surfaces; and (*d*) an area contact element

forced response accounting for nonlinear interactions at blade-disk joints are performed for the first time for realistic bladed disks.

2 A Method for the Predictive Forced Response Analysis of Bladed Disks With Root Joints

The equation for motion for a bladed disk (see Fig. 1, where one sector of a bladed disk is shown) with friction contact interfaces can be written in the following form:

$$\mathbf{K}_\Sigma \mathbf{q}_\Sigma + \mathbf{C}_\Sigma \dot{\mathbf{q}}_\Sigma + \mathbf{M}_\Sigma \ddot{\mathbf{q}}_\Sigma + \mathbf{f}_\Sigma(\mathbf{q}_\Sigma) = \mathbf{p}_\Sigma(t) \tag{1}$$

where $\mathbf{q}_\Sigma(t)$ is a vector of displacements for all degrees of freedom (DOFs) in the structure considered; $\mathbf{K}_\Sigma$, $\mathbf{C}_\Sigma$, and $\mathbf{M}_\Sigma$ are stiffness, viscous damping, and mass FE matrices used for description of linear forces; $\mathbf{f}_\Sigma(\mathbf{q})$ is a vector of nonlinear interface forces, which is dependent on displacements DOFs at interface nodes; and $\mathbf{p}_\Sigma(t)$ is a vector of excitation forces. Thus, the problem of modeling bladed disks with friction interfaces at the blade roots can be separated into three major parts: (i) modeling of the bladed disk assembly, or its components, when only linear forces are allowed for (i.e., constructing matrices $\mathbf{K}_\Sigma$, $\mathbf{C}_\Sigma$, and $\mathbf{M}_\Sigma$); (ii) modelling of the friction contact interaction at the root contact surfaces (calculation of $\mathbf{f}_\Sigma(\mathbf{q})$), and (iii) combining the models for the bladed disk and the contact interfaces. Approaches developed to resolve these issues in the analysis of bladed disks with friction interaction at blade roots are discussed in this section together with a multiharmonic formulation of the equation of motion and a method for calculation of the amplitudes of vibration.

2.1 Models for Blades and a Disk. Models for bladed disks with linear forces only allowed for are constructed using the finite element method. This is now a well-established method widely used in practice in the gas-turbine industry. Commercial FE software packages available allow stiffness and mass matrices to be routinely calculated for large-scale FE models. A specific feature necessary for the FE models created for the analysis of bladed disks with friction contact interfaces require introduction mating nodes at all contact surfaces where nonlinear contact interaction can be expected. These mating nodes can have the same spatial coordinates, but the stiffness, $\mathbf{K}_\Sigma$, and mass, $\mathbf{M}_\Sigma$, matrices of the FE model for the bladed disk are calculated assuming that these nodes are disconnected and, hence, that all contact surfaces are free. The total number of degrees of freedom, N, in a large-scale FE bladed disk model is usually too large to permit nonlinear forced response calculations to be made using the matrices $\mathbf{K}_\Sigma$ and $\mathbf{M}_\Sigma$ directly. In order to make use of these models in nonlinear forced response analysis to be feasible, we apply the modal synthesis method developed in Ref. [15] and which can efficiently reduce the size of large FE models. To do this reduction, all DOFs of a bladed disk, $\mathbf{q}_\Sigma$, can be expressed through a selected subset of DOFs—so-called "master" DOFs, $\mathbf{q}^m$, and special modal DOFs, ξ, in the following way:

$$\underset{N\times 1}{\mathbf{q}_\Sigma} = \underset{N\times 1}{\begin{Bmatrix} \mathbf{q}^m \\ \mathbf{q}^S \end{Bmatrix}} = \underset{N\times n}{\begin{bmatrix} \mathbf{I} & \mathbf{0} \\ \mathbf{B} & \mathbf{\Phi} \end{bmatrix}} \underset{n\times 1}{\begin{Bmatrix} \mathbf{q}^m \\ \xi \end{Bmatrix}} = \underset{N\times n}{\mathbf{T}} \underset{n\times 1}{\begin{Bmatrix} \mathbf{q}^m \\ \xi \end{Bmatrix}} \tag{2}$$

Here, $\mathbf{q}^S$ is a vector of so-called "slave" DOFs, which are eliminated after reduction; and $\mathbf{I}(n\times n)$ is the identity matrix. The number, n, of DOFs retained in the reduced model, $\mathbf{q}=\{\mathbf{q}^m,\xi\}^T$, can be much smaller than total number of DOFs in the original structure, N, i.e., $n = size(\mathbf{q}^m) + size(\xi) \ll N$. Matrices $\mathbf{B}$ and $\mathbf{\Phi}$ used in Eq. (2) are determined from the solution of the following two conjugated problems:

1. Each jth column of matrix $\mathbf{B}$ is determined from a solution of the following static problem with respect to the vector of slave DOFs, $\mathbf{q}^S$:

$$\mathbf{K}_\Sigma \mathbf{q}_\Sigma = \mathbf{0} \tag{3}$$

when the corresponding master coordinate $\mathbf{q}_j^m = 1$ and all the other master DOFs are zero.

2. The jth column of matrix $\mathbf{\Phi}$ is the jth mode shape obtained for vector of slave DOFs, $\mathbf{q}^S$, from solution of the following eigenproblem when all master DOFs are fixed (i.e., when $\mathbf{q}^m = \mathbf{0}$):

$$\mathbf{K}_\Sigma \mathbf{q}_\Sigma = \omega^2 \mathbf{M}_\Sigma \mathbf{q}_\Sigma \tag{4}$$

For analysis of variable contact and friction at root joints, master degrees of freedom are selected at the mating nodes of the blade root and disk contact surfaces. In addition, master nodes are also selected in the blade body to ensure acceptable accuracy of the dynamic model condensation. An example of master nodes used for forced response analysis of a bladed disk with friction at blade roots is shown in Fig. 1.

Substitution of Eq. (2) into Eq. (1) gives a reduced equation of motion for the bladed disk

$$\mathbf{K}\mathbf{q} + \mathbf{C}\dot{\mathbf{q}} + \mathbf{M}\ddot{\mathbf{q}} + \mathbf{f}(\mathbf{q}) = \mathbf{p}(t) \tag{5}$$

where $\mathbf{K} = \mathbf{T}^T \mathbf{K}_\Sigma \mathbf{T}$; $\mathbf{M} = \mathbf{T}^T \mathbf{M}_\Sigma \mathbf{T}$; $\mathbf{C} = \mathbf{T}^T \mathbf{C}_\Sigma \mathbf{T}$ and $\mathbf{p} = \mathbf{T}^T \mathbf{p}_\Sigma$. The ratio, n/N, of the number of DOFs before and after mode synthesis method reduction can take values of 10^{-2}–10^{-3}.

2.2 Multiharmonic Balance Equation of Motion. Steady-state periodic regimes of vibration response are sought by making a transformation of the equation of motion (5) formulated in time domain into the frequency domain. In order to search for a periodic vibration response, the time variation of all DOFs of the system is represented as restricted Fourier series, which can contain as many and such harmonic components as are necessary to approximate the solution with a desired accuracy, i.e.

$$\mathbf{q}(t) = \mathbf{Q}_0 + \sum_{j=1}^{n} \mathbf{Q}_j^c \cos m_j \omega t + \mathbf{Q}_j^s \sin m_j \omega t \tag{6}$$

where n is the number of harmonics kept in the multiharmonic solution; $\mathbf{Q}_0$, $\mathbf{Q}_j^c$, and $\mathbf{Q}_j^s$ $(j=1,\ldots,n)$ are vectors of harmonic coefficients for the system DOFs; m_j $(j=1,\ldots,n)$ are the specific harmonics that are kept in the displacement expansion in addition to the constant component, and ω is the fundamental vibration frequency. In accordance with the multiharmonic balance method, the expansion from Eq. (6) is substituted into Eq. (5) which is sequentially multiplied by $(\cos m_j\omega)$ and $(\sin m_j\omega)$ and then integrated over the vibration period. As a result, equations for determining all the harmonic components are obtained in the following form:

$$\mathbf{R}(\mathbf{Q}) = \mathbf{Z}(\omega)\mathbf{Q} + \mathbf{F}(\mathbf{Q}) + \mathbf{P} = \mathbf{0} \tag{7}$$

where $\mathbf{Q}=\{\mathbf{Q}_0, \mathbf{Q}_1^c, \ldots, \mathbf{Q}_n^s\}^T$ is a vector containing all harmonic coefficients for displacement; $\mathbf{P}=\{\mathbf{P}_0, \mathbf{P}_1^c, \mathbf{P}_1^s, \ldots, \mathbf{P}_n^s\}^T$ is a vector of the harmonic coefficients of excitation forces, which for bladed disks are usually due to the aerodynamic forces caused by inhomogeneous gas flow and $\mathbf{F}(\mathbf{Q})=\{\mathbf{F}_0(\mathbf{Q}), \mathbf{F}_1^c(\mathbf{Q}), \ldots, \mathbf{F}_n^s(\mathbf{Q})\}^T$ is a vector of multiharmonic nonlinear friction contact forces acting at the blade-disk interfaces. The dynamic stiffness matrix involved in Eq. (7) has the form

$$\mathbf{Z}(\omega) = \begin{bmatrix} \mathbf{K} & \mathbf{0} & \mathbf{0} & \cdots & \mathbf{0} \\ \mathbf{0} & \mathbf{K} - (m_1\omega)^2\mathbf{M} & m_1\omega\mathbf{C} & \cdots & \mathbf{0} \\ \mathbf{0} & -m_1\omega\mathbf{C} & \mathbf{K} - (m_1\omega)^2\mathbf{M} & \cdots & \mathbf{0} \\ \cdots & \cdots & \cdots & \cdots & m_n\omega\mathbf{C} \\ \mathbf{0} & \mathbf{0} & \mathbf{0} & \cdots & \mathbf{K} - (m_n\omega)^2\mathbf{M} \end{bmatrix} \tag{8}$$

The multiharmonic balance formulation avoids the conventional time-consuming integration of equation. Instead, the nonlinear algebraic equation (7) is formed with respect to harmonic coefficients of displacement. The matrix of multiharmonic dynamic stiffnesses in Eq. (8) is formed from the stiffness, damping, and mass matrices of the linear part of the structure. Although it is quasi-diagonal, the matrix in Eq. (7) represents a simultaneous system of equations since coefficients for all harmonics are interdependent through a vector of multiharmonic nonlinear friction contact forces acting at blade-disk joints $\mathbf{F}(\mathbf{Q}) =\{\mathbf{F}_0(\mathbf{Q}), \mathbf{F}_1^c(\mathbf{Q}), \ldots, \mathbf{F}_n^s(\mathbf{Q})\}^T$.

2.3 Solution of the Nonlinear Equations and Tracing of the Solution. Equation (7) represents a nonlinear set of equations with respect to $\mathbf{Q}$. One of the most efficient methods for solution of the nonlinear equations is the Newton–Raphson method, which possesses quadratic convergence when an approximation is close enough to the solution. An iterative solution process is expressed by the following formula:

$$\mathbf{Q}^{(k+1)} = \mathbf{Q}^{(k)} - \left(\frac{\partial \mathbf{R}^{(k)}}{\partial \mathbf{Q}}\right)^{-1} \mathbf{R}(\mathbf{Q}^{(k)}) \tag{9}$$

where superscript (k) indicates the number of the current iteration. By differentiating Eq. (8) with respect to $\mathbf{Q}$, a recurrence formula can be rewritten in the form

$$\mathbf{Q}^{(k+1)} = \mathbf{Q}^{(k)} - \left[\mathbf{Z}(\omega) + \frac{\partial \mathbf{F}(\mathbf{Q}^{(k)})}{\partial \mathbf{Q}}\right]^{-1} \mathbf{R}(\mathbf{Q}^{(k)}) \tag{10}$$

The matrix $\mathbf{Z}(\omega)$ is a multiharmonic dynamic stiffness matrix introduced in Eq. (7). A matrix of derivatives, $\mathbf{K}_{\text{nln}}(\mathbf{Q}) = \partial\mathbf{F}(\mathbf{Q})/\partial\mathbf{Q}$, also called "a tangent stiffness matrix," describes the stiffness properties of the friction contact interfaces determined for a current vector of multiharmonic amplitudes, $\mathbf{Q}$. The vector of nonlinear friction contact forces acting at blade-disk joints $\mathbf{F}(\mathbf{Q})$ and the tangent stiffness matrix of the friction contact interface, $\mathbf{K}_{\text{nln}}(\mathbf{Q})$ fully describe interaction of bladed and disk at blade-disk joints and allows the nonlinear forced response to be determined.

2.4 Friction Contact Modeling: Area Contact Elements. Special friction area contact elements have been developed to model friction contacts of blade and disk at the blade root contact surfaces. The friction contact elements allow for variation of area of the contact patches during bladed disk vibration, friction stresses with effects of variable normal stresses on stick-slip transitions and friction stresses' levels. Moreover unilateral character of blade-disk interaction along normal to the contact surfaces can be described. This unilateral interaction occurs due to the fact that only compressing normal stresses can act at the contact surfaces but not the tensile stresses. Because of that when the mating contact surfaces are temporarily separated during vibrations the normal stresses become equal to zero and cannot take negative values. In order to model blade-disk interaction at the contact patches of the blade roots the area contact elements are distributed over the surfaces where nonlinear forces can be expected (as shown in Fig. 1(*d*)). The friction area contact element developed allows automatic determination of all possible contact interaction states for a small area covered by the contact element including stick, slip, and separation. Friction contact models for time-domain analysis were developed in paper [16] and friction contact elements for frequency-domain analysis were developed in paper [14].

Table 1 Stresses of the friction contact interaction

Status	Tangential force σ_t	Normal force σ_n
Contact Slip: $\xi\mu\sigma_n$	Stick: $k_t(u_t - u_t^{(0)}) - \xi\mu\sigma_n^{(0)}$	$\sigma_0 + k_n u_n$
Separation	0	0

The friction contact elements developed in paper [14] are extended here to modeling area contact for analysis of bladed disks with blade-disk contact interfaces. In contrast to paper [14], these friction area contact elements express contact stresses but not contact forces in terms of the relative displacements along a direction tangential to the contact surface, $u_x(\tau)$, and a normal relative displacement, $u_y(\tau)$. There are several major possible states of the contact interaction and expressions for tangential and normal components of the interaction force are shown for each of these in Table 1.

Here $u_t^{(0)} = u_t(\tau_{stick})$ and $\sigma_n^{(0)} = \sigma_n(\tau_{stick})$ are values of the tangential displacement and of the normal stresses at the beginning of the current stick state, τ_{stick}, and σ_0 is static normal stresses which are due to action of centrifugal, thermoelastic, and static aerodynamic forces. k_t and k_n are contact stiffness coefficients for tangential and normal deformations accordingly, and $\xi = \text{sgn}(\sigma_t(\tau_{slip})) = \pm 1$ is a sign function. Equations that are used to determine time instants when contact state changes are given in Table 2.

Since periodic steady-state vibrations are analyzed, the relative displacements, $x(\tau)$ and $y(\tau)$ can be expressed as a Fourier series with a restricted number of harmonics

$$u_t(\tau) = \mathbf{H}_{-}^T(\tau)\mathbf{X}; \quad u_n(\tau) = \mathbf{H}_{-}^T(\tau)\mathbf{Y} \tag{11}$$

where $\mathbf{H}_{-}=\{1, \cos m_1\tau, \sin m_1\tau, \ldots, \cos m_n\tau, \sin m_n\tau\}^T$; m_j are numbers of harmonics that are used in the multiharmonic expansion, and $\mathbf{X}$ and $\mathbf{Y}$ are vectors of harmonic coefficients of relative motion in the tangential and normal directions, respectively. The nondimensional time, $\tau = \omega t$, is introduced here using the principal frequency, ω, of the multiharmonic vibrations which defines period of the vibrations.

A method developed in Ref. [14] allows the exact determination of the contact stresses and tangent stiffness matrix of the friction contact interface as a function of relative displacements for a gen-

Table 2 Conditions of the friction contact state transition

Stick to slip	Slip to stick	Contact to separation
$\sigma_t(\tau) = \pm\mu\sigma_n(\tau)$ $\xi\dot{\sigma}_t < \mu\dot{\sigma}_n$	$\xi k_t \dot{u}_t(\tau) = \mu k_n \dot{u}_n(\tau)$ $\xi k_t \ddot{u}_t < \mu k_n \ddot{u}_n$	$\sigma_n = 0$ $\dot{u}_n < 0$

eral case of multiharmonic vibrations. In accordance with the method, the interaction stresses given in Table 1 are expanded into Fourier series

$$\sigma_t(\tau) = \mathbf{H}_-^T(\tau)\mathbf{S}_t(\mathbf{X},\mathbf{Y}); \quad \sigma_n(\tau) = \mathbf{H}_-^T(\tau)\mathbf{S}_n(\mathbf{Y}) \tag{12}$$

The vectors of multiharmonic components for tangential, $\mathbf{S}_t(\mathbf{X},\mathbf{Y})$, and normal, $\mathbf{S}_n(\mathbf{Y})$, stresses are obtained in an explicit form as functions of vectors of harmonic coefficients of relative motion along tangential and normal directions to the contact surface, $\mathbf{X}$ and $\mathbf{Y}$.

The contact area can be now covered by the area contact elements. These elements are usually chosen to be relatively small to allow distributions of the traction and normal stresses to be accurately interpolated over each of the elements. The values of the contact stresses are evaluated at a set of nodes usually located within and on boundaries of the area contact elements. For each node, the tangential friction forces and normal unilateral forces are calculated in the local coordinate system with axes directed along normal and tangential directions of the contact surface that are defined for a current point, xyz. The contact stresses in global coordinate system, $\overline{xyz}$, are then interpolated using the contact forces evaluated at several nodes of the contact element area in the form

$$\bar{\boldsymbol{\sigma}} = \sum_j^{n_{nodes}} \mathbf{N}_j(x,y)\mathbf{R}(x_j,y_j)\boldsymbol{\sigma}(x_j,y_j) = \sum_j^{n_{nodes}} \mathbf{N}_j(x,y)\bar{\boldsymbol{\sigma}}(x_j,y_j) \tag{13}$$

where $\bar{\boldsymbol{\sigma}}=\{\sigma_{\bar{x}},\sigma_{\bar{y}},\sigma_{\bar{z}}\}^T$ is a vector of contact stresses interpolated; $\boldsymbol{\sigma}(x_j,y_j)=\{\sigma_t,\sigma_n\}^T$ is a vector of contact stresses calculated at the jth point, (x_j,y_j); n_{nodes} is number of nodes for the area contact element; $\mathbf{R}(x_j,y_j)$ is the so-called "rotation" matrix describing rotation of for the local coordinate system with respect to a coordinate system which is global and used for analysis of the whole structure. $\mathbf{N}_j(x,y)$ are conventional shape functions used in isoparametric finite elements. The standard FE procedure for the reduction of the contact stress distribution to the nodes of the finite element mesh can be applied. This procedure is based on equality of works performed by the nodal forces and the stresses distributed over the area of the element, which gives the following expression for the nodal force:

$$\mathbf{f}_j = \int_A N_j(x,y)\bar{\boldsymbol{\sigma}}(x,y)dA = \mathbf{H}_-^T(\tau)\mathbf{F}_j \tag{14}$$

where $\mathbf{f}_j=\{f_x,f_y,f_z\}^T$ is a vector of nodal forces at the jth node of the area contact element and $\mathbf{F}_j=\{\mathbf{F}_x,\mathbf{F}_y,\mathbf{F}_z\}^T$ is a vector of harmonic coefficients for the jth nodal forces. From Eqs. (12), (13), and (14), we derive expressions for harmonic coefficients of nodal forces in the form

$$\mathbf{F}_j = \int_A N_j(x,y)\bar{\mathbf{S}}(x,y)dA \tag{15}$$

where $\bar{\mathbf{S}}=\{\bar{\mathbf{S}}_0,\bar{\mathbf{S}}_1^{(c)},\ldots,\bar{\mathbf{S}}_n^{(s)}\}$ is a vector of harmonic coefficients for $\bar{\boldsymbol{\sigma}}$.

For the simplest case of the area element with one node located in the middle of the area, the multiharmonic components of the nodal forces can be expressed in the form

$$\mathbf{F} = \begin{Bmatrix} \mathbf{F}_t \\ \mathbf{F}_n \end{Bmatrix} = A\begin{Bmatrix} \mathbf{S}_t(\mathbf{X},\mathbf{Y}) \\ \mathbf{S}_n(\mathbf{X},\mathbf{Y}) \end{Bmatrix} \tag{16}$$

where A is area covered by the eth contact element. The tangent stiffness matrix of this contact element is determined by differentiating Eq. (16) with respect to vectors $\mathbf{X}$ and $\mathbf{Y}$

$$\mathbf{K}_e = \begin{bmatrix} \mathbf{K}_{tt} & \mathbf{K}_{tn} \\ \mathbf{0} & \mathbf{K}_{nn} \end{bmatrix} = \frac{\partial \mathbf{F}}{\partial\{\mathbf{X},\mathbf{Y}\}} = A\begin{bmatrix} \partial\mathbf{S}_t/\partial\mathbf{X} & \partial\mathbf{S}_t/\partial\mathbf{Y} \\ \mathbf{0} & \partial\mathbf{S}_n/\partial\mathbf{Y} \end{bmatrix} \tag{17}$$

Owing to analytical expressions obtained for $\mathbf{S}_t(\mathbf{X},\mathbf{Y})$ and $\mathbf{S}_n(\mathbf{Y})$ calculations of the tangent stiffness matrix for the contact interface can be made exactly and very fast. Further details of the contact force vectors and the stiffness matrix derivation can be found in Ref. [14]. Vectors of multiharmonic components of the contact forces, $\mathbf{F}_e$, and tangent stiffness matrices, $\mathbf{K}_e$, are calculated for all contact elements and added to the vector of nonlinear friction contact forces $\mathbf{F}(\mathbf{Q})$ and the tangent stiffness matrix of the friction contact interface, $\mathbf{K}_{\text{nln}}(\mathbf{Q})$.

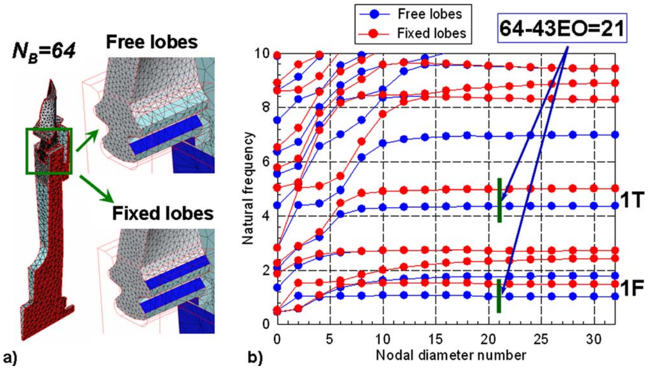

Fig. 2 Model (*a*), natural frequencies of the bladed disk with different contact conditions and frequency range of interest (*b*)

3 Numerical Investigations

The method developed has been applied to analysis of realistic bladed turbine and fan bladed disks of gas-turbine engines. One of the considered test cases was a bladed turbine disk from a test rig of the EU-funded project ADTurb (see [17,18]). A sector of the FE model used in the analysis is shown in Fig. 2(*a*). The FE model is constructed using tetrahedral 10 node finite elements. The total number of blades in the bladed disk analyzed is 64. The number of DOFs in the FE model of one sector comprises 73,245 DOFs. Root damping is analyzed at contact surfaces of the first lobe of the two-lobe firtree blade root. First, a linear bladed disk model was analyzed. To assess a range of the possible variation of the resonance frequencies due to slip at blade root, the natural frequencies were calculated for two extreme cases: (i) a case when there is no contact between bladed and disk at the first lobe, and (ii) a case when all contact surfaces are fully stuck and slip does not occur. Due to confidentiality requirements, all frequencies in this paper are normalized by the first blade-alone resonance frequency and the forced response levels are also normalized. Calculated natural frequencies are shown for all possible nodal diameters numbers in Fig. 2(*b*). One can see that variation of the contact condition at the first lobe of the bladed disk can significantly affect the resonance frequencies.

The blade-disk interaction at the contact surfaces is essentially nonlinear since slip-stick or contact-separation transitions can occur at the contacting surfaces and, moreover, the contact area and contact conditions can vary during period of vibration. In order to predict forced response levels and damping caused by friction at the root contact surfaces the developed friction area contact elements are applied at the contact surfaces of interest. The FE model of the bladed disk is constructed for this purpose with the contact surfaces set to be free and the friction one-node area contact elements are distributed uniformly over these surfaces to describe nonlinear friction contact interaction between the blades and the disk. The reduced model obtained by application of the modal synthesis method has 332 DOFs. These DOFs includes 282 master DOFs (3 DOFs for each of 94 master nodes) and 50 modal coor-

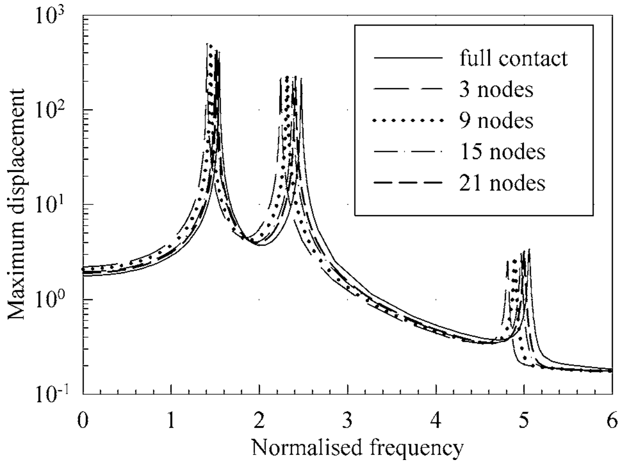

Fig. 3 Forces response of the bladed disk with stuck contact surfaces modeled by different number of the area contact elements

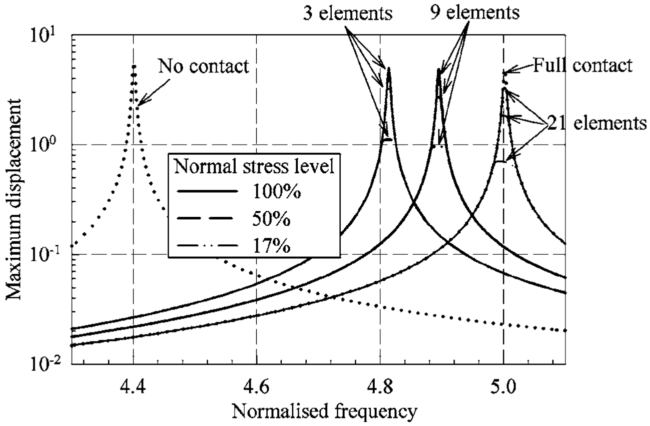

Fig. 5 The forced response levels for different levels of the static normal stresses and different numbers of the friction area elements applied at the contact surfaces

dinates. From 94 master nodes $4 \times 21 = 84$ are chosen on blade-disk mating contact surfaces at two contact patches of the blade root and are uniformly distributed over the contact surfaces. 10 master nodes are chosen at airfoil of the blade.

Damping loss factor, η, due to material and aerodynamic damping was assumed to be 0.001. Aerodynamic forces exciting the vibration analyzed were determined from aerodynamic calculations and are distributed over the blade airfoils. Excitation by 43th engine-order is considered which corresponds to a vibration mode of a tuned bladed disk with $64-43=21$ nodal diameters and frequency range corresponding to first flap-wise (1F) mode and first torsional (1T) mode are analyzed. A green line marks a frequency range for which the forced response analysis is performed. Friction coefficient at the contact surfaces was assumed to be 0.3. Total damping including effects of friction forces and variation of stiffness of the blade-disk joints due to variation of the contact areas and slip-stick transitions at the contact interfaces were determined in process of calculations by applied the friction area contact elements.

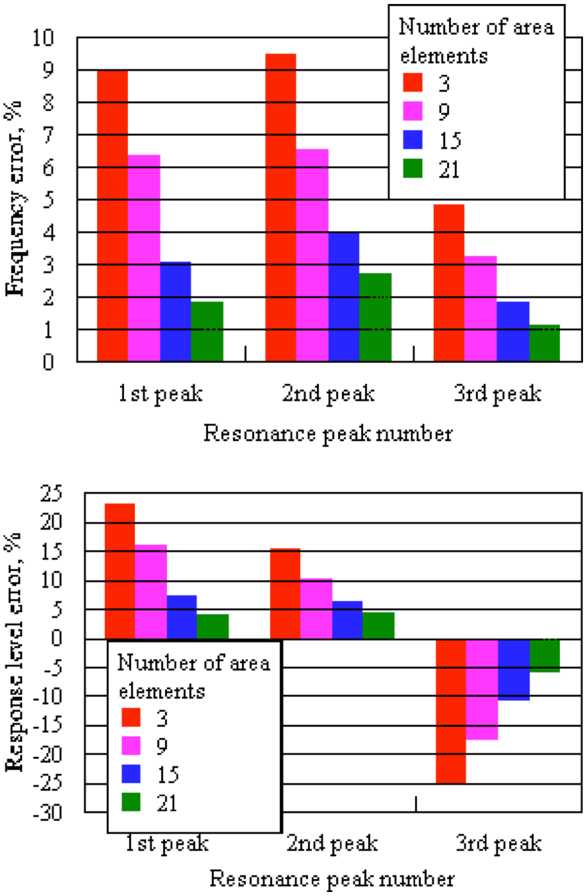

Fig. 4 Errors in prediction of the resonance characteristics for different number of the area contact elements: (*a*) For resonance frequencies and (*b*) for resonance amplitudes

The method developed reduces the number of DOFs in the whole structure to the number of degrees of DOFs where nonlinear contact forces are applied. Hence, the size of the resulting nonlinear equation is proportional to number of the friction contact elements applied to the bladed disk and, accordingly, the speed of calculations is dependent on number of these elements. In order to chose the number of contact elements providing acceptable accuracy for the area contact modeling together with high speed of calculation, an investigation of influence of the choice of number of the area elements on forces response levels and values of the resonance frequencies is performed. Four cases of (i) 3, (ii) 9, (iii) 15, and (iv) 21 one-node area contact elements applied over each of two (left and right) contact patches of the first lobe of the firtree root.

In each of the considered cases, the friction area contact elements cover the whole area of the contact patches; hence, area of contact represented by each element for these cases is 14.17, 4.73, 2.83, and 2.02 mm^2, accordingly. In order to explore the capability of the relative small number of the area contact elements to model a full stuck condition, the forced response was calculated with the large normal load excluding possibility of slip-stick transition at the contact patches. Since for this case the structure with friction contact elements exhibits linear behavior without friction damping, the forced response is compared with the forced response of linear structure determined for the FE model obtained for a case of fixed firtree lobes. Closeness of the resonance frequencies and amplitudes obtained for the model with the friction contact elements and from the FE model with fixed firtree lobes indicates accuracy of the contact modeling for a case of full contact. The calculated forced responses are compared in Fig. 3. This comparison is used to choose number of the area contact elements required in the analysis.

Errors in the prediction of the resonance frequencies and amplitudes are shown in Fig. 4. One can see that for the case of 21 area contact elements, for each of the two contact patches accept-

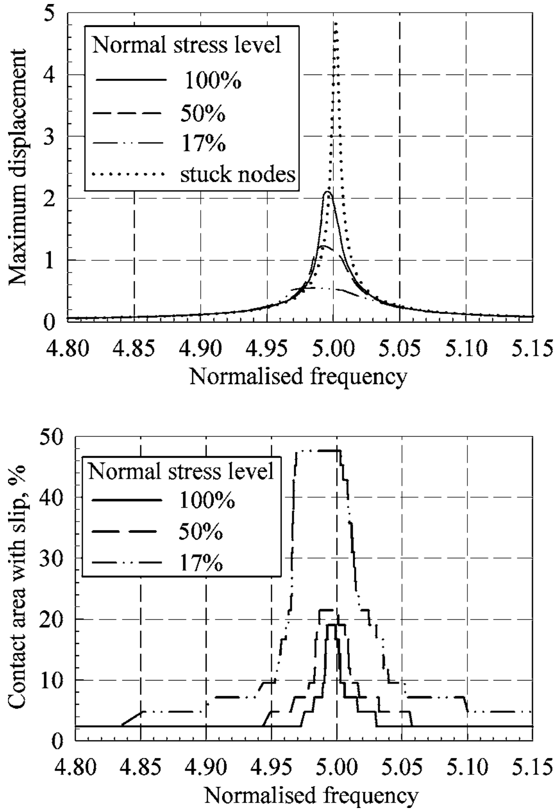

Fig. 6 Effects of different levels of the static normal stresses: (*a*) Forced response; and (*b*) contact area where slip occurs

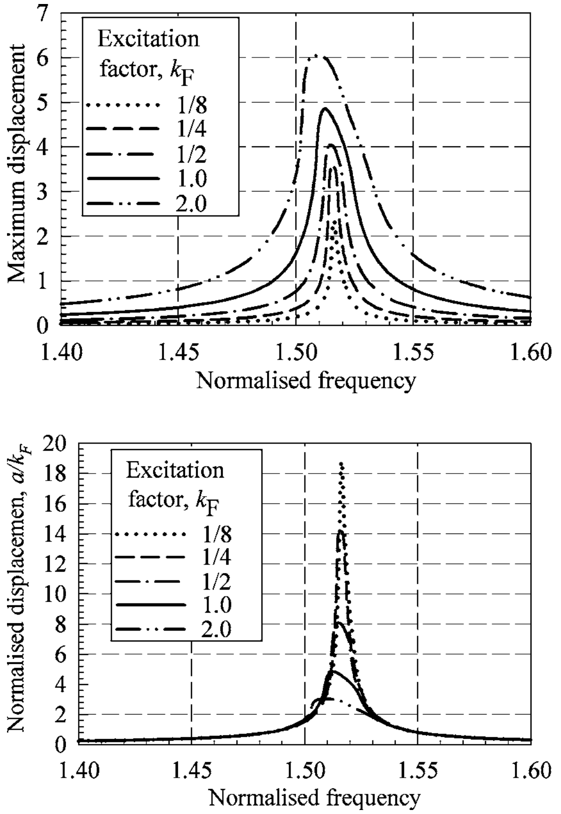

Fig. 8 Effects of the excitation level on the forced response in frequency range of 1F mode: (*a*) Displacement; and (*b*) displacement normalized by the excitation level

able accuracy is achieved for first 3 resonance frequencies (error <2.7%) and resonance amplitudes (error <5.8%).

Moreover, realistic normal stresses which are due to action of the centrifugal forces were calculated and then these static stresses are used in the forced response analysis for the area contact elements. Variation of the normal stresses over the contact patches is accounted for and hence different normal stress levels are applied to different area contact elements. Three different levels of the static normal stresses were studied, namely 100%, 50%, and 17% of the maximum level. These static stress levels occur in the bladed disk analyzed at rotation speeds: 100%, 70%, and 40% of the maximum rotation speed, respectively.

Results of calculation of the forced response levels for cases of 3 different levels of the normal stresses and for 3 cases of the number of the friction contact element applied over each contact patch are shown in Fig. 5. For comparison, forced responses calculated for two linear systems are also plotted there: (i) the forced response for a case when there is no contact with the disk at the first lobe of the blade root; and (ii) the forced response for a case when there is full contact at blade-disk joints and slip does not occur. One can see that there is more than an 8% shift in the resonance frequency between these two extreme linear cases. When 21 friction contact elements are applied at each contact, surface forced response level outside the vicinity of the resonance frequency is practically coinciding with that of the linear system with full contact. For these frequencies, the level of relative displacements is too small to cause slip at the contact interfaces or variation of the contact area. The resonance frequency for 100% level of the static normal stresses is very close to resonance frequency of this linear system. For cases of 3 and 9 friction contact elements per contact surface, there is a difference, although small, in resonance frequencies, which is due to a decrease in stiffness of the blade-disk joints when too small a number of the contact elements is used for contact modeling. In all of the following figures, results obtained with 21 friction contact elements at each of the contact surfaces are shown.

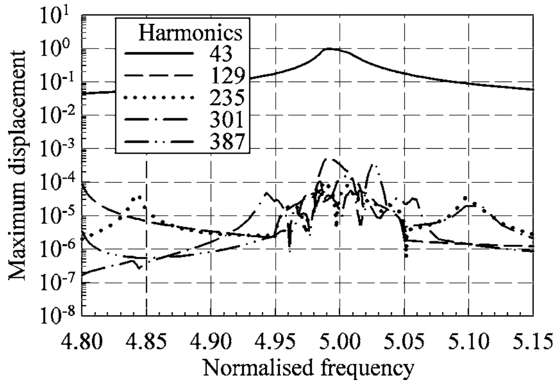

Fig. 7 Harmonic components for the multiharmonic forced response (calculated for the case of 50% of the normal stress level)

The effect of the level of the static normal stresses on levels of forced response is demonstrated in Fig. 6(*a*) for excitation frequencies in the range of 4.8–5.15 corresponding to 1T mode. The forced response of the linear system with full contacts is shown here for comparison.

The method allows determination of not only the forced response but also contact conditions at each point of the over area covered by the friction contact elements, including occurrence slipping parts. The size of the contact area where slip occurs related to the whole size of the contact patches is shown Fig. 6(*b*). One can see that the resonance frequency is not significantly af-

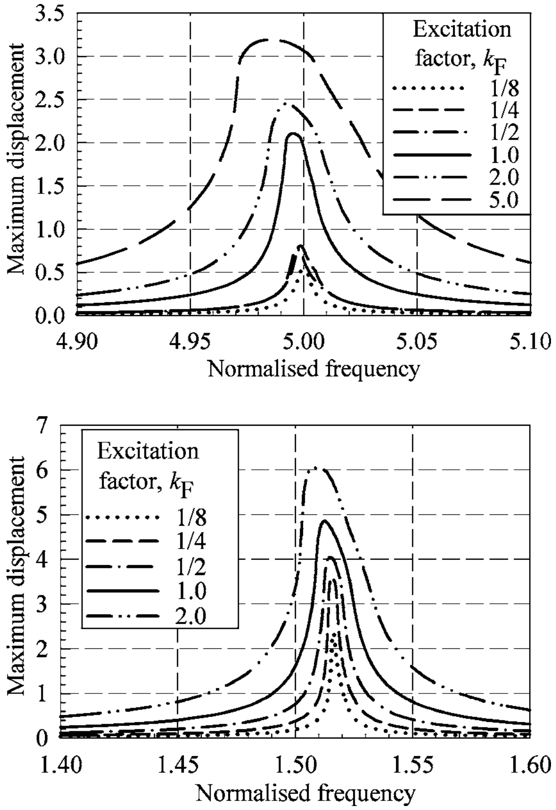

Fig. 9 Effects of the excitation level on the forced response in frequency range of 1T mode: (*a*) Displacement; and (*b*) displacement normalised by the excitation level

fected by the level of normal stresses and accordingly by effects of number of slipping nodes at the contact surface. Yet, the level of forced response is very sensitive to the normal stress level since the size of the contact area is involved in slip-stick transitions, and, therefore, the vibration energy is dissipated by the friction forces at these parts of the contact area. For the case considered, accounting for root damping reduces resonance amplitude in 2.5 times for 100% level of the normal stresses and in 10 times for 17% level. For the resonance frequency, 18% (for 100% normal stress level) and 22% (for 50% normal stress level) and 48% (for 17% normal stress level) of the whole contact area is subjected to slip at least over small time interval.

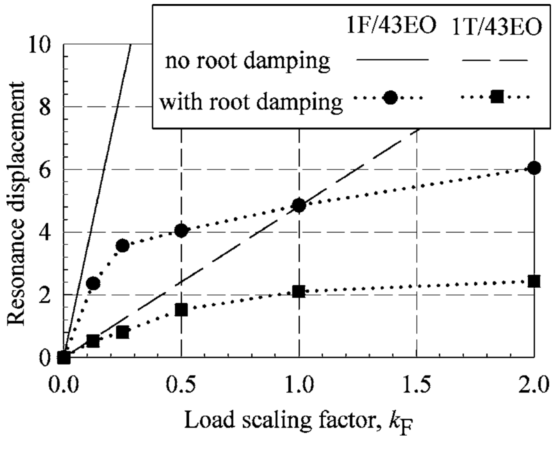

Fig. 10 Effects of the excitation level on the resonance displacement

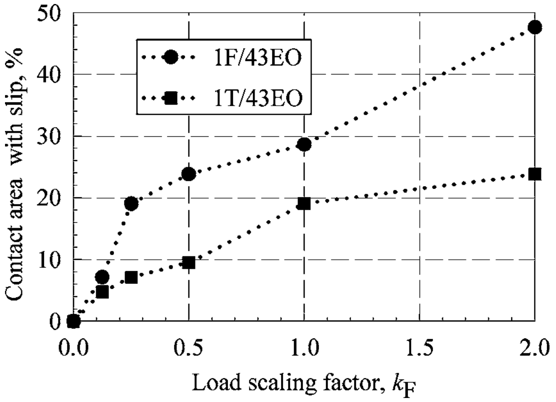

Fig. 11 Effects of the excitation level on the slipping area at resonance frequency

It is also important to note that although the friction forces produce strongly nonlinear blade-disk interaction at root joints, the harmonic coefficients of the multiharmonic forced response were small for all harmonics except of that coinciding with excitation harmonic. In the calculations, the first 6 odd multiplies from 1 to 9 of the excitation harmonic, 43EO are kept. An example of the amplitudes for all these harmonics in the multiharmonic expansion for displacement is shown in Fig. 7. One can see that the 43rd harmonic is predominant in the forced response and contribution of all the other can be neglected.

The effect of the excitation level on the response level is demonstrated in Fig. 8 for a frequency range including 1F mode, and in Fig. 9 for a frequency range including 1T mode. Distribution of the excitation loads over the blade airfoil in all cases was the same, but these loads were multiplied by a factor k_F with values from 1/8 to 5. In Figs. 8(*a*) and 9(*a*), the amplitude of the displacement is plotted. One can see that shape of the forced response curves significantly differs for the different levels of excitation. In Figs. 8(*b*) and 9(*b*), in order to clearly demonstrate the nonlinear dependency of this amplitude to excitation levels, it is normalized by dividing by k_F. For the case of the linear structure, the displacement normalized by k_F would be identical for all forced response levels, but they differ here and the highest level of excitation produces the smallest value of the normalized forced response. This is because at higher levels of vibration the larger part of the contact area starts slipping and therefore friction damping increases.

The resonance amplitude level as a function of level of excitation is plotted in Fig. 10 for both resonance modes analyzed: 1F and 1T. These functions have essentially nonlinear character. For comparison, straight lines show the resonance amplitudes that

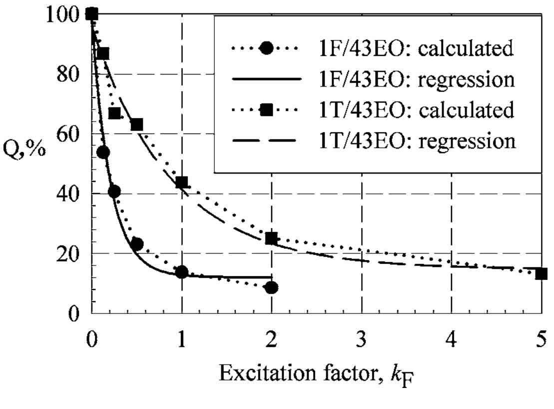

Fig. 12 Dependency of the *Q*-factor on the excitation level

Table 3 Approximation for the *Q*-factor as a function of the excitation level

Approximation coefficient	Mode	
	1F	1T
c_0	12.18	14.75
c_1	86.04	81.28
c_2	0.486	0.112

would realize if there were no friction damping at the blade root. Relative size of the slipping part of the contact area is shown in Fig. 11 for both resonating modes.

The calculations performed allow the determination of the damping in the structure caused by friction at blade root joints. The characteristics of the total damping in the structure, $Q=1/\eta$ (η is the total damping loss factor) were obtained directly from the calculated forced response functions in vicinity of the resonance frequency. The Q-factor extracted from results of the forced response is plotted as a function of excitation level in Fig. 12. The regression analysis was made for the calculated function and it was found that the three-parameter exponential function $Q=c_0+c_1e^{-c_2k_F}$ with values for the coefficient values given in Table 3 provides a good approximation for the Q-factor as a function of the excitation level.

4 Conclusions

An effective method for predictive analysis of inherent damping at blade-disk root joints has been developed. The method can use large-scale models for bladed disks with variable contact and friction at root joints. In order to achieve high speed of calculation, the multiharmonic balance formulation for nonlinear equation of motion is used. The formulation allows accuracy required to be achieved by keeping necessary number of harmonics in the solution and by choosing those harmonic number that are needed to approximate the solution sought.

The method is based on analytical formulation of friction area contact elements which allows exact calculation of multiharmonic components of interaction forces and of the tangent stiffness matrix of the joints for friction contact. Reduction in size of the model is performed by application of the modal synthesis method.

Acknowledgment

The authors are grateful to Rolls-Royce plc. for providing the financial support for this project and for giving permission to publish this work. The FE model used for the test case is based on the results of the European Community project ADTurB (Project BRPR-CT95-0124). Further details can be found at www.cordis.lu.

References

[1] Kenny, B., Patterson, E. A., Said, M., and Aradhya, K. S. S., 1991, "Contact Stress Distributions in a Turbine Disk Dovetail Type Joint—A Comparison of Photoelastic and Finite Element Results," Strain J. Brit. Soc. Strain Measurement, **27**, pp. 21–24.

[2] Meguid, S. A., Refaat, M. H., and Papanikos, P., 1996, "Theoretical and Experimental Studies of Structural Integrity of Dovetail Joints in Aeroengine Disks," J. Mater. Process. Technol., **56**, pp. 668–677.

[3] Papanikos, P., Meguid, S. A., and Stjepanovic, Z., 1998, "Three-Dimensional Nonlinear Finite Element Analysis of Dovetail Joints in Aeroengine Disks," Finite Elem. Anal. Design, **29**, pp. 173–186.

[4] Sinclair, G. B., Cormier, N. G., Griffin, J. H., and Meda, G., 2002, "Contract Stresses in Dovetail Attachments: I—Finite Element Modeling," Trans. ASME: J. Eng. Gas Turbines Power, **124**, pp. 182–189.

[5] Pierre, C., Ferri, A. A., and Dowell, E. H., 1985, "Multiharmonic Analysis of Dry Friction Damped Systems Using an Incremental Harmonic Balance Method," Trans. ASME, J. Appl. Mech., **52**, pp. 958–964.

[6] Wang, J. H., and Chen, W. K., 1993, "Investigation of the Vibration of a Blade With Friction Damper by HBM," Trans. ASME: J. Eng. Gas Turbines Power, **115**, pp. 294–299.

[7] Yang, B.-D., and Menq, C.-H., 1997, "Modelling of Friction Contact and its Application to the Design of Shroud Contact," Trans. ASME: J. Eng. Gas Turbines Power, **119**, pp. 958–963.

[8] Sanliturk, K. Y., Imregun, M., and Ewins, D. J., 1997, "Harmonic Balance Vibration Analysis of Turbine Blades With Friction Dampers," Trans. ASME, J. Vib. Acoust., **119**, pp. 96–103.

[9] Berthillier, M., Dupont, C., Mondal, R., and Barrau, R. R., 1998, "Blades Forced Response Analysis With Friction Dampers," Trans. ASME, J. Vib. Acoust., **120**, pp. 468–474.

[10] Szwedowicz, J., Sextro, W., Visser, R., and Masserey, P., 2003, "On Forced Vibration of Shrouded Turbine Blades," ASME Paper No. GT-2003-38808.

[11] Petrov, E. P., 2004, "A Method for Use of Cyclic Symmetry Properties in Analysis of Nonlinear Multiharmonic Vibrations of Bladed Disks," ASME J. Turbomach., **126**, pp. 175–183.

[12] Nacivet, S., Pierre, C., Thouverez, F., and Jezequel, L., 2003, "A Dynamic Lagrangian Frequency-Time Method for the Vibration of Dry-Friction-Damped Systems," J. Sound Vib., **265**, pp. 201–219.

[13] Petrov, E. P., and Ewins, D. J., 2004, "Method for Analysis of Nonlinear Multiharmonic Vibration of Bladed Disks Mistuned by Scatters in Characteristics of Friction Contact Interfaces and Blades," ASME Paper No. GT2004-53891.

[14] Petrov, E. P., and Ewins, D. J., 2003, "Analytical Formulation of Friction Interface Elements for Analysis of Nonlinear Multiharmonic Vibrations of Bladed Disks," ASME J. Turbomach., **125**, pp. 364–371.

[15] Craig, R. R., Jr., and Bampton, M. C. C., 1968, "Coupling of Substructures for Dynamic Analysis," AIAA J., **6**(7), pp. 1313–1319.

[16] Petrov, E. P., and Ewins, D. J., 2004, "Generic Friction Models for Time-Domain Vibration Analysis of Bladed Disks," ASME J. Turbomach., **126**, pp. 184–192.

[17] Green, J. S., 2001, "An Overview of a European Collaborative Programme for Forced Response," 6th National Turbine Engine High Cycle Fatigue Conference, Jacksonville, FL.

[18] Aeromechanical Design of Turbine Blades (ADTurB), Project funded by the European Community under the Industrial and Material Technologies Programme (Brite-EuRam III), Contract number: BRPR-CT95-0124, ADTurB Synthesis Report, 2001, 17 pp.